UNIVERZA V LJUBLJANI
FAKULTETA ZA MATEMATIKO IN FIZIKO

DOKTORSKA DISERTACIJA

Manca Mrvar

2018

UNIVERSITY OF LJUBLJANA
FACULTY OF MATHEMATICS AND PHYSICS
DEPARTMENT OF PHYSICS

Manca Mrvar

Calibration of Aerogel Ring-Imaging Cherenkov Detector in Belle II Spectrometer

Doctoral thesis

ADVISER: Assist. Prof. Rok Pestotnik

Ljubljana, 2018

UNIVERZA V LJUBLJANI
FAKULTETA ZA MATEMATIKO IN FIZIKO
ODDELEK ZA FIZIKO

Manca Mrvar

Umeritev detektorja obročev Čerenkova z aerogelskim sevalcem v spektrometru Belle II

Doktorska disertacija

MENTOR: doc. dr. Rok Pestotnik

Ljubljana, 2018

Acknowledgements

If you find a path with no obstacles,
it probably doesn't lead anywhere.

- *Frank A. Clark*

I could not have overcome some of those obstacles without amazing people by my side...

Samo – I was always able to rely on your professional guidance and moral support.

Luka – The best teacher shows you where to look, but doesn't tell you what to see.

Maša, mami in oči – Hvala, ker ste vedno ob meni. Lepo je imeti nekoga, na kogar se lahko zaneseš.

My friends – You taught me that true friendship continues to grow, even over the longest distances.

My fellow collaborators – KEK would not have been a home away from home without you.

All the exceptional people I met during my travels – Every single one of you left a special mark in my life.

You helped me to become who I am today.

Abstract

The Aerogel Ring-Imaging Cherenkov (ARICH) detector provides a charged particle identification in the endcap region of the Belle II spectrometer at the SuperKEKB asymmetric-energy e^+e^- collider in Tsukuba, Japan. The ARICH consists of a double layer aerogel radiator in a focusing configuration, an expansion volume and a plane of hybrid avalanche photodetectors. The methods of the calibration of the photodetectors and the readout electronics are discussed in the dissertation. The hardware calibration improved the separation of charged kaons and pions, which was studied with the $D^{*+} \to D^0(\to K^-\pi^+)\pi_s^+$ decay. The identification algorithm was tested on the simulated sample. The simulation results show the efficiency of the kaon identification above 90 % at the pion misidentification probability of 5 %. The developed procedure was also applied to the sample of collision data that was collected during the detector commissioning phase. Due to limited sample of the measured data, only the reconstructed $D^0 \to K^-\pi^+$ events were used for the performance studies. The results provide slightly decreased performance due to incomplete calibration of the tracking and particle identification system at the beginning of the operation.

Keywords:

The Belle II spectrometer, calibration, Cherenkov photons, the charged kaon/pion separation, hybrid avalanche photodetector, particle identification, Ring-Imaging Cherenkov detector.

PACS:

- 13.25.Ft Hadronic decays of charmed mesons
- 14.40.Lb Charmed mesons
- 29.40.Ka Cherenkov detectors
- 41.60.Bq Cherenkov radiation
- 85.60.Gz Photodetectors

Izvleček

Detektor obročev Čerenkova z aerogelskim sevalcem (ARICH) je namenjen identifikaciji nabitih delcev v smeri naprej detektorja Belle II ob asimetričnem trkalniku pozitronov in elektronov SuperKEKB, ki stoji v kraju Cukuba na Japonskem. ARICH sestavljajo dvoplastni sevalec iz aerogela, prazen prostor za razširjanje fotonov Čerenkova in detektorska ravnina s hibridnimi plazovnimi fotodetektorji. V disertaciji je opisana umeritev detektorja, s katero izboljšamo ločevanje nabitih kaonov in pionov, ki jih neodvisno identificiramo pri razpadih $D^{*+} \to D^0(\to K^-\pi^+)\pi_s^+$. Umeritvene metode in njihov vpliv na izboljšano ločevanje med kaoni in pioni smo preverili na vzorcu dogodkov, dobljenim z računalniško simulacijo. Rezultati simulacije so pokazali, da je z razvito metodo mogoče pravilno identificirati več kot 90 % kaonov ob zahtevi, da delež napačno identificiranih pionov ni večji od 5 %. Postopek smo uporabili tudi na vzorcu podatkov, ki smo jih zbrali pri prvih trkih na trkalniku SuperKEKB. Zaradi majhnega vzorca smo odziv detektorja preverili z uporabo rekonstruiranih razpadov $D^0 \to K^-\pi^+$, pri čemer je identifikacija delcev malenkost slabša zaradi nepopolne umeritve sledilnega ter identifikacijskega sistema ob začetku delovanja eksperimenta.

Ključne besede:

Detektor Belle II, fotoni Čerenkova, detektor obročev Čerenkova, hibridni plazovni fotodetektor, identifikacija nabitih delcev, razlikovanje med nabitimi kaoni in pioni, umeritev.

PACS:

- 13.25.Ft Hadronski razpadi čarobnih mezonov
- 14.40.Lb Čarobni mezoni
- 29.40.Ka Detektorji Čerenkova
- 41.60.Bq Sevanje Čerenkova
- 85.60.Gz Fotodetektorji

Contents

List of Figures

List of Tables

CHAPTER 1

Introduction

The difference between matter and antimatter has been one of the major interests of particle physicists for almost a century. The idea of antimatter appeared in 1928, when Paul Dirac published a paper in which he mathematically described the state of an electron [1]. His equation had two solutions; for both positive and negative energy. While the first solution agreed with experimental results, the latter one proposed the possibility that electron can have a positive charge. He continued working on an understanding of the negative-energy solution and three years later he published another paper, in which he proposed the existence of the anti-electron – a particle with the same mass as an electron, but with an opposite charge, that would annihilate upon contact with an electron [2]. Although particles with the properties of electrons that curve in the opposite direction in a magnetic field were observed experimentally around the same time, their studies were not continued. The positron was therefore discovered in 1932 [3] by accident as the first antiparticle.

In following decades, predictions and discoveries of various particles and anti-particles followed. Elementary particles were classified in the Standard Model (SM) [4–6], currently the best-known theory that describes properties of elementary particles and fundamental forces. It predicts three generations of quarks and three generations of leptons, as well as gauge bosons – carriers of interactions between the particles, illustrated in Fig. 1.1. SM was developed in early 1970s and several experiments were focused on discovery of the theoretically predicted particles. The last ones were discovered quite recently. The heaviest quark, known as *top*, *truth* or simply t quark, completed the three-generation structure of SM in 1995, when it was discovered in two Fermilab experiments – The Collider Detector at Fermilab (CDF) and DØ experiment [7, 8]. Five years later another Fermilab experiment DONUT detected the *tau* neutrino, the last missing lepton [9]. The discovery of the Higgs Boson in 2012, a result of two independent experiments ATLAS and CMS at CERN [10], was the final missing part of the puzzle in the Standard Model. However, despite the Standard Model's great success, several deviations from the theory have been observed. New phenomena, often named New Physics (NP) or Physics Beyond SM, suggest the incompleteness of the current theory. One of most noticeable deviations from SM was the evidence of neutrino oscillations, indicating that neutrinos are not massless contrary to SM predicting.

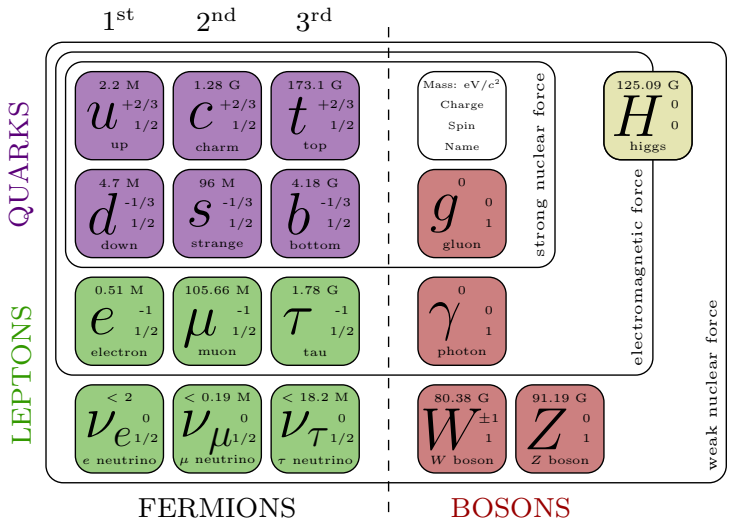

Figure 1.1: Standard Model of particles and interactions [11]. Three generations of quarks and leptons are (currently) the most fundamental particles. Gauge bosons are carriers of interaction between particles.

Particle physics experiments can roughly be divided into three groups. One group includes the experiments for neutrino and muon detection, mainly used for astroparticle physics. The other two groups are based on production of new particles through collisions, but use different approaches. One group of experiments is focused on the energy frontier, where the colliders accelerate particles to very high energies before collisions in order to produce new heavy particles. The main current representatives are the ATLAS and CMS experiments at the Large Hadron Collider (LHC) at CERN in Geneva, Switzerland. The second group of collider experiments is interested in the intensity frontier, which focuses on obtaining precise measurements and high statistics, needed for studies of rare interactions. Important intensity frontier experiments include the LHCb experiment at the LHC, the BESIII experiment at the BEPCII charm factory, the Belle experiment at KEKB B-factory and BaBar B-factory PEP-II [12, 13]. The approaches of the two collider-experiment types are completely different, yet results are complimentary and can together provide a more precise and comprehensive tets for model of particle physics.

The doctoral thesis is based on the Belle II experiment, the successor of the Belle experiment. The Belle experiment used the asymmetric electron-positron collider KEKB at KEK in Tsukuba, Japan. KEKB was the world's highest-luminosity[1] machine, which expanded the possibility to study rare B and D meson and τ decays. The Belle spectrometer was used for particle detection at KEKB. It started taking data in 1999 and ceased operation in 2010, collecting a data sample with an integrated luminosity of about $1000\,\mathrm{fb}^{-1}$. The measurements from the Belle detector provided some important results for particle physics, especially about CP (C – charge, P – parity) violation [13, 14]. One of the most recognized achievements was the observation of phenomenon of CP violation in B meson decays. This experimental result confirmed the theory's prediction, leading to the award of the Nobel

[1]Luminosity: number of interactions per units of cross section and time

Prize in physics in 2008 to Prof. Makoto Kobayashi and Prof. Toshihide Maskawa for their theory describing the origin of the broken *CP* symmetry [15] within the Standard Model.

Upgrades of the KEKB collider and the Belle detector are completed, and the first commissioning data have already been gathered. The improved Belle II detector at SuperKEKB collider will collect 50 times more data and deliver more precise measurements in heavy flavour physics. It is expected that the new experiment will also provide important information about newly discovered physics processes.

1.1 Contents

The design planning of the Belle II spectrometer – based on the Belle spectrometer upgrade – started in the early 2000s. The magnet, used in Belle II, stayed the same, but most other parts have been replaced with more precise and radiation-resistant subsystems. The thesis deals with the hardware components of Aerogel Ring Imaging Cherenkov detector (ARICH), as well as calibration of the physics signals. It is a newly-designed focusing Cherenkov detector, that uses aerogel tiles as a radiator and hybrid avalanche photodetectors for single-photon detection.

The thesis is structured as follows: in the introductory chapters, I will briefly describe the experiment, including a physics motivation, the collider SuperKEKB and the Belle II spectrometer. Then the discussion will continue with particle identification system in Belle II, particularly focusing in the detection of charged particles, based on Cherenkov radiation. With work being related to ARICH detector, I will then discuss in detail its mechanical structure and operation before moving to the central topic.

In the main part, I will concentrate on calibration of ARICH, first discussing the calibration of the detector components' operation, which is crucial to provide reliable signals for further physics analyses. Our detector modules provide binary information about the individual channel being hit. An efficient and correct detection requires continuous parameters monitoring and calibration to exclude false positive or negative signals. The hardware calibration was partially done before the assembly itself and will be later repeated regularly during the operation of the detector. The next chapter will cover the calibration of kaon identification efficiency with respect to the momentum and angular dependencies. The studies have been done using $D^{*+} \to D^0(\to K^-\pi^+)\pi_s^+$ decay (and its charge conjugated mode, $D^{*-} \to \bar{D}^0(\to K^+\pi^-)\pi_s^-$). This decay will be used as a control channel for further physics analyses. I will round off the thesis with a brief summary of the main conclusions.

CHAPTER 2

Belle II Experiment

The Belle II experiment has been designed for studies of rare decays of B and D mesons and τ leptons. It is expected that 50-times more data will be collected than with its predecessor Belle, which corresponds to an integrated luminosity of $50\,\mathrm{ab}^{-1}$. The high statistics will allow studies of very rare processes that have not been observed at a lower level of event rates. Studies will be focused on CP violation in the quark and lepton sector.

The collider, SuperKEKB, is running at the energy of the $\Upsilon(4S)$ resonance (10.58 GeV) for most of the time. This is just above the threshold for production of a pair of neutral or charged B mesons. The $B\bar{B}$ pairs decay through various decay chains into several long-lived particles – pions, kaons, electrons, muons, protons, neutrons, photons and neutrinos. The B decays with neutrinos or multiple other neutral particles in the final state will be the main focus of the measurements [13].

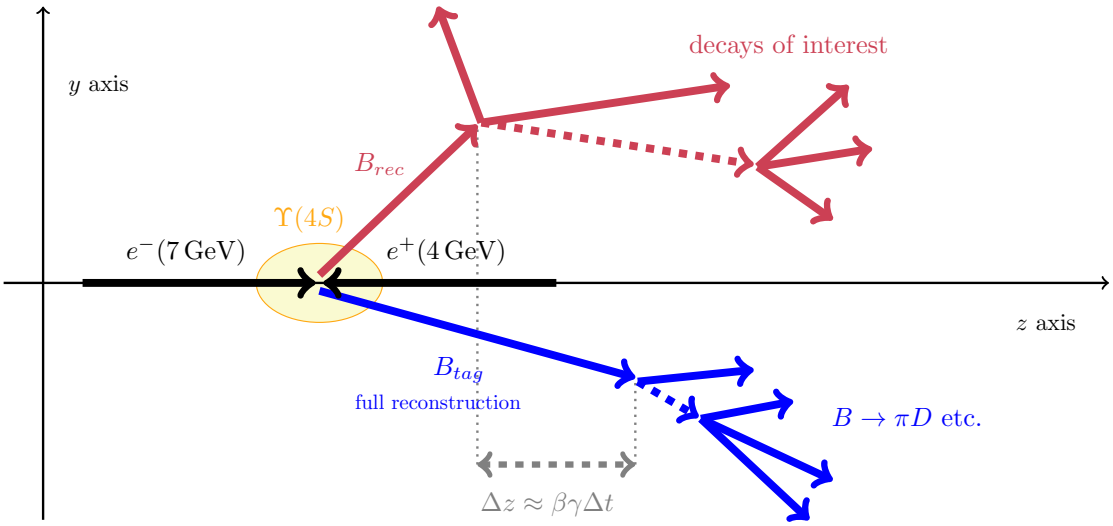

Figure 2.1: Flavour tagging at Belle II. Full reconstruction of one B_{tag} meson provides information about flavour and momentum of the other meson from the $B\bar{B}$ pair. It also excludes decay products from further analysis of B_{rec}. The scale on the figure is amplified in y direction in comparison to z direction.

The $\Upsilon(4S)$ resonance decays in one pair of $B\bar{B}$ mesons only. We reconstruct a decay of one B meson (B_{tag}), and based on that we can determine the flavour and charge of the other $\bar{B}$ meson (B_{rec}) as well as calculate its momentum. We can also exclude the decay products of B_{tag} meson from further B_{rec} analysis. This method is called *flavour tagging* – often referred to as B-tagging in case of B mesons – and it is a very powerful tool for the reconstruction of rare B decays with missing energy due to neutrinos in final states. A schematic presentation of B-tagging is shown in Fig. 2.1. A time difference of the two B-meson decays, Δt, can also be extracted from the full reconstruction of the event, as shown in the same figure, and it is necessary for analyses of the time-dependent CP violation in neutral B-meson decays.

Among dominant collision products are also large samples of charm ($c\bar{c}$) and tau ($\tau^+\tau^-$) pairs. Two D mesons are produced from one $c\bar{c}$ pair and we can again use the tagging method to determine the flavour of D meson of our focus. Both charm and tau decays will also be studied with the Belle II collected data [13, 16].

2.1 SuperKEKB collider

The SuperKEKB collider (Fig. 2.2) is located at the High Energy Accelerator Research Organization (KEK) in Tsukuba, Japan. It uses a 3 km long tunnel 15 m below the surface. SuperKEKB collides beams of electrons at energy of 7 GeV and positrons at energy of 4 GeV. SuperKEKB will mostly collide beams at the center-of-mass energy of $\Upsilon(4S)$ resonance:

$$e^+e^- \to \Upsilon(4S) \to B\bar{B}$$

It is designed, however, to collect data at energies between the energy of $\Upsilon(1S)$ resonance (9.46 GeV) up to near the energy of $\Upsilon(6S)$ resonance (11.25 GeV). The luminosity of the collider will increase up to the final $8 \times 10^{35}\,\mathrm{cm}^{-2}\,\mathrm{s}^{-1}$ by mid 2022 [16], which is 40-times more than at KEKB. Luminosity is given by [17]:

$$\mathcal{L} = f\frac{n_1 n_2}{4\pi\sigma_x\sigma_y}, \tag{2.1.1}$$

where f is a frequency of collisions, $n_{1,2}$ are numbers of particles in bunches and $\sigma_{x,y}$ are horizontal and vertical beam sizes at the interaction point. The event rate can be calculated by multiplying the luminosity with a cross-section for a given process σ_i, $dN/dt = \mathcal{L}\sigma_i$.

In order to reach such a high luminosity, a low-emittance electron beam is produced in a photocathode radio-frequency (RF) electron gun, which produces high quality beams. The electrons for the high energy ring are accelerated in a linear accelerator Linac and injected into a storage ring. Positrons are created by electrons, originating from an electron gun, that collide with a tungsten target and produce electron-positron pairs. Positrons are then focused and directed into a damping ring, where the beam emittance is reduced. They are afterwards accelerated in Linac prior to being injected into the positron storage ring. Both beams circulate in beam pipes before they are collided at a single interaction point [18]. More details about the accelerator design can be found in [19].

An important milestone were the first turns of the SuperKEKB positron and electron beams in February 2016. The detector commissioning phase started at

the beginning of 2018 and the first collisions were recorded on 26th April 2018 at 0:38 a.m. (GMT+09:00). The target luminosity will be achieved gradually in the following years. The planned timeline is shown in Fig. 2.3.

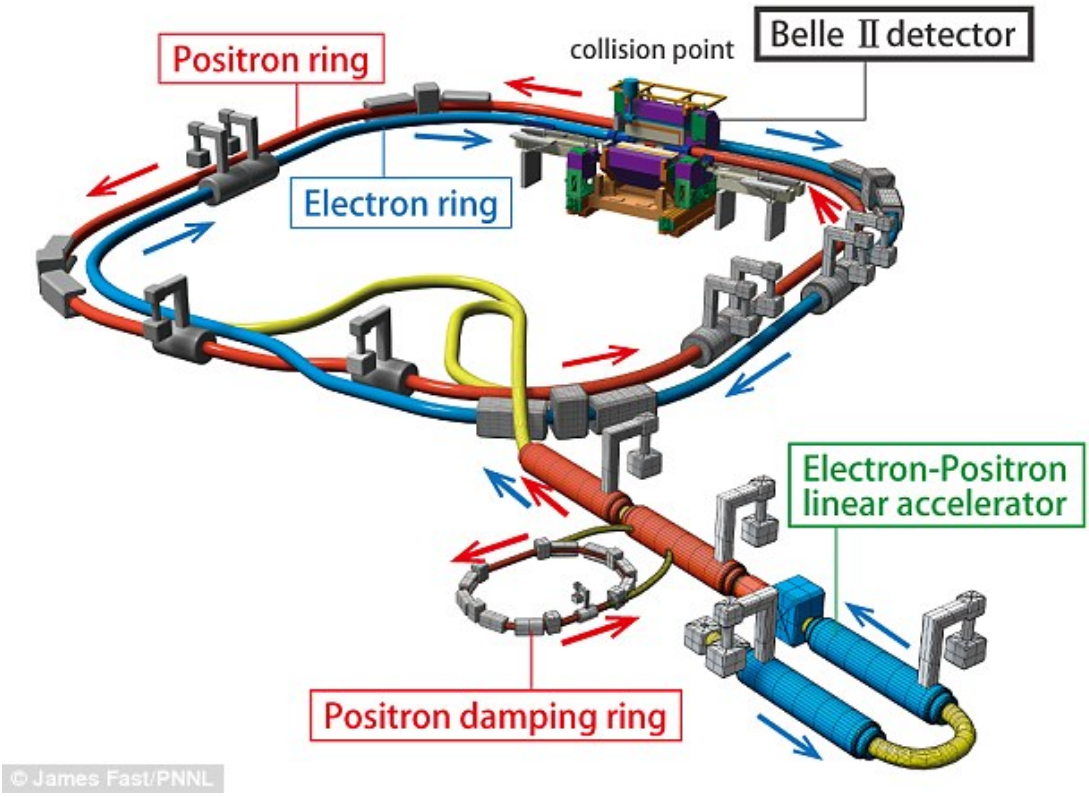

Figure 2.2: SuperKEKB collider with main parts indicated [20].

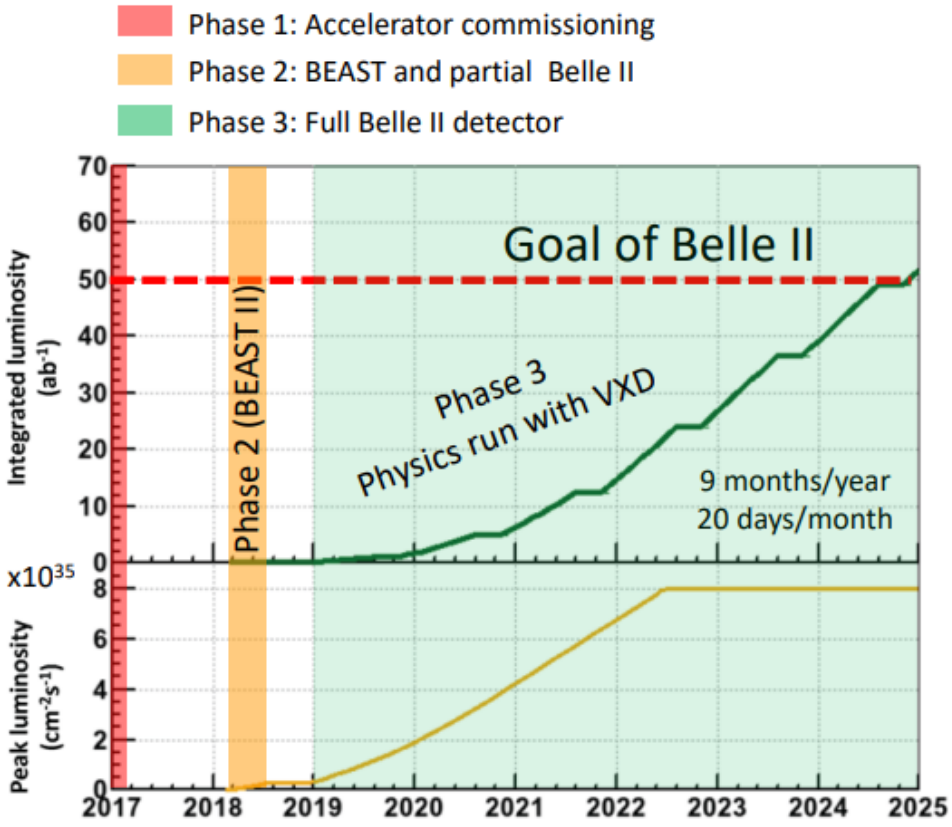

Figure 2.3: A timeline for the luminosity goals for SuperKEKB. A detector commissioning phase (Phase II) was completed in 2018, while the physics runs with the full Belle II detector and high luminosity (Phase III) are planned from the beginning of 2019 [21].

2.2 Belle II Spectrometer

The asymmetrical beam energies result in a relativistic Lorentz boost of the particles, created in the collision. The major part of the decay products is propagated in a direction of the electron beam, towards the forward part of the Belle II spectrometer. Due to the particle boost, Belle II design is asymmetrical and has a more diverse detector coverage in the forward direction.

The very high increase of luminosity will result in ten- to twenty-times higher beam background, increasing the number of fake hits and causing more radiation damage. The higher background rate was the main concern in the efforts to preserve or surpass the performance of the Belle detector [12]. The Belle II detector needs to meet several criteria [16]:

- Excellent impact parameters resolution of approximately 20 µm
- Good momentum resolution over the entire kinematic range (between few 10 MeV/c and 8 GeV/c)
- Precise tracking with a spatial resolution of 100 µm
- Good reconstruction efficiencies for charged particles and photons

- Precise measurements of photon energy and their direction; photon energy resolution is expected to be 1.7 % for the energy range of 3.5 GeV–8 GeV
- Efficient separation of pions and kaons; with kaon identification efficiency over 95 % at less than 1 % of misidentified pions up to momentum of 4 GeV/c
- Efficient identification of electrons (97 %) and muons (89 %)
- Coverage over almost full solid angle

The Belle II detector is divided into several subdetectors, which had to not only fulfil the operational requirements, but also deal with the spatial limitations, as the spectrometer needs to fit into Belle shell, the superconducting solenoid with the iron return yoke. A schematic depiction of both spectrometers is presented in Fig. 2.4. The Belle II detector can be divided into six main parts, described in the following pages.

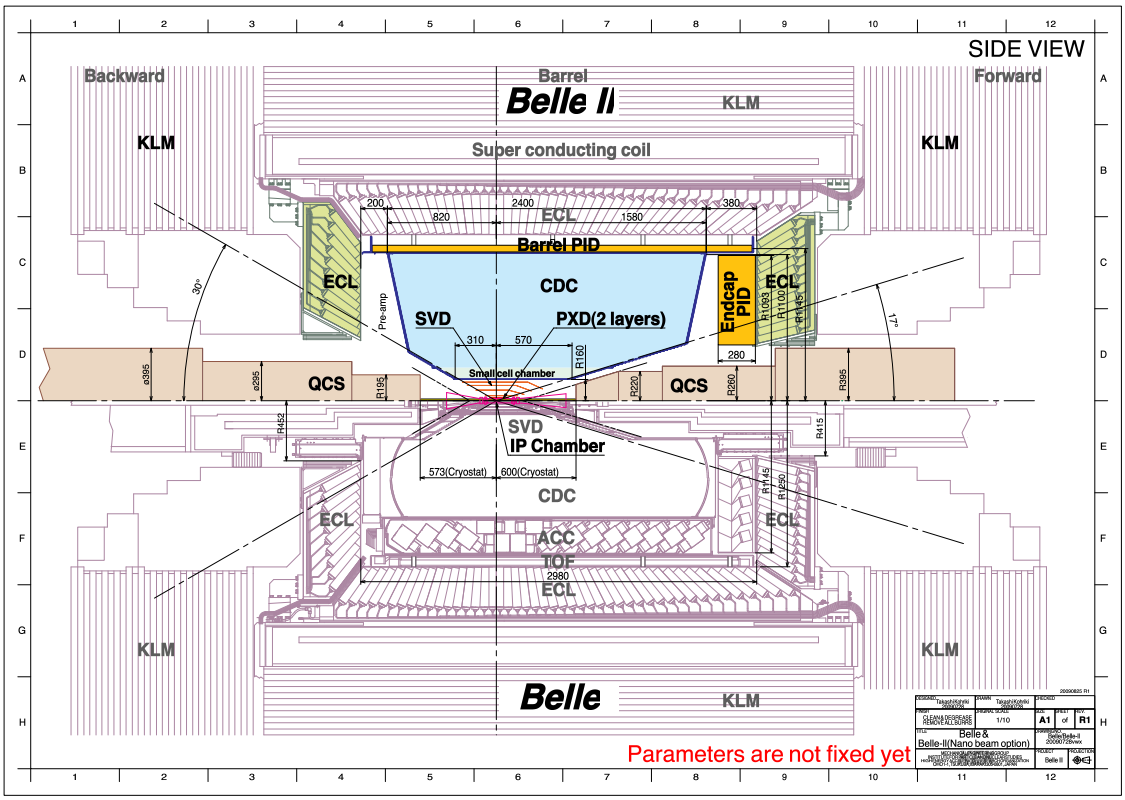

Figure 2.4: A horizontal cross-section of the Belle and Belle II spectrometers. Most components from Belle were replaced or significantly upgraded to meet the performance requirements of Belle II [12].

Vertex Detector (VXD)

The innermost part, Vertex Detector, is made of two very sensitive semiconductor detectors – Pixel Detector (PXD) and Silicon Vertex Detector (SVD). Two layers of pixel silicon detectors are followed by four layers of double-sided silicon strip detectors, as shown in Fig. 2.5. In both, signals are detected through ionizing radiation that produces free charge carriers. The PXD can measure the vertex position of $B\bar{B}$ with a high resolution of 10 µm [12]. The inner detector is able to reconstruct even the trajectories of the particles with a low transversal momentum.

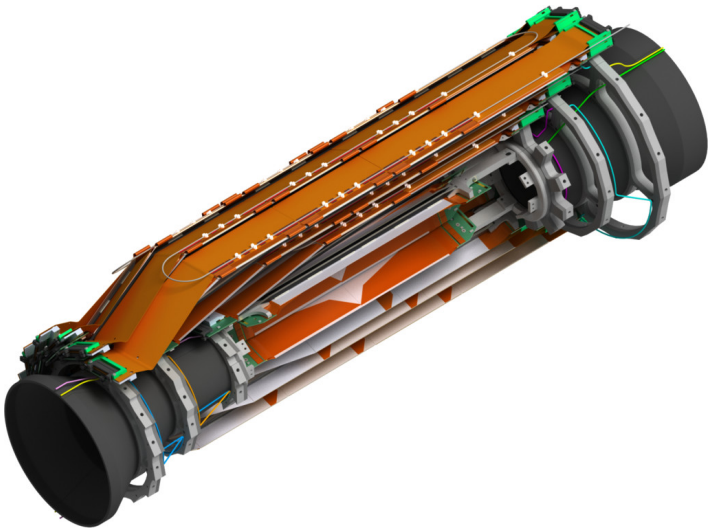

Figure 2.5: A schematic depiction of the vertex detector. It consists of two-layer pixel detector and four-layer silicon vertex detector [22].

During the detector commissioning period with the first beam collisions, the inner detector was replaced with a BEAST system, which consists of one octant of final inner detector as well as different radiation monitors [16]. BEAST was used for the monitoring of background levels and operating conditions during the commissioning phase. The final PXD and SVD will be installed when the electron and positron beams are stable enough to prevent a potential detector damage.

Central Drift Chamber (CDC)

The vertex detector is surrounded by a Central Drift Chamber, which consists of a cylinder, filled with a gas mixture of 50% helium and 50% ethane, and very small drift cells, made of two types of very thin wires. When a charged particle travels through CDC, it ionizes the gas molecules inside. The released charge carriers start moving in an electric field, created by over 42,000 of aluminium wires, that serve as cathodes, and create electron showers on their way to the nearby anodes, some of the 14,000 thin gold-plated tungsten sense wires. CDC in combination with VXD hit information reconstructs the charged particles' trajectories and measures their momenta from the curvature in a magnetic field.

The wires are strung between the forward and backward end-plates and form rectangular cells. Since the CDC cells work as independent proportional chambers, the energy loss within the gas volume can be measured and it provides information about the particle's identity. In addition to that, it gives a reliable information about the particle's charge that can be used as a trigger for the other subdetectors.

Particle Identification (PID) System

The tracking system is followed by a particle identification system. The barrel part is covered by a Time Of Propagation (TOP) counter, whereas the Aerogel Ring Imaging CHerenkov (ARICH) counter covers a forward end-cap area [12, 16]. TOP counter consists of 16 modules, which each measures 270 cm in length and 45 cm in width. Each module is made of two quartz bars, a spherical mirror on one side and an optical prism on the other one. Micro-channel-plate photomultiplier tubes (MCP-PMTs) are used for the read-out [23]. Fig. 2.6 shows the geometry of a single module.

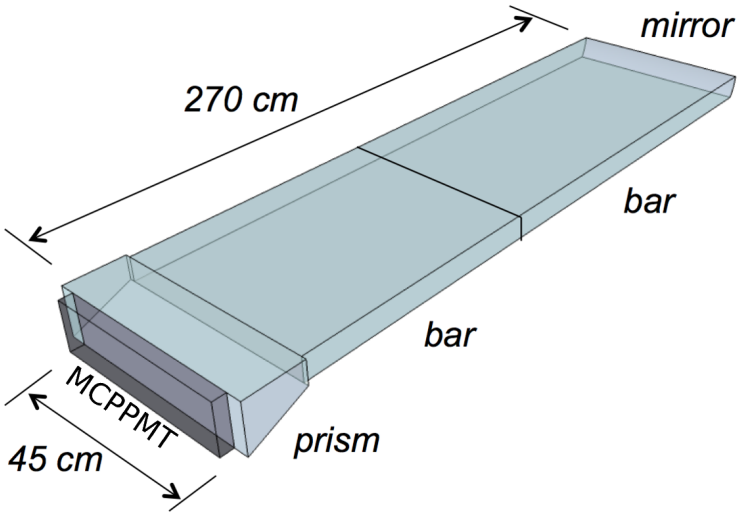

Figure 2.6: One TOP module. It is made of two quartz bars, a spherical mirror on one side and an optical prism on the other one. Micro-channel-plate photomultiplier tubes are used for the read-out [23].

The main purpose of both PID detectors is to distinguish between charged particles, particularly between charged kaons and pions that cannot be identified by the other subdetectors. Their operation is described in Chapter 3. Chapter 4 is dedicated to a detailed ARICH discussion.

Electromagnetic Calorimeter (ECL)

The PID system is surrounded by 43 tons of scintillation crystals, forming an Electromagnetic Calorimeter. More than 8000 crystals cover the barrel region as well as both end-caps [24]. The barrel part of the calorimeter is composed of CsI(Tl) crystals, reused from Belle ECL, whereas the both end-cap parts have been upgraded and crystals have been replaced by faster pure CsI ones. The main purpose is to detect neutral pions and photons in a very wide energy range from a few MeV up to several GeV. Among other main tasks are also a differentiation between electrons and hadrons, a high-efficiency detection of γ-rays, and precise photon energy and position measurements. It can also be used for luminosity measurements [22].

Solenoidal magnet

The listed detectors are surrounded by a solenoidal magnet that creates a homogeneous magnetic field of $B = 1.5\,\mathrm{T}$, parallel to the beam axis. The magnet, used in Belle II, is the same that was used for Belle.

K_L–Muon Calorimeter (KLM)

On the outer side of the magnet there is a K_L–Muon Calorimeter, composed of interchanging layers of iron and detector material to precisely detect muons and long-lived kaons [16]. The detector materials are glass resistive plate counters in the outer region and scintillating fibres in a region closer to the beam pipe. When muon passes through the absorber, it leaves a clean trail of hits over all the layers. A K_L, on the other hand, collides with the iron plates, leaving a cluster of hits behind [22]. The iron plates of KLM serve also as flux return yoke for the solenoid.

The Belle II assembly

A schematic depiction of Belle II is shown in Fig. 2.7. Its upgrade lasted for more than a decade, including subdetectors planning, production and testing. Besides the detectors, a fast and efficient trigger system, a stable data acquisition system (capable of storing large quantities of data) and a precise analysis software for Belle II have been developed. The assembly of most subdetectors was finished before the end of 2017 and they were successfully transported to the final Belle II location. The last missing part, the inner detector (PXD + SVD), joined the Belle II spectrometer at the end of 2018.

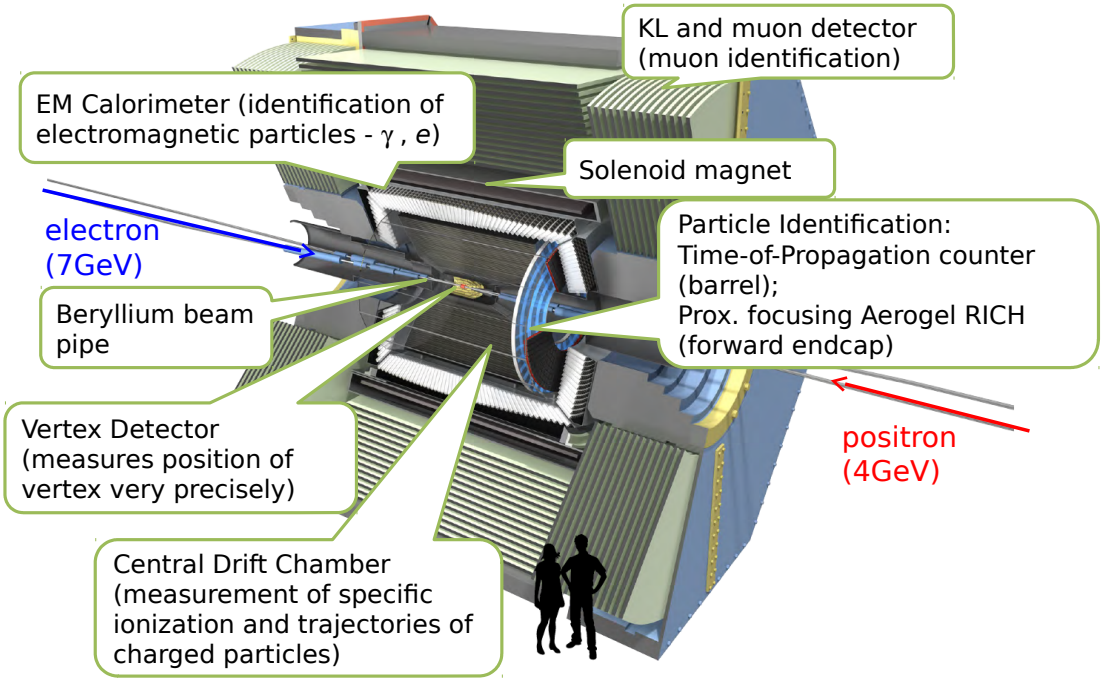

Figure 2.7: Belle II detector with main detector parts indicated [25].

CHAPTER 3

Charged Particle Identification

Efficient identification of long-lived charged particles plays an important role in B-tagging and in studies of rare decays. The charged particle identification performance is evaluated in terms of correct identification and misidentification probabilities. The efficiency is defined as a fraction of correctly identified particles among all reconstructed particles of the same type. Misidentification probabilities, on the other hand, give information about the fraction of particles that are incorrectly identified as particles of some different type [13]. The most important task of charged particle identification at Belle II is an accurate differentiation between kaons and pions. To describe the performance of a particle identification system, we have to study the fraction of kaons, correctly identified as kaons – *kaon identification efficiency*, $\varepsilon_{K\to K}$ – and the fraction of pions, misidentified as kaons, usually referred to as *pion misidentification probability*, $\varepsilon_{\pi\to K}$.

In Belle II, there are two detectors for charged particle identification, the Time Of Propagation (TOP) and Aerogel Ring Imaging CHerenkov (ARICH) counter. They are both novel Cherenkov detectors, designed for Belle II, that cover different solid angles of the spectrometer. Information from both particle identification detectors is combined with the energy loss measurement from the Central Drift Chamber (CDC). Although CDC is mainly a tracking device, the interactions of particles within the CDC volume can provide some information about the identity of the particle.

3.1 Cherenkov Radiation

While CDC uses energy losses from particle collisions with the medium, the dedicated particle identification Cherenkov counters detect charged particles through the effect of Cherenkov radiation. Cherenkov radiation arises when a charged particle moves in a dielectric material faster than the light travels in the same material. The speed of light in a material v_{light} is

$$v_{light} = c_0/n, \tag{3.1.1}$$

where c_0 is the speed of light in vacuum and n is the refractive index of the medium. The refractive index tells us how light propagates through the medium and its value is equal to, or greater than 1 in the optical region.

When a charged particle passes through a dielectric material, it temporarily polarizes molecules close to its trajectory. Created dipoles return to their initial

(stable) states and photons are emitted during this process. When charged particle travels slower than c_0/n, the polarization (Fig. 3.1) is symmetrical and radiation is not seen due to a destructive interference. But when a particle travels faster than c_0/n, polarization is asymmetrical, resulting in a constructive interference, seen as a creation of an electromagnetic shock wave [26, 27].

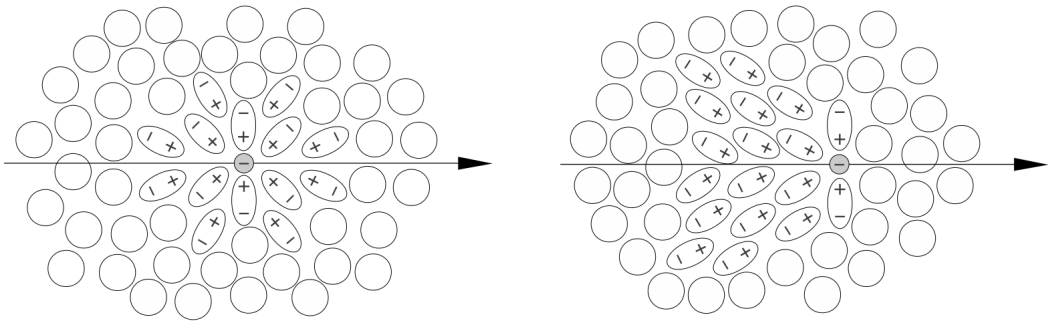

(a) $v_{particle} < c_0/n$ (b) $v_{particle} > c_0/n$

Figure 3.1: Polarization in dielectric material, induced by a charged particle, travelling through the medium with a speed lower (a) and greater (b) than the speed of light in the same medium [28]. When the particle is faster than light, polarization becomes asymmetrical and creates a dipole field.

An electromagnetic shock wave forms as shown in Fig. 3.2. While the particle travels over a distance vt, the shock wave moves a distance of $\frac{c_0}{n}t$. The angle, by which photons are emitted – Cherenkov angle θ_{ch} – is measured relatively to the particle trajectory and is defined with:

$$\cos\theta_{ch} = \frac{1}{vt}\frac{c_0 t}{n} = \frac{1}{\beta n} \tag{3.1.2}$$

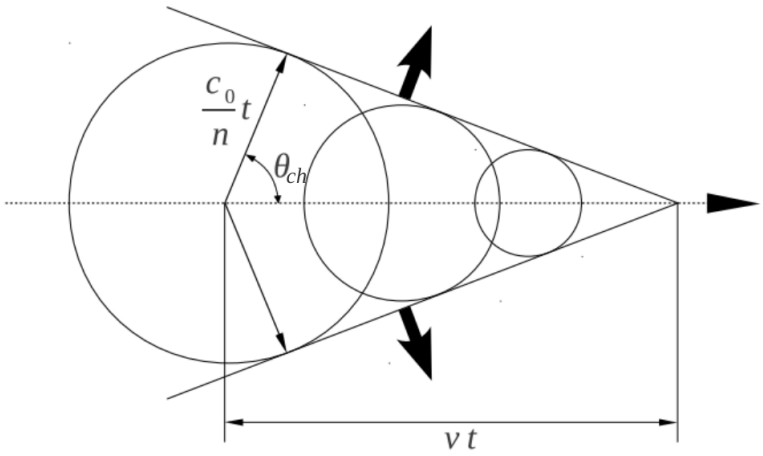

Figure 3.2: Cherenkov radiation. An electromagnetic shock wave is created when a charged particle travels faster than light in a medium. The coherent wavefront is emitted at well-defined Cherenkov angle θ_{ch}.

The maximum Cherenkov angle, when a particle travels at the speed of light, is therefore:

$$\theta_{ch,max} = \arccos\left(n^{-1}\right) \tag{3.1.3}$$

The number of emitted photons depends on the charge of the particle, z, the refractive index of the medium, n, and the thickness of the material, l. It can be calculated as [26, 29]:

$$N_{emitted} = \frac{\alpha z^2}{\hbar c} l \int_{E_1}^{E_2} \sin^2\theta_{ch}(E) dE \tag{3.1.4}$$

where E_1 and E_2 are the limits of optical photon energy interval and α is a fine-structure constant $\alpha = \frac{e_0^2}{4\pi\varepsilon_0\hbar c_0} \approx \frac{1}{137}$.

3.2 Cherenkov Detectors

The Belle II spectrometer has two Cherenkov detectors. In both detectors, the charged particles are (indirectly) identified by their mass m, that can be determined from a relationship between their momentum p and velocity v: $p = \gamma m v$. The momentum is calculated from the radius of the curvature of the particle trajectory in a magnetic field, whereas the particle velocity can be measured using Cherenkov radiation.

The basic operational principle of all Cherenkov detectors is the same. We need a radiator – a material, where Cherenkov photons are emitted; a space where Cherenkov photons can propagate (and often mirrors or lenses that help with focusing Cherenkov photons); and sensors that can detect the photons. The detector design and materials are chosen with respect to the spatial limitations of the detector, desired signal resolution and the ability to distinguish between particles over a necessary momentum range. In particle physics, momentum is normally used instead of velocity, so we are interested in the operational momentum region. A momentum threshold for emitting Cherenkov radiation can be expressed using the equation for relativistic velocity $p = mv/\sqrt{1 - v^2/c_0^2}$, and the relation between the velocity and the refractive index (Eq. 3.1.1) as:

$$p_{th} = \frac{mc_0}{n\sqrt{1 - \frac{c_0^2}{n^2 c_0^2}}} = \frac{mc_0}{\sqrt{n^2 - 1}} \tag{3.2.1}$$

The Cherenkov angle depends on the velocity of the charged particle and the refractive index of the radiator (see eq. 3.1.2). Fig. 3.3 illustrates the Cherenkov angle dependence on the momentum for different particles, emitted in aerogel, showing that the interval for efficient identification is limited. The threshold value can be adjusted over a wide momentum range with a proper choice of radiator. It is possible to separate kaons and pions at momenta as low as a few 10 MeV/c using solid radiators and up to 100 GeV/c using gaseous ones. An example for three different refractive indices (corresponding to the quartz - 1.46, and two types of aerogel - 1.05, 1.01) is shown in Fig. 3.4.

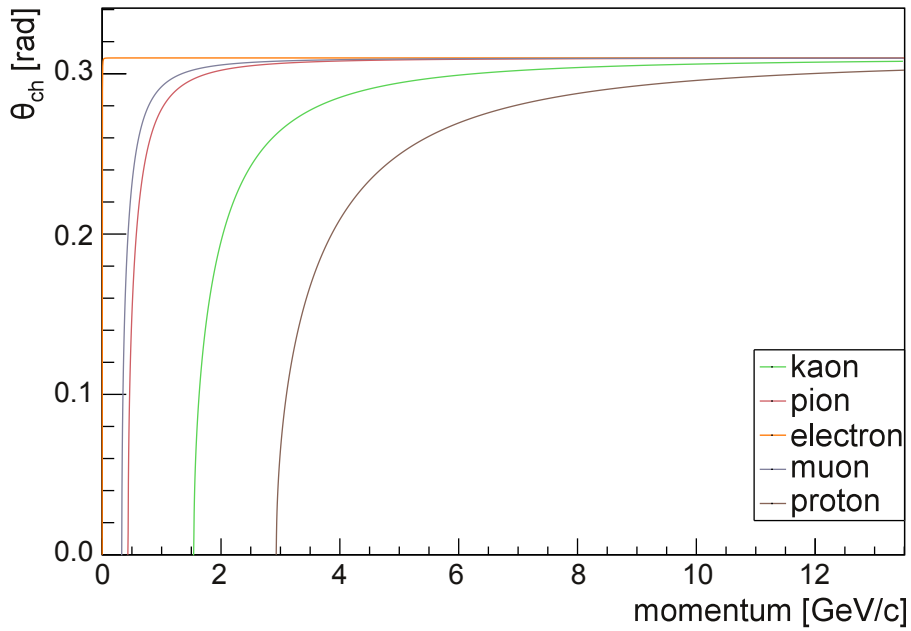

Figure 3.3: A comparison of Cherenkov angle as a function of momentum for photons, emitted within the aerogel radiator with $n = 1.05$ by five different charged particles.

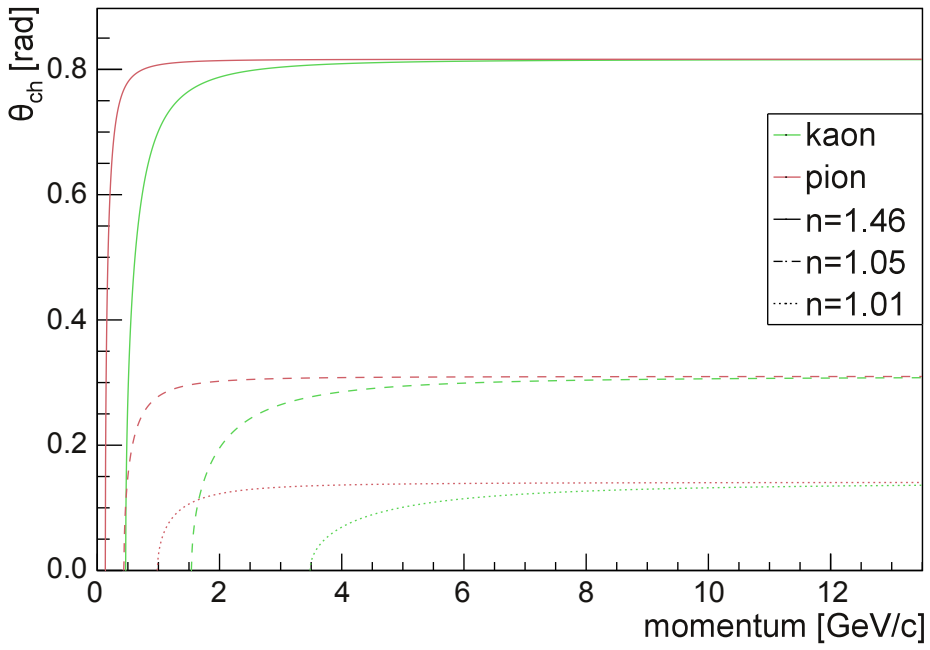

Figure 3.4: Cherenkov angles for kaons and pions as a function of momentum for different types of radiators. Index $n = 1.46$ corresponds to quartz (TOP detector) and the other two to different types of aerogels.

Different types of Cherenkov detectors are known, classified either as threshold or imaging counters. The threshold counters can distinguish between two charged particles, but work in a narrow momentum range between the two momentum

thresholds. The imaging counters can be further divided into differential Cherenkov detectors and ring-imaging Cherenkov detectors. The former work in a very narrow momentum range. They detect photons of one type of particle at a given momentum, whereas photons from the other particle, emitted at different angle at the same momentum, miss the sensor. Only the Ring-Imaging Cherenkov detectors are sensitive over a wider momentum range.

3.2.1 Ring-Imaging Cherenkov Detectors

The Ring-Imaging Cherenkov (RICH) detectors can reconstruct the pattern of the detected photons using either focusing or proximity-focusing design. The former use spherical mirrors for propagating photons to the detector surface. The latter use thin radiators and the photons travel directly to the sensor plane. While the design of various RICH detectors is different, the principle of operation is the same. The pattern of the signal, being either a ring on a detector surface or a particle-characteristic time dependent signal, provides the particle identity information.

Focusing Design

A typical focusing RICH representative at LHCb, RICH1 [30], uses C_4F_{10} gas as a radiator. The emitted Cherenkov photons are reflected from the spherical mirrors and propagated to the sensor plane, outside of the flux of the charged particles, as presented in Fig. 3.5. Photons, emitted at the same azimuthal angle, but from different positions along the particle's path, are collected into a single point on the sensors, that are positioned outside of the track path on the focal plane of the mirrors.

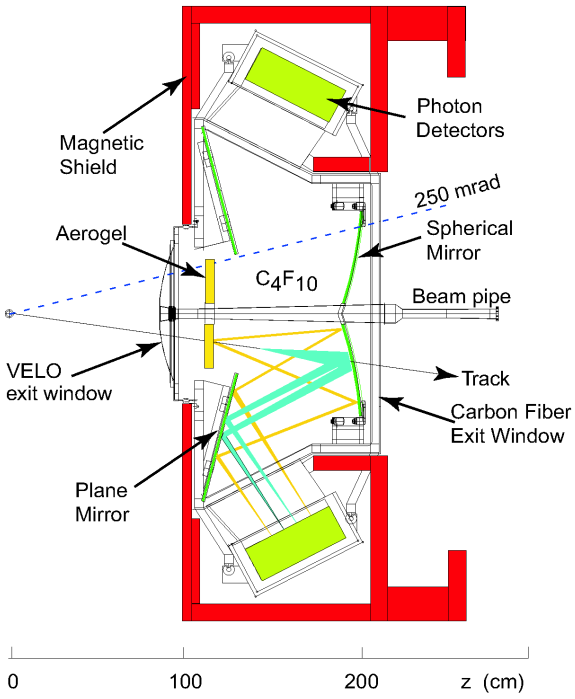

Figure 3.5: The RICH-1 detector at LHCb [31]. The C_4F_{10} gas is used as a radiator. Cherenkov photons are reflected from the spherical mirrors and propagated to the sensor plane.

Proximity Focusing Design

A cone of generated Cherenkov photons in proximity focusing RICH detectors is propagated through the expansion gap between the radiator and the photon detector. A representative, that uses a solid radiator, is the CLEO RICH detector, shown in Fig. 3.6. The Cherenkov photons are emitted in a 1 cm thick LiF radiator and they propagate through 15.6 cm of pure nitrogen, as presented in the figure, before they are detected by multiwire proportional chambers [32].

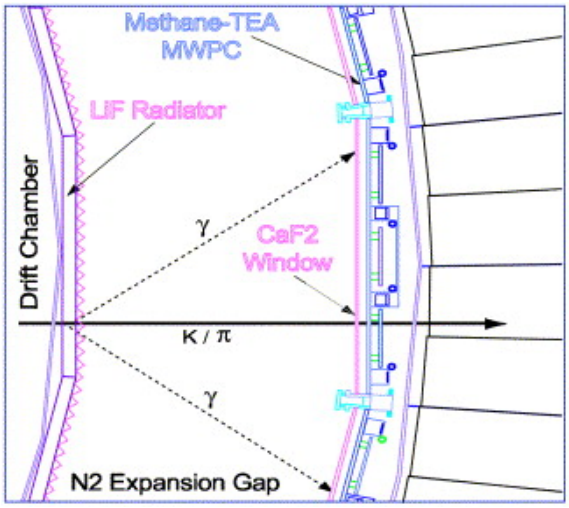

Figure 3.6: A schematic depiction of a proximity focusing CLEO RICH detector and photon propagation between the solid state radiator and photon detectors [32].

New RICH Designs

One of the novel RICH detectors is the Belle II Time-Of-Propagation (TOP) detector. It measures one spatial coordinate and the time of arrival of Cherenkov photons. Fig. 3.7 illustrates the photon propagation in a TOP detector. The charged particle passes the quartz bar and emits photons at different Cherenkov angles for kaons and pions. Emitted photons then travel through the bar and reflect on its borders, which results in a propagation, presented in the figure. Photons that travel to the opposite side of PMTs, reflect from the mirror at the edge and return to the side with readout electronics. The time needed for propagation to MCP-PMTs differs for photons, emitted at different angles. Therefore, particles are identified by the time dependent photon pattern that is detected by PMTs.

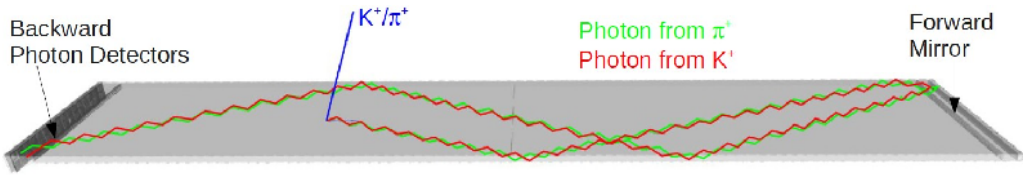

Figure 3.7: A photon propagation in one module of the TOP detector [33]. Photons, emitted at smaller angle, need longer to propagate through the quartz bar. The charged particles are identified by the time of the arrival of Cherenkov photons, detected by MCP-PMTs.

CHAPTER 4

Aerogel Ring Imaging Cherenkov Detector

The Aerogel Ring Imaging Cherenkov (ARICH) detector provides particle identity information in the forward endcap region of Belle II. Its main objective is to achieve better than 4σ separation between kaons and pions in the momentum region between 0.5 GeV/c and 4.0 GeV/c, above the pion momentum threshold for Cherenkov photon emission and below the region where Cherenkov angles of kaons and pions start overlapping. ARICH also discriminates between pions, muons and electrons in the region below 1 GeV/c [34]. Kaons and pions are common B meson decay products, so an excellent degree of performance in particle identification is required for efficient heavy flavour tagging. The detailed description of B-tagging algorithm and the decay products can be found in [13].

The coverage of momentum region required a radiator with a refractive index above that of gaseous radiators and below that of solid ones, and aerogel was a suitable compromise. The main components of ARICH are a double layer aerogel radiator for Cherenkov photons emission, an empty space for a Cherenkov light-cone expansion and a segmented photo sensor plane with the read-out system attached at the back. A schematic depiction of the ARICH detector and its operation is shown in Fig. 4.1.

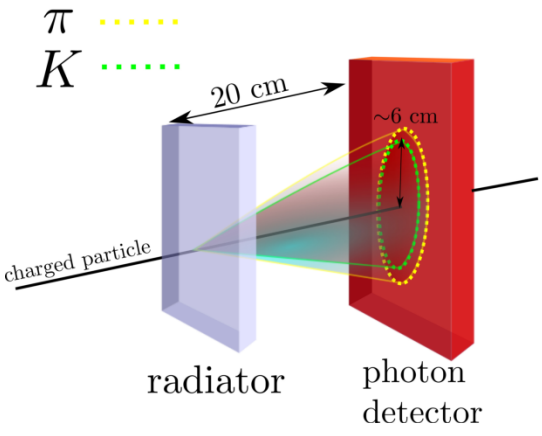

Figure 4.1: A schematic depiction and principle of ARICH operation [34].

4.1 Single Photon Detection

The whole detector design has to ensure a satisfactory collection of photons to identify charged particles. Not all photons emitted in the aerogel (Eq. 3.1.4) are detected. Some photons are already absorbed in the radiator itself, some are reflected from the window of the photo detector or are not converted into photoelectrons at all. Additional loss occurs when photons are emitted close to the edge of the radiator plane and miss the sensors.

The number of detected photons for a particle with a charge z[1] in ARICH can be written as:

$$N_{detected} = \frac{\alpha}{\hbar c} z^2 l \varepsilon_G \int_{E_1}^{E_2} Q(E) T_R(E) T_Q(E) \sin^2 \theta_{ch}(E) dE \qquad (4.1.1)$$

where $Q(E)$ is the photon detection efficiency, $T_{R,Q}(E)$ are radiator and quartz transmittances, and ε_G is the geometrical efficiency – the fraction of the detector plane, covered with active sensors (41 % for ARICH). After taking into account all the photon loss contributions, the expected number of detected photons per track in ARICH is between 10 and 12.

The expected distribution of the hits on the detector plane has a Gaussian shape around the ring. The expected ring size on the detector plane for a pion at 3.5 GeV/c is illustrated in Fig. 4.2. The darker and narrower ring corresponds to the Cherenkov angle width of $\pm 1\sigma$ and the wider one to $\pm 2\sigma$. The ring is drawn for a particle that enters aerogel perpendicularly to the plane, which is true for a small proportion of charged tracks in ARICH, but suffices for an illustration.

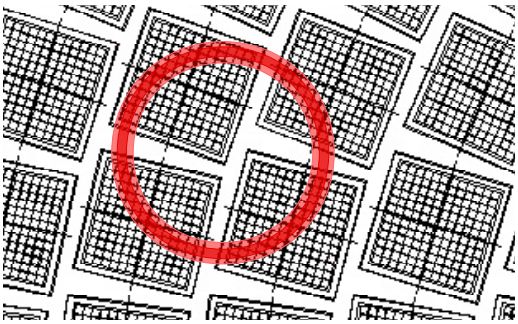

Figure 4.2: A schematic depiction of a size of a Cherenkov ring, corresponding to a pion with momentum of 3.5 GeV/c that enters ARICH perpendicularly to the aerogel plane. Rings are drawn for angles of $\theta_{ch} \pm 1\sigma$ (dark) and $\theta_{ch} \pm 2\sigma$ (light).

From the figure, we can estimate the number of channels, covered by a $\theta_{ch} \pm 2\sigma$ wide ring, to be around 170. If 10 to 12 expected photons are detected on different channels, they occupy 5.9 % to 7.1 % of channels. The probability for two-photon signals on the same channel decreases to 0.5 %.

Most particles enter aerogel at larger impact angles, so that the detected photons form an elliptically-shaped ring, which covers an even larger surface on the detector plane. This decreases the probability for multiple-photon hits on each channel even more, therefore sensors for an efficient single photon detection are needed.

[1] We are only interested in the identification of particles with a charge of $\pm e_0$.

4.2 Detector Design

ARICH has to fit into a 28 cm wide cylinder with an inner radius of 42 cm and an outer radius of 114 cm. The detector plane is a large ring with a total area of roughly 3.5 m^2. Photo sensors are arranged into seven concentric rings with 420 sensors in total. The innermost ring has 42 sensors, while every following one has six more. The radiator plane is divided into four rings with 22, 28, 34 and 40 tile slots, respectively [35]. Each of the four rings requires differently wedge-shaped radiator tiles, whose designs can be found in Appendix A. The segmentations of the detector and radiator planes are shown in Fig. 4.3. The figure also shows planar mirrors at the edges, which reflect photons to the sensor plane as illustrated in Fig. 4.4. The numbering schemes of all components can be found in Appendix B.

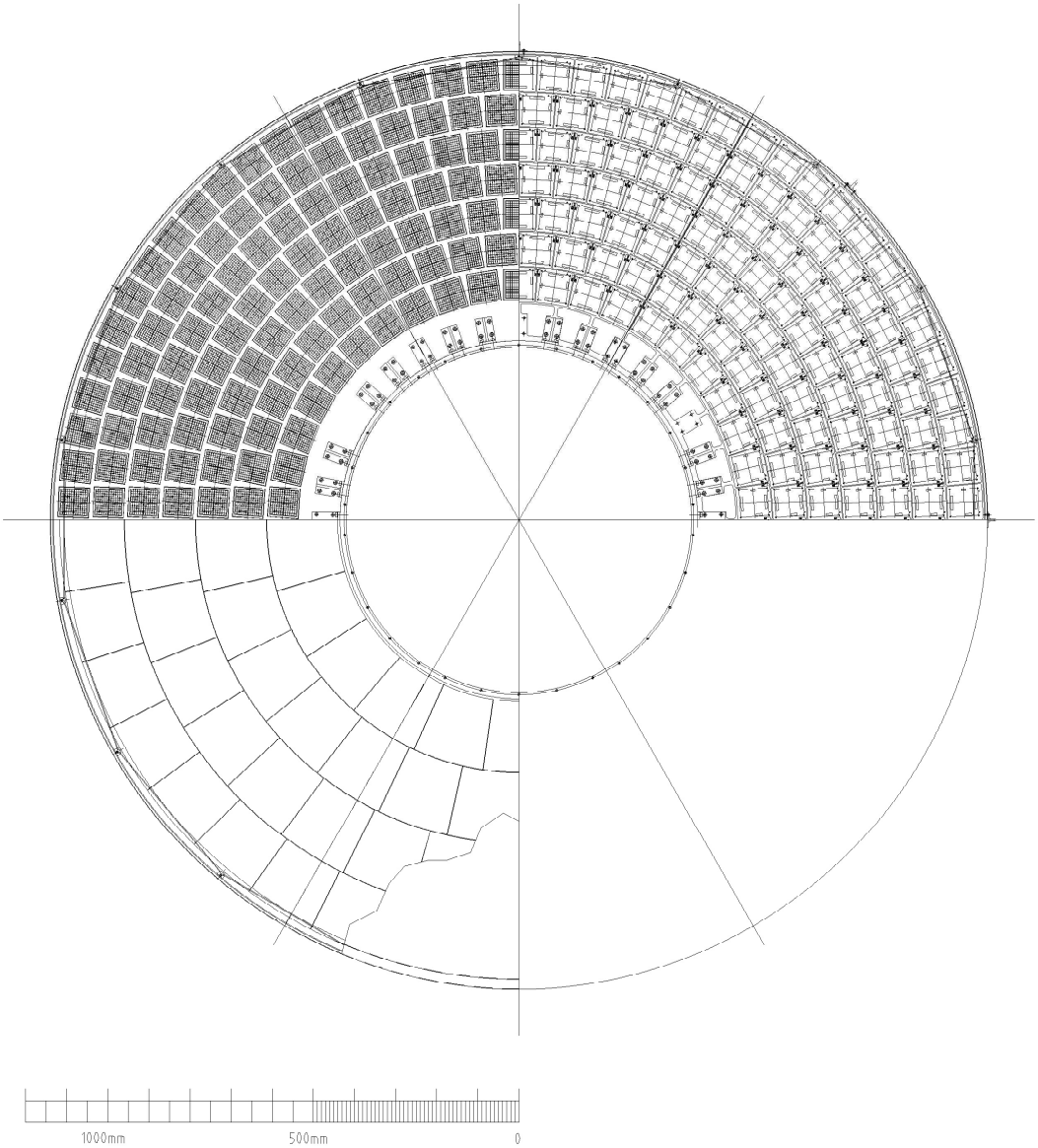

Figure 4.3: A segmentation of ARICH planes [36]. The top part presents the front part of the detector plane with mounted photo sensors (left) and the backside with read-out electronics attached (right). The bottom left quarter shows the radiator segmentation. The lines at 60° angles show the separation between six sectors. Planar mirrors are drawn at the edges of the detector.

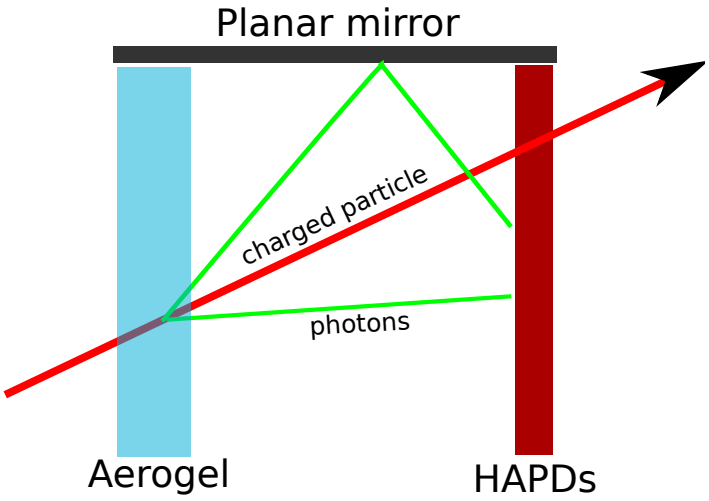

Figure 4.4: Photons, emitted close to the edge of the detector, are reflected to the sensor plane from the planar mirrors [36].

ARICH covers a small proportion of the solid angle, as seen in Fig. 4.5. The aerogel side covers polar angle between 15° and 34°. The sensors can detect photons that reach the detector plane at polar angles between 16° and 31°.

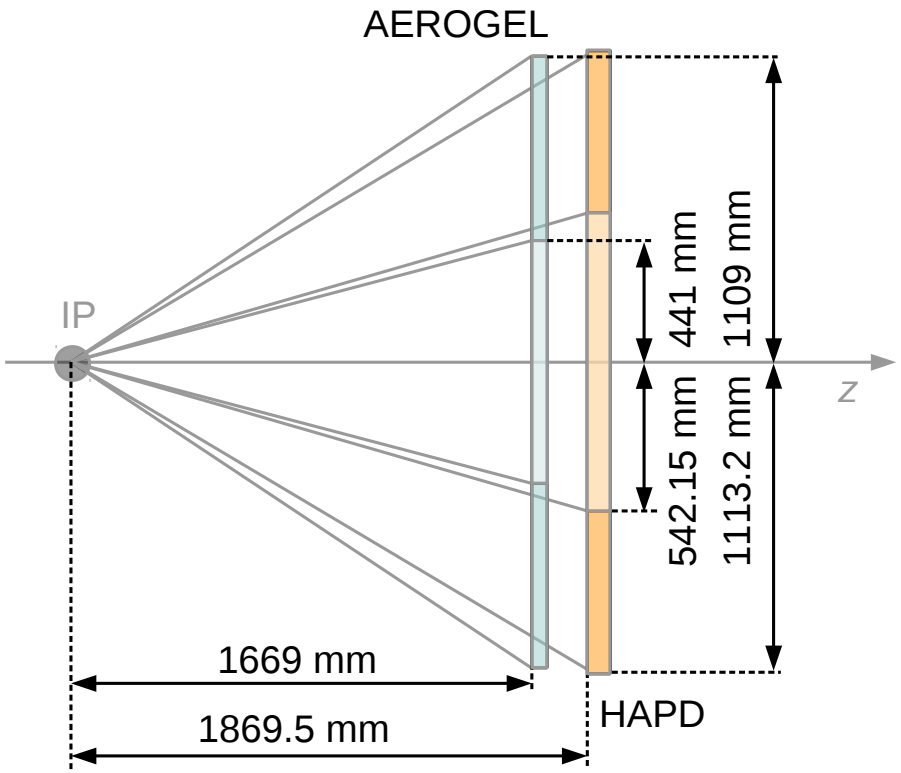

Figure 4.5: A schematic depiction of the ARICH angle coverage. The edges of areas, covered by aerogel tiles and photosensors' sensitive area, are labelled.

4.3 Aerogel

Aerogel is an ultralight material with a good optical transparency. The structure is similar to a gel, where the liquid part is substituted by gas. Aerogels differ based on their molecular structure, density, ability to interact with water, etc. Properties of aerogel are determined during synthesis, which follows three main steps [37]:

a) Gel preparation (gelation of the source solution)

b) Aging of the gel (adding the strength to the gel structure)

c) Drying of the gel (carefully removing the liquid)

The aerogel refractive index, n, typically between 1.003 and 1.11, can be precisely tuned during the synthesis, which makes it a suitable material for various usages, including Cherenkov detectors [38, 39]. A silica aerogel is made of nano-scale sized molecules which consist of numerous siloxane bridges (Si-O-Si), that agglomerate into large structures. A condensed formula of one type of silica aerogel is presented in Fig. 4.6.

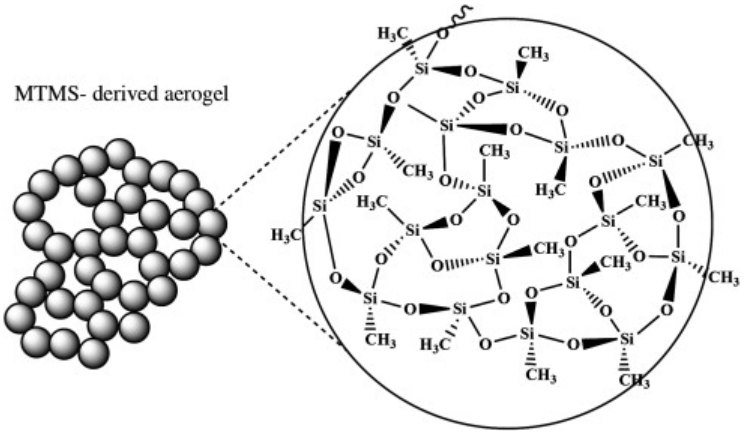

Figure 4.6: A condensed formula of a silica aerogel [40].

4.3.1 Radiator Optimization

A high-transparency and low refractive index were the main reasons to choose aerogel as the ARICH radiator. The radiator design was optimized to collect enough photons on the detector plane, while keeping a good resolution of a single-photon ring. The Cherenkov angle resolution of a track, σ_{track}, depends on a single photon resolution, σ_0, and on a number of detected photoelectrons, N_{pe}:

$$\sigma_{track} = \frac{\sigma_0}{\sqrt{N_{pe}}} \tag{4.3.1}$$

The single photon resolution depends on the pad size a and the radiator thickness d:

$$\sigma_0^2 = \sigma_a^2 + \sigma_d^2 \tag{4.3.2}$$

After taking into account the flat distributions of expected hits over the pad and of emitted photons over the aerogel thickness, the uncertainties for a particle that enters ARICH perpendicularly to the aerogel plane can be expressed as:

$$\sigma_a = \frac{a\cos^2\theta_{ch}}{\sqrt{12}l} \quad \text{and} \quad \sigma_d = \frac{d\cos\theta_{ch}\sin\theta_{ch}}{\sqrt{12}l} \tag{4.3.3}$$

With the pad size of $a = 4.9\,\text{mm}$, an average distance between the radiator and the detector of $l = 18\,\text{cm}$, and $n = 1$, one gets the uncertainties of $\sigma_a \approx 7\,\text{mrad}$ and $\sigma_d \approx d \times 0.45\,\text{mrad}\,\text{mm}^{-1}$.

The number of emitted photons increases with thickness, but so does absorption in the radiator. The optimal thickness of 20 mm was determined from the resolution as a function of radiator thickness, which is presented in Fig. 4.7.

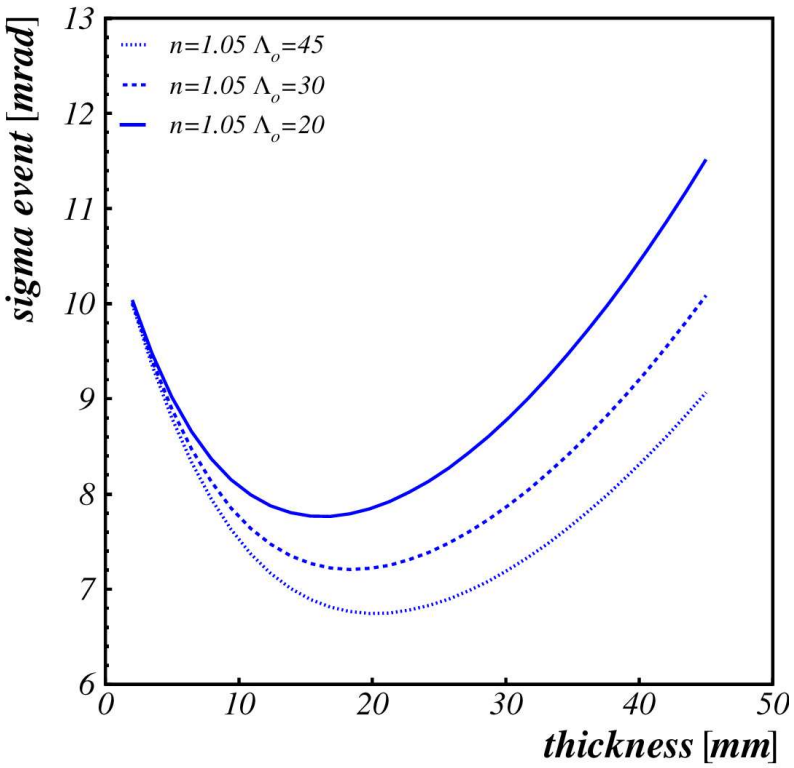

Figure 4.7: A single track resolution as a function of aerogel layer thickness for different values of the absorption length Λ_0 (in mm) [41].

Unfortunately, the number of detected photons with a 20 mm thick radiator is still too low. In order to increase the yield without degrading the resolution, we came up with an innovative solution. Two 20 mm thick aerogel tiles are stacked together, where the refractive index in the second layer is slightly higher than in the first (upstream) layer. If the difference in refractive indices is properly chosen for the given refractive index and geometry, the two resulting rings overlap on the photon detector. The schematic depictions of configurations with the same and different refractive indices of the two layers are compared in Fig. 4.8.

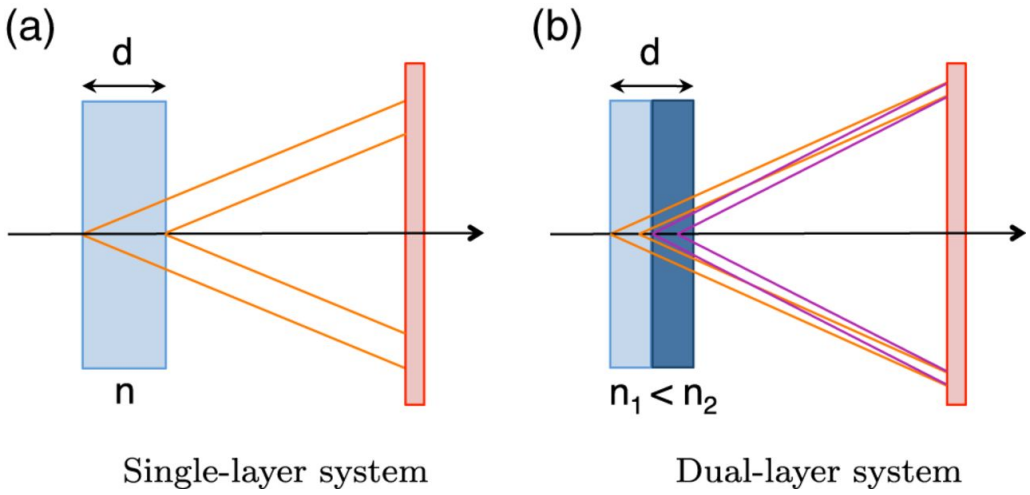

Figure 4.8: A comparison of a single- and a dual-layer focusing scheme. (a) A Cherenkov detector configuration with one layer of radiator. (b) The focusing configuration of radiator, used in ARICH. The total thickness of radiator is the same for both configurations [42].

The advantage of the focusing configuration system is found in a better Cherenkov angle resolution. This was tested with pion beams (with momentum of 0.5 GeV/c – 4 GeV/c) in an experimental setup, consisting of aerogel radiator and an array of Hamamatsu 64-channel position sensitive photomultiplier tubes, enclosed inside a light-tight box [43]. The distance between radiator and photo detector was 20 cm. Results in Fig. 4.9 show that the Cherenkov angle peak width was reduced by 30 % when using a double-layered radiator.

4.3.2 ARICH Radiator

Aerogel is a fragile material and large tiles are both difficult to produce and mount. The plane is therefore segmented into 124 slots, each containing two aerogel tiles with different optical properties.

Optimizing the synthesis resulted in development of a new type of aerogel tiles for ARICH. The important property is a long transmission length Λ_0; the distance at which the original light intensity is reduced by the factor of e:

$$I_x = I_0 e^{-\frac{x}{\Lambda_0}}, \tag{4.3.4}$$

where $I_{0,x}$ are light intensities before entering the material and after a distance x. The main contributions to the signal intensity loss in aerogel are absorption and Rayleigh scattering in the radiator [44]. By changing the solvent in the synthesis, the transmission length of the final aerogel type was extended from 15 mm to 45 mm, which increased the number of propagated Cherenkov photons by up to 2.5-times [45]. A distribution of transmission lengths of both aerogel layers for all installed tiles are shown in Fig. 4.10.

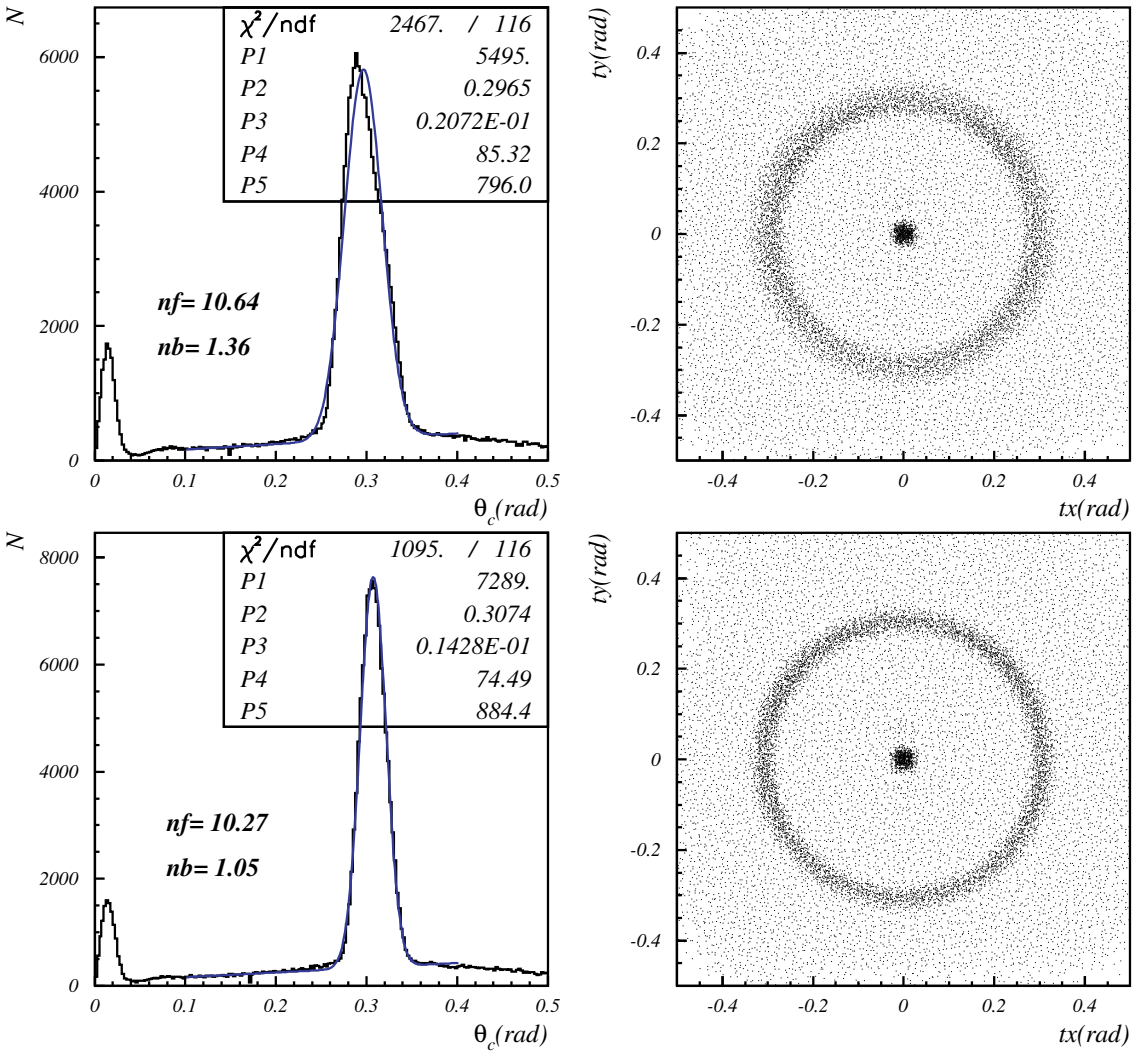

Figure 4.9: Cumulative distribution of Cherenkov photon angle (left) and the Cherenkov ring in a two-dimensional space (right) for a homogeneous radiator (top) and a focusing configuration with refractive indices of $n_{\mathrm{upstr}} = 1.046$ and $n_{\mathrm{downstr}} = 1.056$ (bottom) [43].

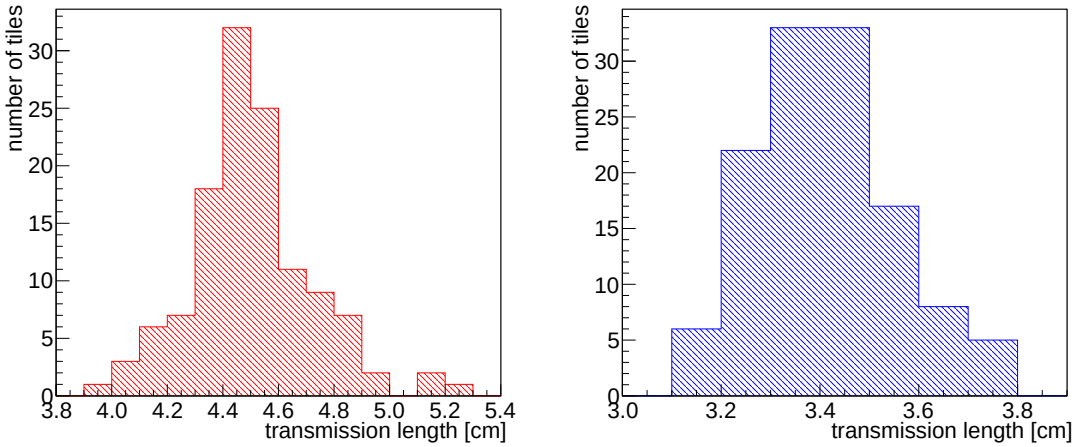

Figure 4.10: Distributions of transmission lengths of installed aerogel tiles. The left histogram shows the upstream tiles with transmission lengths of (4.5 ± 0.2) cm, while the right one shows the downstream ones with values of (3.4 ± 0.1) cm.

Densities of produced upstream and downstream aerogels are roughly $0.160\,\mathrm{g\,cm^{-3}}$ and $0.194\,\mathrm{g\,cm^{-3}}$, respectively. The refractive index n depends on the density ρ of the produced aerogel. They are connected through the equation

$$n = 1 + k\rho, \tag{4.3.5}$$

where the coefficient k depends on the material type and is 0.21 for silica aerogel [46]. These densities correspond to refractive indices of $n_{\mathrm{upstr}} = 1.045$ and $n_{\mathrm{downstr}} = 1.055$ [47]. The distributions of refractive indices for both types of installed tiles are shown in Fig. 4.11.

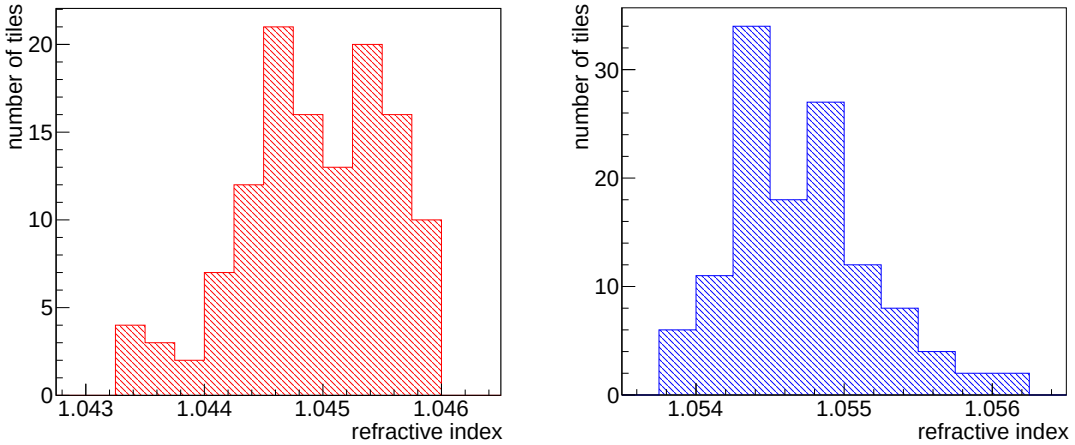

Figure 4.11: The distributions of refractive indices of installed aerogel tiles. The left histogram shows the upstream tiles with refractive index values of $n_{\mathrm{upstr}} = 1.0449 \pm 0.0006$, while the right one shows the downstream ones with $n_{\mathrm{downstr}} = 1.0546 \pm 0.0005$.

They were chosen with respect to the Cherenkov angles. The Cherenkov angle depends on momentum and on the refractive index, as illustrated in Fig. 4.12. Rings

from both layers cannot overlap over the whole momentum region. Therefore, the indices were chosen to get overlapping rings on the detector plane at high momentum of around 3.5 GeV/c, where the separation between kaons and pions is as little as 30 mrad, and the resolution in Cherenkov angle measurement has to be the best. To maintain the best resolution over the whole geometrical acceptance of ARICH, the aerogel tiles were paired in order to get a uniform refractive-index difference all over the plane. A distribution of the difference of the refractive indices of the installed downstream and upstream tile pairs is shown in Fig. 4.13.

The thickness and the optical properties (refractive index, transmission length) for downstream and upstream aerogel tiles are shown in Figs. 4.14, 4.15 and 4.16.

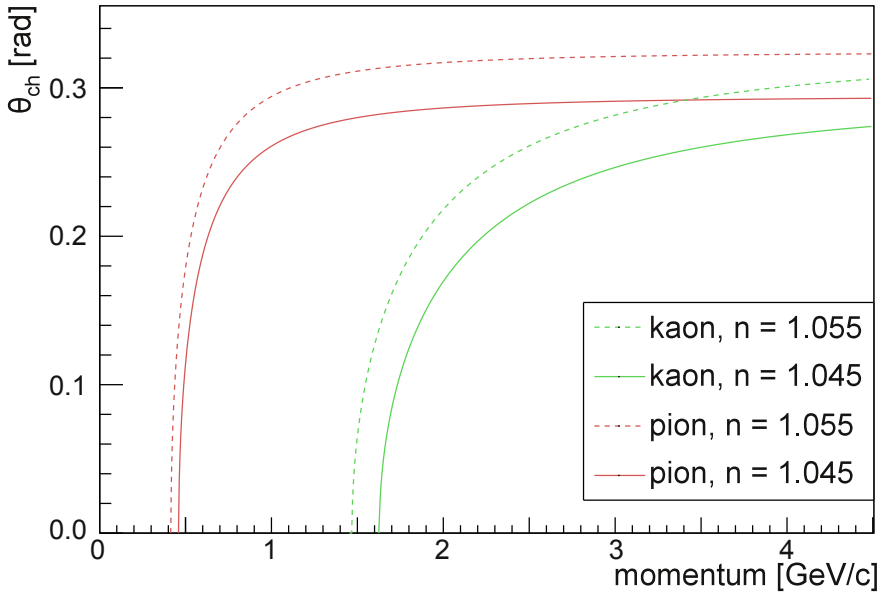

Figure 4.12: The Cherenkov angle as a function of a charged particle's momentum.

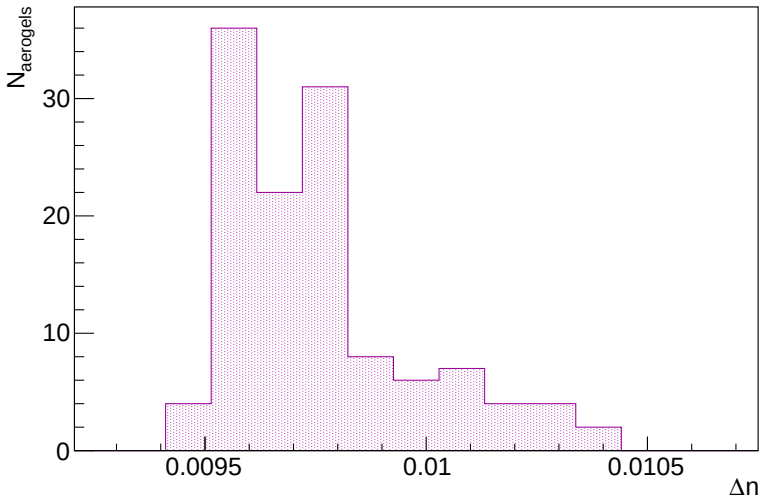

Figure 4.13: The distribution of the difference of the refractive indices of the installed downstream and upstream tile in the same radiator slot. The pairs of the tiles were chosen to get the uniform refractive-index difference. The differences of the installed tiles are $\Delta n = 0.0098 \pm 0.0002$.

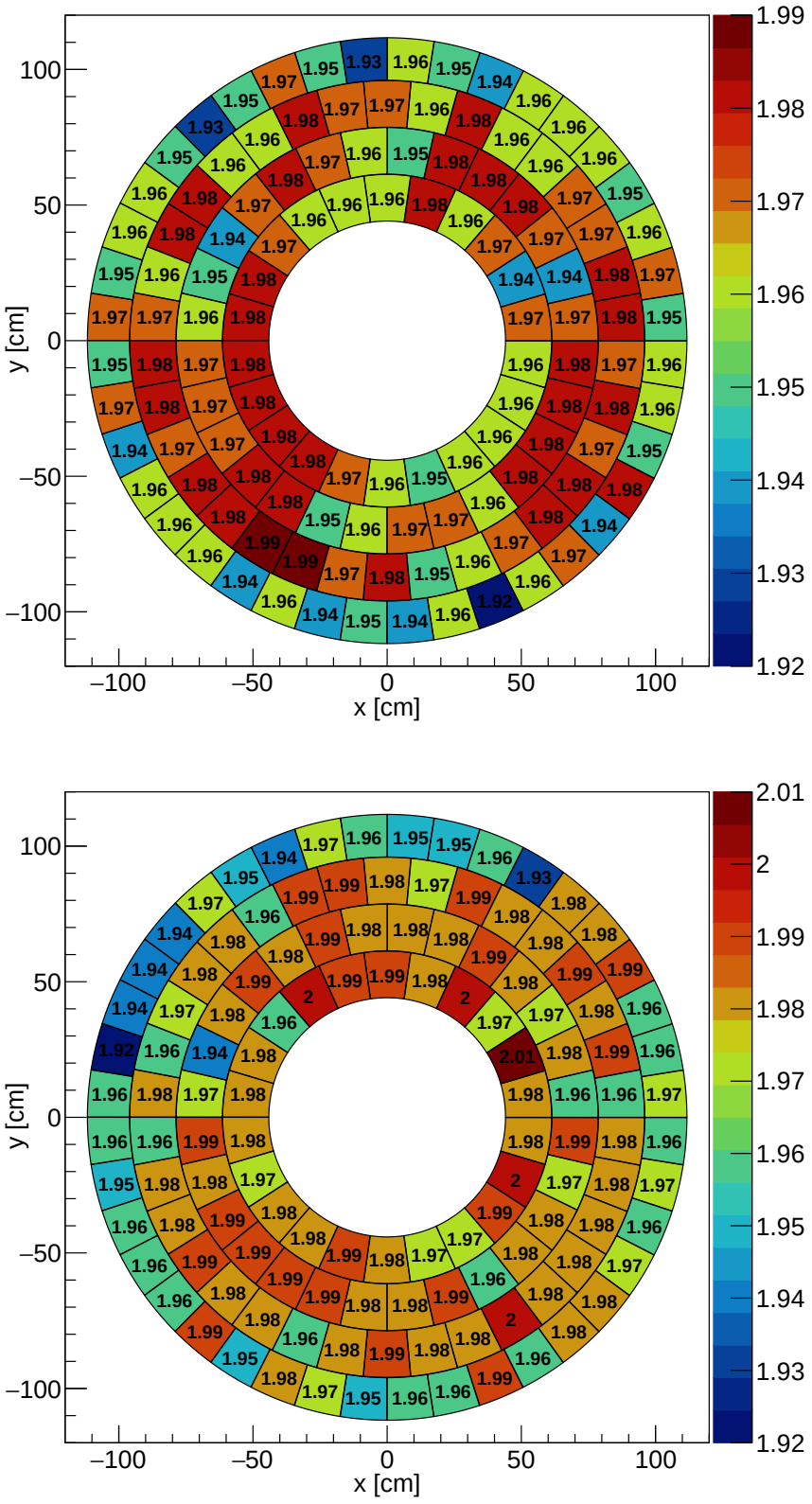

Figure 4.14: The distribution of thickness (in cm) of aerogel tiles on the aerogel plane. The top figure shows the thickness for the upstream tiles and the bottom figure shows the values for the downstream tiles. The average thickness of installed tiles are (1.96 ± 0.01) cm for upstream and (1.97 ± 0.02) cm for downstream tiles.

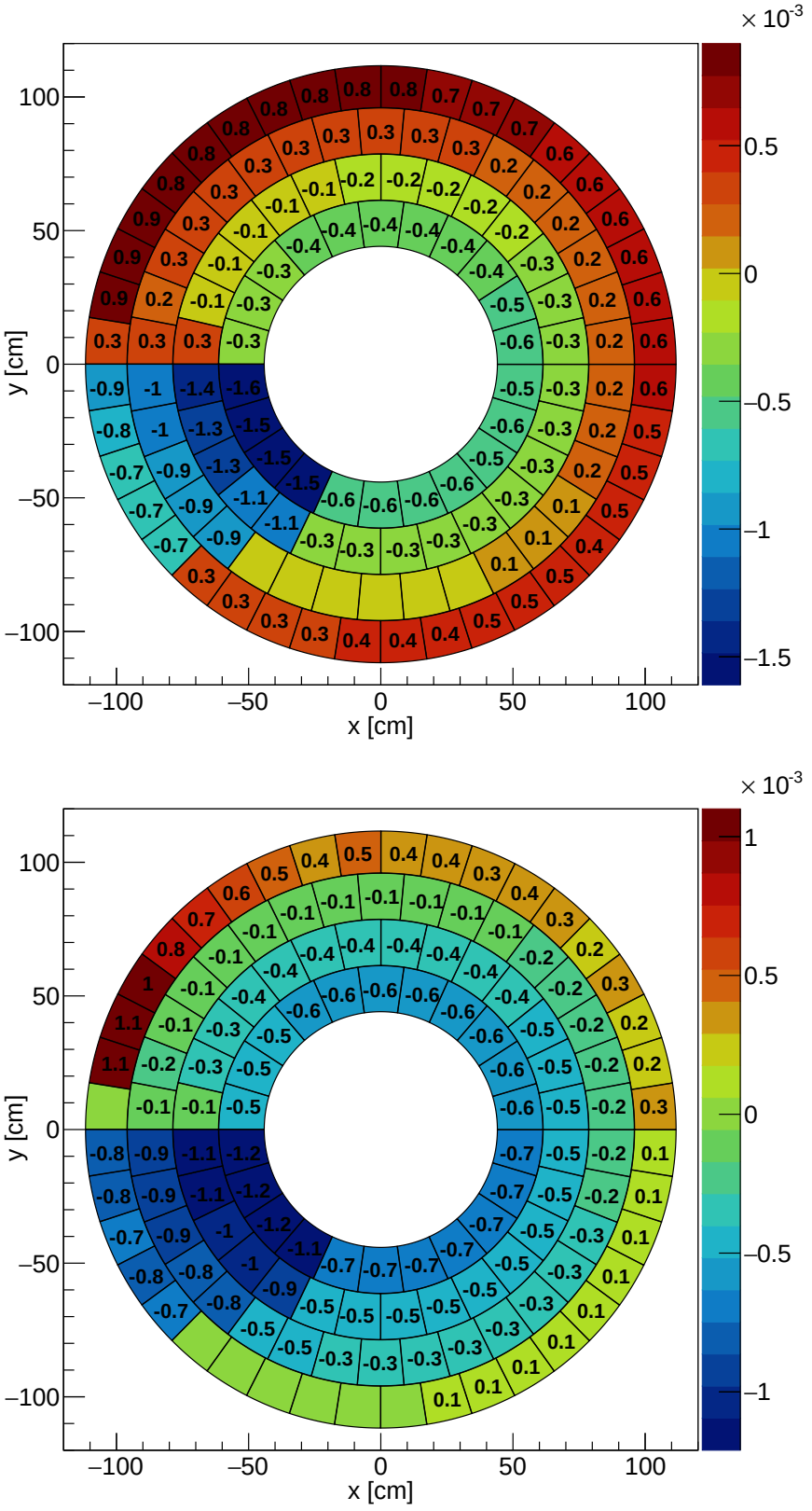

Figure 4.15: The distribution of the difference of the refractive indices of aerogel tiles on the aerogel plane. The difference is calculated as $n_{\text{tile}} - n_{\text{target}}$, where target values are 1.045 and 1.055 for the upstream and downstream tiles, respectively. The top figure shows the differences for the upstream tiles and the bottom figure shows the values for the downstream tiles. The average refractive indices of the installed tiles are 1.0449 ± 0.0006 and 1.0546 ± 0.0005.

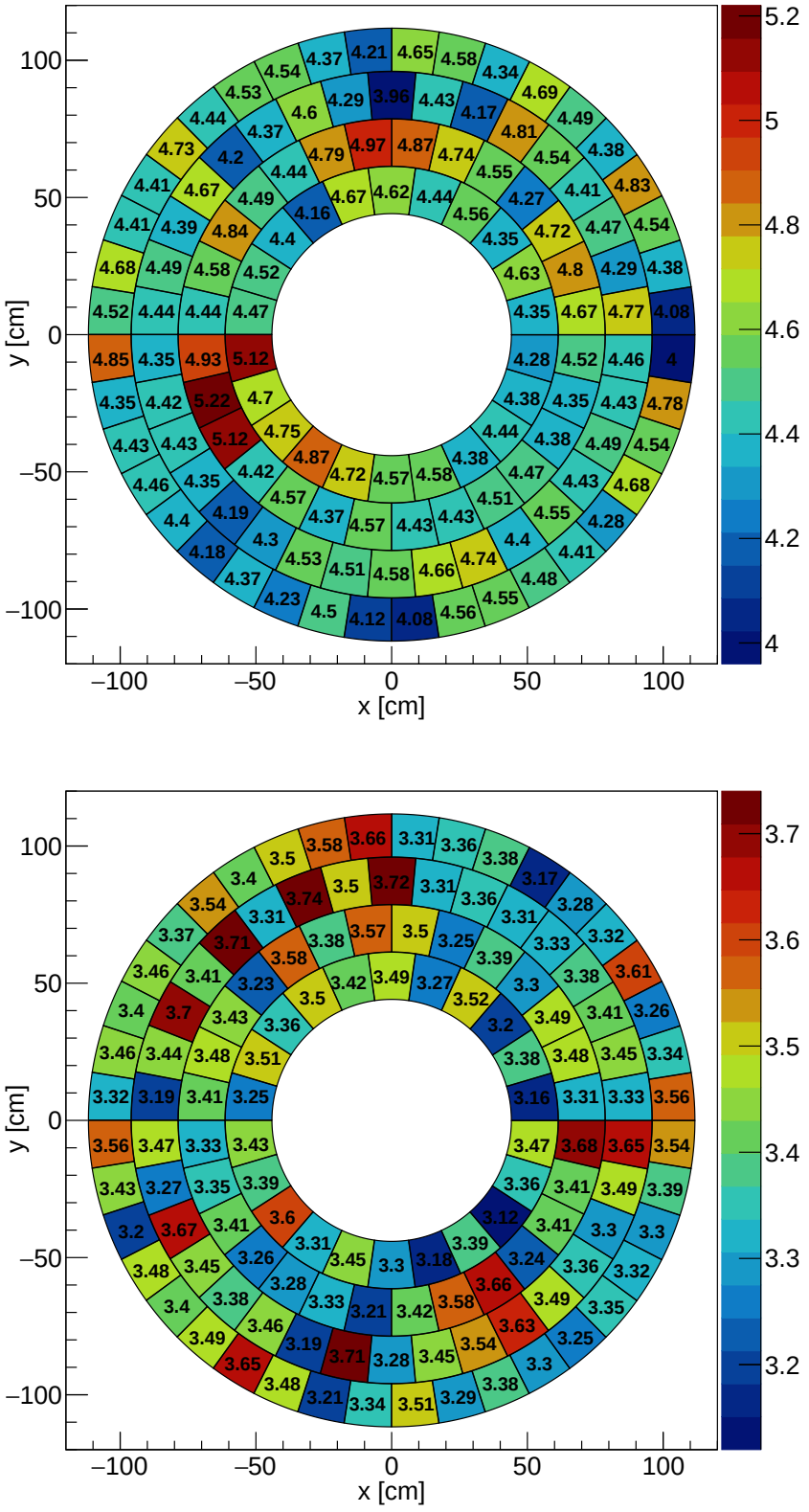

Figure 4.16: The distribution of the transmission lengths (in cm) of aerogel tiles on the aerogel plane. The top figure shows the transmission lengths for the upstream tiles and the bottom figure shows the values for the downstream tiles. The average transmission lengths of the installed tiles are (4.5 ± 0.2) cm for the upstream and (3.4 ± 0.1) cm for the downstream tiles.

4.4 Hybrid Avalanche Photo Detectors

The operational requirements for photo sensors were the capability of efficiently detecting single photons in a high magnetic field of $B = 1.5\,\mathrm{T}$, the tolerance to heavy neutron and gamma irradiation, and the ability to maintain the integrity of the operation during the expected experiment timeframe. The expected fluence in 10-year operation of Belle II at the target luminosity is about 10^{12} neutrons cm^{-2} (1 MeV equivalent) and the expected γ-ray dose is below 100 Gy [42]. This played a decisive role in choosing the Hybrid Avalanche Photo Detectors (HAPDs), that were newly developed in a collaboration with Hamamatsu Photonics.

4.4.1 The HAPD Structure

The HAPD (Fig. 4.17) is a $73\,\mathrm{mm} \times 73\,\mathrm{mm} \times 30\,\mathrm{mm}$ big vacuum tube with ceramic walls, made of quartz window with a bi-alkali photocathode and an electron multiplier. Its structure is similar to photomultipliers, but instead of using dynodes for charge amplification, HAPD uses a silicon avalanche photodiode. The avalanche photodiode (APD) is divided into 4 chips, which are further divided into 6×6 channels, each $4.9\,\mathrm{mm} \times 4.9\,\mathrm{mm}$ in size. The schematic depiction of the chip and channel layout is illustrated in Fig. 4.18. For a more detailed sketch of HAPD, refer to Appendix A.

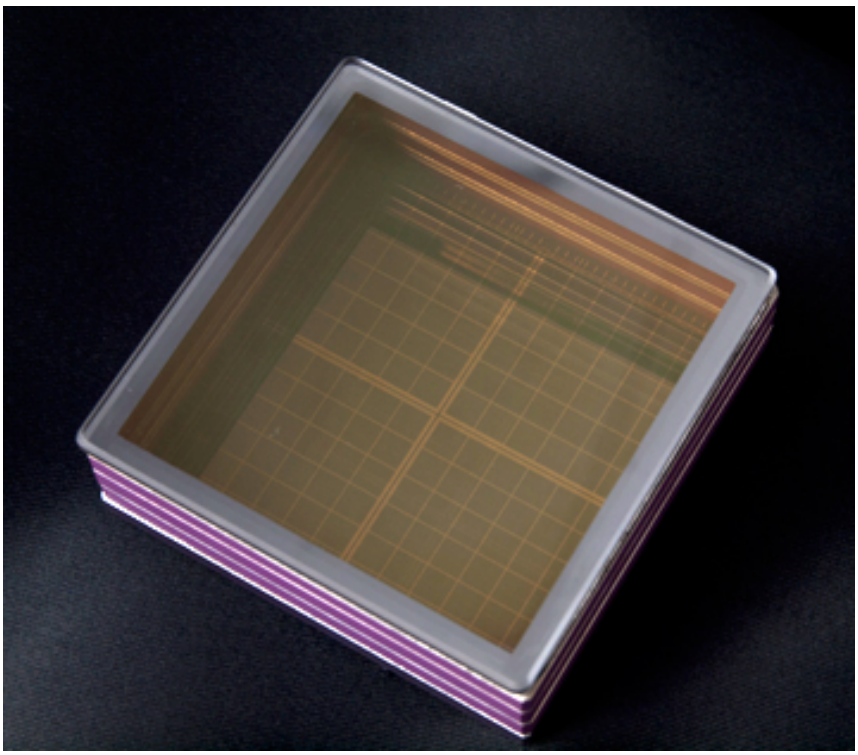

Figure 4.17: A Hybrid Avalanche Photo Detector (HAPD).

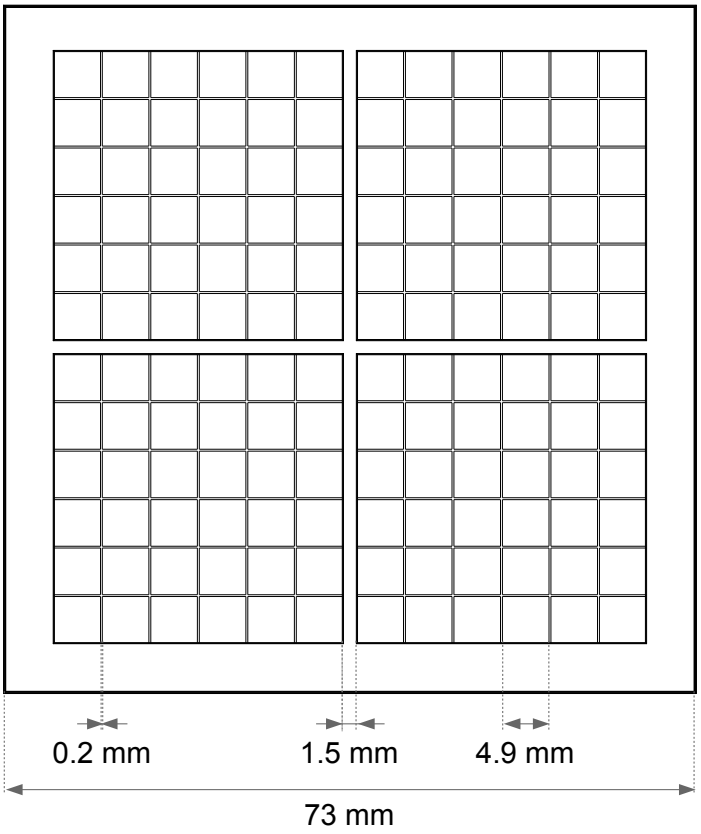

Figure 4.18: A schematic depiction of pixelated avalanche photodiodes (APDs) in HAPD.

4.4.2 Principle of Photon Detection

Photon detection starts after the Cherenkov photon enters the HAPD through the quartz window. The principle of detection is shown in Fig. 4.19.

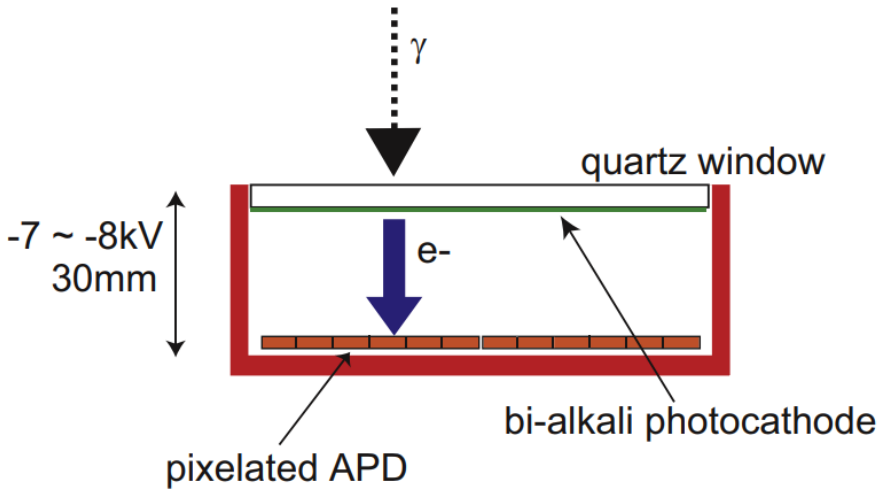

Figure 4.19: A schematic depiction of a single photon detection in HAPD [48].

A Cherenkov photon generates a photoelectron through a photoelectric effect in the bi-alkali photocathode on the bottom side of the quartz. The photoelectron is then accelerated in a vacuum in a high electric field that corresponds to the electric potential difference of 8.5 kV. The accelerated photoelectron hits the pixelated avalanche diode, depositing all of its energy and generating electron-hole pairs, which results in a signal amplification of $\sim$ 1700. Further charge multiplication occurs when the generated electrons create an avalanche inside the APD. The chosen bias voltages (typically between 320 V and 360 V) applied to APD multiply the charge by 40, resulting in a total signal amplification of the HAPD of approximately 7×10^4. The high electron multiplication is needed to achieve a sufficiently high S/N ratio for a single photon detection.

The electric field in a vacuum tube is perpendicular to the photocathode and the APD. Although the electrons have a spiral trajectory in a static magnetic field, the radius of their trajectory is very small, in the order of 0.1 mm. This is significantly less than the size of a channel (4.9 mm $\times$ 4.9 mm), which means that the hit on the sensor corresponds to the position of the photocathode hit.

To ensure homogeneous electric field in the APD, additional voltage (*guard voltage*) of 175 V is applied at the edges of the diodes. It should be applied before the bias voltage, preventing the leakage current getting too high and damaging the sensors. The schematic depiction of voltages, supplied to HAPD, is illustrated in Fig. 4.20.

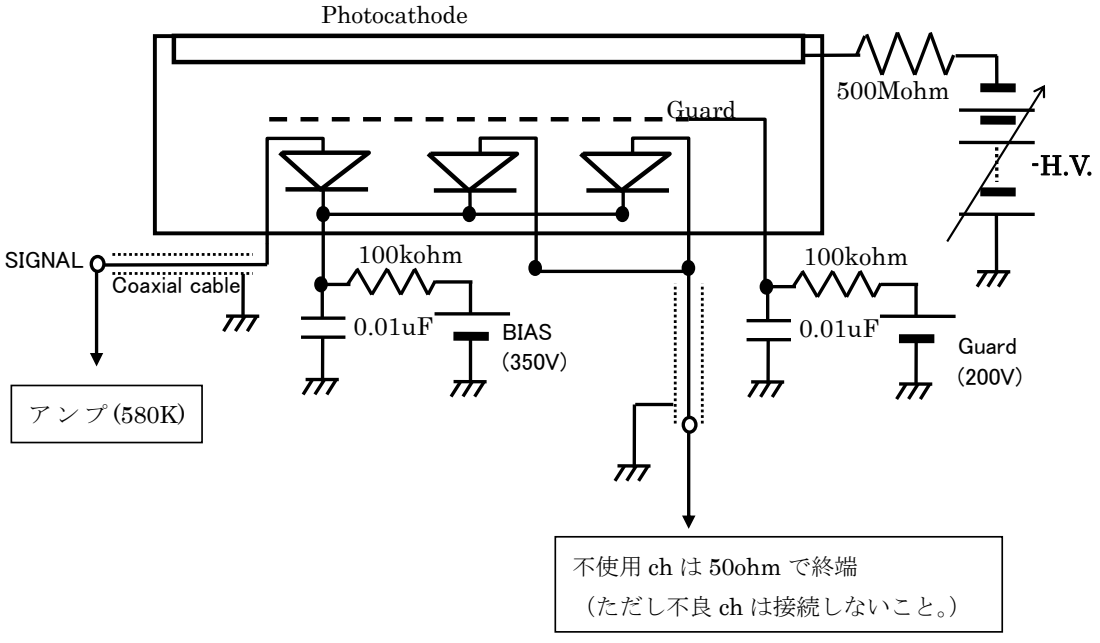

Figure 4.20: A schematic depiction of voltages, supplied to different parts of HAPD [36].

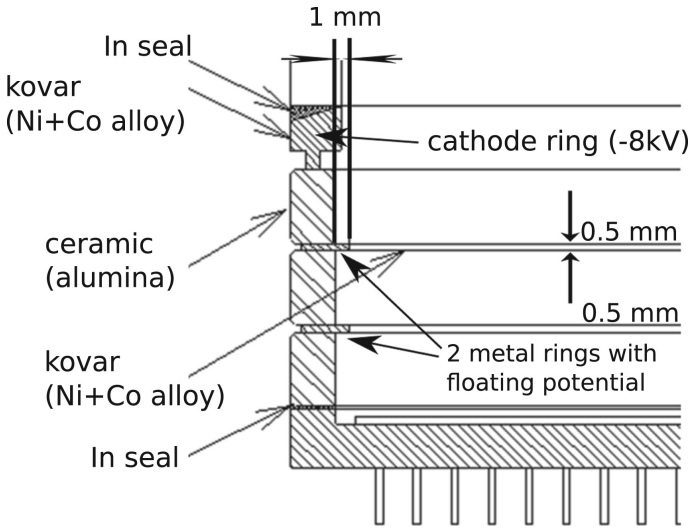

Figure 4.21: A side wall of the HAPD [49].

A side wall of the HAPD is presented in Fig. 4.21. The floating potential on the metal rings at the side wall, marked in the figure, was fixed with the division of the high voltage on the wall of HAPD. It was done using a high voltage board (a voltage divider circuit), shown in Fig. 4.22. The resistivity of high voltage boards, protected with epoxy layer, was measured as a function of temperature, as presented in Fig. 4.23. Temperature monitors were attached above and below the board, and the average value was used for the measurement. The precision of the current measurement was 1 µA, which is the reason for high steps between some of the measurements [50].

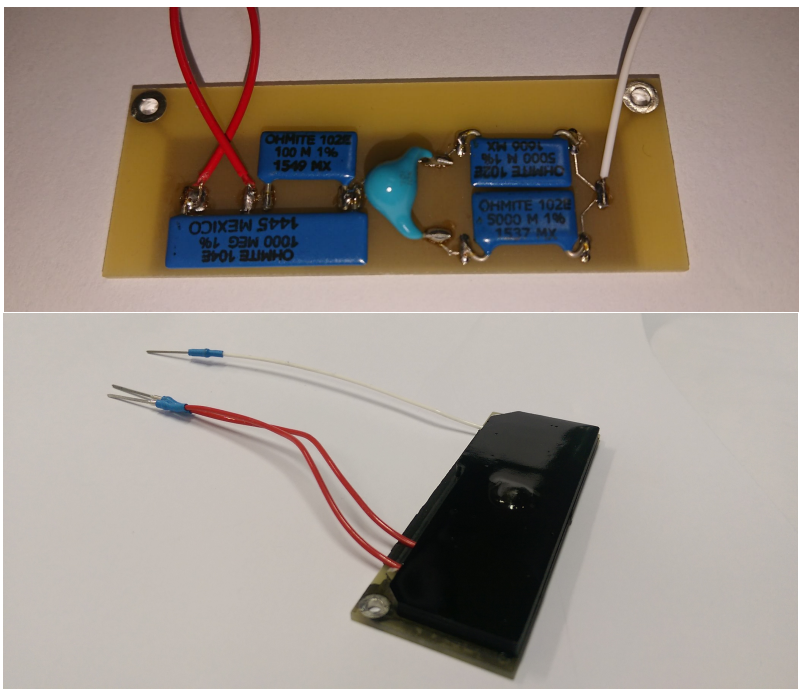

Figure 4.22: Top: A high voltage divider board, that was connected to the side wall of HAPD. Bottom: Before the assembly, the electronic components on the high voltage board were protected with an epoxy layer.

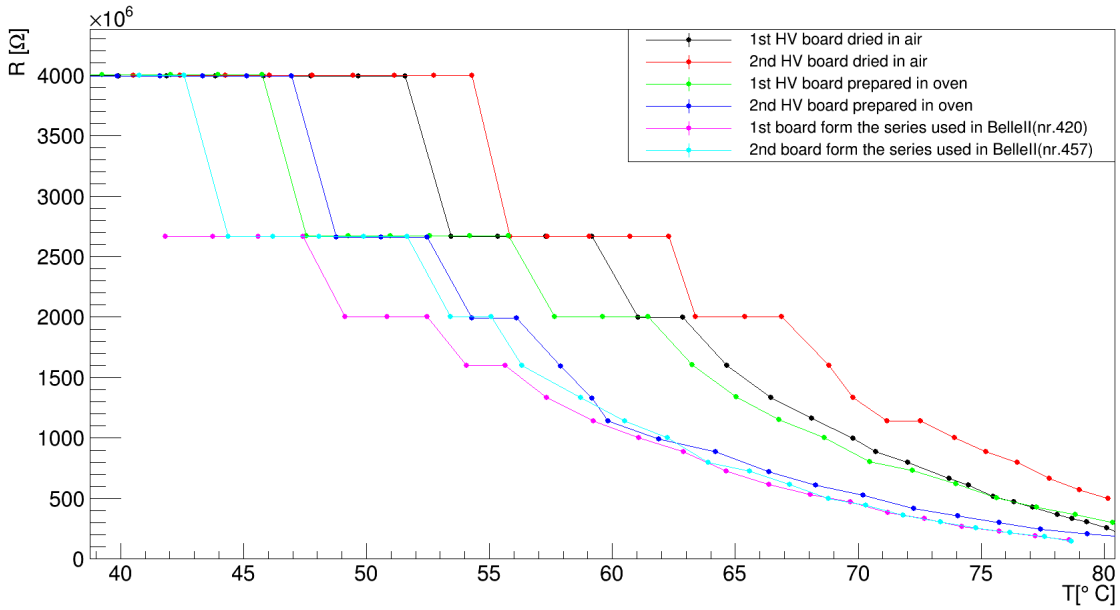

Figure 4.23: The resistivity of high voltage divider board at different temperatures [50]. The pink and turquoise curves present the sample boards from mass production for ARICH.

4.4.3 HAPD Operation Efficiency

Each HAPD channel has a different detection performance, which depends on:

- *Quantum efficiency (QE)*: The probability for the photon to electron conversion in the photocathode. It includes probability for a photoeffect and absorption. It is a function of photon wavelength (see Fig. 4.24).
- *Collection efficiency (CE)*: The fraction of charge collected inside photodiode in ARICH is almost 100 %.
- *Signal gain*: The product of bombardment and avalanche gain. Their dependencies on the sensor voltages are shown in Figs. 4.25 and 4.26.
- *Dark count rate*: The electric signals emitted when there is no incident photon (0.2/HAPD/event).

Quantum efficiency was at first measured by Hamamatsu Photonics. Each sensor was illuminated by laser with a wavelength of 400 nm over the surface of 60 mm × 60 mm in the center of HAPD. The average value of each module was calculated. The average QE for installed HAPDs is (32 ± 3) % (see Fig. 4.27). The wide spread of average quantum efficiencies is the result of an improved photocathode properties during the HAPD production period, as shown in Fig. 4.28.

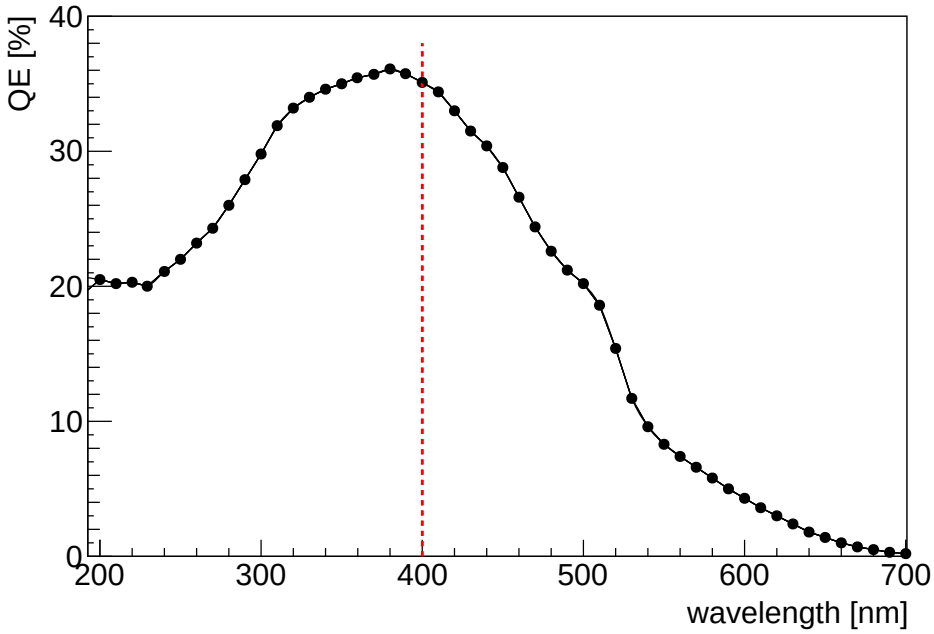

Figure 4.24: A photocathode quantum efficiency as a function of photon wavelength for the HAPD with serial number *KA0530* [51].

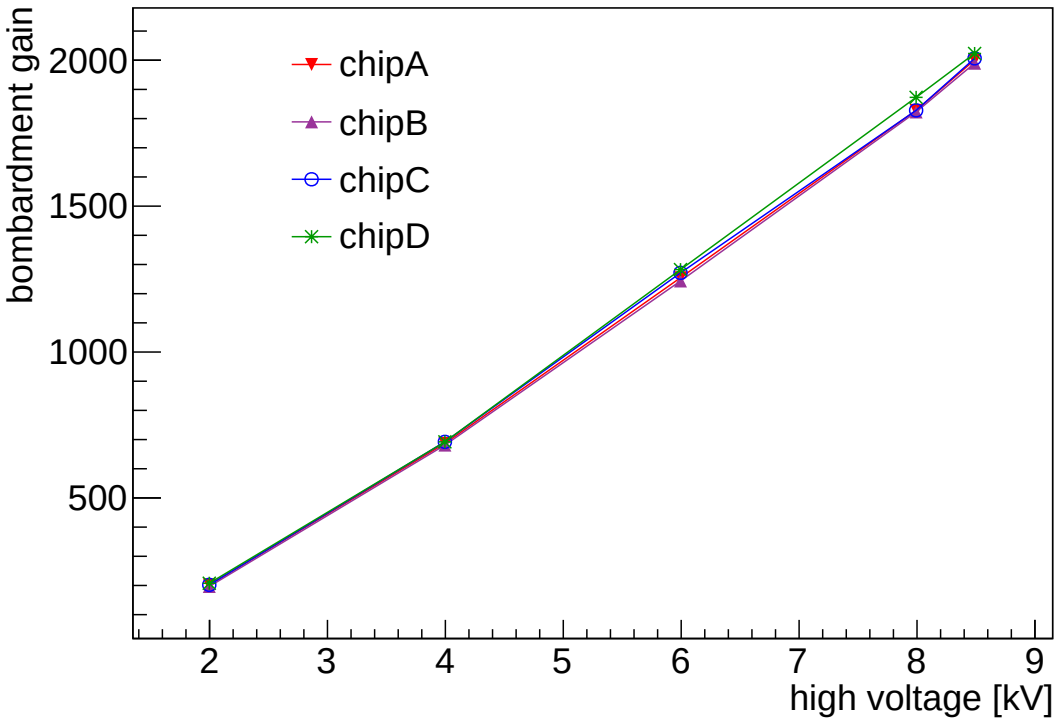

Figure 4.25: Bombardment gain as a function of high voltage for four chips of the HAPD with serial number *KA0530* [51].

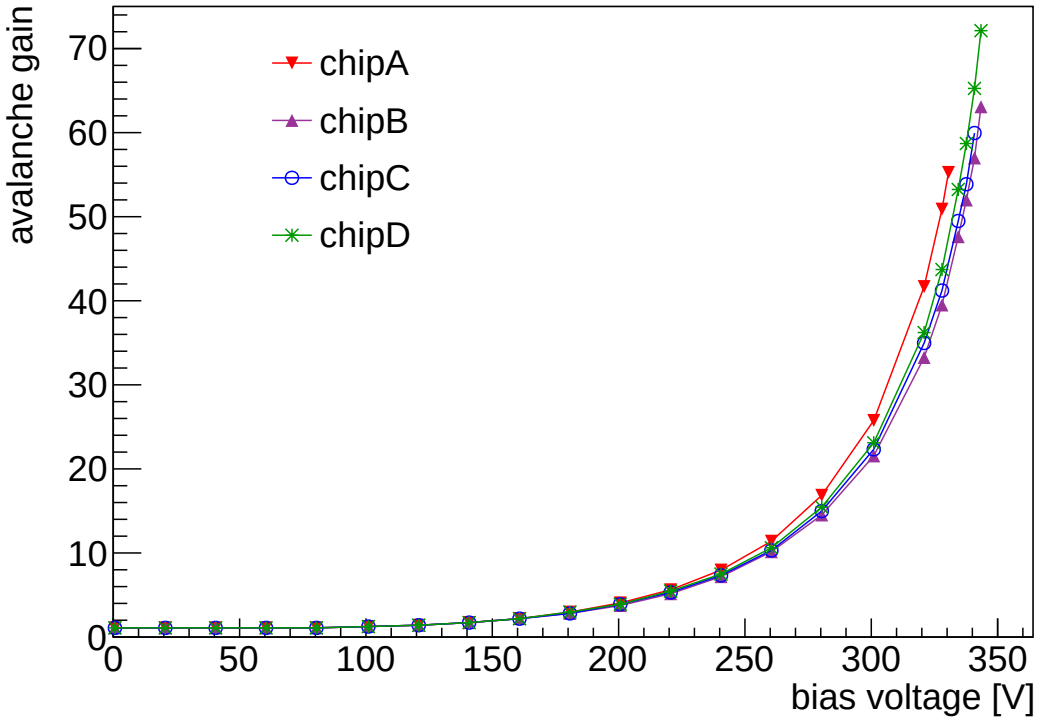

Figure 4.26: Avalanche gain as a function of bias voltage for four chips of the HAPD with serial number *KA0530* [51].

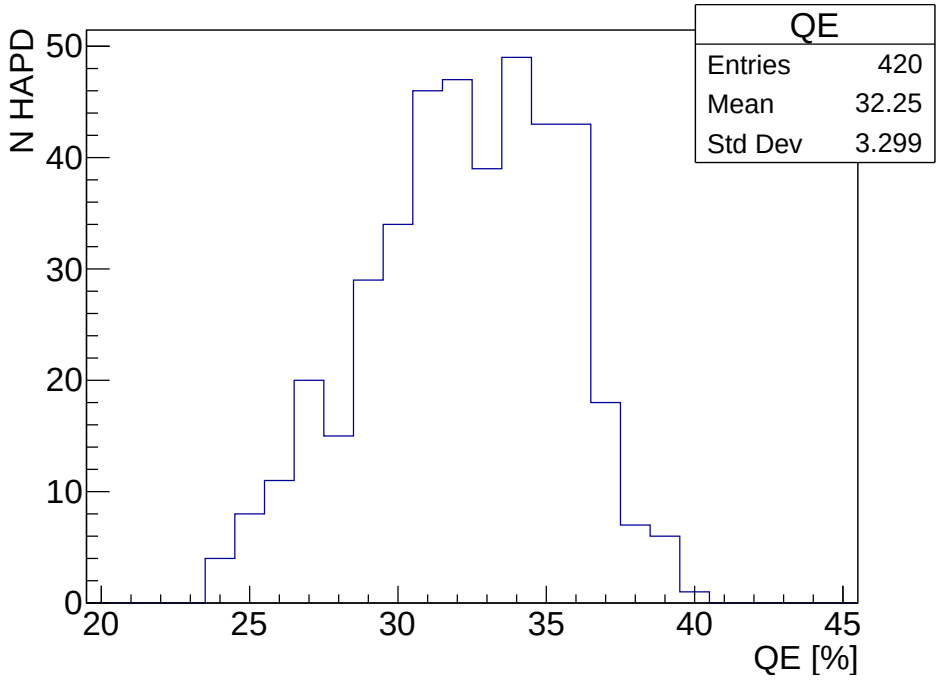

Figure 4.27: The distribution of HAPD quantum efficiency at 400 nm for all installed devices [51].

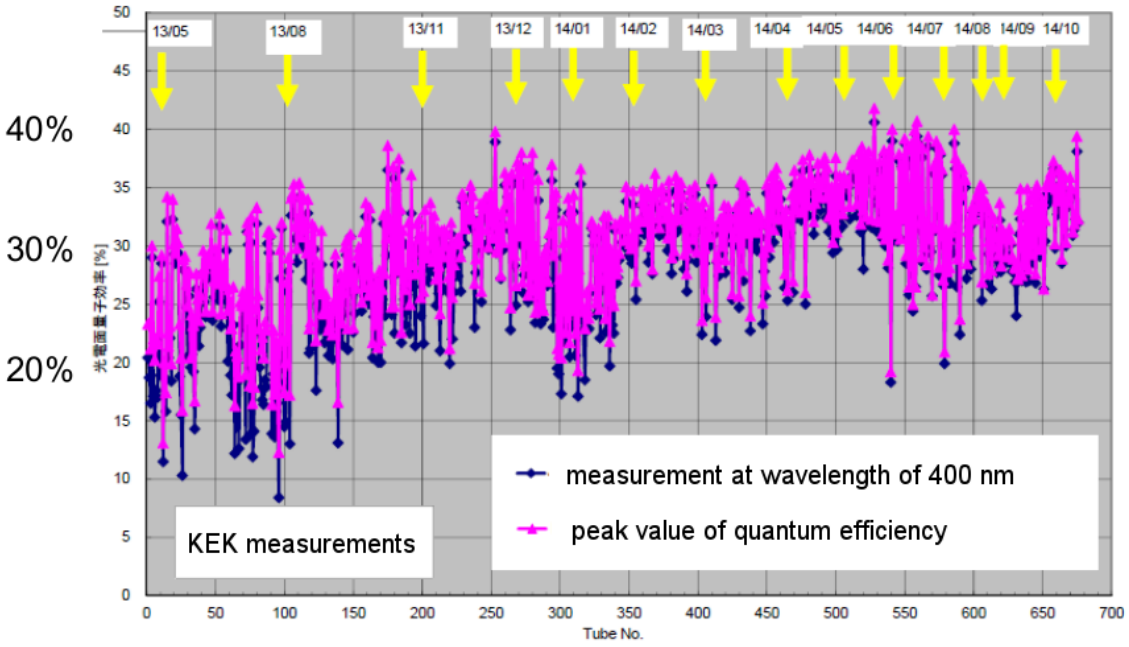

Figure 4.28: The HAPD quantum efficiencies for illumination with 400 nm and peak quantum efficiencies, measured at KEK [52]. The x-axis represents the sequential number of produced HAPD.

Quantum efficiency is not uniform over the whole photocathode; it is higher in the centre and lower at the edges. The non-uniformity is a result of its production method – a deposition of vaporized bi-alkali on the quartz window. To determine sensitivity of the photocathode as a function of position, the photocathode was illuminated in small discrete steps and the measured current was compared with the one from the reference photodiode [53]. The QE was calculated from the comparison of both currents for each step. The result of one scan is shown in Fig. 4.29.

The average quantum efficiency was calculated for the photocathode area that corresponds to each APD channel. A distribution of average quantum efficiency over a detector plane is presented in Fig. 4.30. HAPDs were installed to the detector frame with the tendency of the uniform QE over the sensor plane.

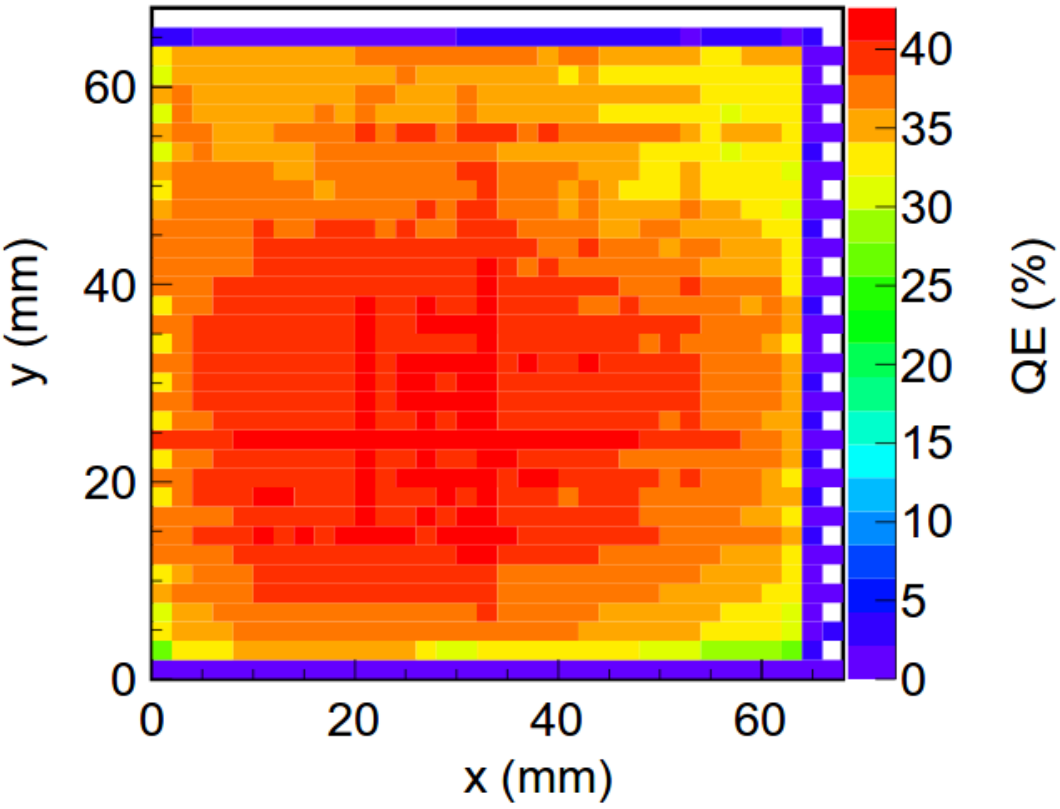

Figure 4.29: An example of a two-dimensional quantum efficiency scan [53].

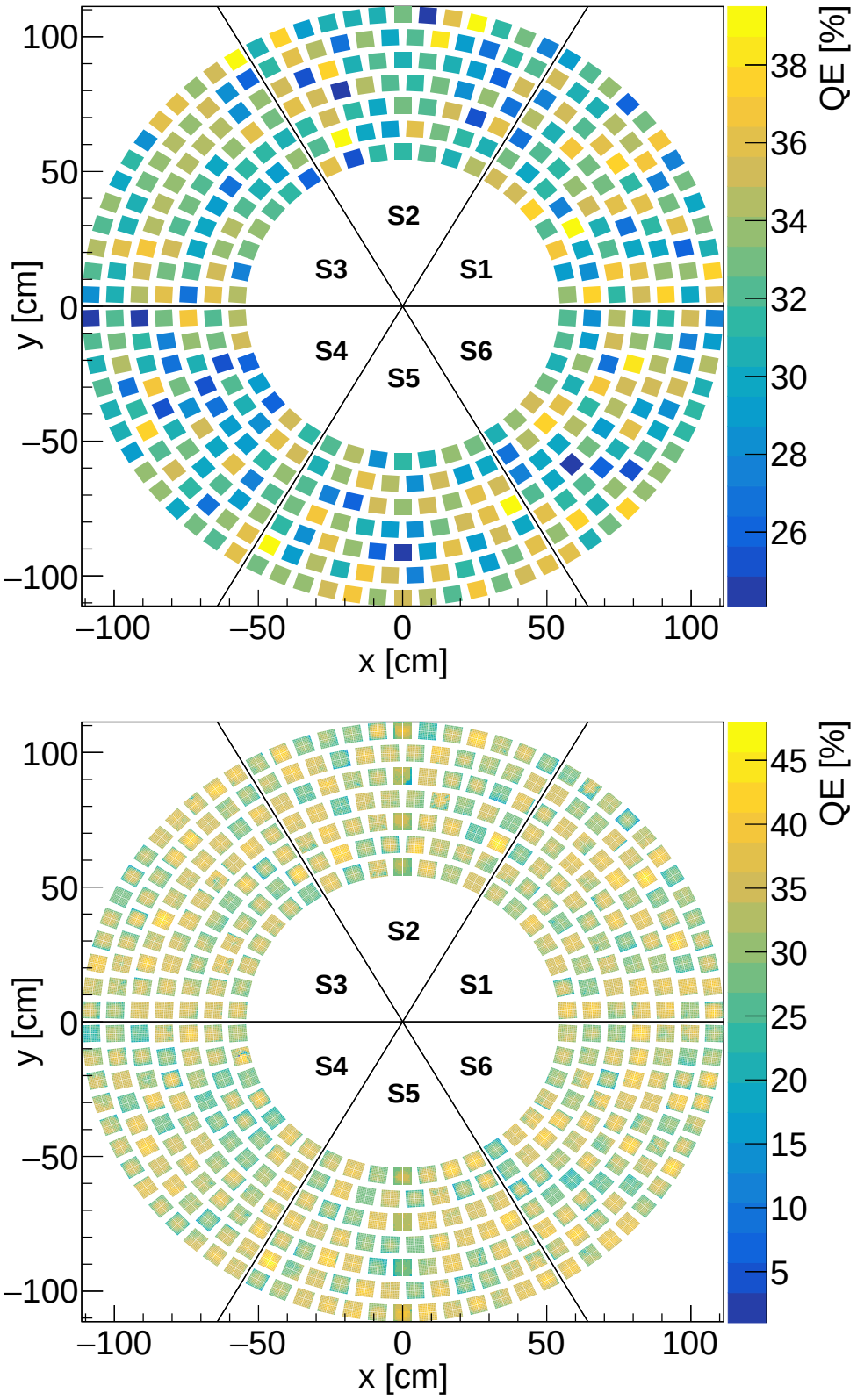

Figure 4.30: Top: The distribution of average HAPD quantum efficiency on the detector plane, measured with 400 nm illumination by Hamamatsu Photonics. The average value of QE of all installed HAPDs is (32 ± 3) %. Bottom: The distribution of average quantum efficiency corresponding to the area of each HAPD channel, measured at KEK. The average value of QE of all installed HAPDs is (32 ± 4) %.

4.5 Data Acquisition

HAPD signals are processed in several steps, from which the first two are specific for ARICH and the following steps are common for the entire Belle II:

1. A primary Front-End readout Board (FEB), attached directly to the back of the HAPDs, digitizes the signal.
2. Merger board collects data from several FEBs and reduces the data size by a zero hit supression.
3. High Speed Link Board (HSLB) applies masking of predefined mapping of unused read out channels.
4. A Common Pipelined Platform for Electronics Readout (COPPER) merges data.
5. Read-Out PCs (ROPC), High Level Trigger (HLT) and Event Builders (EB) further merge, process and skim data on the fly before storing it.

Apart from the signal processing chain, there is a Front-end Timing Switch (FTSW) system, distributing trigger signals among the subsystems and synchronizing them. The Belle II data acquisition is able to cope with a frequency of 30 kHz. More details about it can be found in [54].

The local electronic signal processing is performed in front-end and merger boards. The main parts of FEB are four ASICs *(Application Specific Integrated Circuit)*, one FPGA *(Field Programmable Gate Array)* and connectors for power supply and data cables [55]. Each ASIC is connected to one HAPD chip (36 channels). It amplifies and shapes analog signals from the HAPDs. Furthermore, it needs to discriminate the signals and digitize them. The main components and signal shape development in ASIC is presented in Fig. 4.31. The threshold for discrimination can be set by the electronic parameters, which are listed in Tables 4.1 and 4.2. A detailed information about the operation of ASICs are provided in [55].

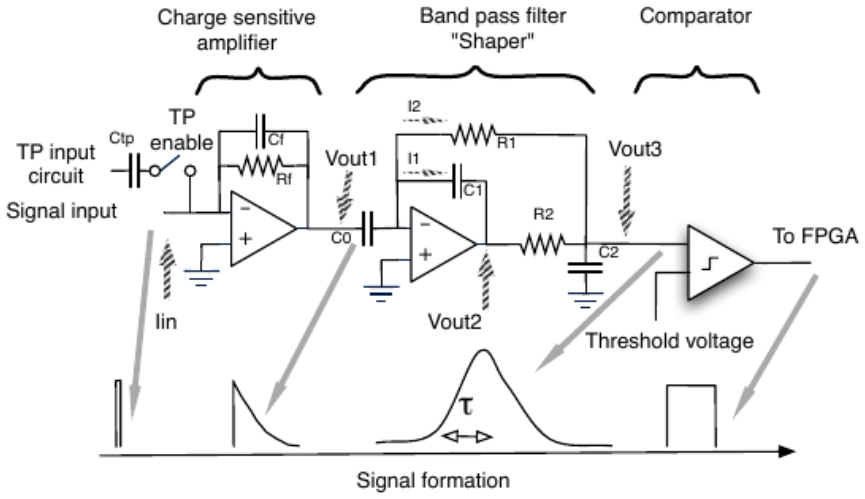

Figure 4.31: The main components of ASIC chip and the signal after each stage of processing [55].

Table 4.1: A list of ASIC parameters that can be set globally for all channels [56].

Name	Function
PHASECMPS	Reverse transfer capacitance for phase compentation
GAIN	Gain (3=min, 0=max)
SHAPINGTIME	Time constant of the shaper (0=min, 3=max)
COMPARATOR	Selection of the comparator (0=unipol, 1=diff)
VRDRIVE	Output drive
MONITOR	Selection of the monitor signal
ID	9 bit chip ID (0x181); read-only

Table 4.2: A list of ASIC parameters that can be set for each channel [56].

Name	Function
DECAYTIME	Decay time of the preamplifier
OFFSET	Coarse offset adjustment
FINEADJ_UNIPOL	Fine offset adjustment for unipolar comparator
FINEADJ_DIFF	Fine offset adjustment for differential comparator
TPNEB	Test pulse enable (1=disable, 0=enable)
KILL	Disable the channel (1=disable, 0=enable)

FPGA, a matrix of configurable logic blocks, is made of a control mechanism and a readout system. Besides the data processing, FEB provides connection for bias and guard voltage supply for HAPD, monitors temperatures, power supply voltages and currents, and can trigger an internal pulse for the test measurements. Parameter monitoring is described in [57], whereas the integrated circuits of the main front-end board operational units are presented in Appendix A. The ASICs are on the front side of the FEB, together with connector for HAPD pins. The FPGA and cable connectors are soldered at the back of the board. A schematic depiction of both sides is shown in Fig. 4.32.

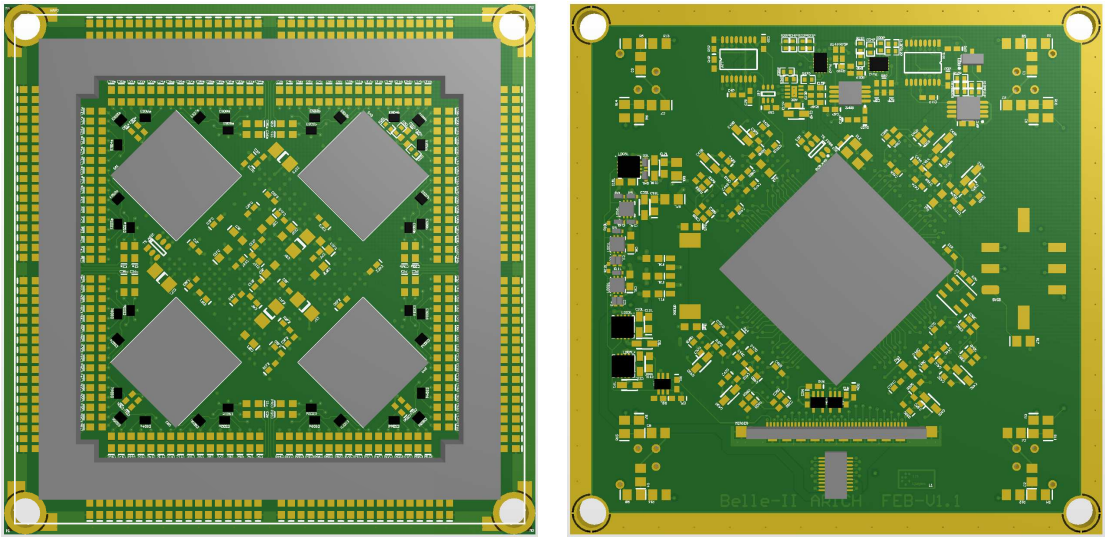

Figure 4.32: The ASIC (left) and FPGA (right) side of a front-end board [36].

Front-end boards constantly collect data and communicate with the merger board. Merger boards, presented in Figs. 4.33 and 4.34, take care of communication with trigger system and read the information from the front-end boards at the time window that corresponds to the trigger timing. One merger board is connected to five or six front-end boards, as presented in Fig. 4.35. Mappings of bias and high voltage cables can be found in Appendix B.

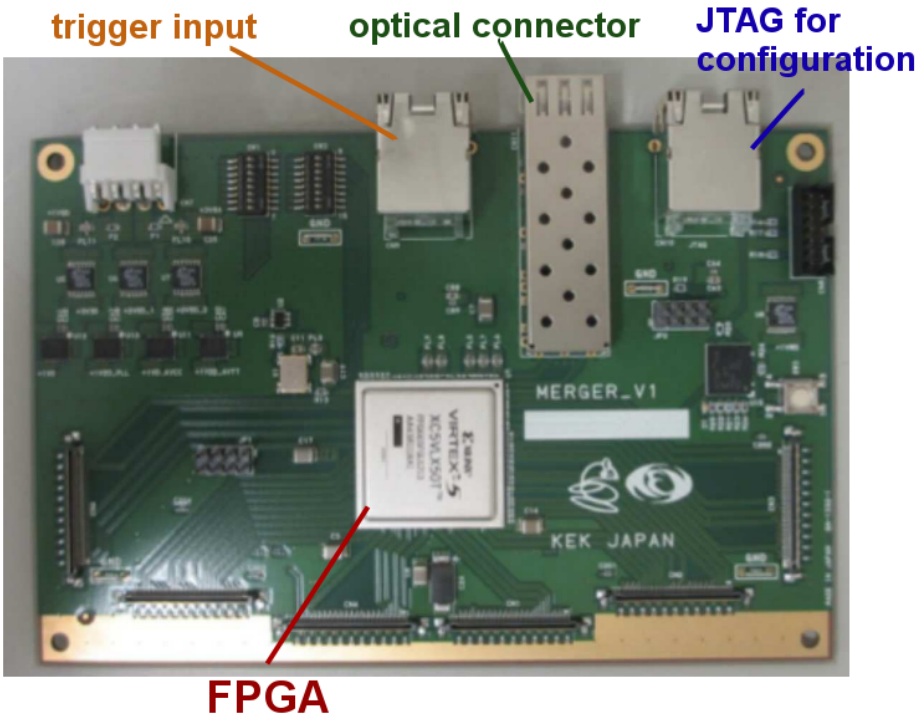

Figure 4.33: Merger board with labelled main components [55]. Optical fibers are used for communication with Belle II HSLB.

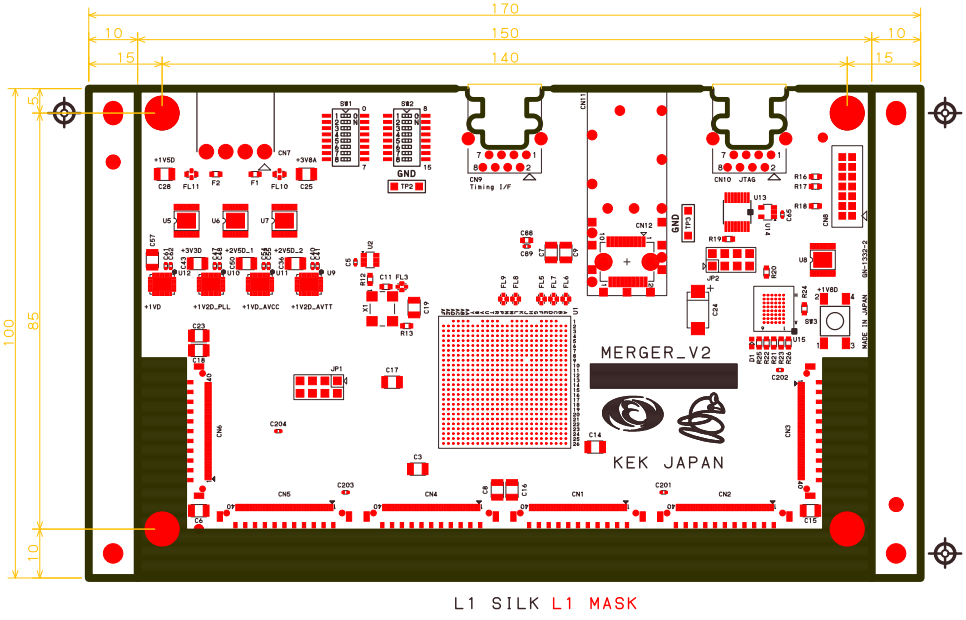

Figure 4.34: A scheme of merger board [36]. Measures are in units of [mm].

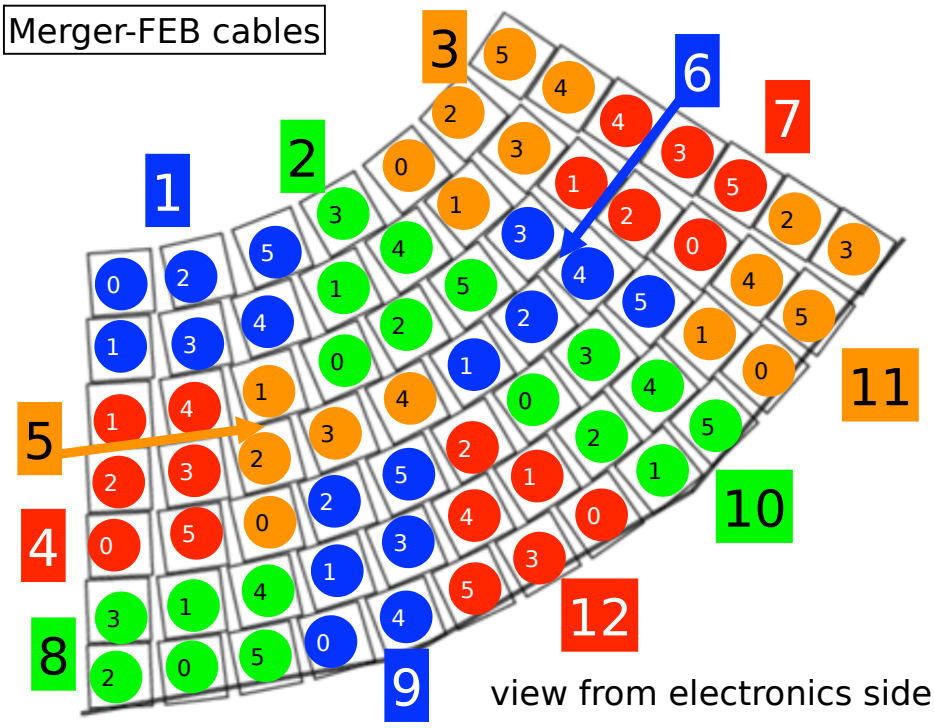

Figure 4.35: The mapping of connections between the front-end and the merger boards for one sector [36]. Ten merger boards have six front-end boars connected and two of them have five front-end boards connected.

4.6 Assembly

All ARICH components underwent several quality assessment measurements before the assembly. Tests of the HAPDs included measurements of leakage currents, determination of quantum efficiency and a performance test in a magnetic field. Voltages and currents on the front-end electronics were monitored and the response of each channel was tested. Currents through high voltage distribution boards were measured with an applied voltage of 9 kV. If all components reached the satisfactory quality and response, the final module was assembled and re-tested. Each sensor module consists of an HAPD, a front-end board and a high voltage distribution board, as seen in Fig. 4.36.

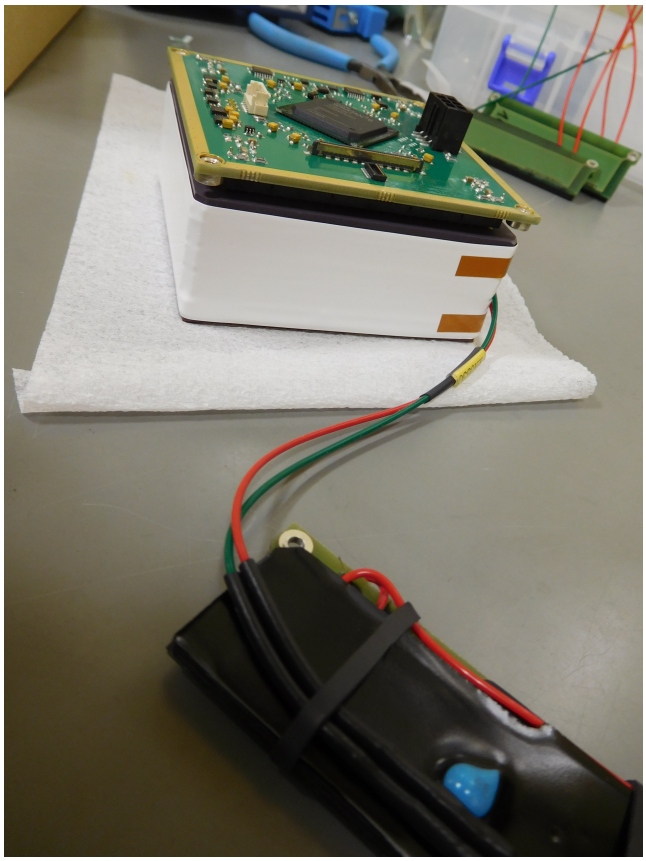

Figure 4.36: One detector module, composed of HAPD, front-end board and high voltage distribution board.

Detector modules were mounted to the aluminium structure, centred using conical screws and tightened equally with a torque screwdriver. The module installation was completed in May 2017. A part of the detector plane is shown in Fig 4.37. Aerogel tiles were installed into the frame at the beginning of 2017. They are fixed to the structure with very thin carbon fibre strings to keep them in place when the detector is in the vertical position. A part of the assembled aerogel plane is seen in Fig. 4.38.

Eighteen planar mirrors were installed at the sides of the detector plane. Their purpose is to reflect photons at the edges of the detector that would otherwise miss the active detector surface, which significantly improves the particle identification efficiency at the edges of the detector. Each mirror is 13.1 cm wide and has a useful reflective length of 37.3 cm, and it can reflect more than 85 % of photons in the wavelength interval between 250 nm and 600 nm. The front surface technology is used to reflect photons from the surface coating, to prevent the emission of additional Cherenkov photons in the glass. Mirrors can also be seen in the photo of the detector plane. The sensor and aerogel planes were combined, and aluminium panels were attached at the edges, as seen in Fig. 4.39.

Figure 4.37: A part of HAPDs mounted on aluminium structure. Planar mirrors are attached to the sides.

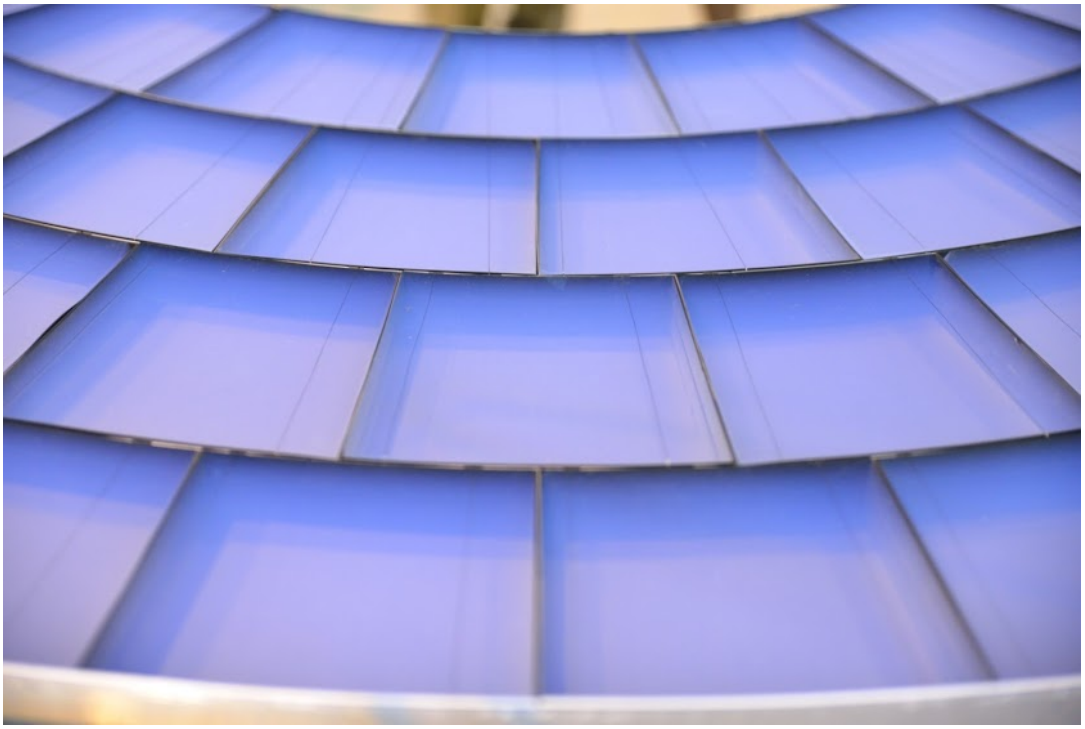

Figure 4.38: A part of the installed aerogel tiles [58].

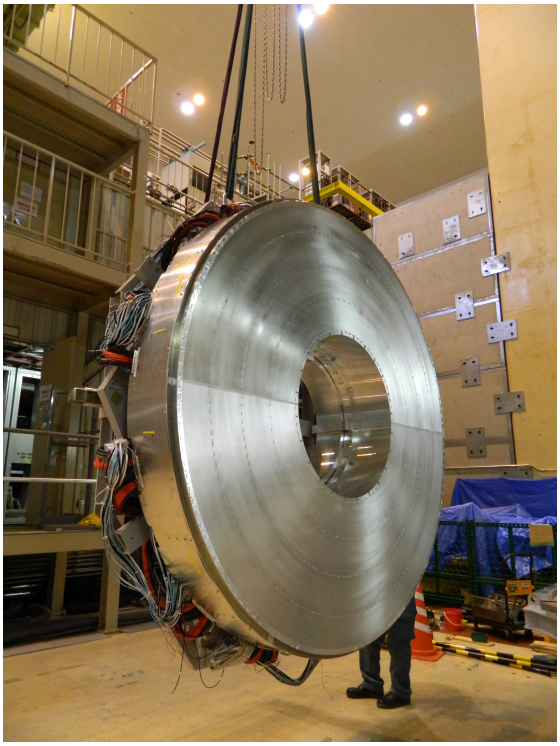

Figure 4.39: The ARICH cylinder after aerogel and sensor planes were combined.

Power supply and data cables were mostly custom-made on-site. Each sector required the following cables:

- Four high voltage cables
- Eight bias and guard bias cables
- 12 cables for low-voltage distribution boards
- 12 low voltage cables for merger boards
- 12 sets of merger board communication cables
- 70 short low voltage cables for supply between the low-voltage distribution board and front-end board
- 70 data cables for communication between front-end and merger boards

High and bias voltage cables are common for a group of modules. The lengths of their inner wires were adjusted on-site to reach the modules, yet not to have an overhead length. Pins were attached to the wires and they were tested before the mounting. A high voltage cable has 21 inner wires and 17 or 18 of them are connected to the modules.

Bias and guard voltage cables required more work, as one cable had 51 inner wires that had to be matched into bundles of five or six wires. After combining them by colour patterns, they were cut to the needed length, pins were attached and wires were fixed to the connector in a specific order. The current measurement confirmed if all wires have a connection and are ordered properly. An example of a custom-made bias cable is shown in Fig. 4.40.

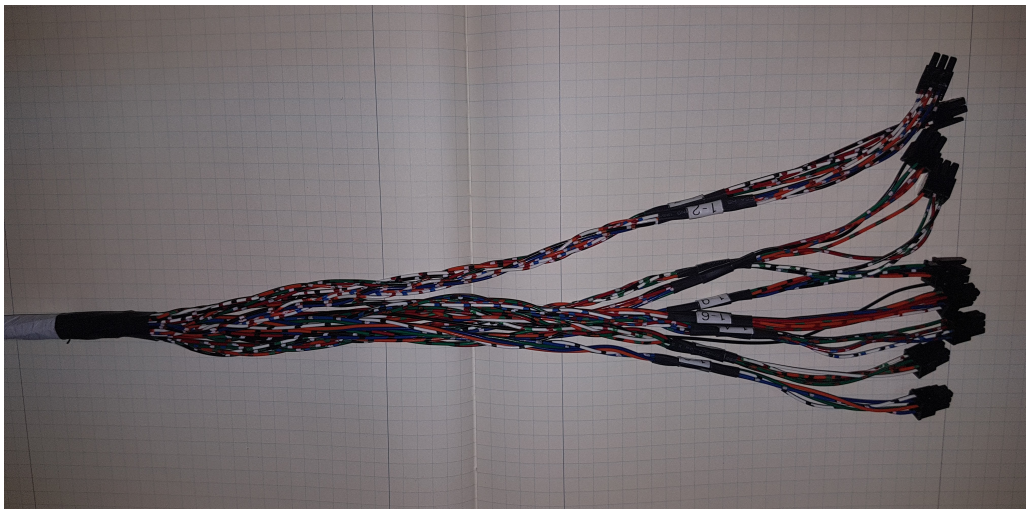

Figure 4.40: A custom-made cable for bias and guard voltage supply of nine modules [36]. The inner cable bundles lengths are equal, because it was used for testing.

Cables were attached at the end, together with merger boards. They had to fit into a limited space at the back of the detector plane, as seen in Fig. 4.41. The back of the detector was covered with aluminium back plane, divided into six panels. Small gaps between aluminium panels were covered with aluminium tape to ensure the lightproofness. ARICH was attached to ECL first, before they were transferred to their position in the Belle II detector.

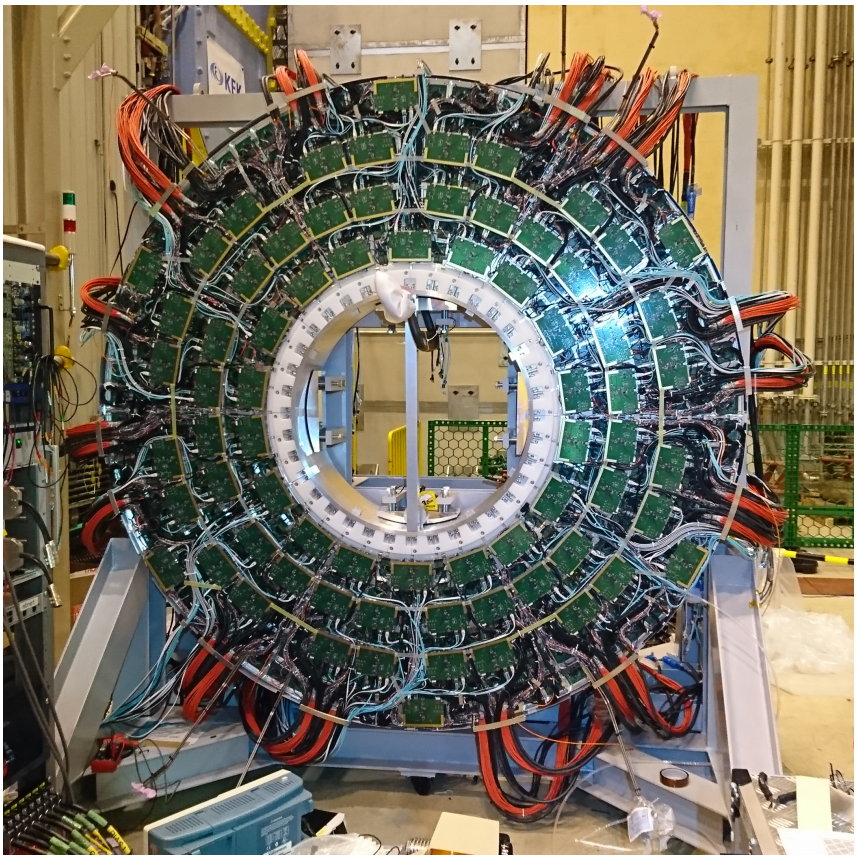

Figure 4.41: Back view of the ARICH with all cables and merger boards mounted.

CHAPTER 5

ARICH Simulation

5.1 Reconstruction Software

The analysis was done using BASF2 (***B**elle **A**nalysis **S**oftware **F**ramework II*) [59], a software framework developed for the Belle II experiment, used for both online and offline data processing. Particles are generated with respect to the chosen solid angle and vertex. In case of studies of physics processes, the EvtGen generator is used. A Geant4 toolkit [60, 61] then simulates a passage of particles through matter, including the detector geometry, particle propagation and physical processes. The framework is based on modules, sequential processing units with tasks varying from simple reading of files to complicated simulations or data reconstructions. The modules are based on the C++ programming language [62] and they are executed using python script [63]. A user can determine the order of modules with respect to the purpose of their work, such as data analyses, simulation studies, displaying events etc, as shown in Fig. 5.1. Modules use parameters from the database, a central storage, including information about the detector geometry, sensor properties and calibration constants. The temporary storage is called datastore and it is accessible from all the modules in a chain. It stores the processed data for each event, such as detector hits and reconstructed track information. The output of BASF2 module chain is saved in root files [64].

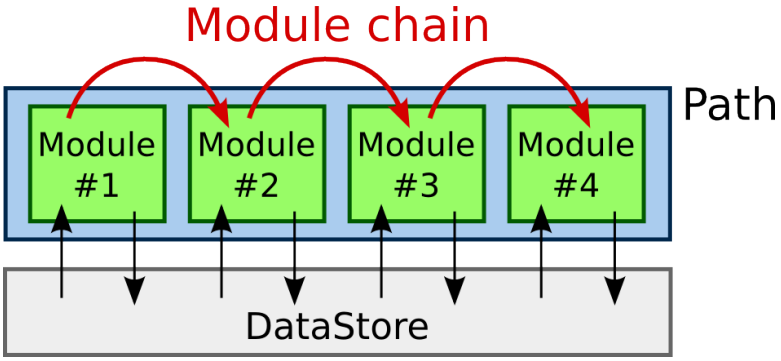

Figure 5.1: The workflow of BASF2 software framework.

5.2 Construction of Maximum Likelihood Function

ARICH uses the maximum likelihood function to determine the identity of charged particles. The basic principle of ARICH reconstruction module follows a few steps:

1. It requires particle track information, that is calculated from the hits in tracking system (PXD, SVD, CDC). A detailed description of tracking algorithms can be found in [65]. Track is extrapolated from CDC into ARICH.

2. Digitized ARICH electronics signals are converted into positional hit information.

3. Maximum likelihood function is constructed for every track that enters ARICH.

A differentiation between kaons and pions is performed by calculating a maximum likelihood function. The basic construction of the likelihood function follows P. Baillon [66] and R. Forty [67]. The likelihood function is constructed in ARICH reconstruction module for each event and evaluated for all five mass hypotheses (for pion, kaon, proton, electron and muon).

For each mass hypothesis, the likelihood function is defined as a product of probabilities p_i for all individual channels i to be hit:

$$\mathcal{L} = \prod_{\text{all channels}} p_i \tag{5.2.1}$$

The probability density function follows the Poissonian distribution:

$$p_i = \frac{e^{n_i} n_i^{m_i}}{m_i!}, \tag{5.2.2}$$

where n_i is an expected (i.e. calculated) total number of hits and m_i is a detected number of hits. The number of hits per channel is not counted in ARICH. The only output information is whether there was a hit in a channel or not, so the probabilities are grouped into two contributions:

$$p_i = \begin{cases} e^{-n_i} & \text{for non-hit channels} \\ 1 - e^{-n_i} & \text{for hit channels} \end{cases} \tag{5.2.3}$$

Using eq. 5.2.3, the likelihood function can be written as:

$$\mathcal{L} = \prod_{\text{all channels}} p_i = \prod_{\text{non-hit}} e^{-n_i} \times \prod_{\text{hit}} \left(1 - e^{-n_i}\right) \tag{5.2.4}$$

Taking the logarithm of likelihood function, the algorithm is simplified, because the average number of hits needs to be calculated for the hit channels only:

$$\begin{aligned}
\ln\mathcal{L} &= \sum_{\text{non-hit}}(-n_i)+\sum_{\text{hit}}\ln\left(1-e^{-n_i}\right) = \\
&= \sum_{\text{non-hit}}(-n_i)+\sum_{\text{hit}}(-n_i)-\sum_{\text{hit}}(-n_i)+\sum_{\text{hit}}\ln\left(1-e^{-n_i}\right) = \\
&= \sum_{\text{non-hit}}(-n_i)+\sum_{\text{hit}}(-n_i)+\left(-\sum_{\text{hit}}(-n_i)+\sum_{\text{hit}}\ln\left(1-e^{-n_i}\right)\right) = \\
&= -\left(\sum_{\text{non-hit}} n_i+\sum_{\text{hit}} n_i\right)+\sum_{\text{hit}}\ln\left(e^{n_i}-1\right)
\end{aligned} \tag{5.2.5}$$

The sum $\left(\sum_{\text{non-hit}} n_i + \sum_{\text{hit}} n_i\right)$ is a number of total expected hits N, whose value is mass hypothesis dependent. The $\ln\mathcal{L}$ can be written as:

$$\ln\mathcal{L} = -N + \sum_{\text{hit}}\ln\left(e^{n_i}-1\right), \tag{5.2.6}$$

where n_i is a sum of signal (n_i^s) and background (n_i^b) contributions. The main background contributions are the Rayleigh scattering of the Cherenkov photons and the electronics noise. The latter one was estimated from the properties of electronics, while the first one is correlated with the signal and is included into the signal contribution. For the physical analyses, the uncorrelated background rates will be more precisely determined from the studies of random trigger events.

The signal contribution is a sum of contributions of all radiator layers $n_i^s = \sum_r n_{i,r}^s$. The expected number of hits on the channel can be analytically calculated for each aerogel layer as:

$$n_{i,r}^s = \varepsilon_i n_{t,r}\int_{\Omega_i} S_r(\theta_r,\phi_r)d\theta_r d\phi_r, \tag{5.2.7}$$

where ε_i is a quantum efficiency and $n_{t,r}$ is a number of photons, propagated from one aerogel tile. $S_r(\theta_r,\phi_r)$ is a hit distribution over the ring:

$$S_r(\theta_r,\phi_r) = \frac{1}{2\pi}\frac{1}{\sqrt{2\pi}\sigma_{\theta_r}}e^{-\frac{(\theta_r-\theta_r^h)^2}{2\sigma_{\theta_r}^2}}, \tag{5.2.8}$$

where θ_r^h is an expected Cherenkov angle for a given mass hypothesis and aerogel layer, θ_r is a measured Cherenkov angle for each aerogel layer and σ_{θ_r} is its uncertainty, ϕ_r is an azimuthal angle and Ω_i is a solid angle that is covered by the i-th channel. Angles, corresponding to the particle track and emitted photons, are defined also in the Fig. 5.2. The integral of $S_r(\theta_r,\phi_r)$ over solid angle Ω_i gives a proportion of the signal, expected on each channel. The schematic depiction of the expected signal distribution and channel coverage is shown in Fig. 5.3. The analytical calculation of the $\int_{\Omega_i} S_r(\theta_r,\phi_r)$ integral can be found in [68].

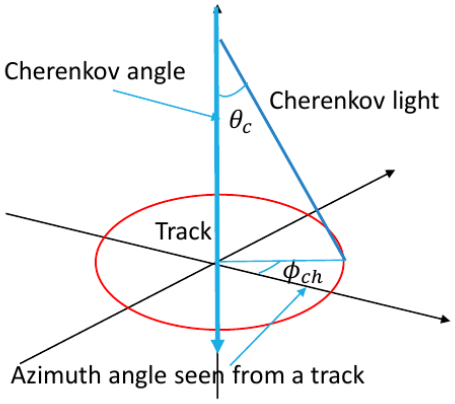

Figure 5.2: The definition of the Cherenkov angle and the azimuthal angle, that corresponds to the detected Cherenkov photon, in a coordinate system of the track [69].

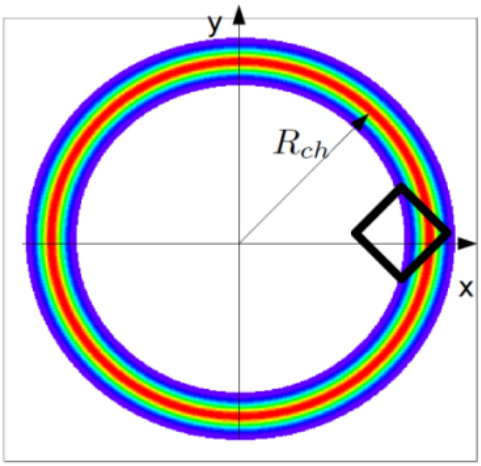

Figure 5.3: A schematic depiction of Gaussian photon distribution around the ring and one channel on a detector plane [70]. The sizes of the ring and the channel are not scaled.

The likelihood function is calculated for all mass hypotheses. Two of them are normally compared, in case of ARICH the likelihoods for a kaon and a pion.

5.2.1 Efficiencies

The cumulative distribution of logarithms of likelihoods for kaon and pion mass hypotheses is shown in Fig. 5.4. From now on, the neutral logarithm will be marked with log. To differentiate between both particles, a limit value of $\log \mathcal{L}_K - \log \mathcal{L}_\pi$ is determined. Particles with $\log \mathcal{L}_K - \log \mathcal{L}_\pi$ value above (below) the chosen limit are classified as kaons (pions). Since this criterion sets the limit for particle identity, the chosen limit is called the PID cut.

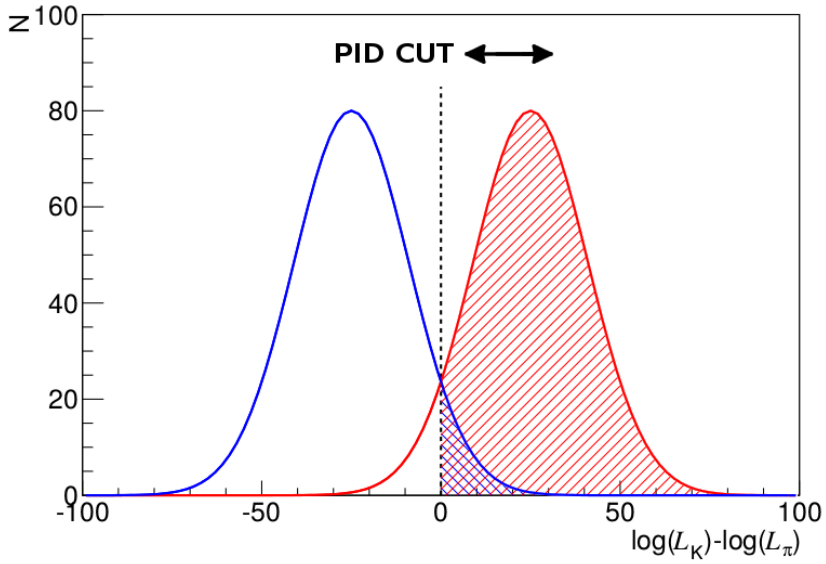

Figure 5.4: The difference of $\log \mathcal{L}$ for two mass hypotheses for two types of charged particles. The PID cut can be moved and the integral of particles with $\Delta \log \mathcal{L}$ above the cut are identified as kaons. The red curve represents the true kaons and the blue one the true pions.

By applying different PID cuts to a cumulative likelihood distribution, as presented in the figure, the kaon identification efficiency $\varepsilon_{K\to K}$ and pion misidentification probabilities $\varepsilon_{\pi\to K}$ are calculated. The kaon identification efficiency and pion misidentification probability are then calculated as:

$$\varepsilon_{\pi\to K} = \frac{N^K_{pass}}{N^K_{all}} \quad \text{and} \quad \varepsilon_{\pi\to K} = \frac{N^\pi_{pass}}{N^\pi_{all}}, \tag{5.2.9}$$

where N^K_{all} (N^π_{all}) is the number of all kaons (pions) that enter ARICH, and N^K_{pass} (N^π_{pass}) is the number of particles that pass the PID cut for a kaon.

5.3 Basic ARICH Performance Studies

A performance of ARICH was studied using simulation, with whole Belle II geometry included. For basic studies, a sample of 5×10^5 charged kaons and 5×10^5 charged pions with momenta between 0.5 GeV/c and 4.0 GeV/c (where ARICH is expected to efficiently differentiate between kaons and pions) originating from the interaction point was used as a particle source. Particles were uniformly distributed over the polar and azimuthal angles. The interaction point of the charged particle with aerogel and its momentum, both obtained from the tracking system, and hits on the ARICH detector plane were used to reconstruct Cherenkov photons. An example of a simulated kaon track and emitted Cherenkov photons in ARICH is shown in Fig. 5.5.

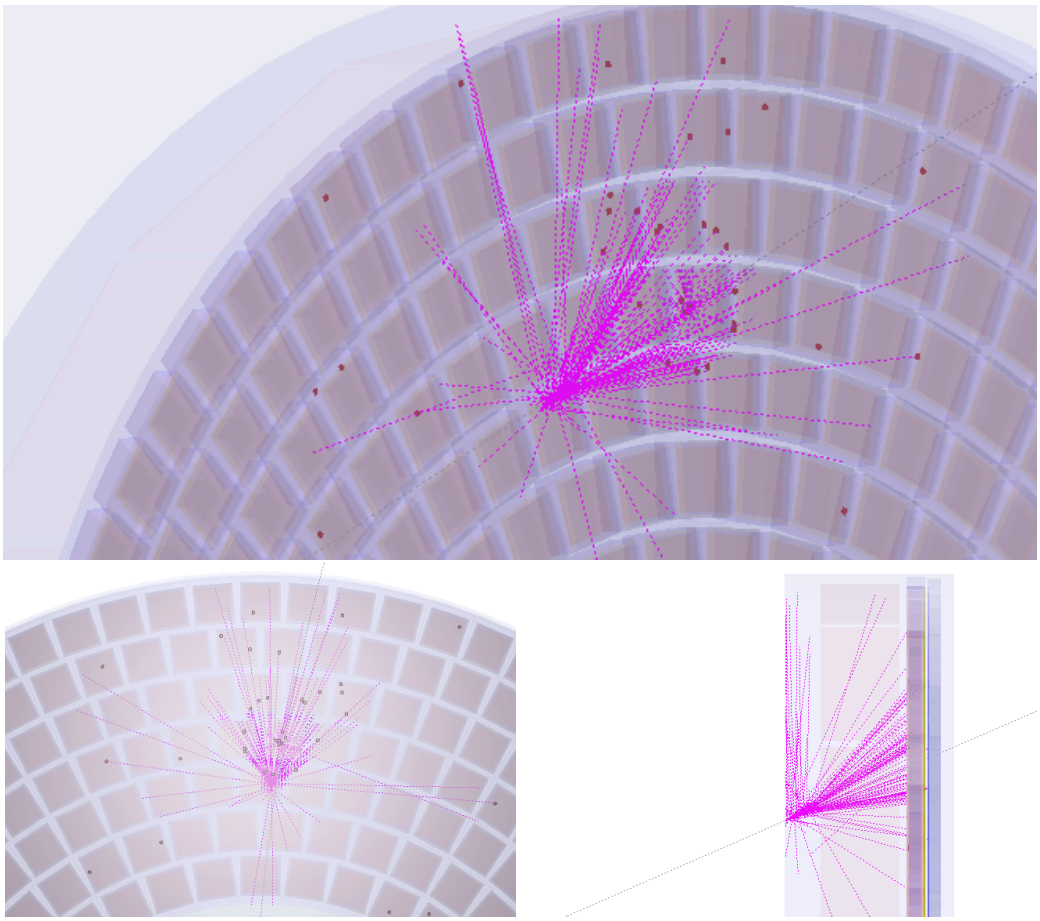

Figure 5.5: A simulated single kaon track and emitted Cherenkov photons in ARICH. The same event is shown from three different angles.

The reconstructed charged particles and Cherenkov photons were used for particle identification. The cumulative momentum and azimuthal angle distributions of reconstructed particles are shown in Figs. 5.6 and 5.7.

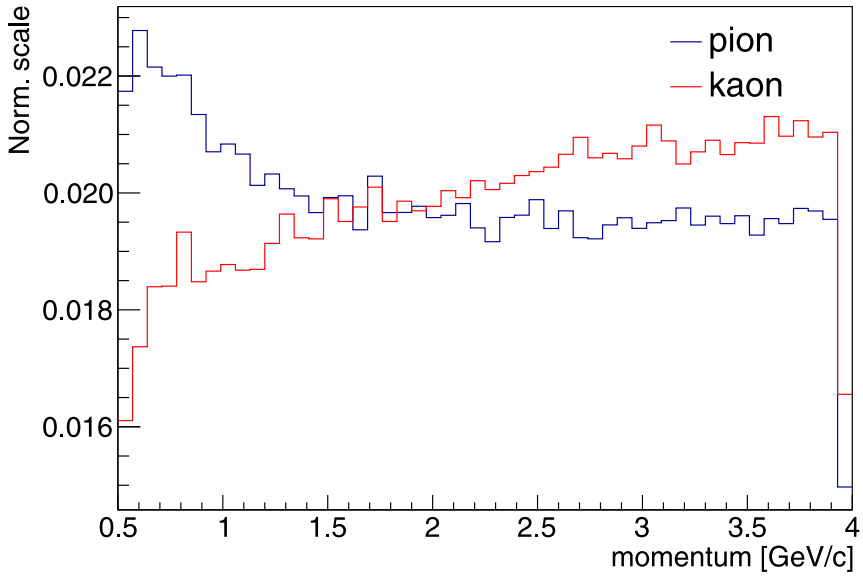

Figure 5.6: A cumulative distribution of the momentum of kaons (red) and pions (blue).

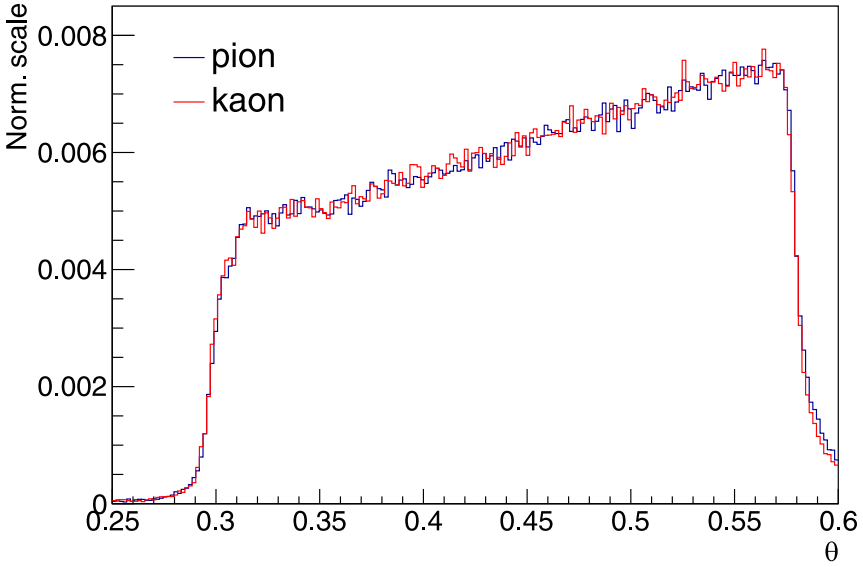

Figure 5.7: A cumulative distribution of the polar angle of kaons (red) and pions (blue).

Due to different momentum distributions of charged particles (Fig. 5.6), only the momentum range of 3.0 GeV/c to 4.0 GeV/c, where both distributions are relatively flat, was used for further calculations. The Cherenkov angle is not needed for a likelihood calculation, but is calculated for each reconstructed photon in the angle range between 0 rad and 0.5 rad with respect to the charged track, assuming that a photon was emitted from the mean emission point of the upstream aerogel layer. Distribution for kaons has a signal peak at around 0.28 rad, but there are also two smaller background peaks at different angles, as seen in Fig. 5.8. The background shape is the result of hits in HAPDs, that come from reflected photons and scattered photoelectrons, and are correlated with incident charged particles, as is illustrated in Fig. 5.9.

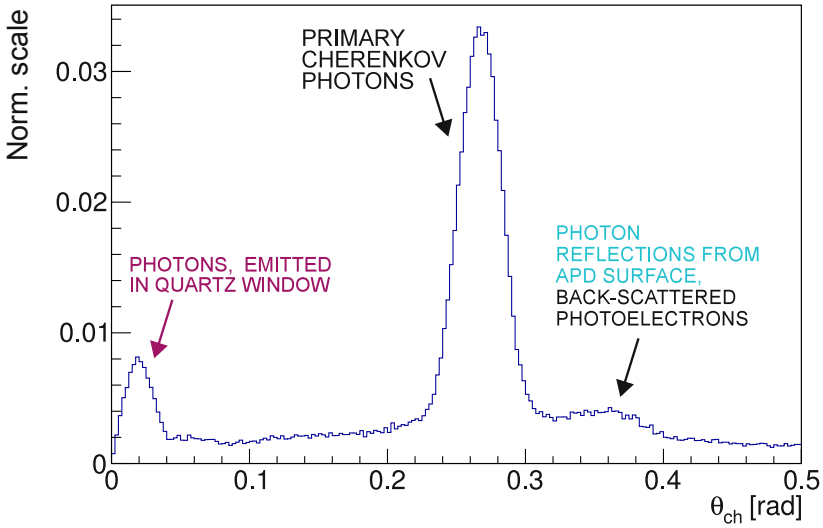

Figure 5.8: Cherenkov angle distribution for kaons with momenta between 3.0 GeV/c and 4.0 GeV/c. Contributions from Fig. 5.9 are marked.

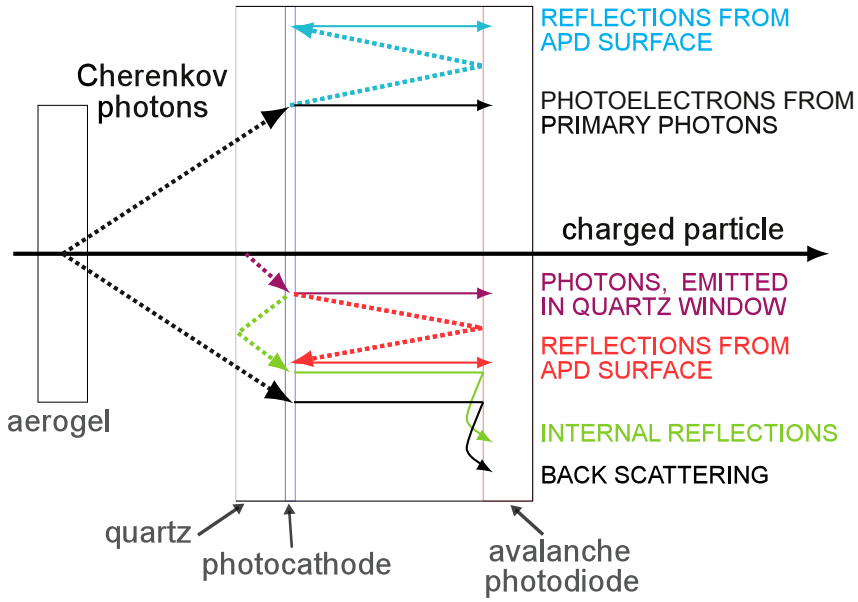

Figure 5.9: A schematic depiction of different contributions to Cherenkov angle distribution [71].

Cumulative distributions of the Cherenkov angle and the number of detected photons per track for both kaons and pions are shown in Figs. 5.10 and 5.11. During the reconstruction, the likelihood function for all mass hypotheses is constructed for each track. A logarithmic likelihood differences of kaons and pions $\log \mathcal{L}_K - \log \mathcal{L}_\pi$ is presented in Fig. 5.12.

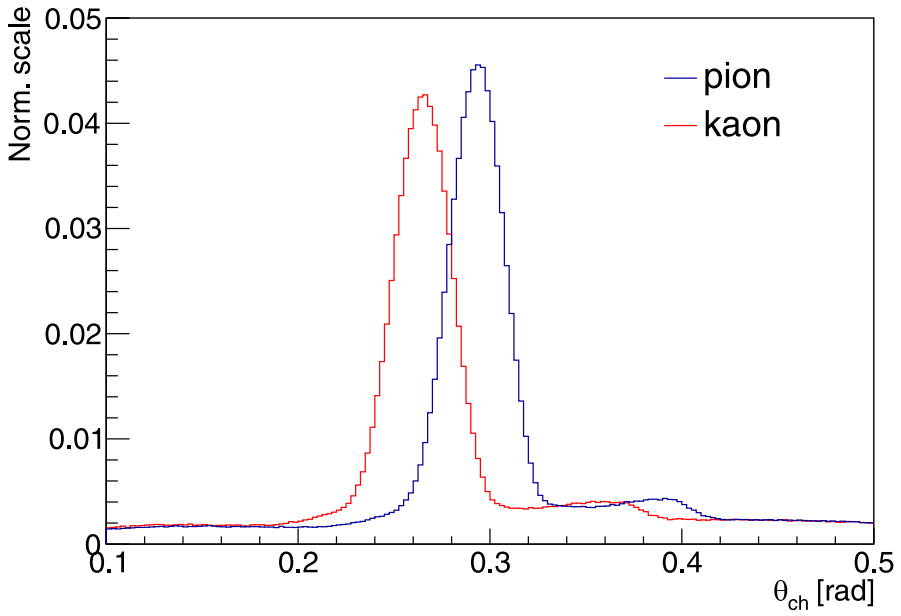

Figure 5.10: A cumulative distribution of Cherenkov angle of kaons (red) and pions (blue) with momentum of 3.0 GeV/c to 4.0 GeV/c.

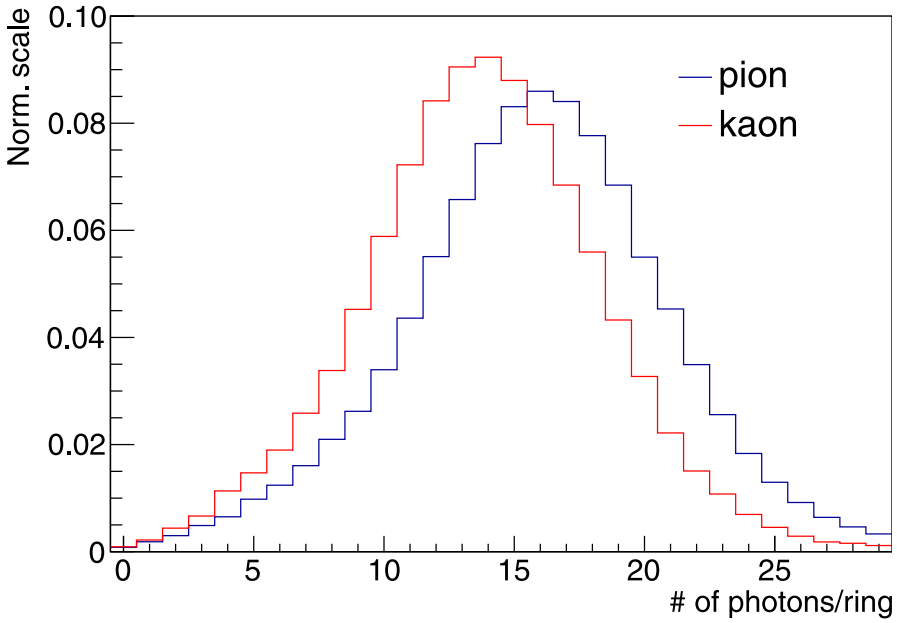

Figure 5.11: A cumulative distribution of the number of reconstructed photons per track for kaons (red) and pions (blue) with momentum of 3.0 GeV/c to 4.0 GeV/c.

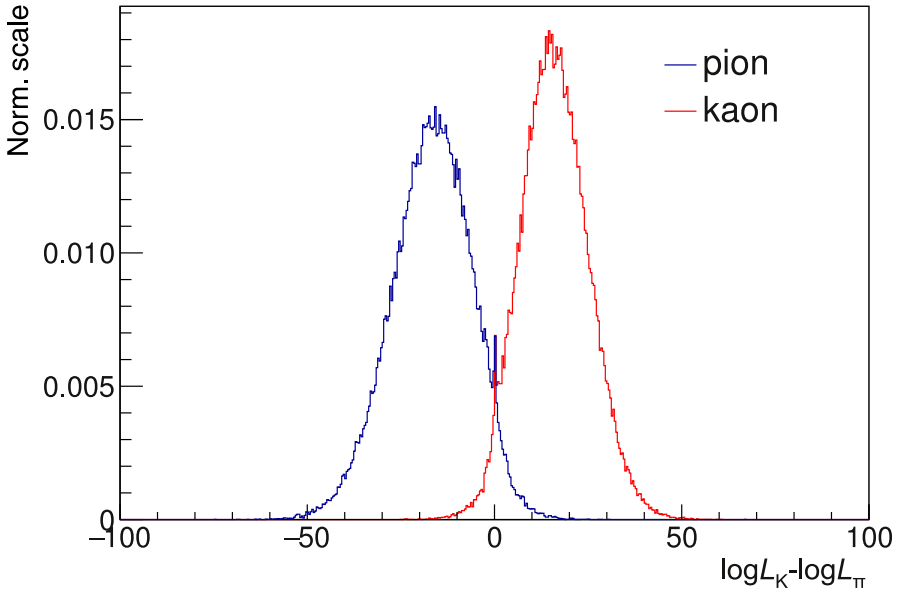

Figure 5.12: A cumulative distribution of likelihood difference of kaon and pion mass hypotheses $\log \mathcal{L}_K - \log \mathcal{L}_\pi$ for kaons (red) and pions (blue) with momentum of 3.0 GeV/c to 4.0 GeV/c.

A kaon identification efficiency, $\varepsilon_{K\to K}$, are usually presented as a function of momentum. Results for three fixed pion misidentification probabilities are shown in Fig. 5.13. Efficiencies were calculated from the $\log \mathcal{L}_K - \log \mathcal{L}_\pi$ difference. Histograms were divided into 50,000 bins in interval between -200 and 200. The PID cut was moved in steps of a bin size and the pion misidentification probability was calculated for each step. When the $\varepsilon_{\pi\to K}$ value was reached, the appropriate kaon identification efficiency was calculated.

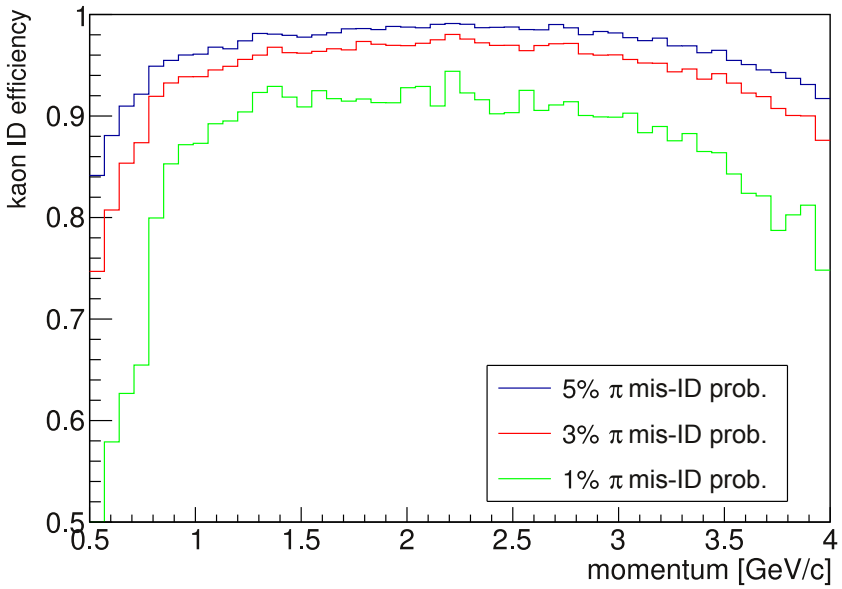

Figure 5.13: Kaon identification efficiency as a function of momentum for three different pion misidentification probabilities.

The efficiency depends on the number of reconstructed photons as well. The efficiency calculation was similar as in the case of momentum dependence. Results for three different $\varepsilon_{\pi\to K}$ values are depicted in Fig. 5.14. There is an efficiency drop at large numbers, which is the result of a low statistics in that range.

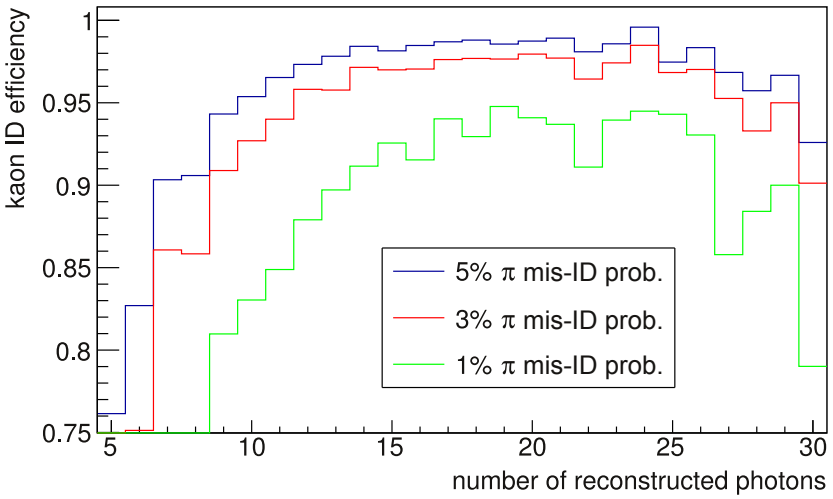

Figure 5.14: Kaon identification efficiency as a function of the number of reconstructed photons for three different pion misidentification probabilities.

The efficiencies also depend on the position and the incident angle of the initial particle. Close to the edge of the detector, a part of the photons is reflected from the mirrors. As is unknown whether a photon was reflected or not, both possibilities need to be considered, and this degrades reconstruction performance. The efficiency as a function of the particle's incident angle, which also corresponds to the polar angle of the detector, is presented in Fig. 5.15. Maximum likelihood function cannot be calculated for particles outside of geometrical acceptance of ARICH.

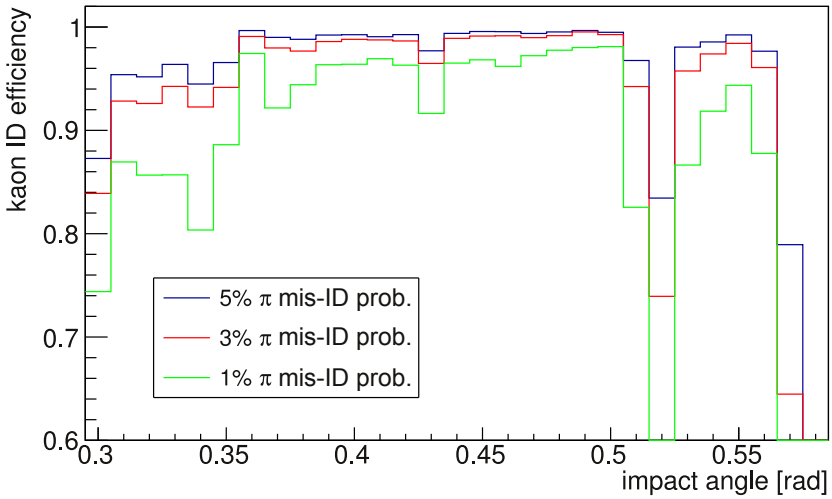

Figure 5.15: Kaon identification efficiency as a function of particle's incident angle for three different pion misidentification probabilities.

The efficiency drop is observed for angles above 0.5 rad, where a significant part of the emitted photons is reflected from the mirrors. Examples for various cases of performance degradation due to the Cherenkov ring overlaps from same or different particles are illustrated in Figs. 5.16 and 5.17. The examples show results for the shortest distance between the interaction point and a planar mirror. The overlaps depend on the particle's momentum, incident angle and the azimuthal position of the track.

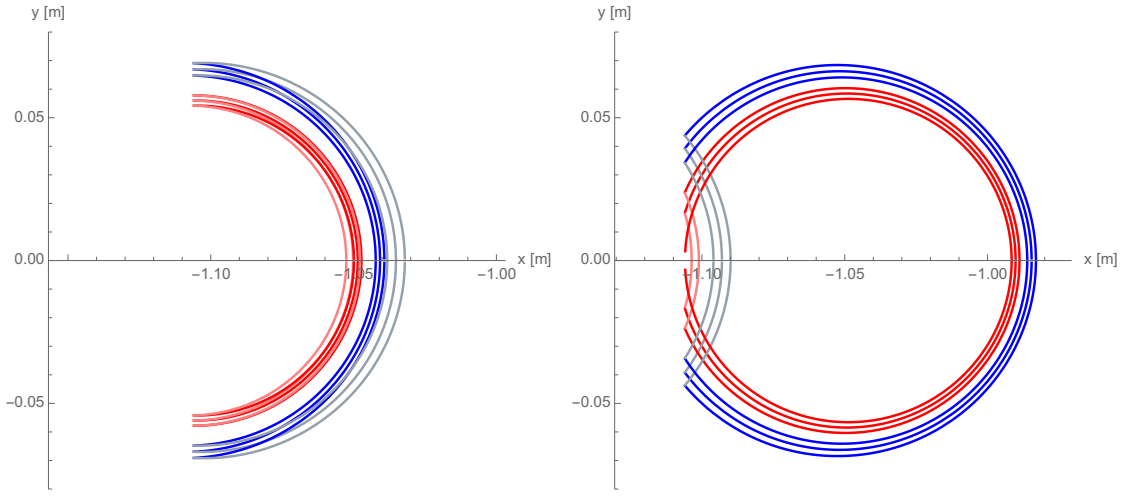

Figure 5.16: A schematic depiction of Cherenkov rings, emitted by kaon (red) and pion (blue), and partially reflected from the planar mirror. The x and y axes correspond to the x-y position on the sensor plane. Left: The overlap of the direct and the reflected photons, emitted by one particle with the momentum of 3.0 GeV/c and the incident angle of 30.4°. Less photons are expected to be detected. Right: Cherenkov photons, emitted by kaon and pion with the momentum of 3.5 GeV/c and the incident angle of 29.1°, propagate to the sensor plane very close to the planar mirror. Both hypotheses for the direct and the reflect photon have to be taken into account, decreasing the resolution of the Cherenkov angle.

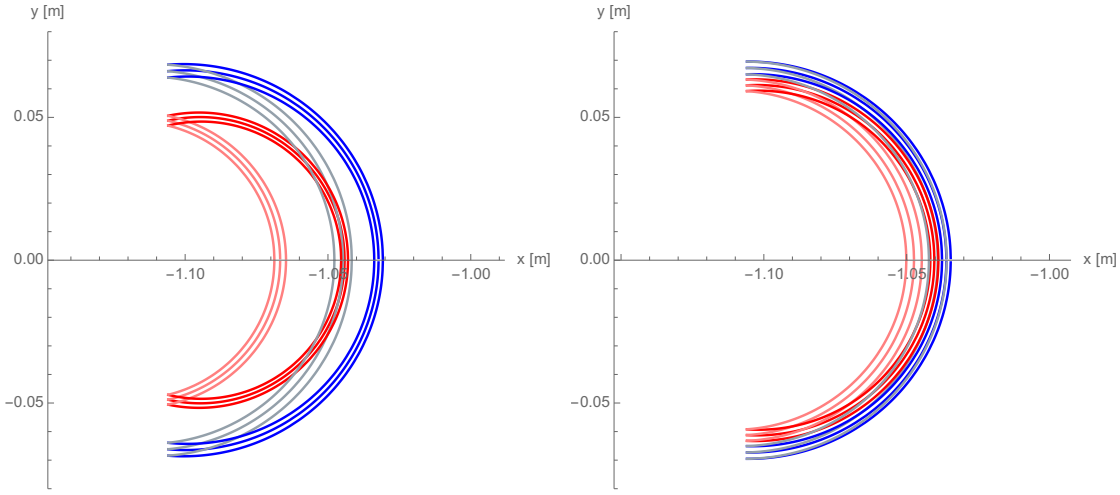

Figure 5.17: A schematic depiction of Cherenkov rings, emitted by kaon (red) and pion (blue), and partially reflected from the planar mirror. The x and y axes correspond to the x-y position on the sensor plane. Left: Rings, emitted by kaon and pion with the momentum of 2.5 GeV/c and the incident angle of 30.2°. The overlap of direct Cherenkov photons, emitted by kaon, and reflected Cherenkov photons, emitted by pion, is seen. Right: Rings, emitted by kaon and pion with the momentum of 4.0 GeV/c and the incident angle of 30.3°. The overlap of the direct and the reflected Cherenkov photons is seen.

5.4 Beam Backgrounds

Background sources in ARICH can be divided into signal correlated and uncorrelated, the latter coming both from the particle beams and ARICH electronics. In Belle II, different sources of beam related backgrounds will affect the performance of all subsystems. The background contributions in ARICH are:

a) *Radiative Bhabha*: e^+e^- scattering, where photons are emitted. Photons interact on iron of magnets producing neutrons.

b) *Two-photon*: new e^+e^- pair is created when the original e^+e^- pair interacts through virtual photons.

c) *Coulomb contribution*: elastic beam scattering on gas in beam pipes.

d) *Touschek*: Coulomb scattering within each beam.

The overview of beam background sources and their shielding can be found in [72, 73]. According to the simulations, the main beam background contributions in ARICH during target luminosity physics runs will be radiative Bhabha and two-photon radiation. They only occur during collisions and highly depend on luminosity. The Coulomb and Touschek scatterings are characteristic for each beam separately, and they are present even during beam storage without collisions. These backgrounds from LER are larger than from HER. Several shields reduce the radiation levels significantly, including the borated polyethylene neutron shield on the inner side of ARICH, around the beam pipe. A comparison of energy distribution of neutrons, entering ARICH, without any shield and with two types of neutron shield

is presented in Fig. 5.18. Based on this study, the polyethylene shield with addition of 10 % of boron was selected.

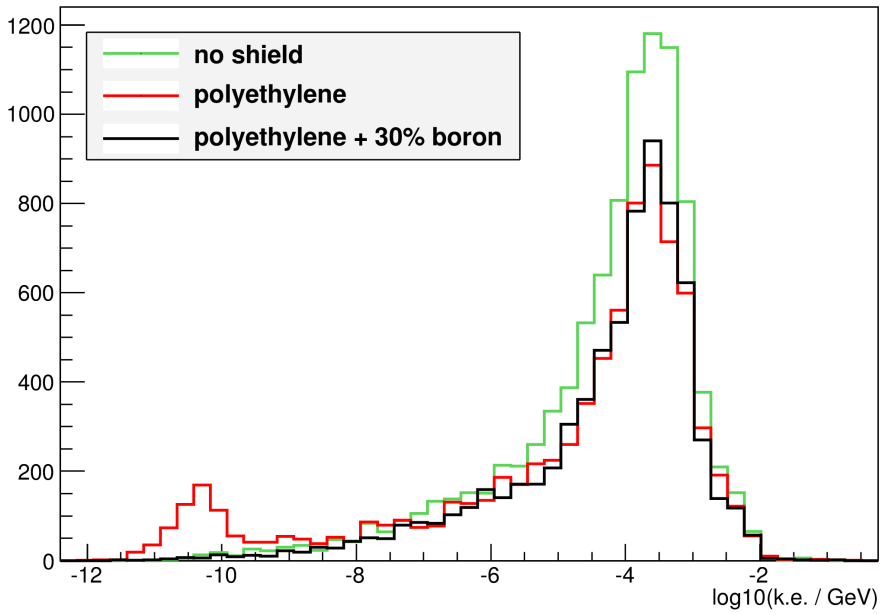

Figure 5.18: Comparison of neutron energy distribution for three different cases – without neutron shield and with two types of shields [74]. The x-axis is a common logarithm of kinetic energy of neutrons in units of GeV, and the y-axis presents a number of neutrons from the simulation. A polyethylene shield slows down the neutrons (see a small peak at $\log_{10}(k.e./GeV) = -10.5$), while the addition of boron in the shield material decreases the neutron flux that reaches ARICH sensors.

5.4.1 Resistance to Radiation

The results of neutron and gamma irradiation confirmed that both HAPDs and FEBs should be able to withstand the 10^{12} of 1 MeV equiv. neutron fluence/cm^2 and γ radiation dose of 100 Gy [75]. Neutrons can induce lattice defects in the silicon APDs. The result is an increased leakage current, which lowers the signal-to-noise ratio and degrades the photon detection efficiency. The front-end electronics can suffer from single event upsets from neutron irradiation, which change the state in chip logic, but can be recovered by rebooting the firmware.

The measured fluence and dose limits were compared to the irradiation levels from a simulation. Different beam backgrounds during peak luminosity operational runs with the full Belle II detector were simulated. Beam background studies were performed during different campaigns, where a simulation followed the changed machine parameters and improved radiation shielding around the beam pipe. The simulation results of the 16$^{\text{th}}$ Monte Carlo campaign, i.e. the last one before the data taking, are shown in Figs. 5.19 and 5.20. The expected irradiation for HAPDs at different concentric rings in 10 years of the Belle II operation is about half of that of the tested one for both HAPDs and FEBs, so a long lifetime of the sensors can be expected.

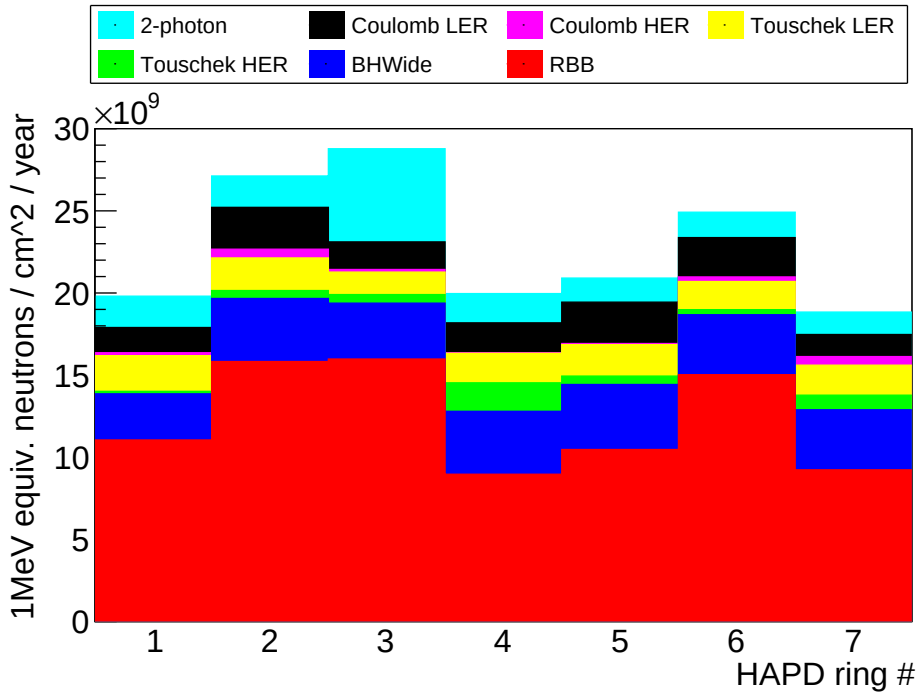

Figure 5.19: 1 MeV equiv. neutron fluence/cm^2/year per HAPD module. The average values per HAPD for each ring are shown. Results were produced with 16$^{\text{th}}$ beam background Monte Carlo campaign; the last one before the data taking, including the final shielding configuration.

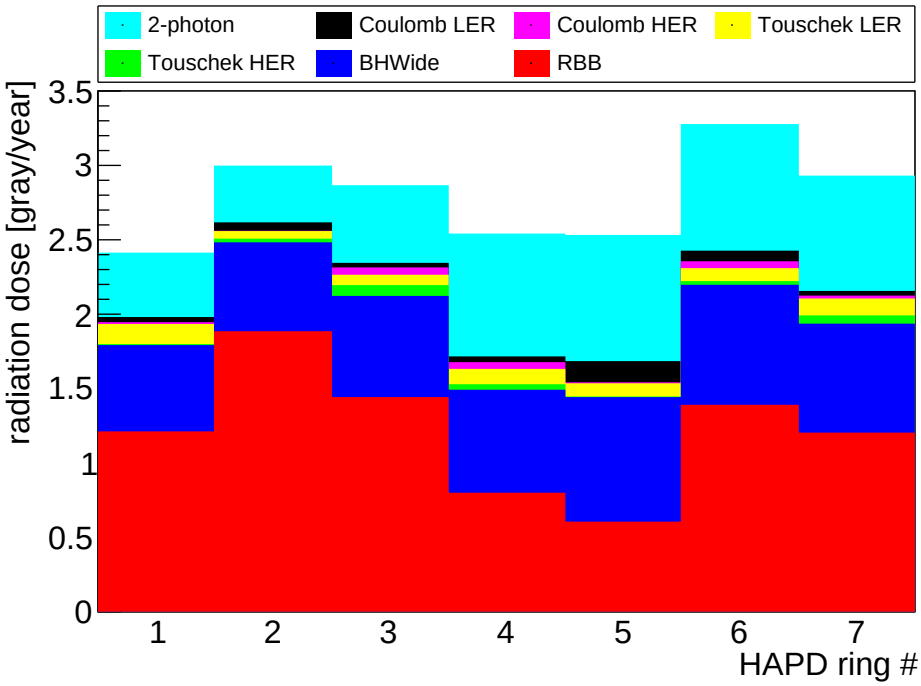

Figure 5.20: The radiation dose per year per HAPD module. The average values per HAPD for each ring are shown. Results were produced with 16$^{\text{th}}$ beam background Monte Carlo campaign; the last one before the data taking, including the final shielding configuration.

5.5 Calibration Effects on ARICH Performance

The ARICH design provides good performance within its spatial and operational requirements. An excellent K/π separation is a result of the optimal radiator thickness and a fine sensor granularity.

The latter one should be equal to, or smaller than, the expected ring width on the detector plane. The radiator thickness was chosen with regards to the best resolution of the single track, i.e. all the combined photons of one ring. In the case of a charged particle's impact angle of 0° and the average of 10 detected photons from the radiator, using Eq. 4.3.1 we get a single track resolution of:

$$\sigma_{ring} \approx \frac{11.4\,\text{mrad}}{\sqrt{10}} \approx 3.6\,\text{mrad} \tag{5.5.1}$$

At a high momentum of 4 GeV/c the Cherenkov angle difference for kaons and pions is $\theta_{ch}(\pi) - \theta_{ch}(K) \approx 23\,\text{mrad}$, which gives an excellent K/π separation of 6σ.

The single track resolution at smaller momentum is worse, but the Cherenkov rings are further apart, which ensures good separation over the whole momentum region. The $\pi^{\pm}$ momenta thresholds are 0.42 GeV/c and 0.46 GeV/c for downstream and upstream layers, respectively (see Eq. 3.2.1). Cherenkov photons are emitted by fast kaons at momenta above 1.47 GeV/c in downstream and 1.63 GeV/c in upstream aerogel layer.

The fraction of pions misidentified as kaons is higher in the region between 0.5 GeV/c and 1.5 GeV/c, where the absence of the detected Cherenkov photons implies that the charged particle was a kaon. Therefore, the analysis algorithm needs to precisely take into account all the inactive region of ARICH to make sure that the misidentification due to wrong masks is eliminated.

The sensitive area is only $\sim 40\,\%$ of the total ARICH region. In addition to that, some channels might stop working during operation. Before the assembly, all HAPDs were tested. There were on average 0.77 inactive channels per HAPD, which accounts for 0.5 % of the total active area. This number is expected to increase slightly during long-term operation. More significant factors could include a potentially inactive chip or the complete malfunction of a sensor due to damage to the HAPD or front-end board, such as increased leakage currents due to radiation, or damage to power supplies. In case of merger board malfunctioning, a region of 5 or 6 HAPDs would be turned off, which presents a significant fraction for a certain area. This would significantly reduce the number of detected photons from a single track. On the other side, some very noisy channels can provide false information about the hit, which contributes to higher background.

The non-calibrated sensors and electronics provide smaller signals and a larger background, which decreases the separation between kaons and pions and results in lower identification efficiencies and larger misidentification rates. The detector calibration is crucial for the optimal detector performance and is carried out in several steps:

a) A calibration of operational parameters, such as the threshold for electronics, sensor gains and masking the problematic channels

b) A calibration with the collected data

c) Efficiencies and misidentification rates, determined using control channels, that can be identified without ARICH information

The first step of the calibration of operational parameters was carried out before assembly. The operational parameters of electronics and HAPDs were monitored during the detector operation. To eliminate the misidentification due to noisy or inactive areas, proper masking has to be taken into account. Therefore, the calibration of masking is provided with offline analysis of collected data. The last step is the determination of identification probabilities using the collision data. Decays that can be identified by their kinematics without particle identification information are used.

CHAPTER 6

Detector Calibration

Calibration of electronics and HAPD operational parameters was performed before the assembly, at the final module tests. The main objectives were to measure the gain for each channel, to align the offsets of the front-end boards and to diagnose the problematic channels. Hardware calibration was done using either illuminated or non-illuminated sensors. Later on, during Phase II, offsets were calibrated again and channel masks were prepared using collision data. The results will be presented in this chapter.

During the Phase II, ARICH encountered a temperature issue. Altogether, ASICs and FPGAs produce 1 W heat per front-end board and 5 W per merger board, summing up to 780 W in total. The thermal coupling between the heat sources and the cooling system was insufficient, which resulted in overheating of the components. The temperature sensors on electronics and additional sensors at the electronics side of the detector were used for monitoring, but with no information about the temperature of the HAPDs, it was decided to keep only a part of ARICH running during Phase II to maintain a cautious stance. Most of the time, a configuration with sectors 1, 4, 5 and 6 was used. After two months of collecting collision data, a configuration with sectors 2, 3 and 6 became the default one. The detector was heating up slowly enough to use the electronics of the whole ARICH for a few hours to also test the overall operation towards the end of Phase II. The temperatures were monitored and their effect on the offset and gain calibration will also be discussed. Despite the larger inactive areas of ARICH during the data collection, the basic performance of the ARICH detector in Phase II was studied and is also presented.

6.1 Module Test Experimental Setup

Before the installation, the modules were tested at the KEK institute. The setup allowed testing of four sensors at once. Modules were attached to the aluminium frame and cables were connected at the back of electronic boards. They had separate readout data cables, bias and a high-voltage power supply, but one used common front-end board power supply. Voltages and leakage currents were monitored through the whole measurement.

A laser was used for the sensor illumination. The laser light was split into four beams, one for each sensor. Approximately equal beam intensity was achieved by using the neutral density filters. The laser fibres were attached to the 3D movable stage, which enabled precise laser scans over the whole sensor plane. The setup was enclosed in a lightproof aluminium box. The setup is presented in Figs. 6.1 and 6.2.

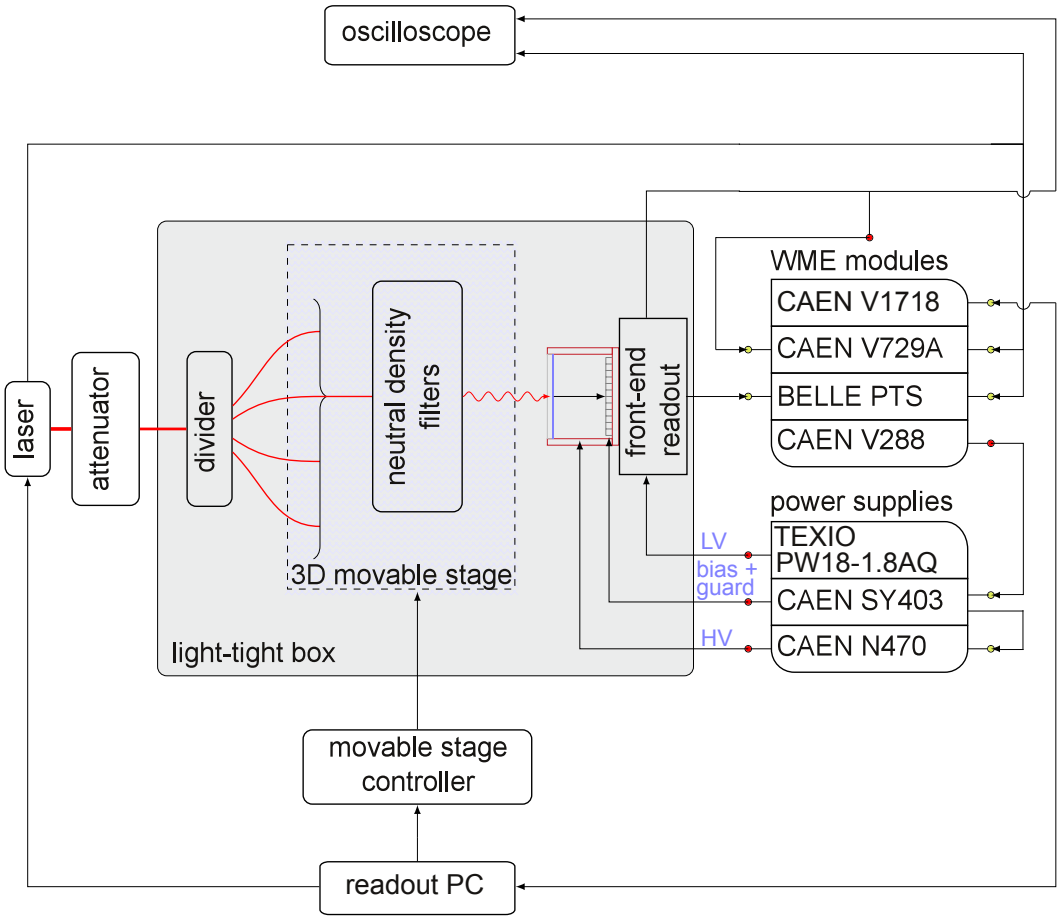

Figure 6.1: A schematic depiction of experimental setup [71].

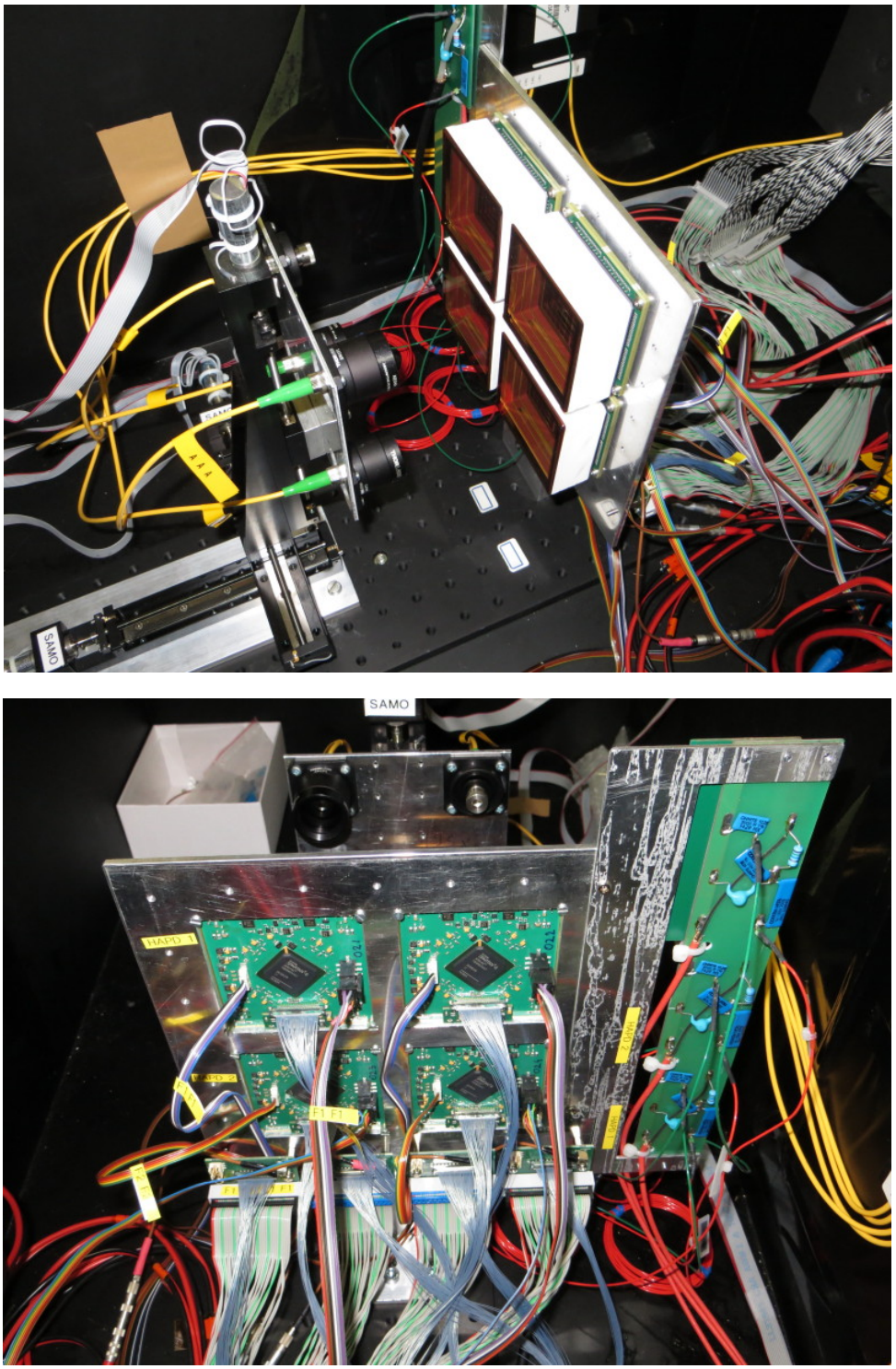

Figure 6.2: A setup for testing four modules at once. A movable stage with split laser beams and modules, mounted to the aluminium frame (top), with power supply and data cables, attached at to the front-end board (bottom) [36].

6.1.1 Laser Choice

Sensors were illuminated by laser pulses. The available lasers provided blue, green and red light. The criteria for the laser choice was the quantum efficiency of the photocathode (Fig. 4.24) and the absorption in APD (Fig. 6.3). Higher quantum efficiency means a higher probability of generation of photoelectrons. A lower absorption length in silicon means less generated electron-hole pairs inside the APD. The wavelengths and corresponding quantum efficiency and silicon absorption are given in Table 6.1.

Module tests included measurements with high voltage supplied to the HAPDs, where photoelectrons were accelerated to the APD. In the absence of an electric field in the vacuum, the diode is still reached by the primary photons that were not absorbed in the photocathode. The green laser was used for the to allow measurements with and without the electric field, in case the latter would be needed.

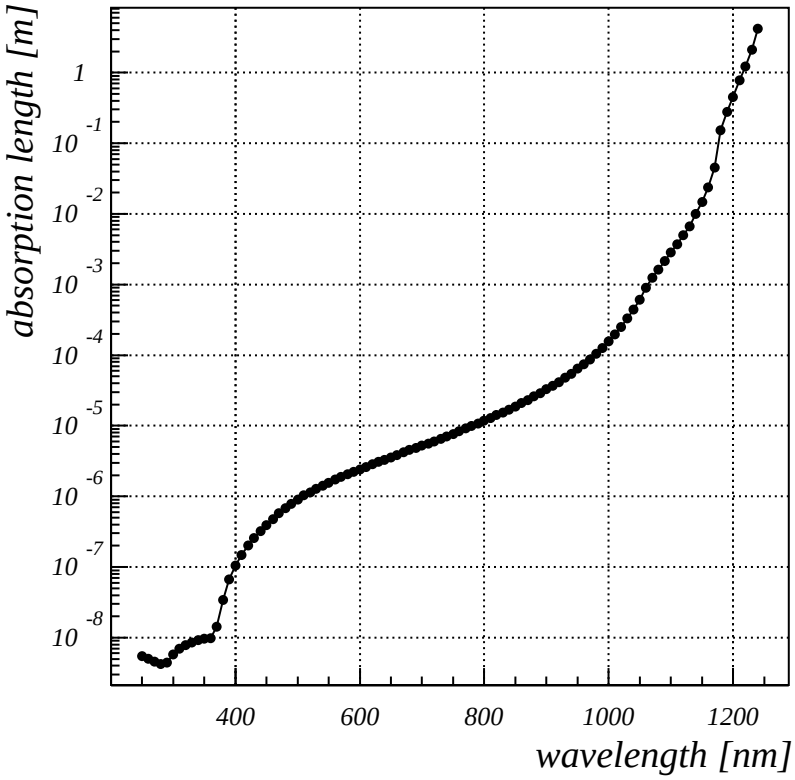

Figure 6.3: Absorption length in silicon for different wavelengths [76].

Table 6.1: HAPD bi-alkali photocathode quantum efficiency (Fig. 4.24) and absorption length x_{abs} in silicon (Fig. 6.3) for three different laser wavelengths.

laser	blue	green	red
λ [nm]	400	520	636
QE [%]	35	10	2
x_{abs} [µm]	0.1	1	3

The laser intensity was calibrated to get an optimal ratio between single-photon

pulses and the rest of the pulses. Ideally, in each laser pulse we would detect exactly one photon and the ratio between triggered and detected events would equal the efficiency of photon detection. In reality, the number of detected photons in a laser pulse follows a Poisson distribution:

$$f(k;\bar{n}) = \frac{\bar{n}^k e^{-\bar{n}}}{k!}, \tag{6.1.1}$$

where $\bar{n}$ is the average photon rate and k is a number of detected photons in a pulse. The proportions of k-photon events can be calculated as:

$$1 = \underbrace{e^{-\bar{n}}}_{0\gamma} + \underbrace{\frac{\bar{n}^1 e^{-\bar{n}}}{1!}}_{1\gamma} + \underbrace{\frac{\bar{n}^2 e^{-\bar{n}}}{2!}}_{2\gamma} + \dots \tag{6.1.2}$$

Since it is unknown how many photons were emitted in each pulse, pulses with more than one photon can distort the measurement. Proportions of pulses with no, one and two or more photons, for a variety of different average numbers of emitted photons, are shown in Table 6.2.

Table 6.2: The proportions of no-, one- and multi-photon pulses for different average numbers of detected photons.

$\bar{n}$	0 γ	1 γ	≥ 2 γ
0	100 %	0.0 %	0 %
0.01	99.0 %	1.0 %	0 %
0.05	95.1 %	4.8 %	0.1 %
0.1	90.5 %	9.0 %	0.5 %
0.2	81.9 %	16.4 %	1.8 %
0.5	60.7 %	30.3 %	9.0 %
1	36.8 %	36.8 %	26.4 %

The laser intensity was set manually with respect to the signal on the oscilloscope with the average number of photons at roughly 0.1. This corresponds to 90 % of events without photons, but keeps the proportion of photon pulses with two- or more-photon pulses at low level of 5 % in events with at least one photon detected.

6.2 Measurements

For both non-illuminated and illuminated sensor measurements, the threshold value was varied in discrete steps. Different measurements used either step or voltage scale for a threshold limit, calculated as:

$$voltage = -1250\,\mathrm{mV} + k \times step, \tag{6.2.1}$$

where k is a coefficient of 2.44 mV. The scale is also presented in Fig. 6.4.

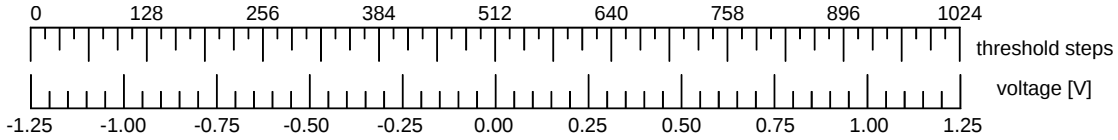

Figure 6.4: Threshold steps and corresponding voltage scale for threshold scans.

6.2.1 Non-illuminated Sensors

The signal of a non-illuminated sensor is a combination of measured noise from the HAPD and electronics. The signal amplitude (either current or output voltage) changes with time, as illustrated in Fig. 6.5. If the threshold is moved in steps and all the transitions of the noise amplitude over the threshold are counted each time, the distribution has a Gaussian shape. Measurements of the number of events, where the signal surpasses the set threshold limit, are called threshold scans. The mean value of the distribution is the baseline, which can be adjusted for each channel, using the electronics parameters.

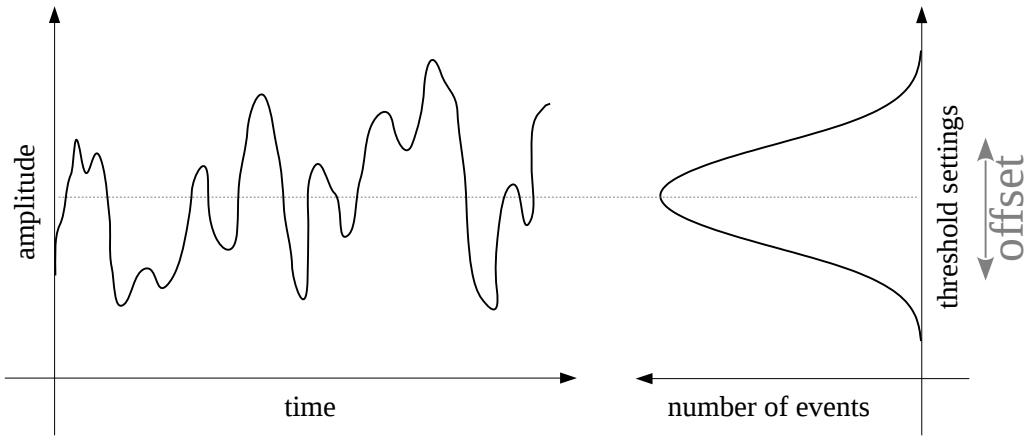

Figure 6.5: Schematic depiction of combined noise from HAPD and electronics (left) and threshold scan (right) of a single channel.

6.2.2 Illuminated Sensors

Sensors are illuminated by a pulse laser, which also sends the trigger information to match time windows of the laser pulse and data acquisition. Threshold scans of illuminated sensors, measured with the edge detection principle, use signals before the digitization in ASIC (as seen in Fig. 6.6) and provide information about the number of detected photons. A schematic depiction of the measurement of up to three-photon signals is shown in Fig. 6.7. There is a time evolution of signals shown at the top. The middle plot shows the ASIC digitization. The last plot presents the counting of the events, where the transition from 0 to 1 is detected.

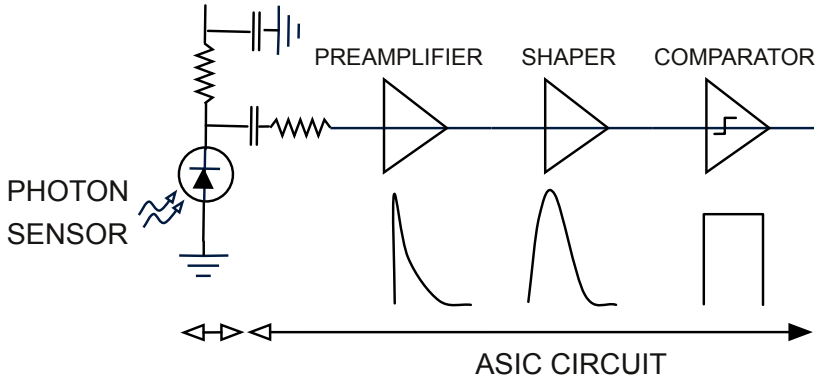

Figure 6.6: Time dependent signal after amplification, shaping and digitization [55].

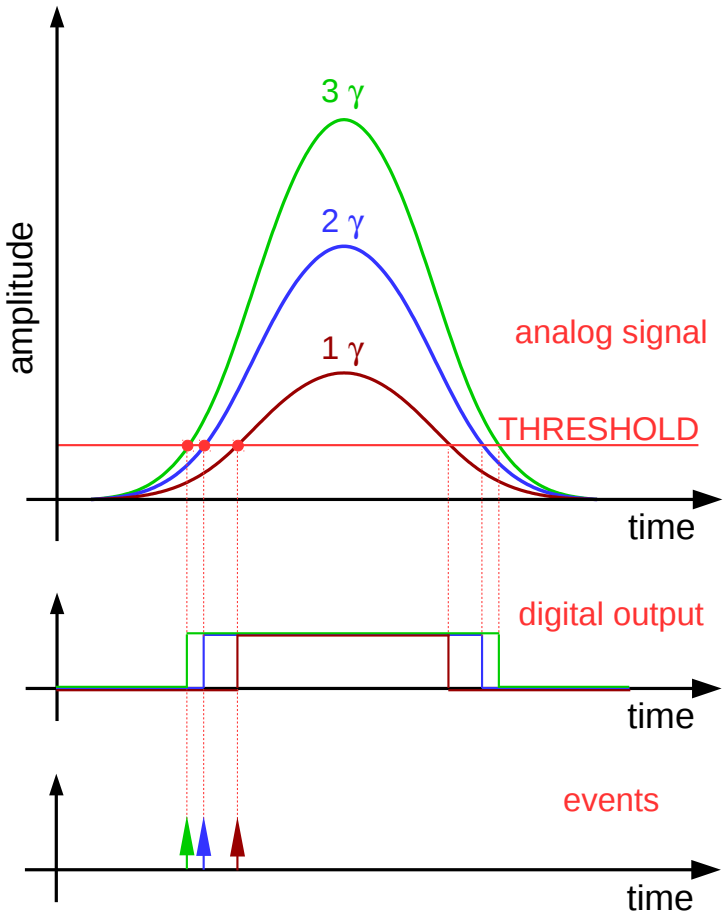

Figure 6.7: A schematic depiction of the edge detection principle. Signal current on a photodiode is time-dependent and only the events corresponding to the laser time trigger are detected. Top: Time evolution of one-, two- and three-photon signals before the ASIC digitization. Middle: Digitized signals. Bottom: Counting of the events, where the 0 to 1 transition is detected.

The threshold is moved in discrete steps. At every step, a number of transitions over the threshold is counted. This results in the threshold scan as seen in Fig. 6.8. A clear pedestal is seen around the threshold step of 520. Threshold scans differentiate between n-photon signals, as presented in the figure. Only a small part of events have at least three-photon signals, as seen from the step 615 on.

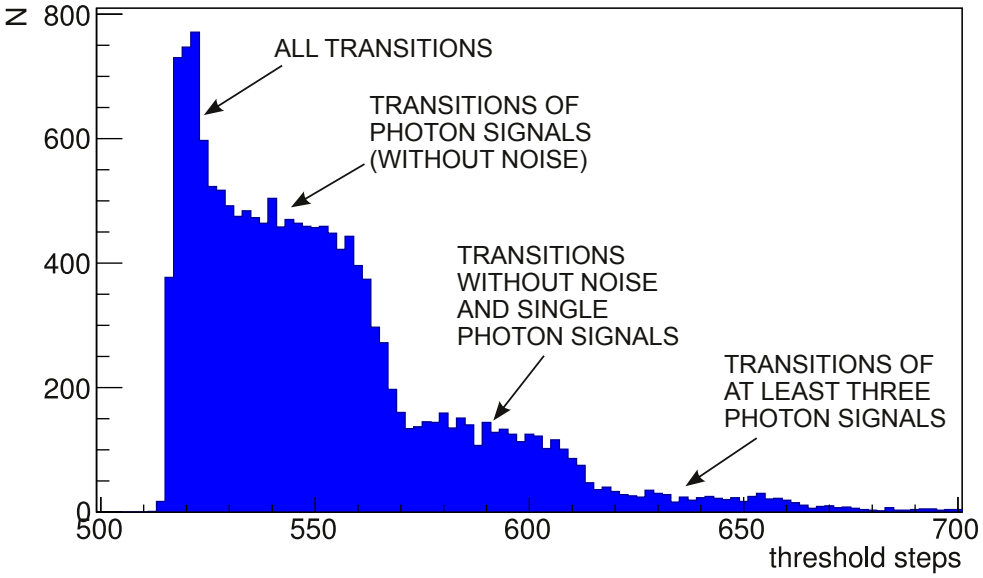

Figure 6.8: An example of a cumulative threshold scan of one HAPD channel, where only the centre of the channel was illuminated by laser.

Threshold scans were acquired for each channel separately. The output of every channel was measured only during the illumination. Taken together, 144 scans per module were acquired, with laser illumination on the positions, marked in Fig. 6.9. The threshold scans for the properly working channels of the same HAPD have similar signal amplitudes heights, as seen in Fig. 6.10.

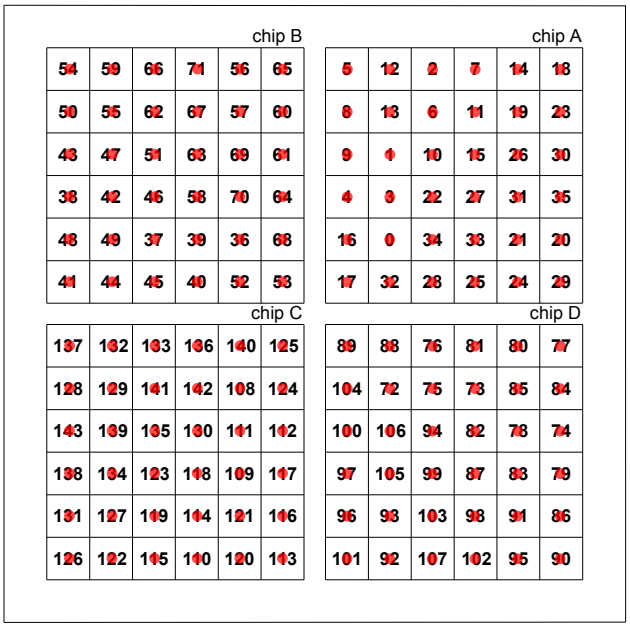

Figure 6.9: Positions of laser illumination of the centre of channels during threshold scans. Measurement was done for one channel at once. Channel ID numbers are also written.

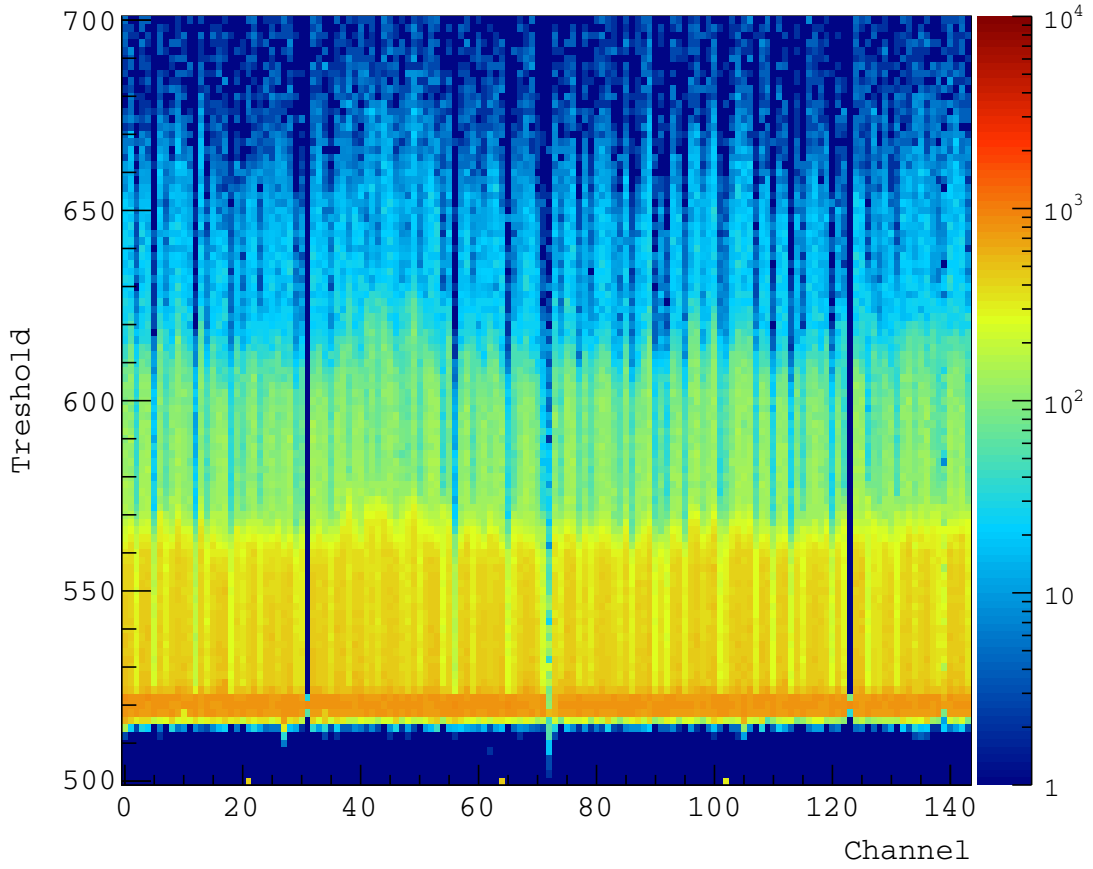

Figure 6.10: Threshold scans for all 144 channels of one HAPD. The output was acquired for the illuminated channel only.

6.3 Offset Calibration of Front-End Electronics

The threshold for each channel has to be set high enough to prevent false signals from the noise of the electronics, yet low enough to detect a single photon signal. Quantitatively, this means setting the threshold limit 3.5σ above the noise baseline of the channel, where the probability of detecting a signal, triggered by noise, is only 0.23 ‰. Because channels cannot have different threshold values, this means fixing the threshold for signal detection and moving the noise baseline for each channel far enough below it.

6.3.1 Signal Baseline at Different Offsets

ARICH electronics channels have noise distributed around different output voltages. The offset settings, designed in ASIC (Table 4.2), allow users to move the baseline in several discrete steps. Two types of settings – coarse and fine – are divided into sixteen steps each. For each channel, a total of 32 threshold scans with different offsets were taken. An example of one scan is shown in Fig. 6.11. Distributions were fitted with a Gaussian function [77] and the mean value was taken as a baseline for each step. The mean values for coarse and fine offset steps were plotted and fitted separately with a linear function, as seen in Fig. 6.12.

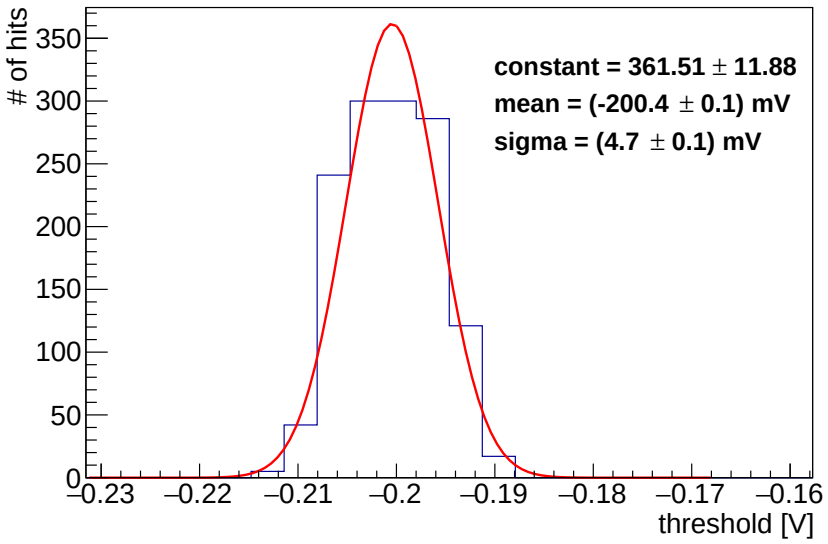

Figure 6.11: A single channel threshold scan for one of the coarse offset steps [78].

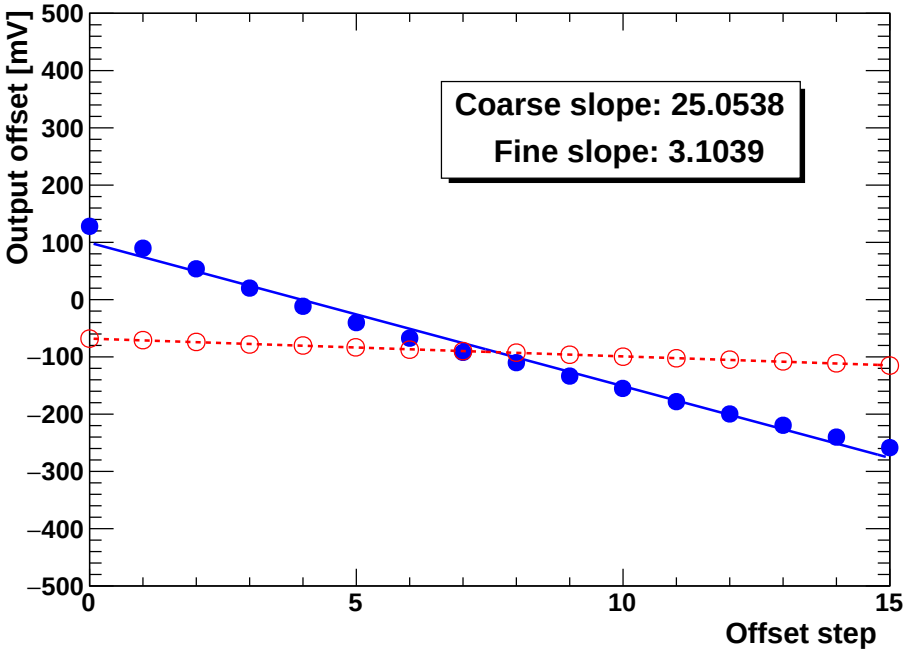

Figure 6.12: Baselines for all offset steps of one channel. Values are fitted separately for coarse and fine settings. The slope is in units of mV/step [78].

Measurements for coarse settings were used to determine the voltage range that can be used as a baseline of the whole ASIC. For the example, presented in Fig. 6.13, this range can be set between $-130\,\mathrm{mV}$ and $20\,\mathrm{mV}$. This range varies for different ASICs, therefore four ASICs with the overlapping ranges were mounted on the same front-end electronics board. This ensured that the same baseline can be set for the whole front-end board.

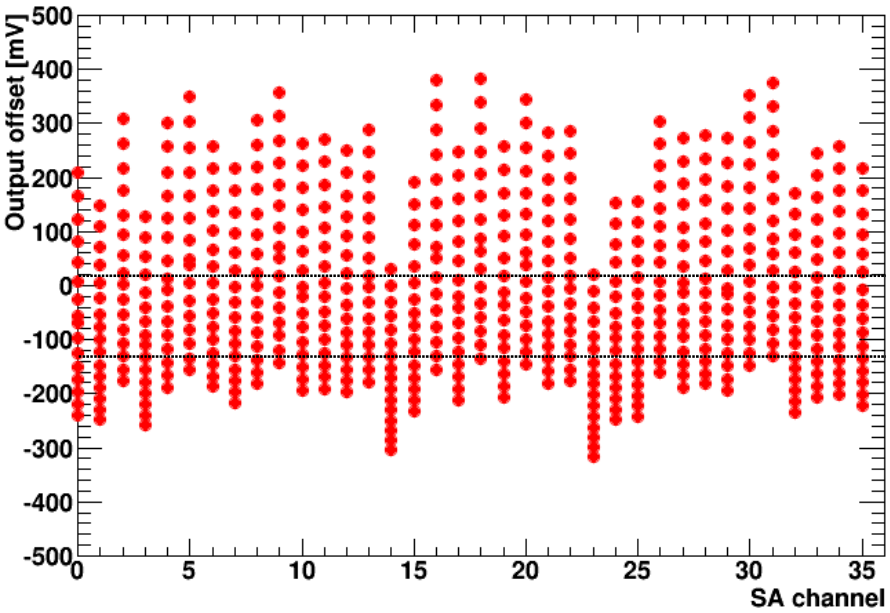

Figure 6.13: The baseline values for coarse offset settings for all channels of one ASIC. The common baseline can be set anywhere between −130 mV and 20 mV [78].

6.3.2 Calibration

At the beginning of the experiment, the noise distributions for different channels were similar. The majority of channels had a width of less than 10 mV (see Fig. 6.14), which is considerably less than the height of a single photon signal.

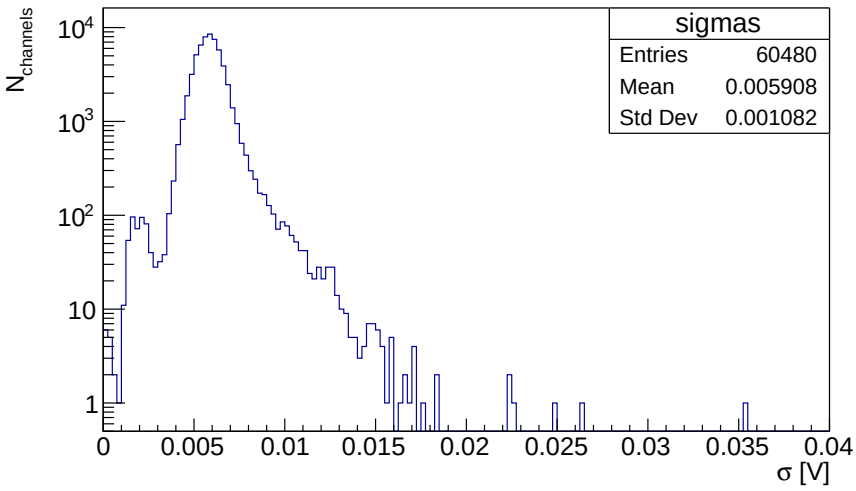

Figure 6.14: A distribution of the widths of Gaussian functions, fitted to the noise distributions of channels of all installed modules (an example of a fit is shown in Fig. 6.11). The y-axis is in a logarithmic scale.

Since noise distributions were similarly narrow, we simplified the calibration method and aligned the baselines of all channels instead. During long-term operation of ARICH, leakage currents in electronics components are expected to increase and

noise distributions might change. The baselines will have to be moved towards the lower threshold voltages with regards to their noise distribution widths.

The baselines for channels are scattered over a wide voltage range at the fixed offset setting. Fig. 6.15 presents the mean values of Gaussian functions, fitted to the noise distributions for one of the coarse settings for all 420×144 channels. The noise threshold scan before calibration for six modules, connected to one merger board, is shown in Fig. 6.16.

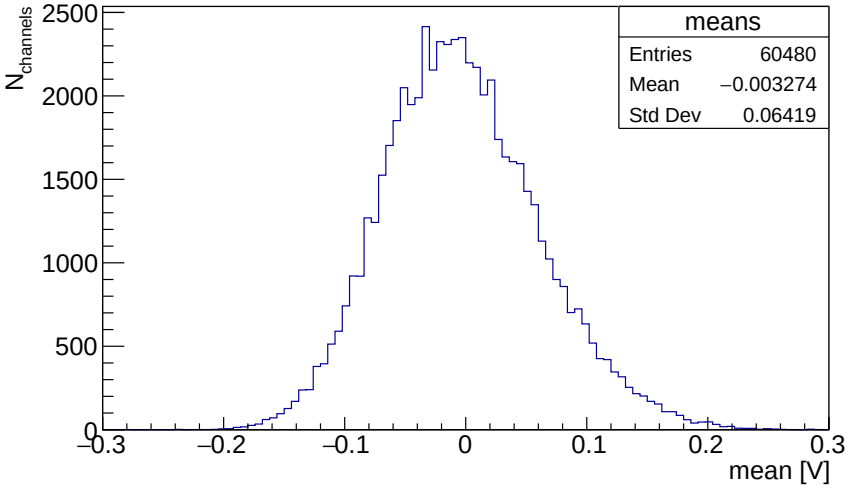

Figure 6.15: A distribution of mean values of Gaussian functions, fitted to the noise distributions of channels of all installed modules (see fit example in Fig. 6.11).

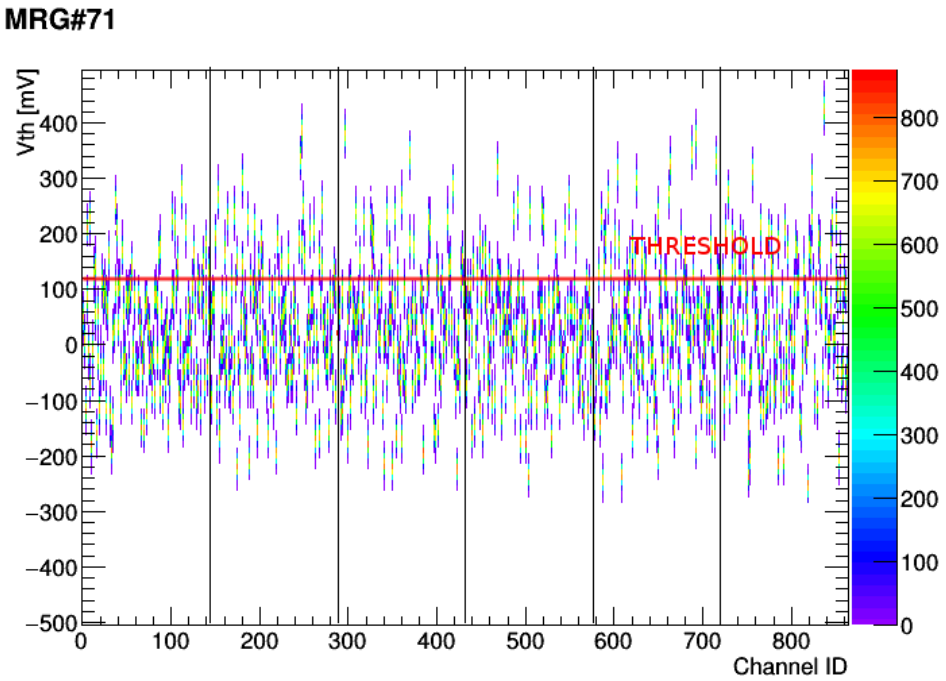

Figure 6.16: A threshold scan of non-illuminated sensors before the offset calibration. Results for six modules (separated by vertical lines), connected to one merger board, are shown. Channel ID numbers for $i-$th module starts with $(i-1) \times 144$. Channel baselines are scattered and many of them are above the set threshold limit.

Since we count the transitions of the signal over the threshold, the non-calibrated offsets would give a large proportion of false negative hit information, because many channels have either the baseline above the set threshold or few hundred mVs beneath it, where the signal cannot be detected even for multiple-photon events. On the other hand, channels where noise is distributed close to the threshold, would provide a signal even when there is no hit. The aligned offsets are set in a few steps:

1. A target value to align baselines is set.
2. A threshold scan of the channels is acquired.
3. Noise distributions are fitted with a Gaussian function to determine the baseline for each channel.
4. From the difference between the channel baseline and the target value, and from the slope of the coarse offset settings, the new offset value is calculated for each channel and uploaded to the front-end boards.
5. Steps 2.∼4. are repeated until all baselines are close to the target value.

Normally, the baselines are roughly aligned after the first try and up to five iterations are sufficient to calibrate the channels. The main reasons for the iterative method are:

a) Non-linearity of the output voltage dependence on offset steps, as seen in Fig. 6.11 (the slope of fitted linear function is only a guideline for offset adjustment)

b) Using the mean slope value for all channels (see Fig. 6.17)

An example of the calibrated channel offsets is shown in Fig. 6.18.

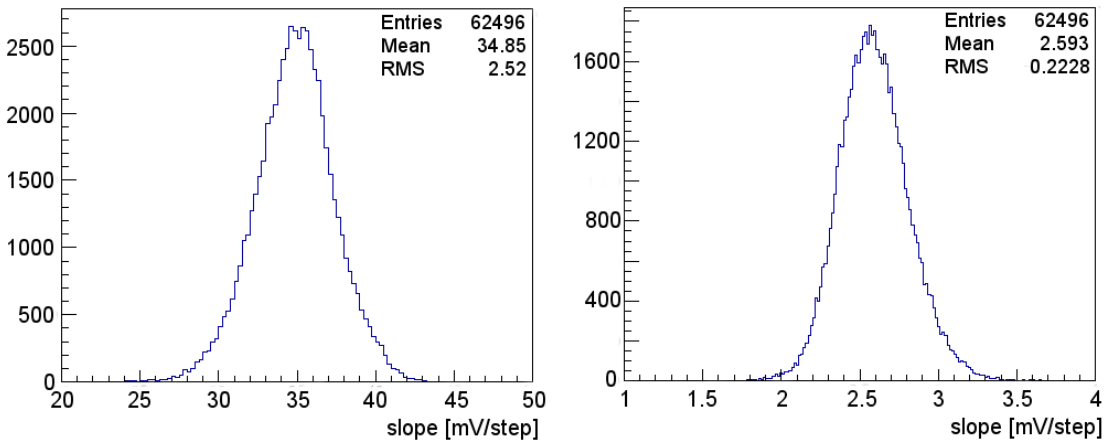

Figure 6.17: Distributions of slopes of fitted linear functions (see Fig. 6.11) to the means values of rough (left) and fine (right) settings. Values for all tested ASICs are plotted.

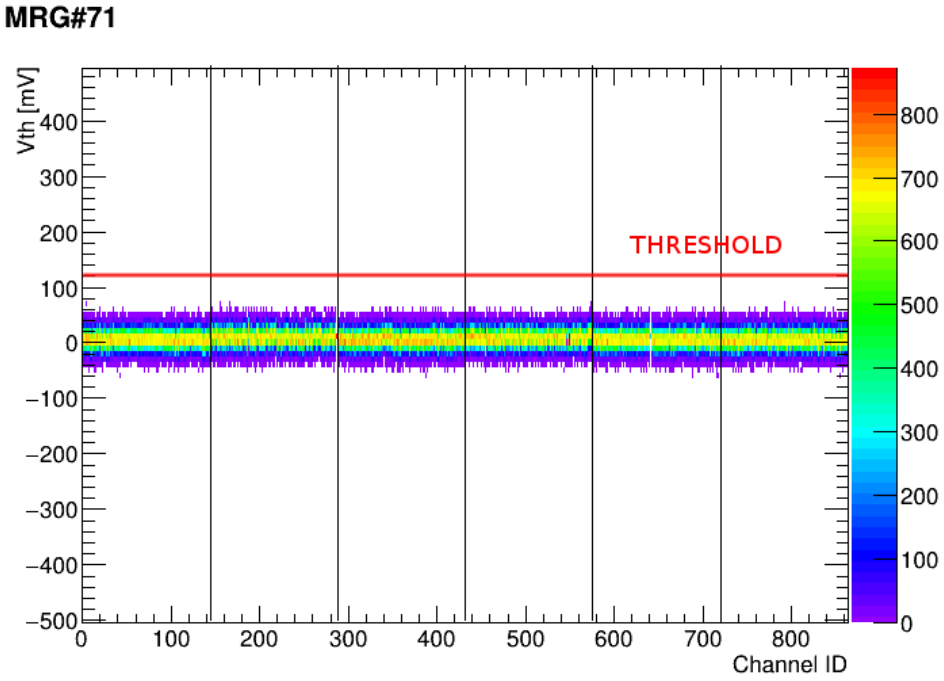

Figure 6.18: A threshold scan of electronics noise after the offset calibration. The channel baselines are aligned well below the threshold limit.

6.4 Signal Gain Measurements

Bombardment and avalanche gains were measured for each of the four HAPD chips by the manufacturer Hamamatsu Photonics. Examples of both gains as a function of corresponding voltages are shown in Chapter 4, Figs. 4.25 and 4.26. In the final module tests (see Chapter 6.1) as well as during the Belle II experiment, bias voltages that correspond to the avalanche gain of 40 are used. The distribution of bias voltages for the installed modules is presented in Fig. 6.19.

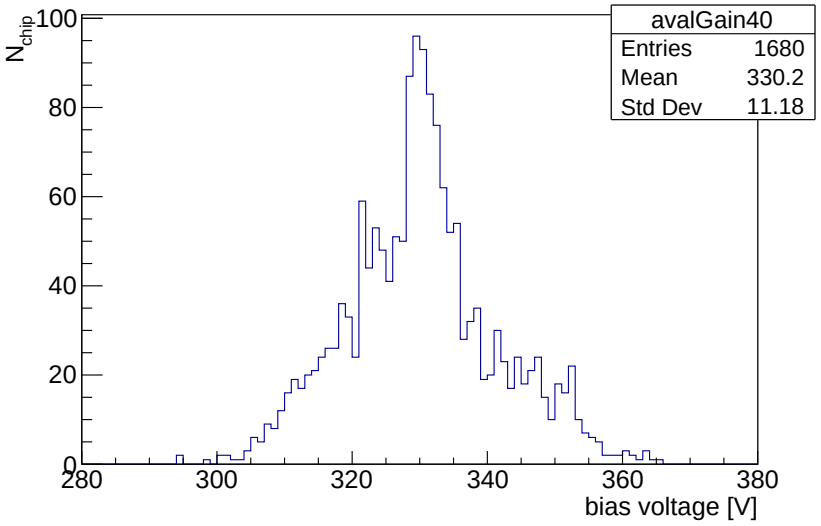

Figure 6.19: A distribution of bias voltages that provide the avalanche gain of 40 for all installed devices [51].

The bombardment gain of the tested modules differs from module to module, because a high voltage of 7 kV was used for all of them. The bombardment gain distribution of all chips of installed modules is shown in Fig. 6.20. The total signal amplification for different channels, calculated as a product of the bombardment and avalanche gains, was in the range of $5.2 \times 10^4 - 6.4 \times 10^4$.

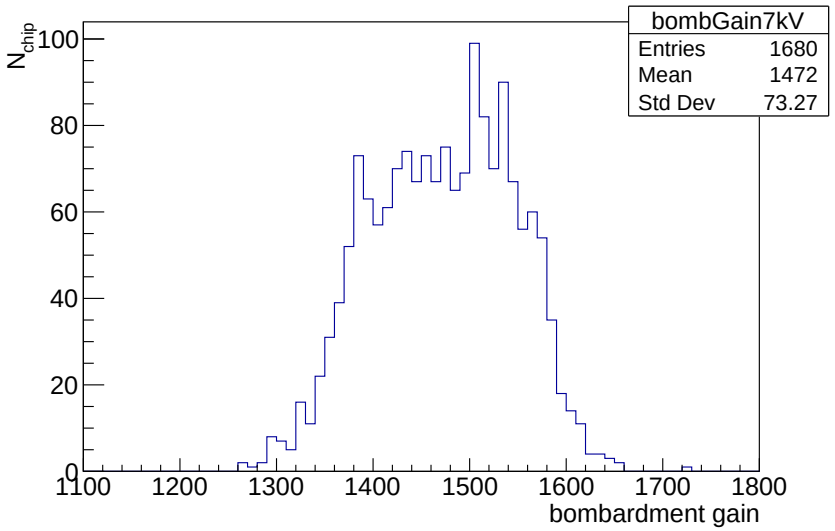

Figure 6.20: A bombardment gain distribution of all installed devices at the applied high voltage of 7 kV that was used in the final module tests [51].

6.4.1 Channel Dependence of Gain

The overall gain was measured for the entire chip, although it varies for every channel. Therefore, the relative gain on the centres of channels was measured in the module test and will be calibrated during the experiment. The gain can be calculated either from the threshold scans or charge collection data. In both cases, the pedestal and one photon signal are fitted separately and the fit parameters are used to calculate the gain. The first one will be used for calibration in Belle II. In this case, the pedestal from the threshold scan is fitted with a Gaussian function and the one photon signal with the scaled and translated error function $A + Berf(\frac{x-C}{D})$, where error function $erf(x)$ is:

$$erf(x) = \frac{1}{\sqrt{\pi}} \int_{-x}^{x} e^{-t^2} dt \tag{6.4.1}$$

An example is illustrated in Fig. 6.21. The signal gain can be calculated from the difference between the mean value of the Gaussian peak and the x-axis translation C of the error function.

The second way is to measure collected charge using an ADC converter. This measurement is acquired for each channel separately, thus it cannot be done during the experiment, but was used for module testing as a crosscheck for the regular threshold scans. For the charge collection scans, the analog signal was integrated in selected interval, as presented in Fig. 6.22.

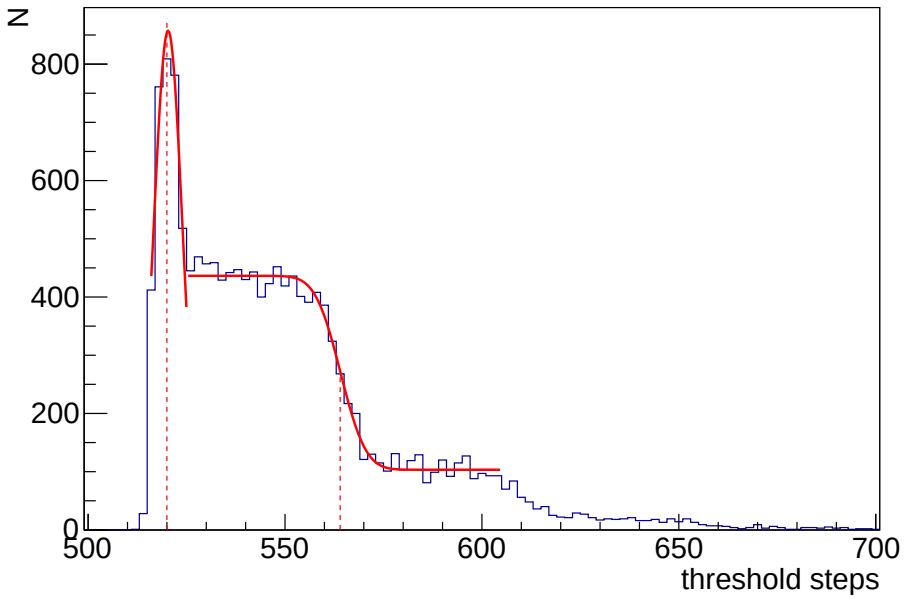

Figure 6.21: A threshold scan of one channel with fitted Gaussian function to the pedestal and error function to the transition between all photon and at least two photon events.

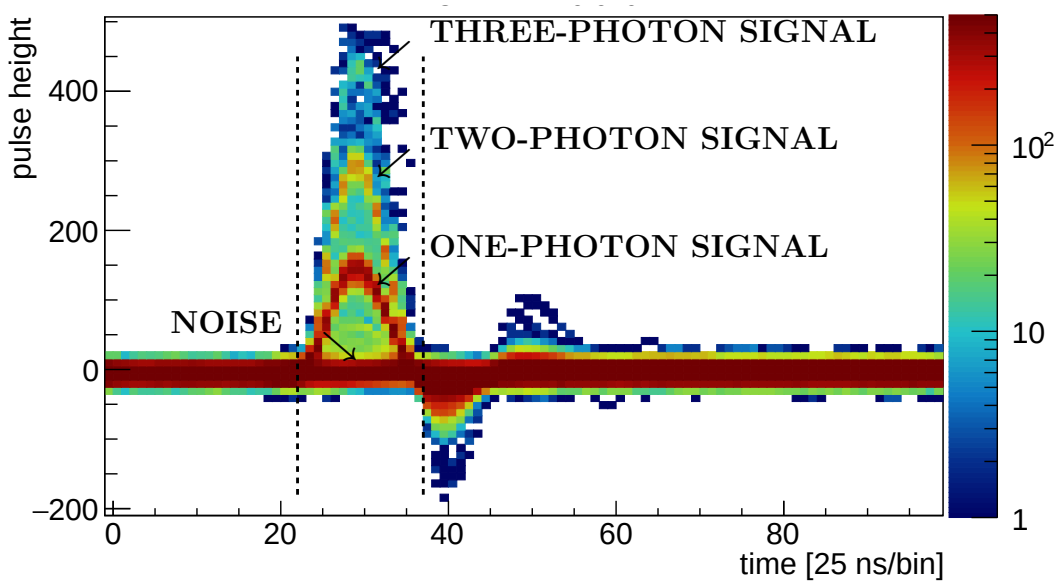

Figure 6.22: A cumulative signal for the charge collection measurement. Pulse height [a.u.] corresponds to the number of detected photons. Vertical lines present the interval at which the signal was integrated.

Integrals of 10^4 events were filled into the charge collection scans. An example is shown in Fig. 6.23. For the gain calculation, the pedestal and one-photon signal were fitted with Gaussian functions, as illustrated in the figure. The relative gain was calculated from the difference of the mean values.

A combined histogram of results for all channels of one module is shown in Fig. 6.24. One can see a noisy channel (72) and two dead channels (31 and 123). The

relative gain distribution over the sensor plane is shown in Fig. 6.25. The most typical gains correspond to the values from 80 [a.u.] to 110 [a.u.].

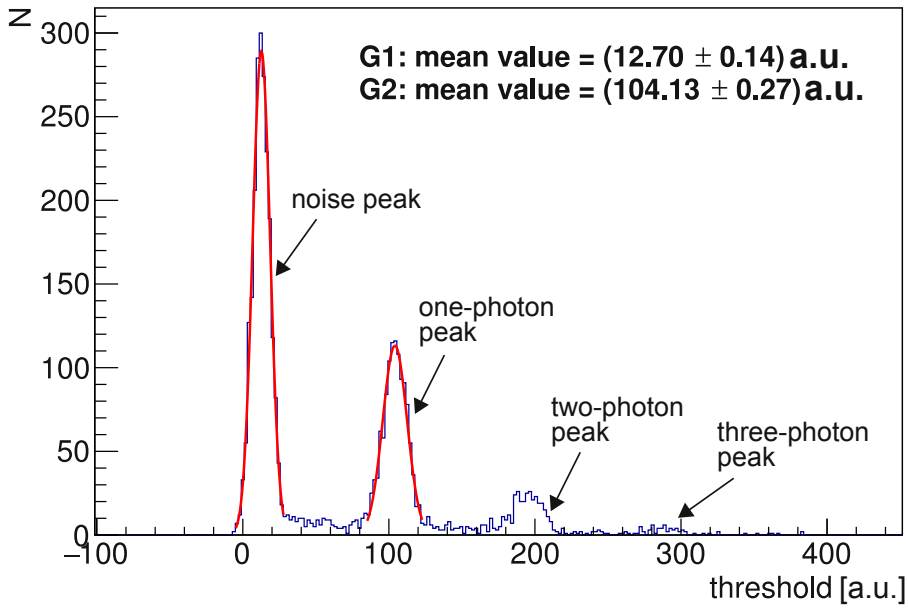

Figure 6.23: A cumulative charge collection plot for a typical channel with fitted Gaussian functions to the pedestal and to the one-photon peak.

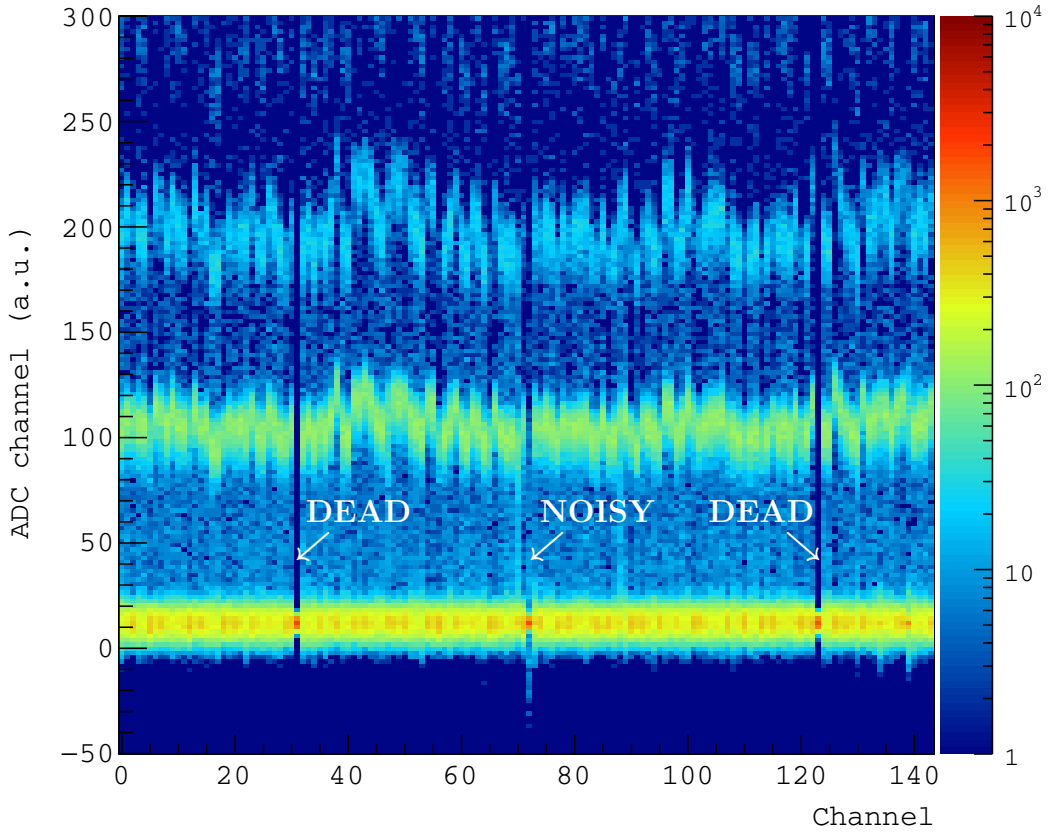

Figure 6.24: A collected charge distribution for all channels of one HAPD. This HAPD has one noisy and two dead channels, as marked in the figure.

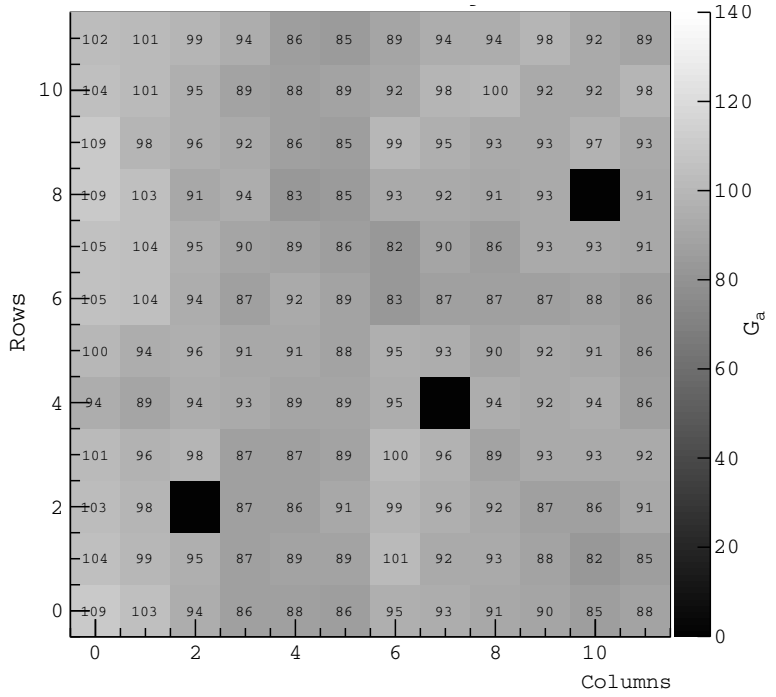

Figure 6.25: The distribution of gain [a.u.] on the centres of the channels. The view from the electronics side is shown.

6.5 Faulty Channels

In Chapter 5, it was shown that false hit information from the sensors affects the likelihood calculation and degrades the kaon/pion separation. To minimize the effect, problematic channels have to be masked in the reconstruction, because we cannot tell whether the hit is due to noise or due to a photon. The channels need to be masked due to several reasons, which can be classified into three categories:

- *Dead channels*: Some channels are permanently dead due to the damage on electronics or the sensor.
- *Noisy channels:* Some channels are permanently very noisy due to large leakage currents in electronics or in the sensor.
- *Inactive clusters of channels:* There can be problematic regions of channels due to various reasons – damage of HAPD or readout electronics, broken cable connectors, damage to power supply or data cables. In case of damage to the bias voltage one chip with 36 channels cannot detect photons. The whole sensor (144 channels) can be inactive due to damage to the front-end readout board or guard or high voltage supply. In the case of damage of merger board, the group of all sensors connected to it cannot be used.

The dead and noisy channels present 0.7 % of the total channels of installed modules. This number is expected to increase after a long-term operation of ARICH. Some sources of faulty channels can be solved by replacing a broken merger board, an HAPD or a front-end board, or using a different power supply cables in the case of damage to the connector pins or cables. This can only be done when the detector is detached from the Belle II and open, which is a very delicate procedure and is

preferably avoided if not absolutely necessary. Nevertheless, some components were replaced during the maintenance period between Phases II and III (see Fig. 2.3).

6.5.1 Permanently Faulty Channels

Permanently faulty channels were identified during the final module test. The dead channels had no signal, while the noisy channels collected some charge, but the cumulative analog signal shape has no clear transition between one-, two- and multi-photon signals. Typical cumulative time dependent signals for properly working and problematic channels are shown in Fig. 6.26.

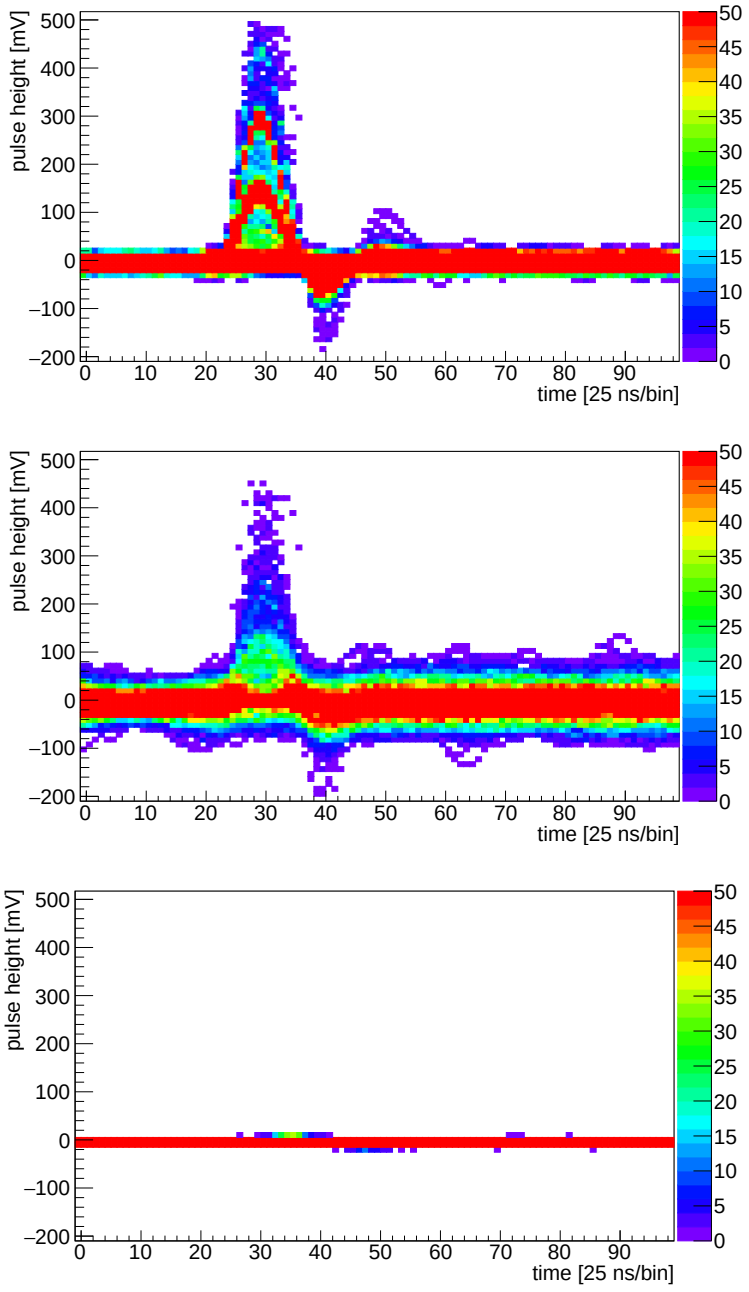

Figure 6.26: A comparison of cumulative time-dependent signals before the digitization in the ASIC for the properly working (top), noisy (middle) and dead (bottom) channels.

Faulty channels can also be identified from the threshold scans, as seen in Fig. 6.27. The downside of these measurements is that they were performed only on the centres of channels.

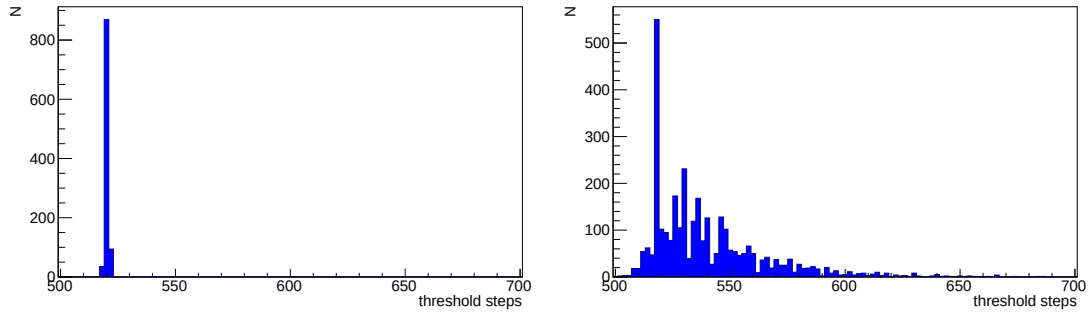

Figure 6.27: Examples of threshold scans over the centre of dead (left) and noisy (right) channels.

6.5.2 Sensor Sensitivity

For the charge collection and threshold scans, signals were collected for one channel at a time with laser illumination on its centre. To find anomalies in channel operation, two more laser scans were acquired. One scan was acquired in y direction, the other one in x. For the y direction scan, the x steps were fixed to the centres of each channel column; twelve per module. The laser was then moved over the y direction in 190 steps, each corresponding to a distance of 359.5 µm. A schematic depiction of the laser movement over the HAPD surface for both scans is shown in Fig. 6.28. During the scan over the y direction, signals from all channels in a row were collected. An example of a scan is shown in Fig. 6.29.

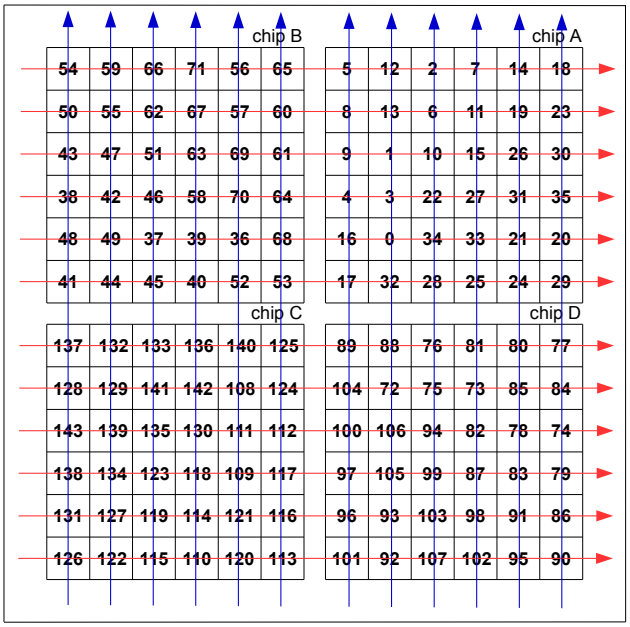

Figure 6.28: A movement of laser for two scans in x (red) and y (blue) direction. A position-dependent sensitivity of HAPDs was tested.

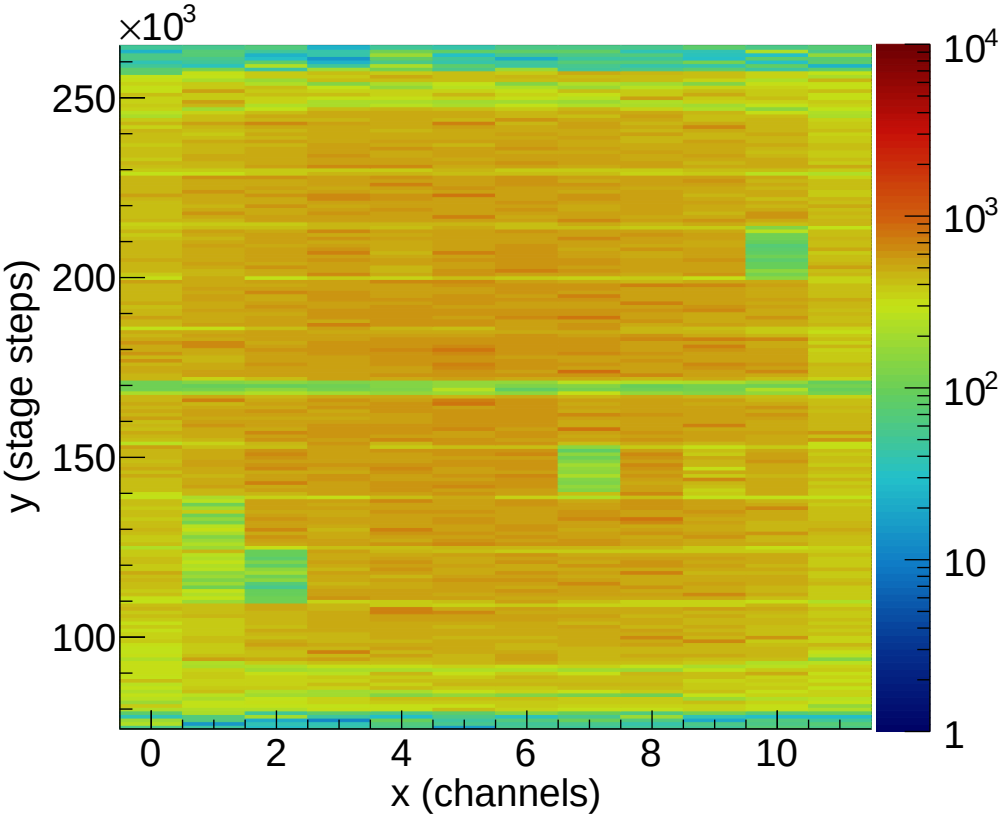

Figure 6.29: Laser scan over the centres of channel columns.

The same scans were performed also in x direction, where the positions of the laser were fixed to the centres of channel rows. From the projection of the laser scan (Fig. 6.30), it is seen that the eighth channel in row 4 induces a signal, regardless of the incident light position. The number of events with a signal above the threshold is slightly higher when the channel is illuminated, but lower than for the rest of the channels. Such channels are noisy and their responses do not correspond to the actual detected photons. For the third channel in row 2 and eleventh channel in row 8, we can see no signal even when the channel is illuminated by the laser. These two channels are dead. The two-dimensional presentation of the same scan is shown in Fig. 6.31.

Fig. 6.30 also shows a distortion at the edges of the rows. This is a result of an inhomogeneous electric field at the edges due to a dielectric material in the walls of the HAPD. The trajectories of the particles close to the edges are illustrated in Fig. 6.32. The effect is gone when HAPD is put into a strong homogeneous magnetic field, parallel to the HAPD's electric field.

Results of the final module tests were carefully checked and the faulty channels were determined from the two-dimensional laser scan and also from the threshold scans of the centres of channels as a crosscheck. Sensors with less than ten problematic channels passed the test, although most of them kept this number well below. Modules with a lower proportion of problematic areas were used for the installation. The distribution of the problematic channels over the sensor plane is presented in Fig. 6.33.

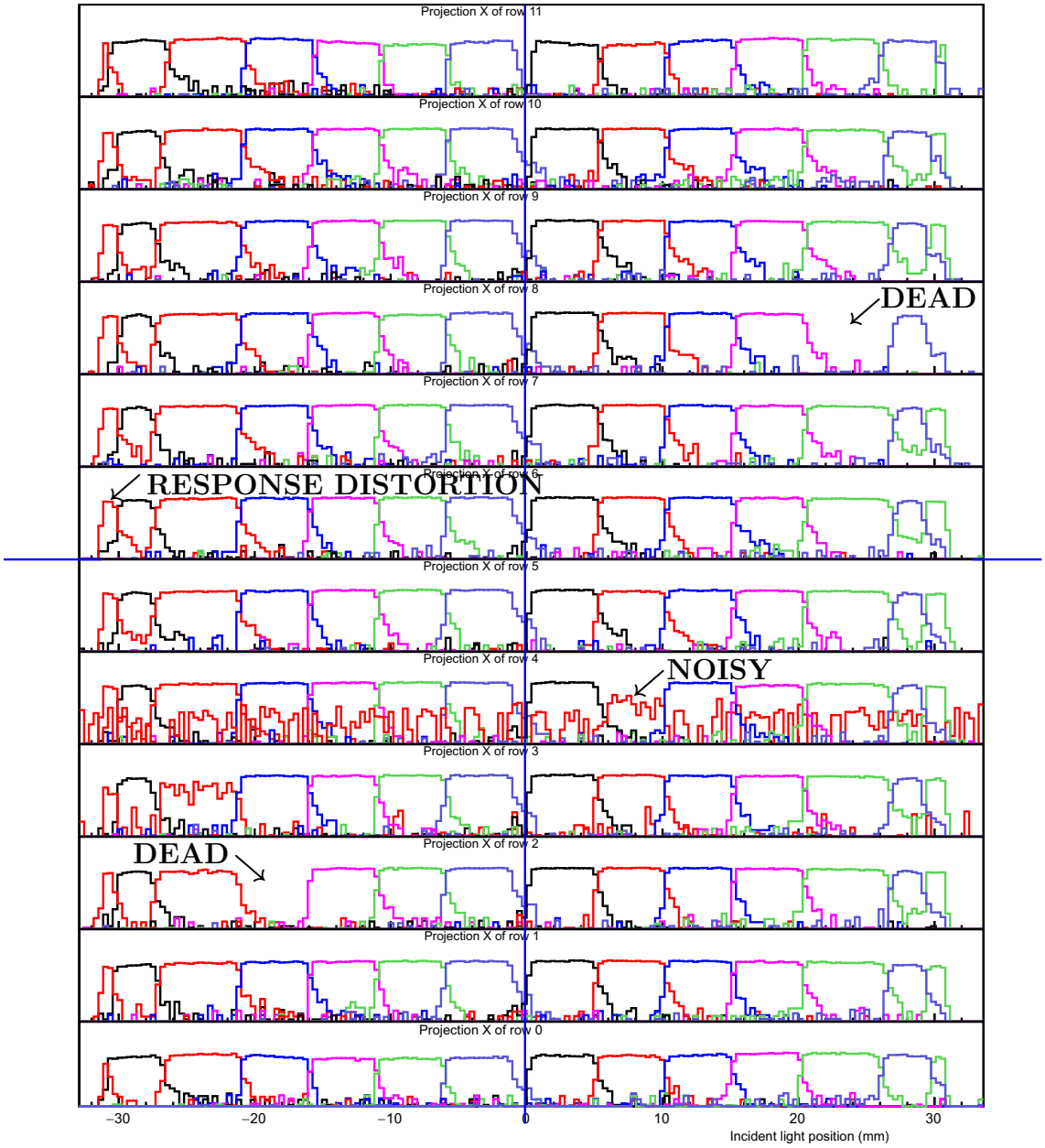

Figure 6.30: A projection of laser scan over the centres of the channel rows. The x-axis shows the position of incident light with respect to the centre of the HAPD. The y-axis represents a number of events in a logarithmic scale with values from 1 to 10^4 for each projection separately. One channel in row 4 is noisy and induces a signal regardless of the laser position. Two dead channels are seen in rows 2 and 8. A distortion at the edges is a result of an inhomogeneous electric field in HAPD, as shown in Fig. 6.32.

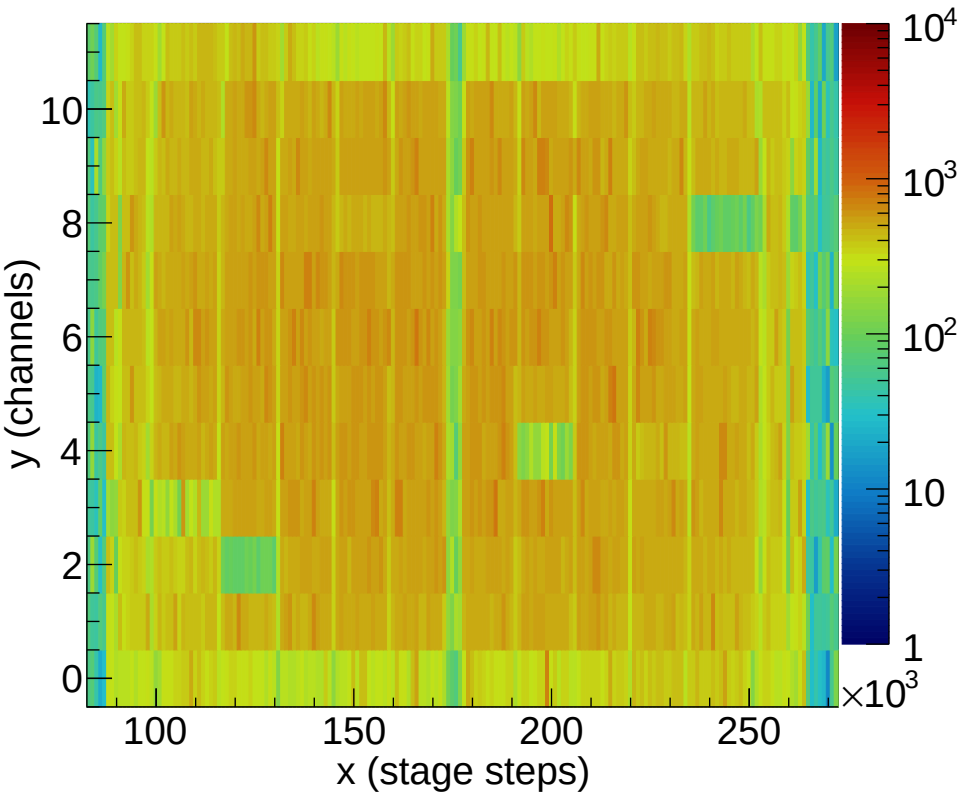

Figure 6.31: Laser scan over the centres of channel rows.

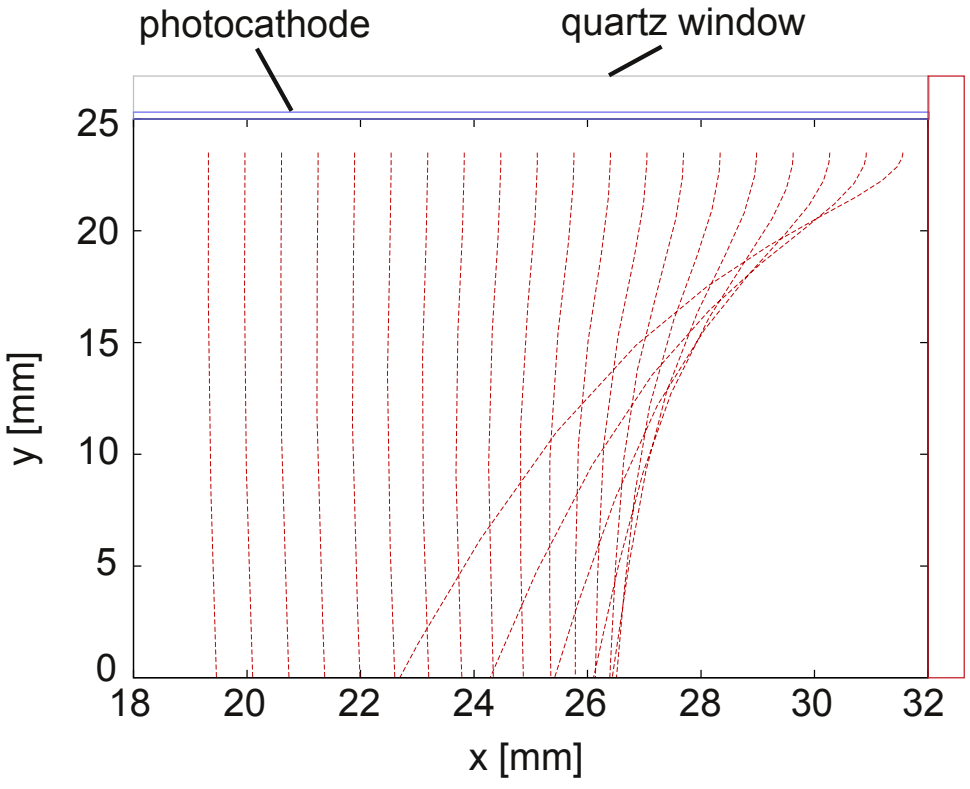

Figure 6.32: A schematic depiction of the trajectories of the photoelectrons at the edges of HAPD due to inhomogeneous electric field [71].

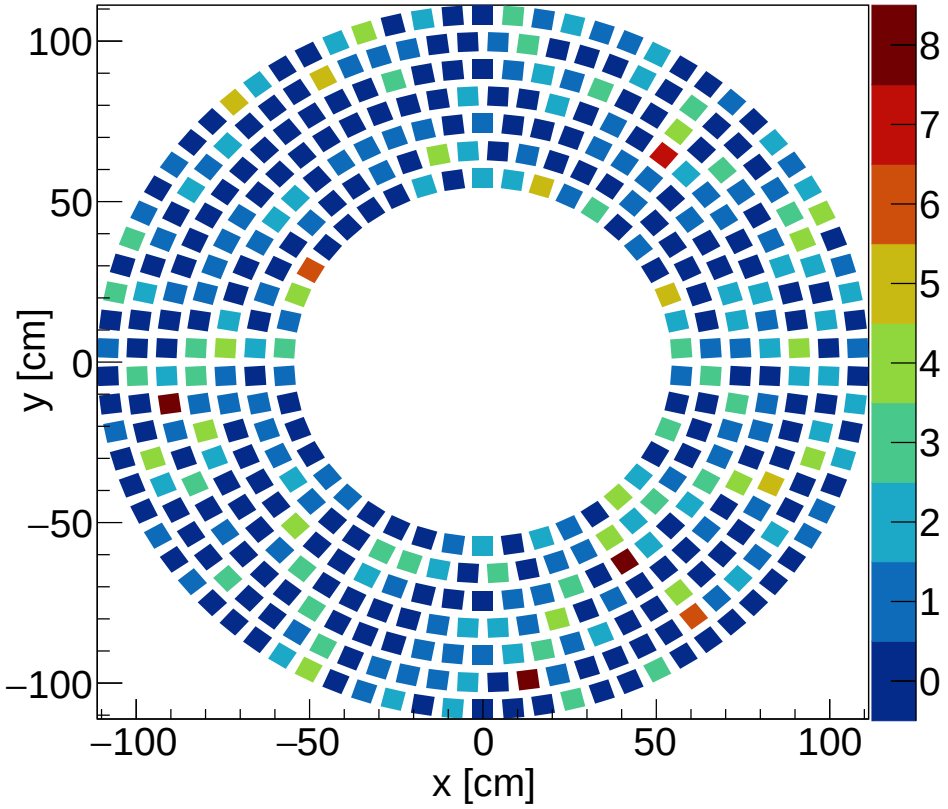

Figure 6.33: The sensor plane distribution of the number of faulty channels per module.

6.5.3 Inactive Channels in Phase II

Some parts of ARICH were inactive during Phase II due to high leakage currents on HAPD power supplies or the lack of communication with merger boards. Mapping of these modules is presented in Fig. 6.34.

Results of the first physics runs during the commissioning phase showed that some channels became noisy later on. The proportion of them is small and it varies from run to run, which implies that some of them appeared to be due to improperly calibrated electronics parameters during certain runs. Therefore, noisy channels from the module test were not masked during Phase II, but determined separately for each run offline. Studies of the full data sample indicated that masking the channels with an occupancy level above 0.15 % should be sufficient to mask the noisy channels without affecting the properly working ones. An example of channel occupancy distribution for one run is shown in Fig. 6.35. Occupancies for all channels[1] before and after applied masking are presented in Figs. 6.36 and 6.37, respectively.

[1]The global channel identification numbers, $chID_G$, are calculated from the HAPD numbering, $hapdID$, and internal channel numbers, $chID_L$, as $chID_G = (hapdID - 1) * 144 + chID_L$.

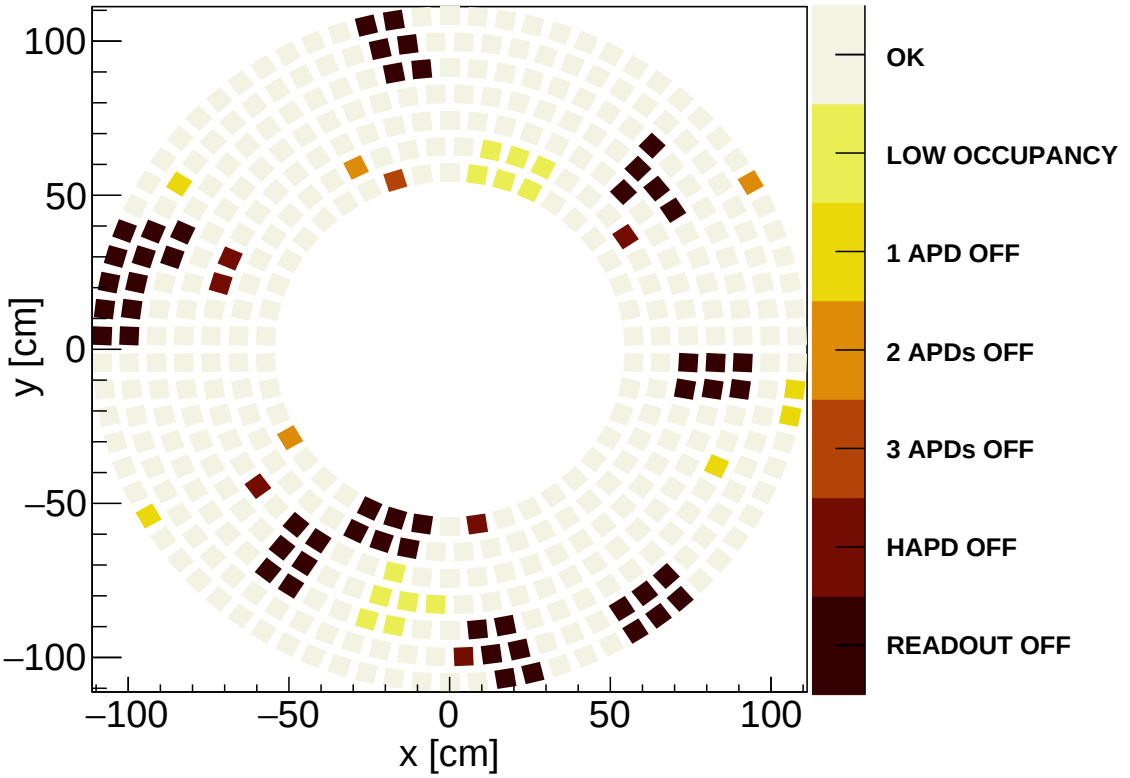

Figure 6.34: Mapping of the inactive part of whole modules during the Phase II runs. Some APDs were turned off due to high leakage currents. Some merger boards had communication issues and the entire readout was inactive.

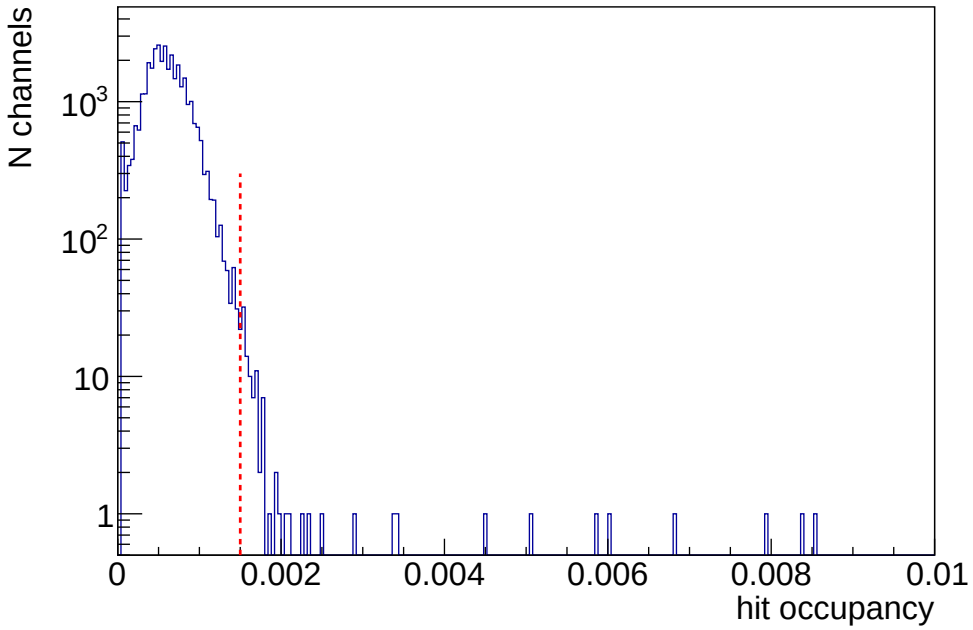

Figure 6.35: Distribution of channel occupancies with cut at 0.15 % (red line) for noisy channels. Note the logarithmic scale on the y-axis.

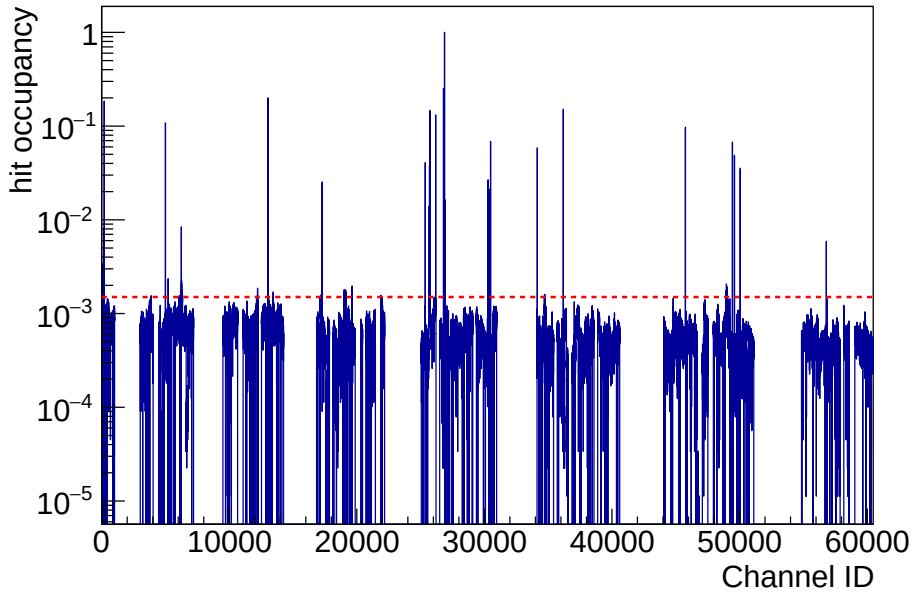

Figure 6.36: The channel occupancy before masking the noisy channels. The red dotted line shows the limit of 0.15 % occupancy, above which the channels are categorized as noisy. Sectors 2 and 3 were turned off, as well as several merger boards. Thus almost half of channels have zero hits.

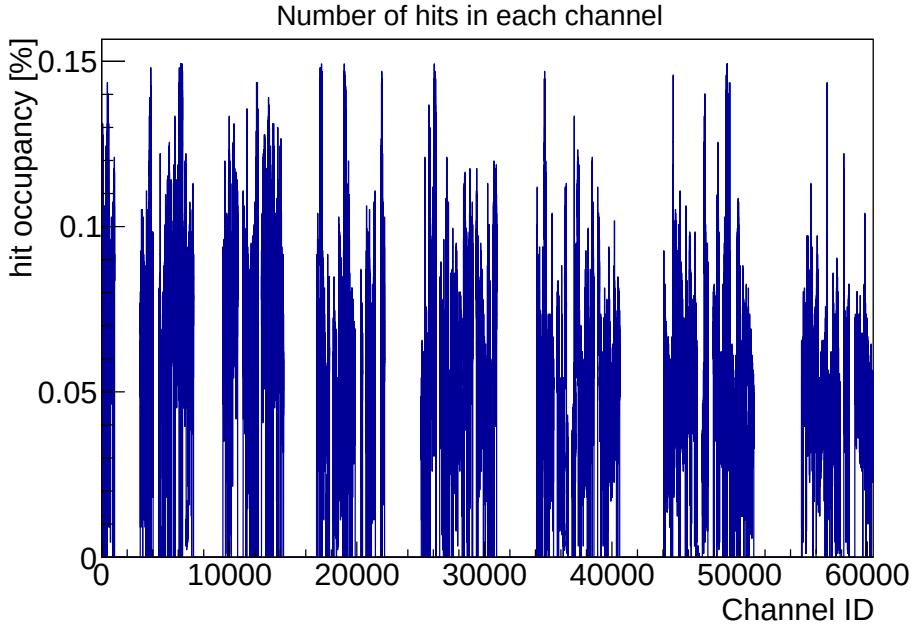

Figure 6.37: The channel occupancy after masking the noisy channels. Hit distribution is not uniform due to lower statistics. Sectors 2 and 3 were turned off, as well as several merger boards. This explains why almost half the channels have zero hits. Channel ID on the x-axis is a global channel number, that can be calculated from HAPD identification number $hapdID$ and HAPD channel number $chID_L$ (refer to Appendix B for the mappings) as $ChannelID = (hapdID - 1) * 144 + chID_L$.

The fixed occupancy limit for masking noisy channels is not the optimal solution, because occupancy plots can differ for different runs. Among the main reasons for the different occupancy distributions are different timing settings of the trigger, offset miscalibration and different threshold settings of the electronics. From a physics perspective, beam backgrounds also increase the hit rate and they depend on the beam size and luminosity. The hit rate is also position dependent, especially if a part of the tracking system is not calibrated properly or included in the run, so the determination of noisy channels should be performed with respect to the occupancies on the nearby channels, instead of globally. The low luminosity and short runs during the Phase II did not allow such a precise method due to the low statistics.

6.5.3.1 Reconstructed Particles

The performance of ARICH in Phase II was studied despite the small sample size and larger inactive areas of ARICH during the collisions. It was evaluated using the events from the Bhabha scattering, illustrated in Fig. 6.38. Even though there are mostly electrons detected in this events, the results can be used for a rough estimation, since the resolution of Cherenkov angle depends mostly on the radiator thickness and size of the channels on the sensors, as it was already discussed in Section 4.3.1.

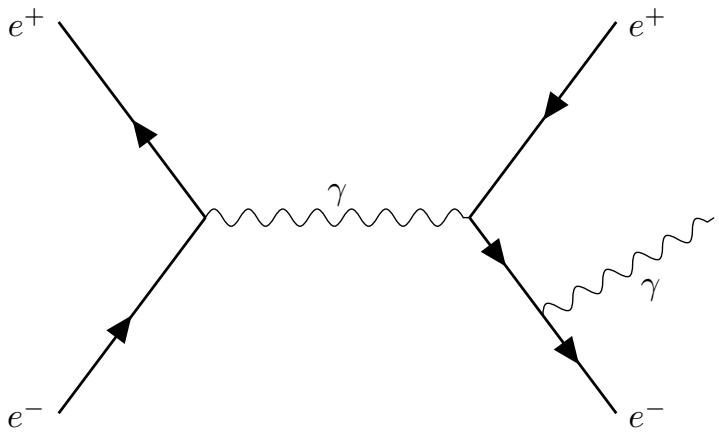

Figure 6.38: An example of a radiative Bhabha scattering.

The Cherenkov angle resolution was estimated using the Phase II sample with the integrated luminosity of $490\,\mathrm{pb}^{-1}$. A selection was applied to the momentum of particles to be between 5.8 GeV/c and 7.4 GeV/c, as seen in Fig. 6.39 left. The worse performance due to reflected photons at the edges of the detector was reduced by the selection of the reconstructed hit positions on the aerogel, which was determined to be between 60 cm and 100 cm, as marked in the same figure (right).

Cherenkov angle distribution, seen in Fig. 6.40, was fitted with linear function and two Gaussian functions:

$$fit = c_0 + c_1 \times \theta_{ch} + N_0 e^{-\frac{(\theta_{ch}-\mu_0)^2}{2\sigma_0^2}} + N_1 e^{-\frac{(\theta_{ch}-\mu_1)^2}{2\sigma_1^2}} \tag{6.5.1}$$

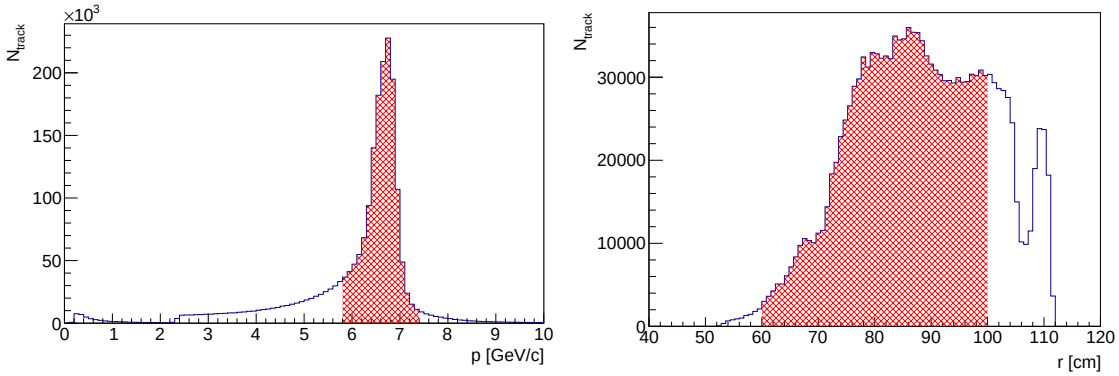

Figure 6.39: Left: A momentum distribution of particles, detected by ARICH, from Bhabha events in Phase II. The red area presents an applied momentum selection of 5.8 GeV/c to 7.4 GeV/c. Right: A distribution of the radius of the particle hits on the aerogel plane. The momentum selection of 5.8 GeV/c to 7.4 GeV/c is applied. The red area presents the chosen radius selection between 60 cm and 100 cm.

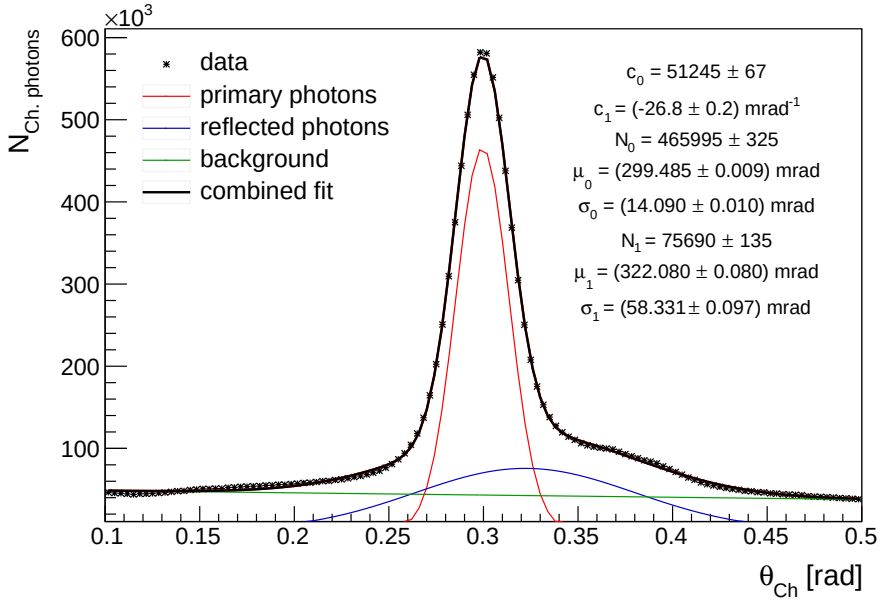

Figure 6.40: The Cherenkov angle distribution of reconstructed photons with an applied momentum selection of 5.8 GeV/c to 7.4 GeV/c and the position selection of the radius of the reconstructed track hit between 60 cm and 100 cm.

The resolution of a single track was estimated from the Eq. 4.3.1, where the single photon resolution was determined from the fitted function in Fig. 6.40, and the average number of detected photons from Fig. 6.41:

$$\sigma_{track} = \frac{\sigma_0}{\sqrt{N_{pe}}} = \frac{(14.09 \pm 0.01)\text{mrad}}{\sqrt{10.34}} \approx 4.4\text{mrad} \tag{6.5.2}$$

The distribution of tracks over the Cherenkov and polar angle is shown in Fig. 6.42. A projection of Cherenkov angle for each polar angle bin was fitted as presented in Fig. 6.40. The mean values of the Gaussian function, fitted to the peak, are fitted

with the red curve. The red curve shows how Cherenkov angle changes with the polar angle (defined in Fig. 5.2), and should be flat in the case of an ideal alignment.

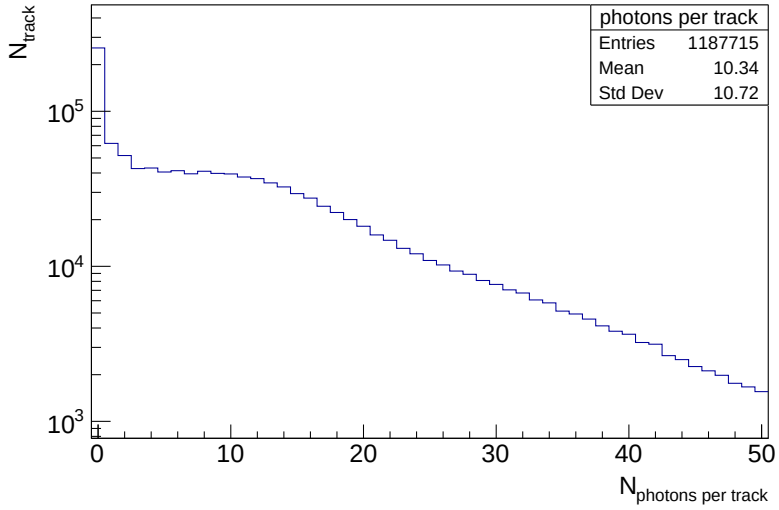

Figure 6.41: The distribution of detected photons per track for the applied selection of momentum range from 5.8 GeV/c to 7.4 GeV/c and the radius from 60 cm to 100 cm.

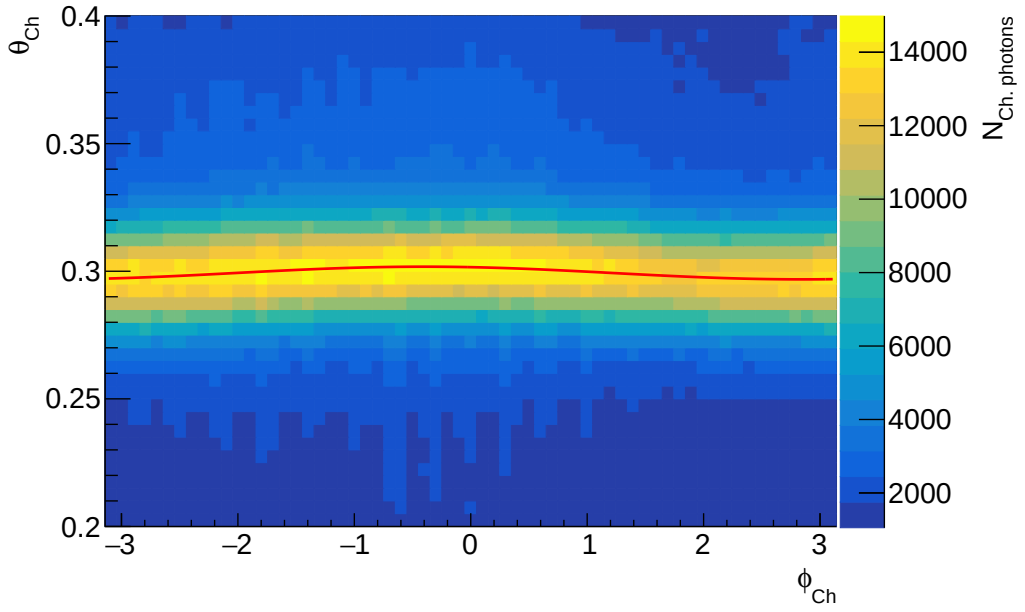

Figure 6.42: The distribution of tracks over the Cherenkov and polar angle is shown.

6.6 Temperature Effects in Phase II

The initial ARICH cooling system, shown in Fig. 6.43, could not transfer heat efficiently enough to keep the temperature at the electronics side below 40 °C. Stainless steel cooling pipes were attached to the aluminium frame, without a direct coupling between the heat sources (electronic chips on the front-end readout boards and merger boards) and the cooling system.

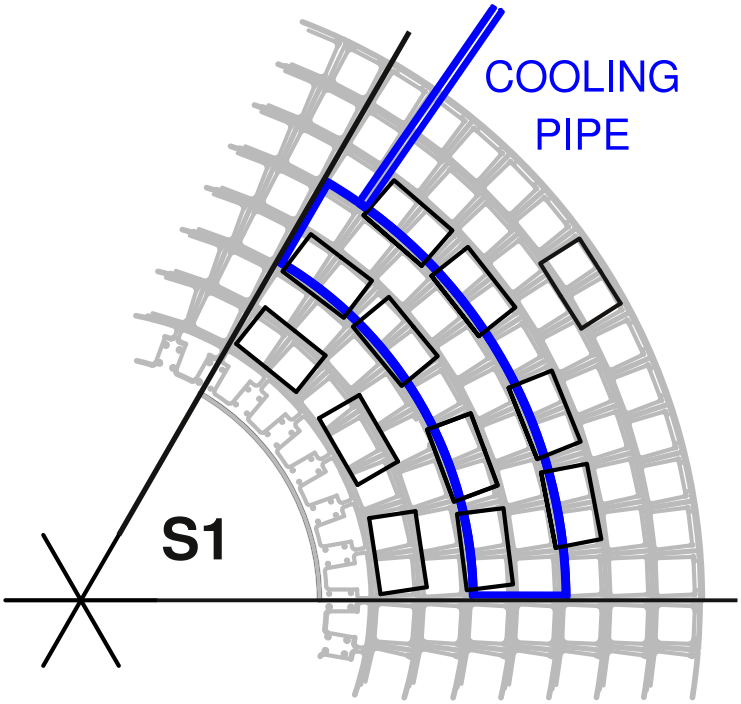

Figure 6.43: Schematic depiction of initial ARICH cooling system for one sector. Stainless steel pipes were attached to the detector frame and cooled with water [36]. The positions of merger boards are marked with black rectangles.

A complete replacement of the cooling system requires a disassembly of ARICH, which could not be realized during data collection with Belle II, so the temporary solution was to install an additional cooling body (seen in Fig. 6.44) on the outer side of the backplane. The main constraint was space availability, so finally one plate was installed on the right outer side of the backplane, as presented in Fig. 6.45. Four temperature sensors were installed between the detector frame and the backplane, as shown in the same figure.

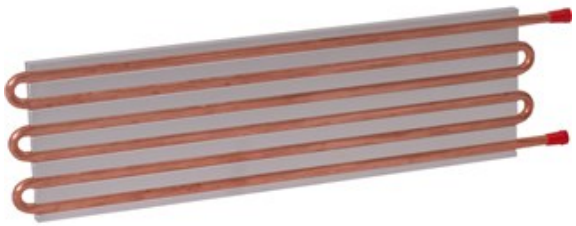

Figure 6.44: A copper-tubed cold plate, used during Phase II [79].

After the installation of an additional cooling body, temperatures of the four sensors were constantly monitored. The longest period of the operation of all six sectors was one day. The temperature monitoring started two hours after the beginning of operation and temperatures increased gradually as seen in Fig. 6.46.

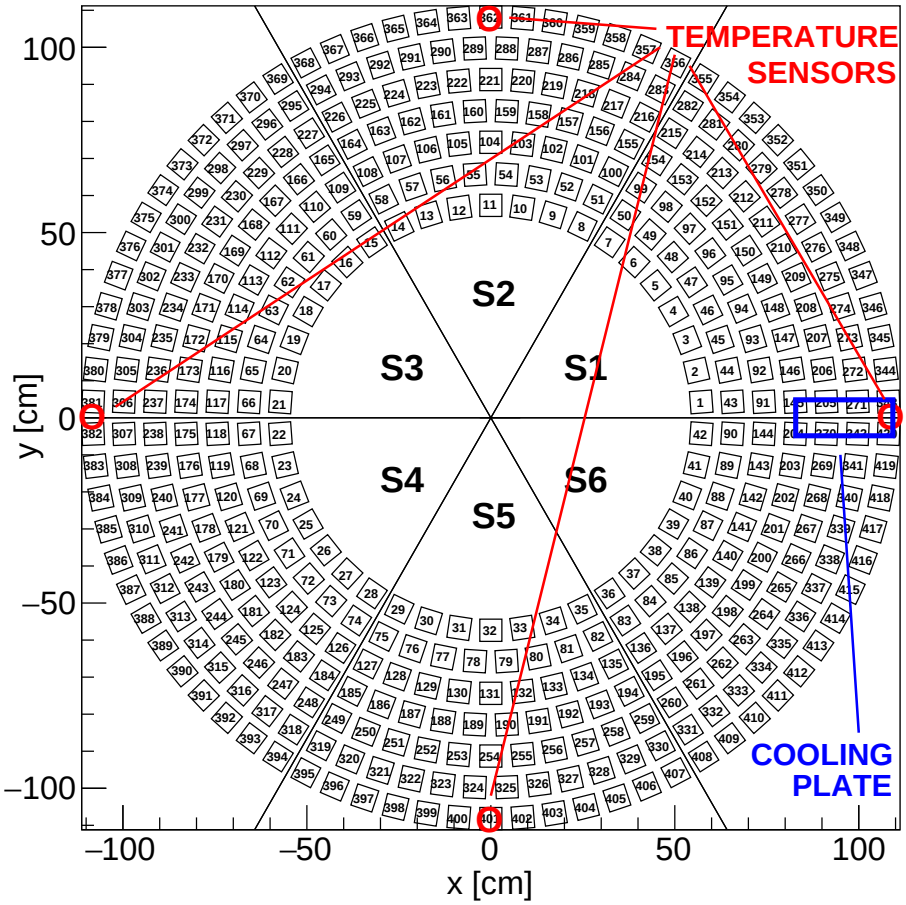

Figure 6.45: A schematic depiction of ARICH electronics side with numbered modules. Four temperature sensors were installed inside, while an additional cooling body was installed on the outer side of the backplane.

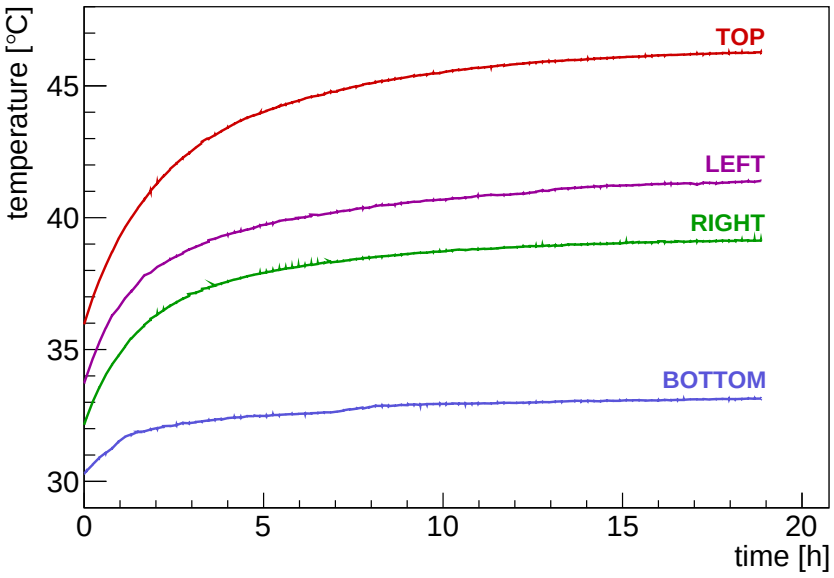

Figure 6.46: Temperatures on four ARICH temperature sensors. Monitoring started two hours after the beginning of operation of full ARICH.

There are additional temperature sensors on the electronic components; two per merger board (one in the FPGA of each merger board and one on the board itself) and two per front-end board (one on the ASIC and other one on the FPGA side). They were also monitored during the ARICH operation. Temperatures of merger boards were measured directly in the FPGA. The front-end board temperature sensors are mounted on the board only, therefore measured temperatures of the front-end boards are lower than the actual temperatures inside its components. The temperature increase for one front-end board per sector is shown in Fig. 6.47. Temperatures at the ASIC side of front-end board (between the front-end board and HAPD) after two and 18 hours of operation for all front-end boards are presented in Fig. 6.48. Mappings of front-end ID numbers can be found in Appendix B.

For more temperature measurement results refer to Appendix C. Time dependencies of temperatures of outermost mergers and electronics boards for each sector are shown there. The temperature changes of the four ARICH temperature sensors and electronics during a week of discontinuous ARICH operation are also presented there.

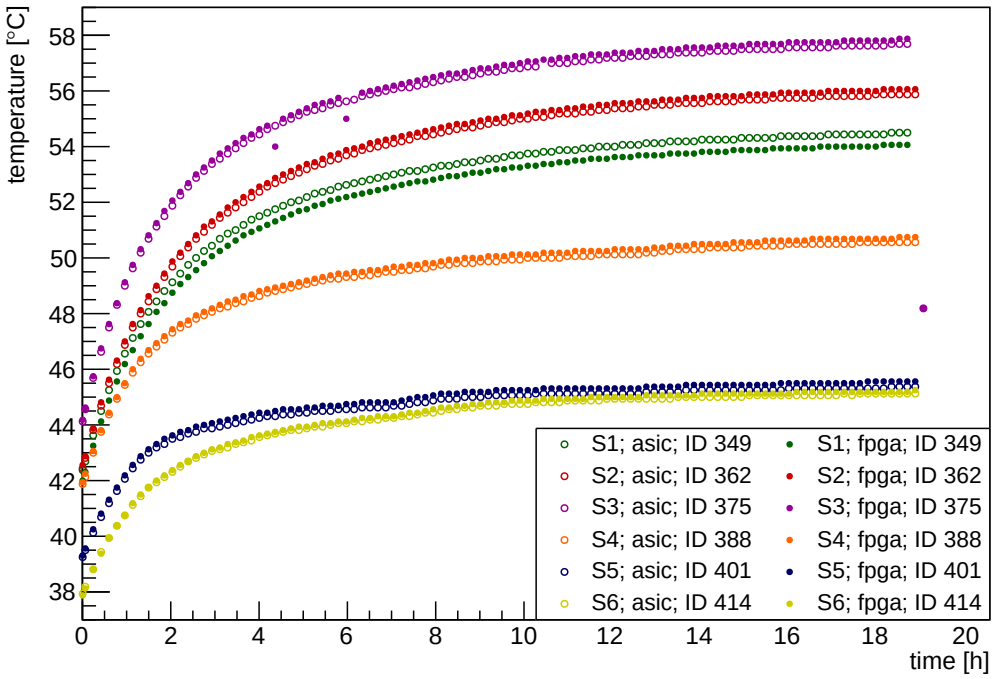

Figure 6.47: Temperatures, measured on the ASIC and FPGA side of front-end boards, for six front-end boards. Results for the boards in the middle of the outer ring for each sector are shown.

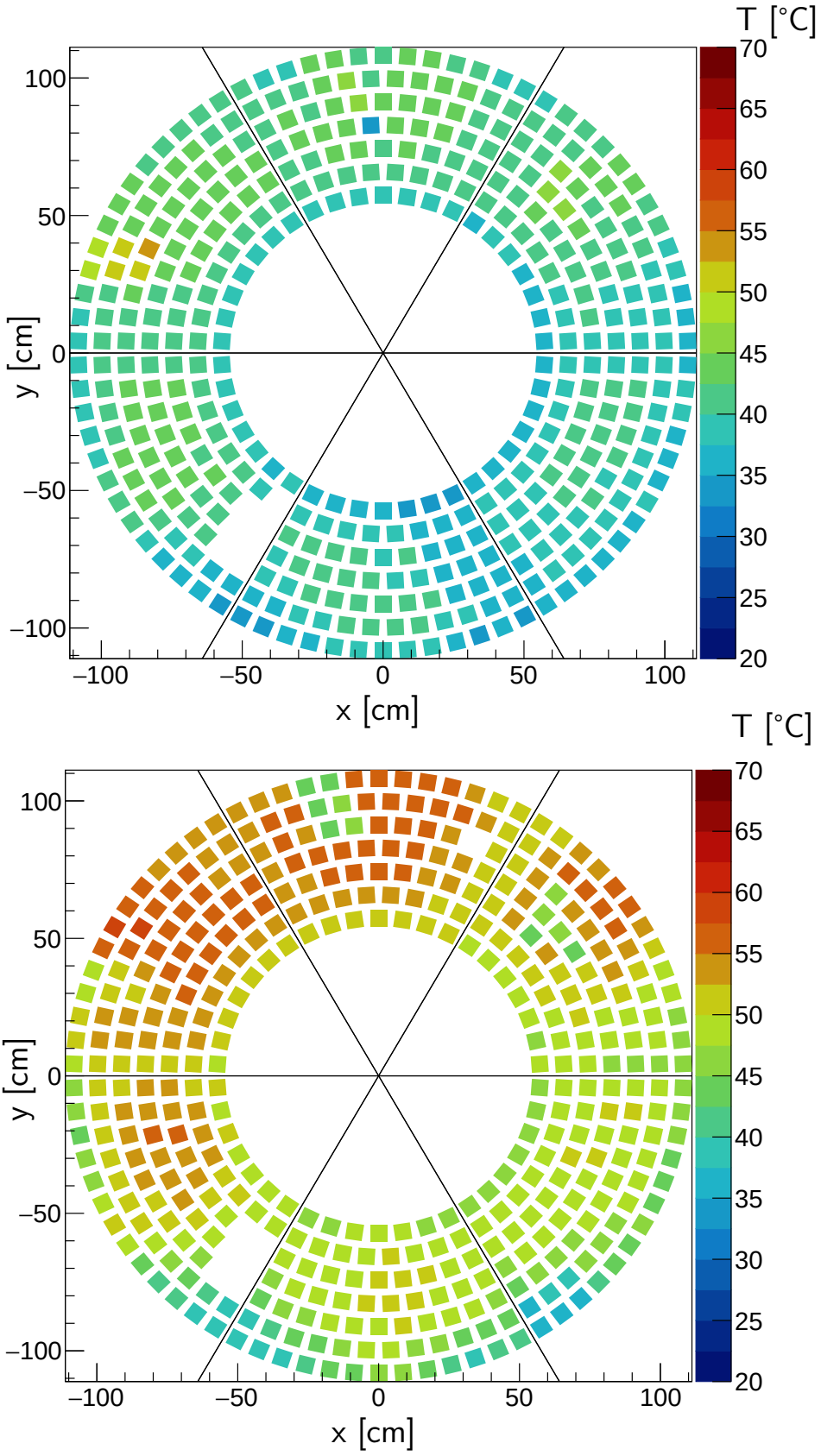

Figure 6.48: Temperatures, measured on the ASIC side of front-end boards, two (top) and 18 (bottom) hours after all electronics components of ARICH have been supplied with electrical power.

6.6.1 Temperature Effects on Calibration

ARICH was mostly operating with three or four sectors at once to prevent overheating. Due to unknown temperatures of the HAPD sensors, the safety limit was set to the maximal temperature of the top sensor of up to 42 °C. This allowed the usage of the entire readout system for up to five hours, if it was turned off for at least three hours prior to that in order to let it cool down. Turning on the readout again required initializing the ARICH data acquisition system, which could not be automatised at that stage. This was one of the main reasons for not iterating between running the entire ARICH readout and turning it off in order to let it cool down throughout the entire Phase II, but only using the full configuration a few times instead. To evaluate the effects of higher temperature on the efficiency of data collection, threshold scans of non-illuminated and illuminated sensors were taken.

6.6.1.1 Noise Measurements

Threshold scans of non-illuminated sensors were taken at three different temperatures at the cable side of ARICH. The low and bias voltages were supplied to front-end boards and HAPDs, and the high voltage was turned off during the measurements. The threshold was moved in steps of 10 mV between −500 mV and 500 mV, and transitions over the threshold for 1000 events were counted. The temperature of the top sensor during the measurements was 29 °C, 35 °C and 39 °C, respectively. The first measurement was acquired 15 minutes after the electronics and sensors were turned on, and the other two were taken one and two hours afterwards. Threshold scans for all modules, except masked ones (see Fig. 6.34), were acquired. The example for module with ID 38 (refer to the mappings in Appendix B) is shown in Fig. 6.49.

Noise distributions of channel 140 for all three temperatures are presented in Fig. 6.50. There is little difference between the noise distribution of one channel at the middle and the high temperature, but they differ from the scan that was taken only 15 minutes after the start of operation. From the histogram fits in the figure, it is seen that the mean value of the Gaussian distribution is slightly shifted at higher temperatures, which could also be a result of relatively large bin widths. A comparison of the height and width of the noise distributions at different temperatures shows increased noise, generated by dark current in the silicon of the photodiodes.

The results of all properly working channels were fitted with Gaussian functions, and their shifts and widths at different temperatures were compared. Results are presented in Figs. 6.51 and 6.52. The standard deviations increased for 2.3 mV (17 %) on average.

The enlarged width of noise distribution caused more hits, generated by electronics noise. If the threshold value is set to 3.5σ above the noise baseline at lowest temperature and the standard deviation increases for 17 % at higher temperature, it means that the set threshold is only 3σ above the baseline at the higher temperature. The probability of detecting the signal, that is triggered by noise, increases from 0.23 ‰ to 1.4 ‰, which is close to the limit that was set for Phase II data analysis, as seen in Fig. 6.35.

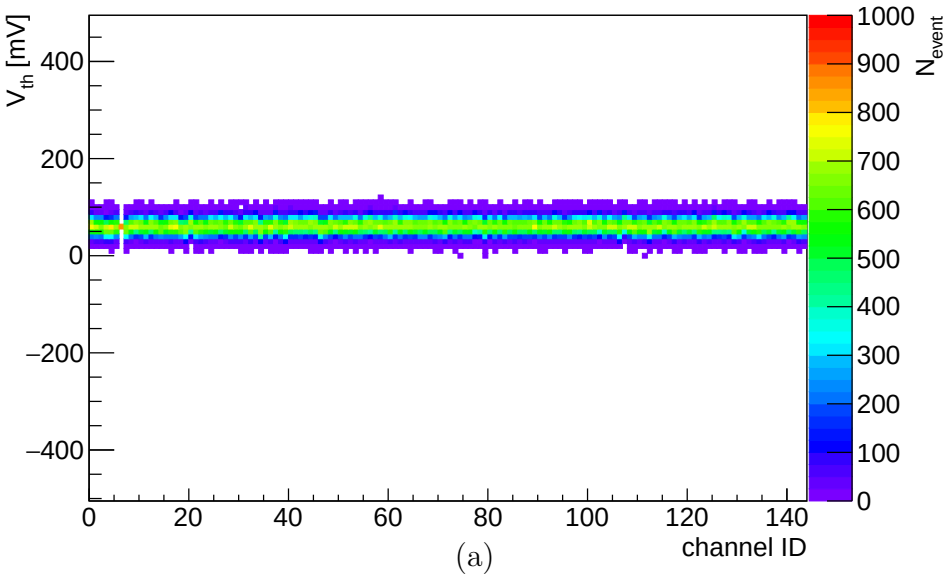

(a)

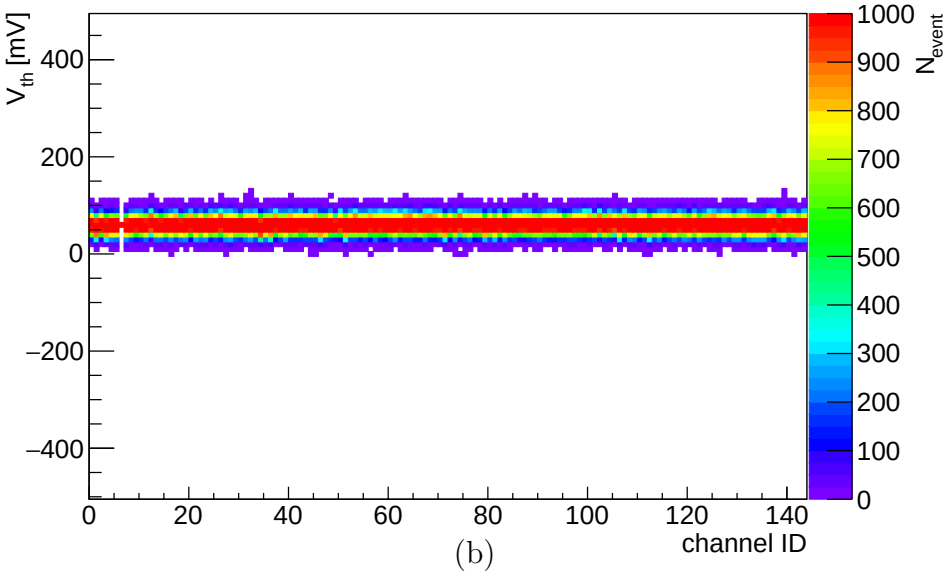

(b)

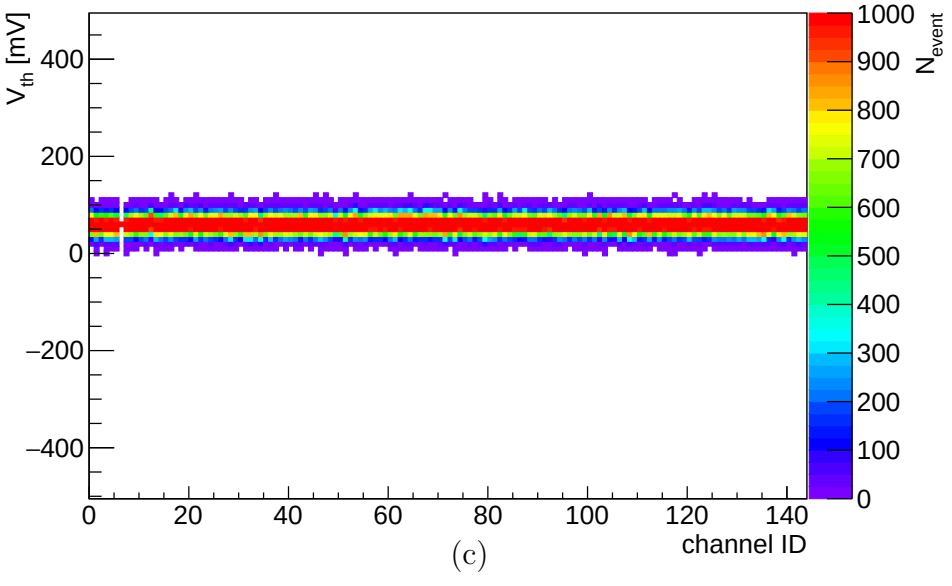

(c)

Figure 6.49: Threshold scan of non-illuminated sensor ($ID = 38$) at three different temperatures of the top temperature sensor: (a) 29 °C, (b) 35 °C, (c) 39 °C.

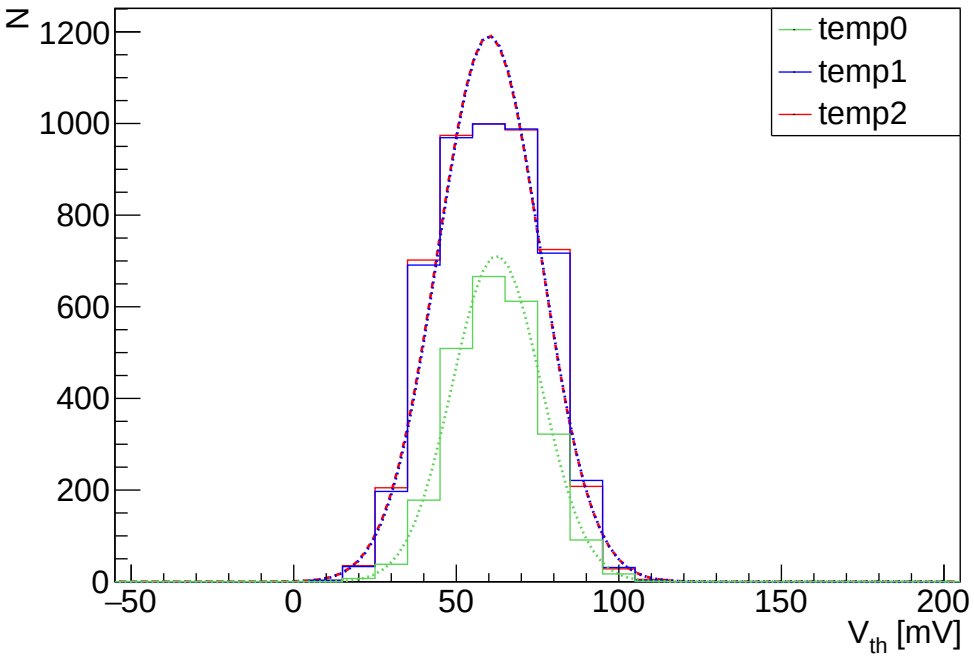

Figure 6.50: Threshold scans of one channel (module 38, channel 140) at three different temperatures at the cable side of ARICH. Results are fitted with a Gaussian function.

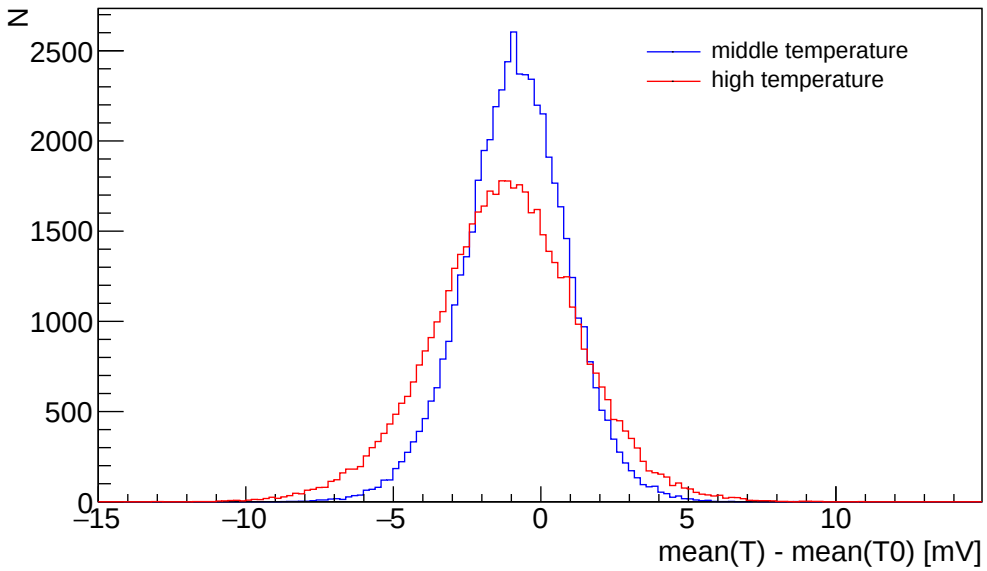

Figure 6.51: Distributions of the shifts of mean value of a Gaussian function at higher temperature. The shift is calculated as the difference of the mean value at temperature of the top sensor of 35 °C (39 °C) and 29 °C for the middle (high) temperature.

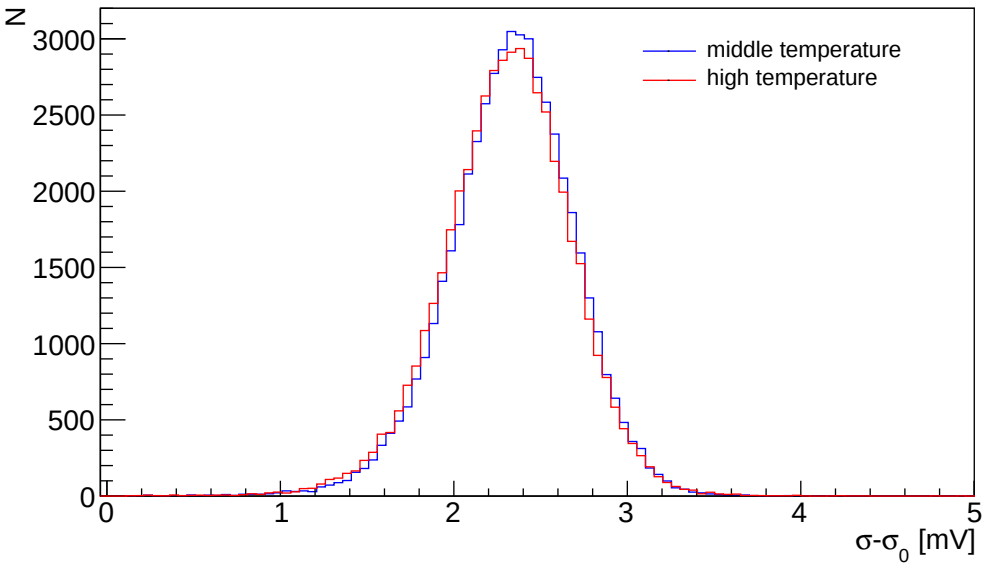

Figure 6.52: Distributions of the difference of a Gaussian function standard deviations at higher temperatures. It is calculated as the difference of the Gaussian standard deviation at a temperature of the top sensor of 35 °C (39 °C) and 29 °C for the middle (high) temperature.

6.6.1.2 Gain Measurements

Threshold scans of sensors, illuminated by LED light, were acquired at temperatures of 32 °C, 34 °C and 41 °C. Fibres were installed to the HAPD side of the detector plane at positions, shown in Fig. 6.53.

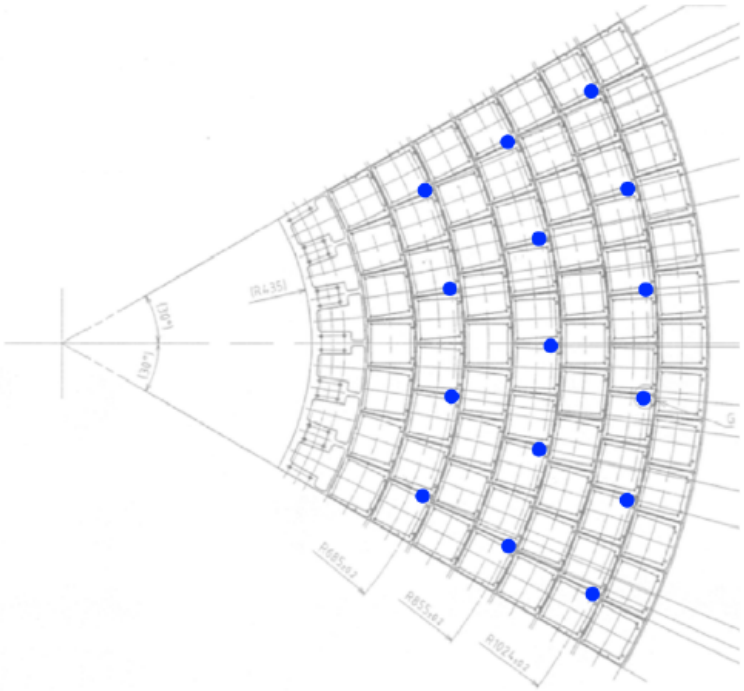

Figure 6.53: Positions of installed fibres from a LED diode for calibration of the gain and studies of channel response [80].

The measurements were taken with the full ARICH detector, but the main principle was the same as at gain measurements in the module test, described in Section 6.2.2. Bias voltages that correspond to the avalanche gain of 40 and the high voltage of 6 kV were supplied to modules. An estimate of average bombardment gain (based on Figs. 4.25 and 6.20) is approximately 1200 – 1250, accounting to the total gain of 5×10^4.

Threshold scan results of all channels of one module at different temperatures are shown in Fig. 6.54. The results look similar, but a comparison of the threshold scan for one channel at three different temperatures in Fig. 6.55 shows that the channel gain decreases with temperature. This has to be taken into account at the threshold determination to keep the efficient signal detection.

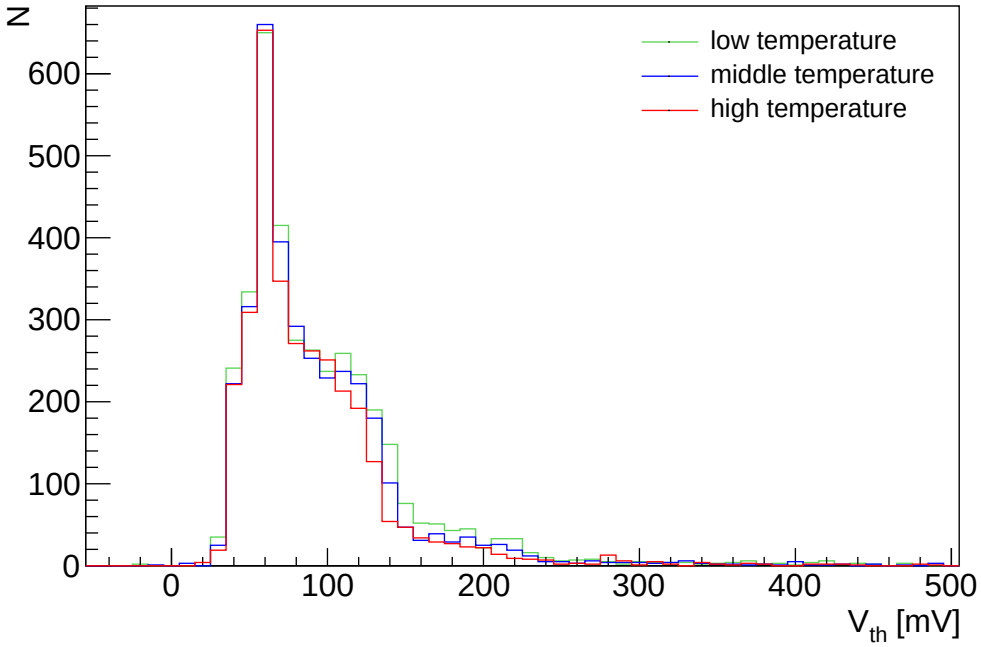

Figure 6.55: A comparison of the threshold scan of one channel (module 38, channel 140) at three different temperatures of the ARICH top temperature sensor; 32 °C, 34 °C, 41 °C.

The total gains were determined for all channels. The threshold scan was fitted with a Gaussian function to the pedestal and an error function to the transition between at least one-photon and at least two-photon signals, as described in Section 6.4.1 and illustrated in Fig. 6.56. Fitting was performed in three steps:

1. A bin with a maximal value $V_{N=max}$ was found and a Gaussian function was fitted to it in a range that corresponded to the $V_{N=max} \pm 0.6 \times RMS$. The Gaussian function parameters – a mean value, V_{mean}, and a Gaussian standard deviation, σ – were used to determine more precise fitting range and initial parameters for fitting the pedestal in the following step.
2. The pedestal peak was fitted with a Gaussian function in the range of $V_{mean} \pm 3 \times \sigma$.
3. The transition between at least one-photon and at least two-photon events was fitted with the error function in the range between $V_{mean} + 3 \times \sigma$ and $V_{mean} + 150\,\text{mV}$.

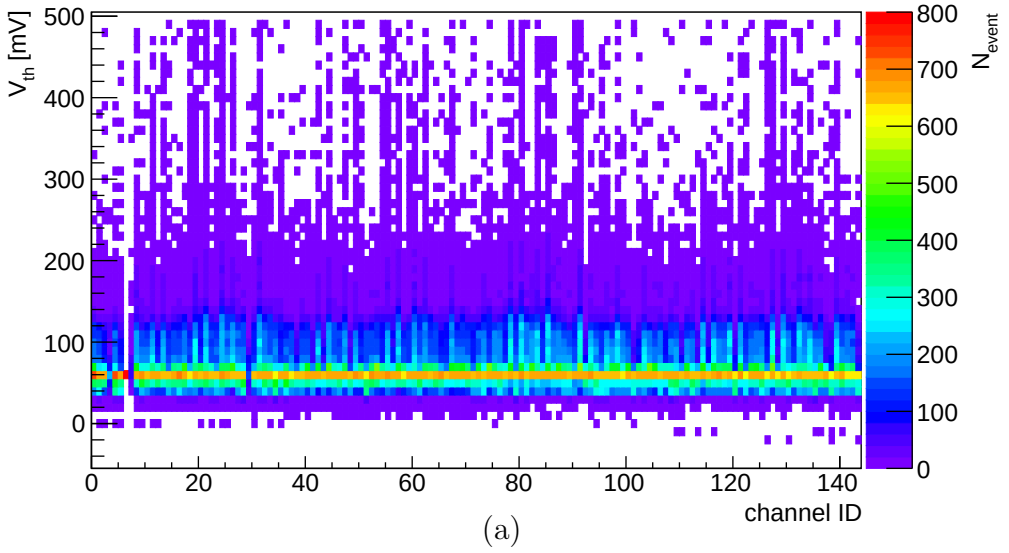

(a)

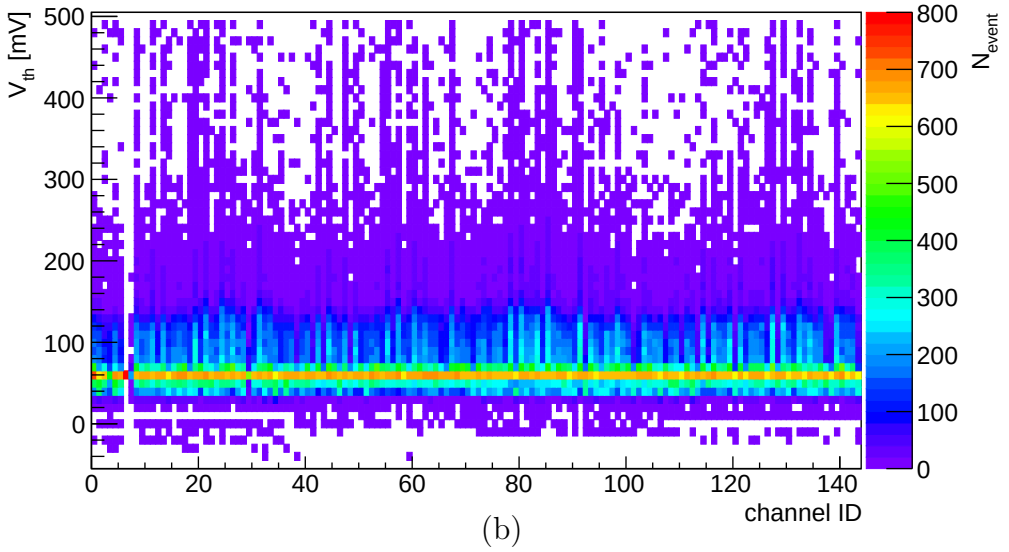

(b)

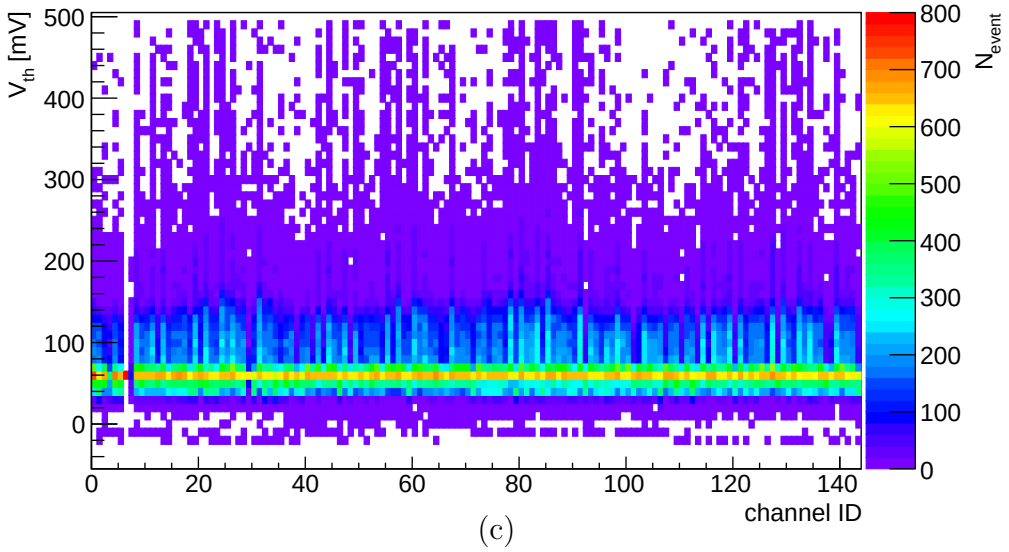

(c)

Figure 6.54: Threshold scan of illuminated sensor ($ID = 38$) at three different temperatures of the top temperature sensor: (a) 32 °C, (b) 34 °C, (c) 41 °C.

Gains (in the units of mV) were calculated from the difference between the mean values of both fits, as marked in the same figure. A pulse height, presented in the threshold scan as the x-axis, depends on the input charge. The signal amplification in ASICs was measured for one sector of the installed modules and results are shown in Fig. 6.57. The total electron multiplication was therefore calculated from the gain, determined from the threshold scan, using the equation:

$$\text{charge multiplication}[e^-] = \frac{\text{gain [mV]}}{10.7\text{mV fC}^{-1} \times 1.6 \times 10^{-4}[\text{fC}/e^-]} \tag{6.6.1}$$

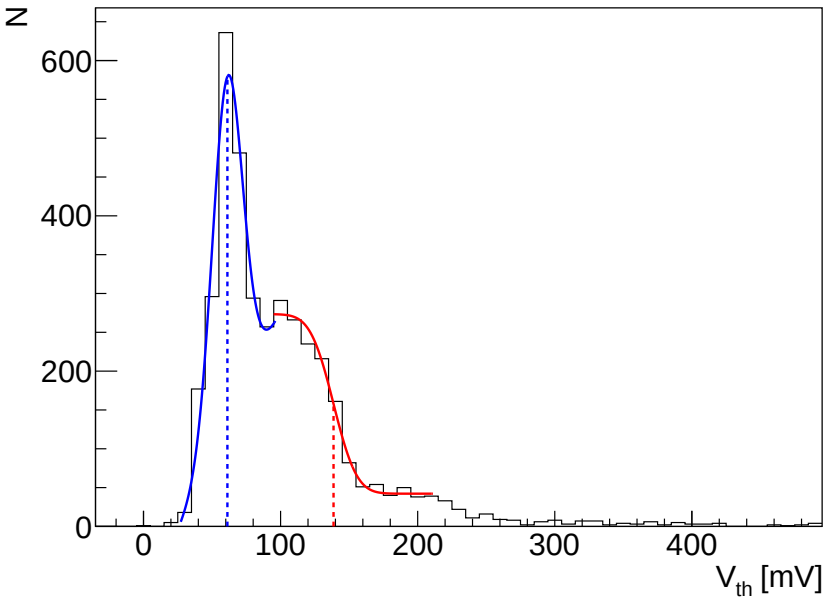

Figure 6.56: Fitted threshold scan of one channel (module 38, channel 140). Total gain was calculated from the differences of the mean values of the functions, marked with dotted lines.

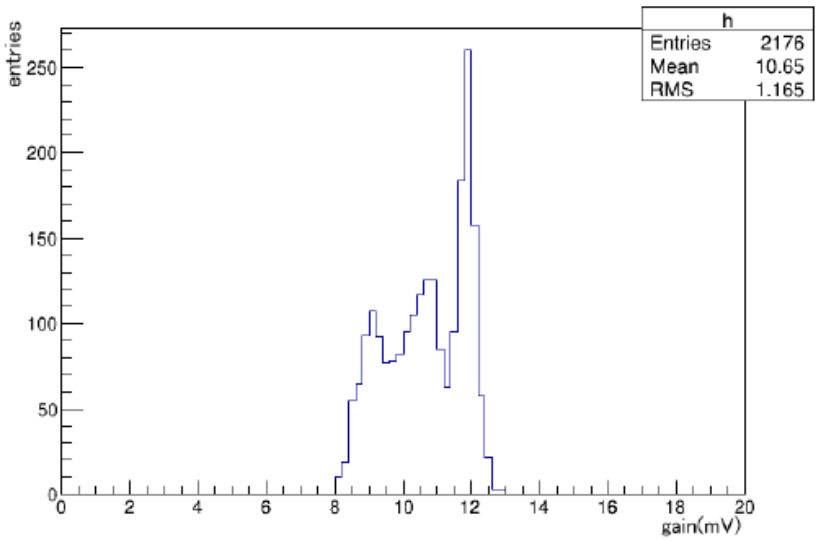

Figure 6.57: The output pulse height [mV] before the comparator as a function of input charge [fC], based on measurements of one sector of installed modules [81].

A distribution of total gains for all channels is shown in Fig. 6.58. During the Phase II the gain was not calibrated regularly and the results in the figure indicate that partial loss of signal due to a high set threshold might have occurred when the detector reached higher temperatures. The ARICH cooling system, shown in Fig. 6.59, was installed during the shut down period between the Phases II and III, so lower temperatures are expected during the Phase III operation. However, the gain will be calibrated more often to prevent signal loss due to low gain, which can cause particle misidentification, especially in a region below the kaon threshold.

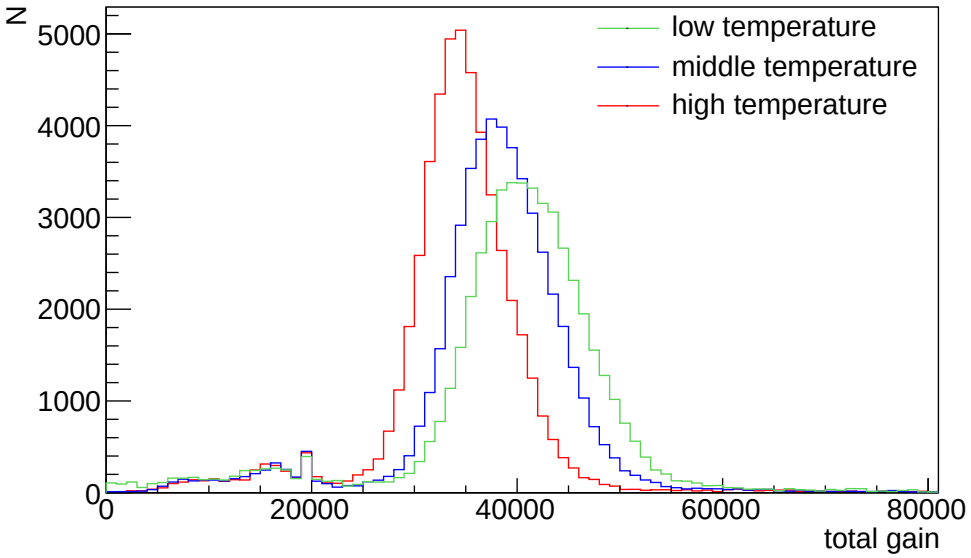

Figure 6.58: Total gains of all active channels at three different temperatures of the ARICH top temperature sensor; 32 °C, 34 °C and 41 °C.

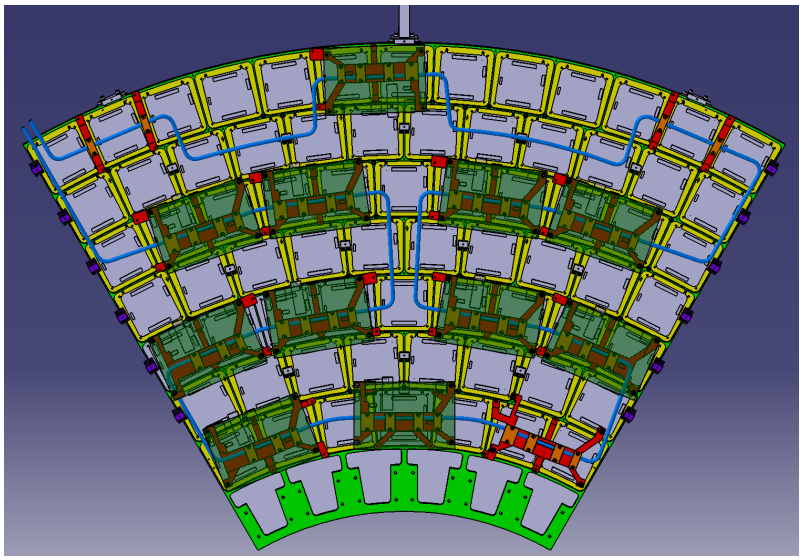

Figure 6.59: Upgraded ARICH cooling system, installed between Phases II and III. Red parts are the additional aluminium structures that provide coupling between the FPGAs on merger boards and the cooling pipes.

CHAPTER 7

ARICH Performance

Performance of ARICH is evaluated by the determination of the quality of separation between kaons and pions. Quantitatively, the identification of particles is studied by determination of the efficiency of kaon identification and the corresponding fraction of pions, misidentified as kaons. Both values have to be studied using control channels, where an identity of the charged particles can be determined from their kinematic properties, without information from ARICH. The decay channel $D^{*+} \to D^0(\to K^-\pi^+)\pi_s^+$, and its charge-conjugated mode $D^{*-} \to \bar{D}^0(\to K^+\pi^-)\pi_s^-$, are good candidates that fulfil this requirement. From this point on in the analysis, all cases where D^{*+} and D^0 related channels are mentioned, charge-conjugated modes will also be implied unless stated otherwise.

The mass of charged D^{*+} meson is $(2010.26 \pm 0.05)\,\mathrm{MeV/c^2}$ and the mass of D^0 meson is $(1864.83 \pm 0.05)\,\mathrm{MeV/c^2}$ [17]. The mass difference of D mesons is just above the mass of charged pions ($(139.570\,61 \pm 0.000\,23)\,\mathrm{MeV/c^2}$), leaving only a small amount of energy for the daughter pion. Hence the pion denoted by π_s^+ from D^{*+} decay is slow, with momentum of a few MeV/c in the D* rest frame, and does not reach ARICH. Its charge is determined from the curvature of the trajectory in the tracking system (see Sections 2.2 and 2.2). The charge of the slow pion determines the flavour of the accompanying neutral D^0: positive pion is produced with D^0 (decaying preferentially to $K^-\pi^+$), and negative pion with a $\bar{D}^0$ (decaying preferentially to $K^+\pi^-$). The fast charged particles, K^- and π^+ from D^0 decay, that enter ARICH, are identified based on their charge – a negative particle is a kaon and a positive one is a pion. Using this kinematic and charge information, ARICH particle identification can be evaluated independently.

7.1 Monte Carlo and Data Samples

The Monte Carlo (MC) samples of D^{*+}, produced in generic continuum $c\bar{c}$ events near the energy of $\Upsilon(4S)$ resonance, which contained all the $c\bar{c}$ fragmentation products, were used for the control channel studies. The expected number of events N can be calculated from the cross section σ_{event} and integrated luminosity L_{int} as:

$$N = L_{int} \times \sigma_{event}, \tag{7.1.1}$$

where luminosity can be calculated using Eq. 2.1.1.

Table 7.1: Comparison of branching fractions, used in Belle II software, and the current PDG values [82] for the decays, used in the analysis. The values also apply to the charge-conjugated modes.

Decay channel	Belle II MC assigned Br	Current PDG Br
$D^*(2010)^+ \to D^0\pi_s^+$	0.6770	0.677 ± 0.005
$D^0 \to K^-\pi^+$	0.0389	0.0389 ± 0.0004
$D^0 \to K^+\pi^-$	1.3745×10^{-4}	$(1.48 \pm 0.07) \times 10^{-4}$

The Belle II experiment target integrated luminosity of $50\,\mathrm{ab}^{-1}$ and the $c\bar{c}$ production cross section of $\sigma_{c\bar{c}} = 1.3\,\mathrm{nb}$ [16] indicate that the detector will collect 65 billion $c\bar{c}$ events in total. Furthermore, the number of collected events of interest decreases due to charm fragmentation fractions [83] and branching fractions for D^{*+} and D^0 meson decays, as summarised in Table 7.1. While the large proportion of D^{*+} mesons decays into D^0 and π_s^+, only a small proportion of D^0 decays into K^- and π^+. Efficiencies for detection and reconstruction of decays, as well as fractions of events, passing the selection criteria, impact the total number of selected decays. The best estimation for the expected selected number of $D^{*+} \to D^0(\to K^-\pi^+)\pi_s^+$ is the yield, obtained from $1\,\mathrm{ab}^{-1}$ of Belle data, which is 2.61×10^6 $K^-\pi^+$ pairs [84]. By scaling to $50\,\mathrm{ab}^{-1}$, the total signal yield of this channel at Belle II is expected to be around 130 million.

The limited solid angle coverage of ARICH reduces the number of D^{*+} decays useful for ARICH performance analysis. Monte Carlo simulations show that around 10 % of the charged particles[1], originating from this control channel, enter the geometrical acceptance of ARICH. The expected signal sample size is therefore around 13 million events.

For simulations for efficiency studies, Monte Carlo (MC) samples corresponding to $50\,\mathrm{fb}^{-1}$ of Phase II and $1\,\mathrm{ab}^{-1}$ of Phase III data were used. Beam backgrounds were added to 80 % of the generated MC sample, while the rest of the sample was used without beam backgrounds added. The studies were performed with two MC campaigns (MC8 and MC9), hence official samples were produced with different versions of reconstruction software. The software was still being developed at the time of the analysis, and therefore the results of the newer MC9 samples[2] will be presented.

The amount of collected data during Phase II is small, $490\,\mathrm{pb}^{-1}$, therefore the results are presented in Section 7.4 only as an example. When larger sample size will be available, the method will provide a ratio between efficiencies from simulation and data, and the systematic differences between them will be determined.

7.2 Analysis Method

The particle identification performance was evaluated by calculating the kaon identification efficiencies and pion fake rates. All data was analysed using BASF2 software,

[1] Using MC samples it was determined that ARICH likelihood is calculated for 10.2 % kaons and 10.4 % pions from this control channel.

[2] produced by software version release-00-09-02

release-00-09-02. The PID criterion for the basic studies of ARICH performance and possible reconstruction software improvements, described in Section 5.3, was formulated as the difference between the likelihood logarithms, $\log \mathcal{L}$. Another way – more common for the performance studies with decay modes – is defining a PID criterion as the ratio between likelihoods:

$$PID_{K/\pi} = \frac{\mathcal{L}_K}{\mathcal{L}_K + \mathcal{L}_\pi}, \tag{7.2.1}$$

Particles with $PID_{K/\pi}$ value above (below) a chosen value are classified as kaons (pions). This definition is normally used for particle identification selection at physics analyses. The $PID_{K/\pi}$ value of 0.5 is equivalent to the $\log \mathcal{L}_K - \log \mathcal{L}_\pi$ of a value 0.

The reconstruction of the D^{*+} decay was performed based on the kinematic properties of the decay products. The momentum of charged particles was obtained from the tracking system. Particle candidates were assigned a nominal mass of kaons and pions, as explained below. The momentum and invariant mass of mother particle D^0 (and grandmother particle D^{*+}) were reconstructed using four-momenta of the daughter particles.

Decay reconstruction was performed in few steps. All the charged particles in an event were used as potential candidates for the kaon and the pion D^0 daughter track, or the slow pion π_s. The selection criteria were applied based on d_0 and z_0, defined as the projections of the distance of the closest approach in $r-\phi$ and $r-z$ planes [12], respectively. Particles with impact parameters $|d_0| < 2\,\mathrm{cm}$ and $|z_0| < 4\,\mathrm{cm}$ were selected in order to remove badly reconstructed tracks and tracks arising from long lived particles (K_S, Λ_C).

The reconstruction method was performed in the following steps:

1. Slow pion π_s^+ was used for identity-tagging of kaons and pions from D^0 decay (based on their charge).

2. All combinations of charged kaons and pions were chosen as candidates for D^0 reconstruction.

3. Negatively-charged tracks, entering the geometrical acceptance of ARICH, were chosen as a sample of true kaons. They were assigned a nominal kaon mass. Positively-charged tracks from the event were assigned a nominal pion mass.

4. Positively-charged tracks, entering the geometrical acceptance of ARICH, were chosen as a sample of true pions. They were assigned a nominal pion mass. Negatively-charged tracks from the event were assigned a nominal kaon mass.

5. The momentum of kaon and pion candidates, and their assigned kaon (pion) masses were used for the reconstruction of D^0 candidates. All combinations of kaon and pion candidates per event were reconstructed. Only candidates with loose selection on the invariant mass of combinations, $1.75\,\mathrm{GeV/c^2} \leq M(K\pi) \leq 1.98\,\mathrm{GeV/c^2}$ were retained for further analysis.

6. Slow pion and reconstructed D^0 were combined into D^{*+}. Reconstructed events with a mass difference $M(K\pi\pi_s) - M(K\pi)$ between $0.12\,\mathrm{GeV/c^2} and 0.17\,\mathrm{GeV/c^2}$ were retained for the analysis.

While a D^{*+} mass distribution is a combination of several Gaussian functions and possesses a rather complex background shape, a D^0 mass distribution has a linear combinatorial background and a simpler signal shape. The latter one was used to determine the number of reconstructed events due to less fit parameters needed.

Samples of kaon and pion tracks, selected in the above selection procedure, were used to determine the ARICH performance. In the following we refer to these samples as a kaon and a pion sample.

7.2.1 Selection Criteria

The majority of the background in selected $K\pi$ combinations can be removed using a tight selection criterion on a mass difference

$$\Delta M = M(K\pi\pi_s) - M(K\pi) \tag{7.2.2}$$

Additional selections were applied, based on D^{*+} decay studies from the Belle experiment [85]. They were adjusted according to the Belle II MC samples to reduce the background. The final selection was as follows:

- A selection, based on kinematic properties of D mesons:
  - D^{*+} momentum in the center-of-mass frame: $p(D^{*+}) \geq 1.5\,\mathrm{GeV/c}$ *(see Fig. 7.1)*
  - A decay angle of a D^0 meson, calculated as the angle between the momentum of a D^0 and the momentum of a K^+ in the rest frame of D^0: $|\cos\theta_{D^0}| \leq 0.8$ *(see Fig. 7.2)*
- A selection, based on invariant masses:
  - Invariant mass of D^0: $1.82\,\mathrm{GeV/c^2} \leq M(K\pi) \leq 1.91\,\mathrm{GeV/^2c}$
  - $D^{*+} - D^0$ mass difference: $4.0\,\mathrm{MeV/c^2} \leq (\Delta M - m(\pi^+)) \leq 8.0\,\mathrm{MeV/c^2}$ *(determined from the ΔM distribution, see Fig. 7.3)*
  - Reverse mass, calculated as the invariant mass of kaon and pion candidates, with swapped mass assignments: $1.856\,\mathrm{GeV/c^2} \leq M_{rev}(K^+\pi^-) \leq 1.874\,\mathrm{GeV/c^2}$ *(determined from the $M(K^-\pi^+)$ distribution as the mean value $\pm 1\sigma$, see Fig. 7.4)*

Using these selection, the background was significantly reduced, while the majority of signal events was kept. The effects of different selection on the mass difference of D mesons is presented in Fig. 7.5.

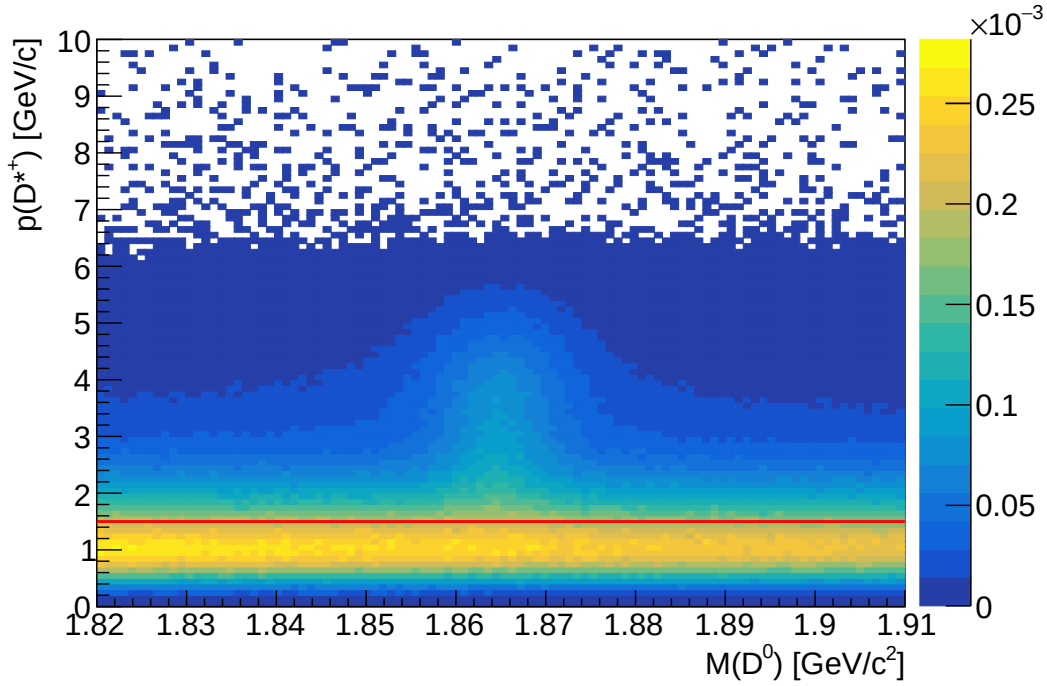

Figure 7.1: Two-dimensional distribution of D^0 mass and D^{*+} momentum in the centre-of-mass frame. The chosen selection is marked with red lines.

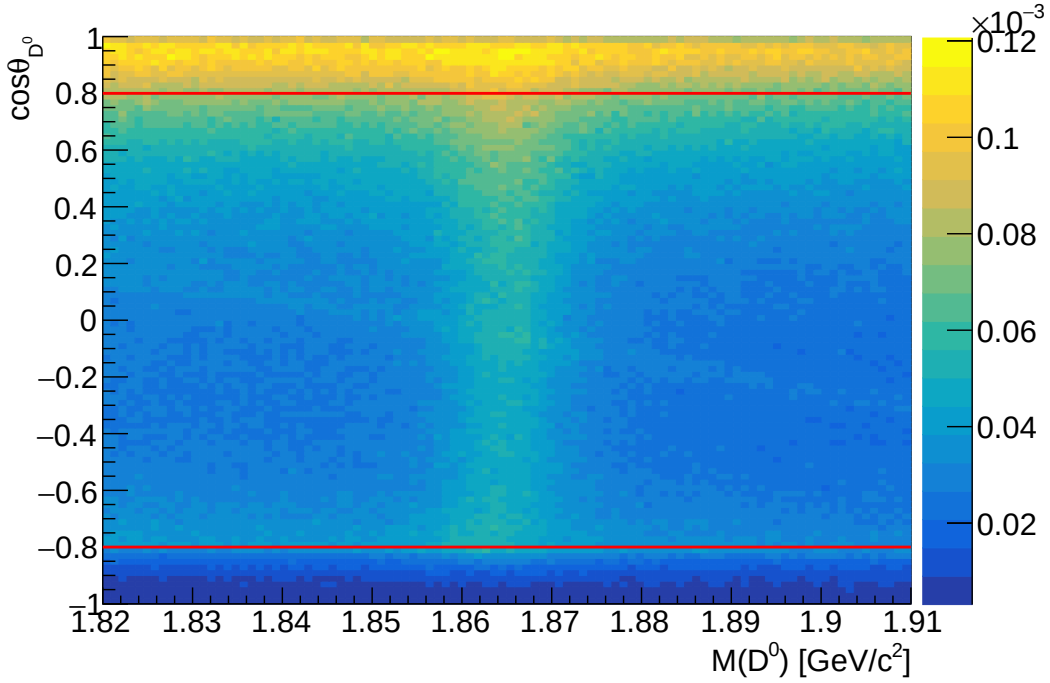

Figure 7.2: Two-dimensional distribution of D^0 mass and the cosine of the angle between D^0 and K^- is the D^0 rest frame. The selected region is marked with red lines.

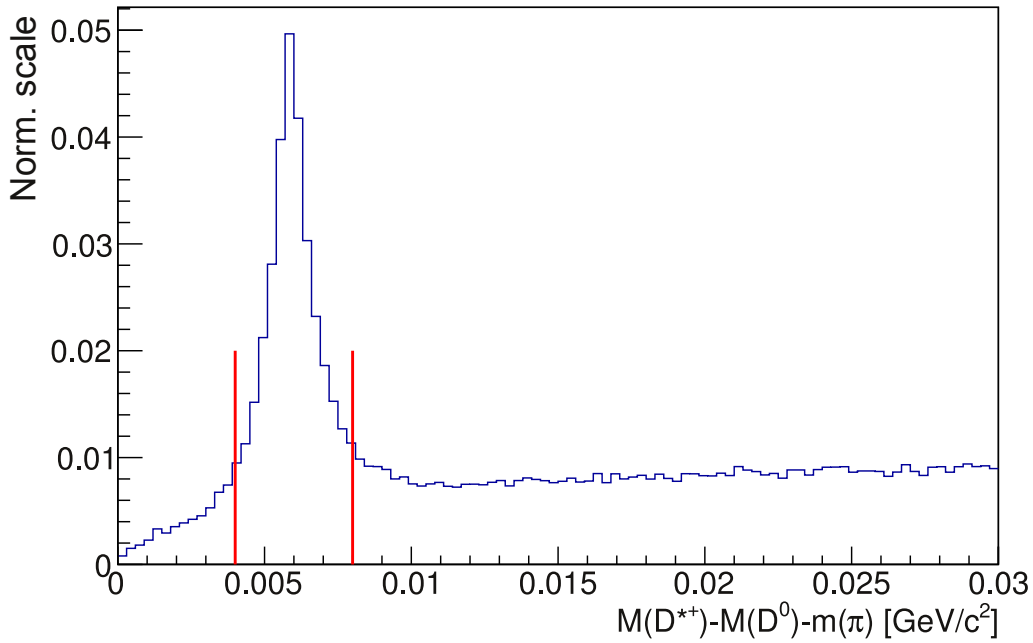

Figure 7.3: The energy release for the kaon sample. The selected signal mass difference interval is marked with red lines.

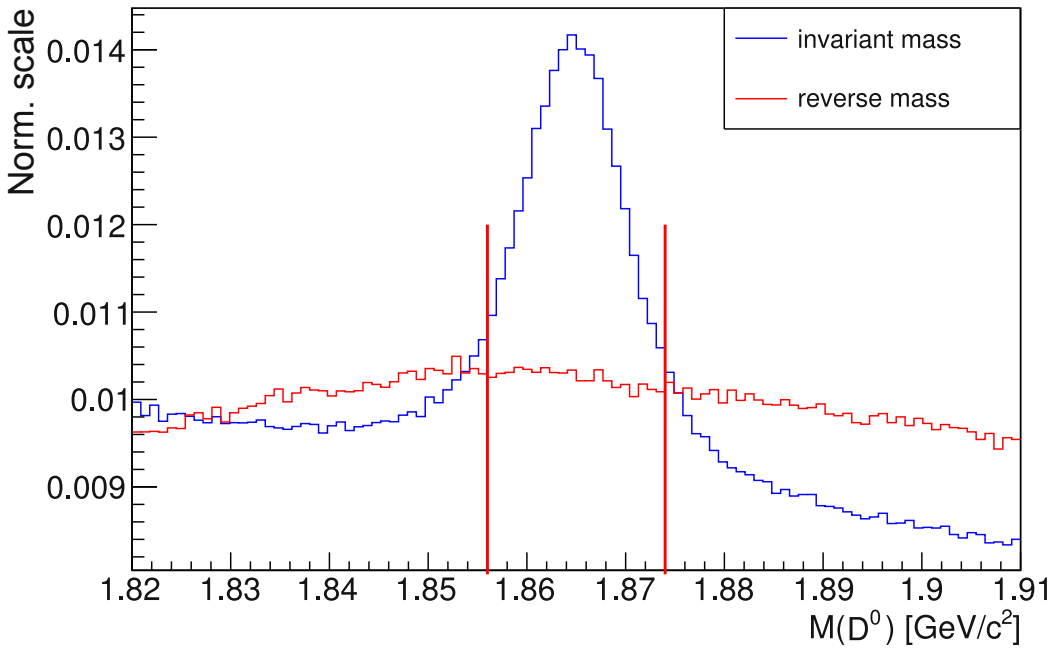

Figure 7.4: Invariant mass of kaon pion pairs (blue) and reverse mass (see text; red) with swapped pion and kaon mass assignments. The selected interval in the reverse mass is marked with red vertical lines.

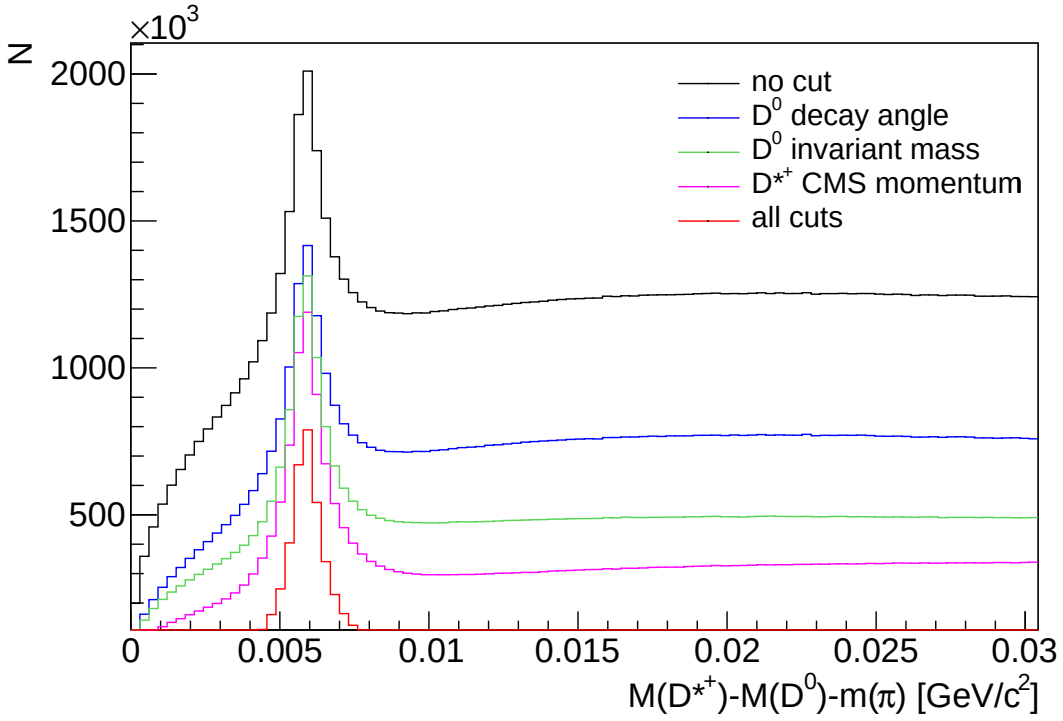

Figure 7.5: Effects of various selection criteria on the mass difference $\Delta M - m(\pi^+)$.

7.2.2 Extraction of Physical Parameters

The number of events for efficiency calculations in simulated (MC) sample was obtained from the D^0 invariant mass fits, as shown in Fig. 7.7. The fit was performed on a distribution of the invariant mass deviation from the nominal mass of D^0, $m(D^0) = 1.864\,84\,\mathrm{GeV/c^2}$. Data sets were fitted using RooFit, a data analysis framework based on ROOT and developed by CERN. It is a widely used framework for data processing in high energy physics research. More details about it can be found [86].

Mass distributions were fitted using the maximum likelihood fitting method, which maximises the product of Poisson probabilities in each data bin. It is implemented in RooFit as the minimisation of a RooFit calculated likelihood function by the ROOT implementation of MINUIT. The asymmetric uncertainties were calculated using MINOS. The reader can find information about the calculation method in the reference manual [87]. For some samples the asymmetry between the positive and negative uncertainty on the fitted yields is large, as can be seen in the example in Fig. 7.6.

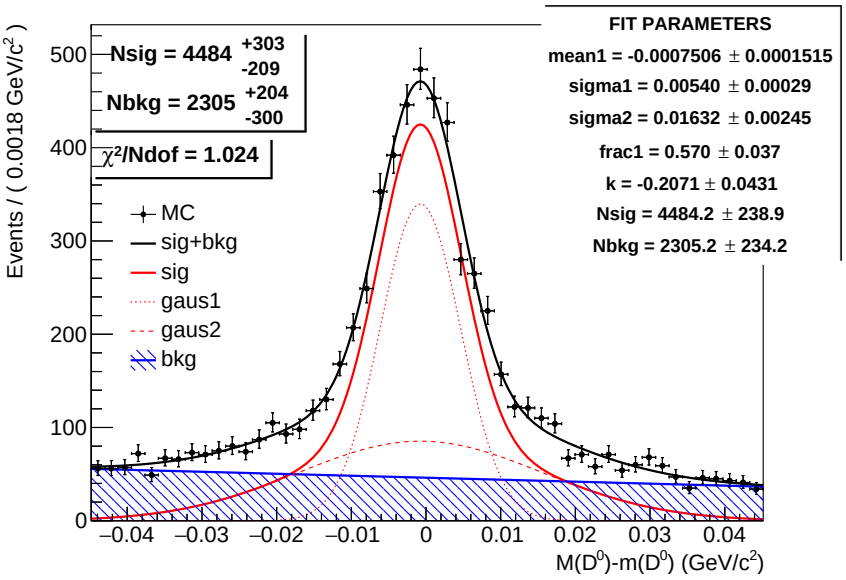

Figure 7.6: D^0 mass fit without any PID cut applied. Kaon sample with momentum between 0.5 GeV/c and 1.0 GeV/c and $\cos\theta$ between 0.90 and 0.92 is shown.

The D^0 invariant mass was fitted with a combined probability density function *pdf*, consisting of a sum of a linear function for background and one (or two) Gaussian functions for the signal. The entire fitting function in the case of one Gaussian can be written as:

$$pdf = Nbkg \times k \times M + Nsig \times g(\mu_1, \sigma_1, M) \tag{7.2.3}$$

where M is the mass difference $M(K\pi) - m(D^0)$, k is the coefficient of the linear function, and $g(\mu_1, \sigma_1, M)$ is a Gaussian function, defined as $g(\mu, \sigma, x) = \frac{1}{\sigma\sqrt{2\pi}} e^{-\frac{1}{2}\left(\frac{x-\mu}{\sigma}\right)^2}$. If one Gaussian function is not enough to describe the signal shape, two functions with the same mean value are used and the proportion of the narrower Gaussian function $frac1$ is used to determine the ratio between the two functions:

$$\begin{aligned} PDF =& Nbkg \times kM + \\ Nsig \times & \Big(frac1 \cdot g1(\mu_1, \sigma_1, M) + (1 - frac1) \cdot g2(\mu_1, \sigma_2, M) \Big) \end{aligned} \tag{7.2.4}$$

Parameters μ and σ from the PDF are written as *mean* and *sigma* on the plots to enhance the readability.

The fitting method was iterative. Initially each sample was fitted with a single Gaussian signal *pdf*. In the case of a poor fit ($\chi^2/Ndof$ larger than 1.4), the fit was repeated using two Gaussian functions for the signal. The bin-by-bin agreement between fit and dataset is presented by the pull distribution, where pull for each bin is defined as the difference between the value of the fit function N_{fit} and the number of events N_{events}, divided by the Poissonian uncertainty of the number of events:

$$\text{Pull} = \frac{N_{fit} - N_{events}}{\sqrt{N_{events}}}. \tag{7.2.5}$$

Examples of fits and their pull distributions are presented in Fig. 7.7. To see how the signal shape changes for different bins, refer to Appendix D.

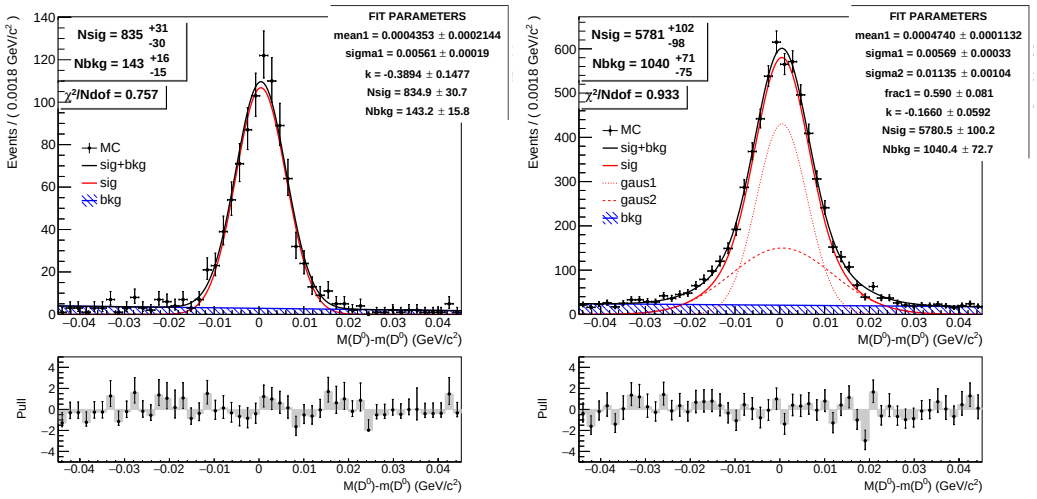

Figure 7.7: $K\pi$ invariant mass fits without PID cut applied. Two samples with momentum between 3.0 GeV/c and 3.5 GeV/c and $\cos\theta$ between 0.82 and 0.84 (left) and 0.88 and 0.90 (right) are shown. The first sample (left) was fitted with a single Gaussian function to describe the signal, while for the second (right) two Gaussians were used.

After performing the fit to the full D^0 sample, signal shape parameters (mean values, standard deviations and ratio between the two Gaussian functions, fitted in Fig. 7.7) were fixed and used for the fit of subsamples of the events with different PID cuts applied. The floating parameters in the fits of subsamples were the slope of the linear function, and yields of signal and background. The slope for the background fit was not fixed because it is PID cut dependent. The number of signal events, as well as its uncertainty, were subsequently used for the efficiency calculation. Examples of one of the typical cuts of $PID_{K/\pi} > 0.6$ are shown in Fig. 7.8.

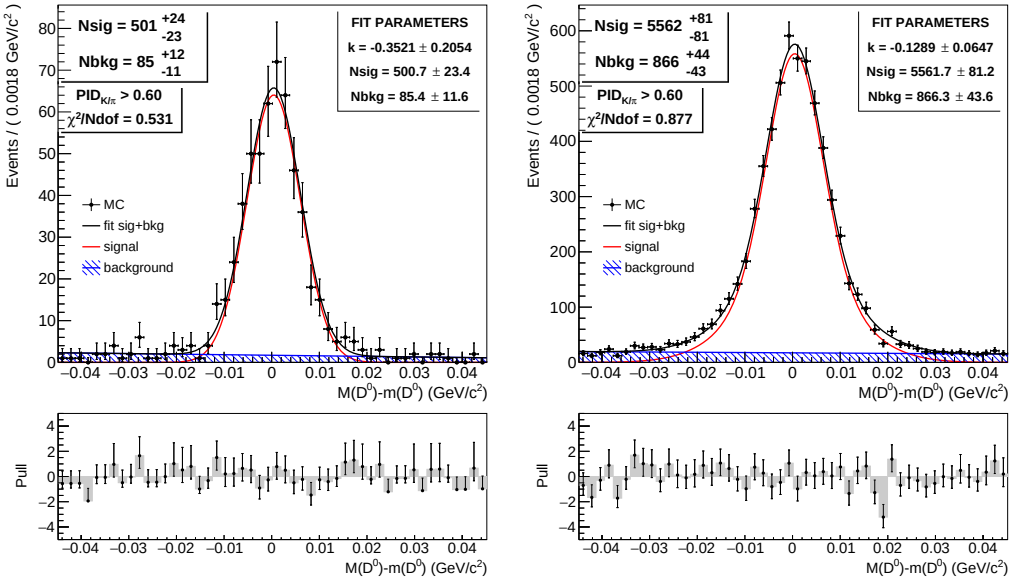

Figure 7.8: D^0 mass fits with cut $PID_{K/\pi} > 0.6$ applied. Two samples with momentum between 3.0 GeV/c and 3.5 GeV/c and $\cos\theta$ between 0.82 and 0.84 (left) and 0.88 and 0.90 (right) are shown.

7.2.3 Efficiency Calculations and Statistical Uncertainty

The efficiencies and misidentification probabilities were calculated using information about the number of signal events with and without PID cut applied. Both kaon identification efficiency, $\varepsilon_{K\to K}$, and a fraction of pions misidentified as kaons, $\varepsilon_{\pi\to K}$, were calculated using the Eq. 5.2.9.

The calculation of the efficiency uncertainties was more complex. The efficiency with symmetric uncertainties is:

$$\varepsilon = \frac{A \pm \sigma_A}{N \pm \sigma_N}, \tag{7.2.6}$$

where A is a subsample of N. Taking into account the correlation factor between σ_A and σ_N, the uncertainty on the efficiency, σ_ε, can be expressed as:

$$\sigma_\varepsilon^2 = \frac{1}{N^2}\left(\varepsilon^2\sigma_N^2 + \sigma_A^2 - 2\varepsilon^{3/2}\sigma_A\sigma_N\right) \tag{7.2.7}$$

In case of asymmetric uncertainties

$$\varepsilon^{+\sigma_{\varepsilon_+}}_{-\sigma_{\varepsilon_-}} = \frac{A^{+\sigma_{A_+}}_{-\sigma_{A_-}}}{N^{-\sigma_{N_-}}_{+\sigma_{N_+}}}, \tag{7.2.8}$$

the efficiency uncertainties are calculated by combining positive and negative uncertainties of the numbers of events. The upper limit σ_{ε_+} is calculated using the positive uncertainty of the subsample σ_{A_+} and the negative uncertainty of the entire sample σ_{N_-}. The lower limit for efficiency σ_{ε_-} is calculated by combining σ_{A_-} and σ_{N_+}. The uncertainties are determined conservatively by this approach.

Efficiencies were determined for several $PID_{K/\pi}$ cuts. They were chosen in steps of 0.05 for $PID_{K/\pi}$ values between 0.05 and 0.90, and in steps of 0.01 for $PID_{K/\pi}$ values between 0.90 and 0.99.

7.3 Results of Monte Carlo Simulations

The kaon identification efficiency $\varepsilon_{K\to K}$ and pion fake rate $\varepsilon_{\pi\to K}$ were studied with respect to different momenta and polar angles of the charged kaons and pions.

MC samples for Phase III were studied first due to the availability of better statistics, and also to exploit a better tracking information arising from the full vertex detector. The total number of simulated events in which at least one charged particles was selected with specified selection criteria and had an ARICH PID information is 320,000. Results for Phase II were obtained using the same analysis method and selection, but using a different momentum and polar angle binning due to the lower statistics. In total there are 18,000 simulated Phase II events with charged tracks carrying the PID information of ARICH. In the following examples of results obtained using MC9 simulation with beam backgrounds are presented.

7.3.1 Properties of Charged Particles

The MC samples were chosen for kaons and pions separately, requiring that a charged track (either a kaon or a pion according to the generated MC information) arising from a D^0 decay is within the ARICH geometrical acceptance. The geometrical acceptance depends on the solid angle covered by ARICH, as well as on the particle's impact angle, as the particle should pass the aerogel side first and produce Cherenkov photons that can be detected by HAPDs. The acceptance of ARICH is calculated from the polar angle coverage of aerogel tiles, extending from $\theta = 15^\circ$ to $\theta = 34^\circ$ (see Fig. 4.5).

Studies were performed for particles momenta from 0.5 GeV/c to 4.0 GeV/c, where ARICH is expected to distinguish between kaons and pions efficiently. Below the momentum of 0.5 GeV/c neither of these charged particles emit Cherenkov photons, so identification by ARICH cannot be performed. The distributions of charged particles' momenta and polar angles are shown in Figs. 7.9 and 7.10.

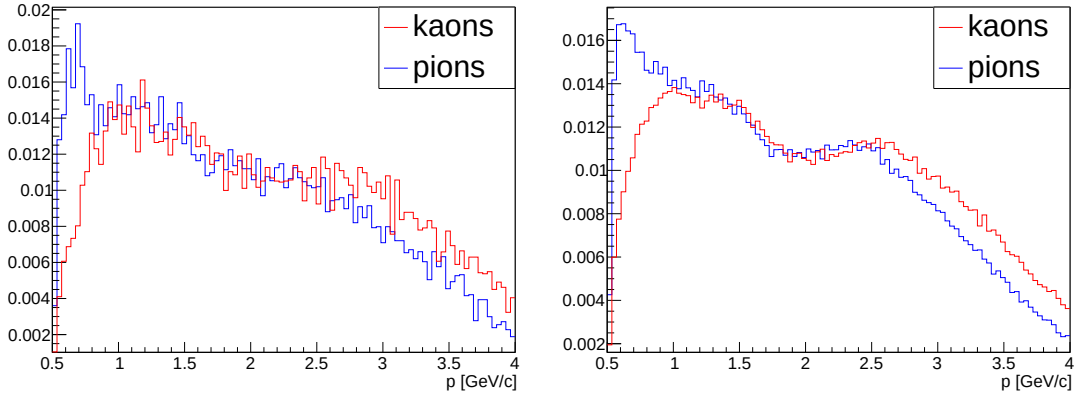

Figure 7.9: A comparison of kaon and pion momentum distributions in ARICH geometrical acceptance in Phase II (left) and III (right) for particles coming from a $D^{*+} \to D^0(\to K^-\pi^+)\pi_s^+$ decay.

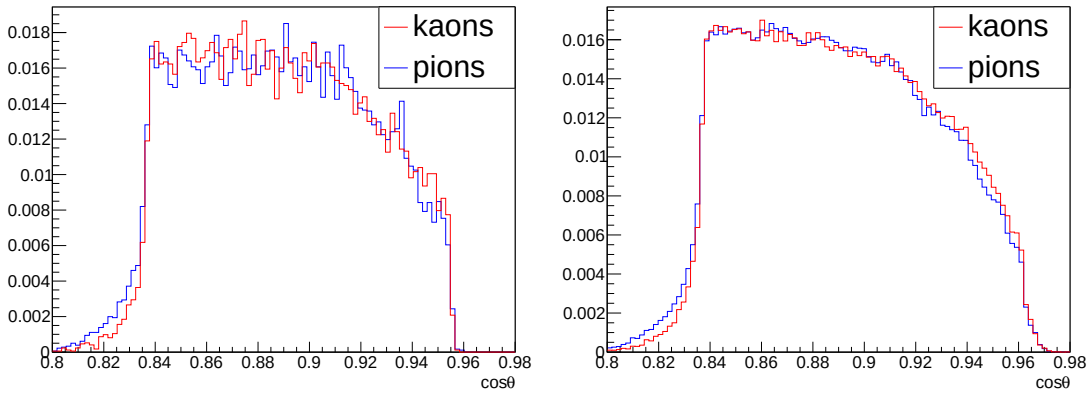

Figure 7.10: A comparison of kaon and pion incident angle distributions in ARICH geometrical acceptance in Phase II (left) and III (right) for particles coming from a $D^{*+} \to D^0(\to K^-\pi^+)\pi_s^+$ decay.

The $PID_{K/\pi}$ values obtained from ARICH Phase III samples are presented in Figs. 7.11 and 7.12.

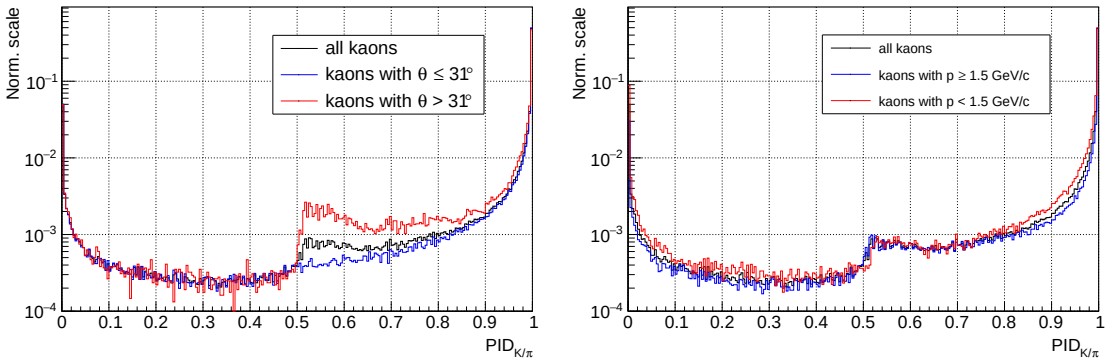

Figure 7.11: A $PID_{K/\pi}$ values of kaons (Phase III). Left: Comparison for the entire sample and two subsamples with different impact angles. Right: Comparison for the entire sample and two subsamples with different momenta.

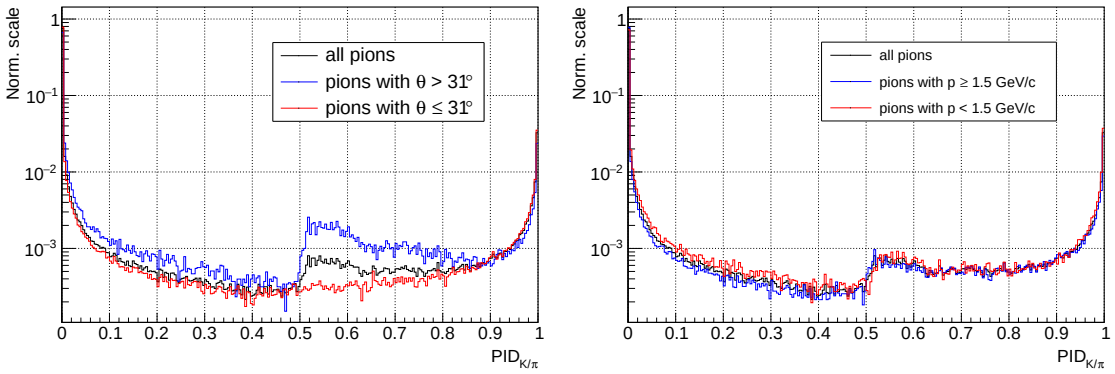

Figure 7.12: A $PID_{K/\pi}$ values of pions (Phase III). Left: Comparison for the entire sample and two subsamples with different impact angles. Right: Comparison for the entire sample and two subsamples with different momenta.

7.3.2 Kaon Efficiencies as Function of Pion Misidentification Probabilities

7.3.2.1 The Sample Binning

The kaon identification efficiency and pion misidentification probability were studied for different charged particle momenta and incident angles, with respect to the geometrical acceptance of ARICH. The p and $\cos\theta$ intervals were divided into 7 equidistant bins for Phase III, while Phase II samples were divided into 3 equidistant bins over $\cos\theta$ and 3 non-equidistant bins for p. The latter binning was chosen to provide adequate statistics for particle identification studies, while still keeping the bin separation at the threshold for kaon Cherenkov photon emission at 1.5 GeV/c. The two-dimensional distributions of momentum and cosine of the polar angle of the charged kaons, originating from D^{*+}, as well as the chosen $p - \cos\theta$ binning, for both Phase II and III are shown in Fig. 7.13, and also give in the tables in Appendix D. Particles are produced close to the interaction point, so their incident angle also corresponds to the polar angle on the detector plane, which is presented in Fig. 7.14.

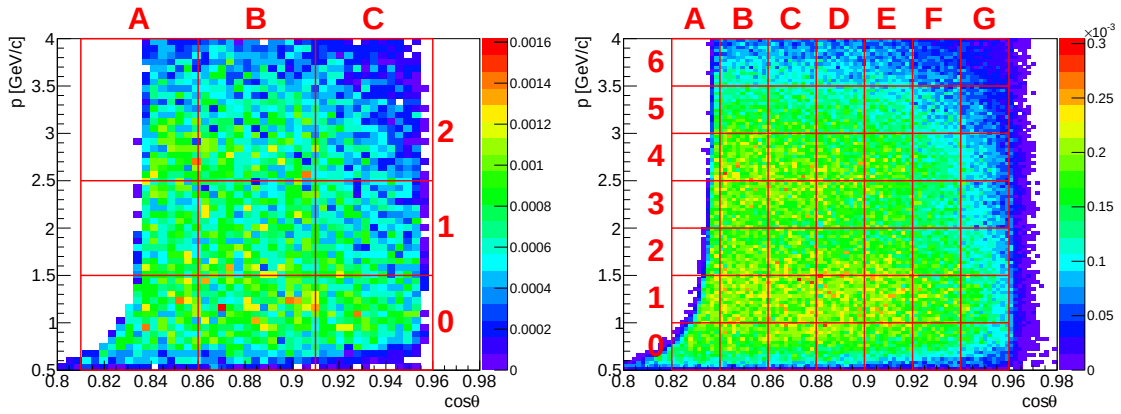

Figure 7.13: The binning for kaon momentum and incident angle for Phases II (left) and III (right).

When dividing kaon and pion samples into momentum and $\cos\theta$, the $K\pi$ invariant mass was divided into 20 bins for Phase II, and into 50 (40) bins for Phase III samples with (without) beam background. The number of mass bins was increased by a factor of two in the case of samples with no momentum and polar angle division.

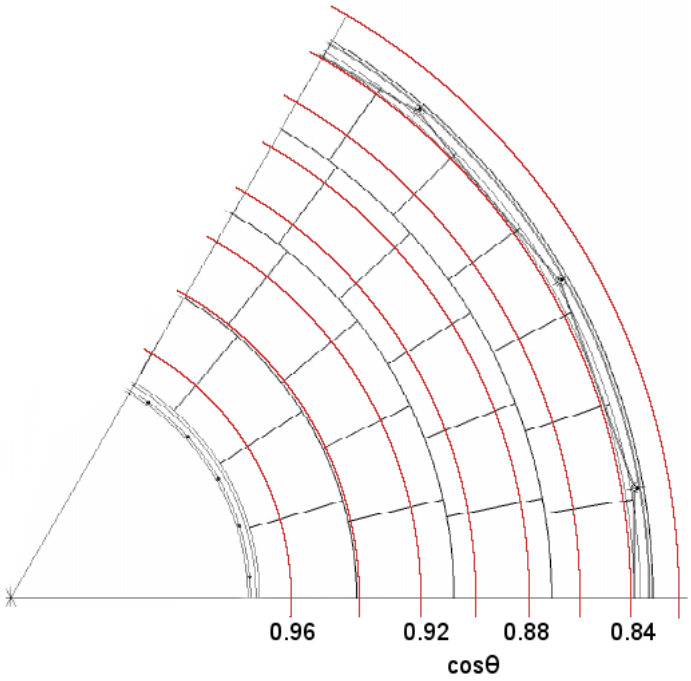

Figure 7.14: The presentation of the cosine of the polar angle on the aerogel plane.

7.3.2.2 Phase III Simulations

MC simulations show a high ARICH kaon identification efficiency over most of the $p - \cos\theta$ region at $PID_{K/\pi}$ cuts below 0.8. The dependence of kaon identification efficiency on different pion misidentification probabilities, obtained by using different $PID_{K/\pi}$ selection, are presented in Fig. 7.15. The entire sample reaches $\varepsilon_{K\to K}$ of

$\sim$ 96 % at large $\varepsilon_{\pi\to K}$ of $\sim$ 10 %. At lower pion misidentification probability of 5 %, one can still correctly identify approximately 90 % of kaons. For other $PID_{K/\pi}$ selections, efficiencies and misidentification rates are given in the Appendix E. The results for all $PID_{K/\pi}$ selection criteria are presented in the Appendix F.

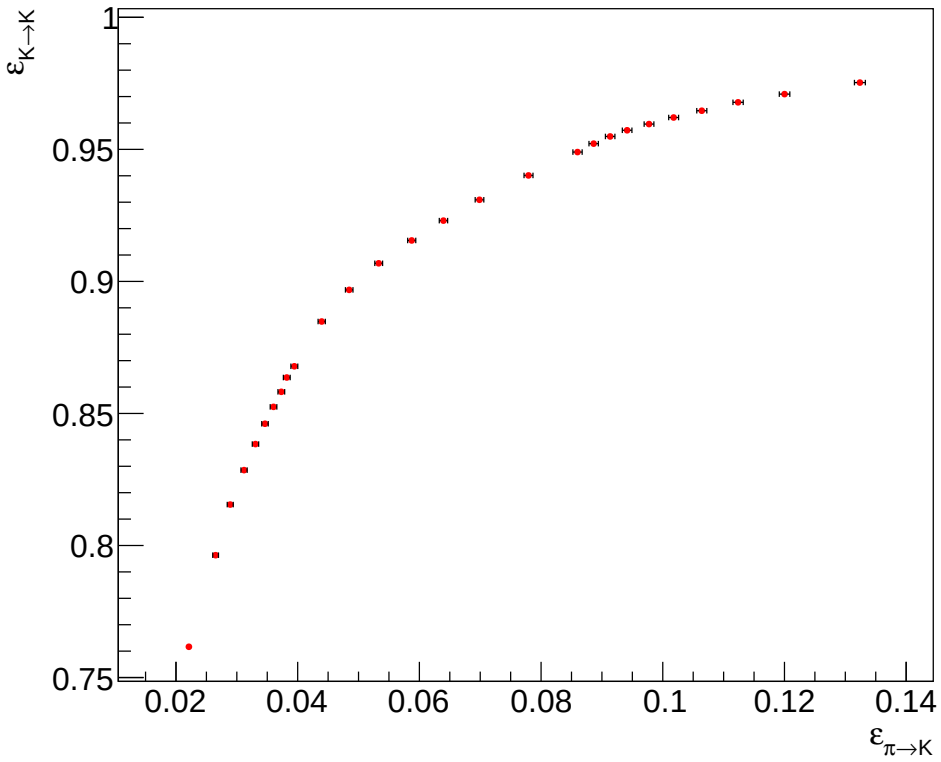

Figure 7.15: The kaon identification efficiency with respect to the pion misidentification probability for the entire Phase III sample.

The identification efficiency varies with the momentum and polar angle of the charged particle. In Fig. 7.16, $\varepsilon_{K\to K}$ for two fixed $\varepsilon_{\pi\to K}$ (5 % and 10 %) is shown. The efficiency is lower for the region between pion and kaon thresholds (between approximately 0.5 GeV and 4.0 GeV), where pion Cherenkov rings are smaller and the absence of the detected Cherenkov photons may imply that the charged particle was a kaon. The efficiency for $\cos\theta$ at the edge of acceptance is low due to the poorer ARICH performance at large incident angles of charged particles, where a part of the detected photons is reflected from the mirrors (see Figs. 5.16 and 5.17).

Dependence of $\varepsilon_{K/\pi\to K}$ on $PID_{K/\pi}$ for two $p-\cos\theta$ bins is shown in Fig. 7.17. Results are plotted for $PID_{K/\pi}$ cuts in steps of 0.1 up to 0.9 and 0.02 from 0.9 on to enhance the readability. The first plot shows bin 1A at low momentum and high polar angle of incident particles. With $\varepsilon_{K\to K}$ of only 73 % at pion misidentification probability of 5 %, it is an example of poor identification efficiency and high misidentification rates. Conversely, bin 5E in the second plot shows an excellent ARICH performance, where the efficiency of 98 % is achieved with a low pion misidentification probability of 6 %.

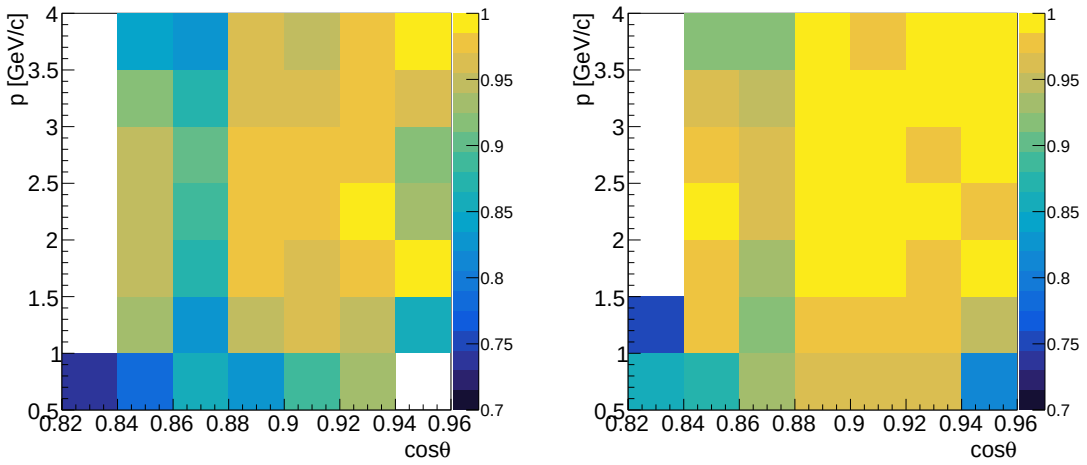

Figure 7.16: The kaon identification efficiencies for Phase III data at fixed pion misidentification probabilities of 5 % (left) and 10 % (right). Values in $p - \cos\theta$ bins with efficiency below 70 % are not plotted. Low efficiency is a result of poorer identification of the particles at the edges of ARICH.

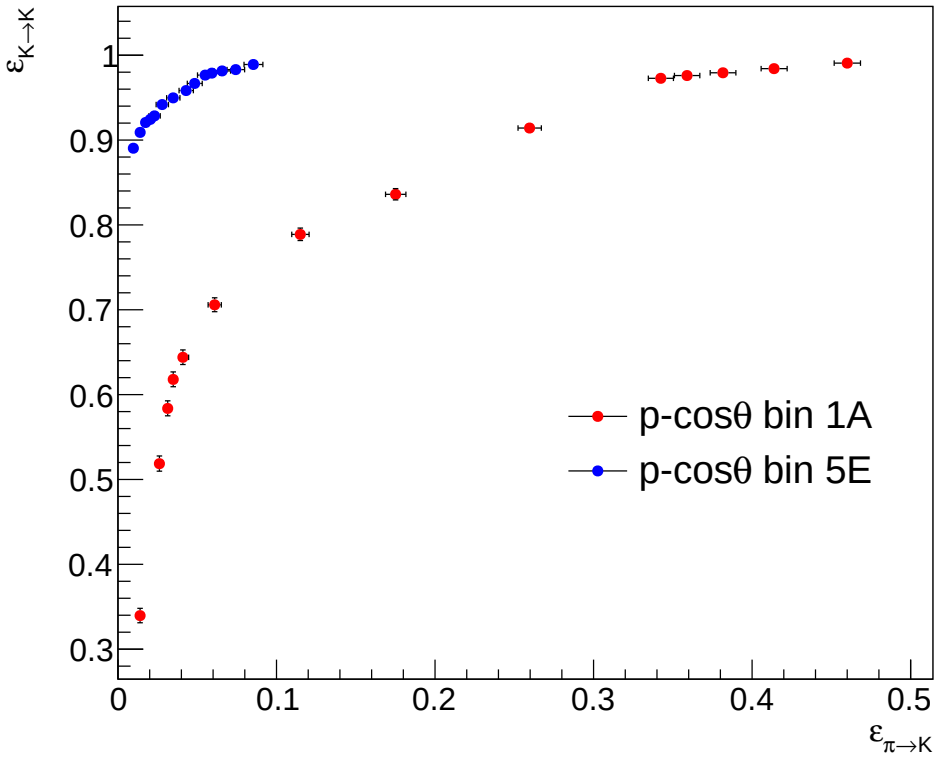

Figure 7.17: An example of Phase III $\epsilon_{K\to K}$ and $\epsilon_{\pi\to K}$ for $p - \cos\theta$ bins with low (bin 1A) and high (bin 5E) kaon identification efficiency.

7.3.2.3 Phase II Simulations

The results of entire Phase II simulated sample reach higher ARICH kaon identification efficiency than the entire simulated sample in Phase III for the same $PID_{K/\pi}$ selection, as seen in Fig. 7.18. This can be a result of slightly different distribution

of particles momenta and incident angles. he entire sample reaches $\varepsilon_{K\to K}$ of $\sim 97\,\%$ at large $\varepsilon_{\pi\to K}$ of $\sim 10\,\%$. At lower pion misidentification probability of $5\,\%$, one can still correctly identify approximately $92\,\%$ of kaons.

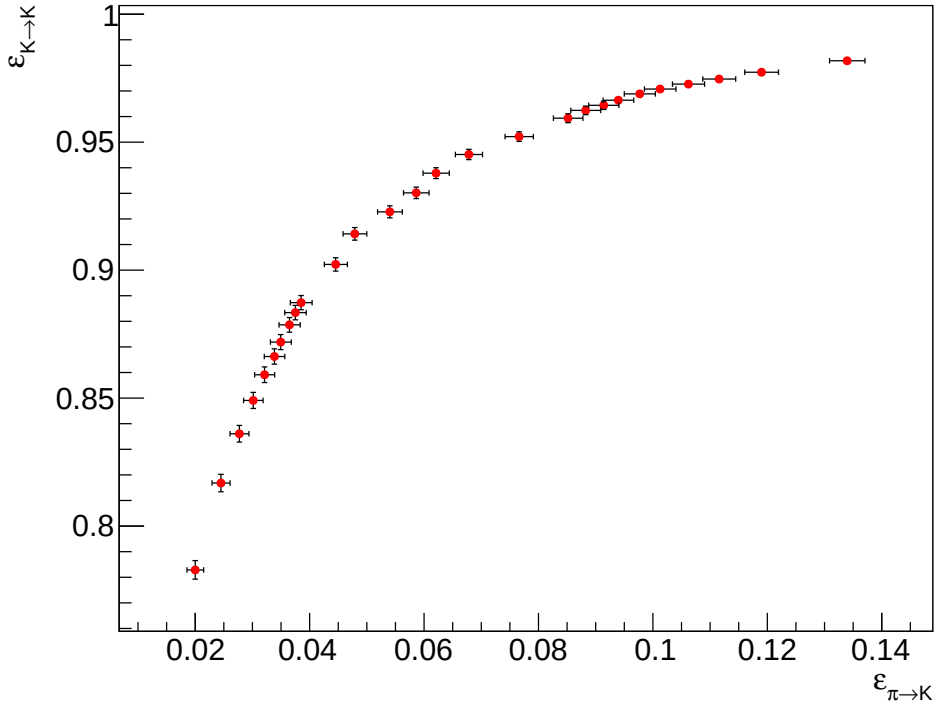

Figure 7.18: The kaon identification efficiency with respect to pion misidentification probability of the entire Phase II sample.

The identification efficiency varies with the momentum and polar angle of the charged particle. In Fig. 7.19, $\varepsilon_{K\to K}$ for two fixed $\varepsilon_{\pi\to K}$ ($5\,\%$ and $10\,\%$) is shown. The efficiency for $\cos\theta$ at the edge of acceptance is low due to the poorer ARICH performance at large incident angles of charged particles, where a part of the detected photons is reflected from the mirrors (see Figs. 5.16 and 5.17).

Dependence of $\varepsilon_{K/\pi\to K}$ on $PID_{K/\pi}$ for two $p - \cos\theta$ bins is shown in Fig. 7.20. Results are plotted for $PID_{K/\pi}$ cuts in steps of 0.1 between 0.05 and 0.85, and 0.02 from 0.91 on to enhance the readability due to large statistical uncertainties. The first plot shows bin 1A at low momentum and high polar angle of incident particles. With $\varepsilon_{K\to K}$ of only $82\,\%$ at pion misidentification probability of $5\,\%$, it is an example of poor identification efficiency and high misidentification rates. Conversely, bin 2B in the second plot shows an excellent ARICH performance, where the efficiency of $95\,\%$ is achieved with a low pion misidentification probability of $5\,\%$.

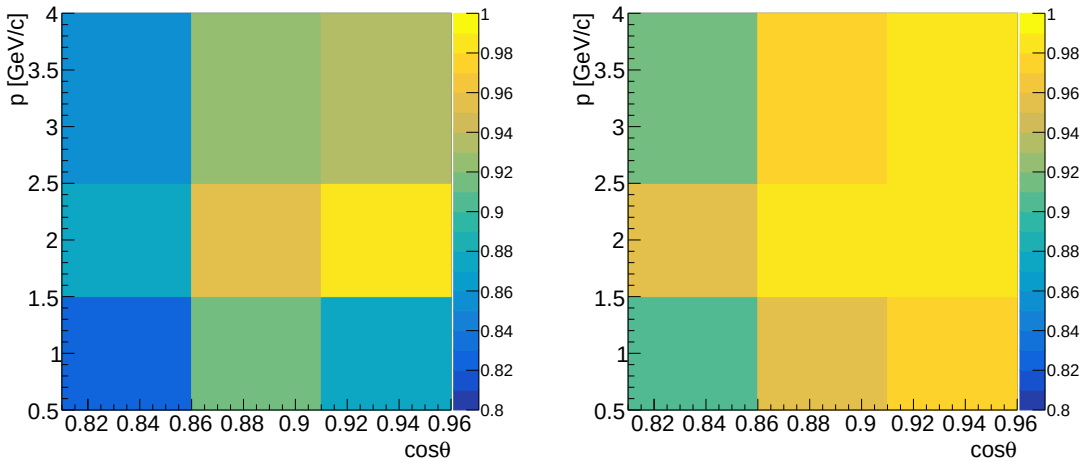

Figure 7.19: The kaon identification efficiencies for Phase II samples at fixed misidentification probability rates of 5 % (left) and 10 % (right).

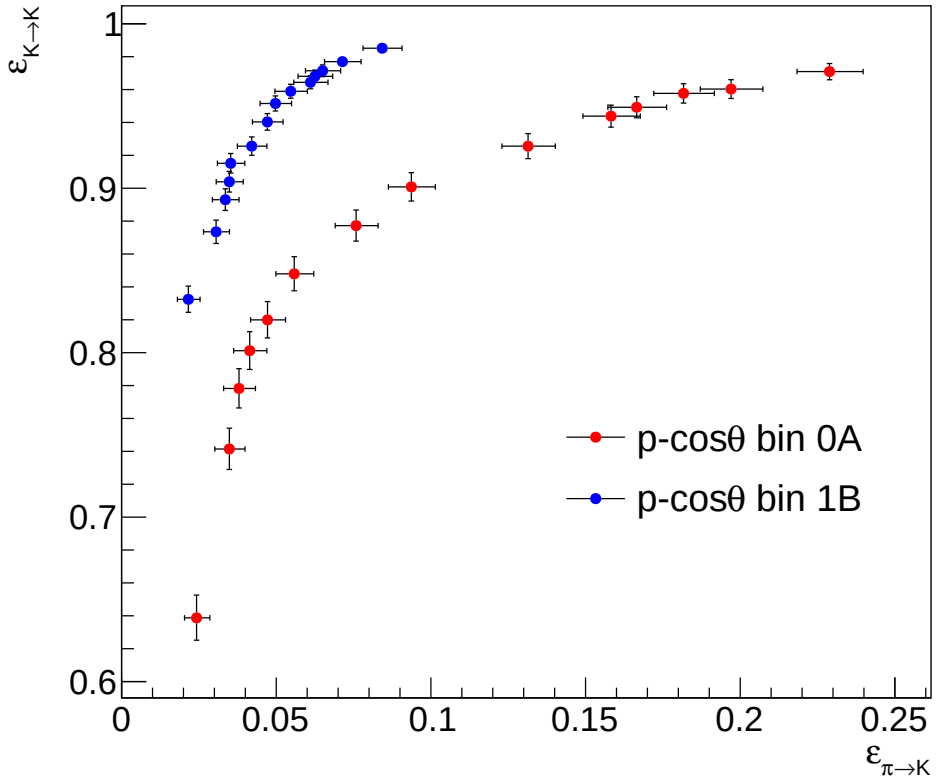

Figure 7.20: Examples of Phase III samples for $p - \cos\theta$ bins with low (bin 1A) and high (bin 2B) kaon identification efficiency.

7.3.3 Kaon Efficiencies and Pion Misidentification Probabilities Rate as a Function of Particle Momentum

The momentum dependence of efficiencies was studied using very fine binning of 100 MeV/c and 50 MeV/c for Phases II and III, respectively. Due to a small size of the Phase II MC samples, no angle range selection was applied. The Phase III results not only include the entire geometrical range samples, but also the results of the three ranges with the interval limits of the cosine of the polar angle of 0.81, 0.86, 0.91 and 0.96 (where the lower limit is excluded and upper limit is included in the angle interval).

7.3.3.1 Phase III Simulations

The result of the sample with no geometrical selection for a typical $PID_{K/\pi}$ selection of 0.6 (Fig. 7.21) shows a high kaon identification efficiency of above 90 % for most of the momentum range, while keeping the pion misidentification probability below 10 %. The efficiency decreases to 80 % for very low momentum particles ($p \sim 0.5\,\mathrm{GeV/c}$), which have slightly higher pion misidentification probabilities of between 10 % to 15 %. The tabulated $\varepsilon_{K\to K}$ and $\varepsilon_{\pi\to K}$ values for all momentum ranges at the $PID_{K/\pi}$ selection of 0.6 are given in the Appendix E. The results for all $PID_{K/\pi}$ selection criteria are presented in the Appendix F.

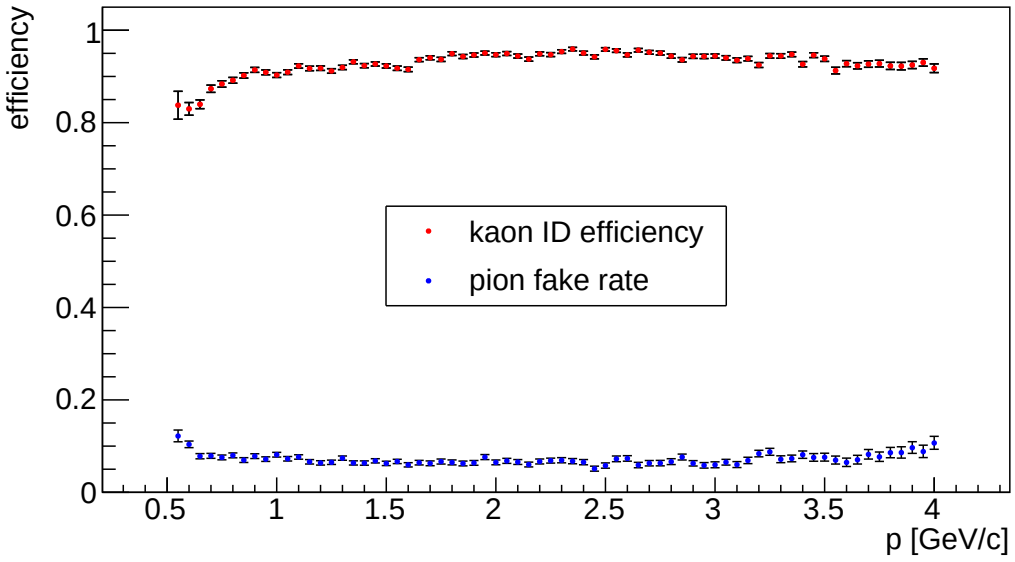

Figure 7.21: The kaon identification efficiencies and pion misidentification probabilities for one of the typical selections of $PID_{K/\pi} > 0.6$. No selection on the polar angle is applied.

The example in Fig. 7.22 presents results of three different incident angle ranges with applied selection of $PID_{K\pi} > 0.6$. The effect of the lower efficiency at the edges of the momentum interval is the most significant for the low $\cos\theta$(the incident angle above 30.7°) and least prominent for the middle values of the incident angle (between 24.5° and 30.7°). The pion misidentification probabilities for fixed $PID_{K/\pi}$ selection, on the other hand, do not vary much with momentum, but highly depend on the incident angle, which will be further discussed in the next section.

The efficiency dependence on $PID_{K/\pi}$ cuts was presented in the previous section 7.3.2. The values of $\varepsilon_{K/\pi\to K}$ depend on both the incident angle and the momentum of the charged particle, while the tendency of $\varepsilon_{K\to K}$ as a function of $\varepsilon_{\pi\to K}$ for different momentum and angle selection is similar. This can also be seen in Fig. 7.23, where the efficiencies as a function of the charged particle's momentum are compared for three $PID_{K/\pi}$ selections of 0.1, 0.6 and 0.9 for the angle interval of 24.5°–30.7°. The kaon identification efficiency and pion misidentification probability are both almost constant over the momentum range between 2.0 GeV/c and 3.5 GeV/c for all selected $PID_{K/\pi}$. For the selection of $PID_{K/\pi} > 0.1$, the kaon identification efficiency exceeds 90 % on the entire momentum range, while keeping the pion misidentification probability below 15 %.

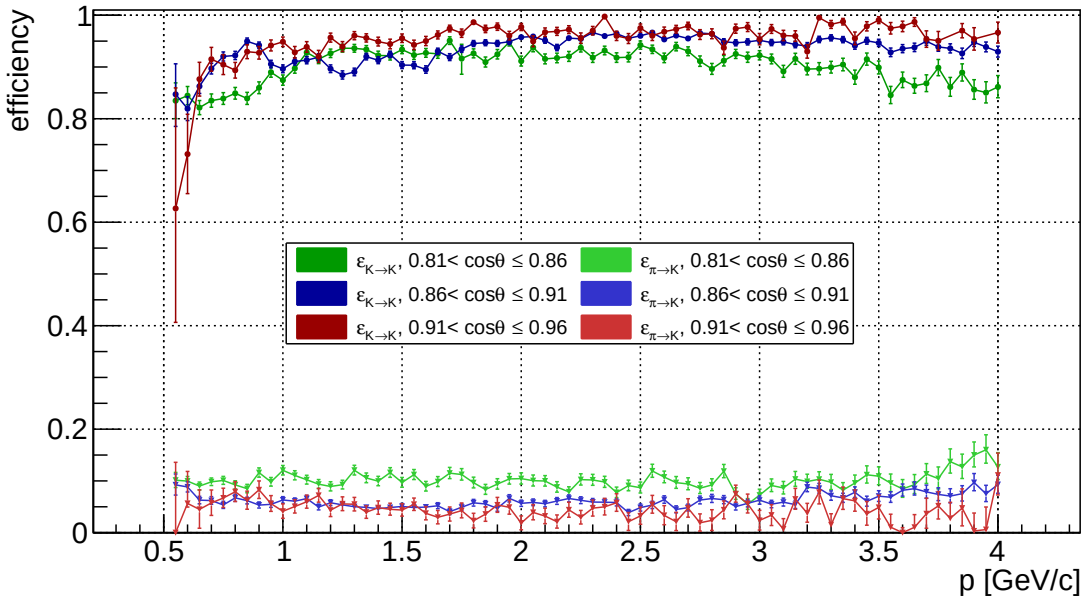

Figure 7.22: The kaon identification efficiencies and pion misidentification probabilities for the selection criterion of $PID_{K/\pi} > 0.6$. The results of three different incident angle ranges (16.3°–24.5°, 24.5°–30.7°, 30.7°–35.9°) are shown.

The data analyses use the $PID_{K/\pi}$ values to select the particles for further studies. The detector performance, however, needs to be evaluated also by comparison of the kaon identification efficiencies with respect to the fixed pion misidentification probabilities. The plot in Fig. 7.24 shows kaon identification efficiencies (with no incident angle selection) at the fixed pion misidentification probability of 5 %. It can be seen that kaon identification is good for the momentum range between 1.5 GeV/c and 3.5 GeV/c, while it drops below 90 % at lower and higher momenta.

In Fig. 7.25 a comparison of efficiencies is shown at different fixed pion misidentification probabilities for the samples with the incident angle of charged particle between 24.5° and 30.7°. One can see that the performance is comparable for most of the momentum range at higher pion misidentification probabilities of 10 %. For the $\varepsilon_{\pi\to K}$ of 3 % and 5 % the efficiencies are constant in the narrow momentum range between 2.5 GeV/c and 3.0 GeV/c, while dropping significantly at low and high momenta.

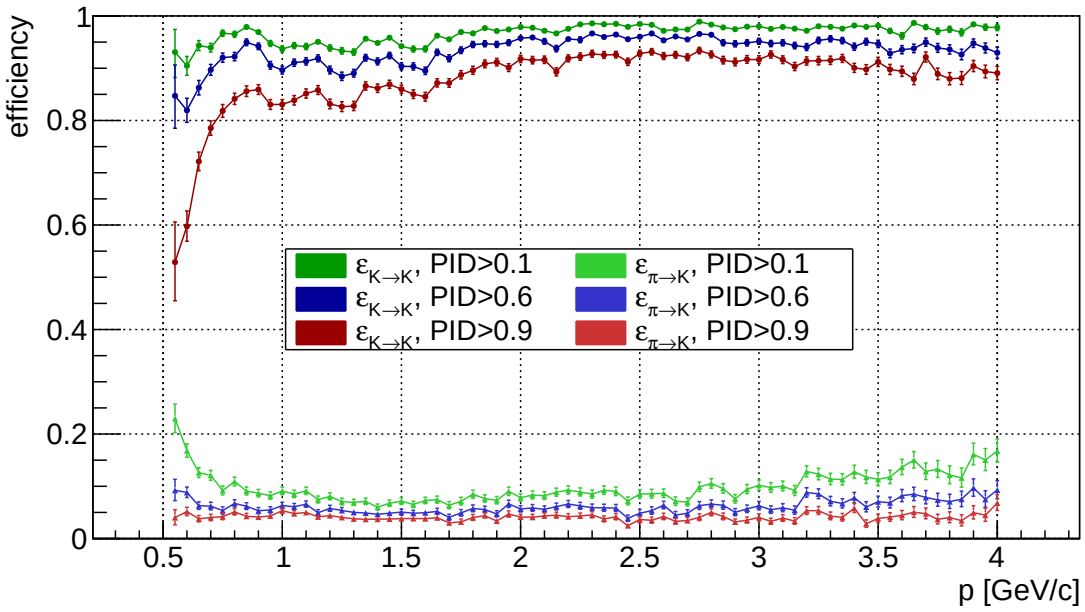

Figure 7.23: The kaon identification efficiencies and pion misidentification probabilities of the sample with the charged particle's incident angle between 24.5° and 30.7°. The results of three different $PID_{K/\pi}$ selections (above 0.1, 0.6, 0.9) are shown.

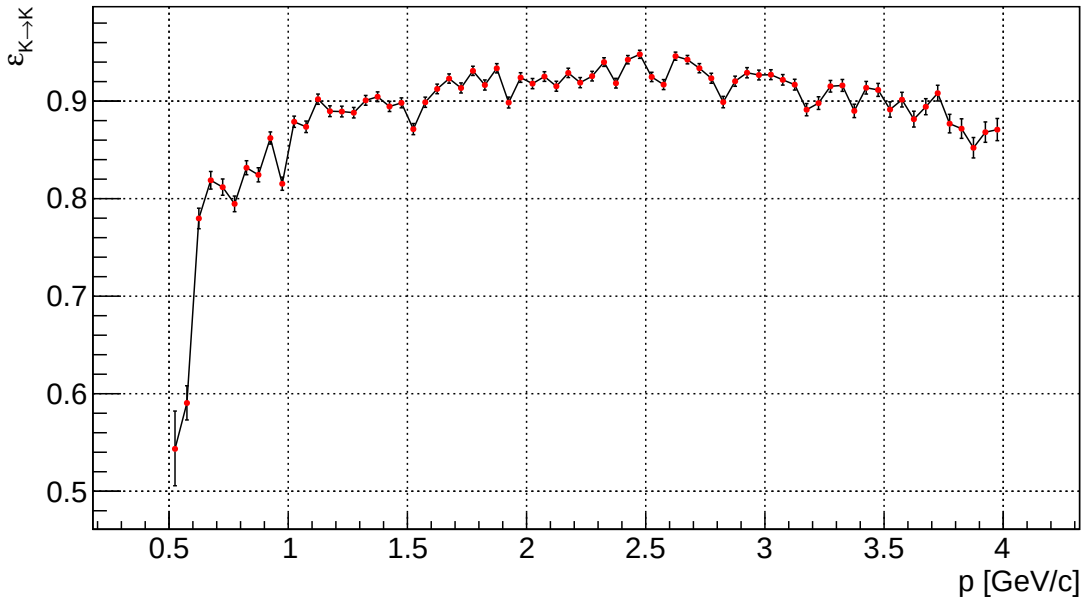

Figure 7.24: The kaon identification efficiencies as a function of a charged particle's momentum for fixed pion misidentification rate of 5 %. No selection is applied to the incident angle of charged particle.

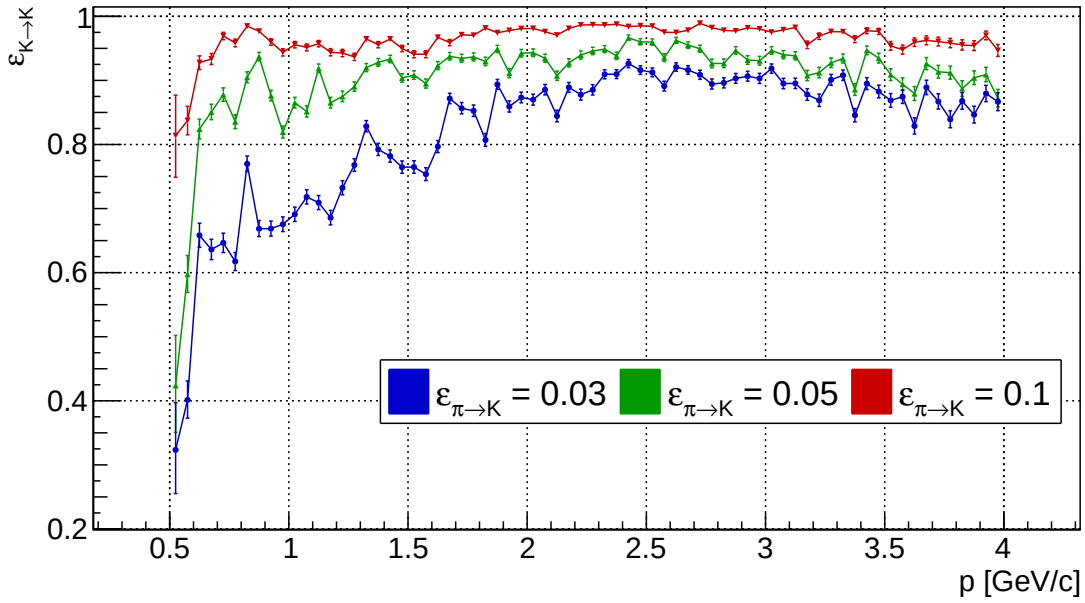

Figure 7.25: The kaon identification efficiencies as a function of a charged particle's momentum at three different fixed pion misidentification probabilities of 3 %, 5 % and 10 %. The sample with the incident angle range between 24.5° and 30.7° is included.

7.3.3.2 Phase II Simulations

The Phase II samples are small, therefore the binning over the momentum range is 100 MeV/c, which is twice as large as for Phase III and there is also no selection over the incident angle. The results of three typical $PID_{K/\pi}$ selections of 0.1, 0.6 and 0.9 (Fig. 7.26), show poorer performance at large cuts. In general, pion misidentification probabilities are higher than for Phase III samples at the same $PID_{K/\pi}$ cuts; being on average 5 %, 10 % and 15 % for the presented selections, respectively.

Figure 7.27 shows the kaon identification efficiency at three different fixed pion misidentification probabilities. It can be seen that the $\varepsilon_{\pi\to K}$ of 5 % does not give $\varepsilon_{K\to K}$ close to, or higher than, 90 % on the entire momentum range. If one wants to have good kaon identification in Phase II, the pion misidentification probabilities of 10 % should be allowed.

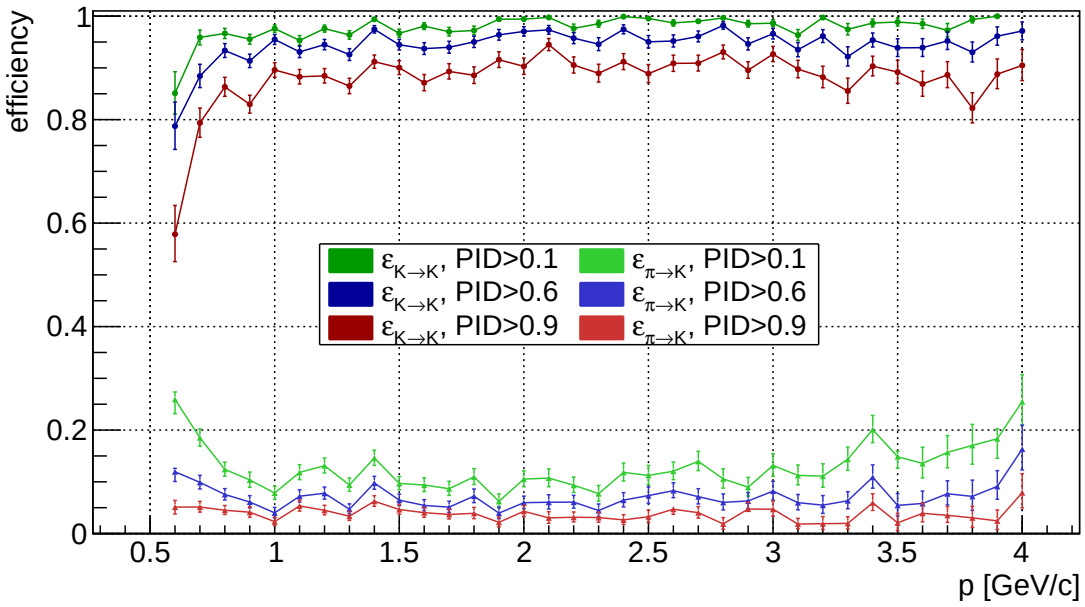

Figure 7.26: The kaon identification efficiencies and pion misidentification probabilities for the sample with the particle incident angle between 11.5° and 36.9°. The results at three different $PID_{K/\pi}$ selections (above 0.1, 0.6, 0.9) are shown.

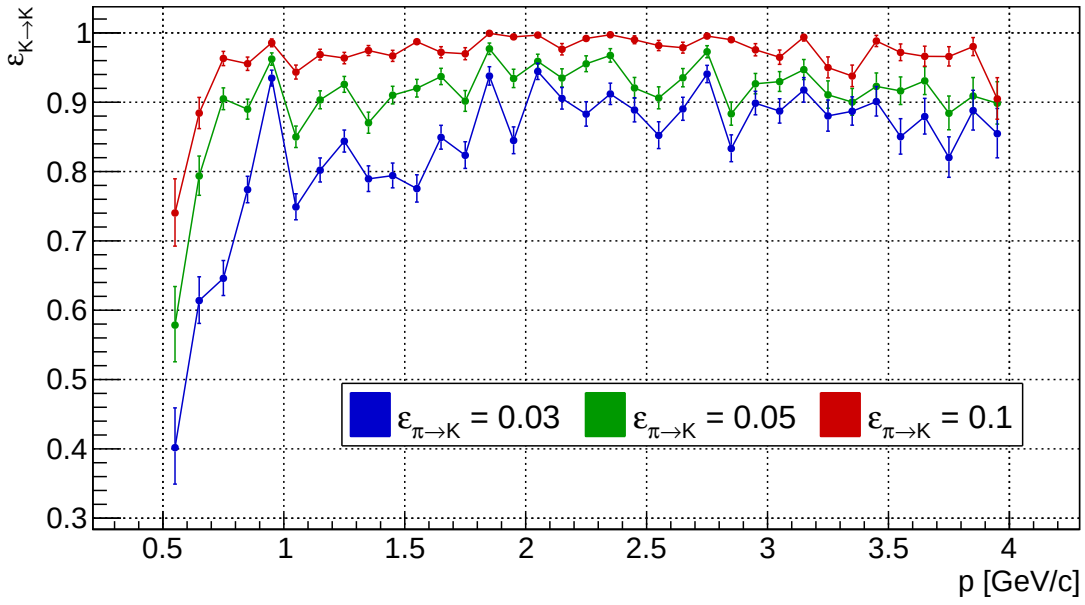

Figure 7.27: The kaon identification efficiencies as a function of the charged particle's momentum at three different fixed pion misidentification probabilities of 3 %, 5 % and 10 %. The incident angle range between 11.5° and 36.9° is selected.

7.3.4 Kaon Efficiencies and Pion Misidentification Probabilities as a Function of Particle Incident Angle

The polar angle dependence of efficiencies was studied using very fine binning of 0.005 and 0.0025 over most of the cosine of polar angle[3] for Phases II and III, respectively. The Phase II sample was too small for applying selection on the momentum range, therefore the whole interval of $p = [0.5, 4.0]$ GeV/c was used. The Phase III results not only include the samples without the momentum selection, but also the results with division of momentum between three bins with the interval limits of 0.5 GeV/c, 1.5 GeV/c, 2.5 GeV/c and 4.0 GeV/c (where the lower limit is excluded and the upper limit is included into momentum interval).

7.3.4.1 Phase III Simulations

The results of the sample with no additional momentum range selection at a typical $PID_{K/\pi}$ selection of 0.6 (Fig. 7.28) shows a high kaon identification efficiency above 90 % for the most of the angle range. The poor performance is seen for the region with cosine of polar angle between 0.84 to 0.855, which corresponds to the angles between 31° to 33°. The $\cos\theta$ range with lower efficiencies also has the corresponding higher pion misidentification probabilities, which additionally decrease the detector performance in the given region. Inferior performance is expected, as a large proportion of photons is reflected from the mirrors, as it was already presented in Chapter 5, Figs. 5.16 and 5.17. The tabulated values of $\varepsilon_{K\to K}$ and corresponding $\varepsilon_{\pi\to K}$ for all angle bins at the applied selection of $PID_{K/\pi} > 0.6$ are given in the Appendix E. The results for all $PID_{K/\pi}$ selection criteria are presented in the Appendix F.

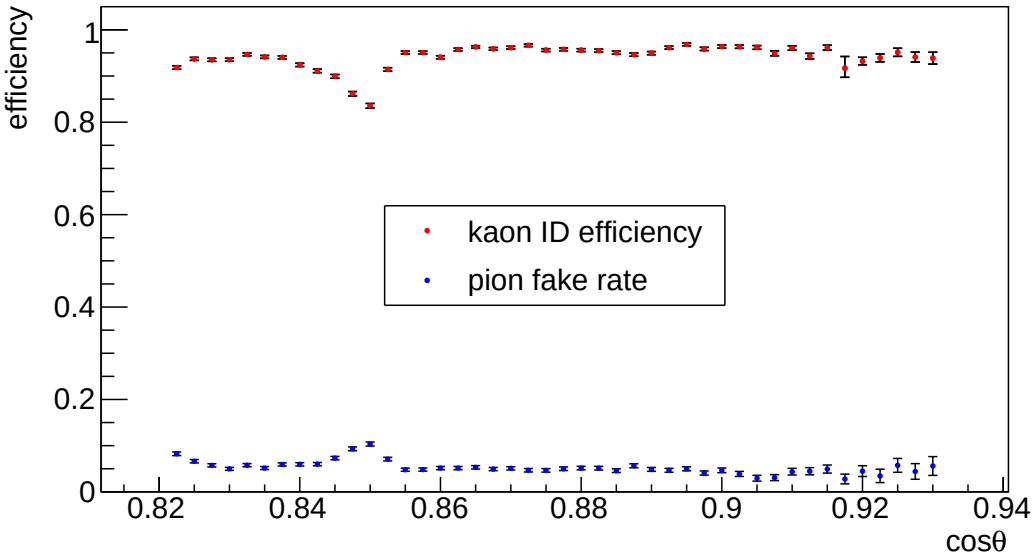

Figure 7.28: The kaon identification efficiencies and pion misidentification probabilities for the typical cut of $PID_{K/\pi} > 0.6$. The entire momentum range is included.

[3]For some samples, bins with $\cos\theta > 0.93$ were skipped due to a very wide signal peak for pions and small sample sizes.

The same selection of $PID_{K/\pi} > 0.6$ was also applied to the samples, divided into three different momentum ranges. The results, shown in Fig. 7.29, as well show little dependence on the polar angle of the charged particle, with the exception of the problematic region around $\cos\theta \sim 0.85$. While the separation in that region is less efficient for all three momentum ranges, the absolute values of $\varepsilon_{K/\pi\to K}$ differ significantly, as seen in the figure. The same $PID_{K/\pi}$ selection gives reasonably high $\varepsilon_{K\to K}$ above 85 % for high momentum particles, but the corresponding pion misidentification probability is up to 20 %.

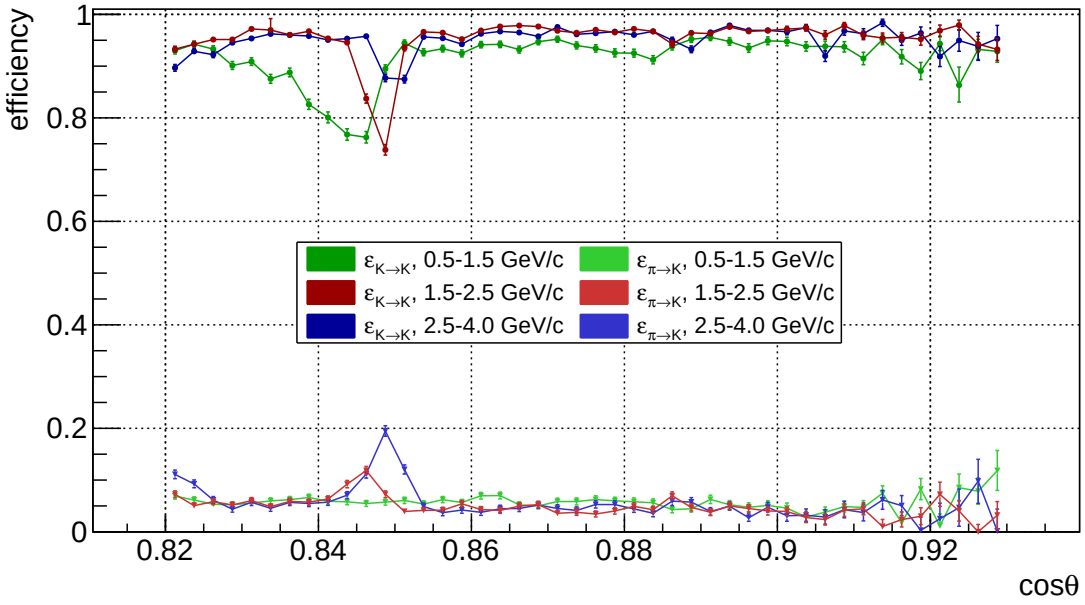

Figure 7.29: The kaon identification efficiencies and pion misidentification probabilities for typical cut of $PID_{K/\pi} > 0.6$. Results for three different momentum ranges are shown.

Different $PID_{K/\pi}$ selections were also compared for the high momentum region with the most efficient kaon identification (2.5 GeV/c–4.0 GeV/c). Fig. 7.30 illustrates that all three compared selections provide a good kaon identification efficiency above 90 % in the region of $\cos\theta > 0.855$ (with the small exception of the $PID_{K/\pi} > 0.9$ selection for a few bins), while keeping the misidentification rate of pions below 10 %. None of the applied selection provide an excellent performance in the region of $\cos\theta < 0.855$, but the efficiencies are again higher in the region around the $\cos\theta \sim 0.83$.

The results at polar angles of $\cos\theta > 0.92$ with a wider signal peak in that region sometimes provide higher efficiencies at larger $PID_{K/\pi}$ selection. Examples of fits of kaon samples with $PID_{K/\pi}$ selection above 0.6 and 0.9 are presented in Fig. 7.31. This is a result of lower signal-to-noise ratio as well as small sample size, which result in a larger fluctuations of the background when $PID_{K/\pi}$ selection is applied.

The kaon identification efficiency was also studied with respect to the fixed pion misidentification probabilities. From the plot in Fig. 7.32 it can be seen that the kaon identification efficiency at $\varepsilon_{\pi\to K} = 5\,\%$ is constant for the $\cos\theta$ range between 0.86 and 0.91, while it decreases to 85 % at large impact angles.

Fig. 7.33 shows a comparison of the efficiencies for different fixed pion misidentification probabilities. All three selected pion misidentification probabilities provide a good kaon identification above $\cos\theta > 0.855$. With requirement of the pion misidentification rate to be 5 %, ARICH can correctly identify up to 85 % of kaons in the poorly efficient region of $\cos\theta \sim 0.85$.

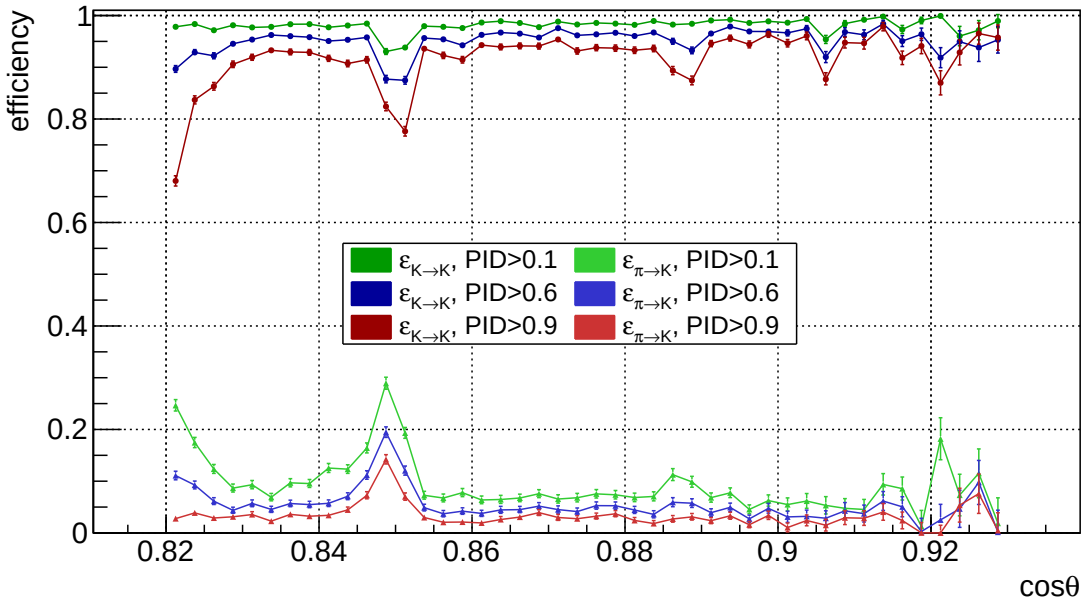

Figure 7.30: The kaon identification efficiencies and pion misidentification probabilities for charged particle momentum between 2.5 GeV/c and 4.0 GeV/c. The results for three different $PID_{K/\pi}$ selections (0.1, 0.6, 0.9) are shown.

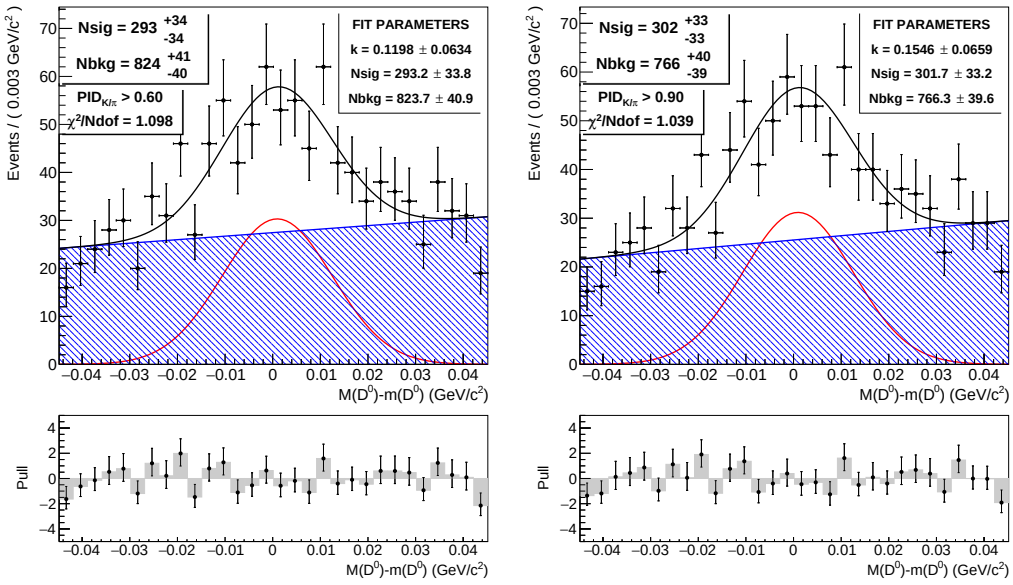

Figure 7.31: D^0 mass fit with $PID_{K/\pi}$ selections of 0.6 (left) and 0.9 (right) applied. The momentum range between 2.5 GeV/c and 4.0 GeV/c and the cosine angle between 0.925 and 0.9275 are selected.

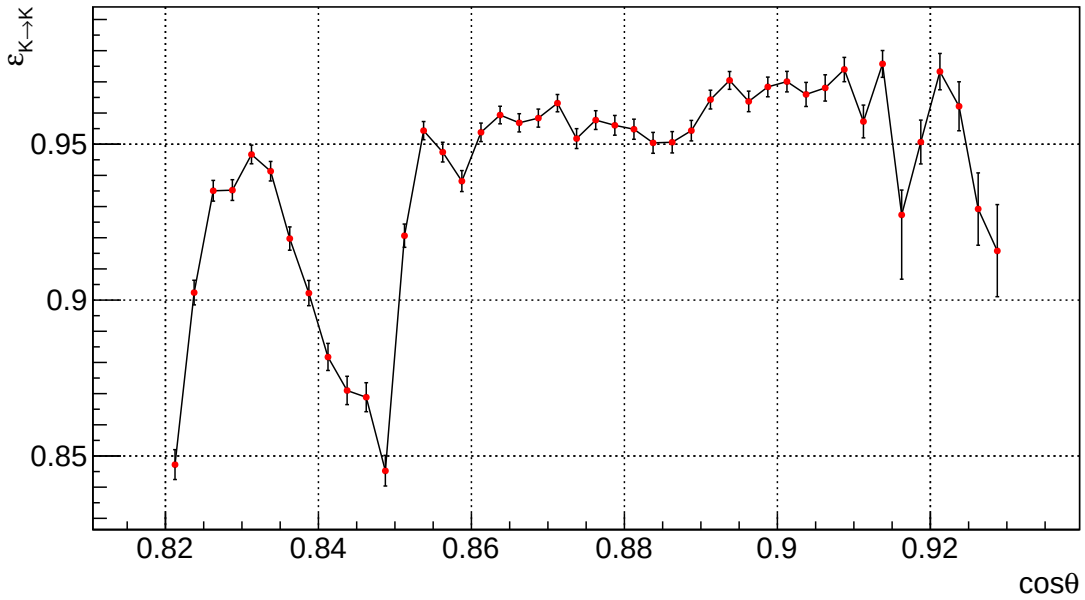

Figure 7.32: The kaon identification efficiencies as a function of the charged particle's polar angle for the fixed pion misidentification rate of 5 %. No selection on momentum range is applied.

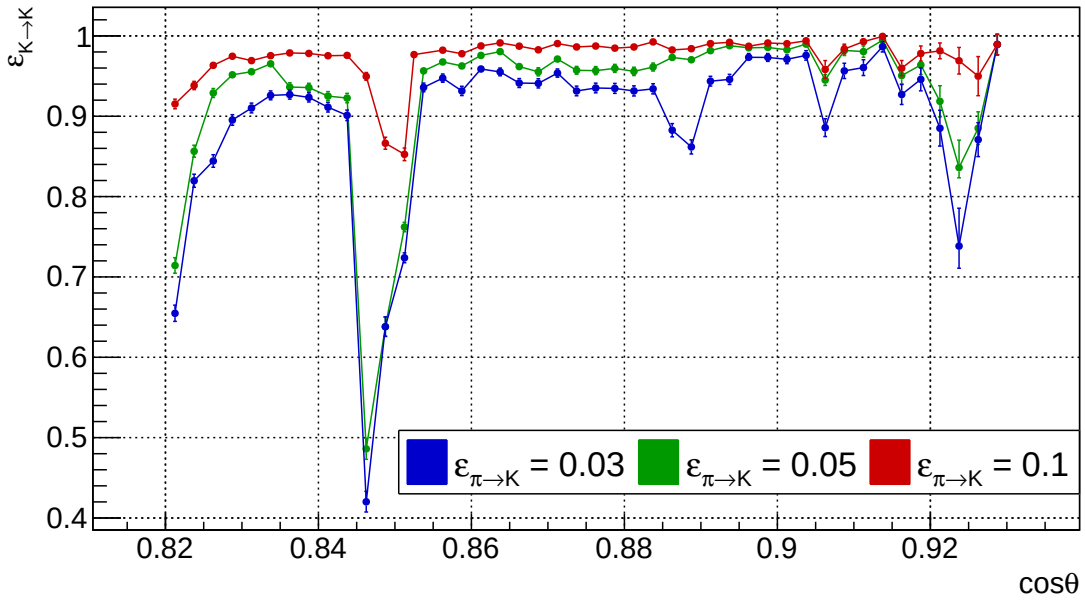

Figure 7.33: The kaon identification efficiencies as a function of the cosine of the charged particle's polar angle at three different fixed pion misidentification rates of 3 %, 5 % and 10 %. The momentum range between 2.5 GeV/c and 4.0 GeV/c is selected.

7.3.4.2 Phase II Simulations

The small Phase II sample required larger angle bins with no selection over the momentum applied. The results at the three typical $PID_{K/\pi}$ selections of 0.1, 0.6 and 0.9 (Fig. 7.34) show an efficient K/π separation for all selections. The performance is similar to the results in Phase III. The kaon identification efficiencies

are high over the entire plotted angle range, although the pion misidentification probabilities are slightly higher than in Phase III. If one requires a high $\varepsilon_{K\to K}$ of at least 90 % over most of the momentum region, the pion misidentification probability limit should be set to up to 10 %, which is also seen from the plot in Fig. 7.26. As the Phase II is not dedicated to detailed physics analyses, but to the detector commissioning, it can be concluded that the expected performance is good over the entire angle range.

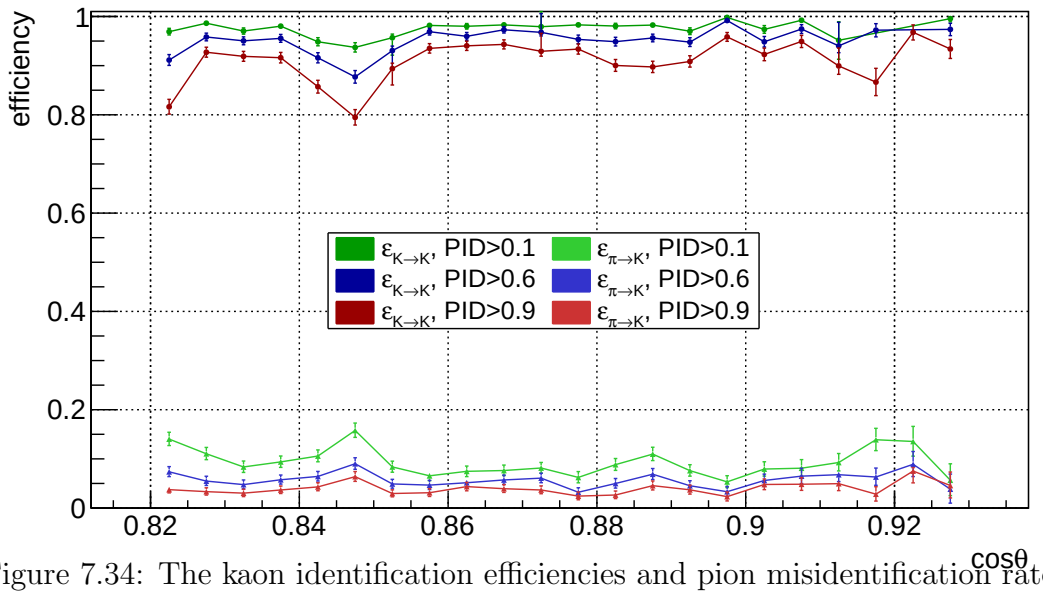

Figure 7.34: The kaon identification efficiencies and pion misidentification rates for charged particle with momentum between 0.5 GeV/c and 4.0 GeV/c. The results of three different $PID_{K/\pi}$ selections (0.1, 0.6, 0.9) are shown.

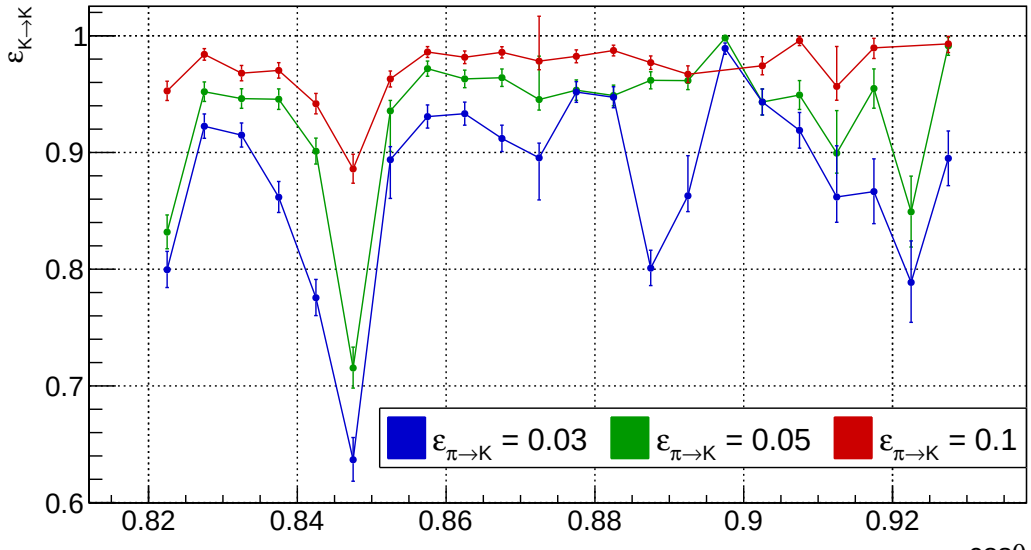

Figure 7.35: The kaon identification efficiencies as a function of the cosine of the particle's polar angle at three different fixed pion misidentification rates of 3 %, 5 % and 10 %. The momentum range between 0.5 GeV/c and 4.0 GeV/c is selected.

7.4 Particle Identification Performance in Phase II

During the Phase II commissioning with beam collisions, lasting from the end of April to mid-July 2018, the data with integrated luminosity of $490\,\mathrm{pb}^{-1}$ was collected; which is only 1 % of the sample size that was used for Phase II MC studies. The ARICH temperature issue, described in Section 6.6, led to the operation of only three or four sectors at once. About 15 % of the detector modules were constantly inactive during the entire, or larger part of, the commissioning phase, mostly because of distortion in the communication with the merger boards, as presented in Fig. 6.34. The expected number of detected kaons from D^{*+} decay, based on the MC simulations and halved because of the inactive areas of ARICH, is approximately 90. This number should be slightly lower due to occasional temporary exclusion of ARICH from the runs because of rebooting of the electronics. Thus the samples were not large enough to perform detailed studies, but adequate for demonstrating the ARICH performance.

Data was analysed using two decay channels, $D^{*+} \to D^0(\to K^-\pi^+)\pi_s^+$ and only part of it, the $D^0 \to K^-\pi^+$ decay. Particles were reconstructed using a simple algorithm, as explained for the example of kaon that enters the geometrical acceptance of ARICH:

a) Charged particle was assigned a kaon mass *(named kaon from now on)*

b) The other particles in the event were selected as pion candidates *(named pion from now on)*

c) Kaon's momentum and mass were combined with pion's momentum and mass to get an invariant mass of D^0

d) In the case of D^{*+}, another particle with the same charge as the first pion candidate and assigned pion mass is combined with D^0

The algorithm for the selection of the pion sample is the same, except that kaon and pion masses for the construction of the D^0 are swapped.

7.4.1 $D^{*+} \to D^0(\to K^-\pi^+)\pi_s^+$ Decay

A D^{*+} decay was reconstructed using collected data. At first, the masses of both D mesons for the entire sample were checked. Results in Figs. 7.36 and 7.37 show, that peaks are seen for both D^0 mass and a mass difference between D mesons. The D^{*+} mass peak is seen only after applying a selection to either the D^0 mass or mass difference of D^{*+} and D^0 mesons, ΔM, as shown in Fig. 7.38. The selection, applied o the mass difference between D mesons, reduces the background significantly.

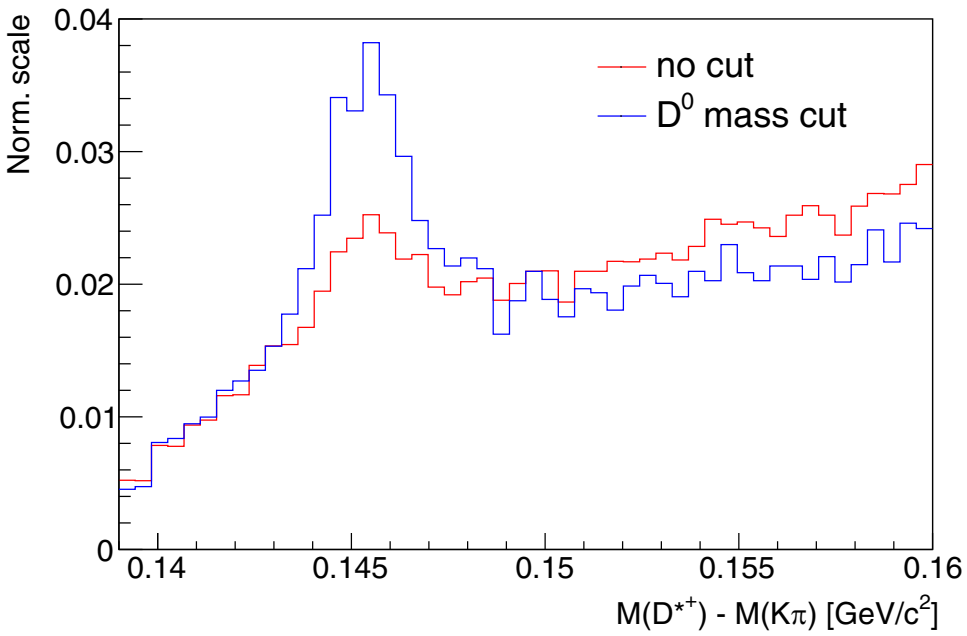

Figure 7.36: A difference between invariant mass of D^{*+} and D^0. A comparison of the entire sample and the sample with the cut on D^0 mass of $1.82\,\mathrm{GeV/c^2} \leq M(K\pi) \leq 1.91\,\mathrm{GeV/c^2}$ is presented. The y-axis is normalized.

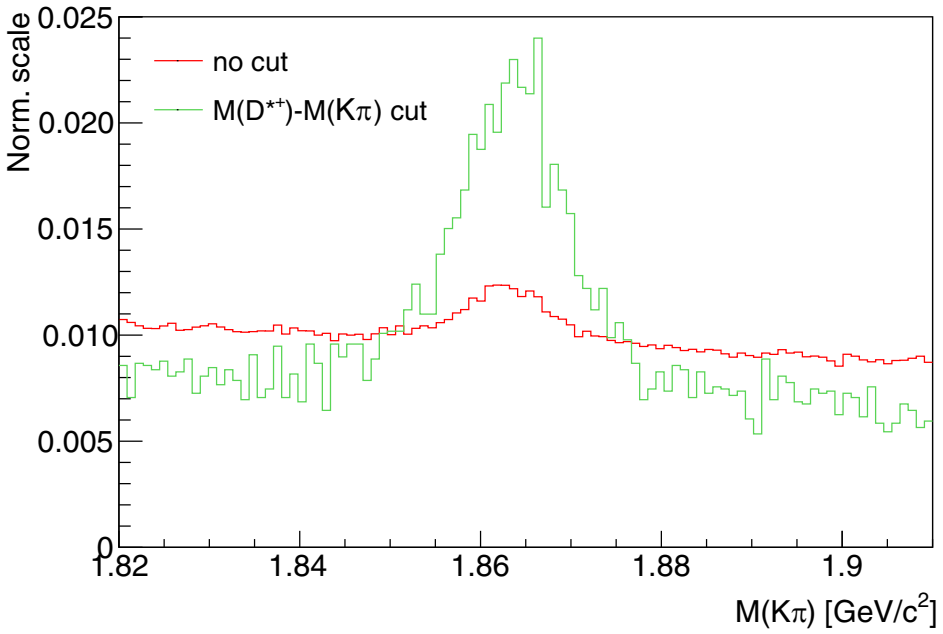

Figure 7.37: A D^0 invariant mass. A comparison of the entire sample and the sample with the cut on the mass difference ΔM of $0.139\,\mathrm{GeV/c^2} \leq \Delta M \leq 0.160\,\mathrm{GeV/c^2}$ is presented. The y-axis is normalized.

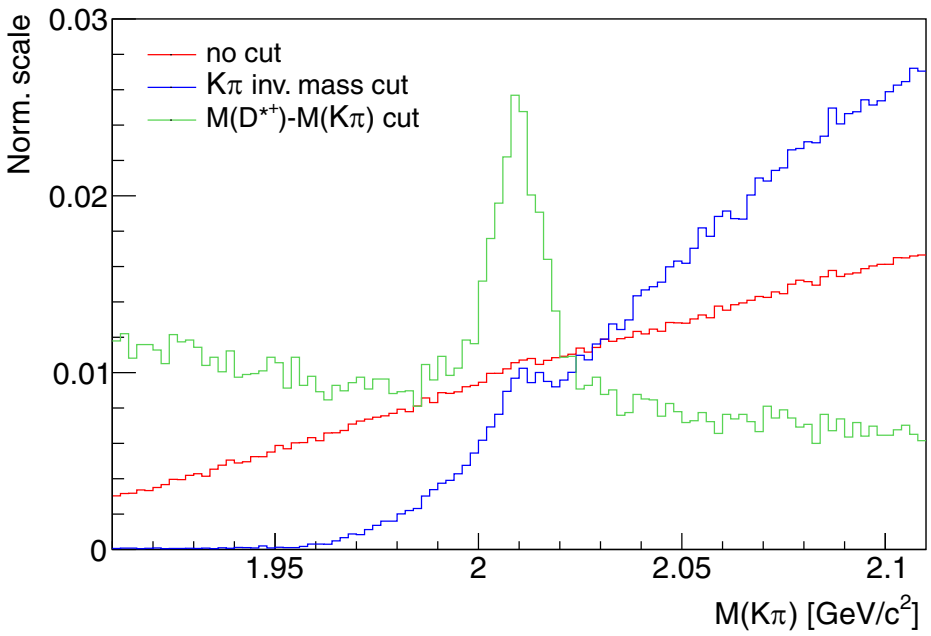

Figure 7.38: A D^{*+} invariant mass for an entire sample, a sample with a selection of $1.82\,\mathrm{GeV/c^2} \leq M(K\pi) \leq 1.91\,\mathrm{GeV/c^2}$ and a sample with a selection of $0.139\,\mathrm{GeV/c^2} \leq \Delta M \leq 0.160\,\mathrm{GeV/c^2}$ is presented. The y-axis is normalized.

A difference between the masses of the D mesons of $0.139\,\mathrm{GeV/c^2} \leq \Delta M \leq 0.160\,\mathrm{GeV/c^2}$ was applied to the sample of kaons (pions). Additionally, mass cuts of $1.91\,\mathrm{GeV/c^2} \leq M(D^{*+}) \leq 2.11\,\mathrm{GeV/c^2}$ and $1.82\,\mathrm{GeV/c^2} \leq M(K\pi) \leq 1.91\,\mathrm{GeV/c^2}$ were applied. Only kaon (pion) tracks with the momentum of $0.5\,\mathrm{GeV/c} \leq p \leq 4.0\,\mathrm{GeV/c}$ were selected. The mass deviation of D^0 was fitted with a Gaussian function for the signal and a linear function for the background. Signal parameters were fixed and the subsample of kaons (pions), that entered ARICH, were fitted with a fixed Gaussian shape and linear function, as seen in Fig. 7.39 (7.40). A number of K^- (π^+) from D^{*+} decay that entered the geometrical acceptance of ARICH, obtained from the fit, is 72 (84).

However, the mass distribution fits indicate that there is a shift in the signal peak for pions that enter ARICH. Samples were fitted again, but this time the mean value of the signal Gaussian function was not fixed, as seen in Figs. 7.41 and 7.42. The signal shifts were calculated from the comparison of values for both the fixed and floating mean value of the fitted Gaussian function, and the results are presented in Table 7.2.

Table 7.2: Signal peak shifts, calculated as the difference between mean values of the Gaussian function for subsample, when charged particle enters ARICH, and the entire sample. The corresponding values of the signal events N_{sig} are also presented.

Particle	Shift ($\mathrm{MeV/c^2}$)	N_{sig} (no shift)	N_{sig} (shift)	N_{sig} loss[a]
kaon	0.33	72 ± 13	72 ± 13	0 %
pion	3.65	84 ± 14	92 ± 14	9 %

[a] Loss of events if mean value is fixed is calculated as $\frac{N_{sig}(\text{shift}) - N_{sig}(\text{no shift})}{N_{sig}(\text{shift})}$.

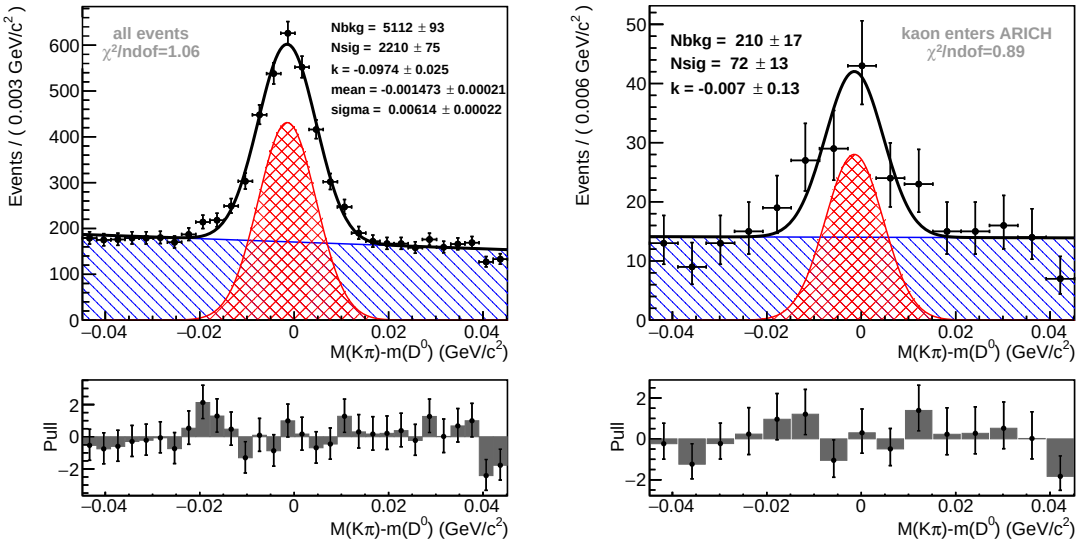

Figure 7.39: A deviation of the D^0 mass, when the momentum of kaon from the decay chain is between 0.5 GeV/c and 4.0 GeV/c. Left: A sample of kaons, entering any part of the solid angle. Right: Kaons enter ARICH. The mean value and the standard deviation of the Gaussian function, fitted to signal peak, are fixed.

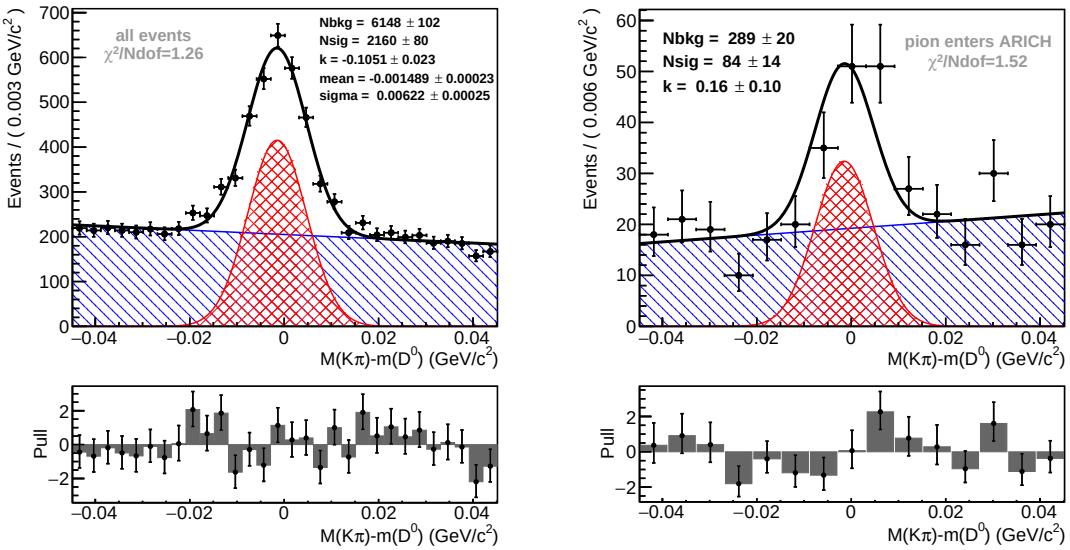

Figure 7.40: A deviation of the D^0 mass, when the momentum of pion from the decay chain is between 0.5 GeV/c and 4.0 GeV/c. Left: A sample of pions, entering any part of the solid angle. Right: Pions enter ARICH. The mean value and the standard deviation of the Gaussian function, fitted to signal peak, are fixed.

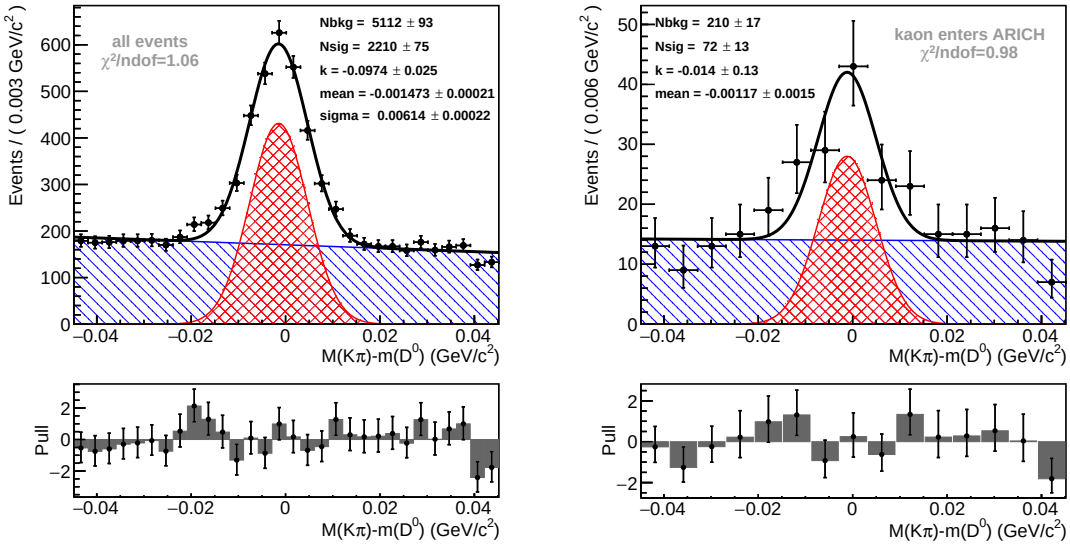

Figure 7.41: A deviation of the D^0 mass, when the momentum of kaon from the decay chain is between 0.5 GeV/c and 4.0 GeV/c. Left: A sample of kaons, entering any part of the solid angle. Right: Kaons enter the ARICH. Only the standard deviation of the Gaussian function, fitted to signal peak, is fixed.

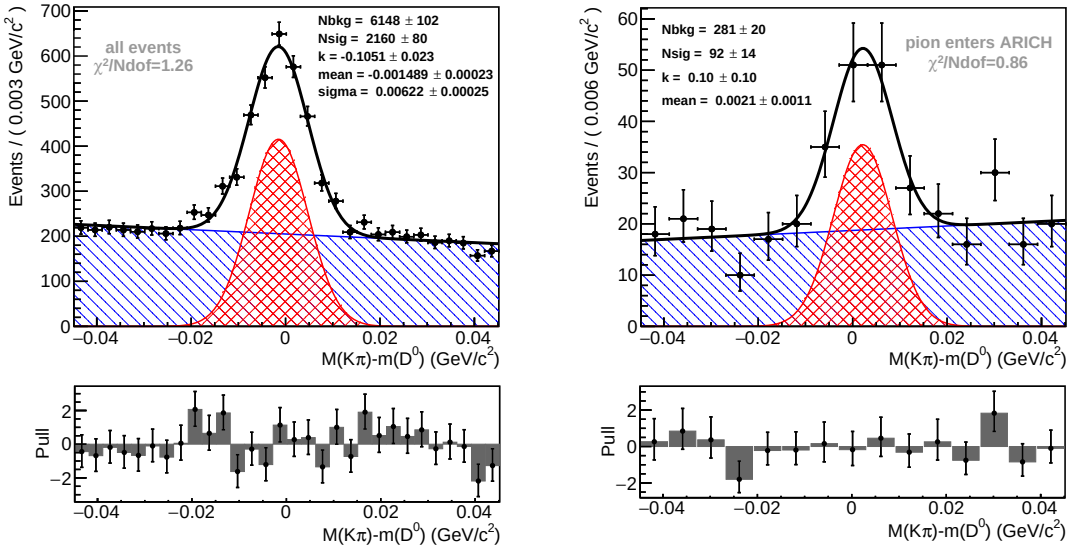

Figure 7.42: A deviation of the D^0 mass, when the momentum of pion from the decay chain is between 0.5 GeV/c and 4.0 GeV/c. Left: A sample of pions, entering any part of the solid angle. Right: Pions enter the ARICH. Only the standard deviation of the Gaussian function, fitted to signal peak, is fixed.

7.4.2 $D^0 \to K^-\pi^+$ Decay

The main selection criterion that reduces the background of D^0 mass distribution from D^{*+} decay is the mass difference between D^{*+} and D^0. Using only $D^0 \to K^-\pi^+$ decay, without the possibility of the ΔM selection, results in higher background and therefore increases the uncertainty of the number of signal events from the fit. However, the number of the reconstructed D^0 decays is almost ten times larger than for the number of the D^{*+} decays, as seen in Fig. 7.43 for kaon sample and Fig. 7.44 for pion sample, so it is a better choice to test the performance. The only selection was applied to the momentum of the kaon (pion), which was limited to between 0.5 GeV/c and 4.0 GeV/c.

Once again, the signal mass peak for the events, when one of the particles transverses ARICH, is shifted in comparison to the signal mass peak of the entire sample. Samples were fitted again with the mean value for the Gaussian function floating, as seen in Fig. 7.45 for kaon sample and Fig. 7.46 for pion sample. The size of the shifts and the corresponding numbers of the events are listed in Table 7.3.

Table 7.3: Signal peak shifts, calculated as the difference between the mean values of the Gaussian functions, fitted to the subsample, when charged particles enter ARICH, and to the entire sample. The corresponding values of signal events N_{sig} are also presented.

Particle	Shift (MeV/c^2)	N_{sig} (no shift)	N_{sig} (shift)	N_{sig} loss[a]
kaon	1.7	613 ± 78	628 ± 78	2 %
pion	5.3	434 ± 85	573 ± 85	24 %

[a] Loss of events if mean value is fixed is calculated as $\frac{N_{sig}(\text{shift}) - N_{sig}(\text{no shift})}{N_{sig}(\text{shift})}$.

Statistics of 600 events is too low to deliver solid conclusions, but can provide some more insight into the particle identification performance. A sample of events, when kaon (pion) enters ARICH, was selected for three different $PID_{K/\pi}$ cuts of 0.1, 0.6 and 0.9, as seen in Fig. 7.47 (7.48). Charged particles that surpass the $PID_{K/\pi}$ cut are identified as kaons in ARICH. For all three selections, kaon identification efficiency and pion misidentification probability were calculated, and the results are presented in Table 7.4. Large misidentification probabilities could be a result of ARICH misalignment and insufficient sensor calibration. However, the results show that all three presented $PID_{K/\pi}$ selections keep the a large fraction of the signal events, while reducing the background significantly.

Table 7.4: The kaon identification efficiencies and pion misidentification rates for three different $PID_{K/\pi}$ cuts. Values are obtained from Phase II data, presented in Figs. 7.45, 7.46, 7.47 and 7.48.

$PID_{K/\pi}$	$\varepsilon_{K\to K}$[%]	$\varepsilon_{\pi\to K}$ [%]
0.1	95.7 ± 3.0	36.8 ± 8.8
0.6	89.3 ± 3.8	24.3 ± 9.1
0.9	76.4 ± 4.6	5.4 ± 8.1

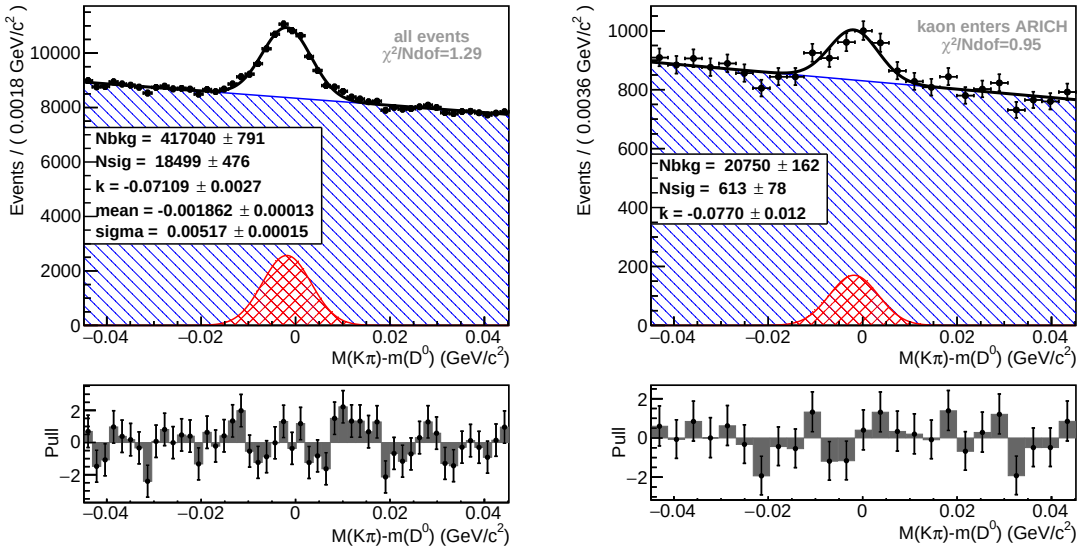

Figure 7.43: A deviation of the D^0 mass, when the momentum of kaon from the decay chain is between 0.5 GeV/c and 4.0 GeV/c. Left: A sample of kaons, entering any part of the solid angle. Right: Kaons enter ARICH.

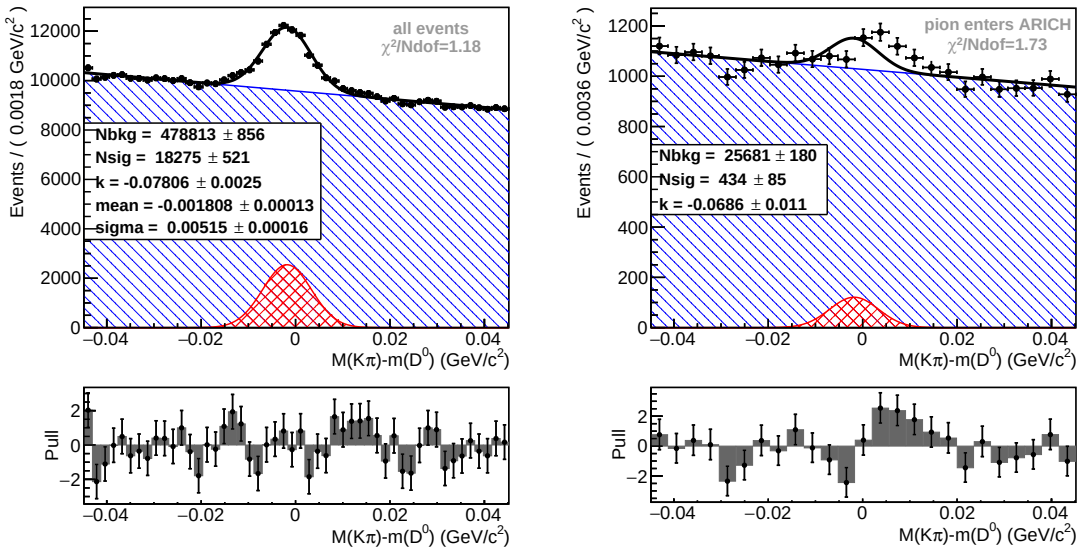

Figure 7.44: A deviation of the D^0 mass, when the momentum of pion from the decay chain is between 0.5 GeV/c and 4.0 GeV/c. Left: A sample of pions, entering any part of the solid angle. Right: Pions enter ARICH.

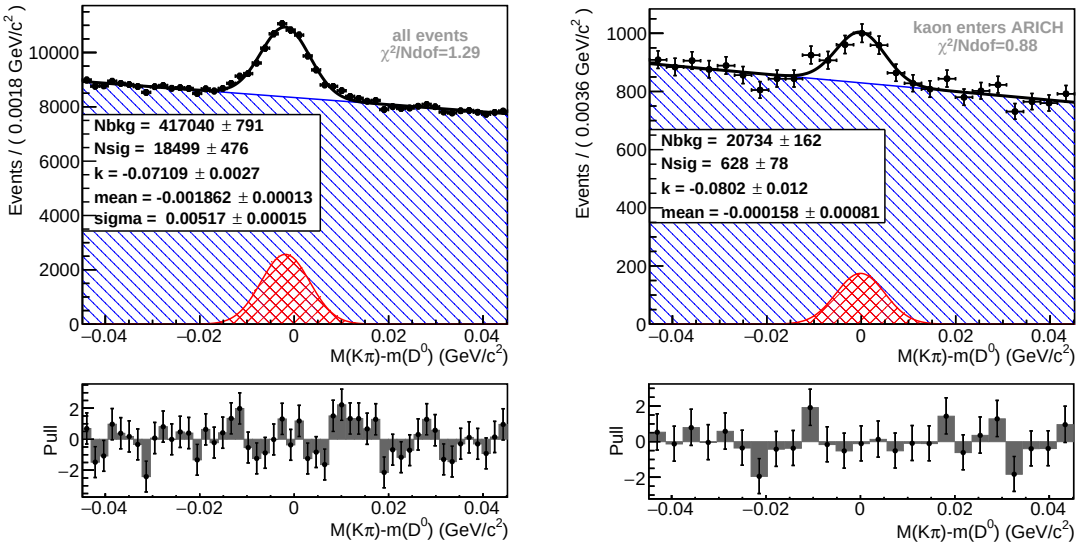

Figure 7.45: A deviation of the D^0 mass, when momentum of kaon from the decay chain is between 0.5 GeV/c and 4.0 GeV/c. Left: A sample of events, when kaon enters any part of the solid angle. Right: A kaon enters ARICH. Only standard deviation of Gaussian function, fitted to signal peak, is fixed.

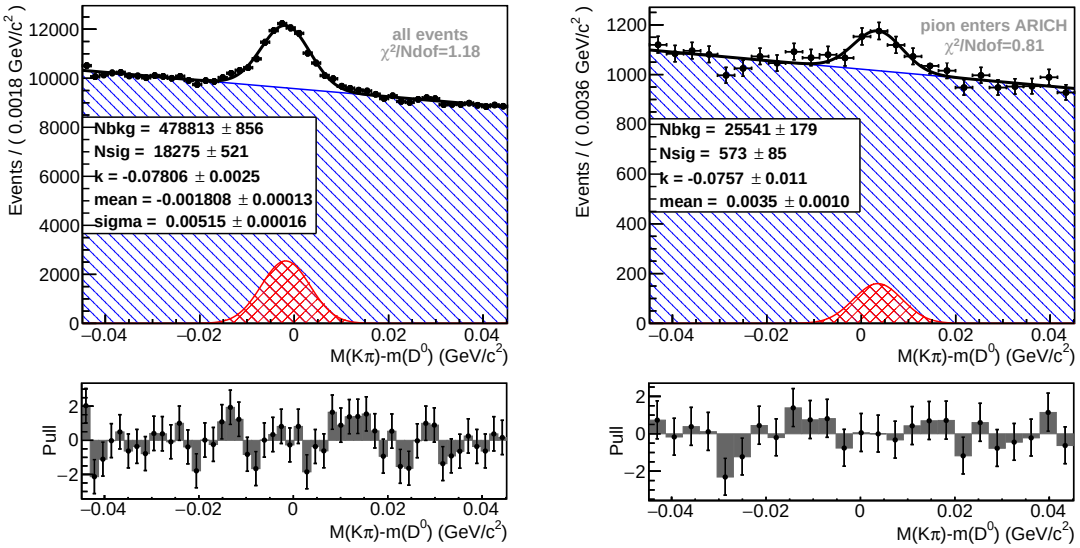

Figure 7.46: A deviation of the D^0 mass, when momentum of pion from the decay chain is between 0.5 GeV/c and 4.0 GeV/c. Left: A sample of events, when pion enters any part of the solid angle. Right: A pion enters ARICH. Only standard deviation of Gaussian function, fitted to signal peak, is fixed.

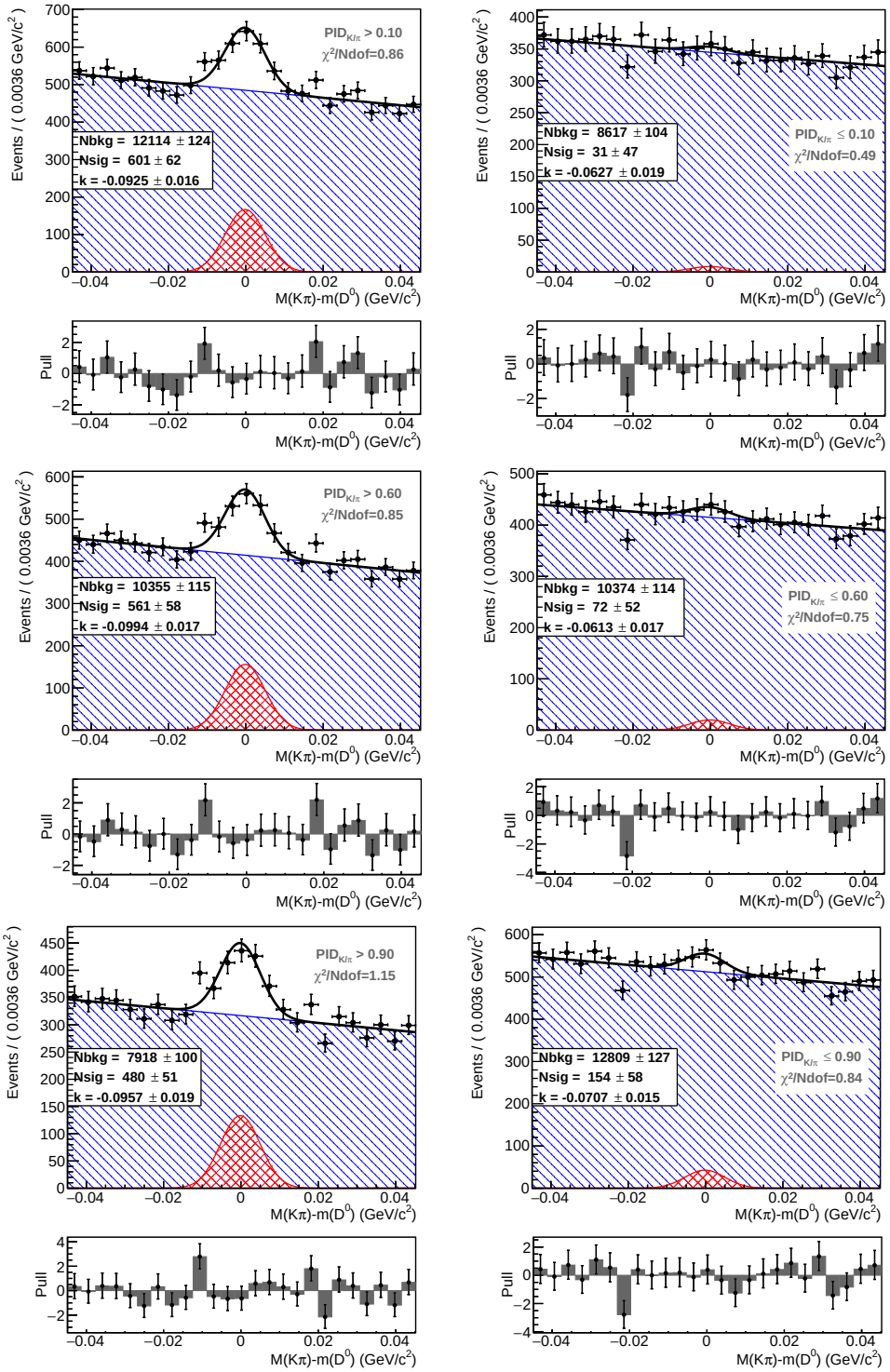

Figure 7.47: A deviation of the D^0 mass, when momentum of the kaon from the decay chain is between 0.5 GeV/c and 4.0 GeV/c and the particle is identified by ARICH. The left (right) plot presents the sample of particles, that fall above (or below) the $PID_{K/\pi}$ selection cut for kaon identification. Different $PID_{K/\pi}$ cuts used are 0.1 (top), 0.6 (middle) and 0.9 (bottom).

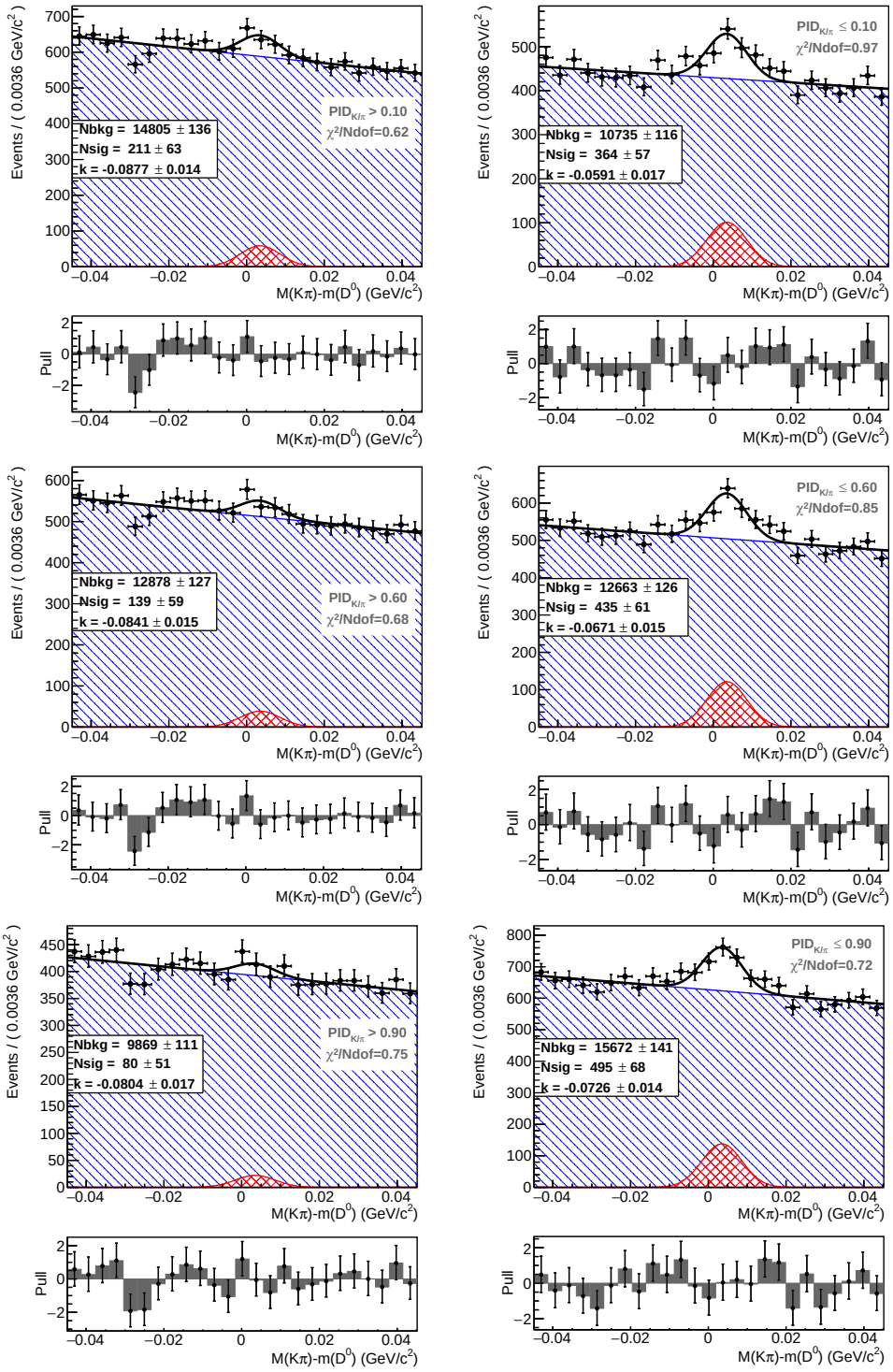

Figure 7.48: A deviation of the D^0 mass, when momentum of the pion from the decay chain is between 0.5 GeV/c and 4.0 GeV/c and the particle is identified by ARICH. The left (right) plot presents the sample of particles, that fall above (or below) the $PID_{K/\pi}$ selection cut for kaon identification. Different $PID_{K/\pi}$ cuts used are 0.1 (top), 0.6 (middle) and 0.9 (bottom).

CHAPTER 8

Summary with Conclusions

The great success of the Belle experiment, which concluded its operation in 2010, was the main motivation for its upgrade. The successor, the Belle II experiment, required an upgraded collider and an improved detector. The SuperKEKB collider successfully stored the electron and positron beams in 2016, and collided particles for the first time two years later. The operation of the Belle II detector started at the beginning of 2018. The commissioning was initially accomplished by the detection of cosmic rays, followed by the low luminosity runs with first collisions at the end of April. The particle identification information in the endcap region of Belle II is provided by the Aerogel Ring Imaging Cherenkov (ARICH) detector, which was assembled at the end of 2017 and joined the runs during the Belle II detector commissioning.

The main objective of ARICH is to provide an efficient charged kaon/pion separation in a momentum region between 0.5 GeV/c and 4.0 GeV/c. The detector consists of three main segments – a double layered aerogel radiator in a focusing configuration, an empty space for expansion of emitted Cherenkov photons, and a segmented sensor plane with Hybrid Avalanche Photo Detectors (HAPDs), attached to an aluminium frame. The back of the sensors is equipped with the front-end readout electronics. The back of the detector is covered with aluminium plates, and the very narrow space in between is equipped with a variety of different voltage power supply and data cables.

The detector components were tested and evaluated before the assembly to ensure the efficient operation. The sensor modules were composed of the HAPD, the front-end readout electronics board and the high voltage distribution board. The methods of the calibration of the gain of the photodetectors and the offset adjustment of the readout electronics are described in the thesis. The results of the determination of the faulty channels due to their damage are also presented.

The second part of the dissertation is dedicated to the studies of the charged kaon/pion separation using control channels $D^{*+} \to D^0(\to K^-\pi^+)\pi_s^+$ and $D^{*-} \to \bar{D}^0(\to K^+\pi^-)\pi_s^-$. The choice of the control channel was based on its kinematic properties. The charge of the slow pion π_s^+ determines the identity of the charged particle from the D^0 decay without the ARICH information. Thus the ARICH performance can be evaluated independently.

The results of the components' measurements before the assembly show that

0.7 % of the channels are not working properly. Most of them are dead, and about one third of the channels is too noisy due to the high leakage currents. The collected collision data from the low luminosity runs shows that the number of channels with larger noise increased. The results indicate the miscalibration of some of the channels, as well as the increased noise due to a higher temperature inside ARICH, as a consequence of the insufficient coupling between the initial cooling system and the heat sources. The noise measurements at different temperatures conclude that wider noise distributions triggered up to six times more events and increased the background hit rates severely, thus the offset calibration is needed not only at the beginning of the operation, but also after the temperature saturates at its maximal value. The total gain of the photon signal decreases with temperature, which degrades the efficiency for the photon collection. Both effects – the noise increase and the gain decrease – result in a poorer efficiency of the particle identification. Before the physical runs with higher luminosity (Phase III, starting in 2019), the initial cooling was upgraded, lowering the expected temperatures inside of ARICH. The total gain and noise are therefore not expected to change to a large extent as during the commissioning phase.

The ARICH identification method was tested on the $D^{*+} \to D^0(\to K^-\pi^+)\pi_s^+$ and $D^{*-} \to \bar{D}^0(\to K^+\pi^-)\pi_s^-$ decays. The simulation results provide the efficiency of kaon identification above 90 % at the misidentification level of pions to kaons of 5 %. The efficiency of the identification strongly depends on the momentum and the incident angle of the charged particle, varying between 70 % and 97 % for the different momentum-angle regions at the probability to misidentify a pion as a kaon with one in twenty cases. For these decays, the part of the sample with a very low efficiency is small and restricted to the particles that enter ARICH very close to its edge. For these particle candidates, photons are reflected from the mirrors and they partially overlap for kaons and pions.

During the detector commissioning phase, Phase II, the same studies could not be performed due to a small sample of only 70 charged kaons and pions originating from the D^{*+}. The samples of the kaons and pions from the $D^0 \to K^-\pi^+$ and $\bar{D}^0 \to K^+\pi^-$ decays were used instead. The number of the reconstructed charged particles that entered ARICH was around 600 for both kaons and pions, respectively. The sample size is still not sufficient for the detailed studies, but provides some insight in the particle identification. The particle identification selection criterion, based on the likelihood ratio between the kaon and the pion mass hypotheses, was applied to the samples of events where one of the charged particles enters ARICH. The kaon identification efficiencies and the pion misidentification rates were calculated from the values, obtained from the fit of the deviation of the D^0 mass. The result of the selection of $PID_{K/\pi} > 0.6$ gives the kaon identification efficiency of (89 ± 4) % at the pion misidentification probability of (24 ± 9) %. The masking of the faulty channels was included in the likelihood calculation, but since it is based on the numbers of expected and detected photons, the particles for which only a small proportion of the Cherenkov ring is detected, are more likely to be misidentified.

The first collected collision data show that ARICH can differentiate between kaons and pions, but larger samples are needed for the detailed performance studies. More data is expected to be collected during Phase III, which will start the physics runs in April 2019.

Bibliography

[1] Paul AM Dirac. 'The quantum theory of the electron'. In: *Proceedings of the Royal Society of London A: Mathematical, Physical and Engineering Sciences*. Vol. 117. The Royal Society. 1928, pp. 610–624.

[2] Paul AM Dirac. 'Quantised singularities in the electromagnetic field'. In: *Proceedings of the Royal Society of London A: Mathematical, Physical and Engineering Sciences* 133.821 (1931), pp. 60–72. ISSN: 0950-1207. DOI: 10.1098/rspa.1931.0130. eprint: http://rspa.royalsocietypublishing.org/content/133/821/60.full.pdf.

[3] Carl D. Anderson. 'The Positive Electron'. In: *Phys. Rev.* 43 (6 1933), pp. 491–494. DOI: 10.1103/PhysRev.43.491.

[4] Sheldon L Glashow, Jean Iliopoulos and Luciano Maiani. 'Weak interactions with lepton-hadron symmetry'. In: *Physical review D* 2.7 (1970), p. 1285.

[5] S Weinberg. 'WEINBERG 1967'. In: *Phys. Rev. Lett* 19 (1967), p. 1264.

[6] Sheldon L Glashow. 'Partial-symmetries of weak interactions'. In: *Nuclear Physics* 22.4 (1961), pp. 579–588.

[7] F. Abe, H. Akimoto et al. 'Observation of Top Quark Production in $\overline{p}p$ Collisions with the Collider Detector at Fermilab'. In: *Phys. Rev. Lett.* 74 (14 1995), pp. 2626–2631. DOI: 10.1103/PhysRevLett.74.2626.

[8] S. Abachi, B. Abbott et al. 'Search for High Mass Top Quark Production in $p\overline{p}$ Collisions at $\sqrt{s} = 1.8$ TeV'. In: *Phys. Rev. Lett.* 74 (13 1995), pp. 2422–2426. DOI: 10.1103/PhysRevLett.74.2422.

[9] K. Kodama, N. Ushida et al. 'Observation of tau neutrino interactions'. In: *Physics Letters B* 504.3 (2001), pp. 218 –224. ISSN: 0370-2693. DOI: https://doi.org/10.1016/S0370-2693(01)00307-0.

[10] G. Aad, T. Abajyan et al. 'Observation of a new particle in the search for the Standard Model Higgs boson with the ATLAS detector at the LHC'. In: *Physics Letters B* 716.1 (2012), pp. 1 –29. ISSN: 0370-2693. DOI: https://doi.org/10.1016/j.physletb.2012.08.020.

[11] M. Lubej. *Standard Model*. http://www-f9.ijs.si/~lubej/SM.pdf.

[12] T Abe, I Adachi et al. 'Belle II technical design report'. In: *arXiv preprint arXiv:1011.0352* (2010).

[13] AJ Bevan, Boštjan Golob et al. 'The physics of the B factories'. In: *The European Physical Journal C* 74.11 (2014), pp. 1–928.

[14] Jolanta Brodzicka, Thomas Browder et al. 'Physics achievements from the Belle experiment'. In: *Progress of Theoretical and Experimental Physics* 2012.1 (2012), p. 04D001.

[15] Nobelprize.org. *The Nobel Prize in Physics 2008*. Ed. by Nobel Media AB 2014. http://www.nobelprize.org/nobel_prizes/physics/laureates/2008/.

[16] E Kou, P Urquijo et al. *The Belle II Physics Book*. 2015.

[17] K Nakamura and Particle Data Group. 'Review of Particle Physics'. In: *Journal of Physics G: Nuclear and Particle Physics* 37.7A (2010), p. 075021. URL: http://stacks.iop.org/0954-3899/37/i=7A/a=075021.

[18] Lei Zang and Takuya Kamitani. 'SuperKEKB Positron Source Target Protection Scheme'. In: (2013).

[19] Yukiyoshi Ohnishi, Tetsuo Abe et al. 'Accelerator design at SuperKEKB'. In: *Progress of Theoretical and Experimental Physics* 2013.3 (2013), 03A011. DOI: 10.1093/ptep/pts083.

[20] J Fast. *SuperKEKB*. http://i.dailymail.co.uk/i/pix/2016/03/02/10/31C312DB00000578-0-image-a-2_1456913455171.jpg.

[21] C Marinas. 'Phase II running of SuperKEKB and Belle II'. In: *The International Conference on B-Physics at Frontier Machines*. 2018.

[22] Belle II Collaboration. *Belle II Experiment*. 2016. URL: https://belle2.jp/.

[23] Boqun Wang et al. 'The assembly of the Belle II TOP counter'. In: *Nuclear Instruments and Methods in Physics Research Section A: Accelerators, Spectrometers, Detectors and Associated Equipment* 766 (2014), pp. 204–207.

[24] Belle-ECL, V Aulchenko et al. 'Electromagnetic calorimeter for Belle II'. In: *Journal of Physics: Conference Series* 587.1 (2015), p. 012045. URL: http://stacks.iop.org/1742-6596/587/i=1/a=012045.

[25] Belle II Collaboration. *Belle II detector*. https://www.belle2.org/e21595/e21770/infoboxContent25430/Belle2.pptx.

[26] William R Leo. *Techniques for Nuclear and Particle Physics Experiments: A How-to Approach*. Springer-Verlag, 1994, p. 24.

[27] John V Jelley. 'Cerenkov radiation and its applications'. In: *British Journal of Applied Physics* 6.7 (1955), p. 227.

[28] Rok Dolenec. 'Time-of-Flight Positron Emission Tomography Using Cherenkov Radiation'. PhD thesis. University of Ljubljana, Faculty of Mathematics and Physics, Department of Physics, 2012.

[29] Jürgen Engelfried. 'Ring Imaging Cherenkov Detectors'. In: *AIP Conference Proceedings*. Vol. 857. 2. AIP. 2006, pp. 340–346.

[30] S. Easo. 'Overview of LHCb RICH detector development'. In: *Nuclear Instruments and Methods in Physics Research Section A: Accelerators, Spectrometers, Detectors and Associated Equipment* 553.1 (2005). Proceedings of the fifth International Workshop on Ring Imaging Detectors, pp. 333 –338. ISSN: 0168-9002. DOI: https://doi.org/10.1016/j.nima.2005.08.063.

[31] CERN Twiki. *LHCb RICH1*. Online, accessed 29. 11. 2018. URL: https://twiki.cern.ch/twiki/pub/LHCb/RICHPicturesAndFigures/rich1-2d.png.

[32] Radia Sia. 'Performance of the LiF-TEA ring imaging Cherenkov detector at CLEO'. In: *Nuclear Instruments and Methods in Physics Research Section A: Accelerators, Spectrometers, Detectors and Associated Equipment* 553.1 (2005). Proceedings of the fifth International Workshop on Ring Imaging Detectors, pp. 323 –327. ISSN: 0168-9002. DOI: https://doi.org/10.1016/j.nima.2005.08.031.

[33] Matthew Barrett. 'Particle identification with the iTOP detector at Belle-II'. In: *Meeting of the APS Division of Particles and Fields (DPF 2013) Santa Cruz, California, USA, August 13-17, 2013*. 2013. arXiv: 1310.4542 [physics.ins-det]. URL: http://inspirehep.net/record/1261025/files/arXiv:1310.4542.pdf.

[34] Luka Šantelj. 'Aerogel RICH counter for the Belle II forward PID'. In: *PoS* (2014), p. 123.

[35] I. Adachi, R. Dolenec et al. 'Construction of silica aerogel radiator system for Belle II RICH Counter'. In: *Nuclear Instruments and Methods in Physics Research Section A: Accelerators, Spectrometers, Detectors and Associated Equipment* 876.Supplement C (2017). The 9th international workshop on Ring Imaging Cherenkov Detectors (RICH2016), pp. 129 –132. ISSN: 0168-9002. DOI: https://doi.org/10.1016/j.nima.2017.02.036.

[36] *Internal Belle II ARICH Documents*.

[37] A Soleimani Dorcheh and MH Abbasi. 'Silica aerogel; synthesis, properties and characterization'. In: *Journal of materials processing technology* 199.1-3 (2008), pp. 10–26.

[38] Makoto Tabata, Ichiro Adachi et al. 'Progress in the development of silica aerogel as a RICH radiator in the Belle II experiment'. In: *Nuclear Science Symposium and Medical Imaging Conference (NSS/MIC), 2013 IEEE*. IEEE. 2013, pp. 1–5.

[39] Lawrence W. Hrubesh. 'Aerogel applications'. In: *Journal of Non-Crystalline Solids* 225.Supplement C (1998), pp. 335 –342. ISSN: 0022-3093. DOI: https://doi.org/10.1016/S0022-3093(98)00135-5.

[40] Hajar Maleki, Luisa Durães and António Portugal. 'An overview on silica aerogels synthesis and different mechanical reinforcing strategies'. In: *Journal of Non-Crystalline Solids* 385 (2014), pp. 55 –74. ISSN: 0022-3093. DOI: https://doi.org/10.1016/j.jnoncrysol.2013.10.017.

[41] S Hashimoto, M Hazumi et al. *Letter of intent for KEK Super B Factory*. Tech. rep. High Energy Accelerator Research Organization, 2004.

[42] S Iwata, I Adachi et al. 'Particle identification performance of the prototype aerogel RICH counter for the Belle II experiment'. In: *Progress of Theoretical and Experimental Physics* 2016.3 (2016).

[43] S. Korpar, I. Adachi et al. 'RICH with multiple aerogel layers of different refractive index'. In: *Nuclear Instruments and Methods in Physics Research Section A: Accelerators, Spectrometers, Detectors and Associated Equipment* 553.1 (2005). Proceedings of the fifth International Workshop on Ring Imaging Detectors, pp. 64 –69. ISSN: 0168-9002. DOI: https://doi.org/10.1016/j.nima.2005.08.008.

[44] Y Maeda, N Kawasaki et al. 'An aerogel Cherenkov detector for multi-GeV photon detection with low sensitivity to neutrons'. In: *Progress of Theoretical and Experimental Physics* 2015.6 (2015), 063H01.

[45] Takahiro Matsumoto, S Korpar et al. 'Studies of a proximity focusing RICH with aerogel radiator'. In: *Nuclear Instruments and Methods in Physics Research Section A: Accelerators, Spectrometers, Detectors and Associated Equipment* 518 (2004), pp. 582–585.

[46] AR Buzykaev, AF Danilyuk et al. 'Measurement of optical parameters of aerogel'. In: *Nuclear Instruments and Methods in Physics Research Section A: Accelerators, Spectrometers, Detectors and Associated Equipment* 433.1-2 (1999), pp. 396–400.

[47] M. Tabata. *ARICH quality assessment data: Aerogel measurements.*

[48] S. Korpar, I. Adachi et al. 'A 144-channel HAPD for the Aerogel RICH at Belle II'. In: *Nuclear Instruments and Methods in Physics Research Section A: Accelerators, Spectrometers, Detectors and Associated Equipment* 766.Supplement C (2014). RICH2013 Proceedings of the Eighth International Workshop on Ring Imaging Cherenkov Detectors Shonan, Kanagawa, Japan, December 2-6, 2013, pp. 145 –147. ISSN: 0168-9002. DOI: https://doi.org/10.1016/j.nima.2014.05.060.

[49] L. Šantelj, I. Adachi et al. 'Studies of a hybrid avalanche photo-detector in magnetic field'. In: *Nuclear Instruments and Methods in Physics Research Section A: Accelerators, Spectrometers, Detectors and Associated Equipment* 845 (2017). Proceedings of the Vienna Conference on Instrumentation 2016, pp. 459 –462. ISSN: 0168-9002. DOI: https://doi.org/10.1016/j.nima.2016.06.037.

[50] Dominik Jan. Private Communication. 2018.

[51] Hamamatsu Photonics K.K. *HAPD data sheets.*

[52] S. Nishida. *HAPD Mass Production.* 19th Belle II General Meeting. Nov. 2014.

[53] Y. Yusa, I. Adachi et al. 'Test of the HAPD light sensor for the Belle II Aerogel RICH'. In: *Nuclear Instruments and Methods in Physics Research Section A: Accelerators, Spectrometers, Detectors and Associated Equipment* 876 (2017). The 9th international workshop on Ring Imaging Cherenkov Detectors (RICH2016), pp. 149 –152. ISSN: 0168-9002. DOI: https://doi.org/10.1016/j.nima.2017.02.046.

[54] S. Yamada, R. Itoh et al. 'Data Acquisition System for the Belle II Experiment'. In: *IEEE Transactions on Nuclear Science* 62.3 (2015), pp. 1175–1180. ISSN: 0018-9499. DOI: 10.1109/TNS.2015.2424717.

[55] Andrej Seljak. 'Proximity Focusing RICH with Aerogel as Radiator: Doctoral Thesis'. PhD thesis. University of Ljubljana, Faculty of Mathematics and Physics, Department of Physics, 2013.

[56] S. Nishida. *SA02 (SA03) Manual*. June 2013.

[57] M Yonenaga, I Adachi et al. 'Development of slow control system for the Belle II ARICH counter'. In: *Nuclear Instruments and Methods in Physics Research Section A: Accelerators, Spectrometers, Detectors and Associated Equipment* 876 (2017), pp. 241–245.

[58] I. Nakamura. *ARICH*. For Belle II Colaboration.

[59] T Kuhr, C Pulvermacher et al. 'The Belle II Core Software'. In: *arXiv preprint arXiv:1809.04299* (2018).

[60] S. Agostinelli, J. Allison et al. 'Geant4—a simulation toolkit'. In: *Nuclear Instruments and Methods in Physics Research Section A: Accelerators, Spectrometers, Detectors and Associated Equipment* 506.3 (2003), pp. 250 –303. ISSN: 0168-9002. DOI: https://doi.org/10.1016/S0168-9002(03)01368-8.

[61] J. Allison, K. Amako et al. 'Recent developments in Geant4'. In: *Nuclear Instruments and Methods in Physics Research Section A: Accelerators, Spectrometers, Detectors and Associated Equipment* 835 (2016), pp. 186 –225. ISSN: 0168-9002. DOI: https://doi.org/10.1016/j.nima.2016.06.125.

[62] Bjarne Stroustrup. *The C++ programming language*. Pearson Education, 2013.

[63] Guido Van Rossum and Fred L Drake Jr. 'The python language reference'. In: *Python software foundation Google Scholar* (2014).

[64] Rene Brun and Fons Rademakers. 'ROOT—an object oriented data analysis framework'. In: *Nuclear Instruments and Methods in Physics Research Section A: Accelerators, Spectrometers, Detectors and Associated Equipment* 389.1-2 (1997), pp. 81–86.

[65] Filippo Dattola. 'Tracking studies for the Belle II detector'. Presented on 20 07 2018. MA thesis. Trieste: Trieste, University of Trieste, 2018.

[66] Paul Baillon. 'Cherenkov ring search using a maximum likelihood technique'. In: *Nuclear Instruments and Methods in Physics Research Section A: Accelerators, Spectrometers, Detectors and Associated Equipment* 238.2-3 (1985), pp. 341–346.

[67] Roger Forty, LHCb Collaboration et al. 'RICH pattern recognition for LHCb'. In: *Nuclear Instruments and Methods in Physics Research Section A: Accelerators, Spectrometers, Detectors and Associated Equipment* 433.1 (1999), pp. 257–261.

[68] Andrej Petelin. 'Identifikacija hadronov z detektorjem obročev Čerenkova v spektrometru Belle'. Bachelor's Thesis. Univerza v Ljubljani, Fakulteta za matematiko in fiziko, Oddelek za fiziko, 2007.

[69] H. Kindo. *Initial performance of Aerogel RICH detector in Belle II experiment*. Presentation at RICH 2018 conference, paper submitted to NIMA Proceedings. 2018.

[70] R. Pestotnik. *Calibration of the Belle II Aerogel Ring Imaging detector*. Presentation at RICH 2018 conference, paper submitted to NIMA Proceedings. 2018.

[71] Mitja Predikaka. 'Karakterizacija modulov za detektor obročev Čerenkova pri spektrometru Belle II: magistrsko delo'. MA thesis. University of Ljubljana, Faculty of Mathematics and Physics, 2015.

[72] M. Iwasaki, Y. Ohnishi et al. 'Beam Background and MDI Design for SuperKEKB/Belle-II'. In: *Conf. Proc.* C1205201 (2012), pp. 1825–1827.

[73] Andrea Fodor. 'Design and Simulation of Beam-background Monitors in the Vicinity of the Electromagnetic Calorimeter for the Belle II Experiment'. PhD thesis. McGill University Libraries, 2017.

[74] Luka Šantelj. Private Communication. 2018.

[75] R. Pestotnik, I. Adachi et al. 'The aerogel Ring Imaging Cherenkov system at the Belle II spectrometer'. In: *Nuclear Instruments and Methods in Physics Research Section A: Accelerators, Spectrometers, Detectors and Associated Equipment* 876.Supplement C (2017). The 9th international workshop on Ring Imaging Cherenkov Detectors (RICH2016), pp. 265 –268. ISSN: 0168-9002. DOI: https://doi.org/10.1016/j.nima.2017.04.043.

[76] Martin A Green and Mark J Keevers. 'Optical properties of intrinsic silicon at 300 K'. In: *Progress in Photovoltaics: Research and Applications* 3.3 (1995), pp. 189–192.

[77] Paul Horowitz and Winfield Hill. *The art of electronics*. Cambridge Univ. Press, 1989.

[78] Yoshida Keisuke. 'The performance evaluation of the photodetector and readout ASIC for particle identification device (A-RICH) at Belle II'. In Japanese only. MA thesis. Tokyo Metropolitan University, Tokyo, 2015. URL: https://www-hep.phys.se.tmu.ac.jp/thesis/doc/2014-Mthesis-yoshida.pdf.

[79] Lytron Direct. *CP15G05 tubed cold plate*. https://www.lytrondirect.com/cp15g05-tubed-cold-plate/cp15g05/.

[80] K. Noguchi. *Monitor System*. 28th Belle II General Meeting. Oct. 2017.

[81] Kouta Noguchi. 'Implementation of monitoring system for the ARICH detector at the Belle II experiment'. In Japanese only. MA thesis. Tokyo Metropolitan University, Hachioji, Japan, 2017. URL: https://www-hep.phys.se.tmu.ac.jp/thesis/doc/2017-Mthesis-noguchi.pdf.

[82] M. Tanabashi, K. Hagiwara et al. 'Review of Particle Physics'. In: *Phys. Rev. D* 98 (3 2018), p. 030001. DOI: 10.1103/PhysRevD.98.030001.

[83] Andreas Meyer. *Charm Fragmentation Fractions*. 2006. URL: http://www.desy.de/~ameyer/hq/node38.html.

[84] Marko Starič, A Abdesselam et al. 'Measurement of D0–$\bar{D}$0 mixing and search for CP violation in D0→ K+ K-, π+ π- decays with the full Belle data set'. In: *Physics Letters B* 753 (2016), pp. 412–418.

[85] S Nishida. 'Study of kaon and pion identification using inclusive D^* sample'. In: *Belle Note* 779 (2005).

[86] Wouter Verkerke and David P. Kirkby. 'The RooFit toolkit for data modeling'. In: *eConf* C0303241 (2003). [,186(2003)], MOLT007. arXiv: physics/0306116 [physics].

[87] F. James. *MINUIT – Function Minimization and Error Analysis*. 1994. URL: https://root.cern.ch/download/minuit.pdf.

APPENDIX A

Technical Drawings

The main technical drawings and electronic circuits of the ARICH components – aerogel tiles, HAPDs and readout electronics – are presented in the following pages. The aerogel designs for upstream and downstream tiles of all four rings are presented in Fig. A.1. Fig. A.2 depicts an HAPD sensor.

ARICH front-end electronics boards are composed of several electronic circuits that provide signal processing, temperature, voltage and current monitoring, communication with merger boards and distribution of HAPD power supplies. Some of the main circuits are presented:

- Temperature sensors: Fig. A.3
- A test pulse generator: Fig. A.5
- Threshold parameters settings: A.4
- Low voltage power supplies: A.6

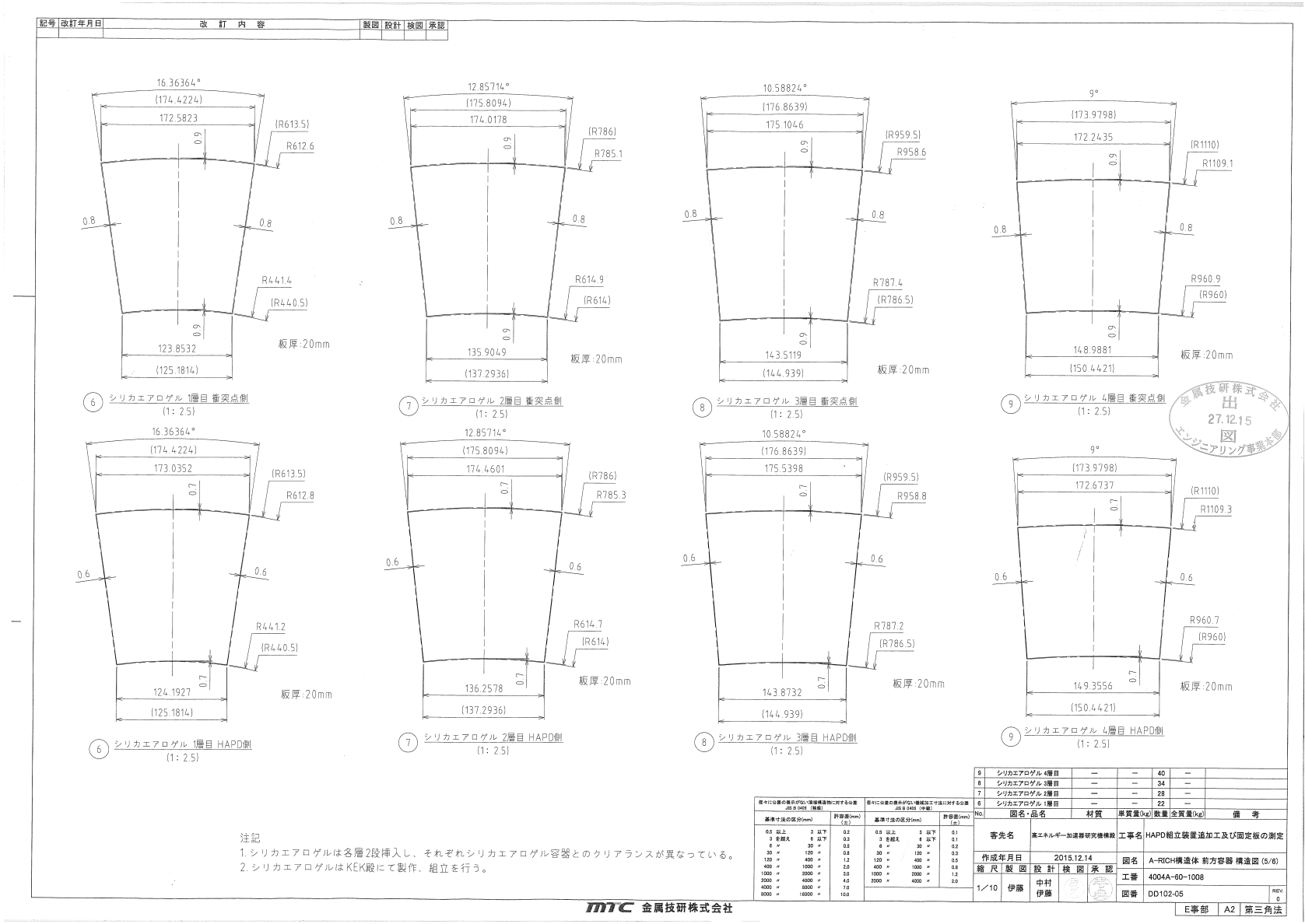

Figure A.1: The shapes and sizes of tiles for each ring are shown. Tile number six corresponds to ring 1; tile seven to ring 2; tile eight to ring 3; tile nine to ring 4. The downstream aerogel tiles are drawn on the top and the upstream tiles on the bottom.

R10947-06-M144 図面 2015/08/26

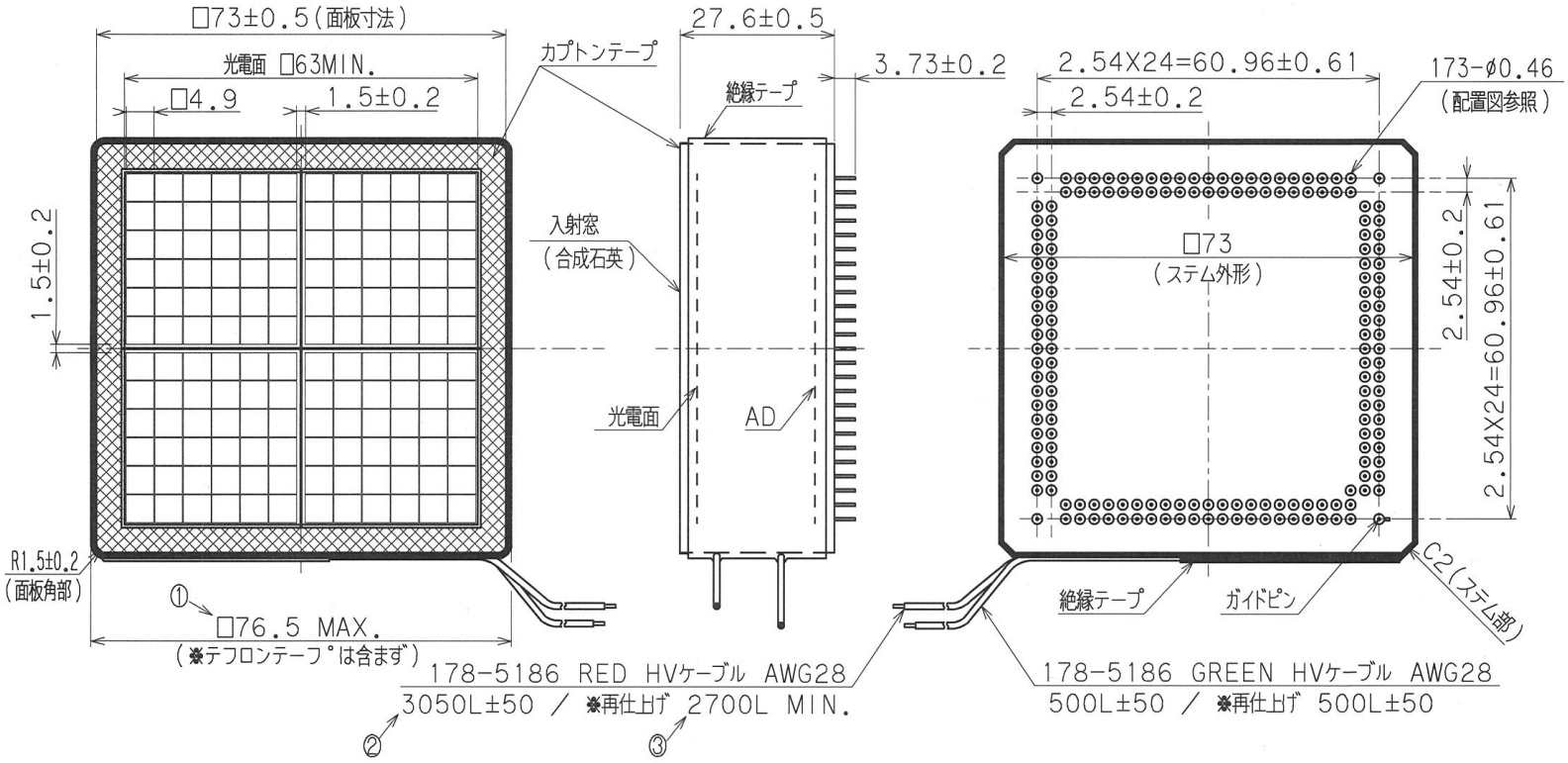

MRAK	日付	変更内容
①	2015. 8.26	寸法変更 □76 MAX.→□76.5 MAX
②	2015. 8.26	寸法変更 3000L→3050L
③	2015. 8.26	寸法と公差変更 2800L±50→2700L MIN.

HAMAMATSU
HAMAMATSU PHOTONICS K.K. Electron Tube Division

Figure A.2: The HAPD technical drawing with main dimensions marked [51].

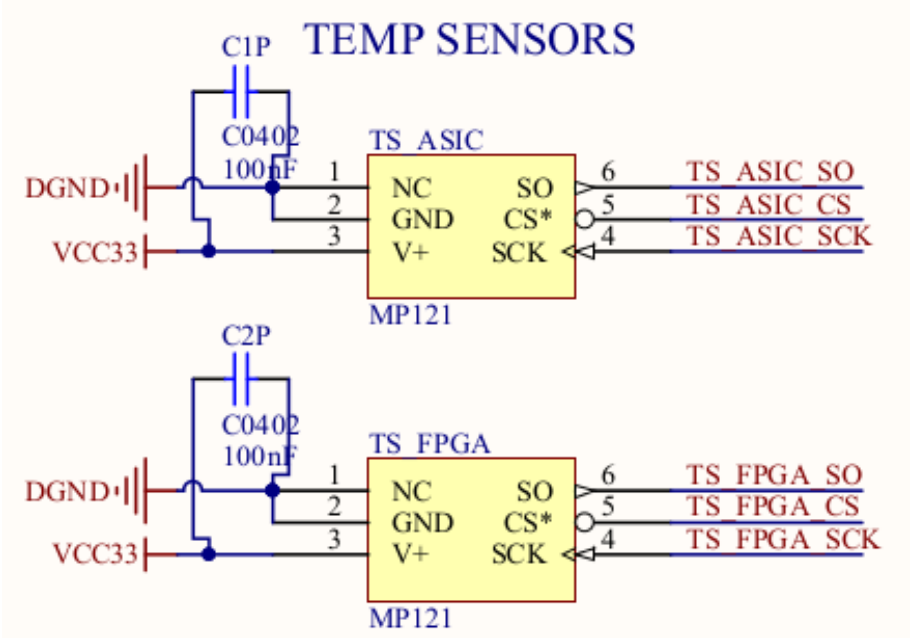

Figure A.3: Schematic depiction of integrated circuit of temperature sensors in front-end board [36].

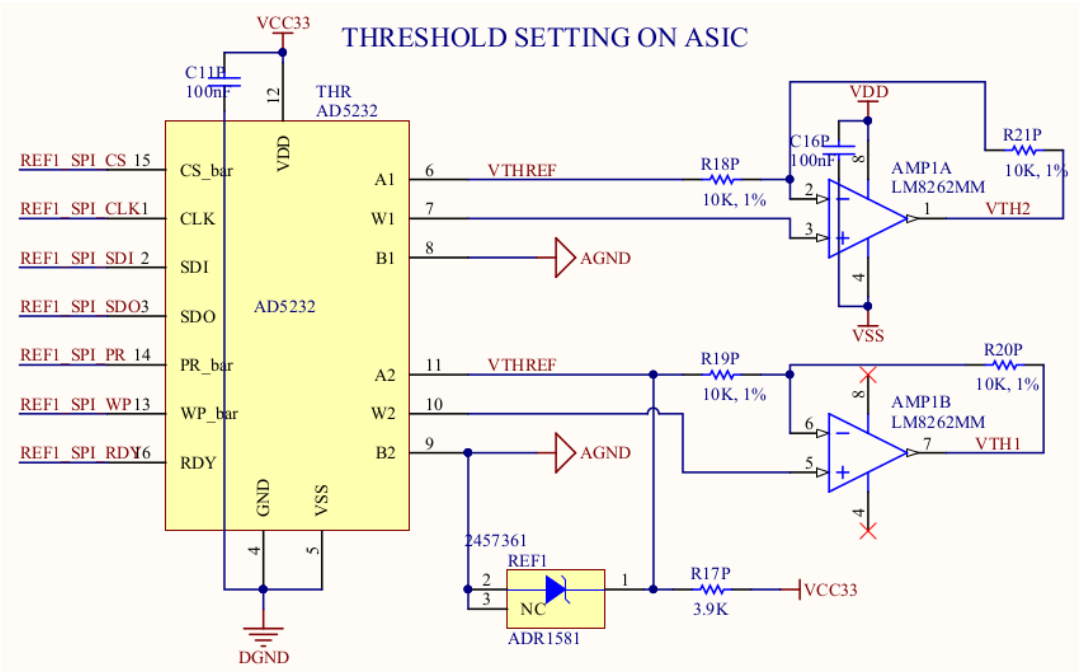

Figure A.4: Schematic depiction of integrated circuit, used for threshold settings, in front-end board [36].

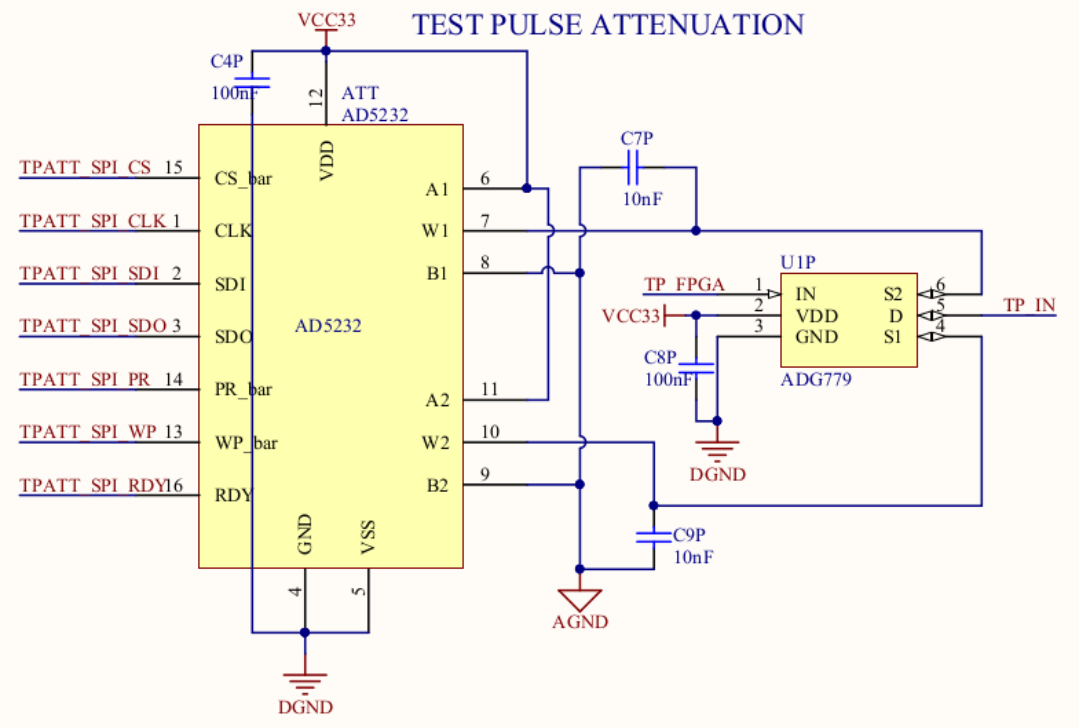

Figure A.5: Schematic depiction of integrated circuit that triggers test pulses in front-end board [36].

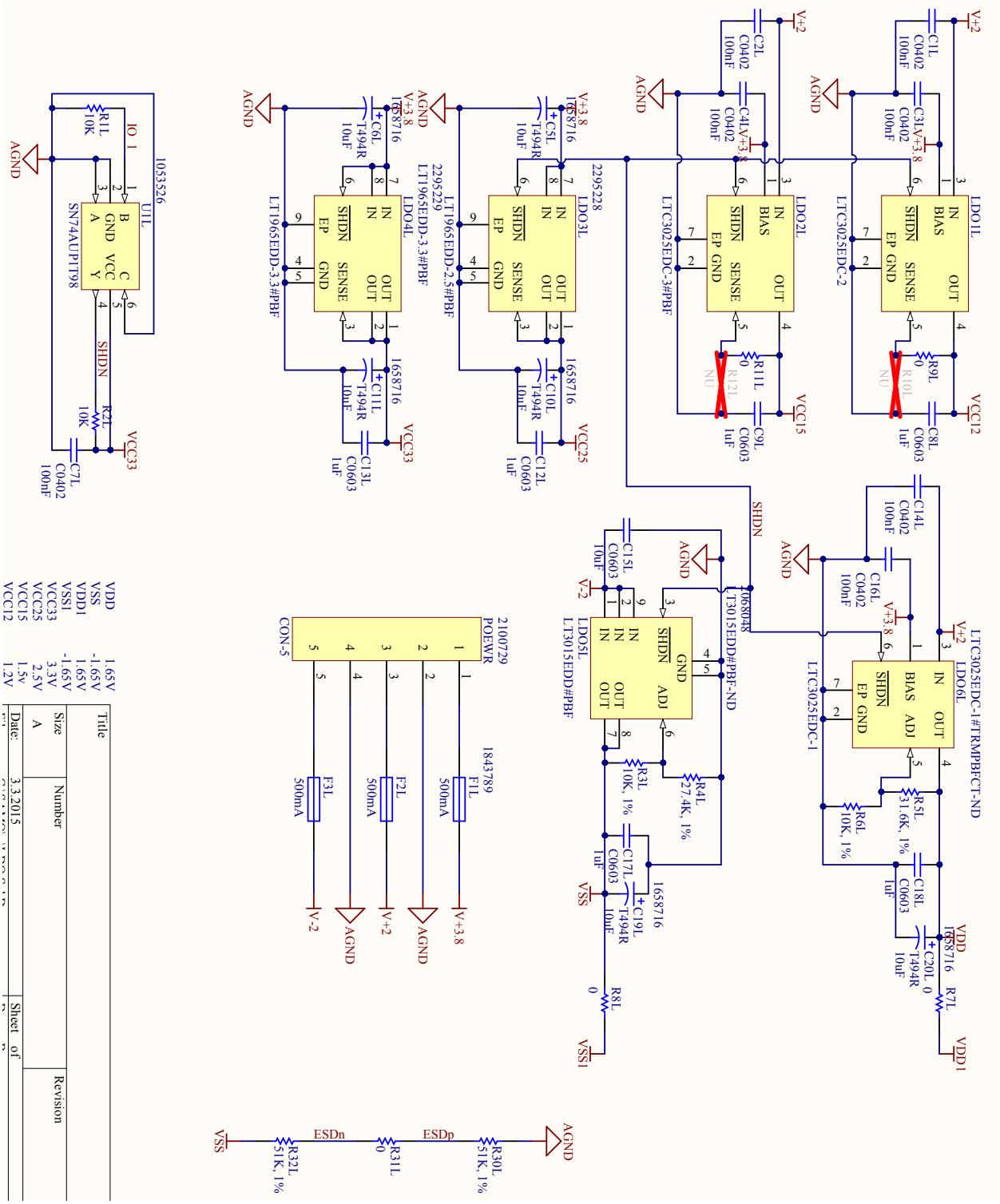

Figure A.6: Schematic depiction of power supply circuits in front-end board [36].

APPENDIX B

Numbering Schemes and Mappings

ARICH is divided into six sectors (labelled from S1 to S6); counting starts from x-axis counter-clockwise, looking from the electronics side. Module numbering (between 1 and 420) starts at x-axis of ring 1 and runs counter-clockwise over all sectors, then continues in ring 2, etc. (Fig. B.1). The mappings of the module channels from the electronics side is given in Fig. B.2.

Merger boards are identified with numbers between 1 and 72, and their counting starts at sector 1 and runs from innermost ring towards the outer ones, as presented in Fig. B.3. The read-out system usually returns merger board serial number instead; this mapping is shown in Fig. B.4.

B.1 Cable Connections

Large number of sensors, installed to the detector plane, and limited cable space resulted in usage of few power supply cables per sector, which were further divided into supply for all sensors. The bias cable mapping for one sector is illustrated in Fig. B.5 and the mapping for high voltage cables is shown in Fig. B.6.

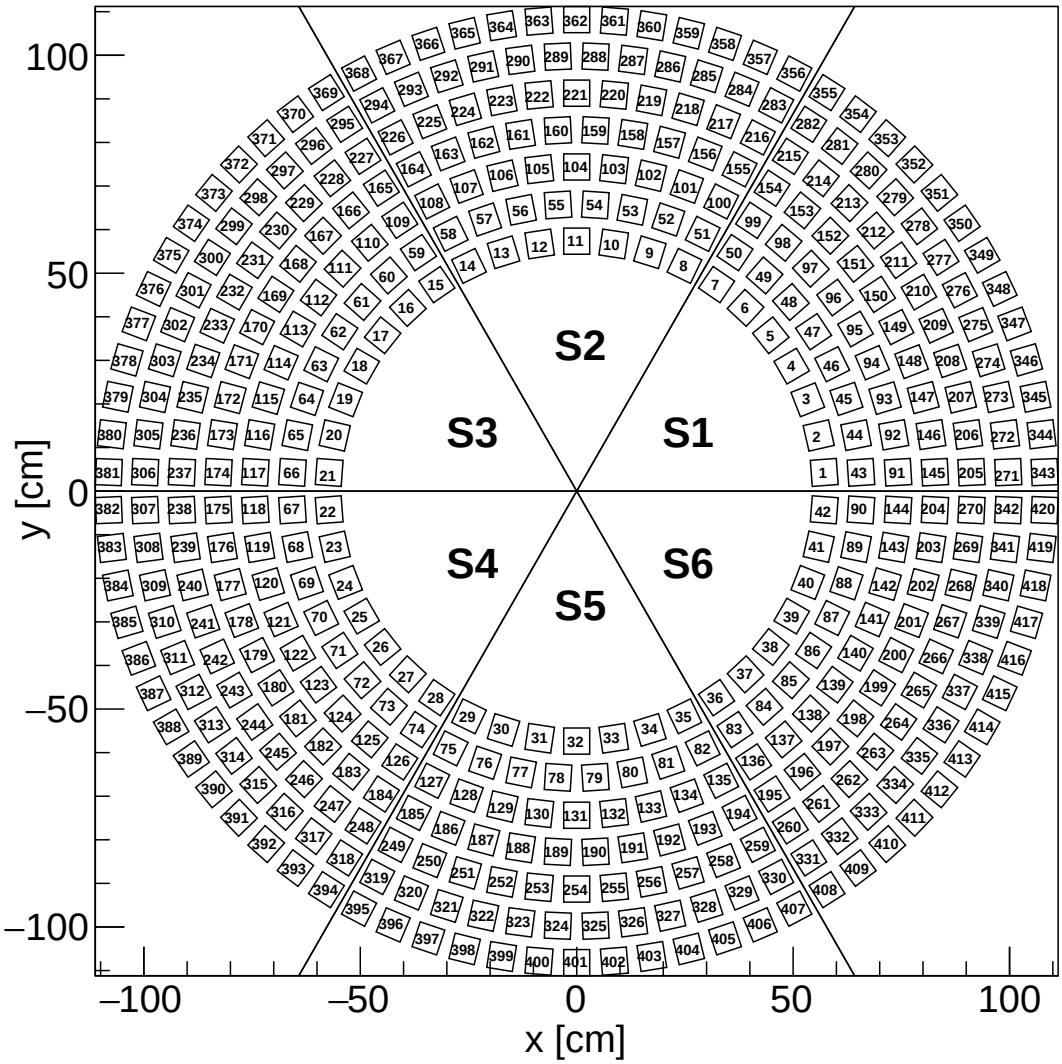

Figure B.1: Numbering scheme [1:420] of modules, made of HAPD and front-end board. It starts at x-axis of innermost ring and runs counter-clockwise over all sectors, before moving to the next ring.

chip B

54	59	66	71	56	65
50	55	62	67	57	60
43	47	51	63	69	61
38	42	46	58	70	64
48	49	37	39	36	68
41	44	45	40	52	53

chip A

5	12	2	7	14	18
8	13	6	11	19	23
9	1	10	15	26	30
4	3	22	27	31	35
16	0	34	33	21	20
17	32	28	25	24	29

chip C

137	132	133	136	140	125
128	129	141	142	108	124
143	139	135	130	111	112
138	134	123	118	109	117
131	127	119	114	121	116
126	122	115	110	120	113

chip D

89	88	76	81	80	77
104	72	75	73	85	84
100	106	94	82	78	74
97	105	99	87	83	79
96	93	103	98	91	86
101	92	107	102	95	90

Figure B.2: Mapping of the ASIC channels from the electronics side.

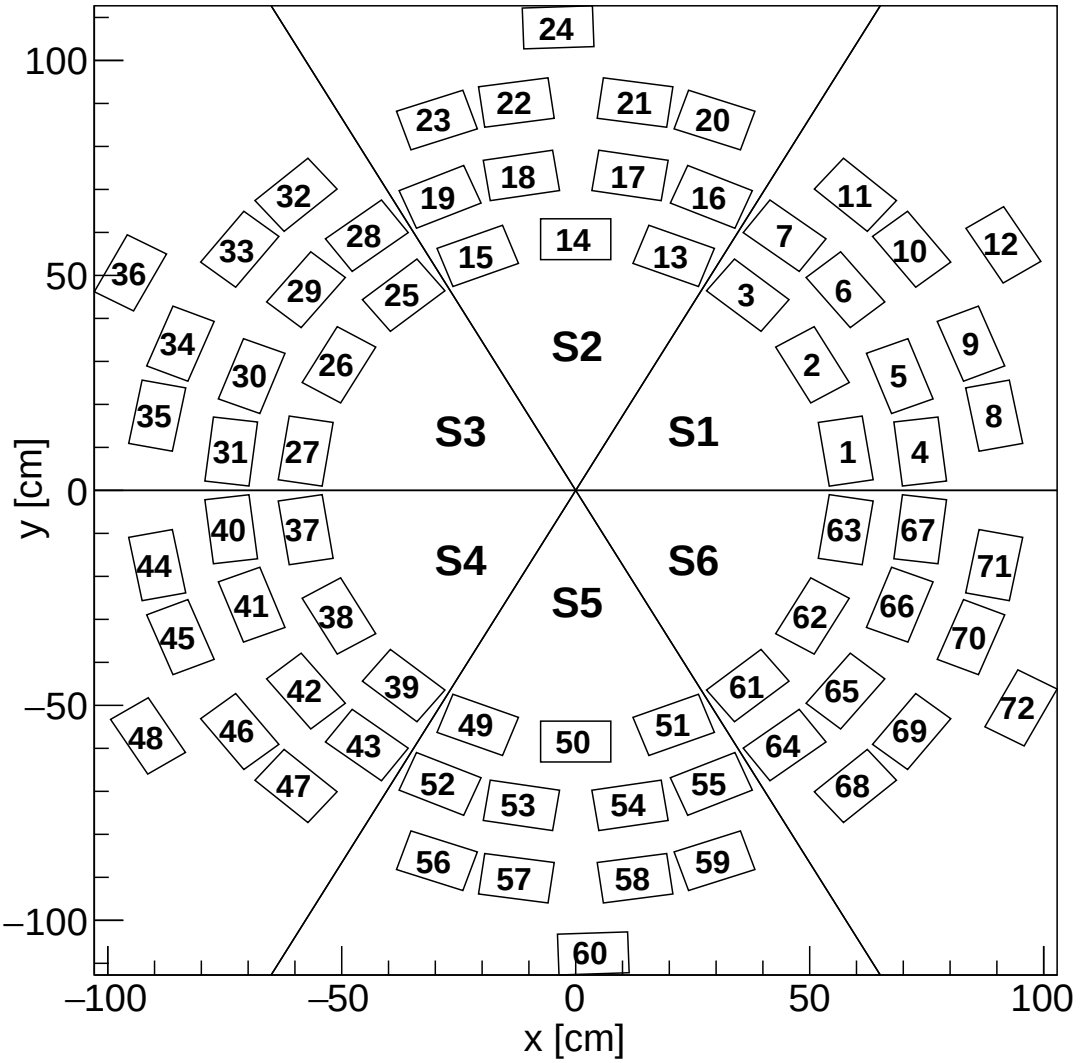

Figure B.3: Numbering scheme [1:72] of merger boards. It starts at x-axis of innermost ring and runs towards the outer part before moving to the next sector.

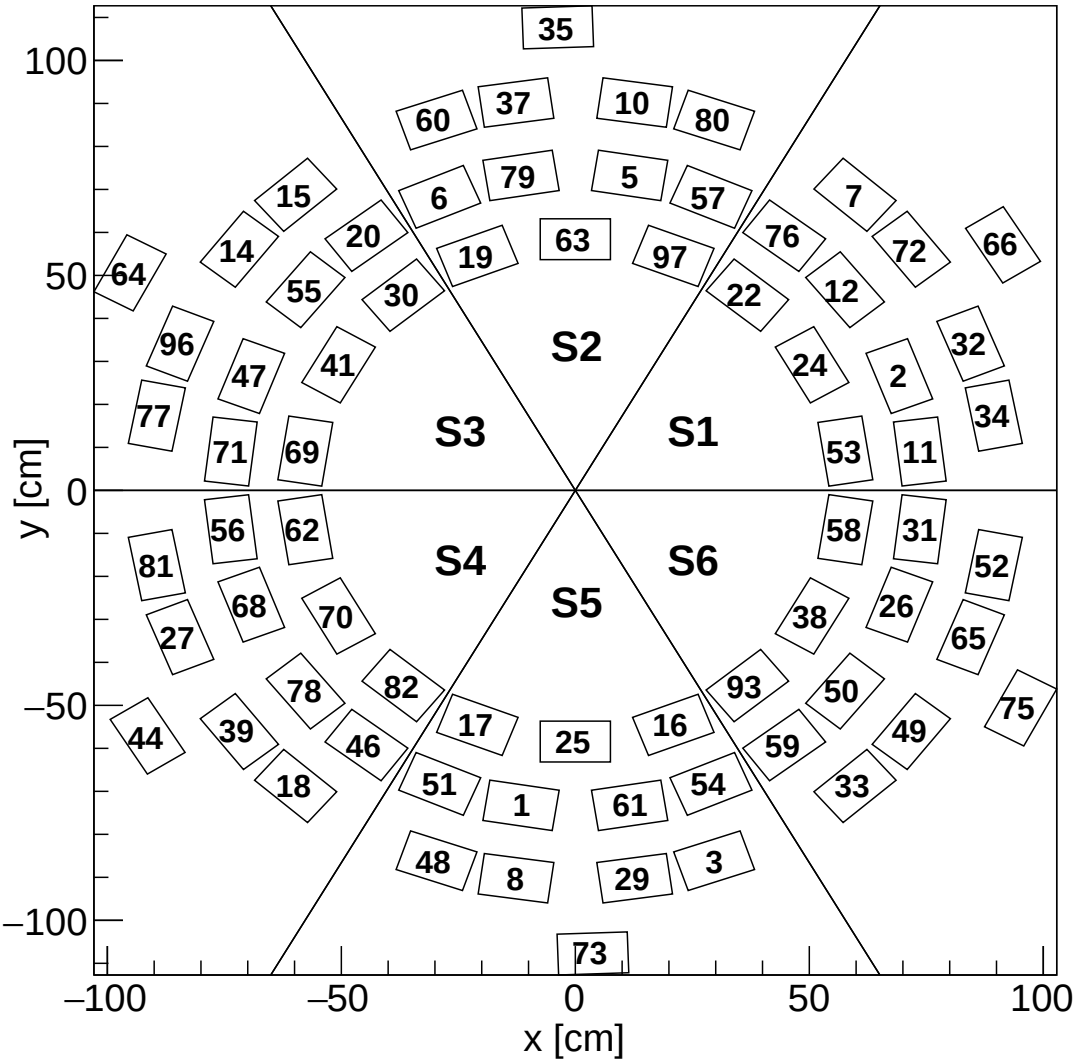

Figure B.4: Serial numbers of merger boards. They are normally presented at the output of read-out electronics.

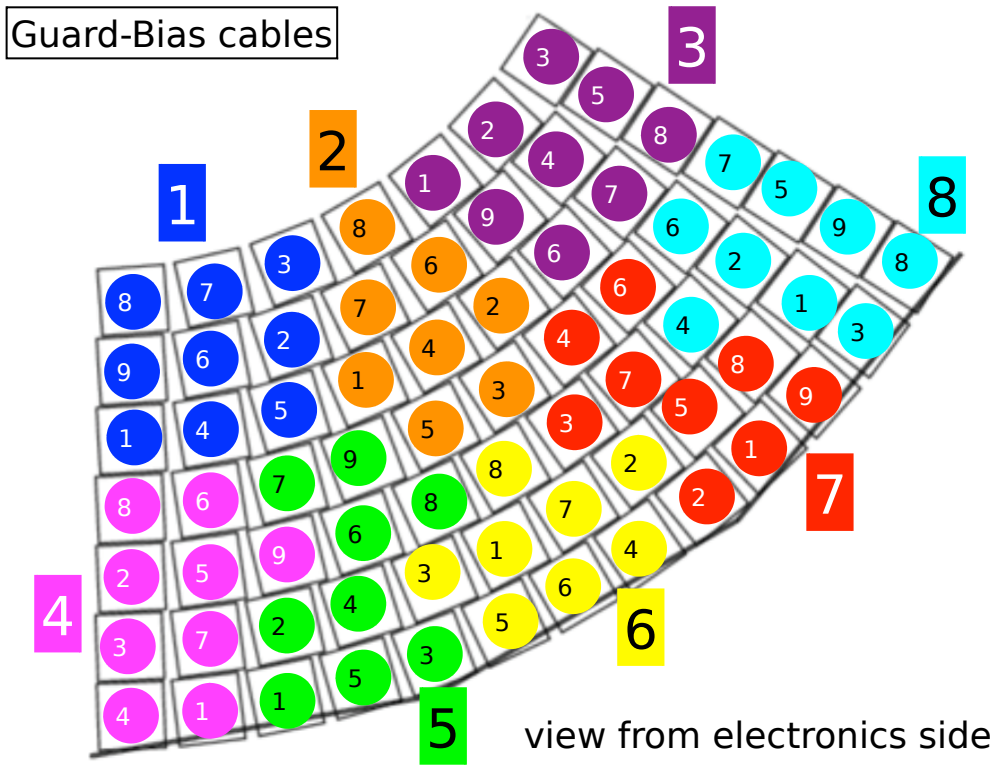

Figure B.5: Eight bias voltage cables per sector were used to supply eight or nine HAPDs each. Inner wires were grouped into bundles of five or six and connected to the front-end board [36].

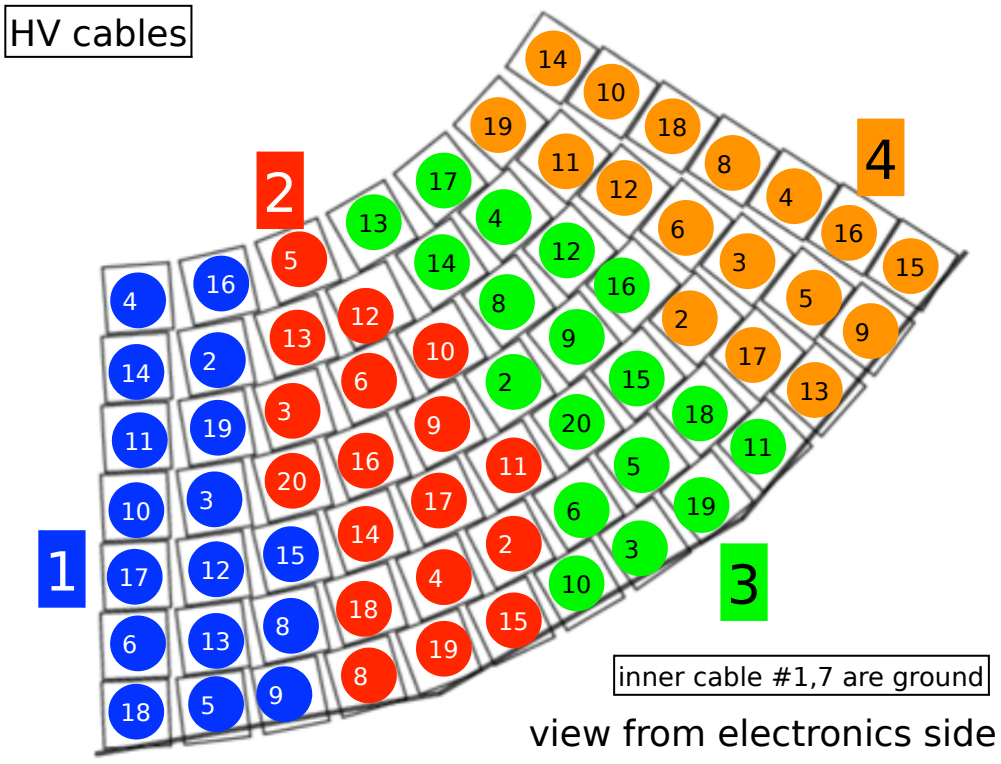

Figure B.6: Four high voltage cables per sector were used. Inner wires were connected to 17 or 18 high voltage distribution boards [36].

APPENDIX C

Temperatures

Temperature measurements during a few-days operation of the ARICH at the beginning of Phase II (starting on 8th February 2018) are presented in this appendix. Merger board temperatures, measured in the FPGA, after two and 18 hours of operation are presented in Fig. C.1. The time dependence of the temperatures on the merger boards at different positions are shown in Figs. C.2, C.4 and C.6. Time-dependent monitored temperatures of the temperature sensors on ASIC (between front-end board and HAPD) and FPGA (on the cable side) sides of few front-end boards are shown in Figs. C.3, C.5 and C.7. Mappings of positions of merger and front-end boards are given in Appendix B.

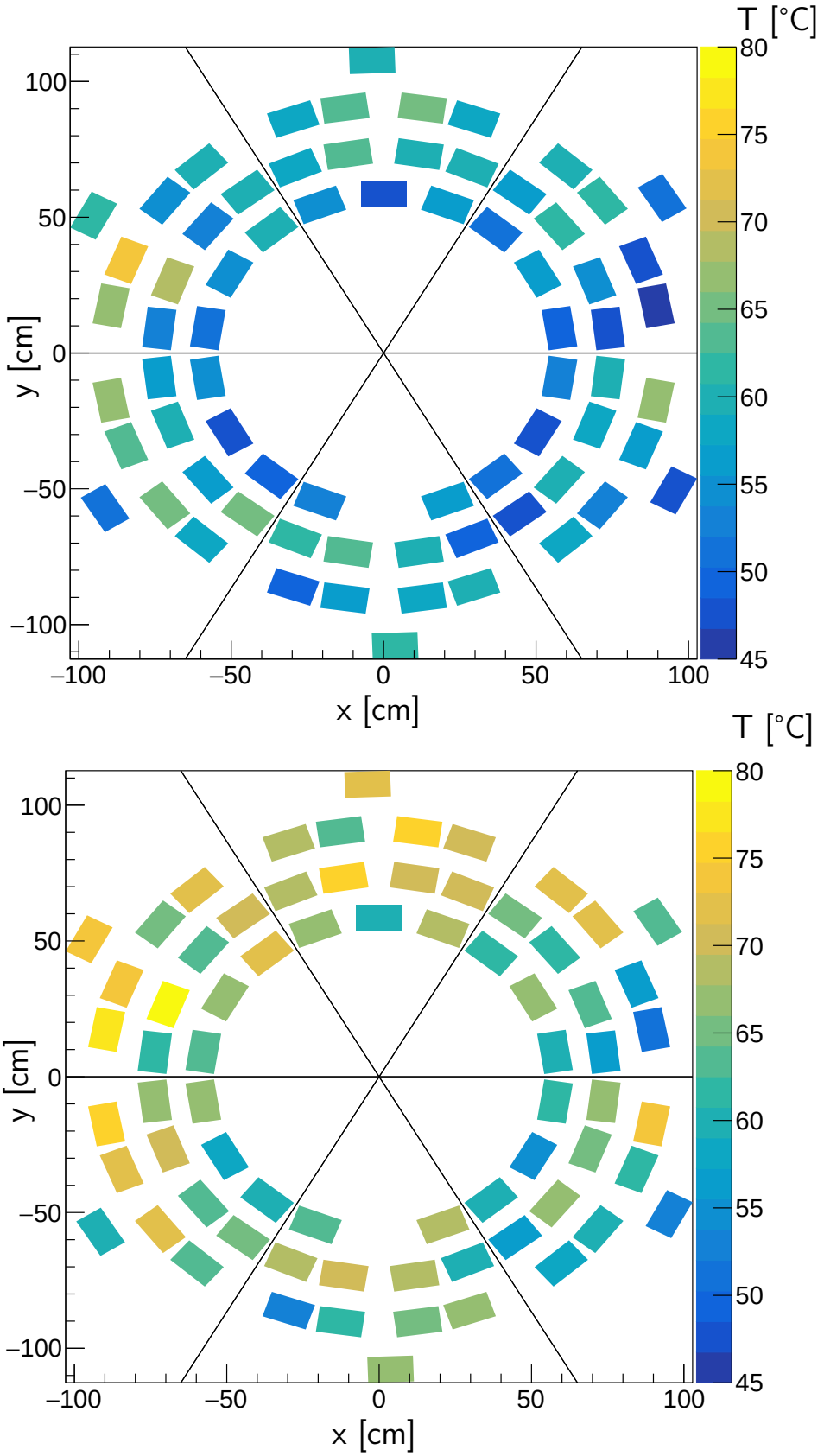

Figure C.1: Temperatures, measured in the FPGA of merger boards, after two (top) and 18 (bottom) hours of all electronics components of ARICH being supplied with electrical power.

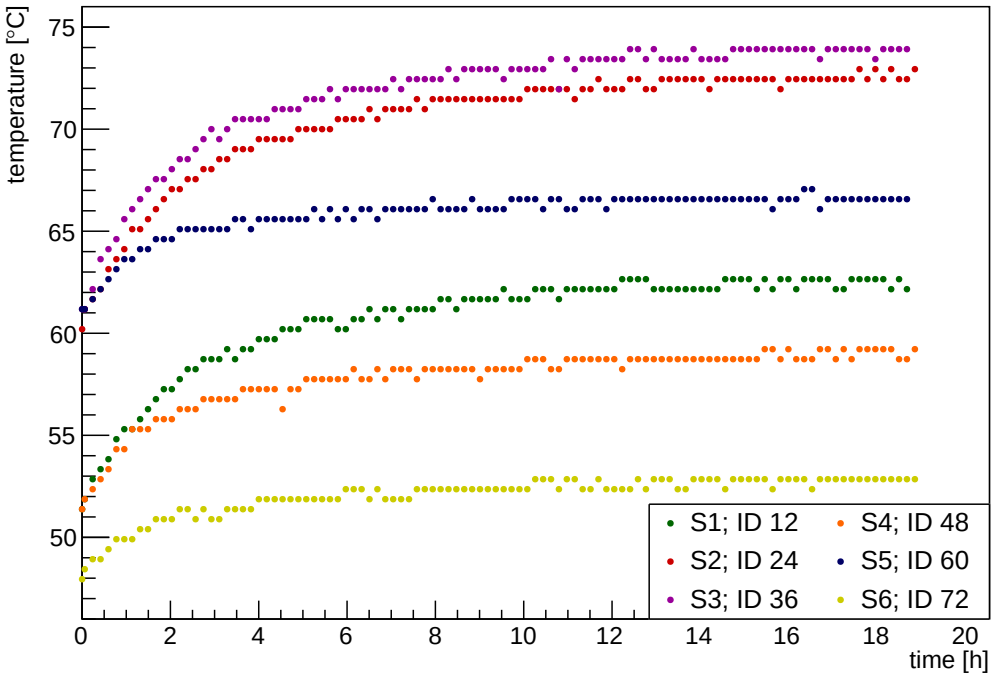

Figure C.2: Temperatures, measured in the FPGA of merger boards, for six merger boards. Results for the outer boards of each sector are shown.

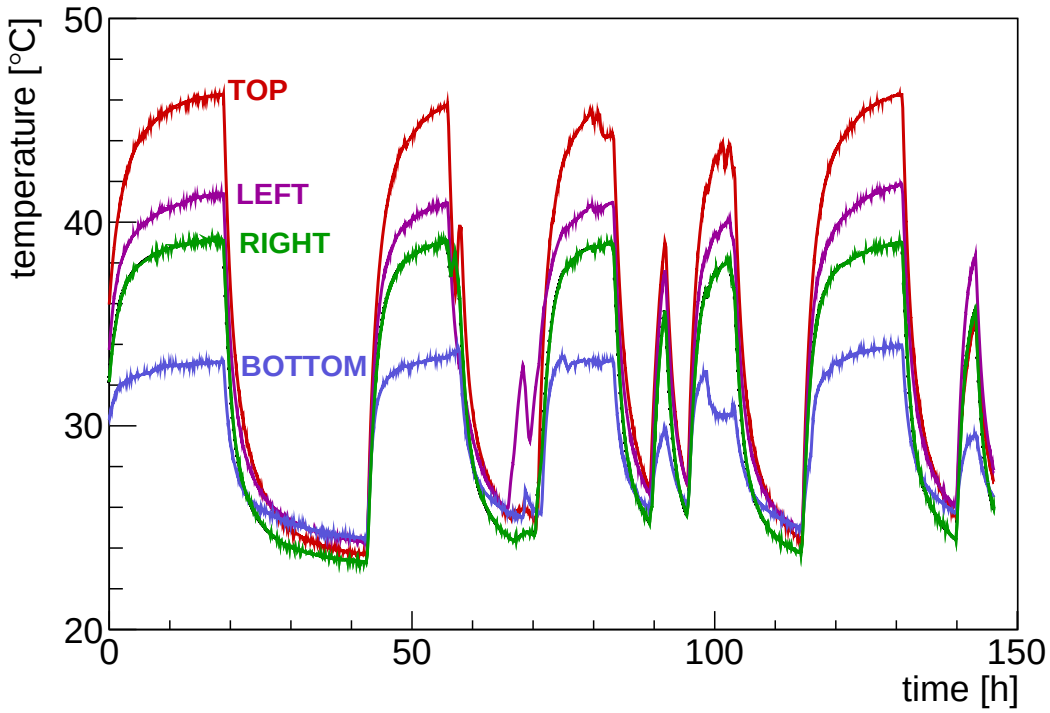

Figure C.3: Temperatures on four ARICH temperature sensors over a week of ARICH operation. Monitoring started two hours after the beginning of discontinuous operation of full ARICH.

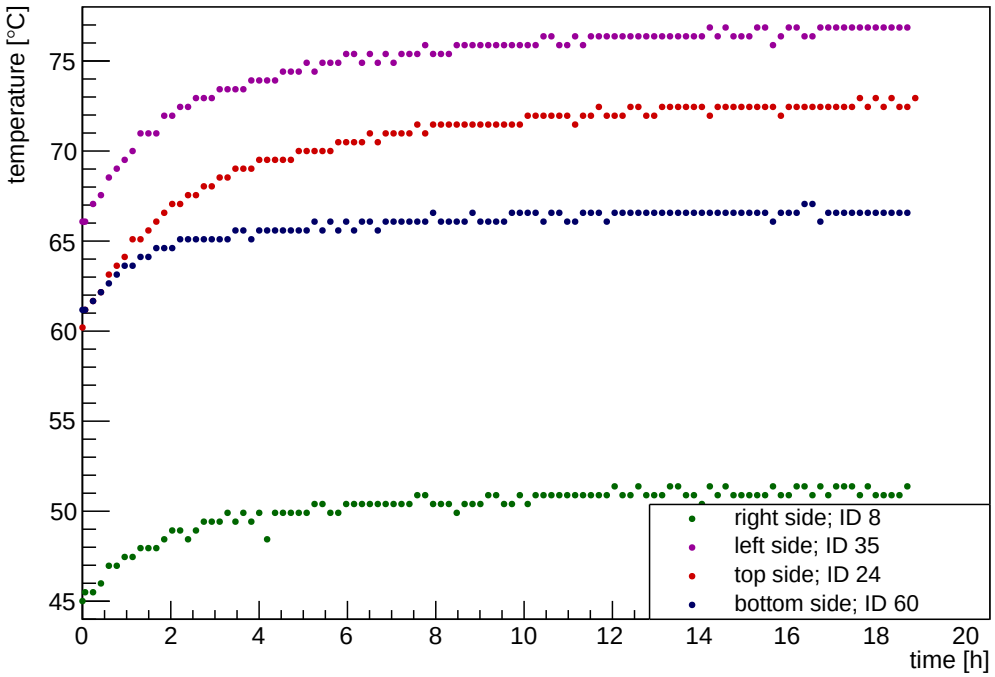

Figure C.4: Temperatures, measured in the FPGA of merger boards, for four merger boards, closest to the ARICH temperature sensors.

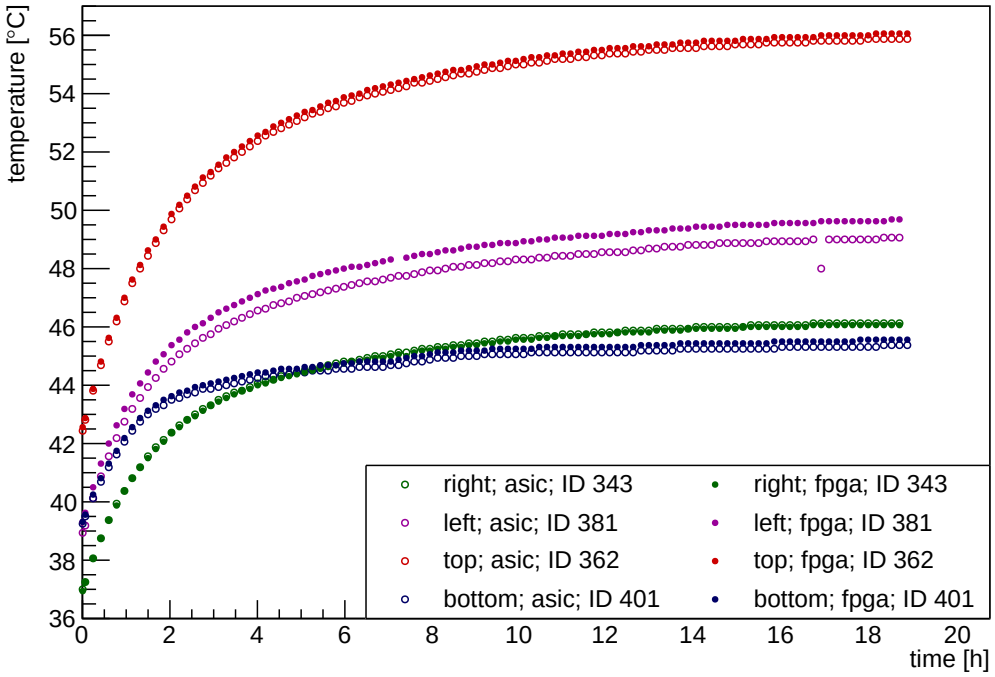

Figure C.5: Temperatures, measured on the ASIC and FPGA side of front-end boards, for four front-end boards, closest to the ARICH temperature sensors.

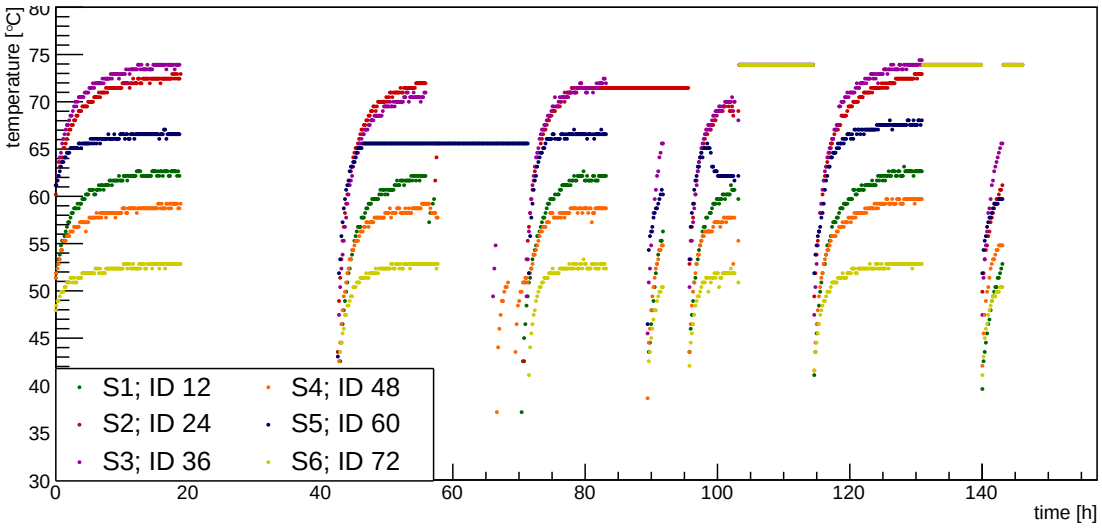

Figure C.6: Temperatures, measured in the FPGA of merger boards, for outermost merger board of each sector. Measurements during a week of discontinuous ARICH operation are shown.

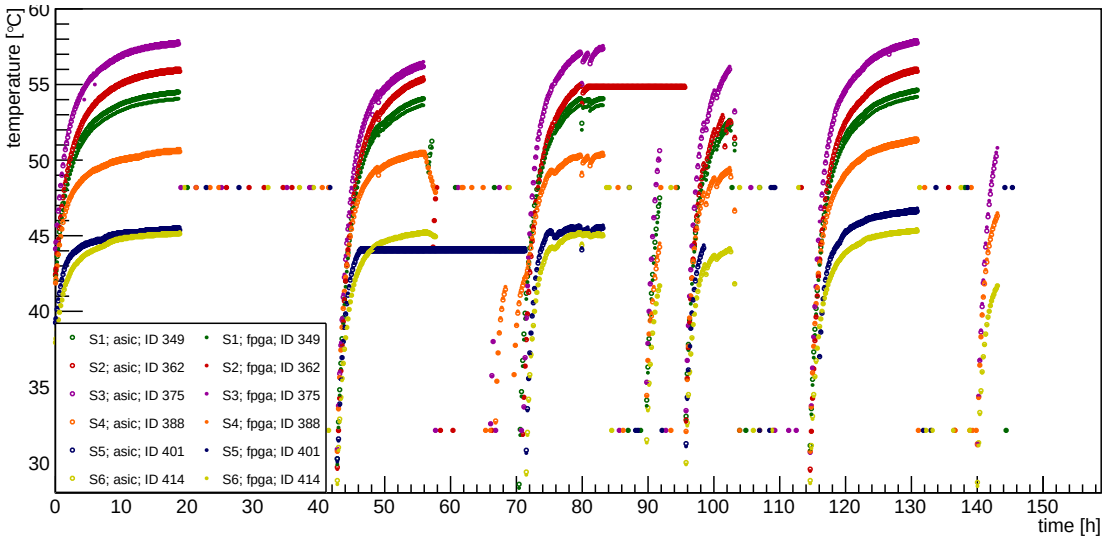

Figure C.7: Temperatures, measured on the ASIC and FPGA side of front-end boards, for front-end boards in the middle of the outer ring for each sector. Measurements during a week of discontinuous ARICH operation are shown.

APPENDIX D

D^0 Mass Fits of Simulated Phase III Sample

The identification of charged kaons and pions from the $D^{*+} \to D^0(\to K^-\pi^+)\pi_s^+$ decay was performed for the various selection of the momentum and the polar angle of the charged particles. The following tables – D.1 and D.2 – give the labelling for the different selection combinations.

The distributions of the D^0 mass deviations for samples of events, when kaon (or pion) enters the ARICH geometrical acceptance, without particle identification selection are presented in the following pages, from Fig. D.1 to Fig. D.16. Figures present results for various momentum and polar angle selections, given in Table D.2.

Table D.1: The labelling of momentum-angle bins for Phase II.

$\cos\theta$	momentum [GeV/c]			
	0.5-1.5	1.5-2.5	2.5-4.0	0.5-4.0
0.81-0.86	0A	1A	2A	3A
0.86-0.91	0B	1B	2B	3B
0.91-0.96	0C	1C	2C	3C
0.80-0.98	0D	1D	2D	3D

Table D.2: The labelling of momentum-angle bins for Phase III.

$\cos\theta$	momentum [GeV/c]							
	0.5-1.0	1.0-1.5	1.5-2.0	2.0-2.5	2.5-3.0	3.0-3.5	3.5-4.0	0.5-4.0
0.82-0.84	0A	1A	2A	3A	4A	5A	6A	7A
0.84-0.86	0B	1B	2B	3B	4B	5B	6B	7B
0.86-0.88	0C	1C	2C	3C	4C	5C	6C	7C
0.88-0.90	0D	1D	2D	3D	4D	5D	6D	7D
0.90-0.92	0E	1E	2E	3E	4E	5E	6E	7E
0.92-0.94	0F	1F	2F	3F	4F	5F	6F	7F
0.94-0.96	0G	1G	2G	3G	4G	5G	6G	7G
0.80-0.98	0H	1H	2H	3H	4H	5H	6H	7H

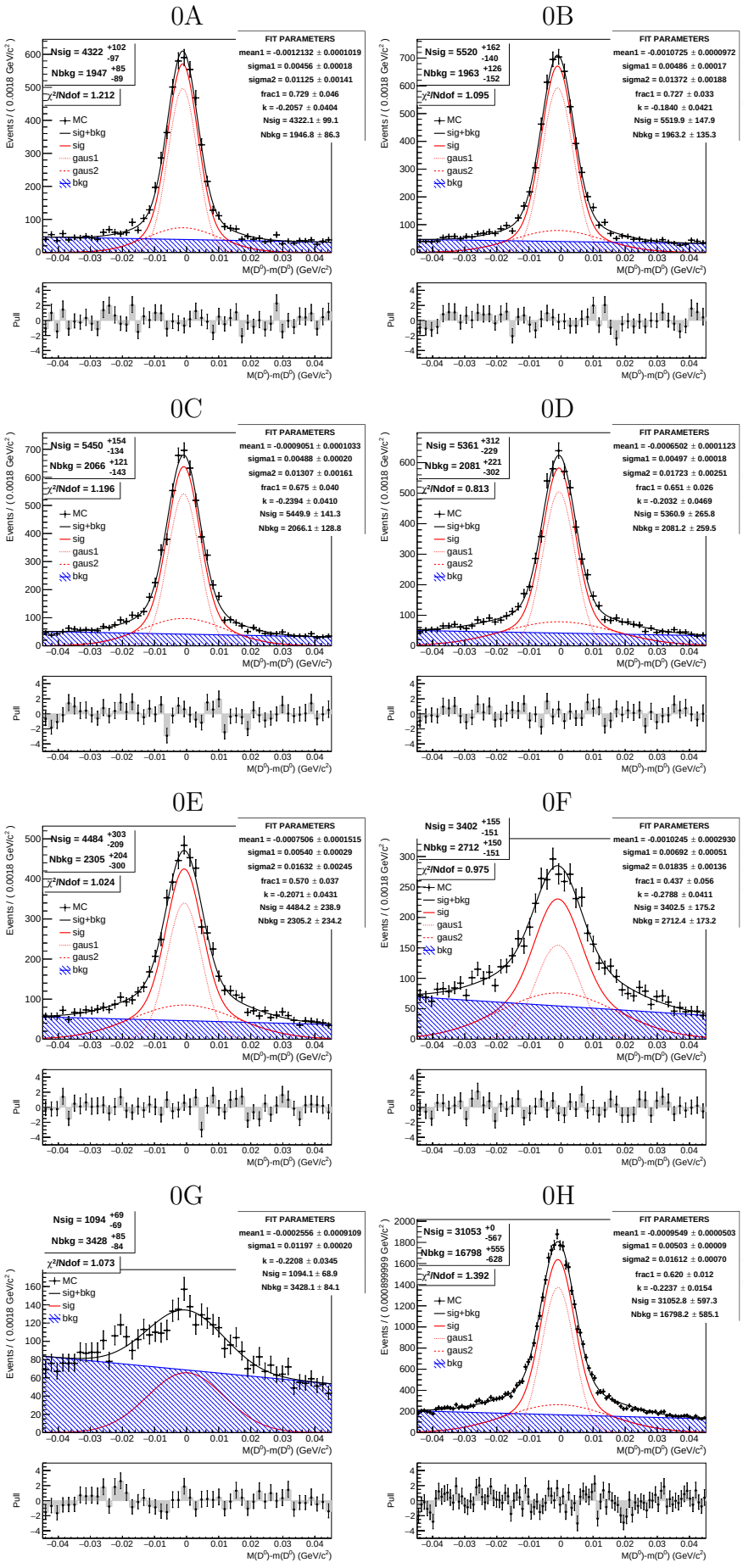

Figure D.1: Fits of kaon sample for momentum from 0.5 GeV/c to 1.0 GeV/c.

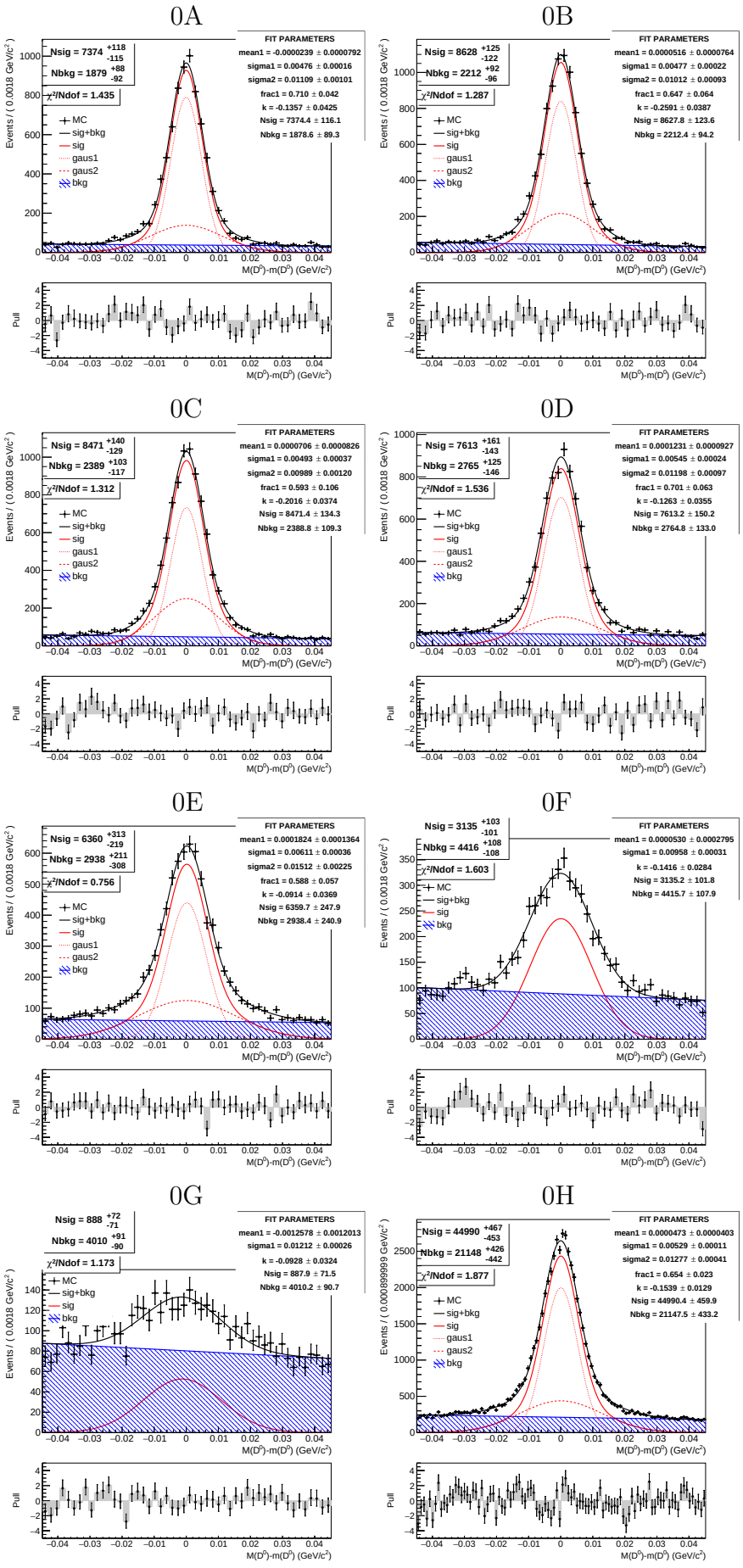

Figure D.2: Fits of pion sample for momentum from 0.5 GeV/c to 1.0 GeV/c.

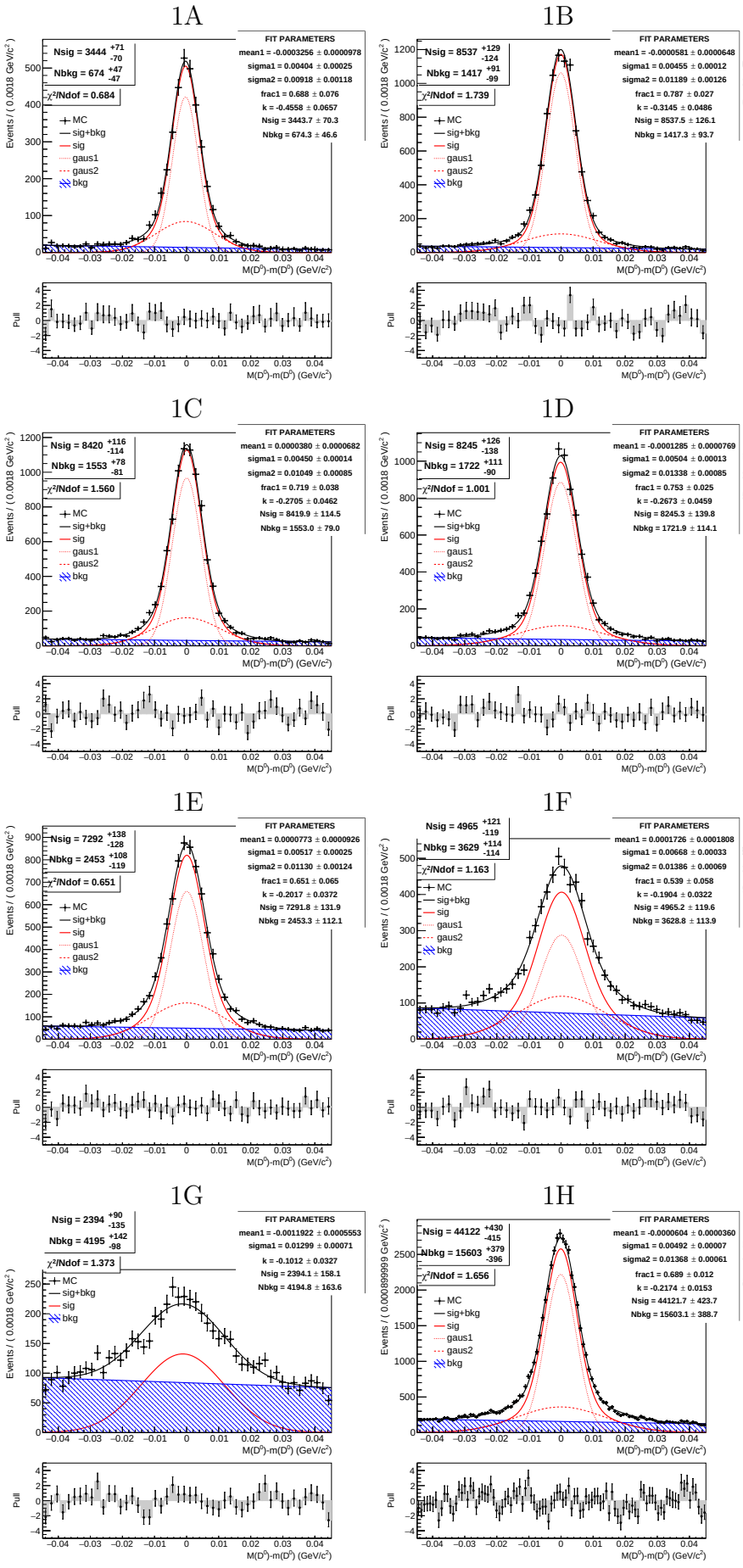

Figure D.3: Fits of kaon sample for momentum from 1.0 GeV/c to 1.5 GeV/c.

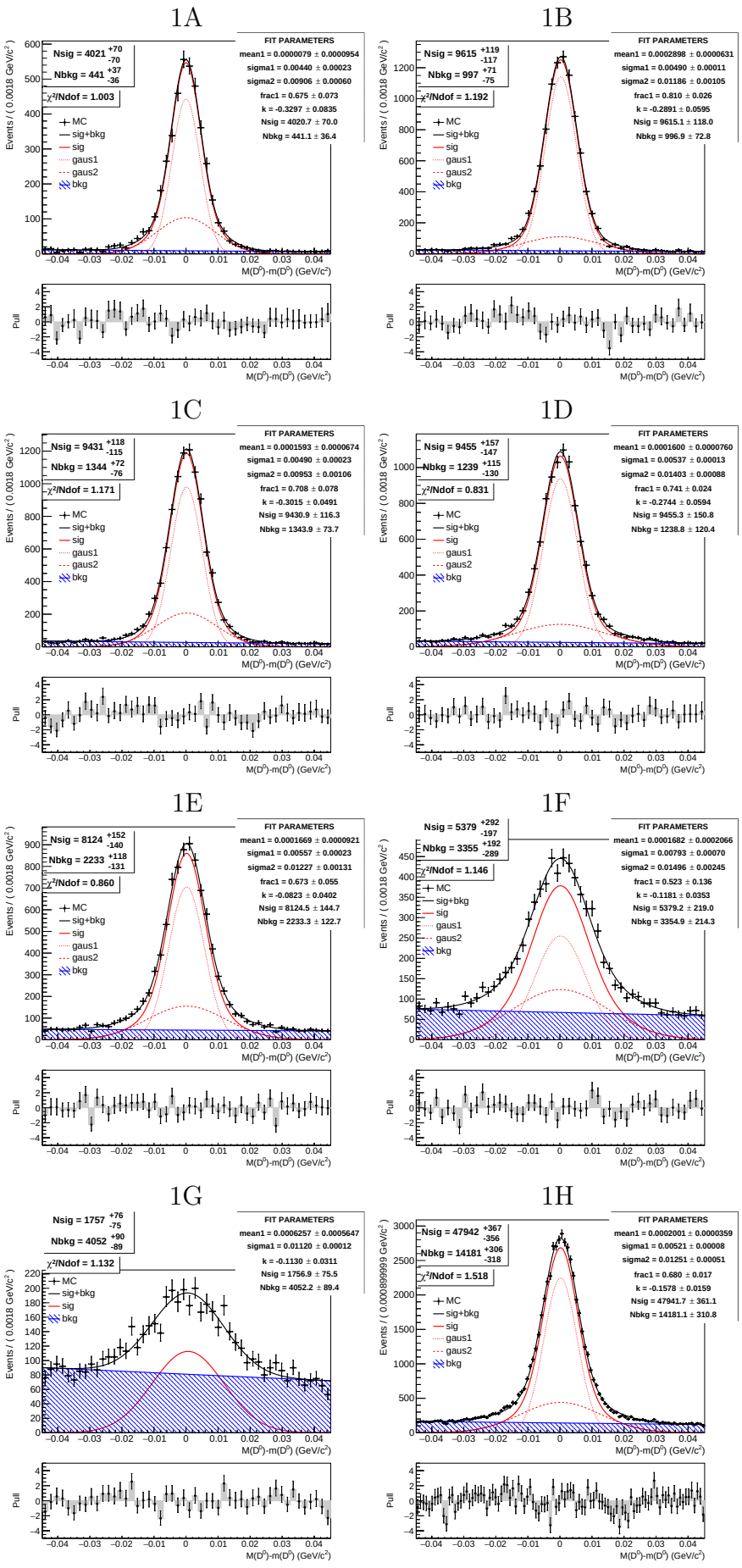

Figure D.4: Fits of pion sample for momentum from 1.0 GeV/c to 1.5 GeV/c.

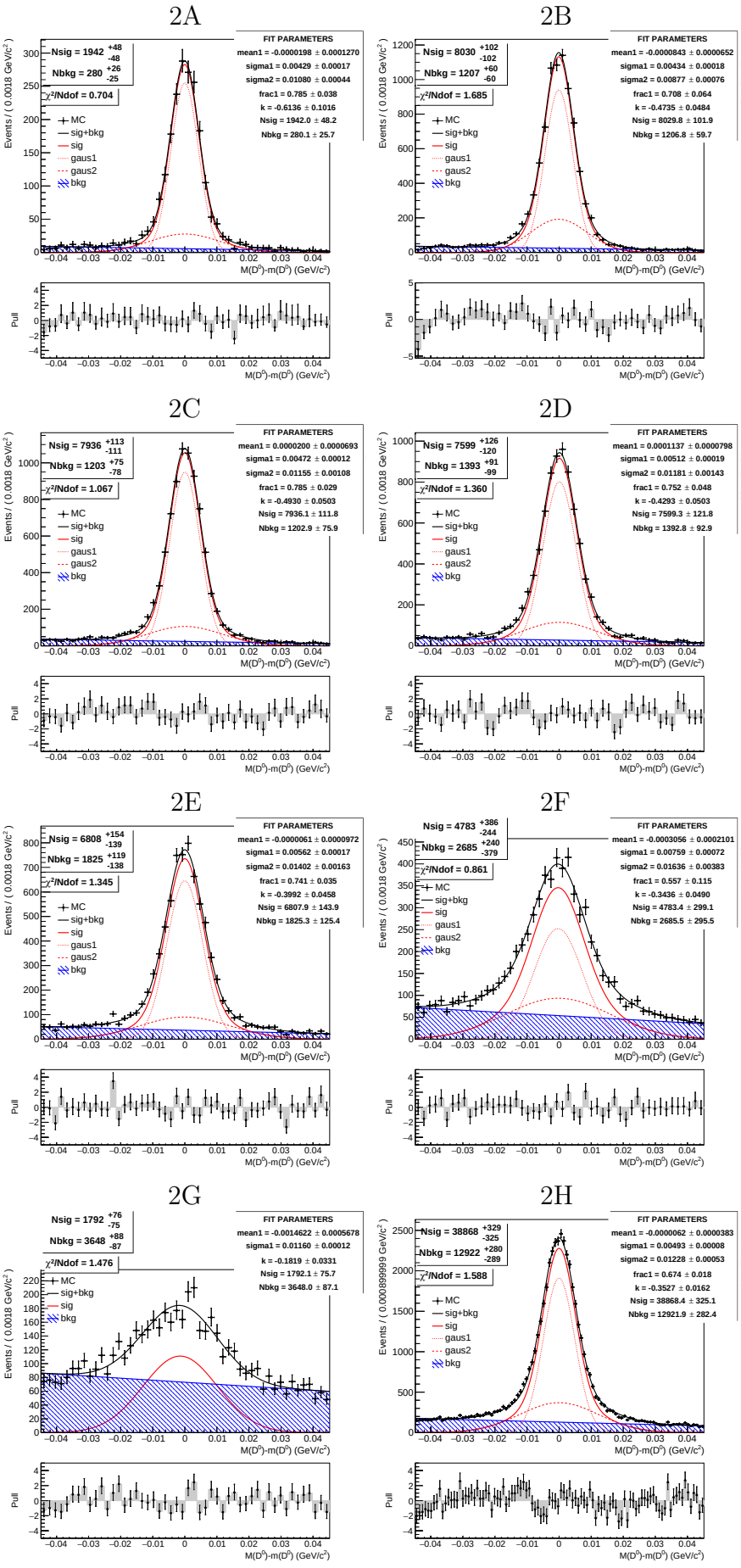

Figure D.5: Fits of kaon sample for momentum from 1.5 GeV/c to 2.0 GeV/c.

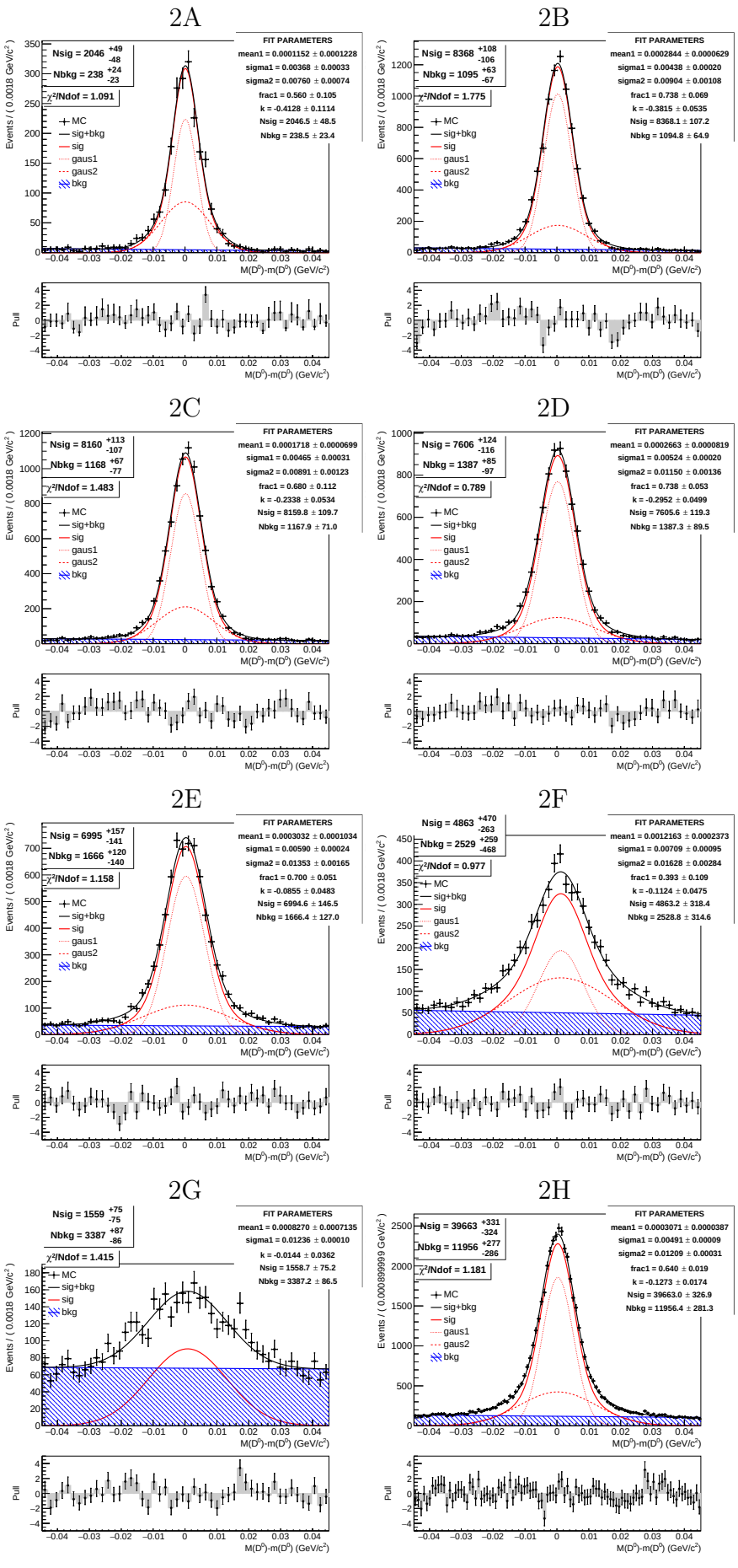

Figure D.6: Fits of pion sample for momentum from 1.5 GeV/c to 2.0 GeV/c.

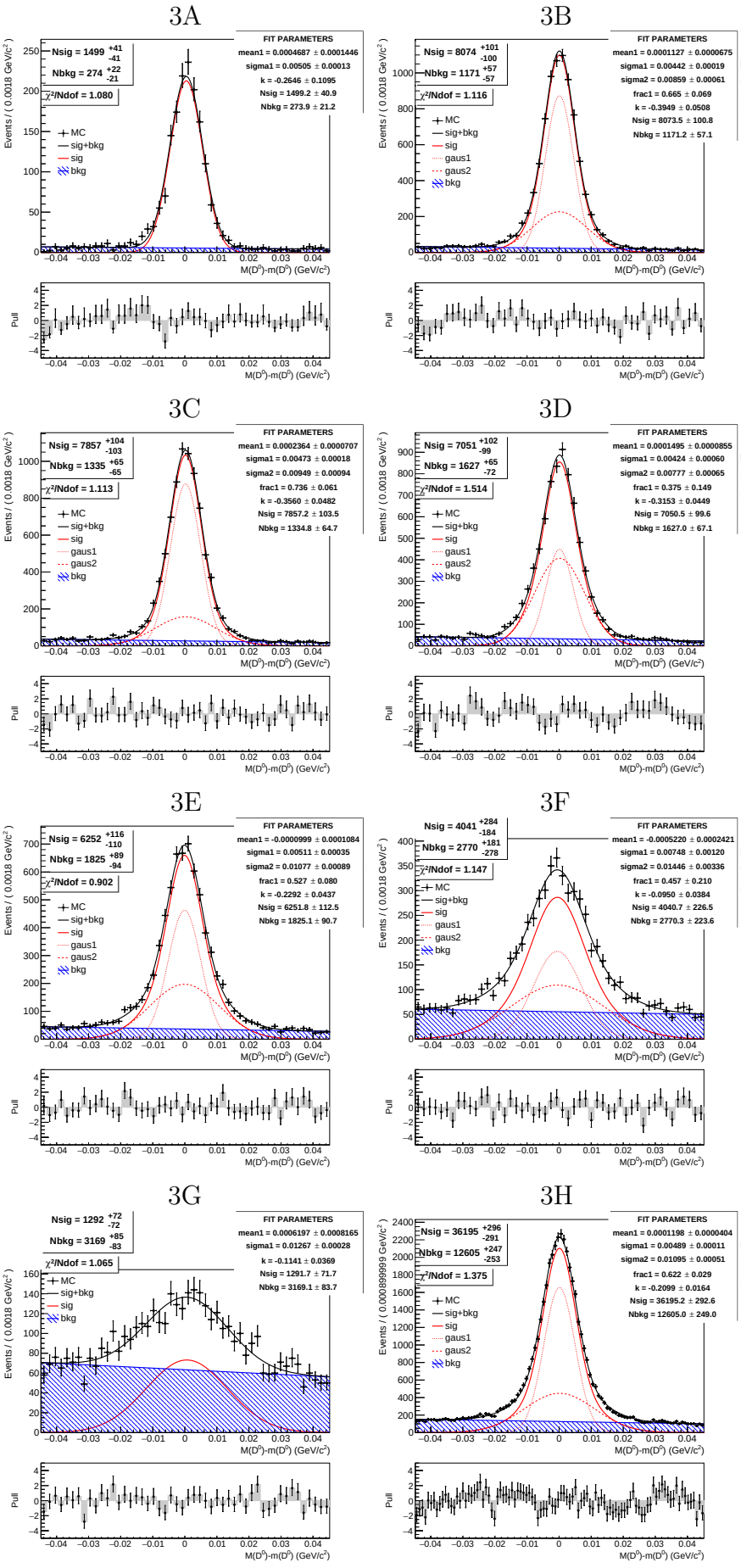

Figure D.7: Fits of kaon sample for momentum from 2.0 GeV/c to 2.5 GeV/c.

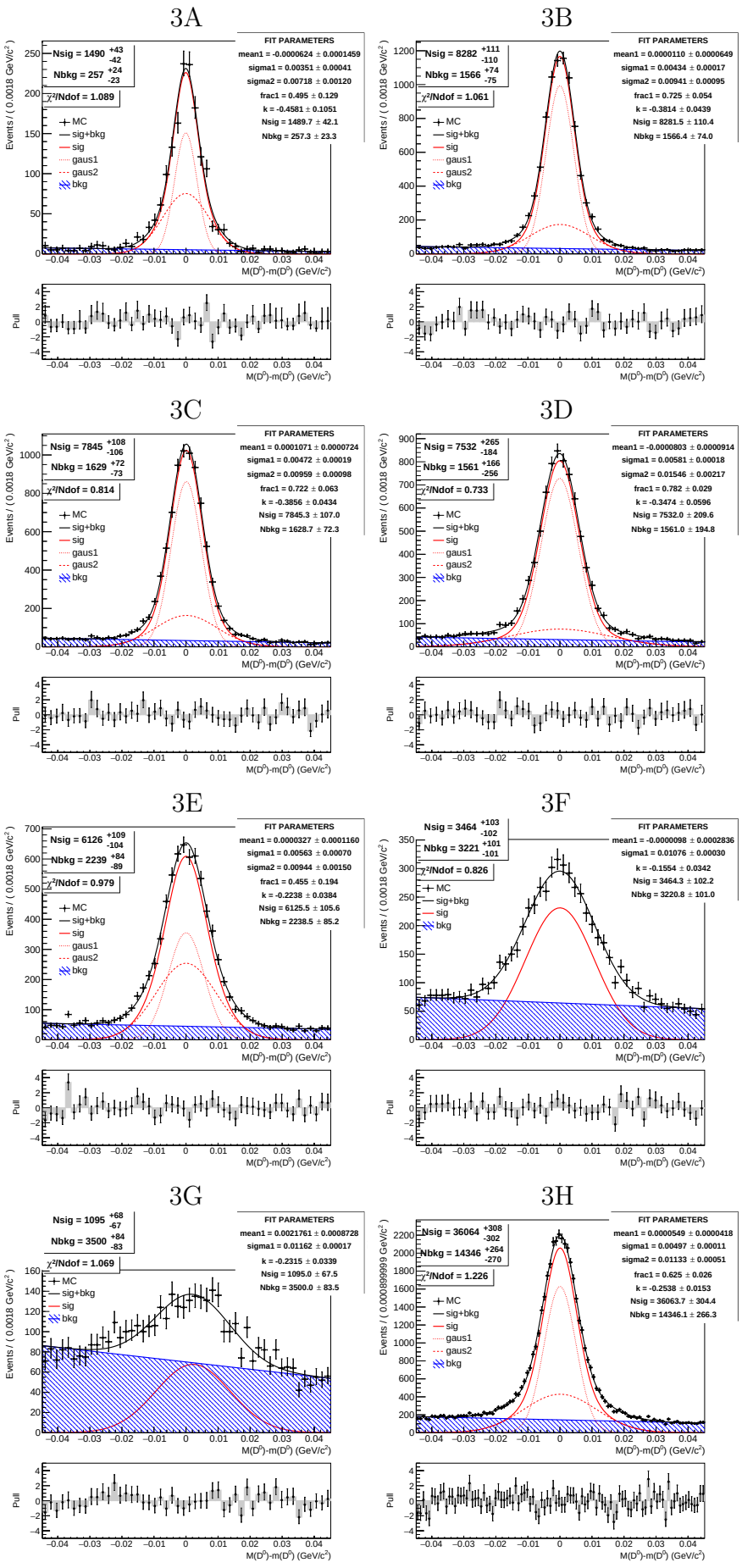

Figure D.8: Fits of pion sample for momentum from 2.0 GeV/c to 2.5 GeV/c.

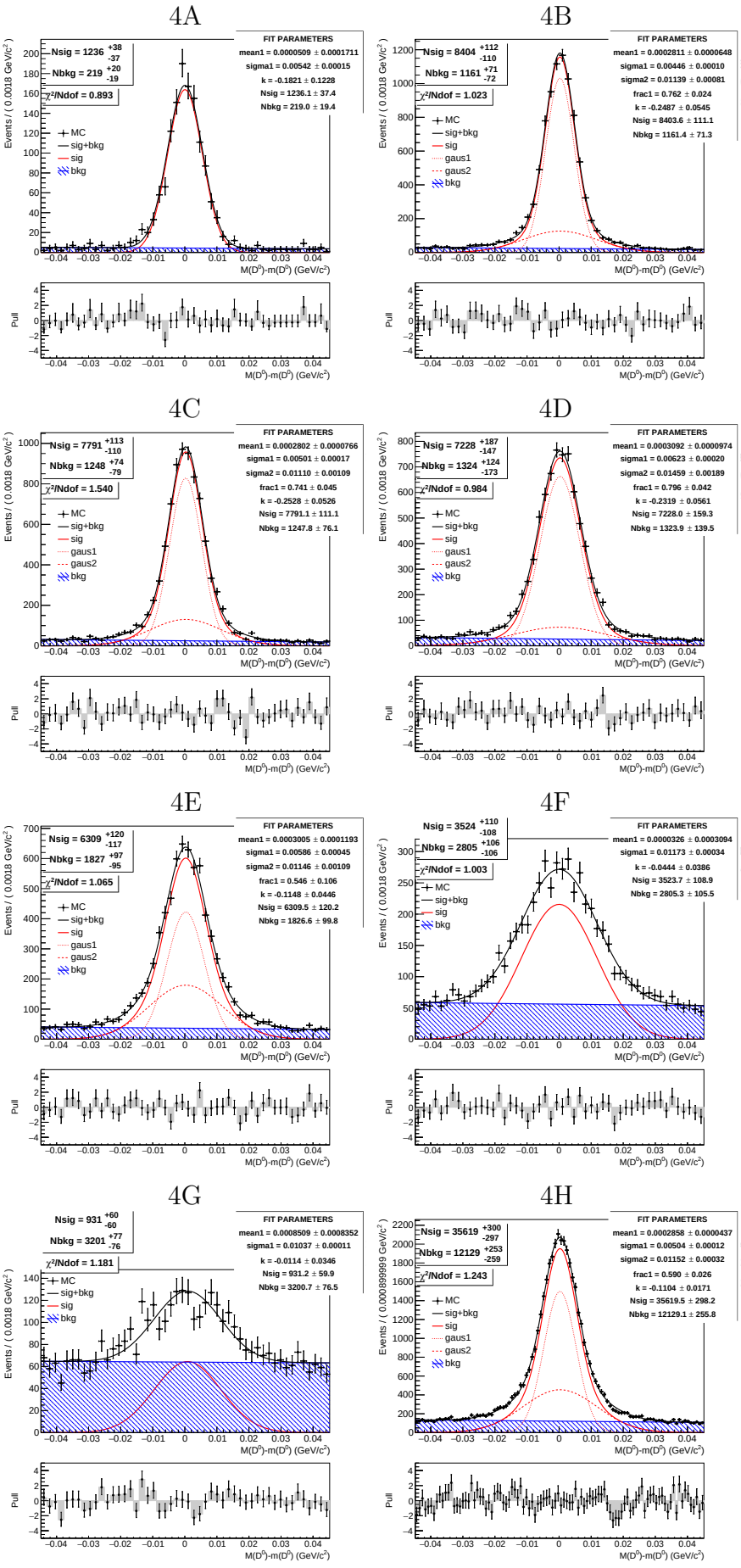

Figure D.9: Fits of kaon sample for momentum from 2.5 GeV/c to 3.0 GeV/c.

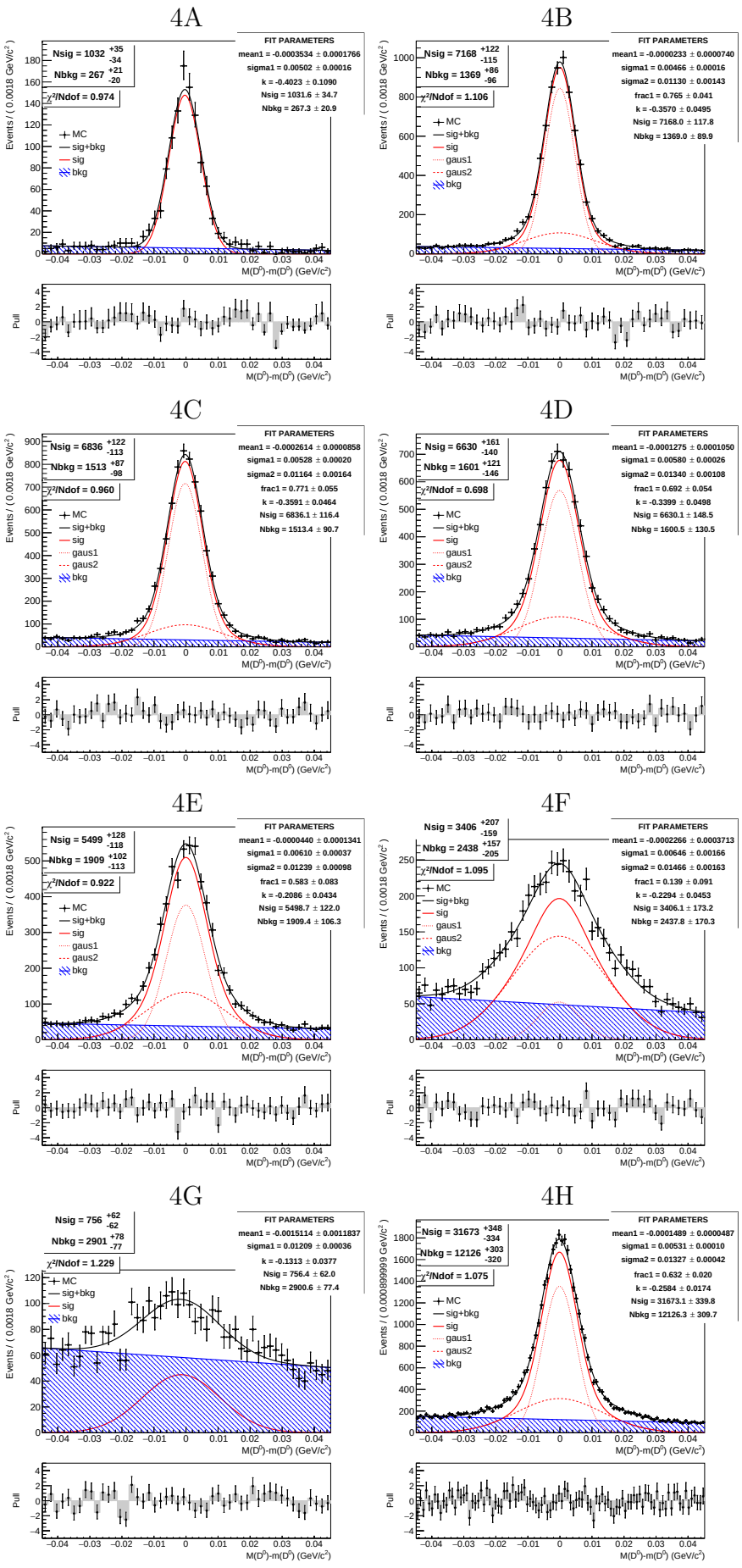

Figure D.10: Fits of pion sample for momentum from 2.5 GeV/c to 3.0 GeV/c.

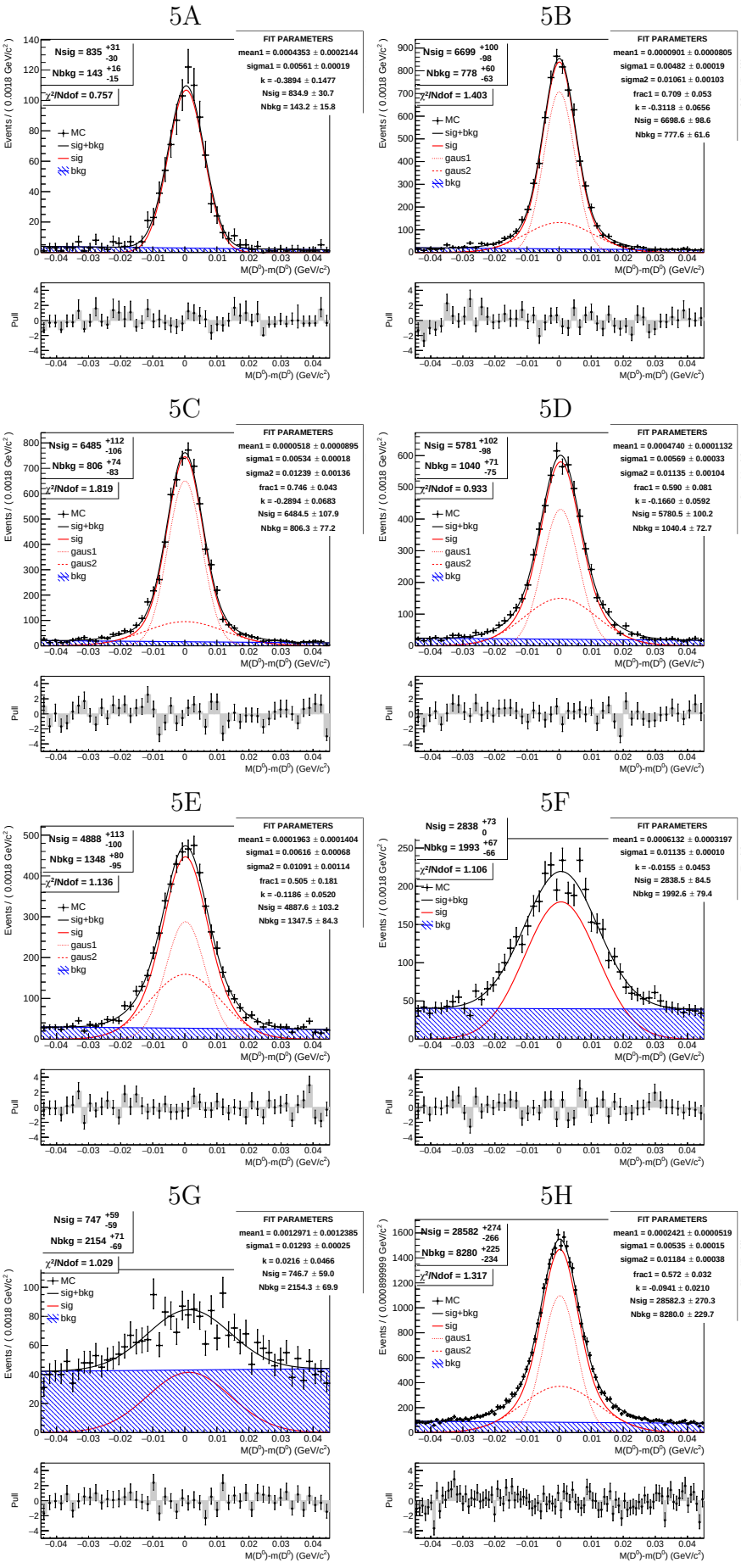

Figure D.11: Fits of kaon sample for momentum from 3.0 GeV/c to 3.5 GeV/c.

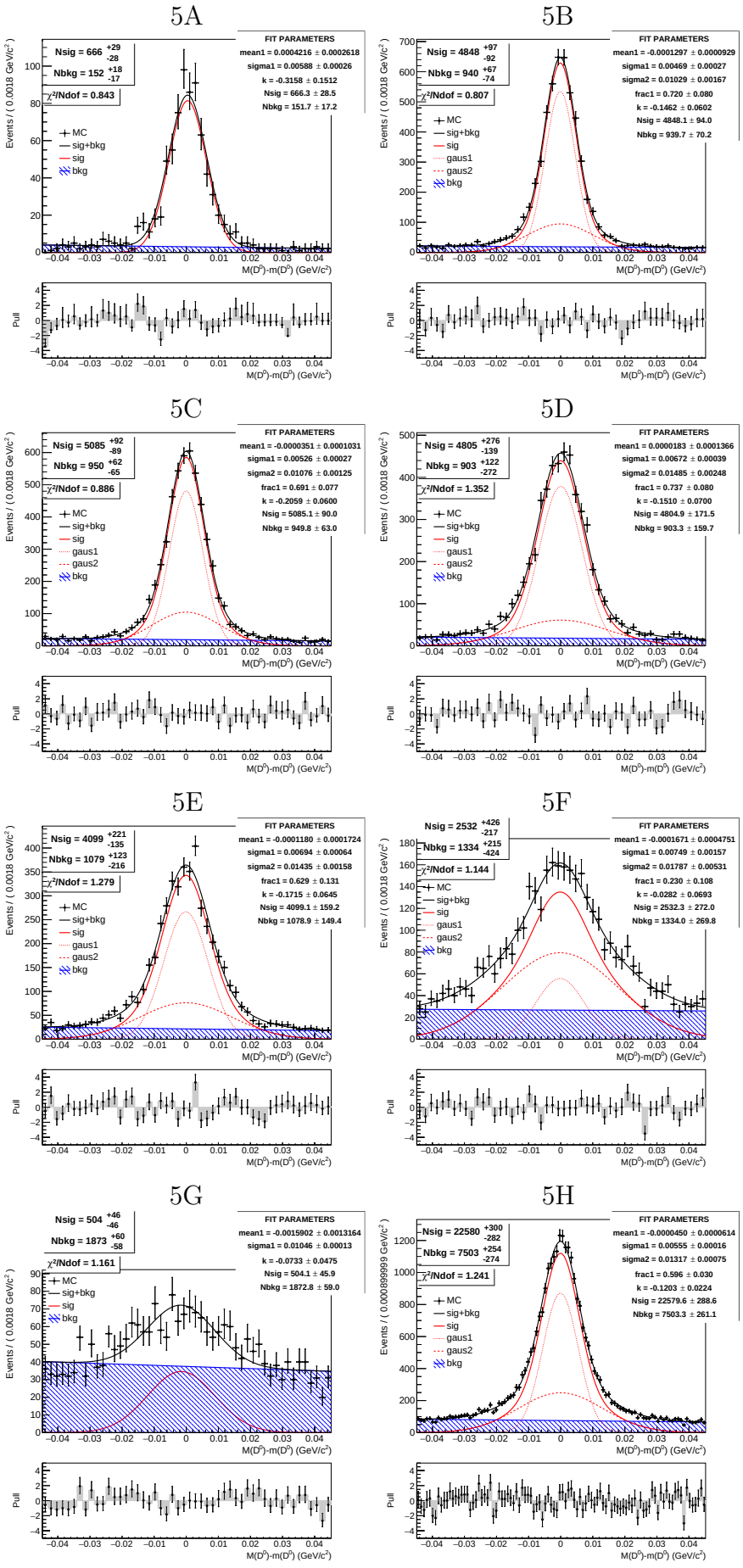

Figure D.12: Fits of pion sample for momentum from 3.0 GeV/c to 3.5 GeV/c.

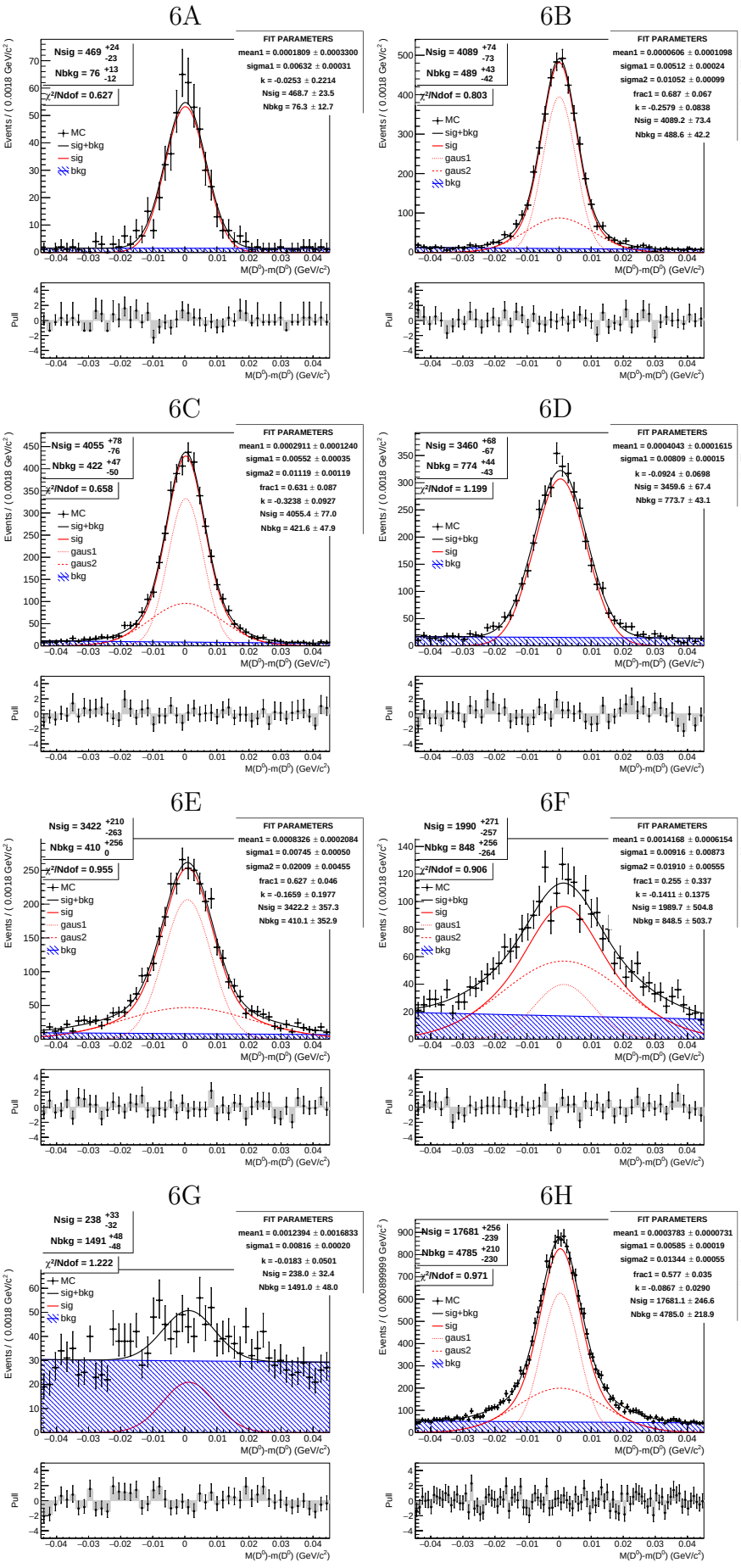

Figure D.13: Fits of kaon sample for momentum from 3.5 GeV/c to 4.0 GeV/c.

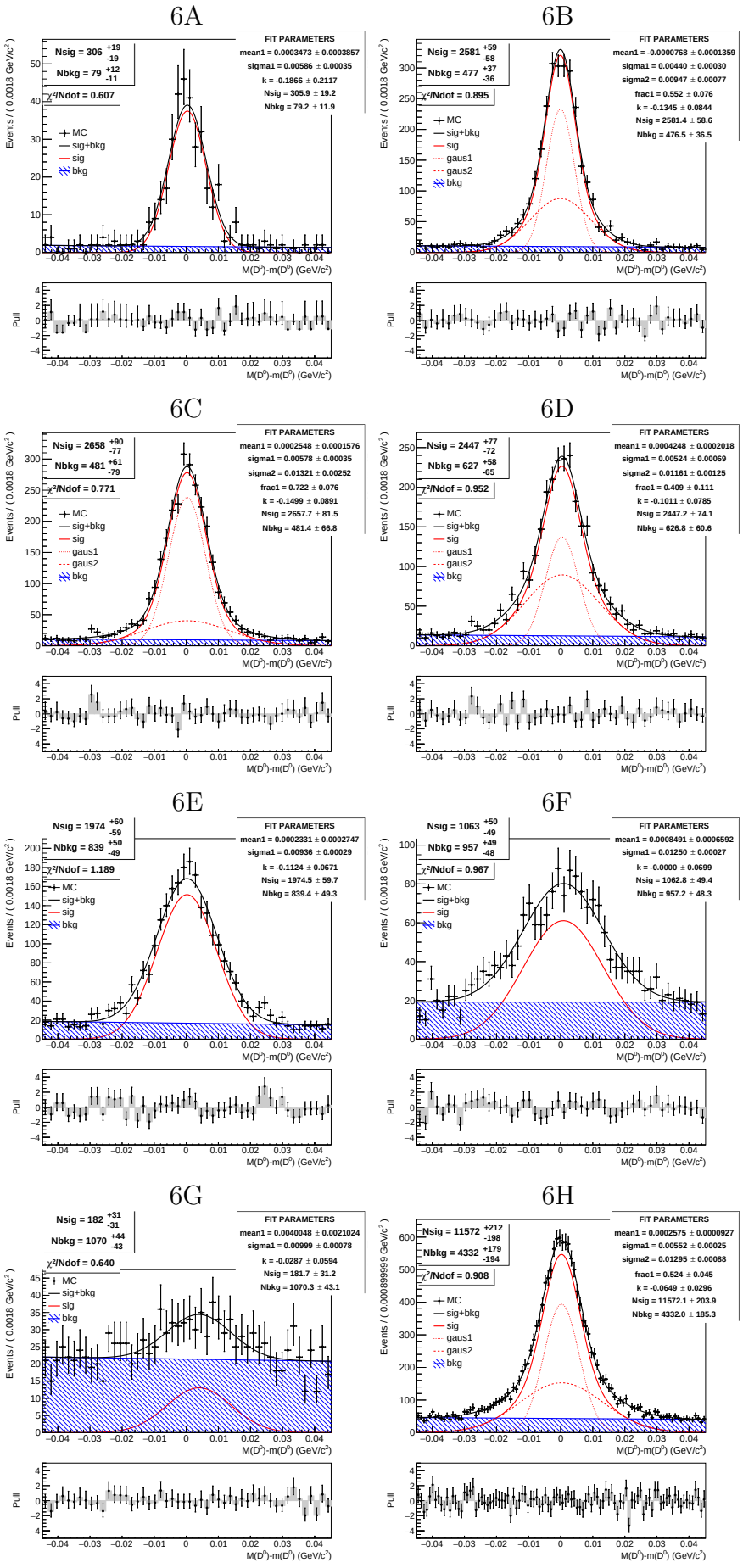

Figure D.14: Fits of pion sample for momentum from 3.5 GeV/c to 4.0 GeV/c.

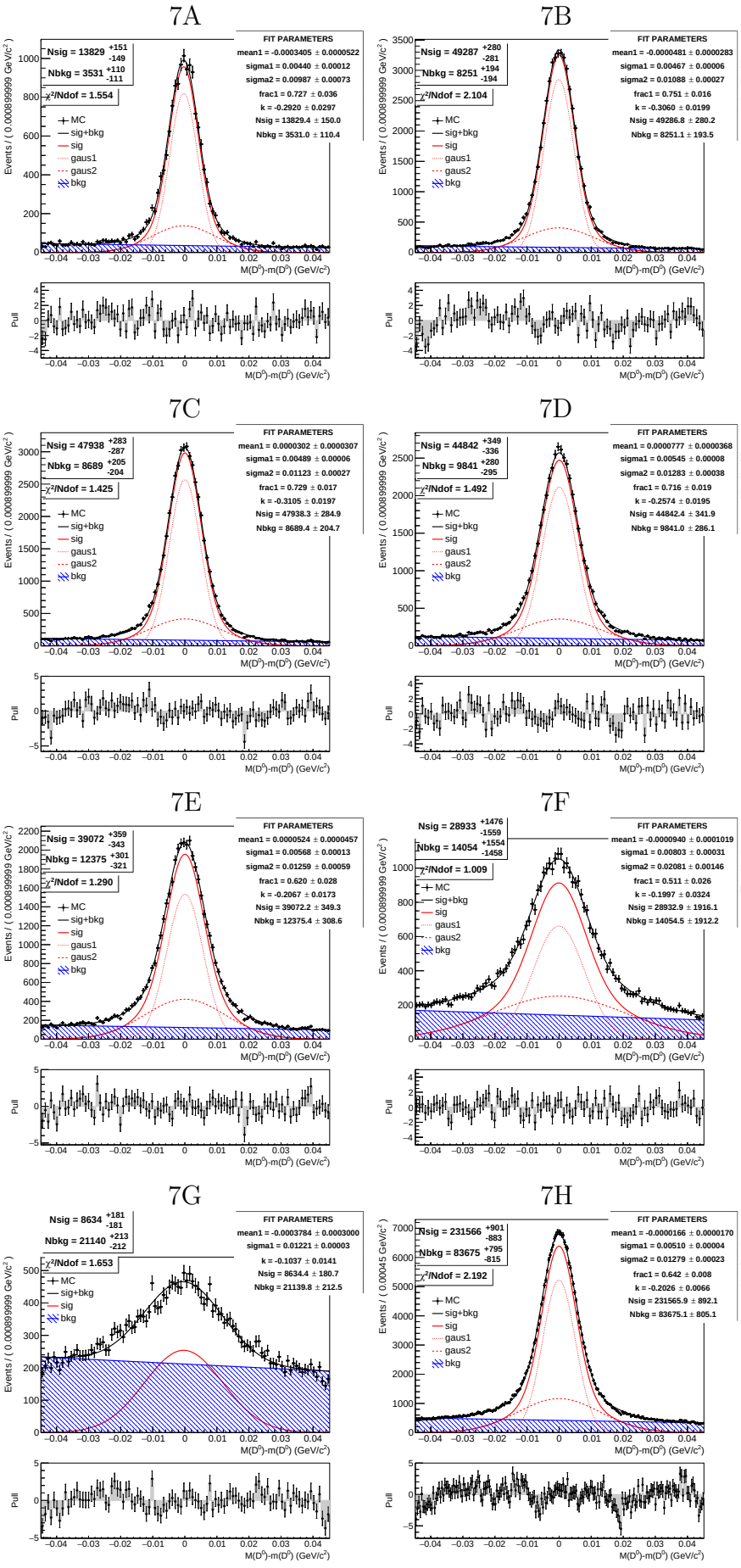

Figure D.15: Fits of kaon sample for momentum from 0.5 GeV/c to 4.0 GeV/c.

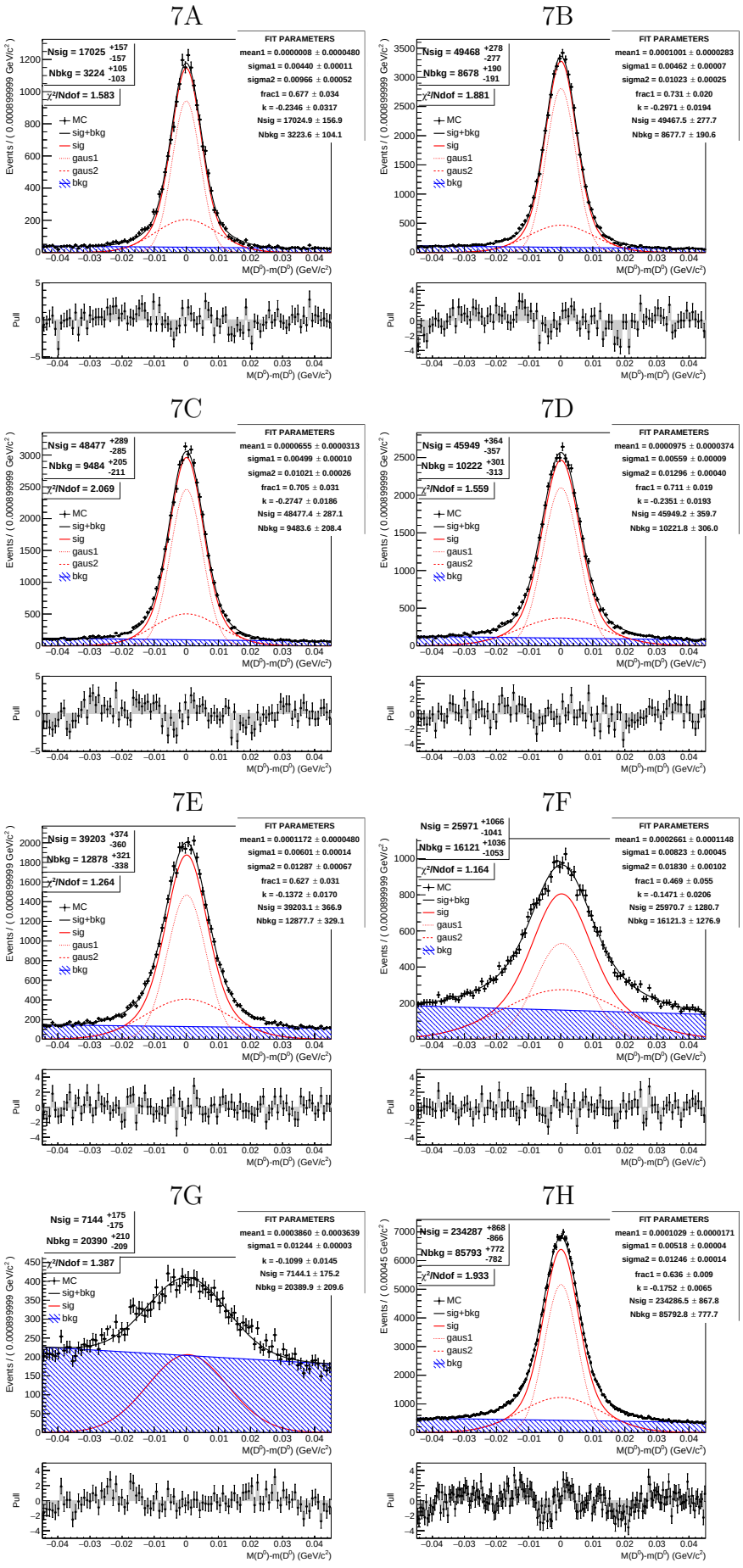

Figure D.16: Fits of pion sample for momentum from 0.5 GeV/c to 4.0 GeV/c.

Appendix D. D^0 Mass Fits of Simulated Phase III Sample

APPENDIX E

Kaon Identification Efficiencies and Pion Misidentification Probabilities in Phase III

Kaon identification efficiencies and pion misidentification probabilities of the Phase III simulated samples are presented in this appendix. Table E.1 shows results of $\varepsilon_{K\to K}$ and $\varepsilon_{\pi\to K}$ for 27 $PID_{K/\pi}$ selections in steps of 0.05 (up to 0.9) and 0.01 (above 0.9). The results are presented for the simulated Phase III sample with no momentum and polar angle division (bin 7H, according to the Table D.2).

Tables E.2 and E.3 show results for a $PID_{K/\pi} > 0.6$ selection for Phase III simulated sample. The kaon identification efficiencies and corresponding pion misidentification probabilities for different momenta ranges with no polar angle division are given in Table E.2, whereas Table E.3 presents the $\varepsilon_{K\to K}$ and $\varepsilon_{\pi\to K}$ for different cosine of polar angle for the entire momentum range.

Appendix E. Kaon Identification Efficiencies and Pion Misidentification Probabilities in Phase III

Table E.1: The kaon identification efficiency and corresponding pion misidentification probability for different $PID_{K/\pi}$ cuts. Results for Phase III sample with no momentum and polar angle division are presented.

$PID_{K/\pi}$	$\varepsilon_{K\to K}$	$\varepsilon_{\pi\to K}$
0.05	$97.53^{+0.04}_{-0.04}$	$13.24^{+0.09}_{-0.09}$
0.10	$97.09^{+0.04}_{-0.04}$	$12.00^{+0.09}_{-0.09}$
0.15	$96.78^{+0.04}_{-0.04}$	$11.24^{+0.08}_{-0.08}$
0.20	$96.46^{+0.04}_{-0.04}$	$10.64^{+0.08}_{-0.08}$
0.25	$96.21^{+0.05}_{-0.05}$	$10.18^{+0.08}_{-0.08}$
0.30	$95.96^{+0.05}_{-0.05}$	$9.77^{+0.08}_{-0.08}$
0.35	$95.72^{+0.05}_{-0.05}$	$9.41^{+0.08}_{-0.08}$
0.40	$95.49^{+0.05}_{-0.05}$	$9.14^{+0.08}_{-0.08}$
0.45	$95.22^{+0.05}_{-0.05}$	$8.86^{+0.08}_{-0.08}$
0.50	$94.90^{+0.05}_{-0.05}$	$8.60^{+0.08}_{-0.08}$
0.55	$94.01^{+0.06}_{-0.06}$	$7.79^{+0.07}_{-0.07}$
0.60	$93.09^{+0.06}_{-0.06}$	$6.99^{+0.07}_{-0.07}$
0.65	$92.30^{+0.06}_{-0.06}$	$6.40^{+0.07}_{-0.07}$
0.70	$91.55^{+0.07}_{-0.07}$	$5.87^{+0.07}_{-0.07}$
0.75	$90.69^{+0.07}_{-0.07}$	$5.33^{+0.06}_{-0.06}$
0.80	$89.68^{+0.07}_{-0.07}$	$4.85^{+0.06}_{-0.06}$
0.85	$88.48^{+0.08}_{-0.08}$	$4.39^{+0.06}_{-0.06}$
0.90	$86.79^{+0.08}_{-0.08}$	$3.95^{+0.06}_{-0.06}$
0.91	$86.35^{+0.08}_{-0.08}$	$3.84^{+0.06}_{-0.06}$
0.92	$85.82^{+0.08}_{-0.08}$	$3.73^{+0.06}_{-0.06}$
0.93	$85.25^{+0.08}_{-0.08}$	$3.60^{+0.05}_{-0.05}$
0.94	$84.61^{+0.09}_{-0.09}$	$3.46^{+0.05}_{-0.05}$
0.95	$83.84^{+0.09}_{-0.09}$	$3.31^{+0.05}_{-0.05}$
0.96	$82.85^{+0.09}_{-0.09}$	$3.12^{+0.05}_{-0.05}$
0.97	$81.54^{+0.09}_{-0.09}$	$2.91^{+0.05}_{-0.05}$
0.98	$79.63^{+0.09}_{-0.10}$	$2.65^{+0.05}_{-0.05}$
0.99	$76.16^{+0.10}_{-0.10}$	$2.21^{+0.04}_{-0.04}$

Table E.2: The kaon identification efficiency and corresponding pion misidentification probability for different momentum bins with $PID_{K/\pi} > 0.6$ selection, applied to the Phase III simulated sample with no polar angle division, is presented.

p [GeV/c]	$\varepsilon_{K\to K}$	$\varepsilon_{\pi\to K}$	p [GeV/c]	$\varepsilon_{K\to K}$	$\varepsilon_{\pi\to K}$
0.50-0.55	$83.78^{+3.01}_{-3.04}$	$12.18^{+1.29}_{-1.25}$	2.25-2.30	$95.39^{+0.40}_{-0.39}$	$6.93^{+0.57}_{-0.55}$
0.55-0.60	$82.99^{+1.37}_{-1.37}$	$10.37^{+0.72}_{-0.71}$	2.30-2.35	$95.92^{+0.37}_{-0.37}$	$6.74^{+0.57}_{-0.56}$
0.60-0.65	$83.98^{+0.95}_{-0.95}$	$7.81^{+0.57}_{-0.56}$	2.35-2.40	$95.06^{+0.40}_{-0.39}$	$6.52^{+0.57}_{-0.56}$
0.65-0.70	$87.34^{+0.79}_{-0.79}$	$7.89^{+0.54}_{-0.53}$	2.40-2.45	$94.25^{+0.43}_{-0.43}$	$5.11^{+0.55}_{-0.53}$
0.70-0.75	$88.38^{+0.69}_{-0.69}$	$7.55^{+0.53}_{-0.51}$	2.45-2.50	$95.86^{+0.38}_{-0.37}$	$5.78^{+0.58}_{-0.56}$
0.75-0.80	$89.17^{+0.62}_{-0.62}$	$7.99^{+0.54}_{-0.52}$	2.50-2.55	$95.59^{+0.37}_{-0.37}$	$7.23^{+0.62}_{-0.61}$
0.80-0.85	$90.22^{+0.57}_{-0.57}$	$6.97^{+0.53}_{-0.51}$	2.55-2.60	$94.67^{+0.42}_{-0.42}$	$7.33^{+0.60}_{-0.59}$
0.85-0.90	$91.42^{+0.54}_{-0.53}$	$7.82^{+0.52}_{-0.51}$	2.60-2.65	$95.68^{+0.38}_{-0.37}$	$5.89^{+0.60}_{-0.58}$
0.90-0.95	$90.89^{+0.52}_{-0.52}$	$7.18^{+0.50}_{-0.49}$	2.65-2.70	$95.22^{+0.40}_{-0.40}$	$6.29^{+0.59}_{-0.57}$
0.95-1.00	$90.30^{+0.52}_{-0.51}$	$8.13^{+0.52}_{-0.50}$	2.70-2.75	$95.06^{+0.41}_{-0.41}$	$6.31^{+0.60}_{-0.58}$
1.00-1.05	$90.92^{+0.51}_{-0.50}$	$7.25^{+0.49}_{-0.48}$	2.75-2.80	$94.40^{+0.45}_{-0.44}$	$6.63^{+0.64}_{-0.62}$
1.05-1.10	$92.28^{+0.48}_{-0.47}$	$7.64^{+0.48}_{-0.47}$	2.80-2.85	$93.61^{+0.48}_{-0.47}$	$7.62^{+0.65}_{-0.63}$
1.10-1.15	$91.73^{+0.49}_{-0.48}$	$6.60^{+0.49}_{-0.47}$	2.85-2.90	$94.35^{+0.45}_{-0.44}$	$6.27^{+0.59}_{-0.57}$
1.15-1.20	$91.79^{+0.49}_{-0.48}$	$6.36^{+0.48}_{-0.46}$	2.90-2.95	$94.34^{+0.47}_{-0.47}$	$5.83^{+0.61}_{-0.58}$
1.20-1.25	$91.18^{+0.50}_{-0.49}$	$6.49^{+0.48}_{-0.46}$	2.95-3.00	$94.42^{+0.44}_{-0.44}$	$5.94^{+0.65}_{-0.63}$
1.25-1.30	$91.95^{+0.47}_{-0.46}$	$7.40^{+0.47}_{-0.45}$	3.00-3.05	$94.03^{+0.47}_{-0.46}$	$6.51^{+0.63}_{-0.61}$
1.30-1.35	$93.17^{+0.43}_{-0.42}$	$6.35^{+0.46}_{-0.45}$	3.05-3.10	$93.51^{+0.50}_{-0.49}$	$5.99^{+0.65}_{-0.63}$
1.35-1.40	$92.34^{+0.45}_{-0.45}$	$6.33^{+0.47}_{-0.46}$	3.10-3.15	$93.86^{+0.48}_{-0.48}$	$6.89^{+0.70}_{-0.68}$
1.40-1.45	$92.70^{+0.45}_{-0.44}$	$6.81^{+0.46}_{-0.45}$	3.15-3.20	$92.47^{+0.53}_{-0.53}$	$8.37^{+0.72}_{-0.69}$
1.45-1.50	$92.28^{+0.45}_{-0.45}$	$6.25^{+0.48}_{-0.47}$	3.20-3.25	$94.47^{+0.49}_{-0.49}$	$8.75^{+0.77}_{-0.74}$
1.50-1.55	$91.78^{+0.47}_{-0.46}$	$6.67^{+0.48}_{-0.46}$	3.25-3.30	$94.43^{+0.49}_{-0.49}$	$7.14^{+0.76}_{-0.73}$
1.55-1.60	$91.52^{+0.49}_{-0.48}$	$5.94^{+0.47}_{-0.45}$	3.30-3.35	$94.77^{+0.49}_{-0.49}$	$7.31^{+0.74}_{-0.71}$
1.60-1.65	$93.64^{+0.43}_{-0.42}$	$6.41^{+0.50}_{-0.49}$	3.35-3.40	$92.65^{+0.58}_{-0.57}$	$8.13^{+0.81}_{-0.78}$
1.65-1.70	$94.04^{+0.43}_{-0.42}$	$6.27^{+0.53}_{-0.51}$	3.40-3.45	$94.61^{+0.52}_{-0.52}$	$7.53^{+0.85}_{-0.81}$
1.70-1.75	$93.69^{+0.45}_{-0.44}$	$6.66^{+0.55}_{-0.54}$	3.45-3.50	$93.82^{+0.57}_{-0.56}$	$7.59^{+0.87}_{-0.84}$
1.75-1.80	$94.94^{+0.41}_{-0.41}$	$6.47^{+0.54}_{-0.53}$	3.50-3.55	$91.27^{+0.72}_{-0.71}$	$6.96^{+0.88}_{-0.84}$
1.80-1.85	$94.32^{+0.44}_{-0.43}$	$6.24^{+0.53}_{-0.51}$	3.55-3.60	$92.77^{+0.66}_{-0.65}$	$6.47^{+0.93}_{-0.88}$
1.85-1.90	$94.64^{+0.43}_{-0.43}$	$6.36^{+0.52}_{-0.50}$	3.60-3.65	$92.30^{+0.68}_{-0.67}$	$7.04^{+0.97}_{-0.92}$
1.90-1.95	$95.06^{+0.40}_{-0.40}$	$7.62^{+0.55}_{-0.54}$	3.65-3.70	$92.68^{+0.71}_{-0.69}$	$8.20^{+1.06}_{-1.01}$
1.95-2.00	$94.71^{+0.42}_{-0.42}$	$6.47^{+0.53}_{-0.51}$	3.70-3.75	$92.78^{+0.73}_{-0.72}$	$7.68^{+1.05}_{-0.99}$
2.00-2.05	$94.96^{+0.42}_{-0.41}$	$6.80^{+0.55}_{-0.54}$	3.75-3.80	$92.28^{+0.78}_{-0.77}$	$8.57^{+1.15}_{-1.09}$
2.05-2.10	$94.41^{+0.43}_{-0.43}$	$6.55^{+0.54}_{-0.52}$	3.80-3.85	$92.23^{+0.82}_{-0.80}$	$8.60^{+1.26}_{-1.19}$
2.10-2.15	$93.75^{+0.45}_{-0.44}$	$6.01^{+0.53}_{-0.51}$	3.85-3.90	$92.48^{+0.79}_{-0.77}$	$9.65^{+1.30}_{-1.22}$
2.15-2.20	$94.90^{+0.41}_{-0.41}$	$6.67^{+0.54}_{-0.53}$	3.90-3.95	$93.02^{+0.80}_{-0.79}$	$8.82^{+1.38}_{-1.30}$
2.20-2.25	$94.73^{+0.43}_{-0.43}$	$6.85^{+0.54}_{-0.53}$	3.95-4.00	$91.77^{+0.95}_{-0.93}$	$10.67^{+1.44}_{-1.36}$

Appendix E. Kaon Identification Efficiencies and Pion Misidentification Probabilities in Phase III

Table E.3: The kaon identification efficiency and corresponding pion misidentification probability for different cosine of polar angle with $PID_{K/\pi} > 0.6$ selection, applied to the Phase III simulated sample with no momentum, is presented.

$\cos\theta$	$\varepsilon_{K\to K}$	$\varepsilon_{\pi\to K}$	$\cos\theta$	$\varepsilon_{K\to K}$	$\varepsilon_{\pi\to K}$
0.8200-0.8225	$91.84^{+0.37}_{-0.36}$	$8.24^{+0.40}_{-0.39}$	0.8750-0.8775	$95.77^{+0.30}_{-0.30}$	$5.00^{+0.39}_{-0.39}$
0.8225-0.8250	$93.70^{+0.33}_{-0.32}$	$6.63^{+0.37}_{-0.36}$	0.8775-0.8800	$95.61^{+0.32}_{-0.32}$	$5.14^{+0.39}_{-0.38}$
0.8250-0.8275	$93.51^{+0.33}_{-0.33}$	$5.74^{+0.35}_{-0.34}$	0.8800-0.8825	$95.48^{+0.32}_{-0.32}$	$5.12^{+0.41}_{-0.40}$
0.8275-0.8300	$93.53^{+0.34}_{-0.33}$	$4.97^{+0.33}_{-0.32}$	0.8825-0.8850	$95.04^{+0.33}_{-0.33}$	$4.58^{+0.40}_{-0.39}$
0.8300-0.8325	$94.67^{+0.30}_{-0.30}$	$5.77^{+0.35}_{-0.34}$	0.8850-0.8875	$94.63^{+0.36}_{-0.36}$	$5.64^{+0.43}_{-0.42}$
0.8325-0.8350	$94.13^{+0.31}_{-0.31}$	$5.15^{+0.33}_{-0.32}$	0.8875-0.8900	$94.95^{+0.34}_{-0.34}$	$4.85^{+0.42}_{-0.41}$
0.8350-0.8375	$94.04^{+0.33}_{-0.33}$	$5.92^{+0.35}_{-0.34}$	0.8900-0.8925	$96.14^{+0.31}_{-0.31}$	$4.67^{+0.43}_{-0.42}$
0.8375-0.8400	$92.41^{+0.36}_{-0.36}$	$5.96^{+0.36}_{-0.35}$	0.8925-0.8950	$96.83^{+0.29}_{-0.30}$	$4.98^{+0.45}_{-0.43}$
0.8400-0.8425	$91.11^{+0.39}_{-0.38}$	$6.00^{+0.36}_{-0.35}$	0.8950-0.8975	$95.86^{+0.35}_{-0.35}$	$4.08^{+0.45}_{-0.44}$
0.8425-0.8450	$89.92^{+0.41}_{-0.41}$	$7.30^{+0.38}_{-0.37}$	0.8975-0.9000	$96.37^{+0.34}_{-0.34}$	$4.65^{+0.51}_{-0.50}$
0.8450-0.8475	$86.16^{+0.48}_{-0.47}$	$9.31^{+0.42}_{-0.41}$	0.9000-0.9025	$96.35^{+0.36}_{-0.36}$	$3.88^{+0.55}_{-0.54}$
0.8475-0.8500	$83.55^{+0.51}_{-0.50}$	$10.35^{+0.44}_{-0.43}$	0.9025-0.9050	$96.18^{+0.41}_{-0.41}$	$2.95^{+0.64}_{-0.62}$
0.8500-0.8525	$91.42^{+0.39}_{-0.38}$	$7.08^{+0.39}_{-0.38}$	0.9050-0.9075	$94.90^{+0.53}_{-0.52}$	$3.08^{+0.66}_{-0.64}$
0.8525-0.8550	$95.09^{+0.30}_{-0.30}$	$4.79^{+0.35}_{-0.34}$	0.9075-0.9100	$96.06^{+0.47}_{-0.47}$	$4.37^{+0.73}_{-0.71}$
0.8550-0.8575	$95.08^{+0.31}_{-0.31}$	$4.82^{+0.34}_{-0.34}$	0.9100-0.9125	$94.31^{+0.60}_{-0.60}$	$4.46^{+0.78}_{-0.77}$
0.8575-0.8600	$94.07^{+0.33}_{-0.33}$	$5.14^{+0.36}_{-0.35}$	0.9125-0.9150	$96.14^{+0.53}_{-0.54}$	$4.93^{+0.88}_{-0.86}$
0.8600-0.8625	$95.74^{+0.29}_{-0.29}$	$5.15^{+0.35}_{-0.35}$	0.9150-0.9175	$91.70^{+2.53}_{-1.98}$	$2.78^{+1.05}_{-1.05}$
0.8625-0.8650	$96.29^{+0.27}_{-0.27}$	$5.31^{+0.37}_{-0.36}$	0.9175-0.9200	$93.24^{+0.81}_{-0.81}$	$4.48^{+1.18}_{-1.16}$
0.8650-0.8675	$95.88^{+0.29}_{-0.29}$	$4.93^{+0.35}_{-0.34}$	0.9200-0.9225	$93.91^{+0.84}_{-0.85}$	$3.45^{+1.45}_{-1.44}$
0.8675-0.8700	$96.15^{+0.28}_{-0.28}$	$5.09^{+0.36}_{-0.35}$	0.9225-0.9250	$95.13^{+0.88}_{-0.88}$	$5.73^{+1.51}_{-1.49}$
0.8700-0.8725	$96.63^{+0.27}_{-0.27}$	$4.67^{+0.38}_{-0.36}$	0.9250-0.9275	$94.10^{+1.07}_{-1.08}$	$4.41^{+1.70}_{-1.68}$
0.8725-0.8750	$95.61^{+0.30}_{-0.31}$	$4.65^{+0.39}_{-0.37}$	0.9275-0.9300	$93.86^{+1.29}_{-1.28}$	$5.60^{+2.03}_{-2.04}$

APPENDIX F

Phase III Simulation Results

In the following pages, Monte Carlo simulation results for Phase III sample of a size $1\,\mathrm{ab}^{-1}$ are presented, as follows:

- Kaon identification efficiencies and pion misidentification probabilities for momentum-angle bins, summarized in Table D.2, are shown in Figs. from F.1 to F.16.
- Kaon identification efficiencies and pion misidentification probabilities for fine momentum binning of $50\,\mathrm{MeV/c}$, are shown in Figs. from F.17 to F.28.
- Kaon identification efficiencies and pion misidentification probabilities for fine binning over $\cos\theta$ of 0.0025, are shown in Figs. from F.41 to F.64.

F.1 Kaon identification efficiencies and pion misidentification probabilities for momentum-angle bins

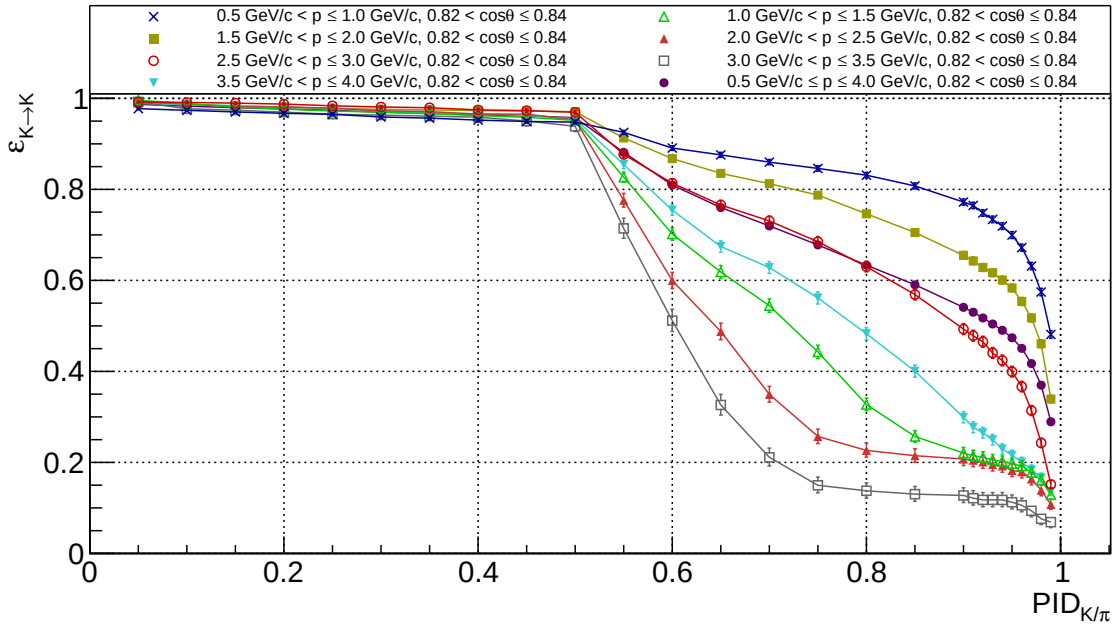

Figure F.1: Kaon identification efficiencies for momentum-angle bins xA.

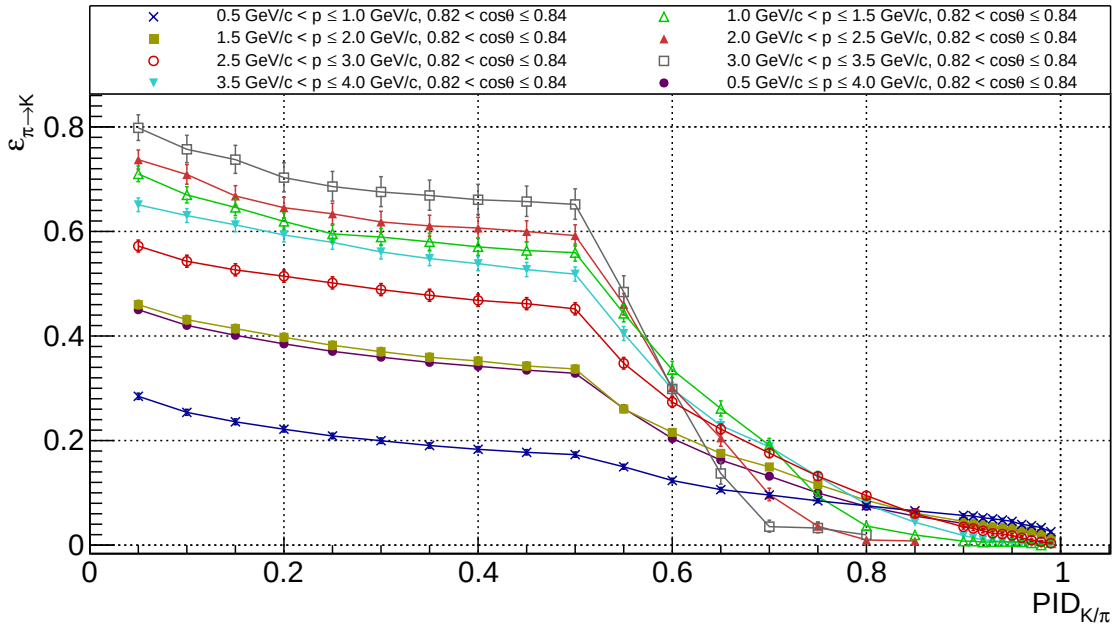

Figure F.2: Pion misidentification probabilities for momentum-angle bins xA.

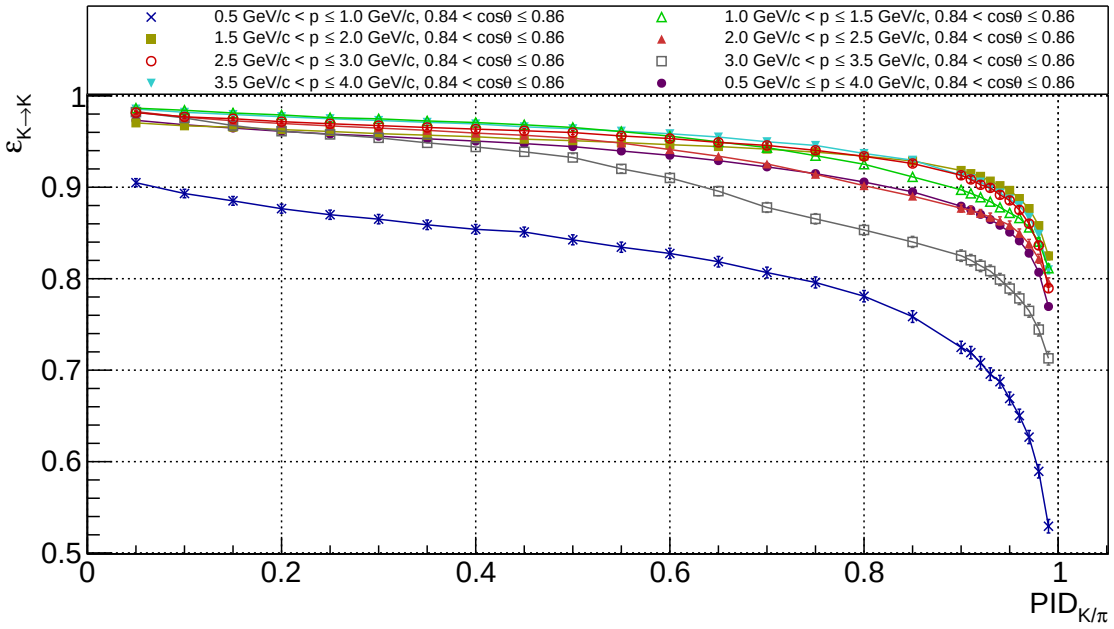

Figure F.3: Kaon identification efficiencies for momentum-angle bins xB.

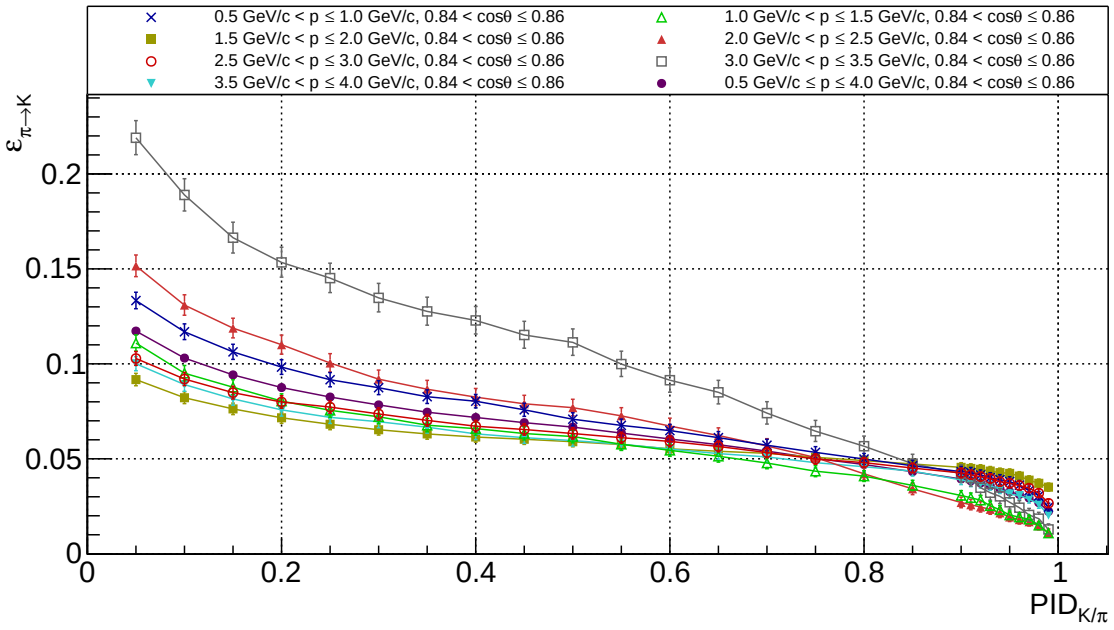

Figure F.4: Pion misidentification probabilities for momentum-angle bins xB.

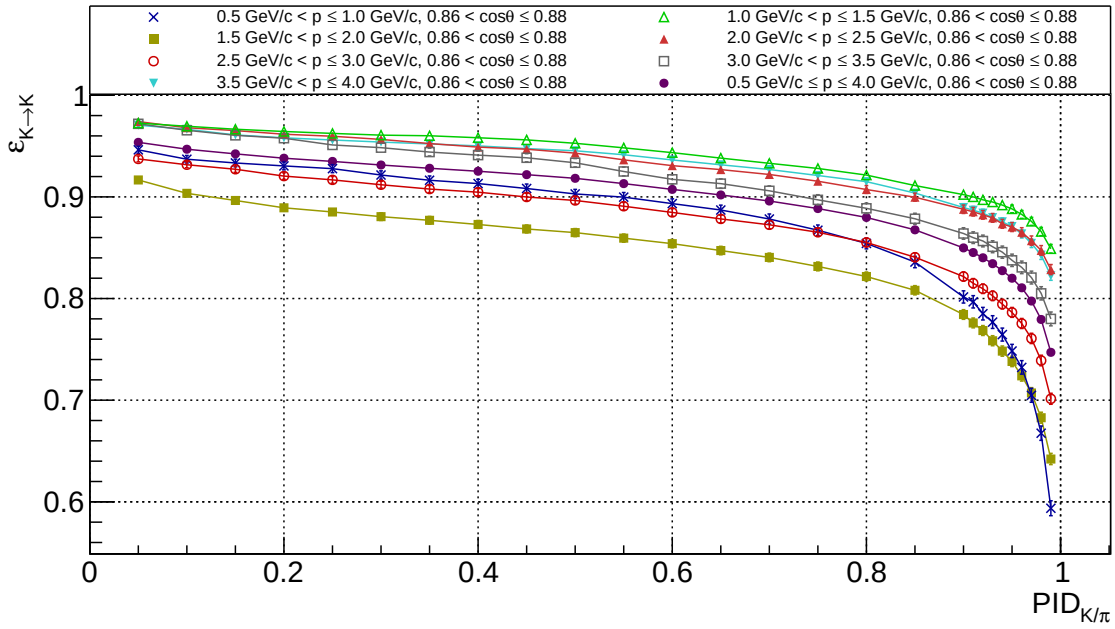

Figure F.5: Kaon identification efficiencies for momentum-angle bins xC.

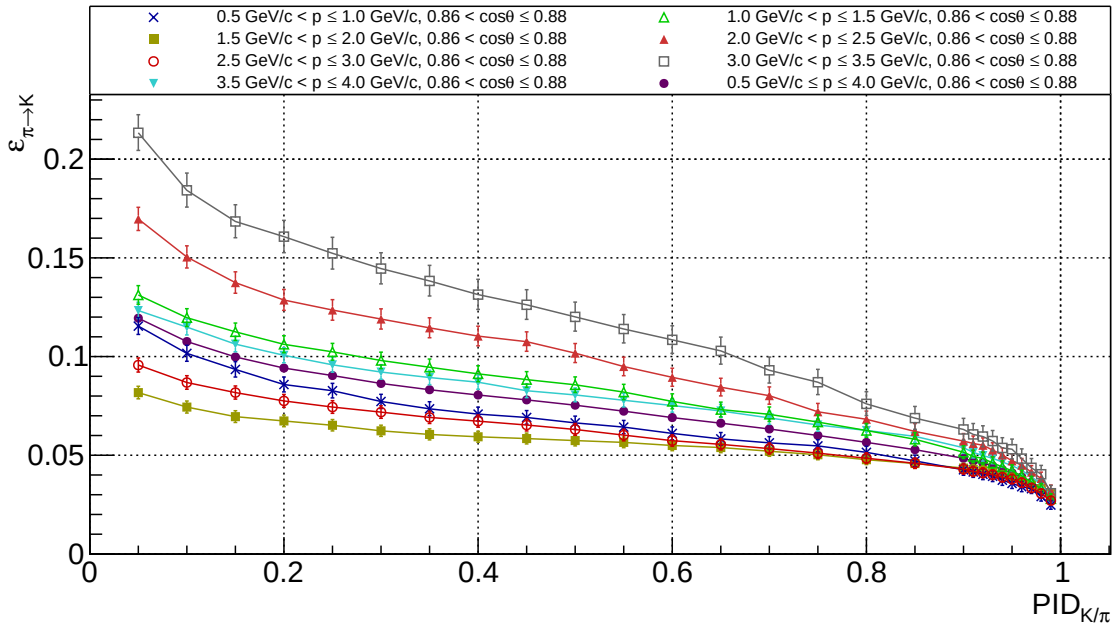

Figure F.6: Pion misidentification probabilities for momentum-angle bins xC.

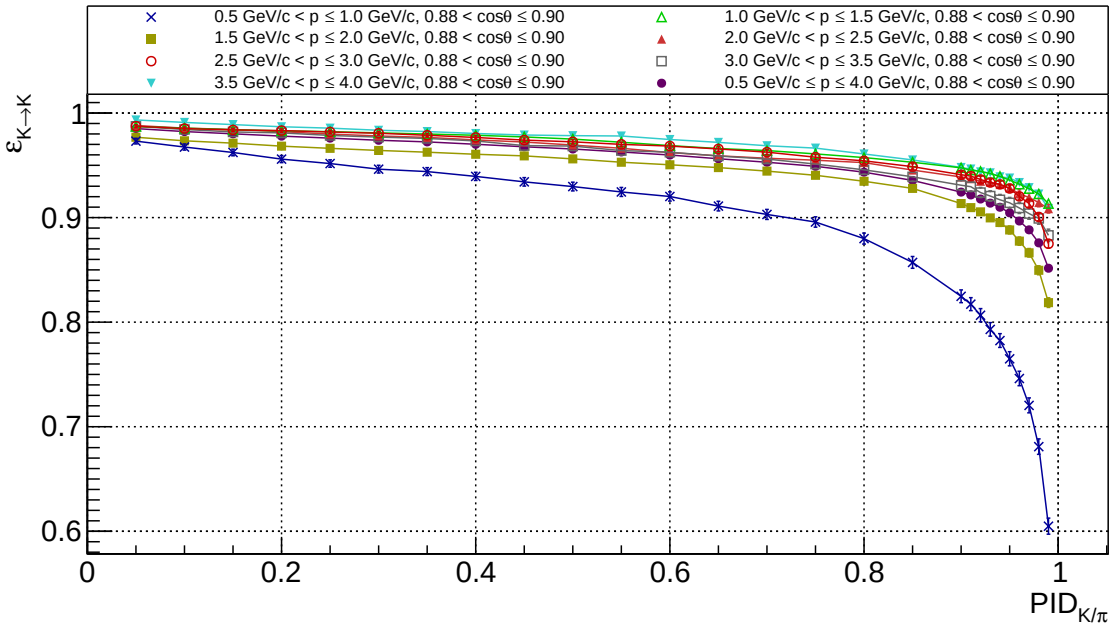

Figure F.7: Kaon identification efficiencies for momentum-angle bins xD.

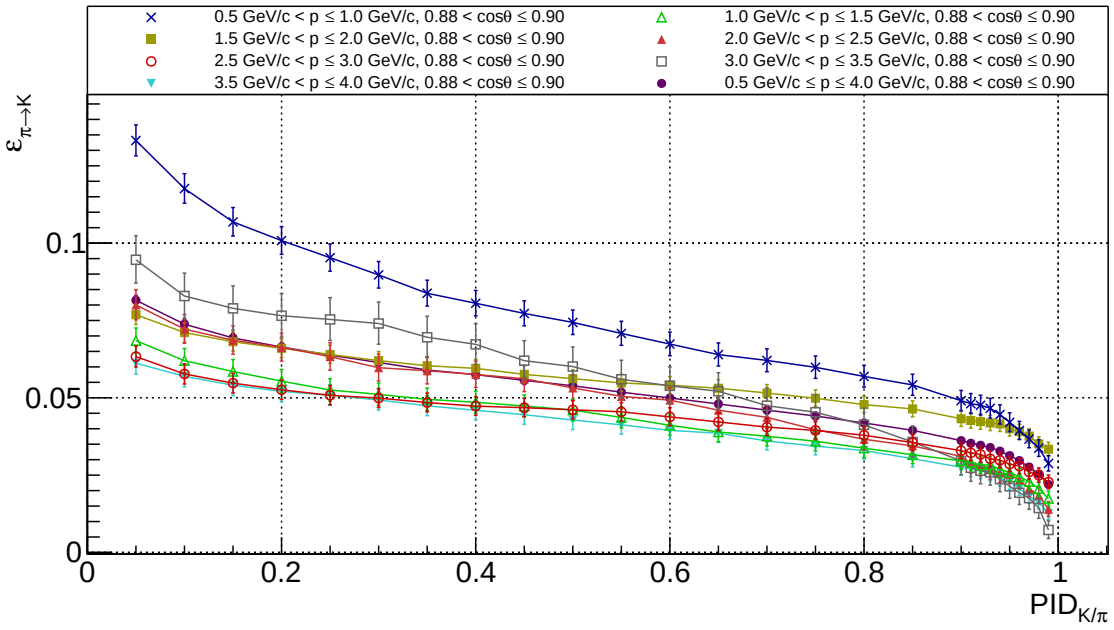

Figure F.8: Pion misidentification probabilities for momentum-angle bins xD.

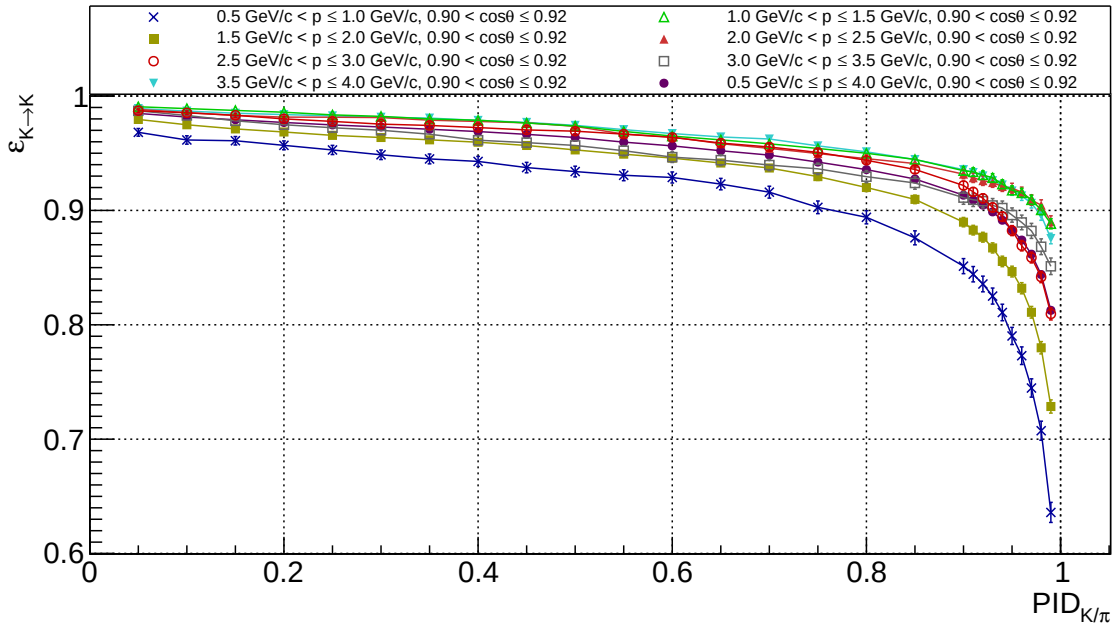

Figure F.9: Kaon identification efficiencies for momentum-angle bins xE.

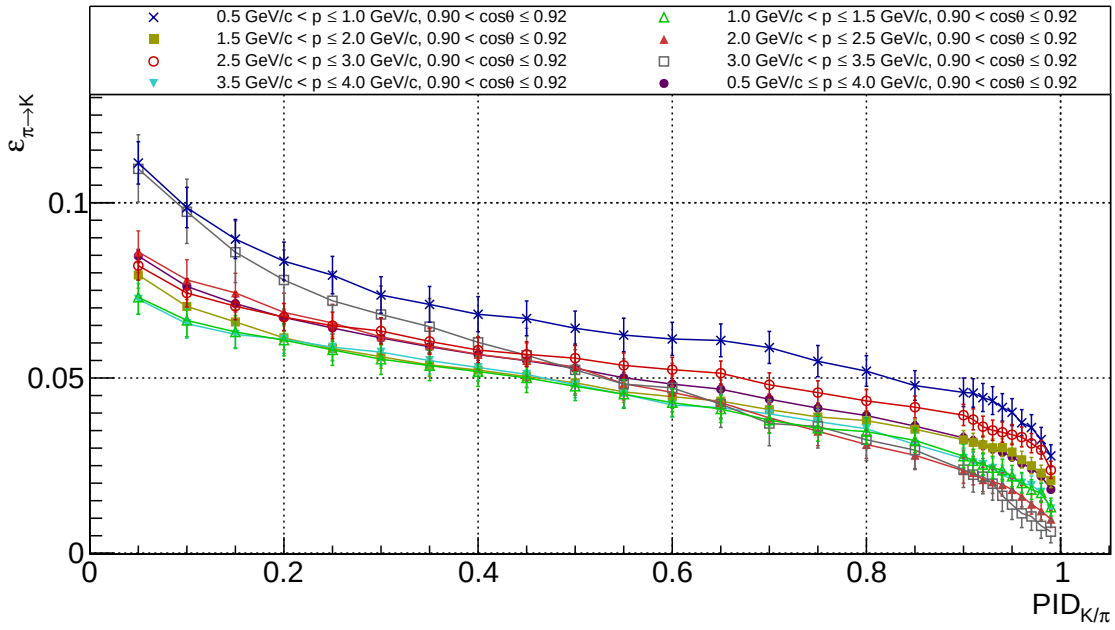

Figure F.10: Pion misidentification probabilities for momentum-angle bins xE.

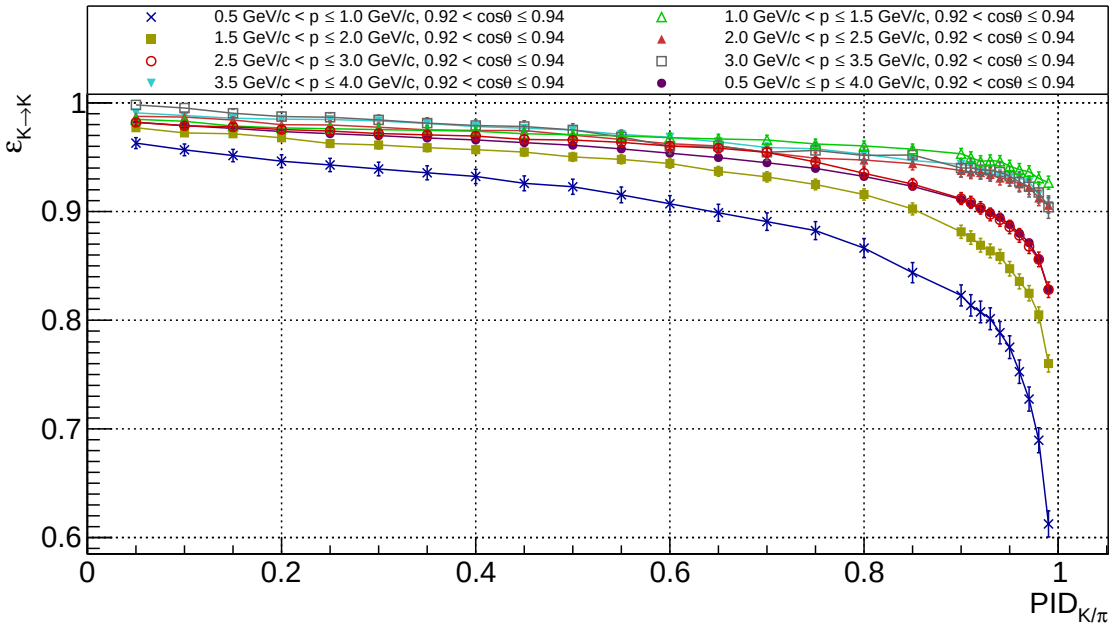

Figure F.11: Kaon identification efficiencies for momentum-angle bins xF.

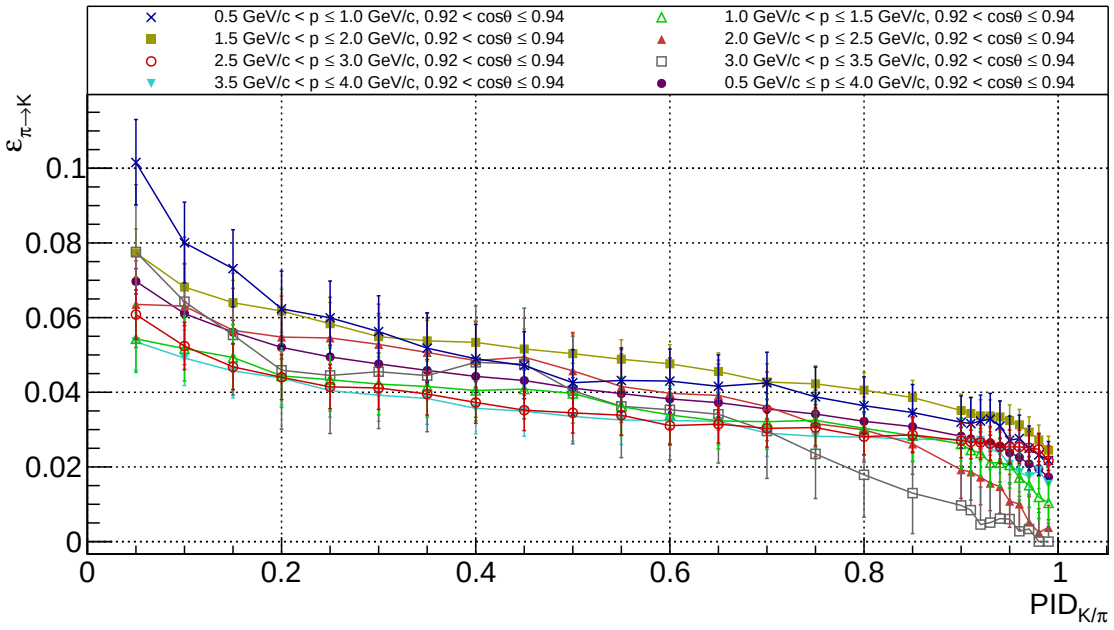

Figure F.12: Pion misidentification probabilities for momentum-angle bins xF.

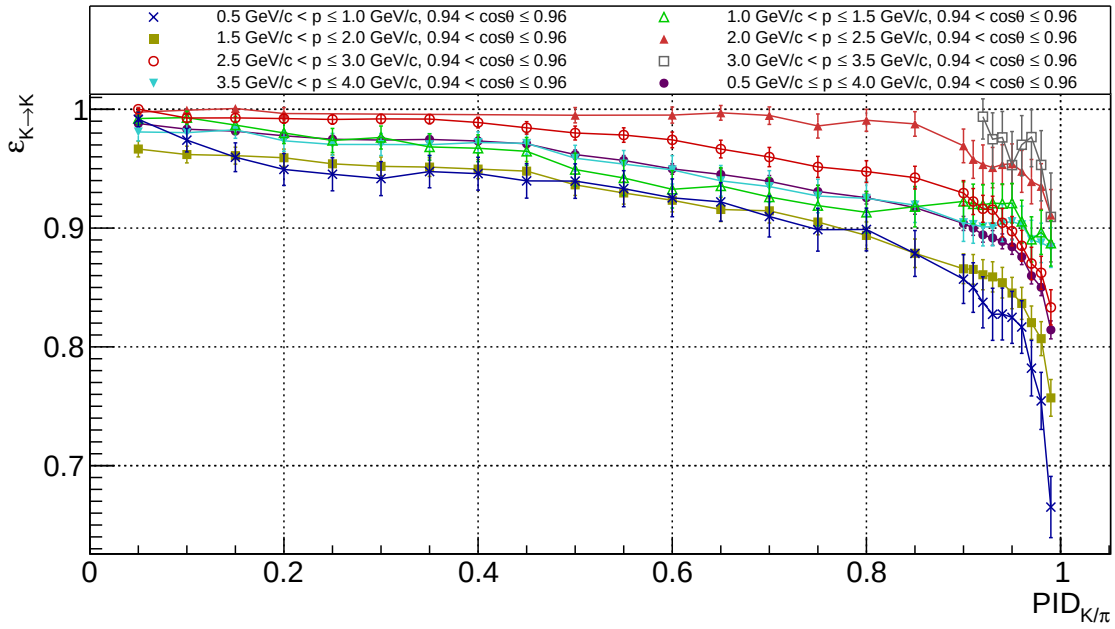

Figure F.13: Kaon identification efficiencies for momentum-angle bins xG.

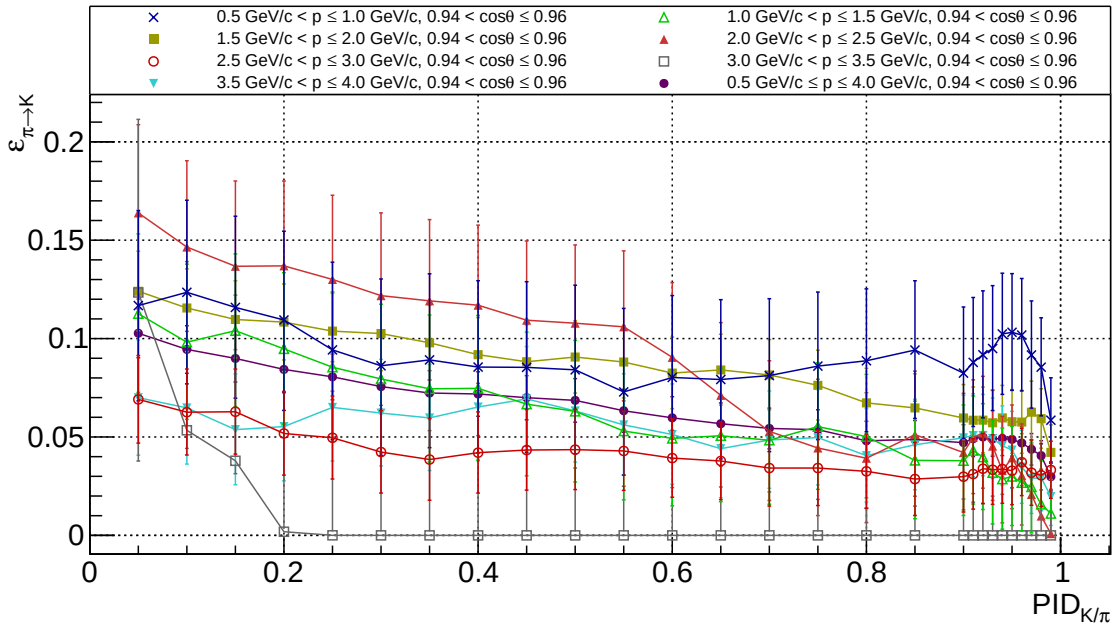

Figure F.14: Pion misidentification probabilities for momentum-angle bins xG.

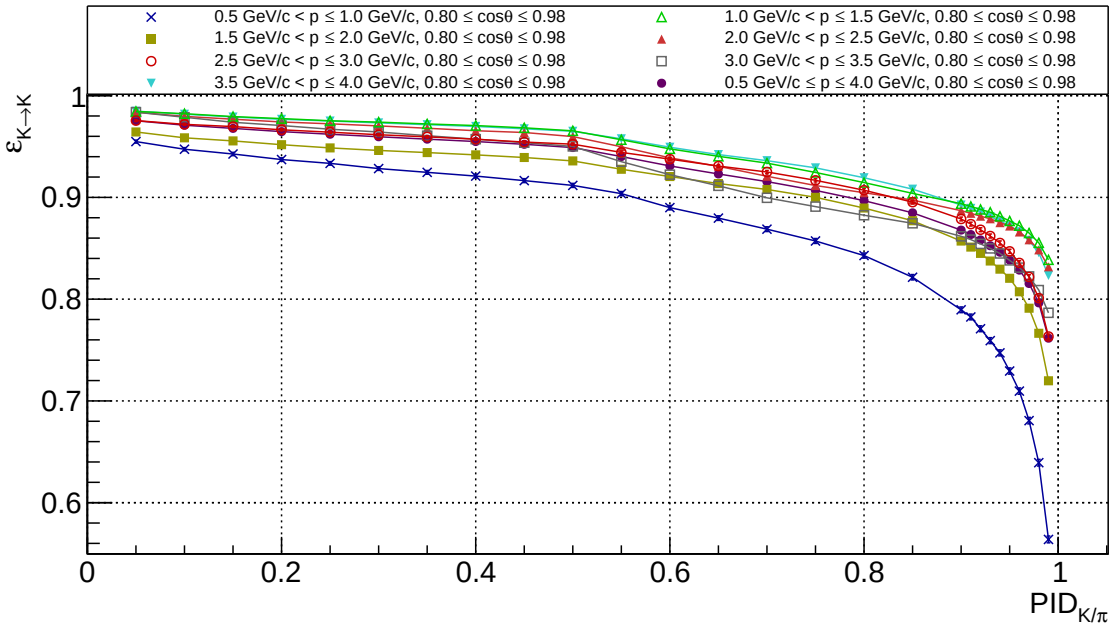

Figure F.15: Kaon identification efficiencies for momentum-angle bins xH.

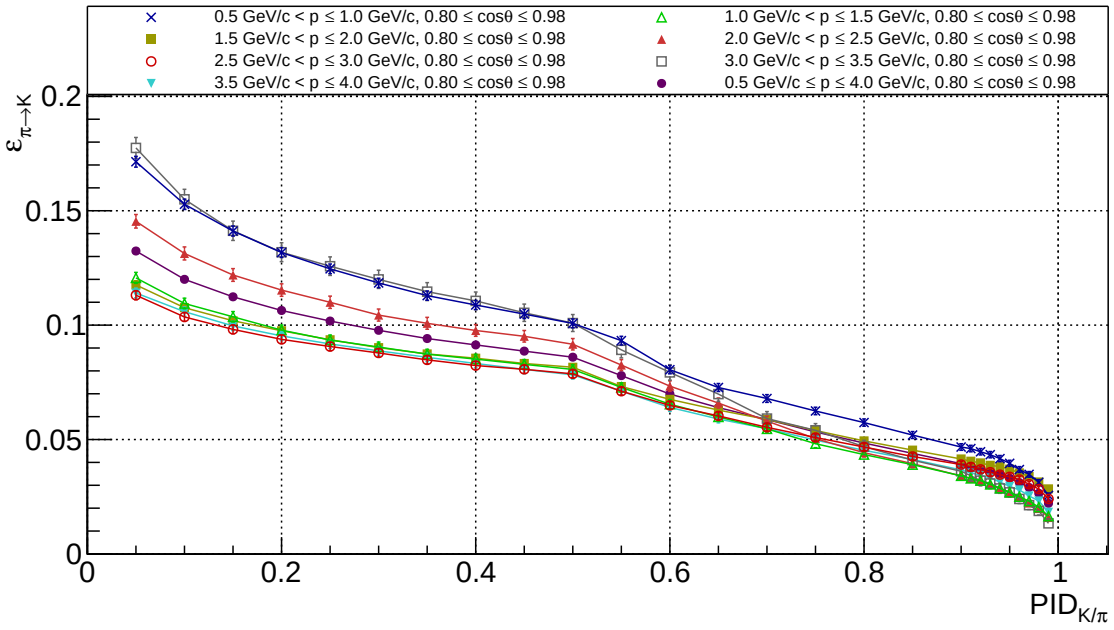

Figure F.16: Pion misidentification probabilities for momentum-angle bins xH.

F.2 Kaon identification efficiencies and pion misidentification probabilities for fine momentum binning

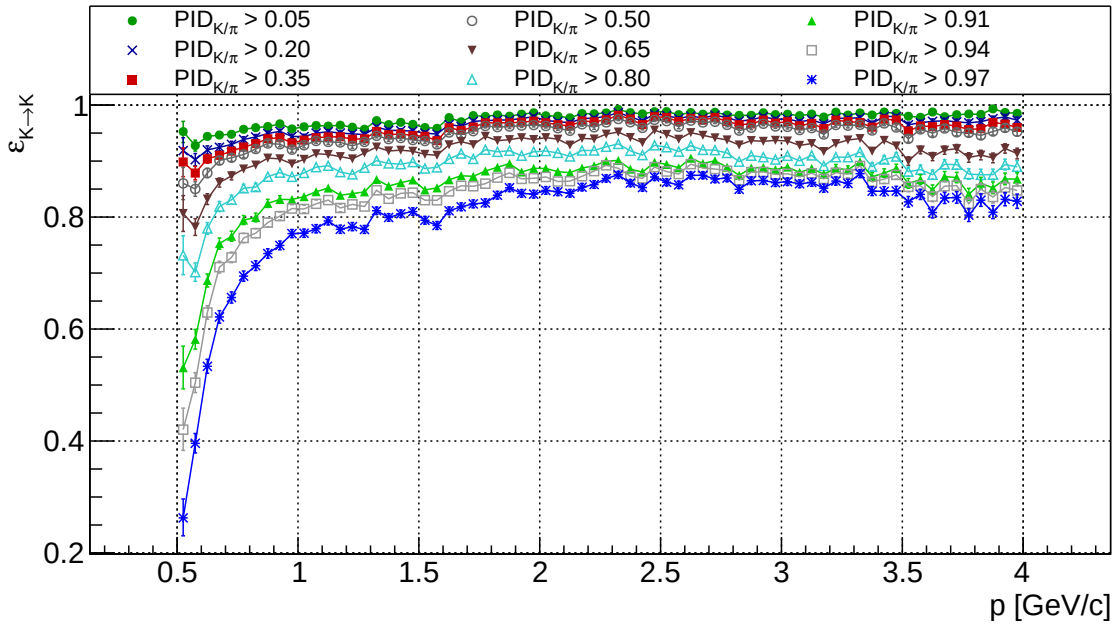

Figure F.17: Kaon identification efficiencies as a function of momentum for whole angle range and different $PID_{K/\pi}$ cuts.

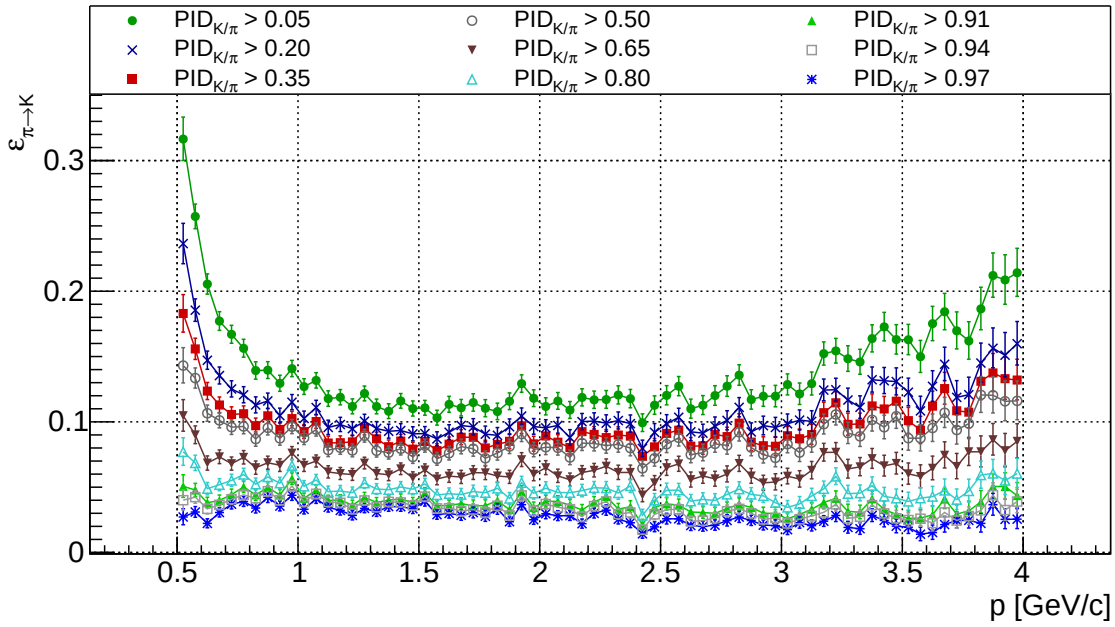

Figure F.18: Pion misidentification probabilities as a function of momentum for whole angle range and different $PID_{K/\pi}$ cuts.

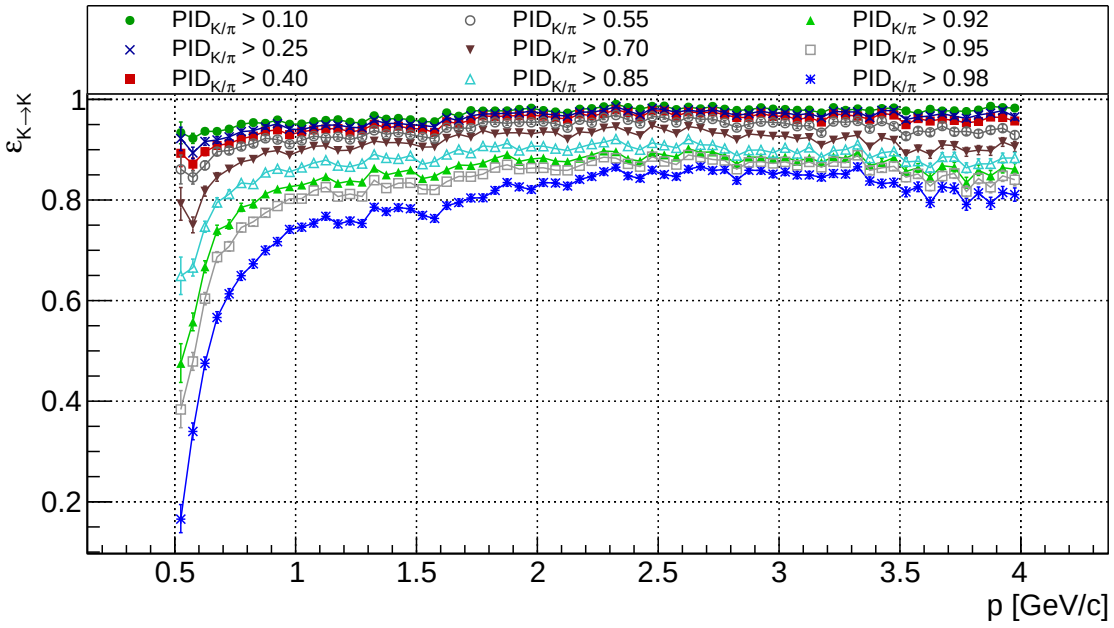

Figure F.19: Kaon identification efficiencies as a function of momentum for whole angle range and different $PID_{K/\pi}$ cuts.

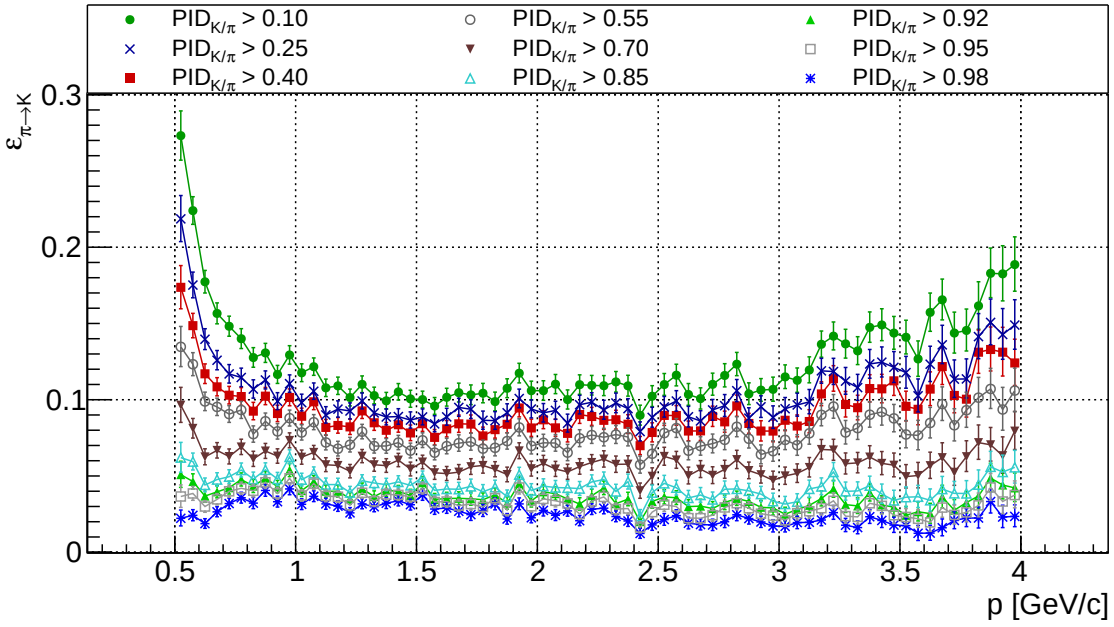

Figure F.20: Pion misidentification probabilities as a function of momentum for the entire angle range and different $PID_{K/\pi}$ cuts.

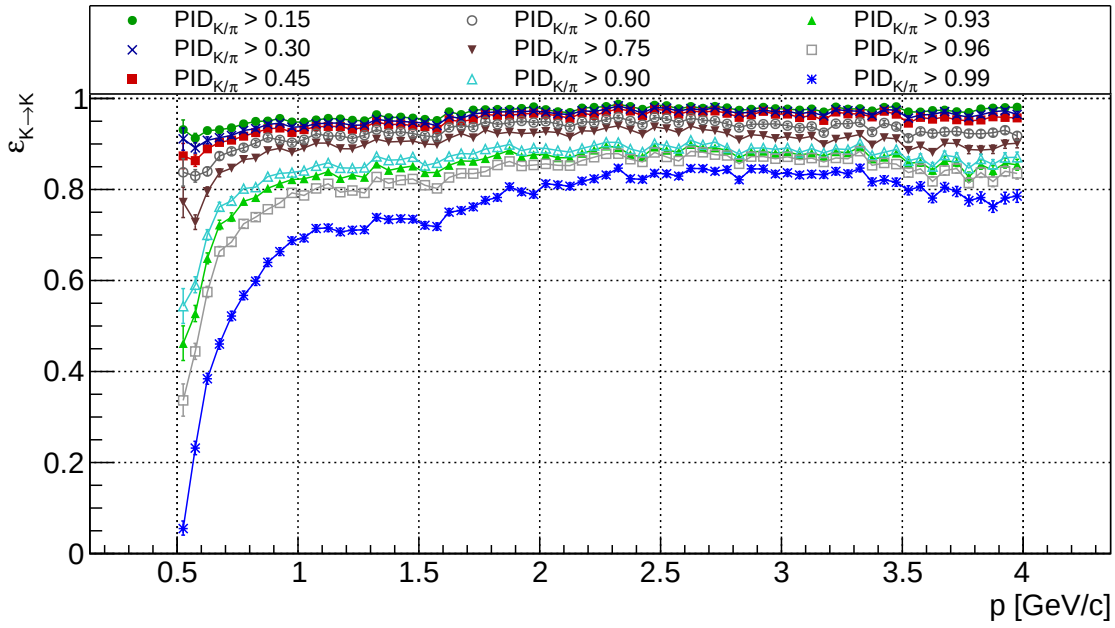

Figure F.21: Kaon identification efficiencies as a function of momentum for the entire angle range and different $PID_{K/\pi}$ cuts.

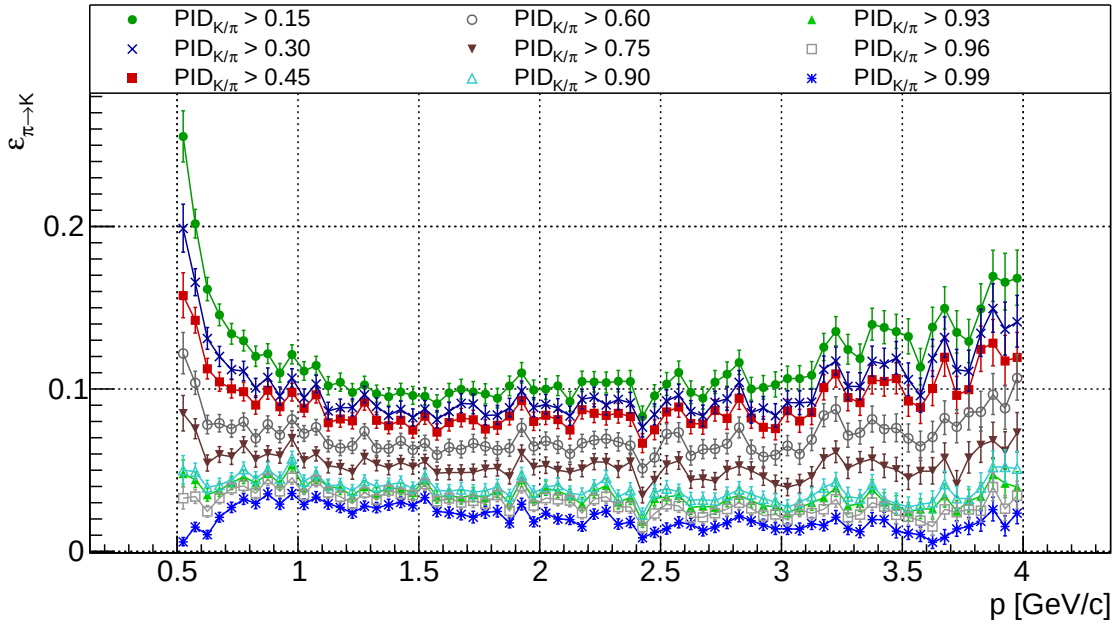

Figure F.22: Pion misidentification probabilities as a function of momentum for the entire angle range and different $PID_{K/\pi}$ cuts.

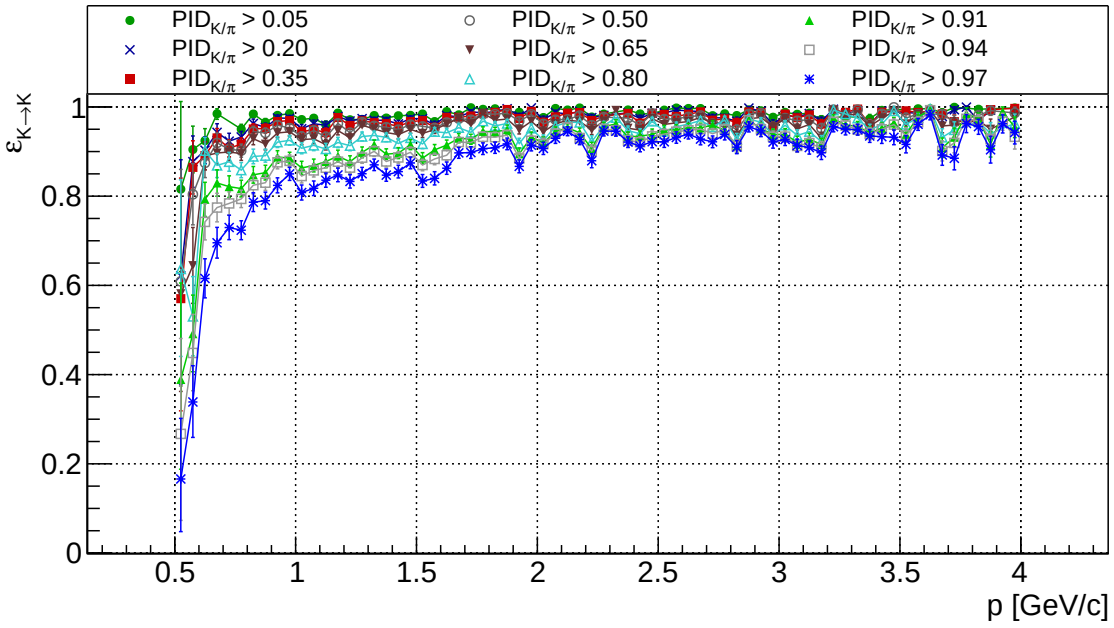

Figure F.23: Kaon identification efficiencies as a function of momentum for the incident angle range between 16.3° and 24.5° and different $PID_{K/\pi}$ cuts.

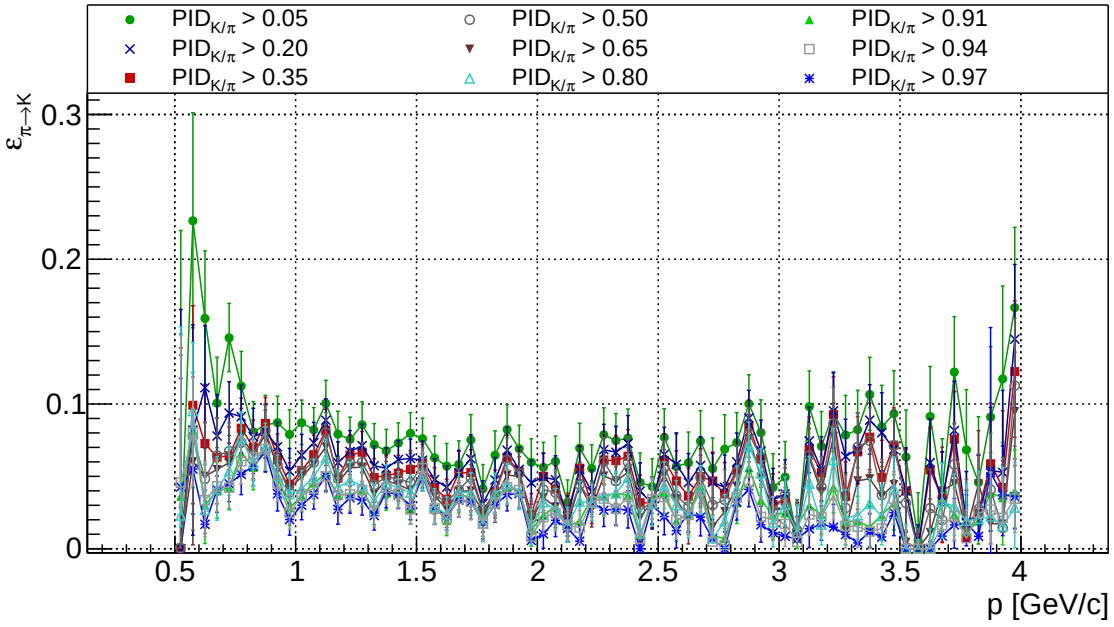

Figure F.24: Pion misidentification probabilities as a function of momentum for the incident angle range between 16.3° and 24.5° and different $PID_{K/\pi}$ cuts.

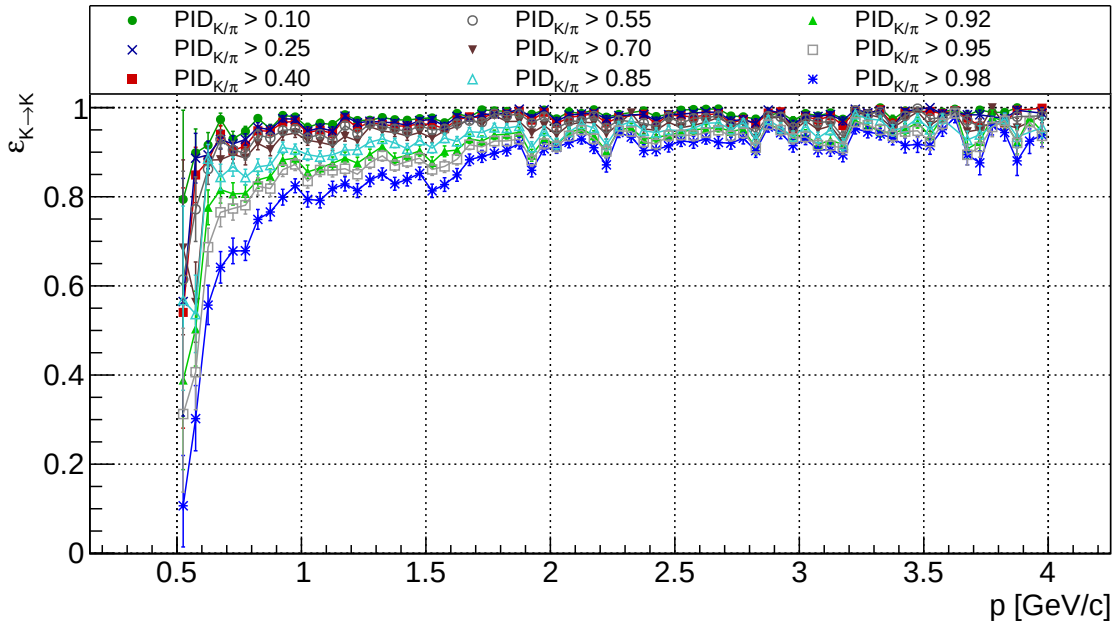

Figure F.25: Kaon identification efficiencies as a function of momentum for the incident angle range between 16.3° and 24.5° and different $PID_{K/\pi}$ cuts.

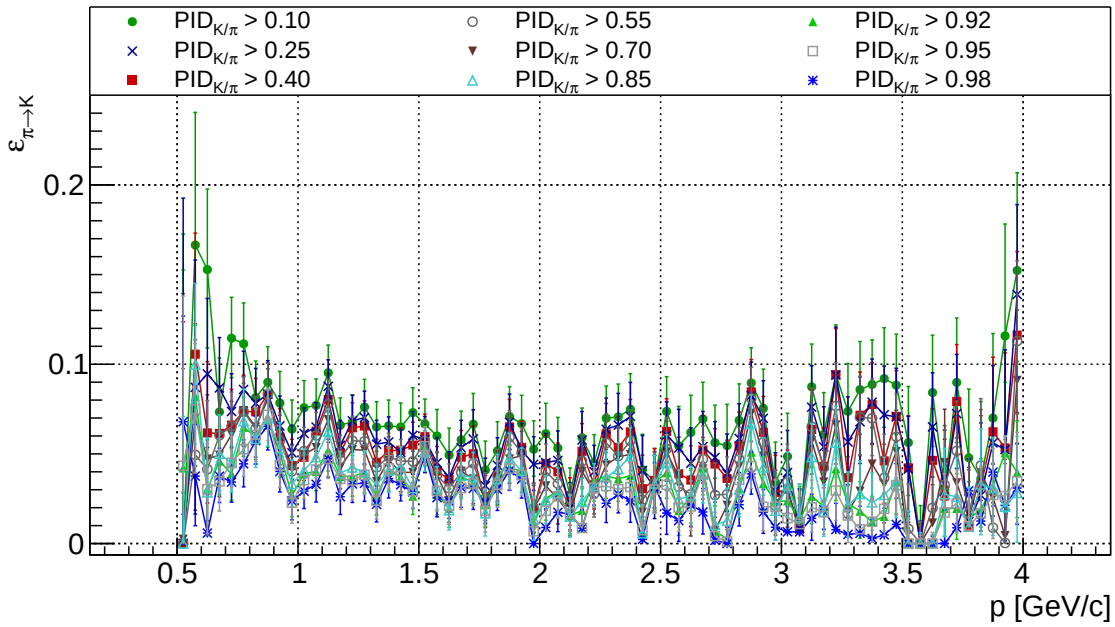

Figure F.26: Pion misidentification probabilities as a function of momentum for the incident angle range between 16.3° and 24.5° and different $PID_{K/\pi}$ cuts.

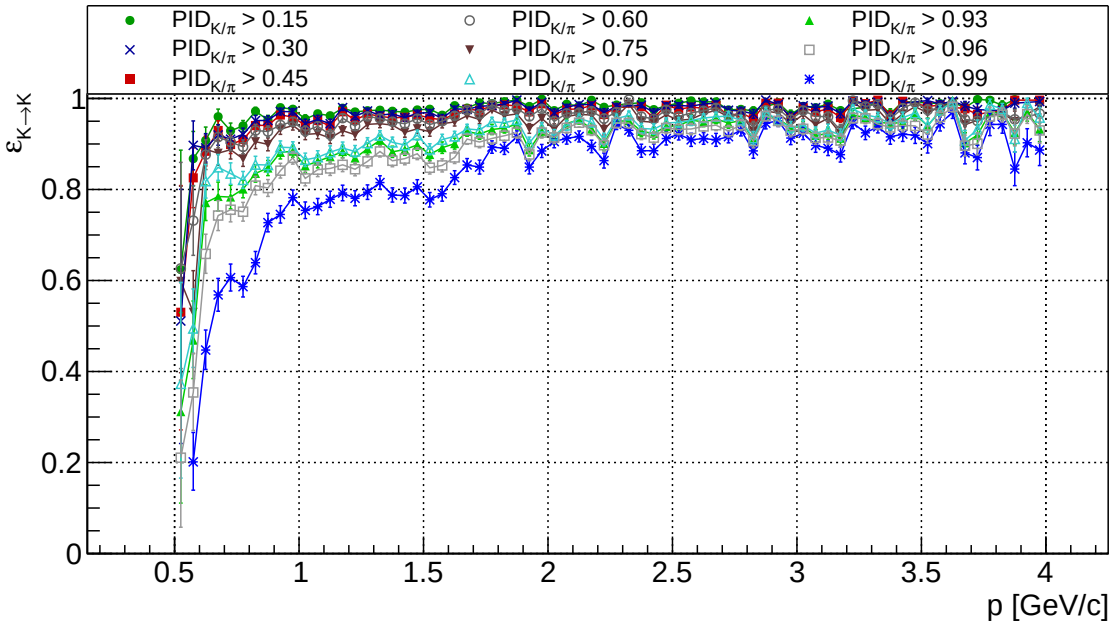

Figure F.27: Kaon identification efficiencies as a function of momentum for the incident angle range between 16.3° and 24.5° and different $PID_{K/\pi}$ cuts.

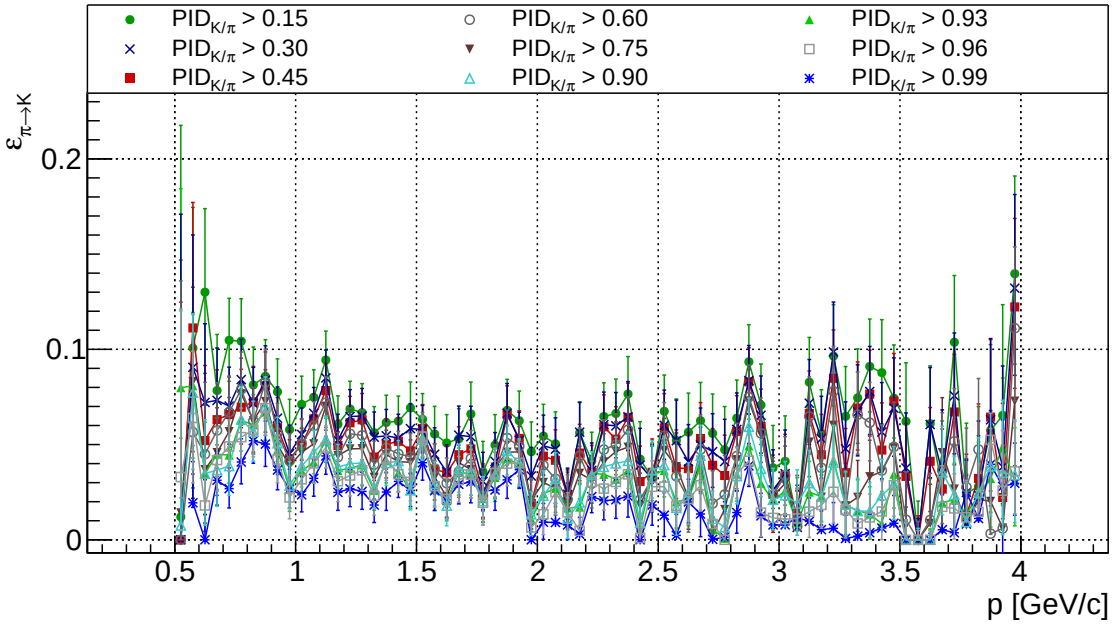

Figure F.28: Pion misidentification probabilities as a function of momentum for the incident angle range between 16.3° and 24.5° and different $PID_{K/\pi}$ cuts.

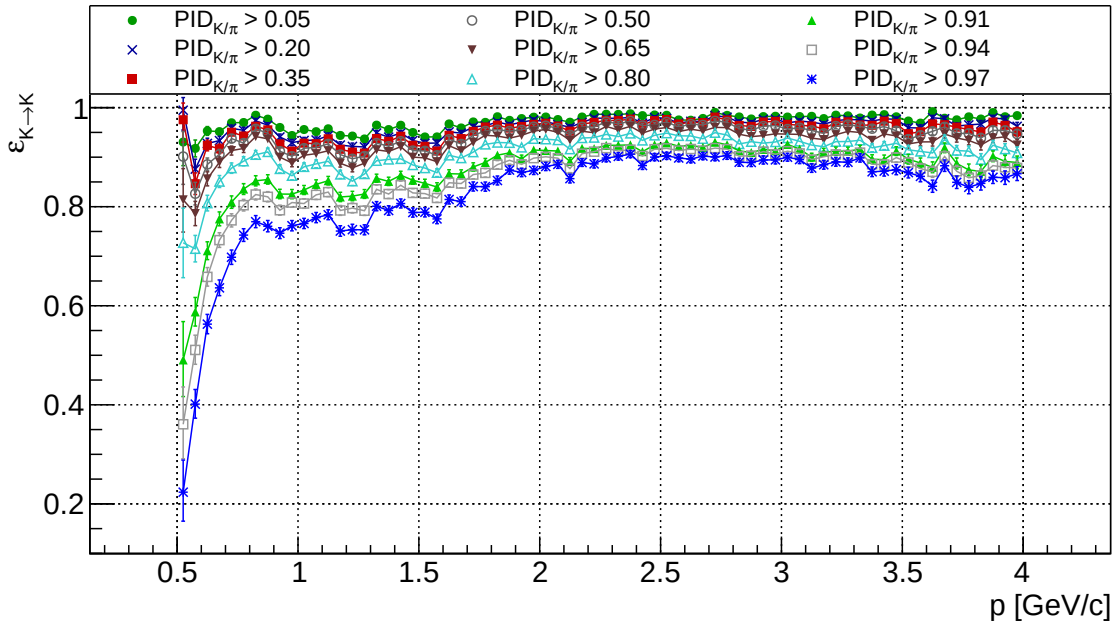

Figure F.29: Kaon identification efficiencies as a function of momentum for the incident angle range between 24.5° and 30.7° and different $PID_{K/\pi}$ cuts.

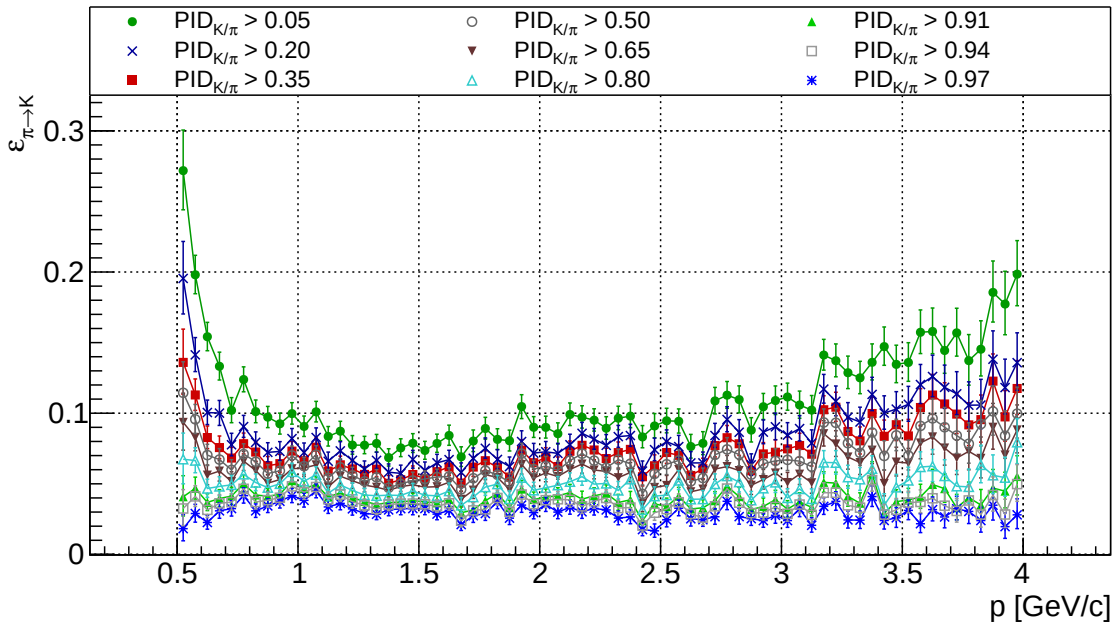

Figure F.30: Pion misidentification probabilities as a function of momentum for the incident angle range between 24.5° and 30.7° and different $PID_{K/\pi}$ cuts.

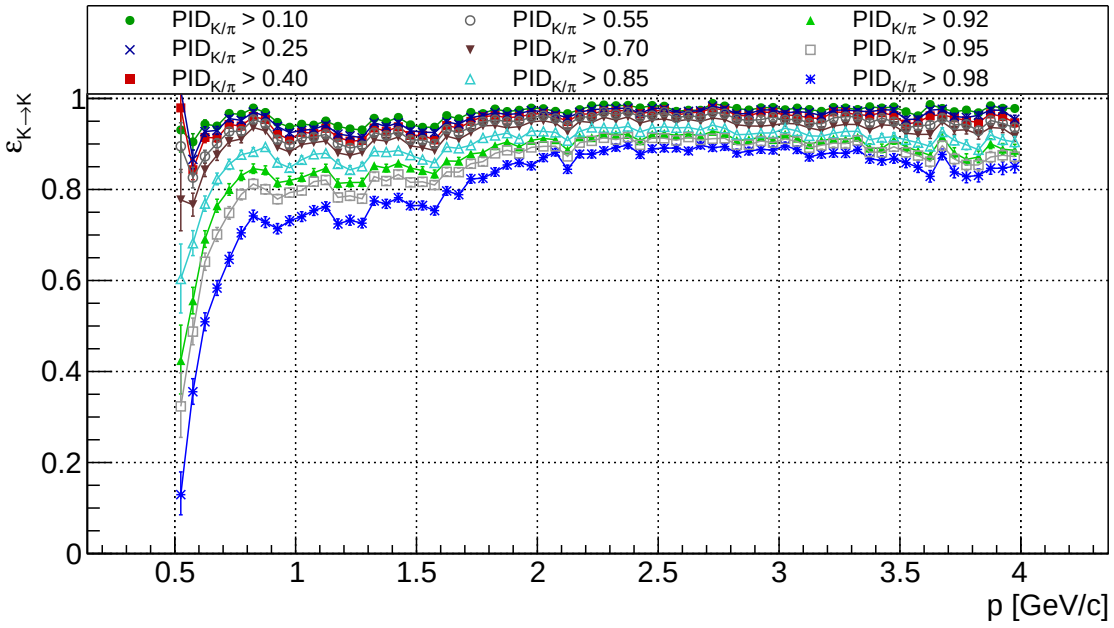

Figure F.31: Kaon identification efficiencies as a function of momentum for the incident angle range between 24.5° and 30.7° and different $PID_{K/\pi}$ cuts.

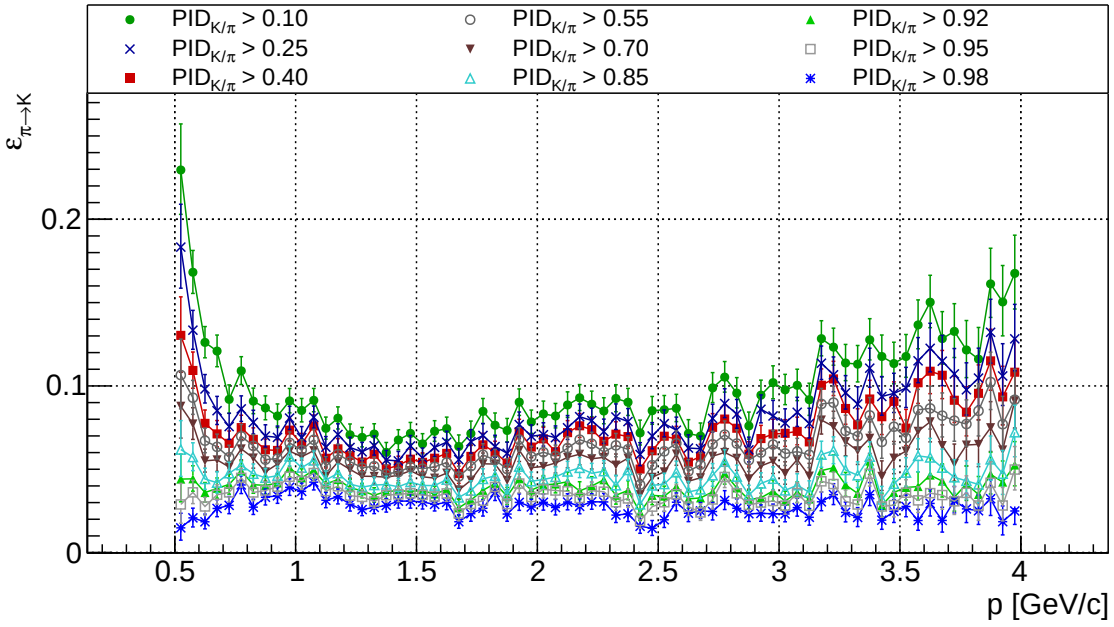

Figure F.32: Pion misidentification probabilities as a function of momentum for the incident angle range between 24.5° and 30.7° and different $PID_{K/\pi}$ cuts.

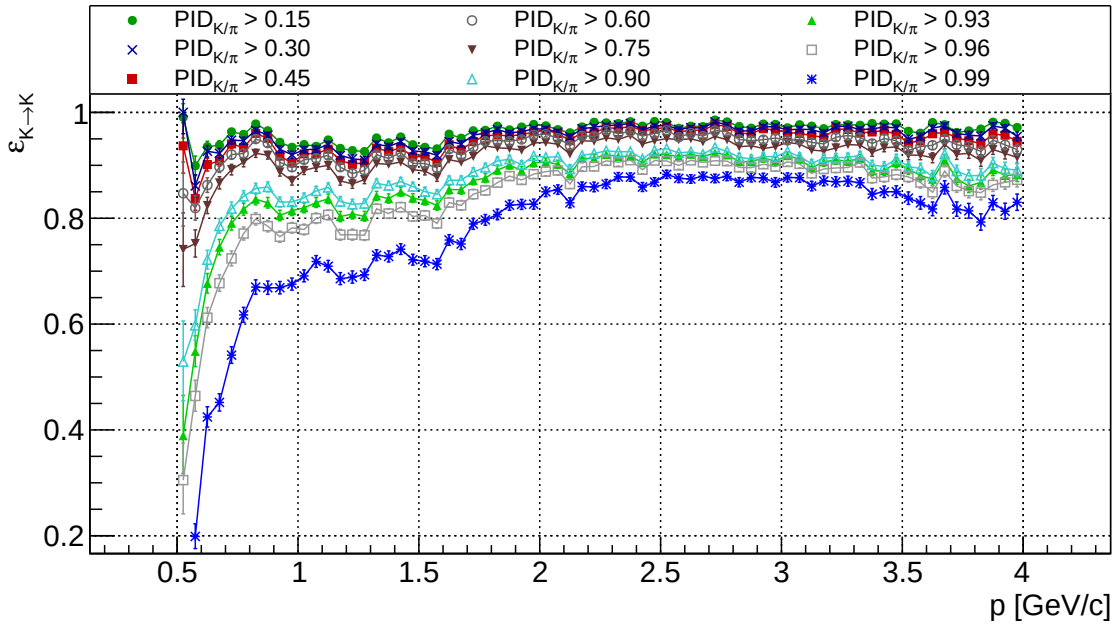

Figure F.33: Kaon identification efficiencies as a function of momentum for the incident angle range between 24.5° and 30.7° and different $PID_{K/\pi}$ cuts.

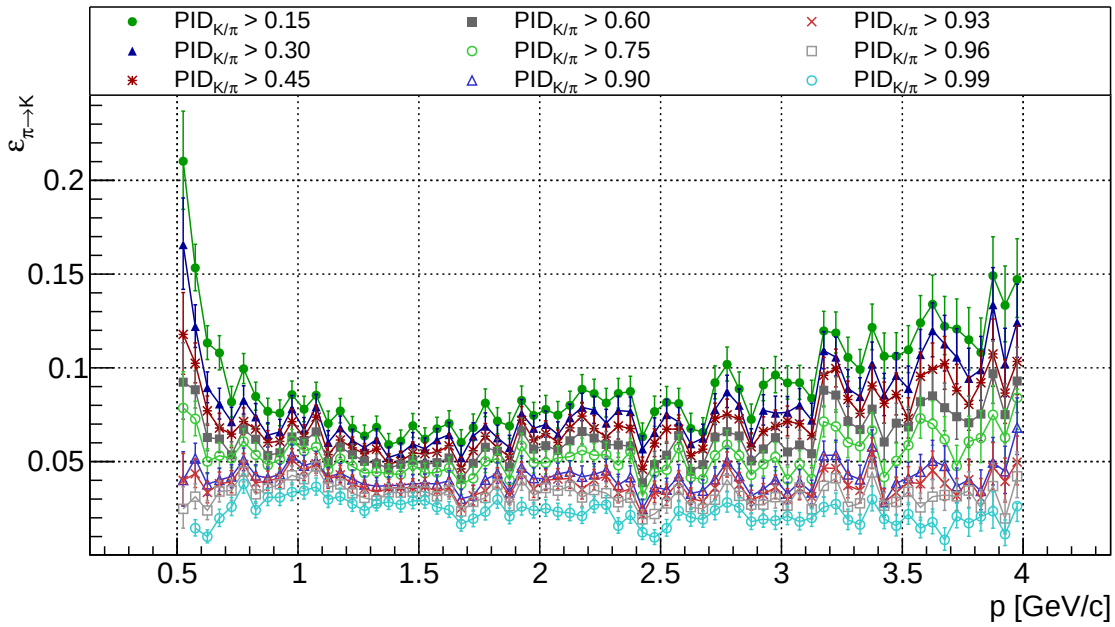

Figure F.34: Pion misidentification probabilities as a function of momentum for the incident angle range between 24.5° and 30.7° and different $PID_{K/\pi}$ cuts.

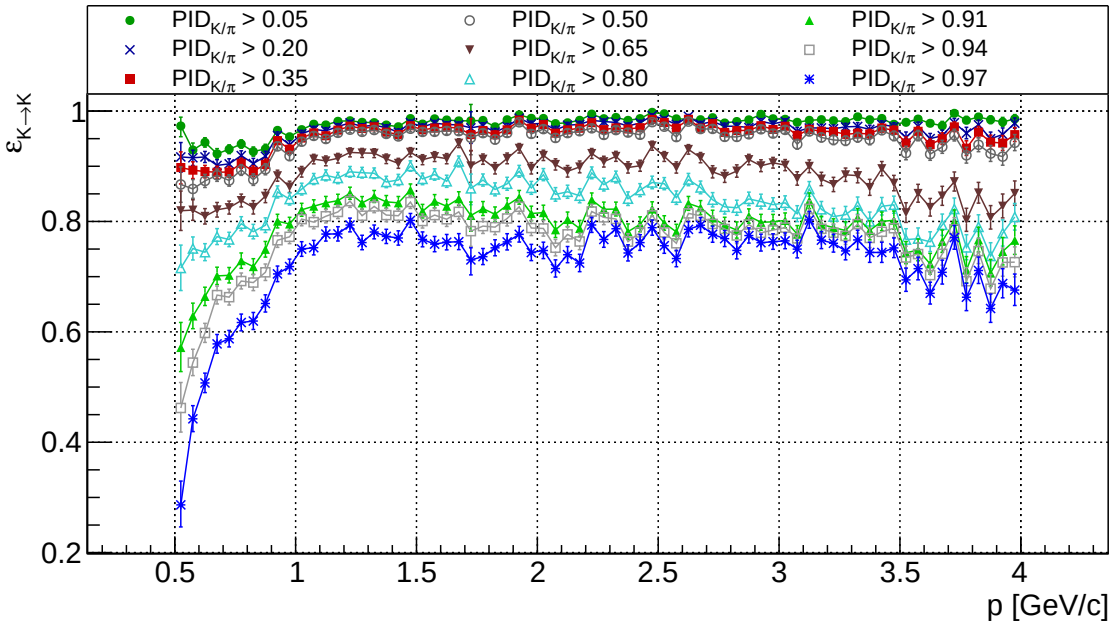

Figure F.35: Kaon identification efficiencies as a function of momentum for the incident angle range between 30.7° and 35.9° and different $PID_{K/\pi}$ cuts.

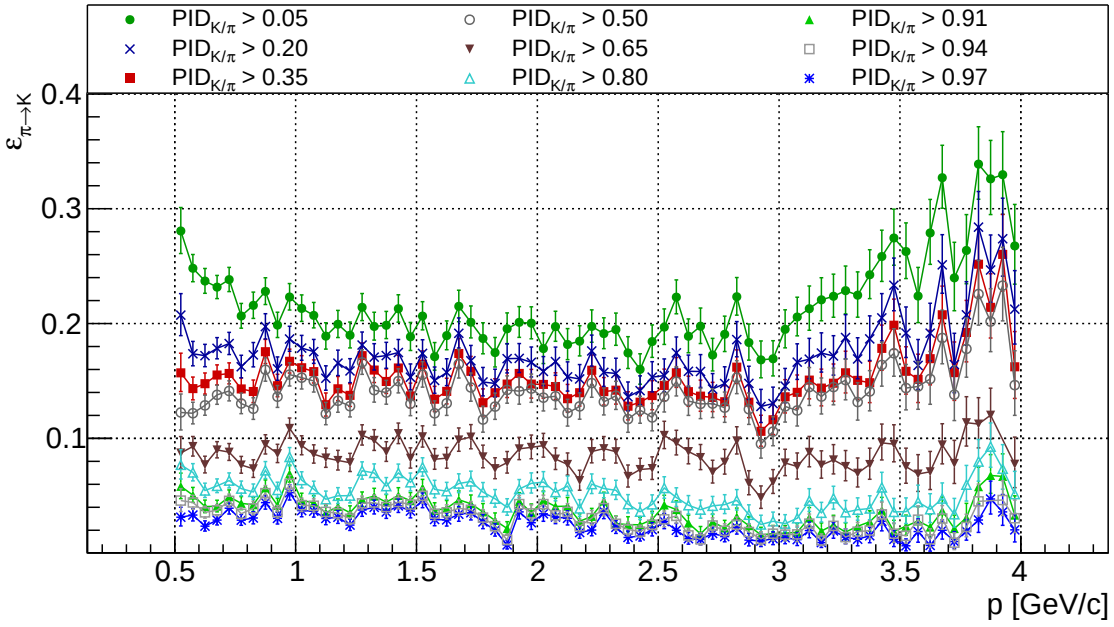

Figure F.36: Pion misidentification probabilities as a function of momentum for the incident angle range between 30.7° and 35.9° and different $PID_{K/\pi}$ cuts.

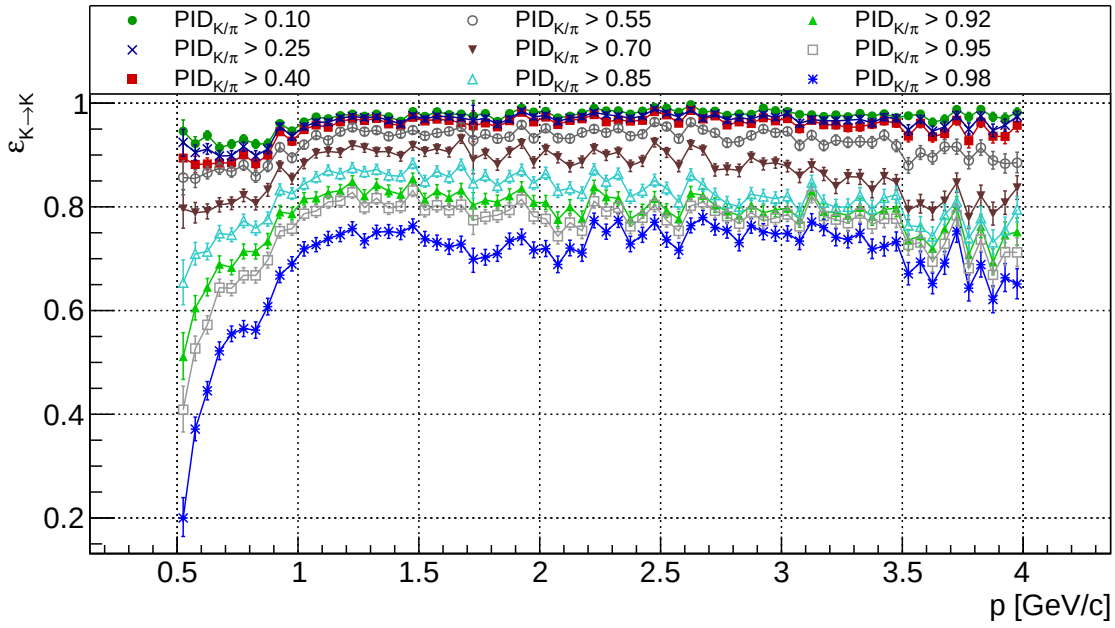

Figure F.37: Kaon identification efficiencies as a function of momentum for the incident angle range between 30.7° and 35.9° and different $PID_{K/\pi}$ cuts.

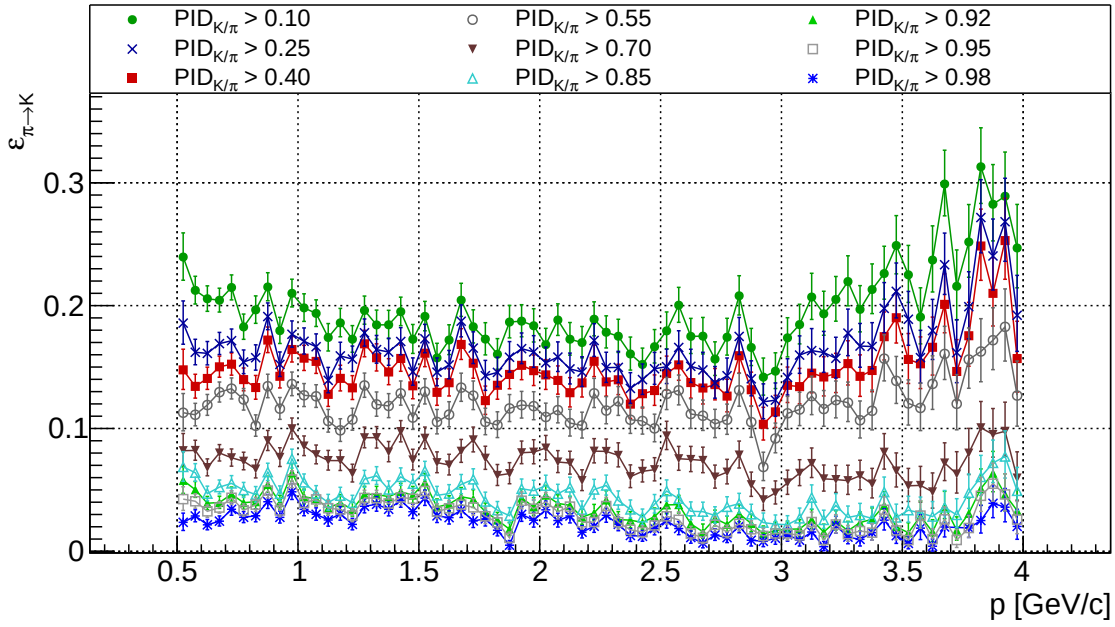

Figure F.38: Pion misidentification probabilities as a function of momentum for the incident angle range between 30.7° and 35.9° and different $PID_{K/\pi}$ cuts.

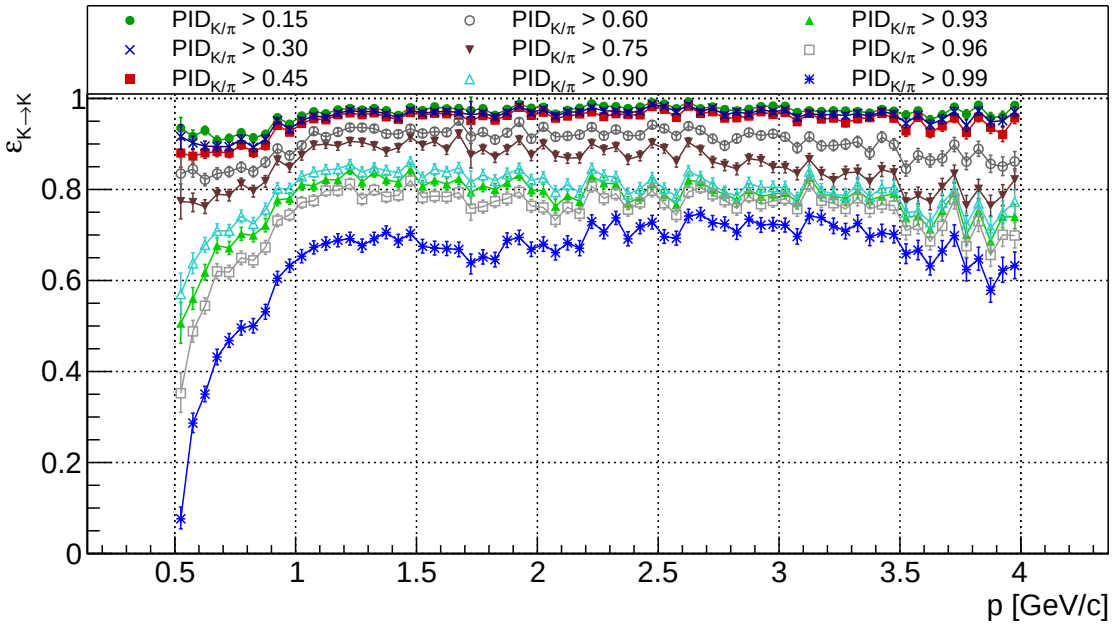

Figure F.39: Kaon identification efficiencies as a function of momentum for the incident angle range between 30.7° and 35.9° and different $PID_{K/\pi}$ cuts.

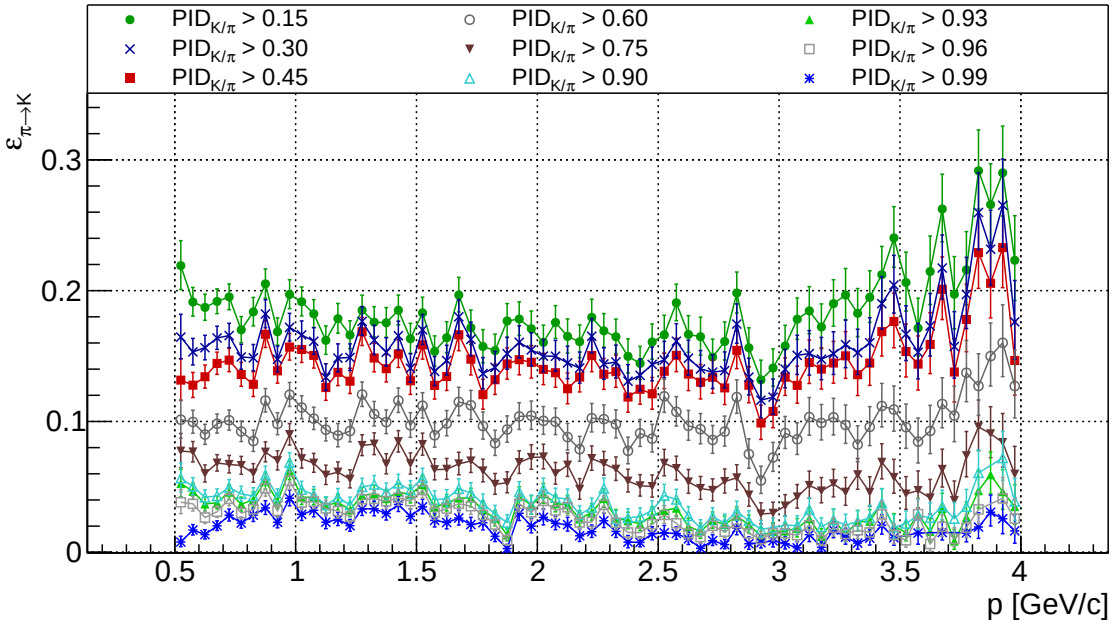

Figure F.40: Pion misidentification probabilities as a function of momentum for the incident angle range between 30.7° and 35.9° and different $PID_{K/\pi}$ cuts.

F.3 Kaon identification efficiencies and pion misidentification probabilities for fine particle's incident angle binning

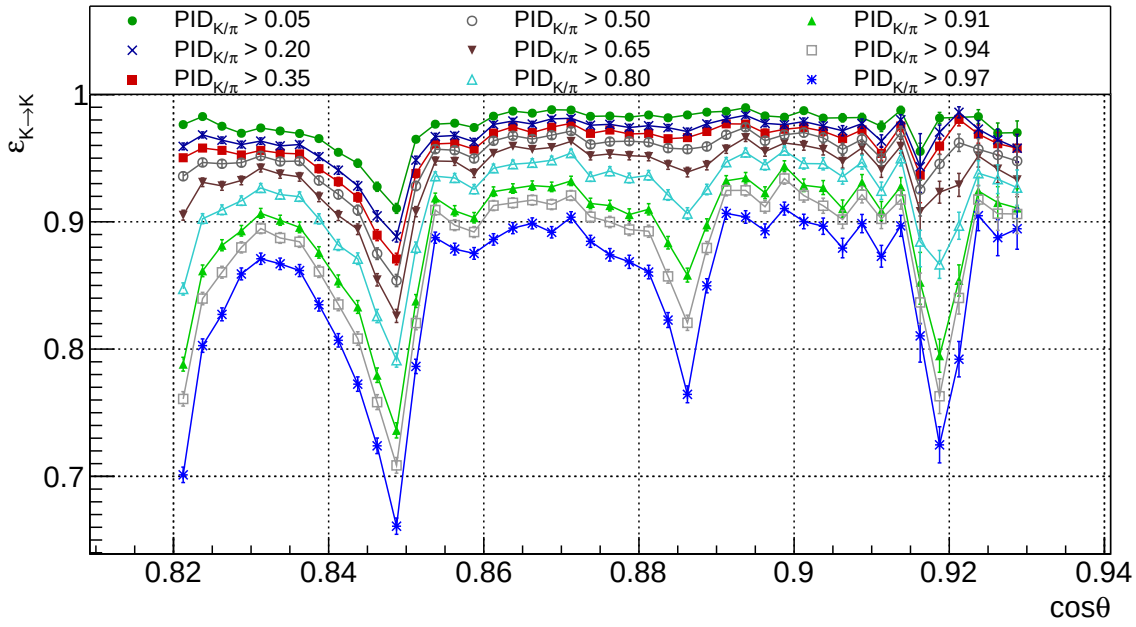

Figure F.41: Kaon identification efficiencies as a function of particle's incident angle for the entire momentum range and different $PID_{K/\pi}$ cuts.

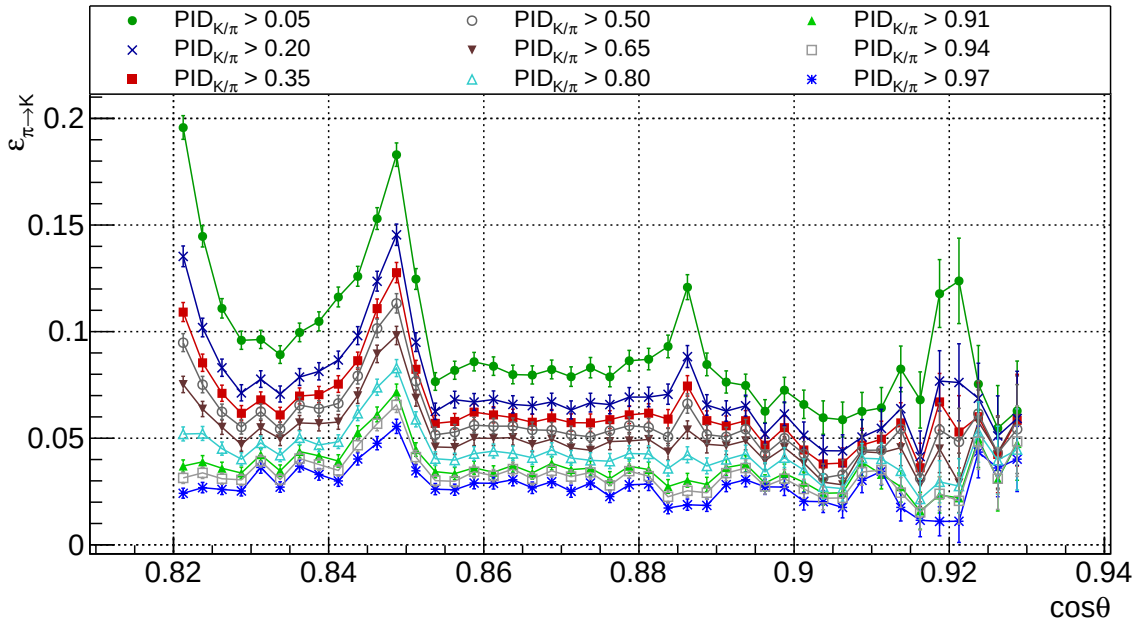

Figure F.42: Pion misidentification probabilities as a function of particle's incident angle for the entire momentum range and different $PID_{K/\pi}$ cuts.

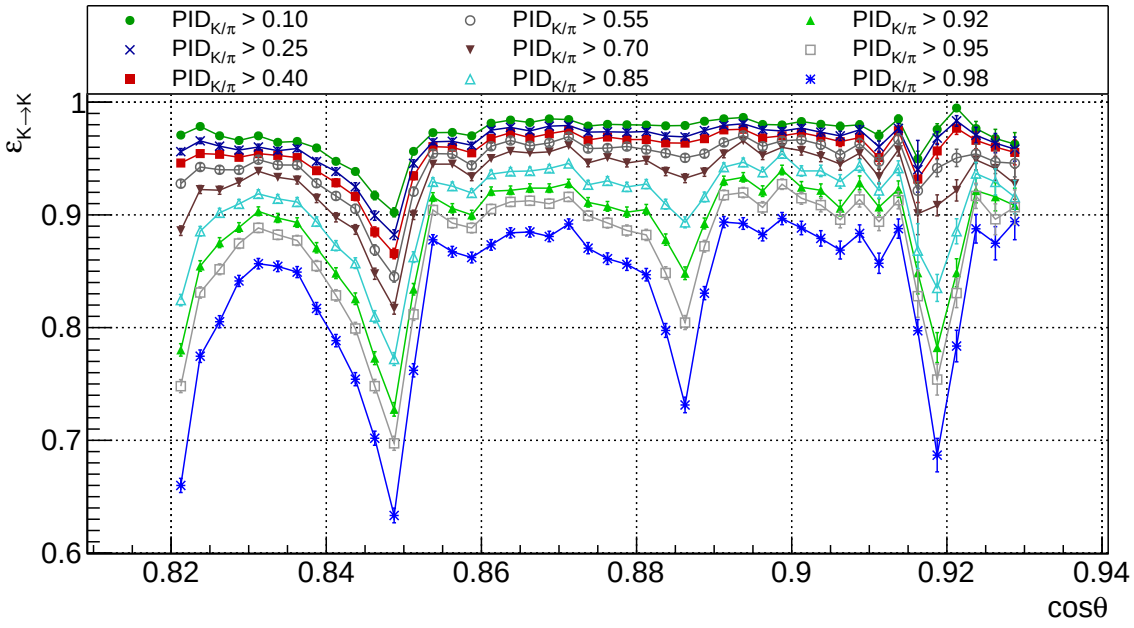

Figure F.43: Kaon identification efficiencies as a function of particle's incident angle for the entire momentum range and different $PID_{K/\pi}$ cuts.

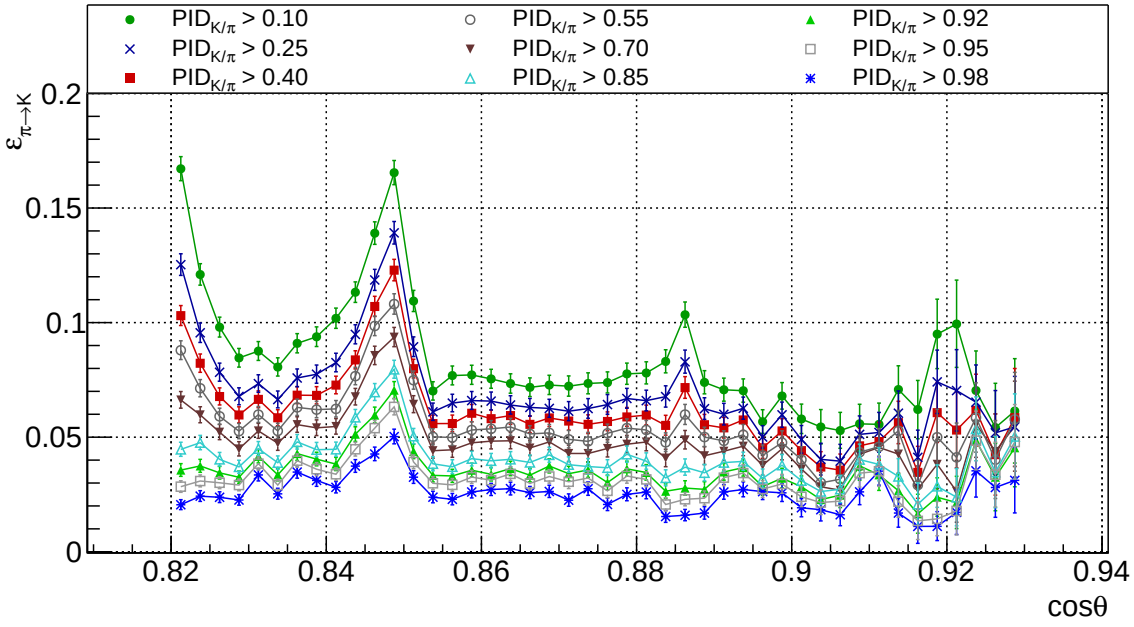

Figure F.44: Pion misidentification probabilities as a function of particle's incident angle for the entire momentum range and different $PID_{K/\pi}$ cuts.

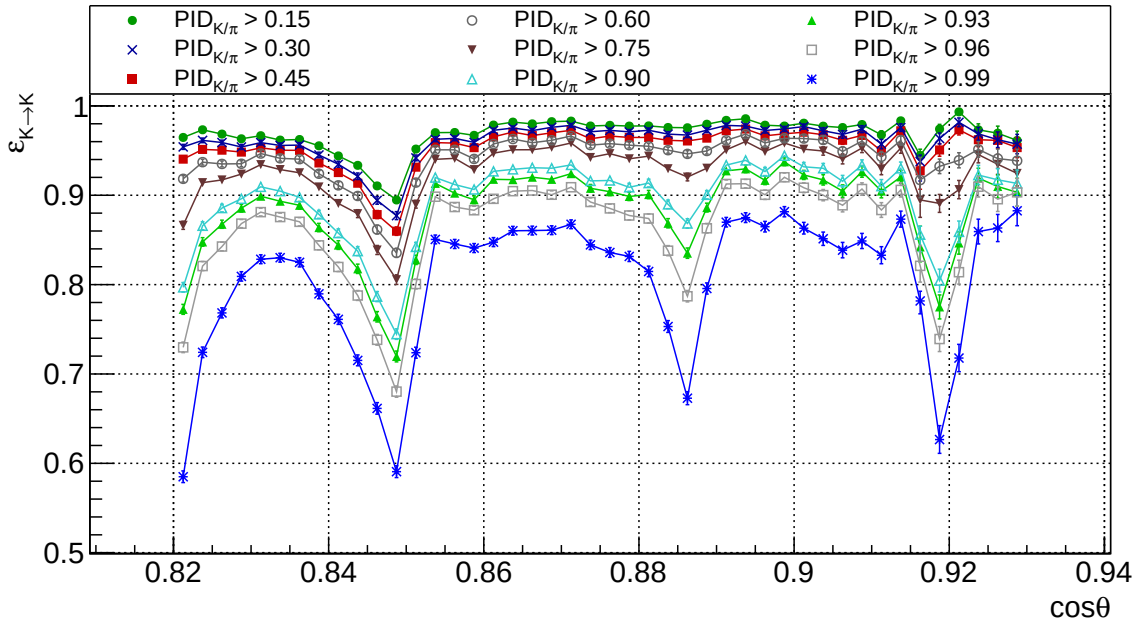

Figure F.45: Kaon identification efficiencies as a function of particle's incident angle for the entire momentum range and different $PID_{K/\pi}$ cuts.

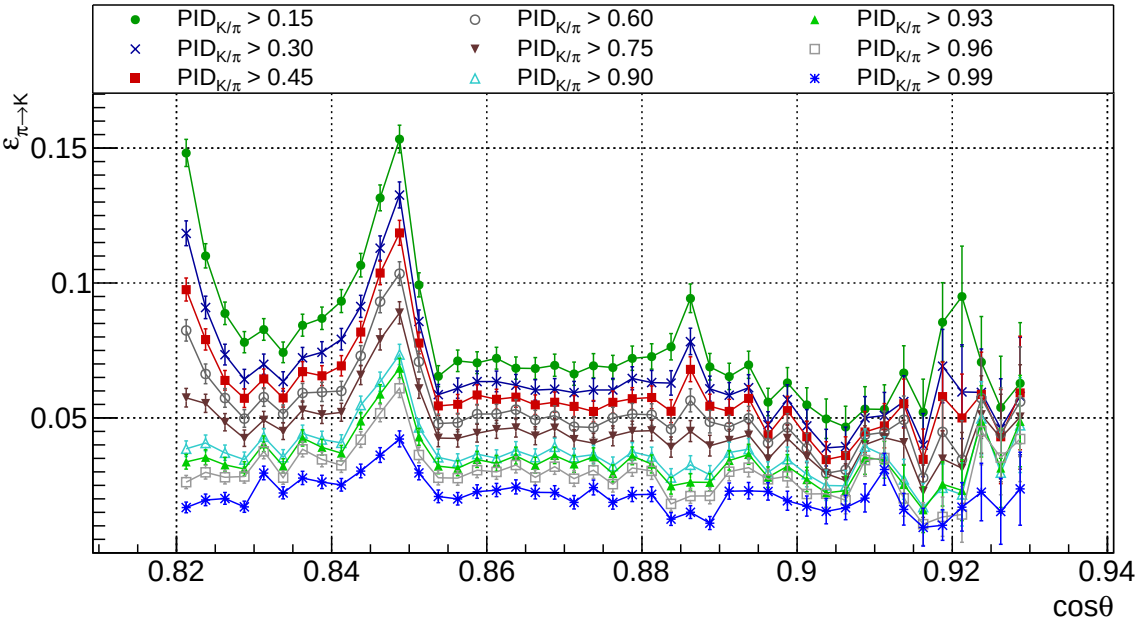

Figure F.46: Pion misidentification probabilities as a function of particle's incident angle for the entire momentum range and different $PID_{K/\pi}$ cuts.

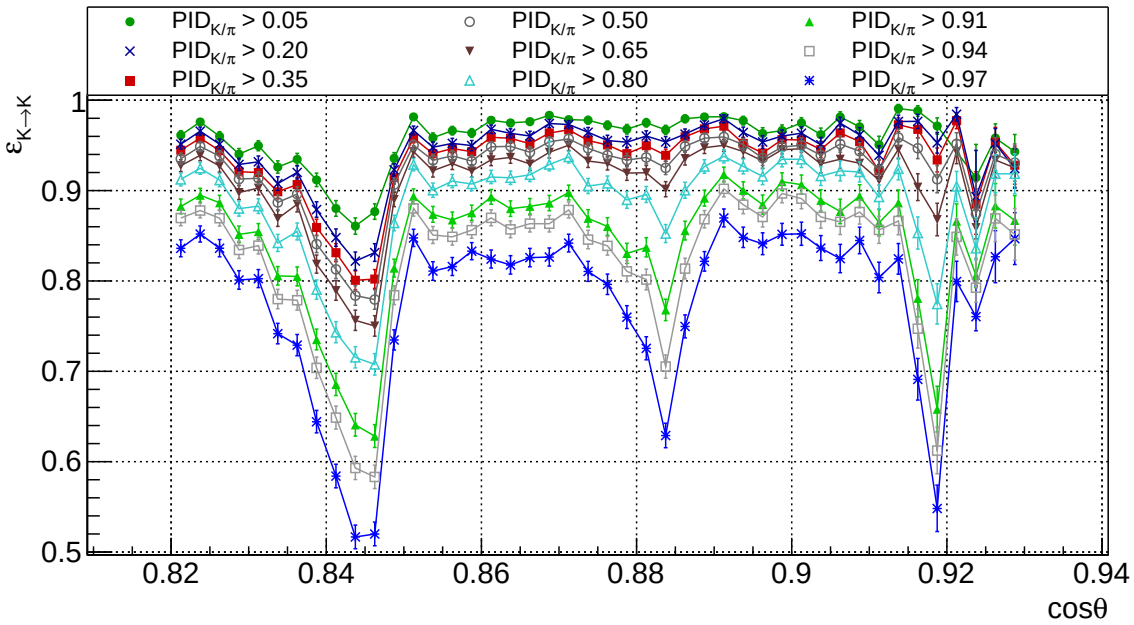

Figure F.47: Kaon identification efficiencies as a function of particle's incident angle for the momentum range between 0.5 GeV/c and 1.5 GeV/c and different $PID_{K/\pi}$ cuts.

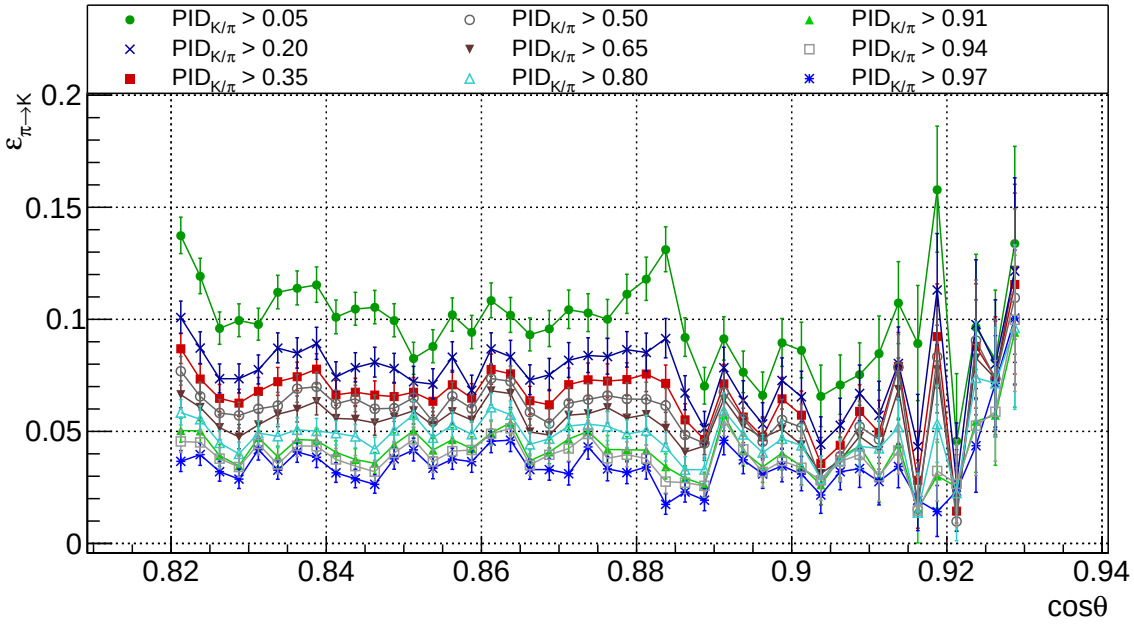

Figure F.48: Pion misidentification probabilities as a function of particle's incident angle for the momentum range between 0.5 GeV/c and 1.5 GeV/c and different $PID_{K/\pi}$ cuts.

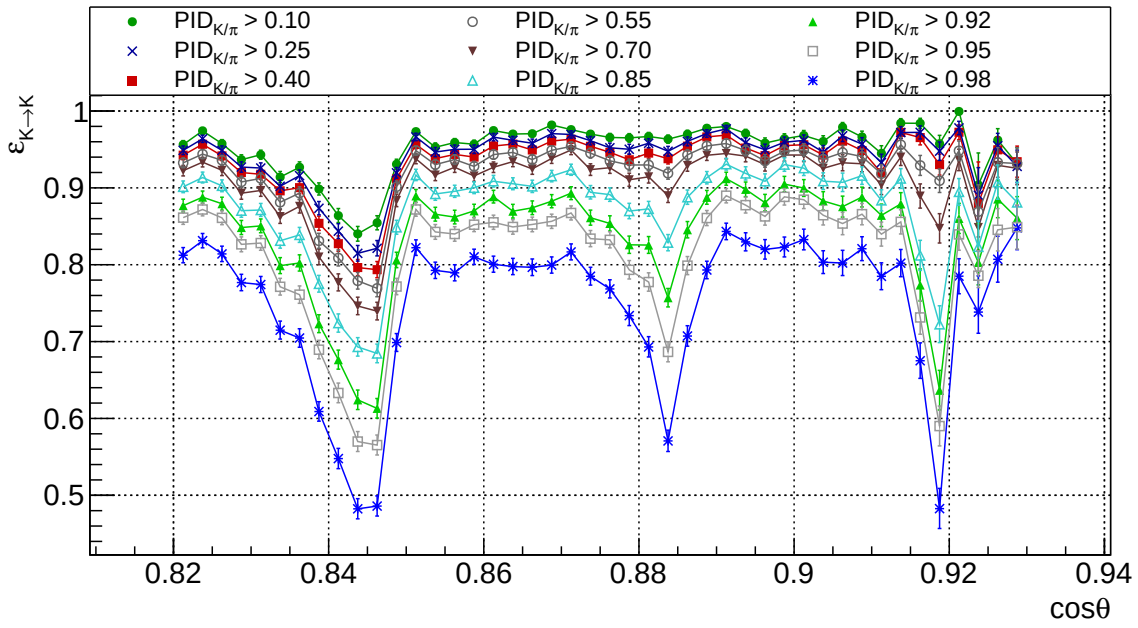

Figure F.49: Kaon identification efficiencies as a function of particle's incident angle for the momentum range between 0.5 GeV/c and 1.5 GeV/c and different $PID_{K/\pi}$ cuts.

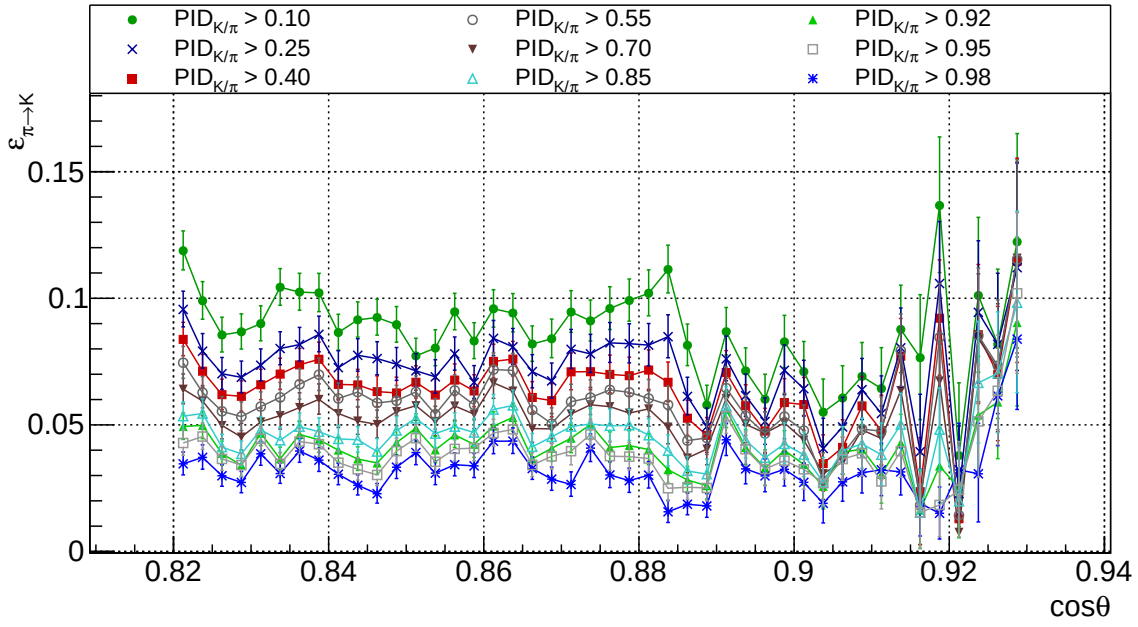

Figure F.50: Pion misidentification probabilities as a function of particle's incident angle for the momentum range between 0.5 GeV/c and 1.5 GeV/c and different $PID_{K/\pi}$ cuts.

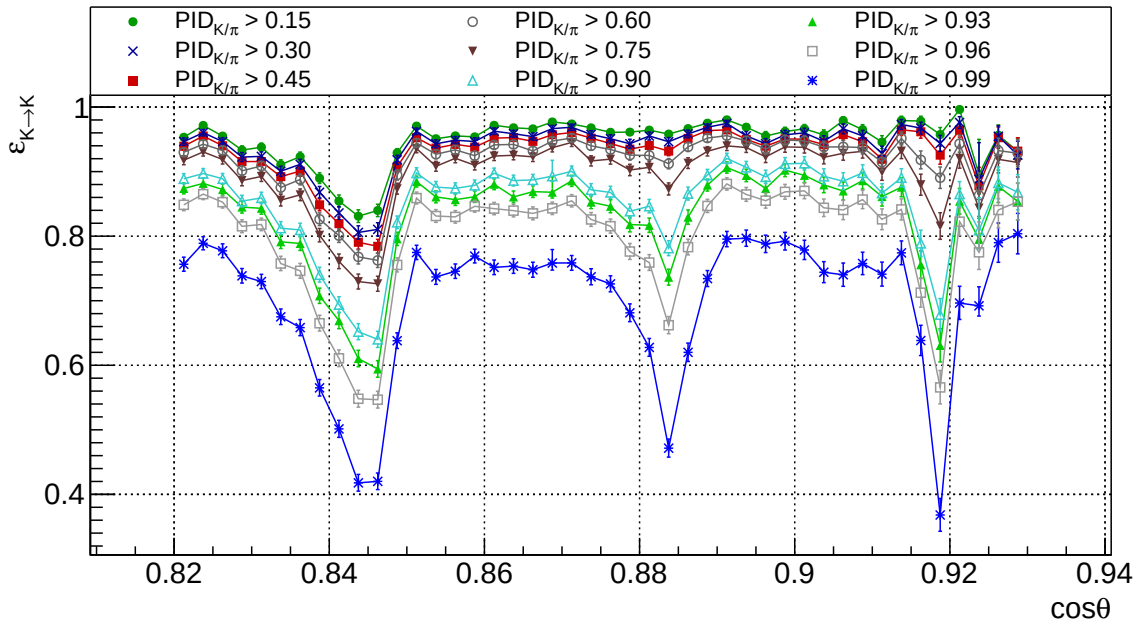

Figure F.51: Kaon identification efficiencies as a function of particle's incident angle for the momentum range between 0.5 GeV/c and 1.5 GeV/c and different $PID_{K/\pi}$ cuts.

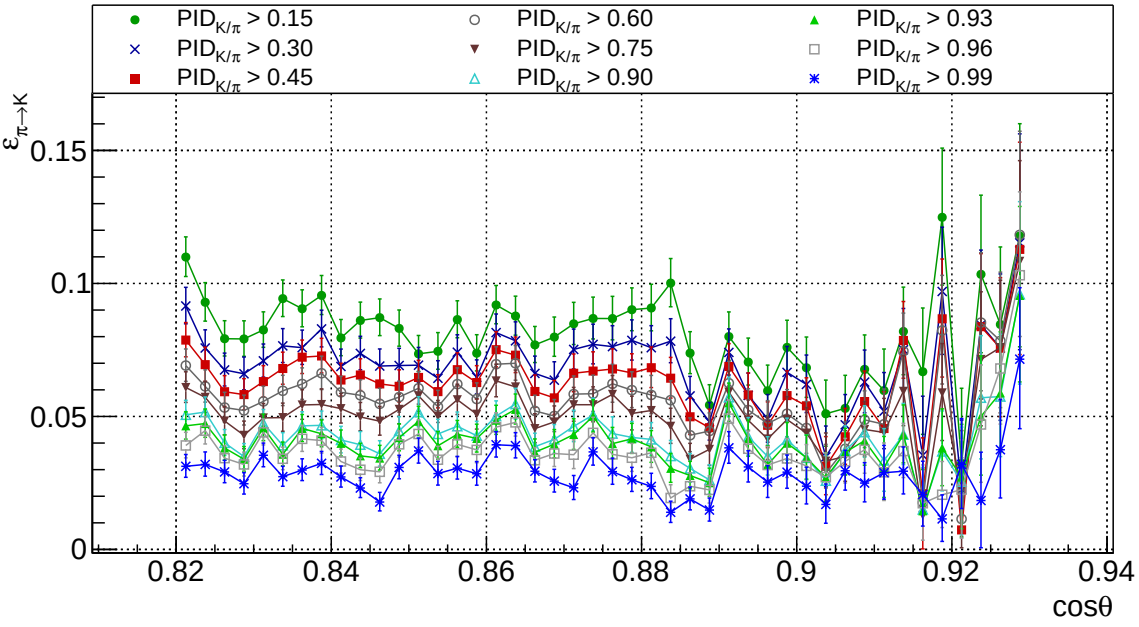

Figure F.52: Pion misidentification probabilities as a function of particle's incident angle for the momentum range between 0.5 GeV/c and 1.5 GeV/c and different $PID_{K/\pi}$ cuts.

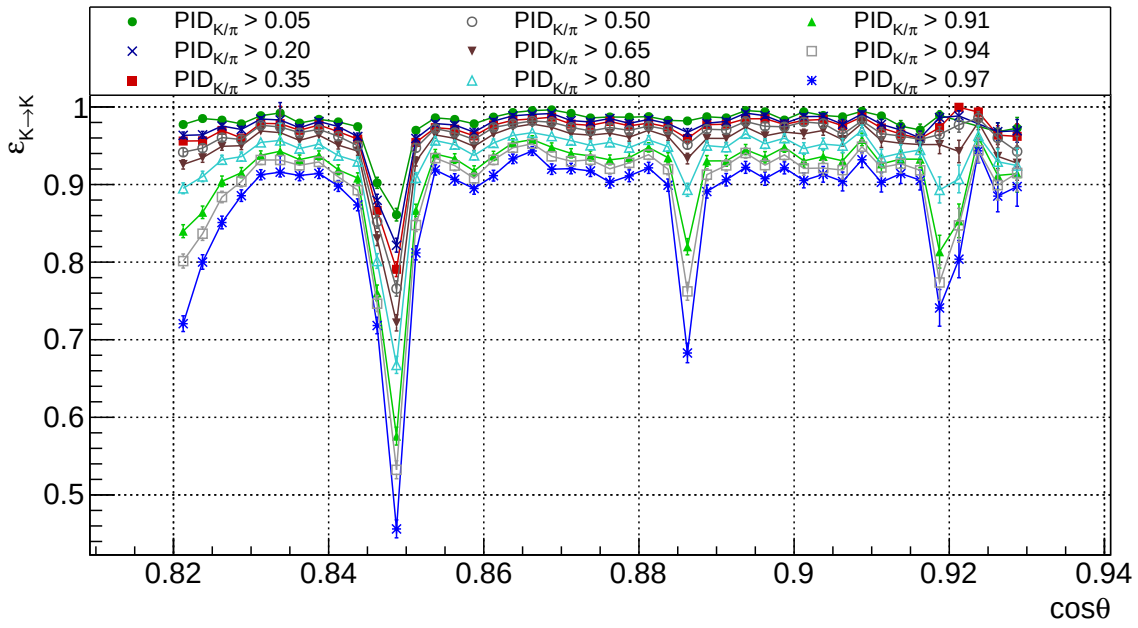

Figure F.53: Kaon identification efficiencies as a function of particle's incident angle for the momentum range between 1.5 GeV/c and 2.5 GeV/c and different $PID_{K/\pi}$ cuts.

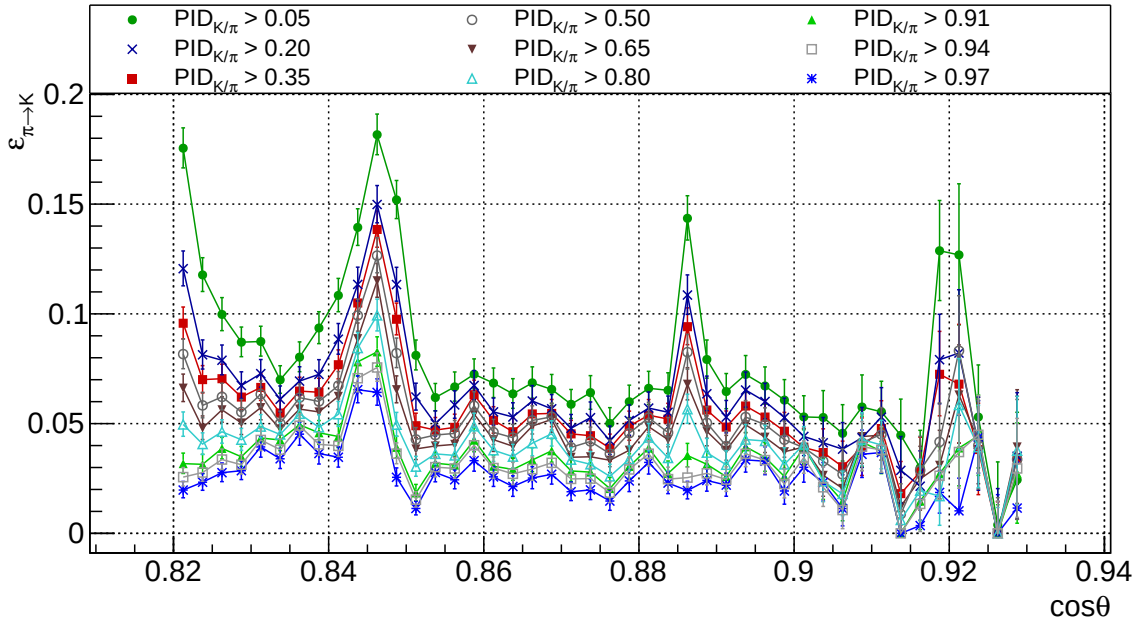

Figure F.54: Pion misidentification probabilities as a function of particle's incident angle for the momentum range between 1.5 GeV/c and 2.5 GeV/c and different $PID_{K/\pi}$ cuts.

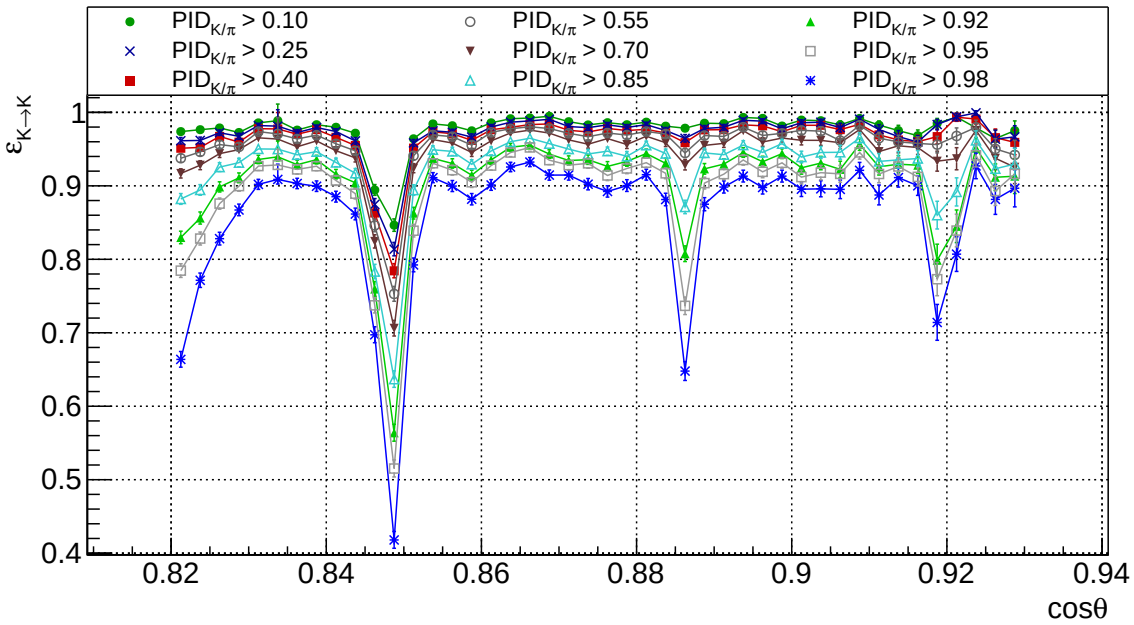

Figure F.55: Kaon identification efficiencies as a function of particle's incident angle for the momentum range between 1.5 GeV/c and 2.5 GeV/c and different $PID_{K/\pi}$ cuts.

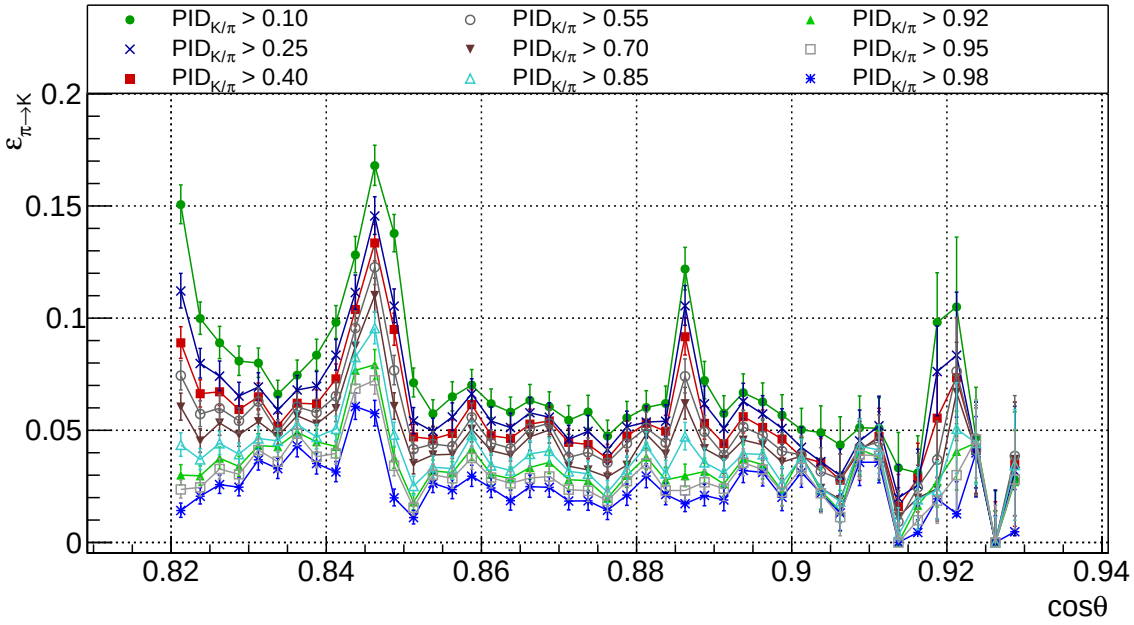

Figure F.56: Pion misidentification probabilities as a function of particle's incident angle for the momentum range between 1.5 GeV/c and 2.5 GeV/c and different $PID_{K/\pi}$ cuts.

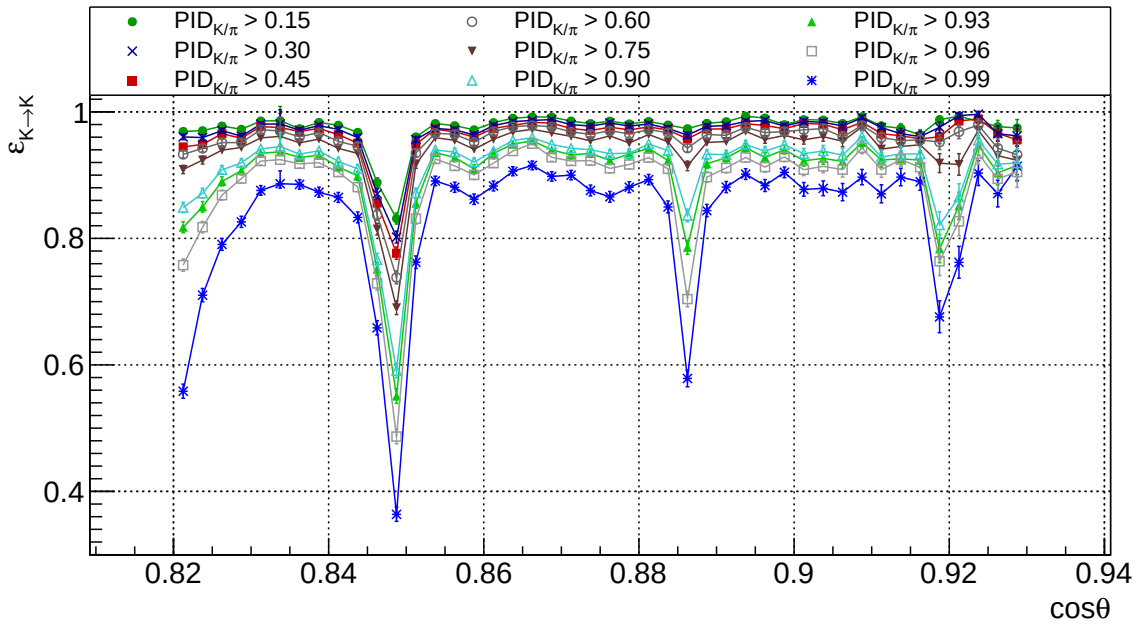

Figure F.57: Kaon identification efficiencies as a function of particle's incident angle for the momentum range between 1.5 GeV/c and 2.5 GeV/c and different $PID_{K/\pi}$ cuts.

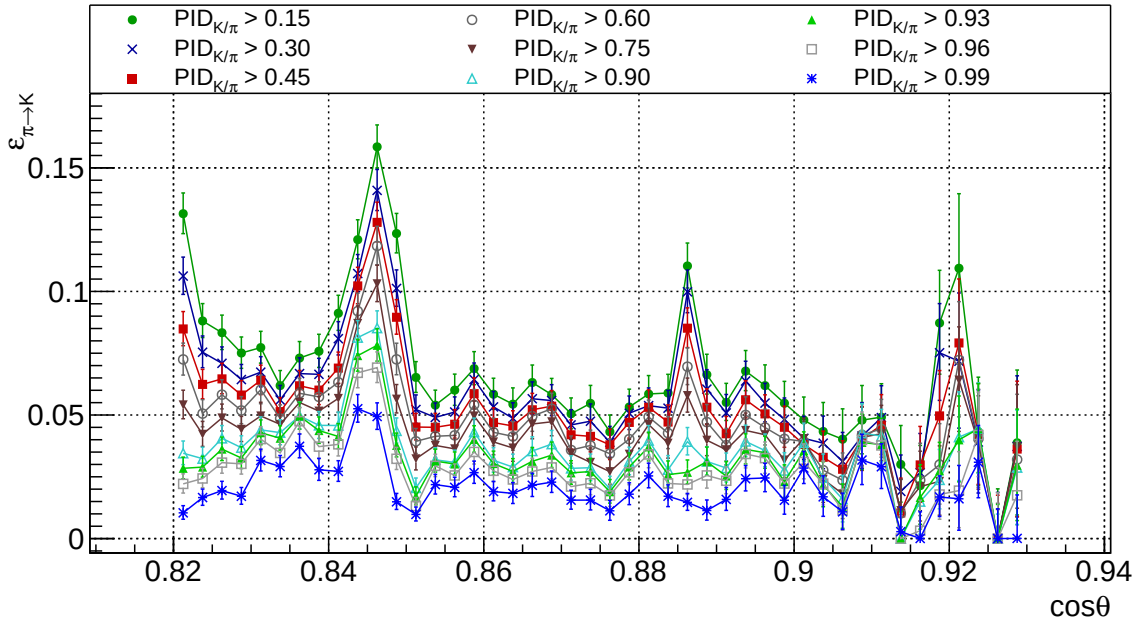

Figure F.58: Pion misidentification probabilities as a function of particle's incident angle for the momentum range between 1.5 GeV/c and 2.5 GeV/c and different $PID_{K/\pi}$ cuts.

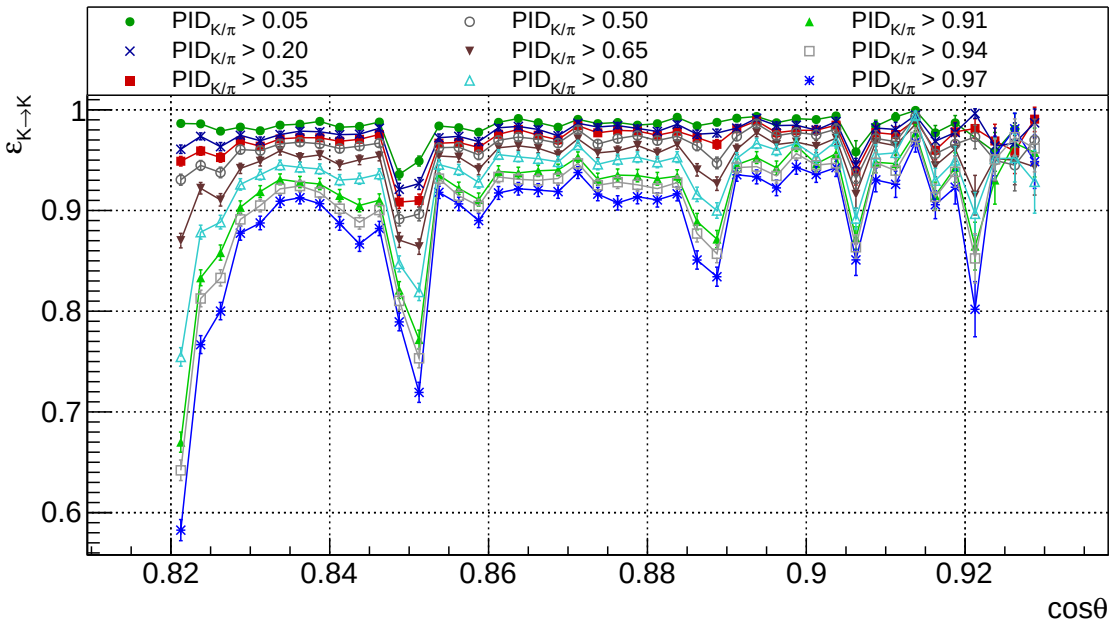

Figure F.59: Kaon identification efficiencies as a function of particle's incident angle for the momentum range between 2.5 GeV/c and 4.0 GeV/c and different $PID_{K/\pi}$ cuts.

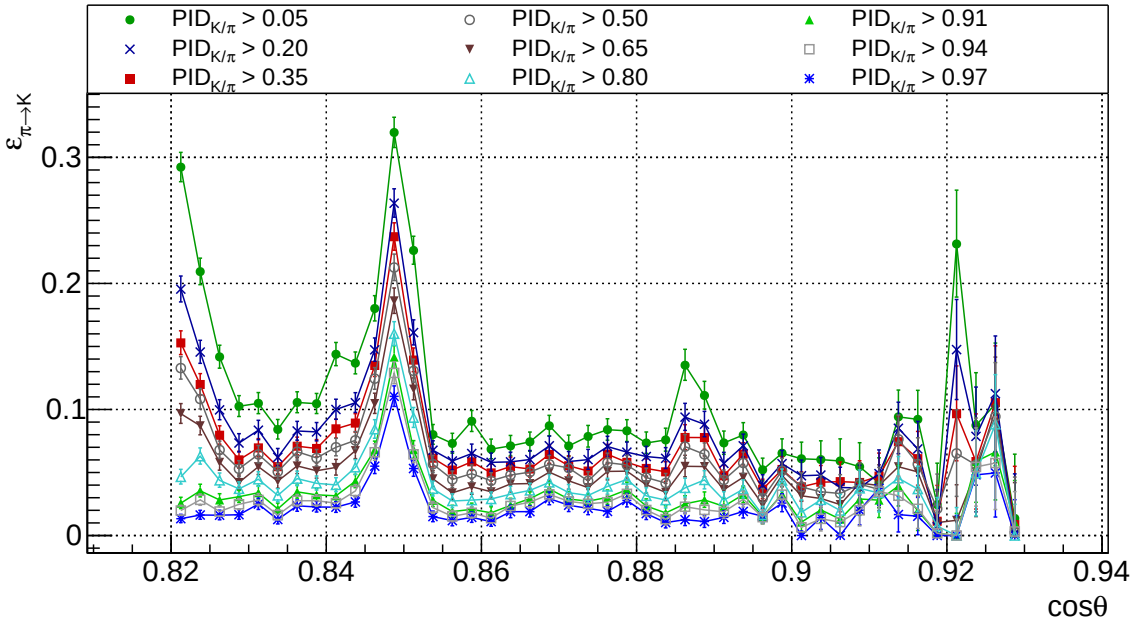

Figure F.60: Pion misidentification probabilities as a function of particle's incident angle for the momentum range between 2.5 GeV/c and 4.0 GeV/c and different $PID_{K/\pi}$ cuts.

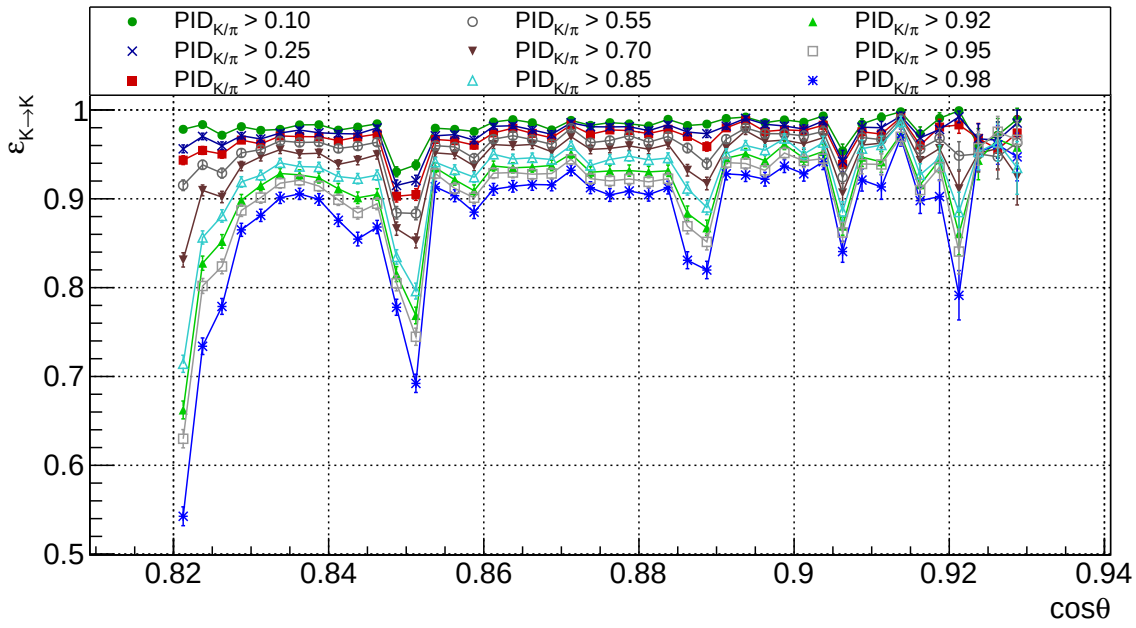

Figure F.61: Kaon identification efficiencies as a function of particle's incident angle for the momentum range between 2.5 GeV/c and 4.0 GeV/c and different $PID_{K/\pi}$ cuts.

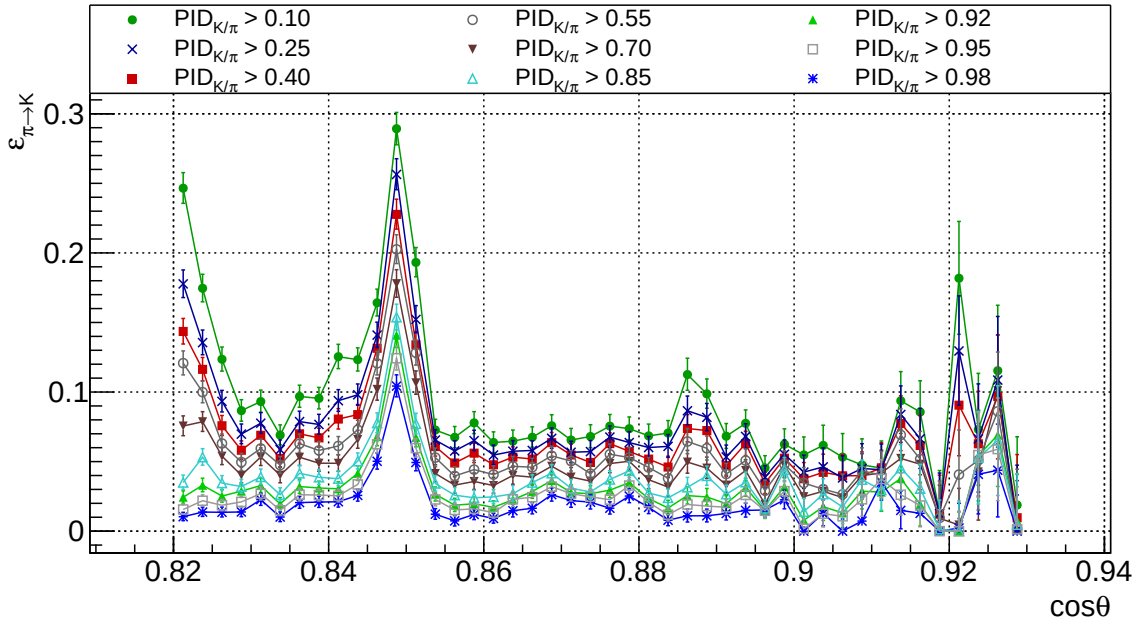

Figure F.62: Pion misidentification probabilities as a function of particle's incident angle for the momentum range between 2.5 GeV/c and 4.0 GeV/c and different $PID_{K/\pi}$ cuts.

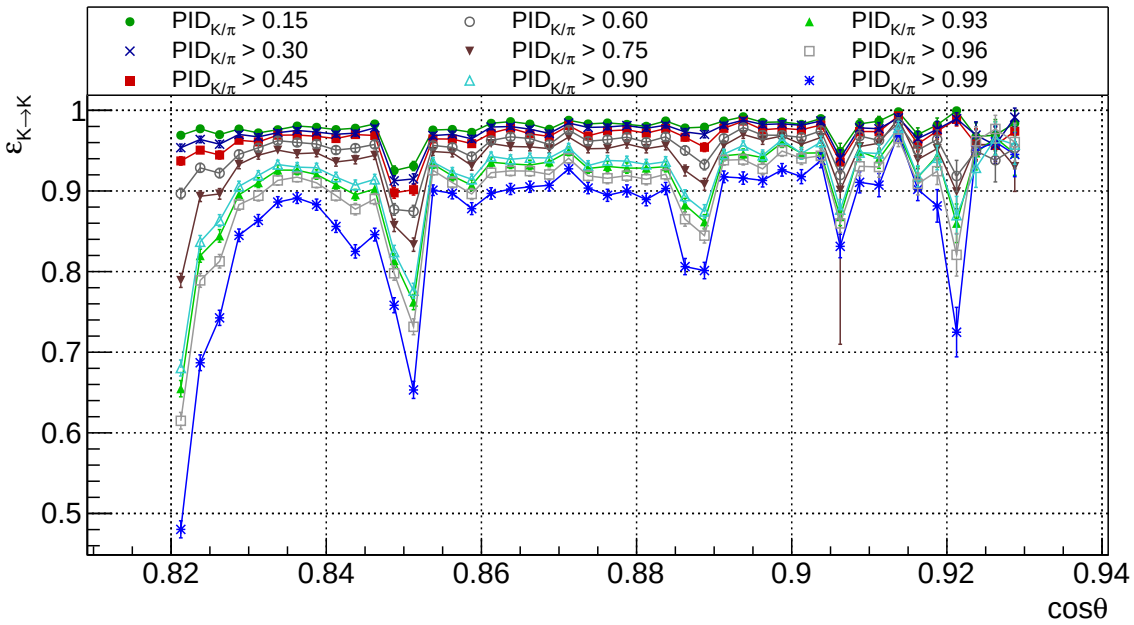

Figure F.63: Kaon identification efficiencies as a function of particle's incident angle for the momentum range between 2.5 GeV/c and 4.0 GeV/c and different $PID_{K/\pi}$ cuts.

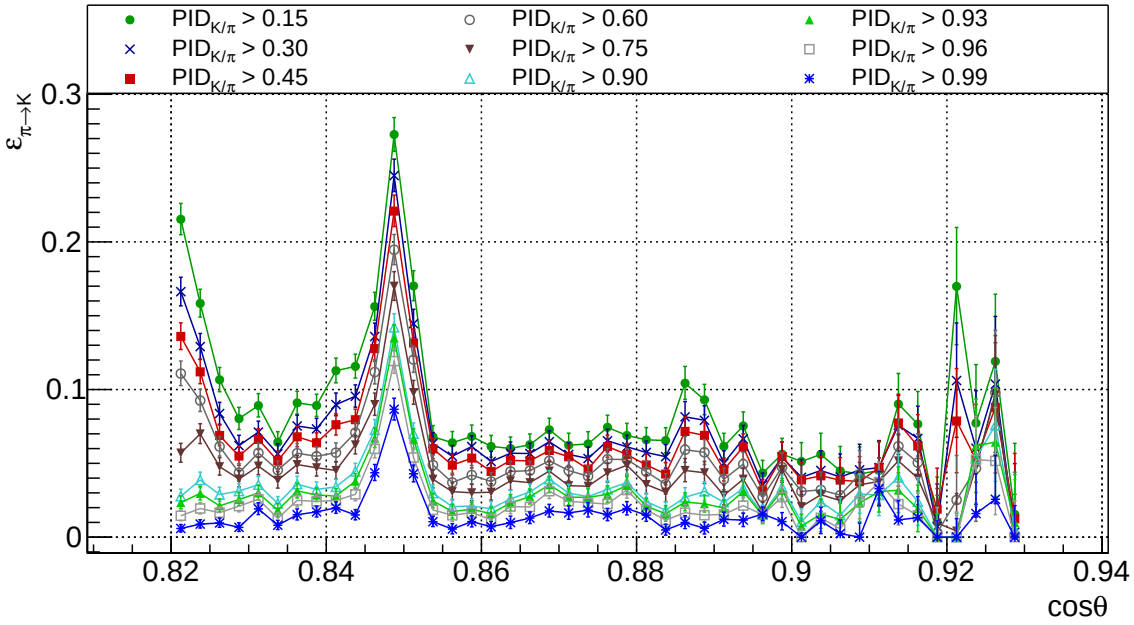

Figure F.64: Pion misidentification probabilities as a function of particle's incident angle for the momentum range between 2.5 GeV/c and 4.0 GeV/c and different $PID_{K/\pi}$ cuts.

POGLAVJE 9

Povzetek v slovenskem jeziku

Eksperimenti, namenjeni proučevanju osnovnih delcev prek njihovih trkov, se delijo na eksperimente pri zelo visokih energijah (trije eksperimenti ob pospeševalniku LHC v CERN-u), kjer je glavni cilj odkritje novih, težjih delcev, in na eksperimente z zelo visoko luminoznostjo (LHCb v CERN-u; Belle ob pospeševalniku KEKB), kjer so glavni cilj zelo natančne meritve redkih razpadov. Meritve z detektorjem Belle so priskrbele pomembne rezultate s študijami redkih mezonov B in D ter leptonov τ. Najpomembnejši dosežek je dokaz o kršitvi simetrije CP pri razpadih mezonov B [13, 14], ki je potrdil teoretske napovedi japonskih fizikov Makota Kobayashija in Toshihide Maskawe, za kar sta leta 2008 prejela Nobelovo nagrado [15].

Naslednik eksperimenta Belle, Belle II, bo zbral 50-krat več podatkov od predhodnika, pri čemer pričakujemo nova odkritja in natančnejše meritve. Doktorska disertacija je posvečena meritvam detektorja obročev Čerenkova z aerogelskim sevalcem, ki skrbi za identifikacijo nabitih delcev. V disertaciji bom na kratko predstavila eksperiment Belle II ter opisala princip identifikacije prek sevanja Čerenkova. Natančno bom predstavila komponente detektorja ARICH ter se v glavnem delu osredotočila na umeritev elektronskih komponent detektorja in študije izkoristkov identifikacije z razpadoma $D^{*+} \to D^0(\to K^-\pi^+)\pi_s^+$ in $D^{*-} \to \bar{D}^0(\to K^+\pi^-)\pi_s^-$.

9.1 Eksperiment Belle II

Eksperiment Belle II je zasnovan za študije redkih razpadov mezonov B in D ter leptonov τ, skupno naj bi zbral vzorec z integrirano luminoznostjo[1] $50\,\mathrm{ab}^{-1}$. Eksperiment sestavljata trkalnik SuperKEKB in sprektrometer Belle II. Trkalnik večino časa deluje pri energiji resonance $\Upsilon(4S)$ (10,58 GeV):

$$e^+e^- \to \Upsilon(4S) \to B\bar{B}$$

Ta energija je ravno nad pragom, potrebnim za nastanek para nevtralnih ali nabitih mezonov B. Pari mezonov $B\bar{B}$ razpadejo preko številnih razpadnih kanalov na različne dolgožive delce – pione, kaone, elektrone, mione, protone, nevtrone, fotone in nevtrine [12, 13]. Prve meritve eksperimenta Belle II so se začele v začetku leta 2018, kot prikazuje slika 9.1. Zajem podatkov pri višji luminoznosti načrtujemo v prvi polovici leta 2019.

[1] luminoznost: število interakcij na enoto preseka in časa

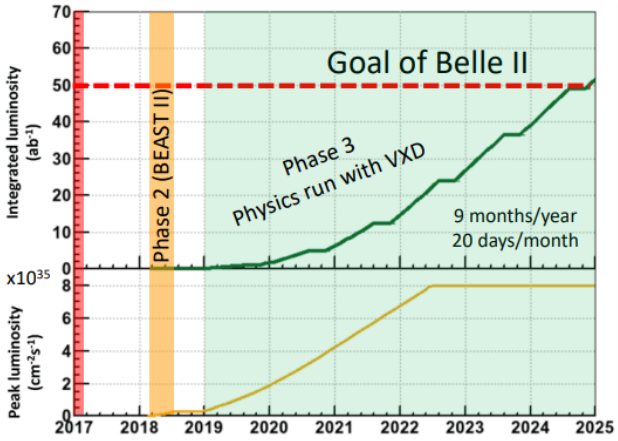

Slika 9.1: Časovnica delovanja pospeševalnika SuperKEKB in eksperimenta Belle II. V drugi fazi (*faza II ali Phase II*) je prišlo do prvih trkov elektronov in pozitronov, ki smo jih zaznali z detektorjem Belle II. Os y prikazuje ciljno luminoznost (spodaj) in pripadajočo integrirano luminoznost (zgoraj). Zajem podatkov pri višji luminoznosti (*faza III ali Phase III*) je načrtovan za začetek leta 2019 [21], kot je razvidno iz slike.

9.1.1 Spektrometer Belle II

Zaradi asimetričnih energij elektronov in pozitronov so produkti trkov pospešeni v smeri curka elektronov. Posledično je tudi detektor Belle II zasnovan tako, da ima boljšo pokritost z raznolikimi detektorskimi sistemi v smeri elektronskega curka. Višja luminoznost bo doprinesla k povečanemu sevalnemu ozadju, ki je bil glavna ovira pri zasnovi novih detektorjev, saj smo želeli obdržati oziroma izboljšati zmogljivost sprektrometra glede na njegovega predhodnika Belle [12, 16]. Spektrometer Belle II je moral zadostiti tudi prostorskim omejitvam, saj smo ohranili skelet in superprevodni magnet. Sestavljajo ga poddetektorji, ki so prikazani na sliki 9.2.

Nadgradnje detektorja Belle II je bila končana leta 2017. Med fazo II je zaradi visokega pričakovanega sevanja detektor verteksov nadomestil detektorski sistem BEAST, sestavljen iz različnih merilnikov sevalnega ozadja. Ta je bil zamenjan z detektorjem verteksov ob koncu leta 2018.

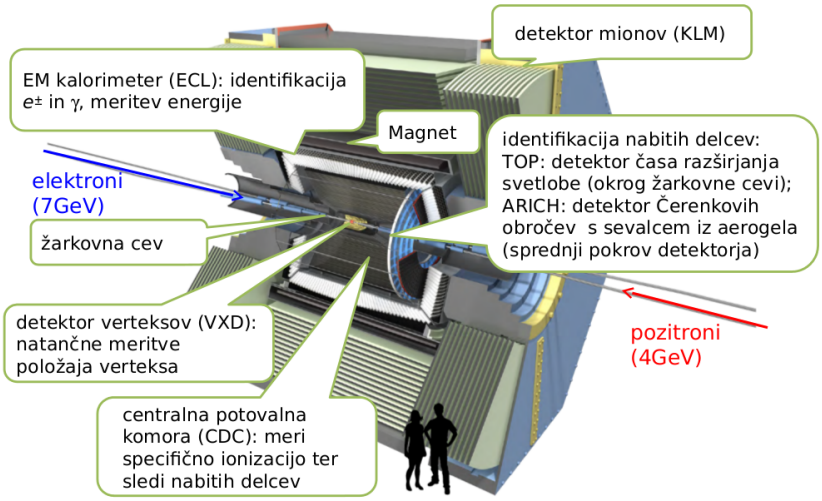

Slika 9.2: Spektrometer Belle II z označenimi glavnimi deli [25].

9.2 Identifikacija nabitih delcev

Uspešnost sistemov za identifikacijo nabitih delcev merimo v deležih pravilno in napačno identificiranih delcev. V primeru detektorjev za identifikacijo delcev v Belle II, določamo deleže kaonov, ki so pravilno identificirani kot kaoni, $\varepsilon_{K\to K}$, in deleže pionov, ki so napačno identificirani kot kaoni, $\varepsilon_{\pi\to K}$. Detektorja TOP in ARICH, ki sestavljata Belle II, spadata v skupino detektorjev sevanja Čerenkova.

9.2.1 Sevanje Čerenkova

Detektorji Čerenkova zaznavajo delce prek sevanja Čerenkova. Nabit delec polarizira molekule, ko potuje skozi dielektrično snov. Nastali dipoli se vrnejo v prvotno stanje in pri tem izsevajo fotone. Kadar delec potuje počasneje od svetlobe v snovi, je polarizacija molekul simetrična in pride do destruktivne interference. V primeru, ko delec potuje hitreje od svetlobe, je polarizacija asimetrična, interferenca pa konstruktivna, kar opazimo kot izsevan elektromagnetni val [26, 27], prikazan na sliki 9.3. Kot Čerenkova (θ_{ch}), pod katerim se izsevajo fotoni, merimo relativno glede na smer delca in ga lahko izračunamo preko enačbe:

$$\cos\theta_{ch} = \frac{1}{\beta n}, \tag{9.2.1}$$

kjer je β razmerje med hitrostjo delca v snovi in hitrostjo svetlobe v vakuumu, ter n lomni količnik snovi. Največji kot Čerenkova, pri katerem se delci izsevajo, je določen z lomnim količnikom snovi kot $\theta_{ch,max} = \arccos\left(n^{-1}\right)$.

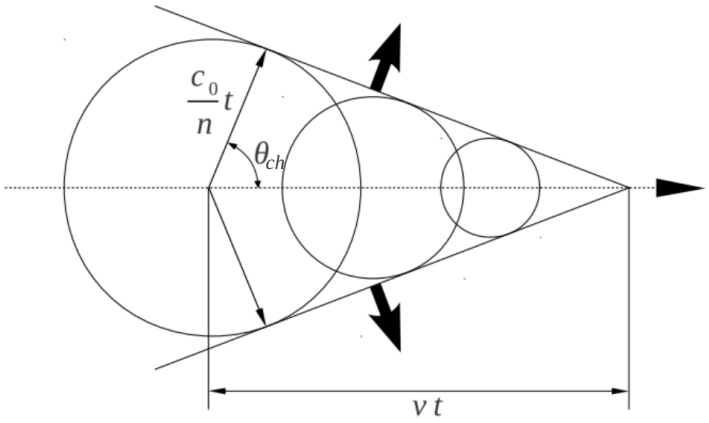

Slika 9.3: Sevanje Čerenkova nastane kot posledica potovanj nabitega delca skozi dielektrično snov hitreje od svetlobe. Elektromagnetni val se izseva pod točno določenim kotom Čerenkova θ_{ch}.

Število izsevanih fotonov je odvisno od naboja delca z, lomnega količnika $n(\nu)$ in debeline snovi l. Določimo ga preko [26, 29]:

$$N_{izsevani} = \frac{\alpha z^2}{\hbar c} l \int_{E_1}^{E_2} \sin^2\theta_{ch}(E) dE \tag{9.2.2}$$

kjer sta E_1 in E_2 meji energijskega intervala optičnih fotonov in $\alpha = \frac{1}{137}$ konstanta fine strukture.

9.2.2 Detektorji sevanja Čerenkova

Osnovna zasnova detektorjev Čerenkova je enaka – sestavljeni so iz sevalca, kjer se izsevajo fotoni Čerenkova; prostora za razširjanje svetlobe (ki pogosto vključuje leče in zrcala za zbiranje svetlobe) in senzorje za zaznavanje fotonov. Izbira vrste sevalca temelji na zahtevah za detekcijo znotraj določenega območja gibalne količine delcev. Primer odvisnosti velikosti kota Čerenkova od gibalne količine kaonov in pionov za tri različne sevalce je prikazan na sliki 9.4.

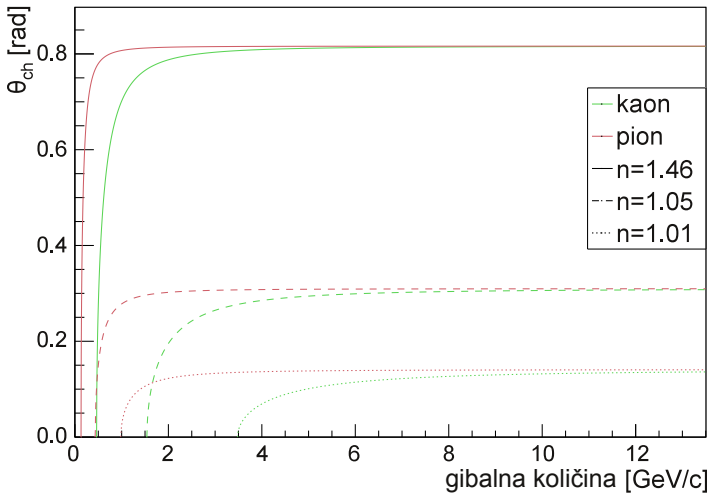

Slika 9.4: Velikost kota Čerenkova za kaone in pione v odvisnosti od gibalna količine. Prikazani so rezultati za tri vrste sevalcev z različnimi lomnimi količniki.

Detektorje sevanja Čerenkova lahko razdelimo na dva tipa – pragovne števce in detektorje obročev Čerenkova. Prvi merijo število zaznanih fotonov in ločujejo med delci v ozkem intervalu gibalne količine med pragovoma, pri katerih lažji in težji delec začneta sevati fotone Čerenkova. Detektorji obročev Čerenkova (*angl. Ring-Imaging CHerenkov; RICH*) rekonstruirajo vpadne delce glede na vzorec zaznanih fotonov, pri čemer merijo tako število zaznanih fotonov kot tudi kot Čerenkova. Fotoni so fokusirani na ravnino senzorjev direktno, ali pa preko leč in zrcal.

9.3 Detektor obročev Čerenkova z aerogelskim sevalcem

Glavna naloga detektorja obročev Čerenkova z aerogelskim sevalcem (*Aerogel Ring Imaging Cherenkov detector; ARICH*) je razlikovanje med kaoni in pioni z ločljivostjo več kot 4σ na intervalu gibalne količine med 0,5 GeV/c in 4,0 GeV/c. Območje je nad pragom gibalne količine, pri kateri pioni izsevajo fotone ter navzgor omejeno z gibalnimi količinami, pri katerih se obroča Čerenkova za kaone in pione začneta prekrivati. ARICH ločuje tudi med pioni, mioni in elektroni na območju gibalne količine pod 1 GeV/c [34]. Glavni deli ARICH-a so sevalec, sestavljen iz dveh plasti aerogela za izsevanje fotonov Čerenkova, prostora za razširjanje svetlobnega stožca Čerenkova in detektorske ravnine s fotonskimi senzorji, kot prikazuje slika 9.5. Fotonski detektorji imajo na zadnjem delu pritrjeno bralno elektroniko.

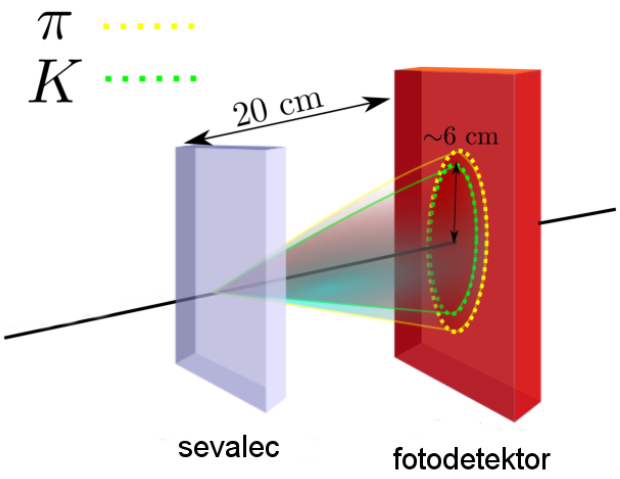

Slika 9.5: Osnovni princip delovanja ARICH-a z označenim sevalcem in fotonskim detektorjem [34].

Fotonski senzorji morajo biti sposobni zaznavati posamezne fotone. Število zaznanih fotonov, $N_{zaznani}$, je odvisno od števila izsevanih fotonov, izkoristka fotosenzorjev senzorjev, $Q(E)$, prepustnosti sevalca, $T_S(E)$, in kvarčnega okna, $T_K(E)$, ter geometrijskega izkoristka, ε_G, ki za ARICH znaša 41 %. Izračunamo ga prek enačbe:

$$N_{zaznani} = \frac{\alpha}{\hbar c} z^2 l \varepsilon_G \int_{E_1}^{E_2} Q(E) T_S(E) T_K(E) \sin^2 \theta_{ch}(E) dE \qquad (9.3.1)$$

Pričakovano število zaznanih fotonov za kaon z gibalno količino med 0,5 GeV/c in 4,0 GeV/c znaša med 10 in 12. Blizu roba detektorja pride do izgube fotonov, zaradi česar so ob robu pritrjena ravna zrcala, ki te izgube zmanjšajo.

9.3.1 Zasnova detektorja

ARICH se prilega v 28 cm širok valj z notranjim radijem 42 cm in zunanjim radijem 114 cm. Skoraj 3,5 m^2 velika detektorska ravnina je prekrita s 420 detektorskimi moduli, razporejenimi v sedem koncentričnih obročev, pri čemer ima notranji obroč 42 senzorjev, vsak naslednji pa šest senzorjev več. Podobno je razdeljena tudi ravnina s sevalcem, le da so aerogelske plošče razporejene v štiri obroče z 22, 28, 34 in 40 odprtinami [35]. Razdeljenost detektorske ravnine in ravnine s sevalcem je prikazana na sliki 4.3.

9.3.2 Aerogel

Aerogel je izredno lahka snov, pri kateri lahko dosežemo dobro optično prepustnost. Aerogeli se razlikujejo glede na njihove kemične in fizikalne lastnosti [37]. Lomni količnik aerogela (navadno med 1,003 in 1,11) je mogoče natančno prilagoditi v postopku sinteze, zaradi česar je primeren za uporabo v detektorjih Čerenkova [38, 39]. Izbira sevalca (odločili smo se za silicijev aerogel) v ARICH-u je bila optimizirana glede na resolucijo obroča Čerenkova za posamezen delec. Ločljivost kota

Čerenkova za posamezen delec, σ_{delec}, je odvisna od kotne resolucije za posamezen zaznani foton, σ_0, in števila zaznanih fotoelektronov, N_{pe}:

$$\sigma_{delec} = \frac{\sigma_0}{\sqrt{N_{pe}}} \tag{9.3.2}$$

Ločljivost zaznavanja posameznega fotona je odvisna od velikosti kanalov na senzorjih in debeline sevalne plošče. Pri upoštevanju enakomerne porazdelitve izsevanih fotonov po debelini sevalca, pričakovanih zadetkov na kanalu senzorja in absorpciji fotonov v sevalcu, dobimo resolucijo posameznega fotona v odvisnosti od debeline sevalca, kot prikazuje slika 4.7. Optimalna debelina sevalca 20 mm bi zagotovila le 5 – 6 zaznanih fotonov na nabit delec, zato smo uporabili dve plasti. Različna lomna količnika plasti poskrbita za prekrivanje obročev Čerenkova na detektorski ravnini, kot prikazuje slika 9.6.

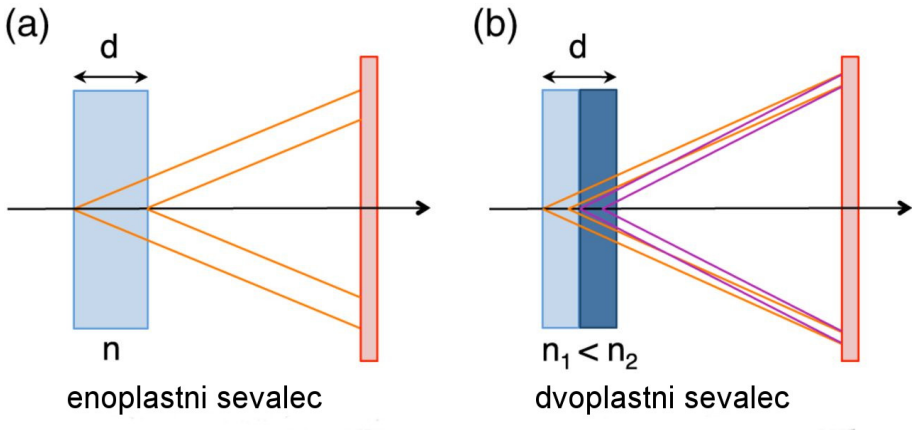

Slika 9.6: Primerjava konfiguracij sevalca z enakima (a) in različnima (b) lomnima količnikoma dveh plasti [42].

Lomna količnika sta bila izbrana tako, da se obroča iz obeh plasti prekrivata pri gibalni količini okoli 3,5 GeV/c, kjer je razlika med kotoma Čerenkova za kaone in pione le 30 mrad. Optične in fizikalne lastnosti plošč aerogela so zbrane v tabeli 9.1.

Tabela 9.1: Lastnosti sevalca v ARICH-u [44–47].

lastnost	prva plast	druga plast
število plošč	124	124
lomni količnik	1,045	1,055
gostota [g cm^{-3}]	0,160	0,194
absorpcijska dolžina[a][cm]	4,5	3,4
debelina [cm]	1,96	1,97

[a] Razdalja Λ_0, pri kateri se začetna intenziteta svetlobe, I_0, zmanjša za faktor e: $I_x = I_0 e^{-\frac{x}{\Lambda_0}}$.

9.3.3 Hibridni plazovni fotonski detektorji

Fotonski detektorji morajo učinkovito zaznavati posamezne fotone v visokem magnetnem polju gostote 1,5 T ter biti odporni na močno nevtronsko in gama sevanje. Tekom 10 let delovanja eksperimenta Belle II je pričakovana doza sevanja zaradi žarkov γ do 100 Gy, $10^{12} n/\mathrm{cm}^2$ pa je pričakovana fluenca ekvivalenta nevtronov z

energijo 1 MeV [75]. Zaradi odličnega delovanja pri visokem obsevanju so bili v sodelovanju s Hamamatsu Photonics razviti hibridni plazovni detektorji (*angl. Hybrid Avalanche Photo Detectors; HAPDs*).

Zaznavanje fotonov v HAPD-ju

HAPD je 73 mm × 73 mm × 30 mm velik vakuumski detektor fotonov s keramičnimi stenami in kvarčnim oknom na vrhu. Na kvarčno okno je naparjena bi-alkalijska fotokatoda, na spodnjem delu pa so pritrjene plazovne fotodiode. Plazovna fotodioda (APD) je razdeljena na štiri čipe, ki so dodatno razdeljeni na 6 × 6 kanalov, velikosti 4,9 mm × 4,9 mm. Shema HAPD-ja je prikazana v dodatku A.

Zaznavanje fotona se prične, ko ta vstopi v HAPD skozi kvarčno okno, kot je prikazano na sliki 9.7. Foton Čerenkova v fotokatodi ustvari fotoelektron preko fotoefekta. Fotoelektron se pospeši v visokem električnem polju (ki ustreza visoki napetosti do 8,5 kV) in zadene plazovno fotodiodo, kjer ustvari približno 1700 parov elektron-vrzel. V plazovni fotodiodi pride do nadaljnjega ojačanja signala, ki je odvisno od njene zaporne napetosti diode. Tipične vrednosti med 320 V in 360 V ojačajo signal za 40-krat, tako da iz enega na koncu dobimo približno 7×10^4 elektronov. Za dosego homogenega električnega polja v APD-ju je na robovih čipov priključena dodatna napetost 175 V, ki poskrbi, da po robovih ne tečejo dodatni električni tokovi.

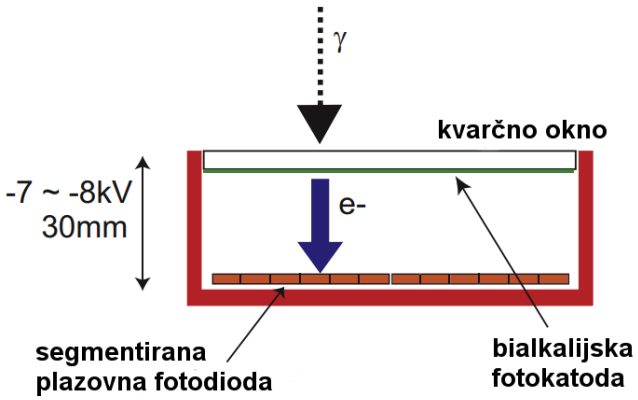

Slika 9.7: Shematski prikaz zaznavanja fotonov znotraj HAPD-ja [48].

Učinkovitost delovanja HAPD-jev

Vsak kanal HAPD-ja ima drugačno učinkovitost delovanja, ki je posledica nekoliko različnih lastnosti materiala. Delovanje je odvisno od učinkovitosti zbiranja naboja znotraj fotodiode, ki za ARICH znaša skoraj 100 %. Do razlike med učinkovitostjo kanalov pride zaradi različnega kvantnega izkoristka fotoelektrode – verjetnosti, da iz fotona dobimo fotoelektron. Kvantni izkoristek ni enakomeren po vsej površini. Do odstopanja pride zaradi naparevanja fotokatode na kvarčno okno. Površinsko občutljivost fotokatode smo izmerili v manjših korakih po celotni površini [53]. Porazdelitev kvantnih izkoristkov po detektorju je predstavljena na sliki 4.30. Kanali se med seboj razlikujejo tudi po ojačanju signala znotraj diode.

9.3.4 Zajemanje podatkov

Signale s HAPD-jev procesiramo v več korakih. Primarno jih obdelamo in digitaliziramo v bralni elektroniki, pritrjeni na HAPD. Signali z bralne elektronike potujejo v združevalno vezje (*angl. merger board*), ki potem naprej komunicira s centralnimi enotami za zajemanje podatkov za celoten detektor Belle II [54].

Glavni deli bralne elektronike ARICH-a so štirje čipi ASIC *(angl. Application Specific Integrated Circuit)*, programabilno vezje FPGA *(angl. Field Programmable Gate Array)* ter priključki za bralne kable in priključitev napetosti [55]. Čipi ASIC ojačajo in oblikujejo signal s HAPD-ja ter ga primerjajo z nastavljeno vrednostjo višine signala in ga ustrezno digitalizirajo. Čip FPGA vzorči signal in procesira podatke. Poleg branja signalov, bralna elektronika spremlja tudi temperature, tokove in napetosti komponent, ter proži notranje signale, ki omogočajo testiranje delovanja. Nastavljivi parametri bralne elektronike so zbrani v tabelah 4.1 in 4.2.

Združevalna vezja skrbijo za komunikacijo med bralno elektroniko ARICH-a in prožilnim sistemom za celoten detektor Belle II, ki zajame podatke ob zaznanih dogodkih. Eno združevalno vezje je povezano s petimi ali šestimi bralnimi vezji.

9.3.5 Sestavljanje detektorja

Vsak detektorski modul sestavljajo HAPD, vezje z bralno elektroniko in vezje za razdelitev visoke napetosti. Vse komponente so bile najprej testirane in šele nato sestavljene v celotni modul. Modul je bil pred sestavljanjem detektorja ARICH še enkrat izmerjen v končnem testu.

Dokončno je bil detektor sestavljen leta 2017. Aerogelske plošče smo namestili v aluminijast okvir in pritrdili s tankimi ogljikovimi vlakni, ki skrbijo, da plošče ostanejo na mestu, ko je detektor postavljen pokončno. Moduli so bili prav tako pritrjeni v aluminijast okvir, kjer smo ob robu namestili tudi 18 ravnih zrcal. Dela obeh ravnin lahko vidimo na slikah 4.37 in 4.38. Napajalni kabli so bili večinoma narejeni po meri za vsak detektorski modul. Detektor je opremljen s kabli za dovajanje visoke, zaporne in zaščitne napetosti na HAPD-je, napajalnih kablov za elektroniko ter kablov za prenos podatkov z bralne elektronike, kot prikazuje slika 4.41.

9.4 Programsko orodje za rekonstrukcijo

Simulacijo in rekonstrukcijo vzorcev Monte Carlo ter analizo podatkov izvajamo s pomočjo programske opreme BASF2 (***B**elle **A**nalysis **S**oftware **F**ramework II*) [59], ki je bila namensko razvita za potrebe eksperimenta Belle II. Za identifikacijo v ARICH-u potrebujemo informacijo o sledi delca, ki jo dobimo iz sledilnega sistema. Elektronske signale z ARICH-a digitaliziramo in s tem pretvorimo v podatek o zadetku na detektorski ravnini. Za vsako sled delca, ki vstopi v ARICH, izračunamo funkcijo največje zanesljivosti, ki temelji na delih P. Baillona [66] in R. Fortyja [67]. Definiramo jo kot produkt verjetnosti p_i za zadetek na i-tem kanalu senzorjev:

$$\mathcal{L} = \prod_{\text{vsi kanali}} p_i \tag{9.4.1}$$

Verjetnostna gostota za zadetke je Poissonova, $p_i = \frac{e^{n_i} n_i^{m_i}}{m_i!}$, pri čemer je n_i pričakovano število vseh zadetkov, m_i pa dejansko število zadetkov. Izračun se

poenostavi, ker v ARICH-u ne štejemo dejanskega števila zadetkov v kanalu, ampak uporabimo samo informacijo o zaznanem signalu. Verjetnosti so tako določene kot:

$$p_i = \begin{cases} e^{-n_i} & \text{kanali brez zadetkov} \\ 1 - e^{-n_i} & \text{kanali z zadetki} \end{cases} \tag{9.4.2}$$

Ob upoštevanju enačb 9.4.1 in 9.4.2 ter logaritmiranju $\mathcal{L}$ dobimo rezultat:

$$\ln \mathcal{L} = -N + \sum_{\text{z zadetki}} \ln \Big(e^{n_i} - 1 \Big), \tag{9.4.3}$$

pri čemer je N število pričakovanih zadetkov, odvisno od masne hipoteze, ki ga lahko zapišemo kot vsoto pričakovanega števila zadetkov po vseh kanalih. Funkcijo izračunamo za pet masnih hipotez (za pion, kaon, proton, elektron in mion).

Pričakovano število delcev n_i je vsota prispevkov signalnih fotonov in ozadja. Večino ozadja dobimo zaradi Rayleigh-jevega sipanja fotonov Čerenkova v sevalcu in elektronskega šuma. Pričakovan prispevek signala izračunamo analitično [68], pri čemer upoštevamo Gaussovo porazdelitev signala po obroču. Funkcijo največje zanesljivosti izračunamo za vseh pet masnih hipotez. Pri identifikaciji navadno primerjamo dve hipotezi – nas najbolj zanimata hipotezi za kaone in pione.

9.4.1 Pričakovana učinkovitost ARICH-a

Učinkovitost delovanja detektorja ARICH smo študirali na simuliranih dogodkih odziva detektorja, ki so temeljijo na orodju Geant4 [60, 61]. Uporabili smo izvor kaonov in pionov, ki so bili izstreljeni iz interakcijske točke in enakomerno porazdeljeni po prostorskem kotu. Za prikaz rezultatov smo uporabili le območje visokih gibalnih količin med 3,0 GeV/c in 4,0 GeV/c, kjer sta porazdelitvi kaonov in pionov po gibalnih količinah konstantni. Za vsako sled delca smo izračunali funkcijo največje zanesljivosti. Skupno porazdelitev razlike logaritmov funkcij zanesljivosti za kaonsko in pionsko masno hipotezo, $\log \mathcal{L}_K - \log \mathcal{L}_\pi$, predstavlja slika 9.8. Med delci razlikujemo tako, da določimo identifikacijsko mejo – mejno vrednost $\log \mathcal{L}_K - \log \mathcal{L}_\pi$, pri kateri so delci nad (pod) mejo identificirani kot kaoni (pioni). Določimo lahko izkoristek identifikacije kaonov in pionov pri različnih identifikacijskih mejah kot:

$$\varepsilon_{K\to K} = \frac{N^K_{nad\ mejo}}{N^K_{vsi}} \quad \text{in} \quad \varepsilon_{\pi\to K} = \frac{N^\pi_{nad\ mejo}}{N^\pi_{vsi}}, \tag{9.4.4}$$

kjer je N_{vsi} število vseh dogodkov, $N_{nad\ mejo}$ pa število delcev, ki preživijo postavljeno mejo identifikacije. Izkoristek identifikacije predstavimo kot funkcijo gibalne količine ali vpadnega kota delca. Primer za tri različne določene deleže narobe identificiranih pionov prikazujeta sliki 9.9 in 9.10.

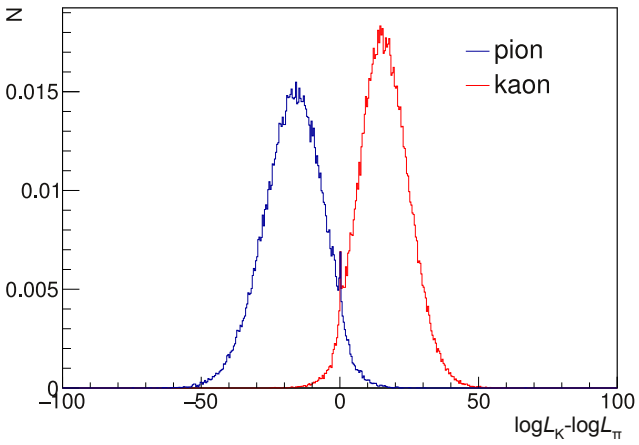

Slika 9.8: Skupna porazdelitev razlike logaritmov funkcij največje zanesljivosti za kaonsko in pionsko masno hipotezo.

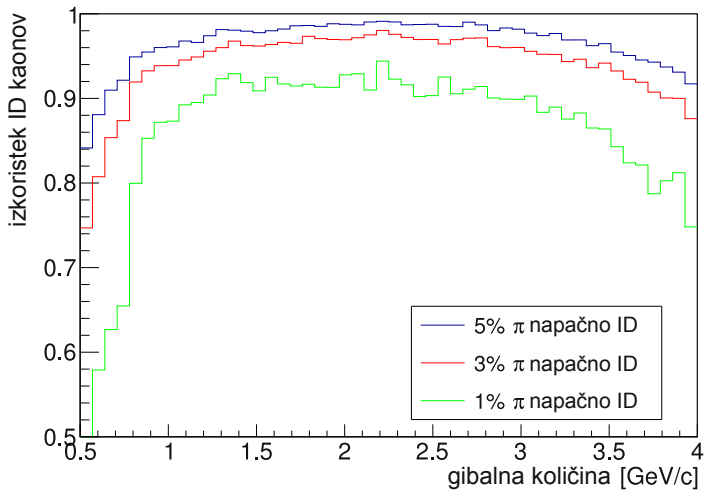

Slika 9.9: Učinkovitost identifikacije kaonov kot funkcija gibalne količine pri treh različnih določenih deležih napačno identificiranih pionov.

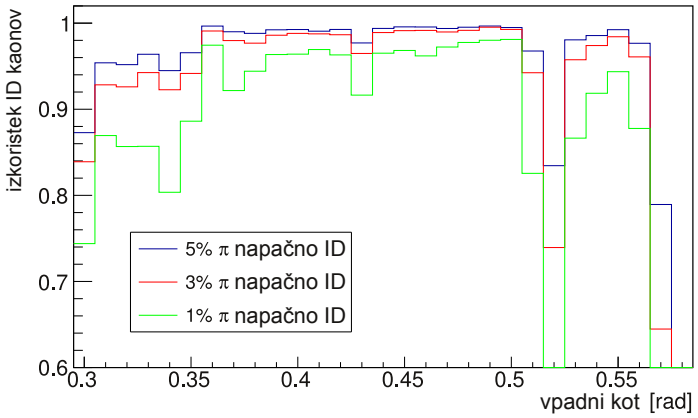

Slika 9.10: Učinkovitost identifikacije kaonov kot funkcija vpadnega kota nabitega delca pri treh različnih določenih deležih napačno identificiranih pionov.

9.4.2 Vpliv umeritve na učinkovitost delovanja ARICH-a

Pri delcih z visoko gibalno količino 4 GeV/c, je razlika kota Čerenkova kaonov in pionov majhna, le 23 mrad. Če delec vpada na ravnino aerogela pravokotno in zaznamo 10 izsevanih fotonov, dobimo ločljivost za sled delca približno 3,6 mrad, kar nam pri teh razliki porazdelitev kotov Čerenkova da izjemno ločljivost 6σ. Ločljivost pri nižjih gibalnih količinah je slabša, vendar sta obroča dlje narazen, kar zagotavlja dobro ločljivost po celotnem območju gibalne količine.

Pioni in kaoni pričnejo sevati fotone Čerenkova pri različnih gibalnih količinah. Za pione sta mejni vrednosti v plasteh aerogela 0,42 GeV/c in 0,46 GeV/c, pri kaonih pa 1,47 GeV/c in 1,63 GeV/c. Delež napačno identificiranih pionov je večji v intervalu med obema pragovoma, saj v primeru, ko ne zaznamo fotonov, predvidevamo, da je bil delec kaon. Zaradi tega moramo pravilno izključiti nedelujoče dele detektorja v metodi računanja funkcije zanesljivosti, da pravilno določimo pričakovano število fotonov.

Umeritev detektorja ARICH izvajamo v več korakih. Kalibracijo parametrov senzorjev in elektronskih komponent, kot so nastavitev odmika ničelnih vrednosti elektronskih kanalov, ojačanje signala in maskiranje nedelujočih kanalov, smo opravili pred sestavljanjem detektorja. Sledila ji je umeritev elektronskih parametrov z zbranimi podatki. V zadnjem koraku bomo izračunali učinkovitost identifikacije z uporabo kontrolnih kanalov, kjer delce lahko identificiramo brez uporabe informacije iz ARICH-a.

9.5 Umeritev detektorskih komponent

Parametre detektorskih komponent smo določili pred sestavljanjem celotnega detektorja. Testirali smo jih v končnih testih modulov, pri čemer smo določili ojačanje signala za vsak kanal, poravnali smo izhodišče signalov na elektroniki in določili problematične kanale. Module smo ponovno umerili med fazo II. V tem času je bila naenkrat aktivna le polovica detektorja ARICH, saj je zaradi neučinkovitega hlajenja prišlo do segrevanja detektorskih komponent. Vpliv temperatur na umeritev bom predstavila na koncu poglavja.

9.5.1 Opis aparature za testiranje

Aparatura omogoča hkratno testiranje štirih modulov, pritrjenih na aluminijasto ogrodje. Merili smo odziv modulov na kratke svetlobne sunke ter odziv pri naključno proženih dogodkih. Pri testiranju osvetljenih detektorjev za določanje površinske občutljivosti smo uporabljali zeleni laser valovne dolžine 520 nm, kar ustreza kvantnemu izkoristku fotokatode 10 % in absorpcijski dolžini v siliciju 1 µm. Izhod laserskega snopa je bil razdeljen na štiri dele, intenziteta pa nastavljena tako, da je ustrezala povprečnemu številu fotonov na prožen dogodek približno 0,1. S tem smo zagotovili zanemarljiv delež večfotonskih signalov. Optična vlakna so bila pritrjena na pomično mizico, kar je omogočalo natančne premike svetlobnega snopa po celotni površini senzorjev. Eksperiment je bil zaprt v svetlobno nepropustni škatli. Shema eksperimenta je predstavljena na sliki 6.1.

9.5.2 Meritve

Opravili smo dve vrsti meritev – brez osvetljevanja modulov in z moduli, osvetljenimi z lasersko svetlobo. Prag diskriminacije smo prestavljali med vrednostma −1,25 V in 1,25 V, pri čemer smo interval razdelili na 1024 korakov. Pri neosvetljenih senzorjih zaznamo signal, ki je posledica šuma HAPD-ja in elektronike, kot prikazuje slika 9.11. Če prag diskriminacije premikamo po različnih vrednostih napetosti, dobimo odziv, ki je prikazan na isti sliki desno. Porazdelitev signala je Gaussova in njeno srednjo vrednost uporabimo za določanje ničelnih vrednosti signala. Nastavimo jo lahko za vsak elektronski signal posebej s spreminjanjem elektronskih parametrov. Princip meritev osvetljenih detektorjev prikazuje slika 9.12. Pri meritvah odziva osvetljenega detektorja štejemo število dogodkov, kjer zaznamo prehod signala z logične 0 na 1. Rezultat takšne meritve prikazuje slika 9.13.

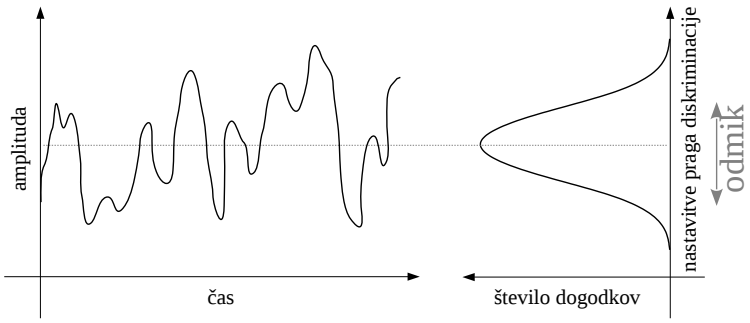

Slika 9.11: Shematski prikaz časovno odvisnega signala enega kanala neosvetljene merilne naprave (levo) in število dogodkov v odvisnosti od praga diskriminacije (desno).

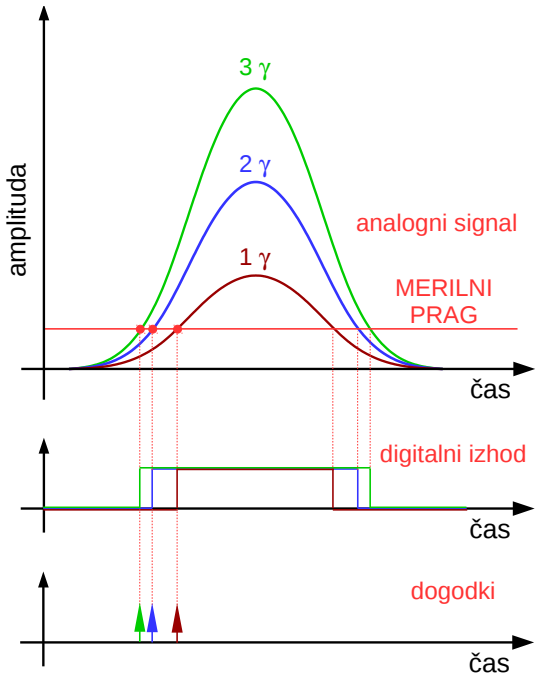

Slika 9.12: Shematski prikaz merjenja prehodov signala čez prag diskriminacije. Zgoraj: Časovni razvoj šuma in eno-, dvo- ter trofotonskega signala pred digitalizacijo. Sredina: Digitalni izhodni signal iz diskriminatorja Spodaj: Štetje dogodkov, kjer zaznamo prehod digitalnega signala z logične 0 na 1.

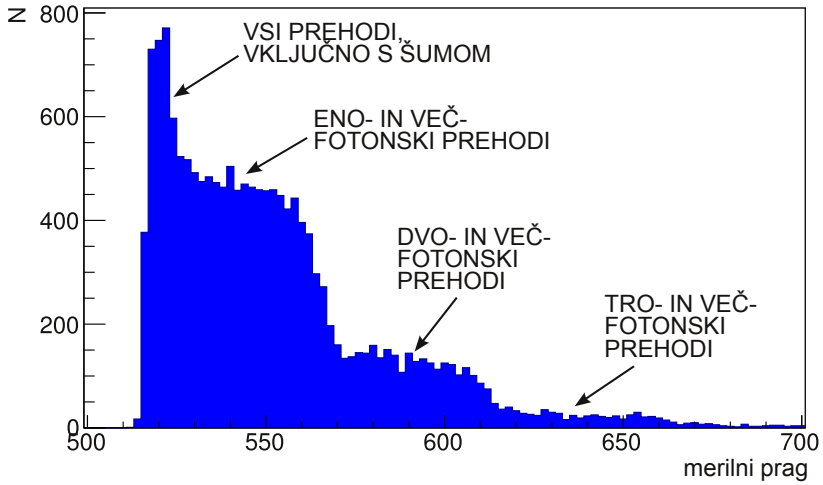

Slika 9.13: Število sunkov v odvisnosti od praga diskriminacije.

9.5.3 Umeritev odmikov ničelnih vrednosti

Elektronski šum kanalov je porazdeljen okoli različnih vrednosti. Ničelno vrednost porazdelitve lahko spreminjamo z nastavljanjem elektronskih parametrov v čipih ASIC, imenovanih *odmik* (*angl. offset*). Vsak čip ima 16 grobih in 16 finih nastavitev odmikov, katerih odzivi so bili testirani. Ničelne vrednosti za posamezen odmik so bile določene s prilagajanjem Gaussove funkcije, kot je razvidno na sliki 9.14 desno. Na isti sliki levo so prikazane ničelne vrednosti za vse nastavitve odmikov enega kanala.

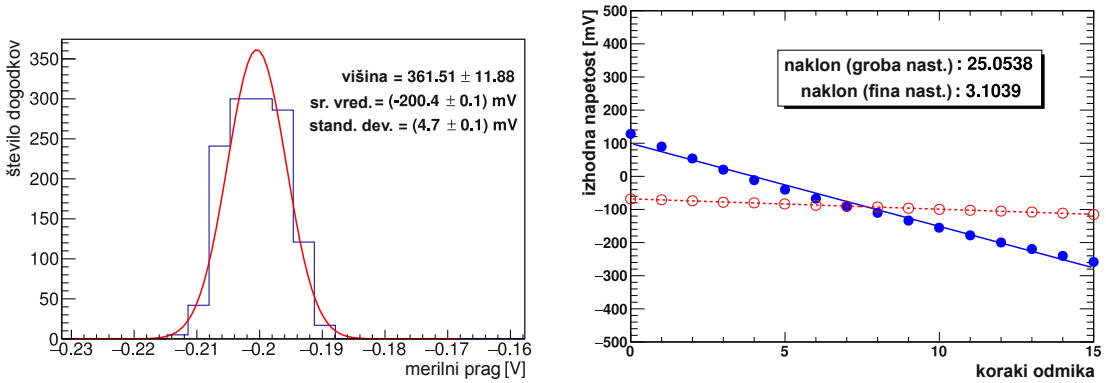

Slika 9.14: Levo: Odziv neosvetljenega kanala za en odmik [78]. Prilagojena je Gaussova funkcija, katere srednja vrednost predstavlja ničelno vrednost šuma. Desno: Ničelne vrednosti za odmike enega kanala. Vrednostim za grobo in fino nastavitev smo prilagodili linearno funkcijo in določili naklon v enotah [mV/korak] [78].

Po prilagajanju Gaussove funkcije šumu smo določili srednjo vrednost in standardni odmik za vsak kanal. Mejo praga diskriminacije nastavili $3{,}5\sigma$ nad ničelno vrednost, pri čemer je verjetnost, da zaznamo signal zaradi šuma le 0,23 ‰. Mejo praga diskriminacije lahko nastavimo le skupno za celotni senzor, zato moramo pri umeritvi premikati ničelne vrednosti posameznih kanalov. Ker so bile širine porazdelitev šuma ob začetku eksperimenta približno enake, smo vse kanale pomaknili na enako ničelno vrednost. Odmike ničelnih vrednosti smo poravnali v več korakih.

Najprej smo nastavili ciljno vrednost, nato pa opravili meritev šuma in iz prilagajanja Gaussove funkcije določili ničelne vrednosti kanalov. Iz razlike med ničelno in ciljno vrednostjo smo določili parametre odmika za vsak kanal in meritev ponovili. Za določanje parametrov odmikov smo uporabili povprečni naklon kanalov. Ker se te za različne kanale malenkost razlikujejo, smo postopek nastavljanja novih parametrov odmika ponovili še nekajkrat, dokler niso bili vsi kanali poravnani. Odzivi kanalov pred in po umeritvi so prikazani na sliki 9.15.

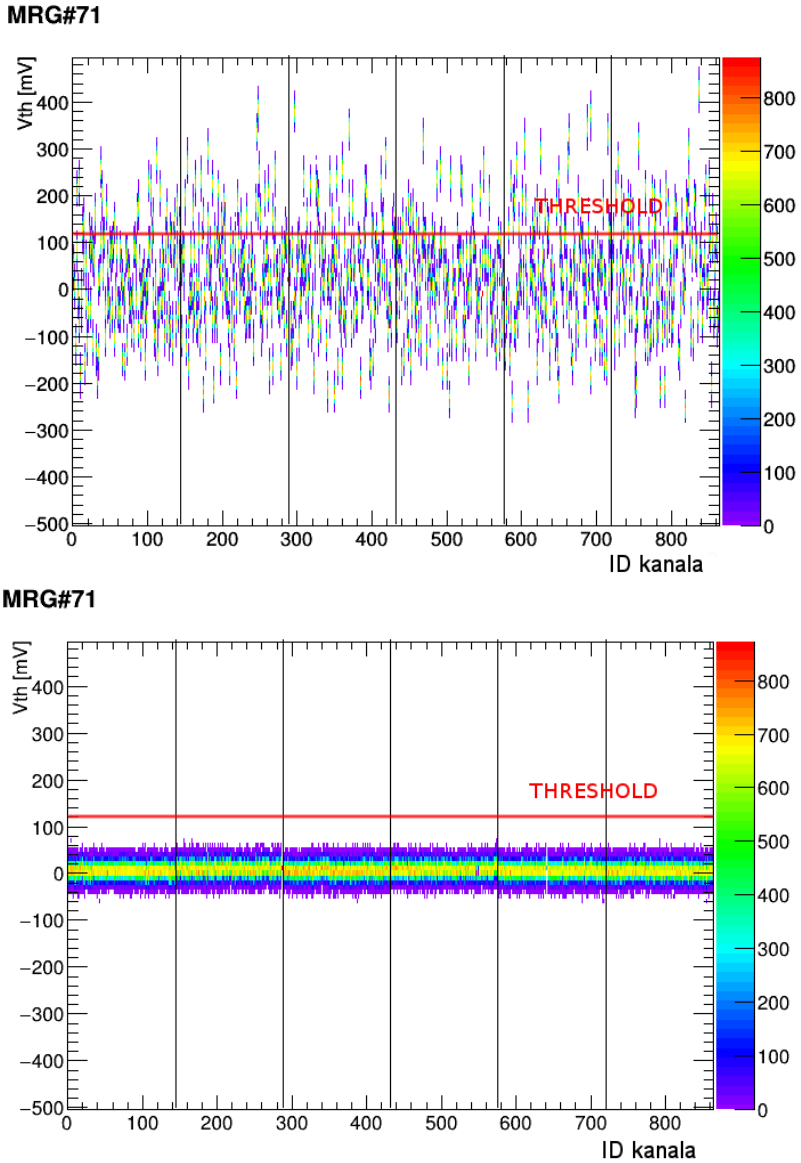

Slika 9.15: Odzivi neosvetljenih kanalov pred (zgoraj) in po (spodaj) umeritvi odmikov. Rezultati so prikazani za šest modulov, ki so med seboj ločeni z navpičnimi črtami. Številke kanalov za $i-$ti senzor se začnejo z $(i-1) \times 144$.

9.5.4 Meritve ojačanja signala

Pri testih modulov smo določili tudi ojačanje signala posameznih kanalov. Določimo ga lahko na dva načina – iz meritev sunkov v odvisnosti od praga diskriminacije (kar bomo uporabljali med eksperimentom Belle II) ali iz porazdelitve po zbranem naboju, kot smo to naredili pri testih modulov. Signale smo integrirali v območju,

ki ga prikazuje slika 9.16, in rezultate 10^4 dogodkov zbrali v histogramu (slika 9.17). Ojačanje kanala smo določili iz razlike srednjih vrednosti Gaussovih funkcij, ki smo ju prilagodili vrhovoma, ki ustrezata šumu in enofotonskemu signalu. Rezultati meritev za 144 kanalov enega HAPD-ja so prikazani na sliki 6.25.

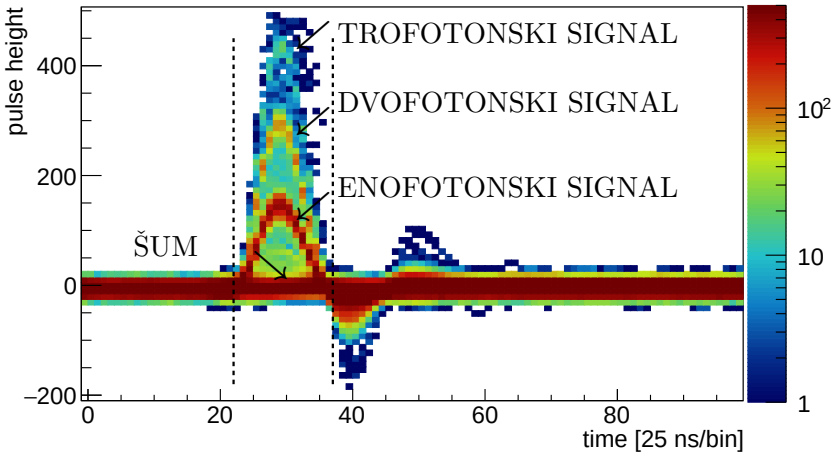

Slika 9.16: Akumulirani analogni signal, kjer je višina pulza odvisna od števila zaznanih fotonov. Os x prikazuje čas, os y pa višino pulza. Signal smo integrirali na območju med navpičnima črtama.

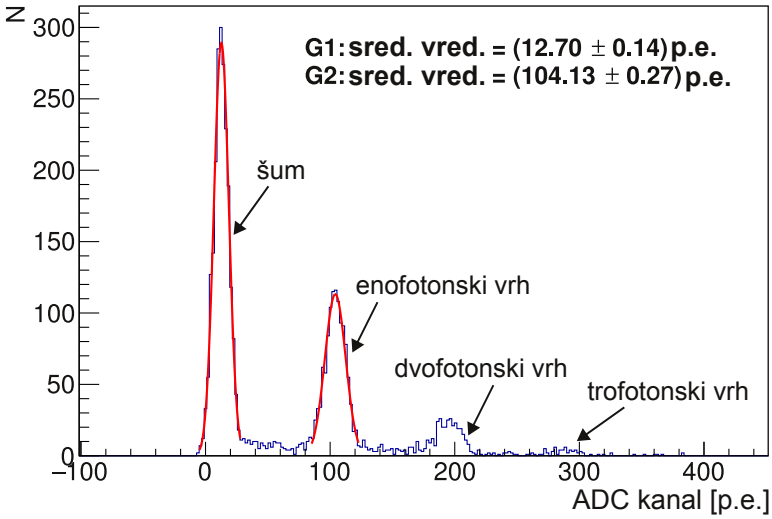

Slika 9.17: Zbran naboj na enem kanalu s prilagojenima Gaussovima funkcijama na vrhovih, ki ustrezata šumu in enofotonskemu signalu.

9.5.5 Neuporabljeni kanali

Nepravilno delujoče kanale v rekonstrukciji maskiramo, saj privedejo do napačnega identificiranja delca. Nepravilno delujoče kanale lahko razdelimo v tri skupine. Prvi so trajno mrtvi kanali zaradi okvare na elektroniki ali senzorju. Drugo skupino predstavljajo kanali, ki imajo zaradi visokega zapornega toka povečan šum in pošiljajo lažne signale o zaznanem zadetku. V zadnjo skupino so zajeta večja območja, ki delujejo nepravilno zaradi okvare celotnega bralnega čipa, nedelujočega napajanja ali napake pri komunikaciji z združevalnimi vezji.

Trajno mrtve in šumeče kanale smo določili pri meritvah pozicijske občutljivosti senzorjev. Z laserjem smo osvetljevali senzor v smeri osi y v korakih velikosti

359,5 µm, pri čemer smo pozicije v smeri osi x fiksirali na sredini kanalov. Podobno smo naredili meritev še v smeri x po sredini vrstic. Ves čas premikanja laserja smo merili odzive vseh kanalov. Primer meritve prikazuje slika 9.18, kjer vidimo odziv šumečih in mrtvih kanalov, prav tako pa tudi popačenje signala na robu senzorja, ki je posledica nehomogenega električnega polja znotraj HAPD-ja. Ko senzorje postavimo v močno magnetno polje, pričakujemo homogen odziv.

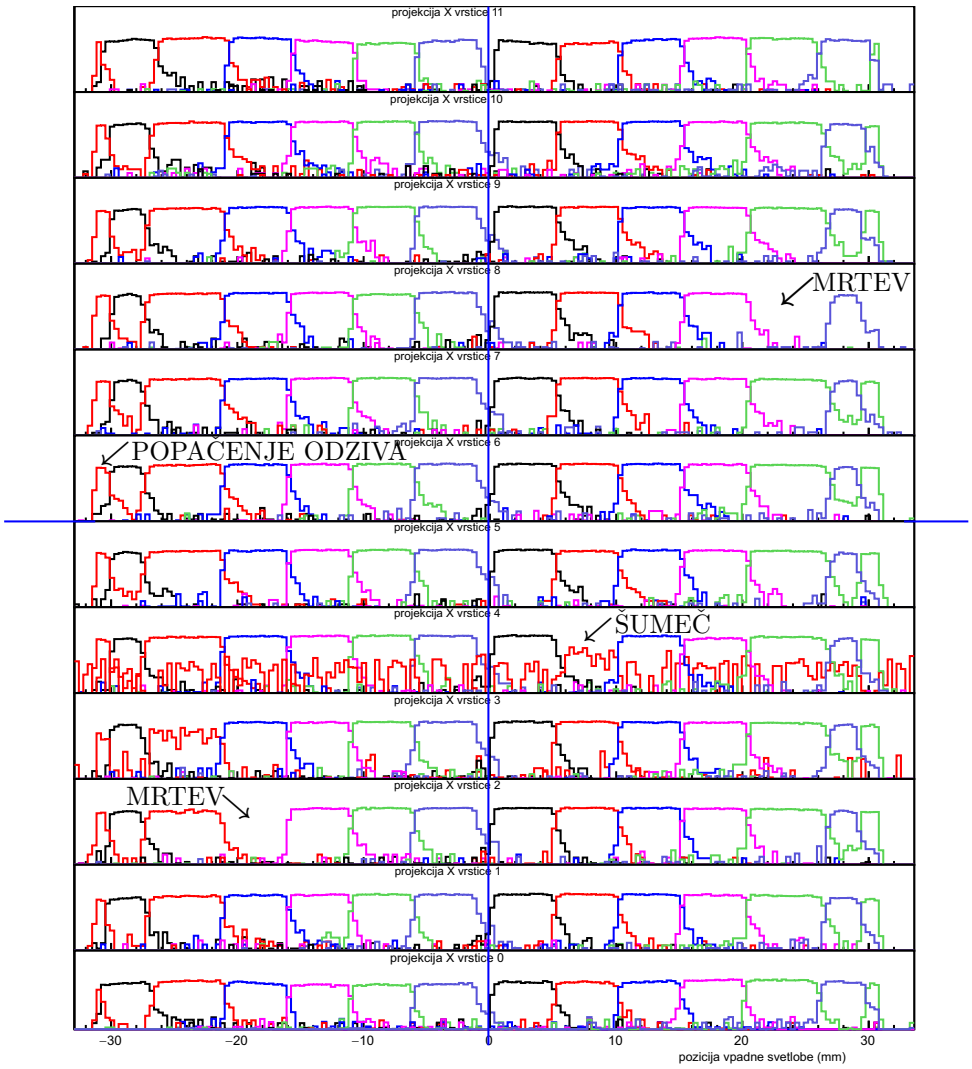

Slika 9.18: Odziv kanalov ob laserskem skeniranju po sredini vrstic kanala. Os x predstavlja pozicijo vpadne laserske svetlobe, os y pa število dogodkov v logaritemski skali z vrednostmi med 1 in 10^4.

Pri nekaterih kanalih se je število zaznanih zadetkov kot posledica šuma povečalo med meritvami v fazi II. Njihov seznam se je sčasoma spreminjal, kar je najverjetneje tudi posledica nepravilne umeritve odmikov ničelnih vrednosti nekaterih kanalov med eksperimentom. Za izboljšanje učinkovitosti identifikacije delcev smo po vsaki meritvi zajete podatke analizirali in maskirali kanale, ki so imeli veliko število zadetkov. Mejo smo določili iz grafov zasedenosti kanalov in jo postavili na 0,15 %, kot prikazuje slika 9.19.

Za oceno učinkovitosti rekonstrukcije sledi delcev v fazi II smo uporabili vzorec dogodkov, kjer je prišlo do sipanja Bhabha. Izbrali smo vzorec z visoko gibalno

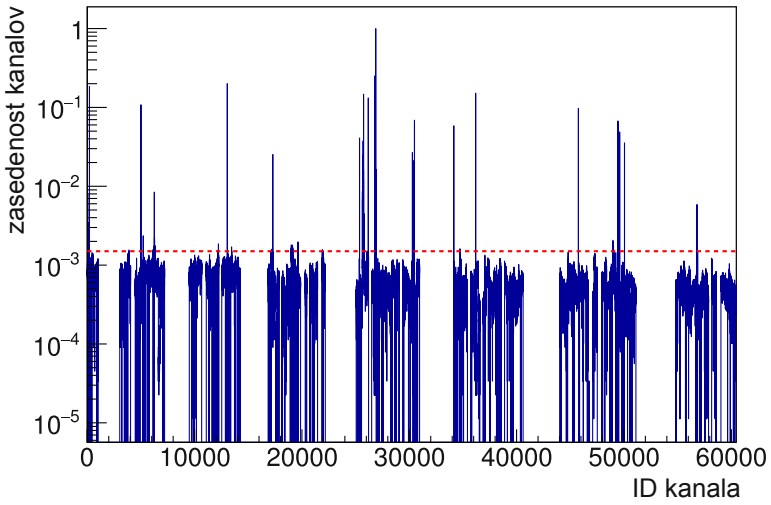

Slika 9.19: Graf zasedenosti kanalov pred maskiranjem. Rdeča črta je meja 0,15 % zasedenosti, nad katero smo kanale označili za šumeče. Podatke smo zajemali s polovico detektorja, zato ima polovica kanalov ničelno zasedenost.

količino elektronov (med 5.8 GeV/c in 7.4 GeV/c) ter izločili sledi delcev, ki zadenejo ARICH blizu roba (meje radija zadetka na aerogelih smo postavili med 60 cm in 100 cm). Določili smo širino porazdelitve kota Čerenkova (ki je odvisna predvsem od širine sevalca in velikosti detektorskih kanalov), kot prikazuje slika 9.20. Standardni odmik vrha za primarne fotone Čerenkova je (14.09 ± 0.01) mrad, kar je že blizu pričakovane širine. Porazdelitev sledi delcev po kotu Čerenkova in polarnem kotu prikazuje slika 9.21. Projekcijam kota Čerenkova pri vsakem intervalu polarnega kota smo prilagodili vsota linearne in dveh Gaussovih funkcij, kot prikazuje slika 9.20. Dobljenim srednjim vrednostim smo prilagodili kosinusno funkcijo, ki je na sliki označena z rdečo. V primeru pravilne poravnave detektorja ARICH znotraj Belle II mora biti ta odvisnost linearna.

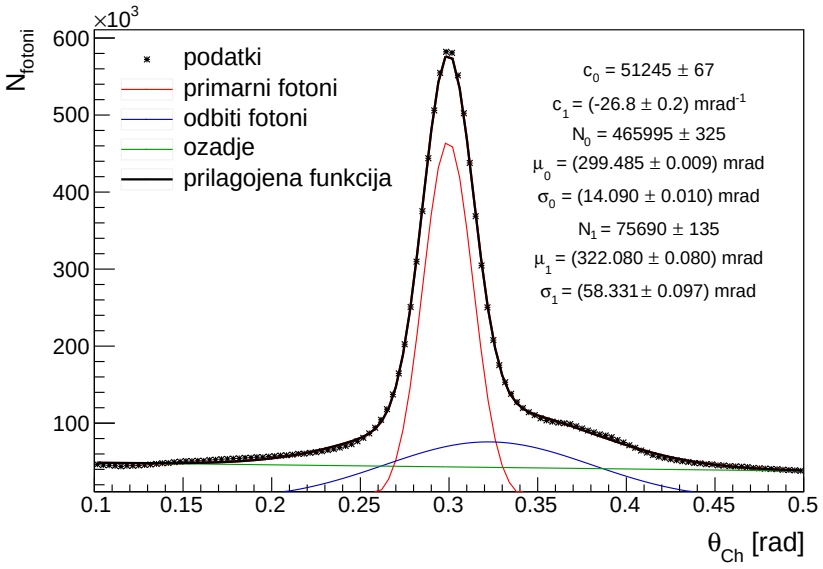

Slika 9.20: Porazdelitev kota Čerenkova pri gibalni količini elektronov med 5.8 GeV/c in 7.4 GeV/c ter radijem zadetka na aerogelu med 60 cm in 100 cm.

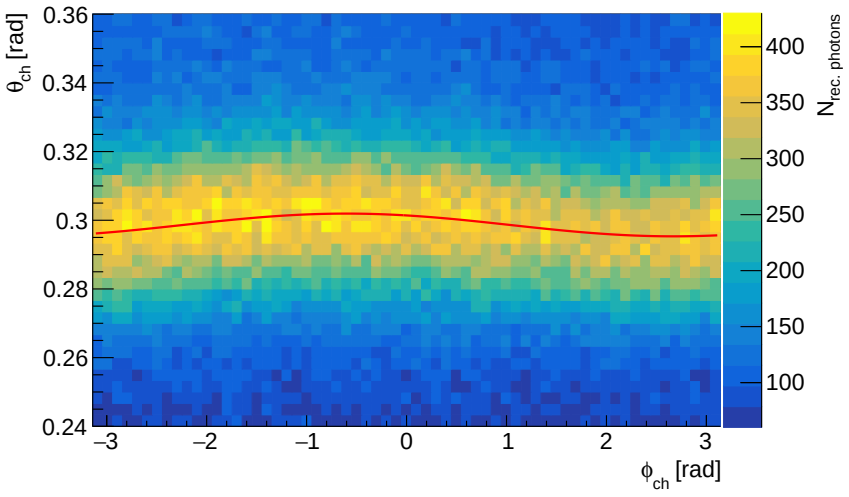

Slika 9.21: Porazdelitev sledi delcev po kotu Čerenkova in polarnem kotu. Srednjim vrednostim Gaussove funkcije, ki opisuje porazdelitev primarnih fotonov Čerenkova za vsak interval polarnega kota, smo prilagodili kosinusno funkcijo, ki je označena z rdečo krivuljo.

9.5.6 Temperaturni vplivi v fazi II

Nezadostno hlajenje ARICH-a je povzročilo segrevanje komponent detektorja. Temperatur HAPD-jev nismo mogli direktno izmeriti, smo pa zato merili temperature na bralni elektroniki ter dodatno namestili še temperaturne senzorje pod zadnjo ploščo ARICH-a, označene na sliki 6.45. Pri višjih temperaturah se poveča temni tok, zato smo se odločili, da najvišja temperatura pri vrhu ARICH-a ne sme presegati 42 °C. S to mejo smo lahko brali podatke s celotnega ARICH-a približno pet ur in preverili vpliv temperature na obliko šuma ter ojačanje signalov.

Meritve šuma

Meritve sunkov neobsevanih senzorjev v odvisnosti od praga diskriminacije smo opravili pri treh različnih temperaturah zgornjega temperaturnega senzorja (29 °C, 35 °C in 39 °C). Prva meritev je bila opravljena 15 minut po začetku napajanja modulov, naslednji dve pa sta si sledili v razmakih ene ure. Razlika med rezultati pri srednji in zgornji temperaturi je zanemarljiva, se pa šum poveča glede na meritev tik po priklopu elektronike. Tipičen primer porazdelitve šuma za en kanal pri vseh treh temperaturah prikazuje slika 9.22.

Standardni odmik se v povprečju poveča za 2,3 mV (17 %). Če je pri umeritvi pri najnižji temperaturi meja diskriminacije $3{,}5\sigma$ nad ničelno vrednostjo, je razlika pri višji temperaturi le še 3σ. Verjetnost, da zaznamo signal, ki ga sproži šum, se v tem primeru poviša s prvotnih 0,23 ‰ na 1,4 ‰.

Meritve ojačanja signala

Temperature zgornjega senzorja pri meritvah ojačanja signala so bile 32 °C, 34 °C in 41 °C. Senzorje smo osvetljevali z LED diodami. Izmerili smo število sunkov kot funkcijo praga diskriminacije za vsak kanal. Ojačanje signala smo dobili iz prilaganja Gaussove funkcije na vrh, ki ustreza vsem prehodom, in Gaussove funkcije napake

na prehodu med eno- in večfotonskimi ter dvo- in večfotonskimi signali, kot prikazuje slika 9.23.

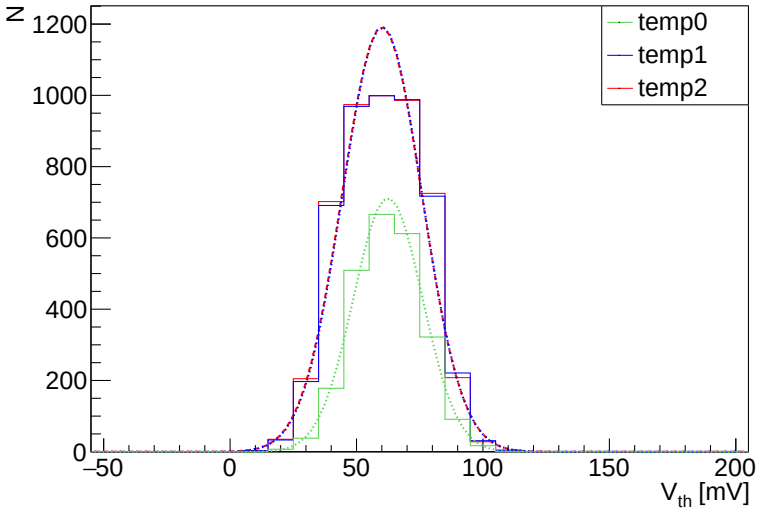

Slika 9.22: Meritve sunkov v odvisnosti od praga diskriminacije za en kanal pri treh različnih temperaturah zgornjega temperaturnega senzorja (32 °C, 34 °C, 41 °C). Rezultatom so prilagojene Gaussove funkcije.

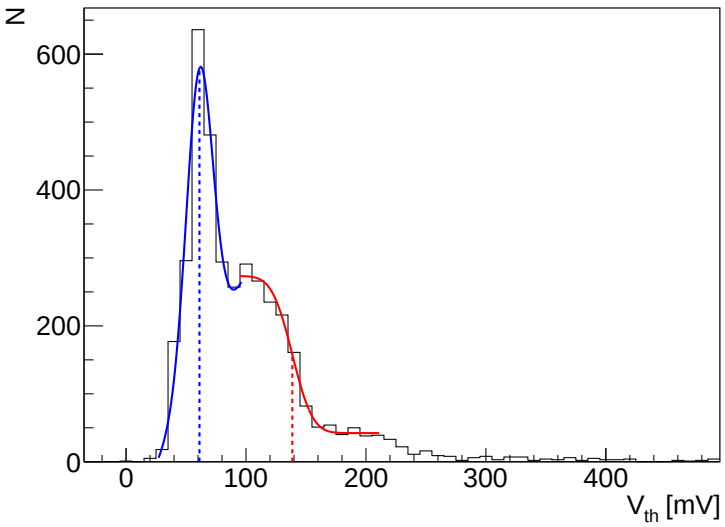

Slika 9.23: Število sunkov kot funkcija praga diskriminacije enega kanala (modul 38, kanal 140). Ojačanje signala določimo iz prilagojene Gaussove funkcije in Gaussove funkcije napake.

Absolutne vrednosti ojačanja smo izračunali kot [81]:

$$\text{ojačanje signala}[e^-] = \frac{\text{ojačanje [mV]}}{10.7\text{mV fC}^{-1} \times 1{,}6 \times 10^{-4}[\text{fC}/e^-]} \tag{9.5.1}$$

Skupno ojačanje signala se zmanjša za povprečno 20 % pri primerjavi rezultatov pri najnižji in najvišji temperaturi, kot prikazuje slika 9.24.

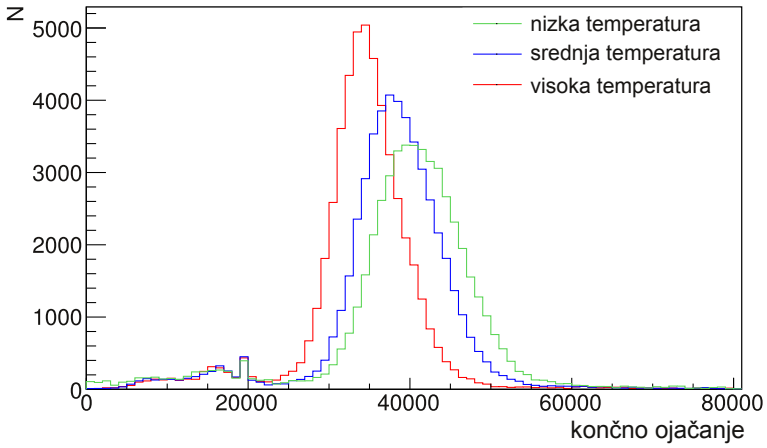

Slika 9.24: Skupno ojačanje signala za vse delujoče kanale pri treh različnih temperaturah zgornjega temperaturnega senzorja v ARICH-u; 32 °C, 34 °C in 41 °C.

9.6 Učinkovitost delovanja ARICH-a

Učinkovitost delovanja detektorja ARICH določimo glede na kvaliteto ločevanja med delci, ki jo izmerimo kot deleže pravilno identificiranih kaonov in napačno identificiranih pionov. Za študije učinkovitosti identifikacije smo uporabili kontrolna kanala $D^{*+} \to D^0(\to K^-\pi^+)\pi_s^+$ in $D^{*-} \to \bar{D}^0(\to K^+\pi^-)\pi_s^-$, pri katerih lahko identiteto nabitega delca določimo neodvisno od ARICH-a. Od tu naprej bomo omenjali samo D^{*+} in D^0, vendar bo analiza zavzemala tudi nabojno konjugirane razpade.

Razlika mas mezonov D je 145,43 MeV/c^2, kar je ravno nad maso nabitega piona $(139{,}570\,61 \pm 0{,}000\,23)$ MeV/c^2. Pri tem ostane malo energije za pretvorbo v kinetično energijo piona, ki ga zaznamo v sledilnem sistemu. Naboj počasnega piona π_s^+ določimo iz ukrivljenosti sledi v sledilnem sistemu, hitri nabit kaon in pion iz razpada pa nato identificiramo na podlagi njunega naboja. S tem dobimo informacijo o vrsti delca, s katero lahko neodvisno preverimo delovanje ARICH-a.

Med delovanjem eksperimenta pričakujemo vzorec podatkov z integrirano luminoznostjo 50 ab^{-1}. Število zaznanih razpadov $D^{*+} \to D^0(\to K^-\pi^+)\pi_s^+$ v celotnem vzorcu lahko ocenimo iz rezultatov eksperimenta Belle, kjer so rekonstruirali $2{,}61 \times 10^6$ parov $K^-\pi^+$ [84]. Če vrednost prilagodimo na luminoznost Belle II, dobimo približno 130 milijonov razpadov. Le okoli 10 % jih identificiramo z ARICH-em. Za študije smo uporabili vzorce Monte Carlo velikosti 50 fb^{-1} za fazo II in 1 ab^{-1} za fazo III. V nadaljevanju bodo predstavljeni rezultati vzorcev MC9, ki so bili simulirani s programskim okoljem BASF2 verzije *release-00-09-02*.

9.6.1 Analizna razpadnega kanala $D^{*+} \to D^0(\to K^-\pi^+)\pi_s^+$

Iz sledilnega sistema smo dobili podatke o trajektorijah nabitih delcev v dogodku. Rekonstrukcijo razpadov D^{*+} smo opravili v več korakih:

1. Naboj počasnega piona π_s^+ smo uporabili za identifikacijo kaona in piona iz razpada mezona D^0.
2. Hitre nabite delce smo izbrali kot kandidate za kaone in pione, pri čemer smo uporabili selekcijo vpadnih parametrov sledi delca d_0 in z_0 (glej tabelo 9.2).
3. Izbrali smo vzorec kaonov, kjer negativno nabit delec vstopi v ARICH; pozitivno nabiti delci so kandidati za pione (in obratno za vzorec pionov).

4. Gibalne količine kandidatov za pione in kaone ter njihove mase smo uporabili za rekonstrukcijo izvornega delca D^0.
5. Počasni pion in rekonstruiran mezon D^0 smo združili v mezon D^{*+}.

Selekcijski parametri, zbrani v tabeli 9.2, so temeljili na izbiri rezov pri podobni analizi pri eksperimentu Belle [85] in bili prilagojeni rezultatom simulacij za Belle II. Najpomembnejša je selekcija na razliki mas mezonov

$$\Delta M = M(K\pi\pi_s) - M(K\pi), \tag{9.6.1}$$

s katero odpravimo večino ozadja in obdržimo večji del signala. Vpliv selekcijskih parametrov na porazdelitev razlike mas mezonov D prikazuje slika 9.25.

Tabela 9.2: Izbira parametrov za rekonstrukcijo razpadov D^{*+}.

selekcijski parameter	vrednost
vpadni parameter v ravnini $r-\phi$	$< 2\,\mathrm{cm}$
vpadni parameter v ravnini $r-z$	$< 4\,\mathrm{cm}$
invariantna masa mezona D^0	$[1{,}82\,\mathrm{GeV/c^2}, 1{,}91\,\mathrm{GeV/^2c}]$
razlika mas $\Delta M - m(\pi^+)$	$[4{,}0\,\mathrm{MeV/c^2}, 8{,}0\,\mathrm{MeV/c^2}]$
obratna invariantna masa[a] D^0_{rev}	$[1{,}856\,\mathrm{GeV/c^2}, 1{,}874\,\mathrm{GeV/c^2}]$
gibalna količina D^{*+} v težiščnem sistemu	$1{,}5\,\mathrm{GeV/c}$
kot med gibalnima količinama D^0 in K^+	$\lvert\cos\theta_{D^0}\rvert \leq 0{,}8$

[a] Invariantna masa, pri kateri kaonu in pionu pripišemo zamenjani masi.

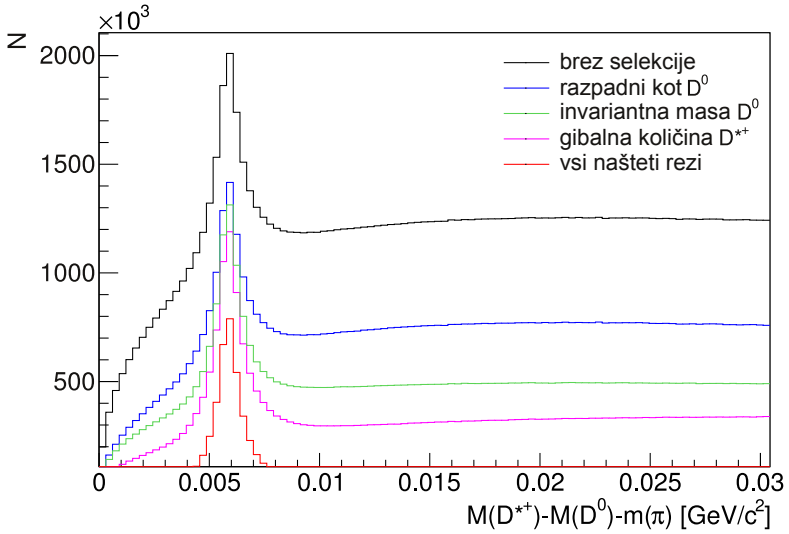

Slika 9.25: Vpliv selekcije na razliko mas D mezonov, zmanjšano za maso počasnega piona; $\Delta M - m(\pi^+)$.

9.6.1.1 Izračuni učinkovitosti identifikacije

Za izračune učinkovitosti identificiranja delcev smo uporabili porazdelitve deviacije invariantne mase D^0. Porazdelitev ima preprosto obliko, kjer ozadje lahko opišemo z linearno funkcijo, signal pa z eno ali vsoto dveh Gaussovih funkcij, kot:

$$PDF = Nbkg \times kM + Nsig \times \Big(frac1 \cdot g1(\mu_1, \sigma_1, M) + (1 - frac1) \cdot g2(\mu_1, \sigma_2, M)\Big) \tag{9.6.2}$$

kjer je M masa $M(K\pi) - m(D^0)$, k je koeficient linearne funkcije, $Nbkg$ in $Nsig$ sta števili dogodkov ozadja in signala, $frac1$ je delež prve Gaussove funkcije, $g(\mu_1, \sigma_1)$ pa predstavlja Gaussovo funkcijo, definirano kot $g(\mu, \sigma, x) = \frac{1}{\sigma\sqrt{2\pi}} \exp(-\frac{1}{2}\left(\frac{x-\mu}{\sigma}\right)^2)$. Srednja vrednost μ_1 je pri obeh Gaussovih funkcijah enaka, standardna odmika funkcij σ_1 in σ_2 pa sta različna. Na histogramih smo namesto μ in σ uporabili oznaki *mean* in *sigma*.

Deleže pravilno identificiranih kaonov, $\varepsilon_{K\to K}$, ter napačno identificiranih pionov, $\varepsilon_{\pi\to K}$, smo določili po enačbi 9.4.4, pri čemer smo mejo identifikacije, $PID_{K/\pi}$, izračunali kot razmerje med funkcijami verjetnosti:

$$PID_{K/\pi} = \frac{\mathcal{L}_K}{\mathcal{L}_K + \mathcal{L}_\pi} \tag{9.6.3}$$

Število signalnih dogodkov, $Nsig$, vzorcev z in brez selekcije $PID_{K/\pi}$ smo določili iz prilagajanja funkcije podatkom po enačbi 9.6.2.

Statistično napako deležev smo določili iz napak parametrov $Nsig$. Če deleže zapišemo kot $\varepsilon^{+\sigma_{\varepsilon_+}}_{-\sigma_{\varepsilon_-}} = \left(A^{+\sigma_{A_+}}_{-\sigma_{A_-}}\right)/\left(N^{-\sigma_{N_-}}_{+\sigma_{N_+}}\right)$, lahko napako zapišemo kot:

$$\sigma^2_{\varepsilon^+_-} = \frac{1}{N^2}\left(\varepsilon^2\sigma^2_{N^-_+} + \sigma^2_{A^+_-} - 2\varepsilon^{3/2}\sigma_{A^+_-}\sigma_{N^-_+}\right) \tag{9.6.4}$$

Deleže smo izračunali za različne meje identifikacije v korakih po 0,05 do vrednosti $PID_{K/\pi} = 0{,}90$ in korakih po 0,01 od vrednosti 0,90 naprej.

9.6.1.2 Prilagajanje funkcij porazdelitvam invariantnih mas

Pri določanju števila dogodkov s selekcijo in brez nje, smo prilagajali funkcijo iz enačbe 9.6.2 porazdelitvi mase mezona D^0, premaknjeni za vrednost nominalne mase $m(D^0) = 1{,}864\,84\,\mathrm{GeV/c^2}$. Funkcije smo prilagajali s pomočjo programskega orodja Roofit [86], ki temelji na orodju ROOT. Primer prilagajanja funkcij masni porazdelitvi prikazuje slika 9.26.

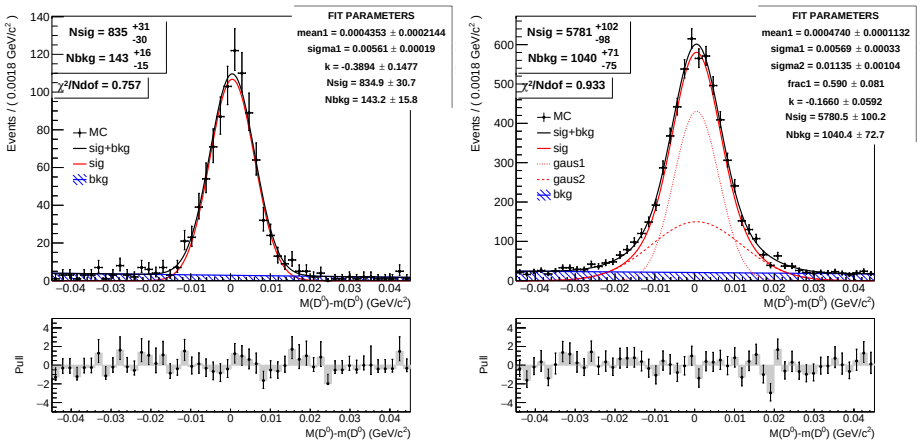

Slika 9.26: Porazdelitve deviacije mase mezonov D^0 za različni območji gibalnih količin in vpadnih kotov. Na sliki sta prikazana primera, kjer signalu prilagodimo eno (levo) in dve (desno) Gaussovi funkciji.

Kvaliteto opisa vzorca s funkcijo smo določili s standardno metodo *hi kvadrata*, kjer je dobro prilagajanje funkcije opisano s parametrom $\chi^2/Ndof \approx 1$. Ujemanje

funkcije z dejanskim vzorcem smo določili tudi porazdelitev normiranih odmikov, $Pull$, ki je za vsako vrednosti na osi x definirana kot razlika med modelsko in izmerjeno vrednostjo, normirano z napako meritve:

$$\text{Pull} = \frac{N_{fit} - N_{dogodek}}{\sqrt{N_{dogodek}}}. \tag{9.6.5}$$

Srednjo vrednost in standardni odmik Gaussove funkcije smo za vzorec brez selekcije fiksirali in parametre uporabili za prilagajanje funkcij vzorcem, kjer smo izbrali rez na meji identifikacije $PID_{K/\pi}$, kot prikazuje slika 9.27. Število signalnih dogodkov obeh vzorcev smo uporabili za izračune izkoristkov identifikacije delcev.

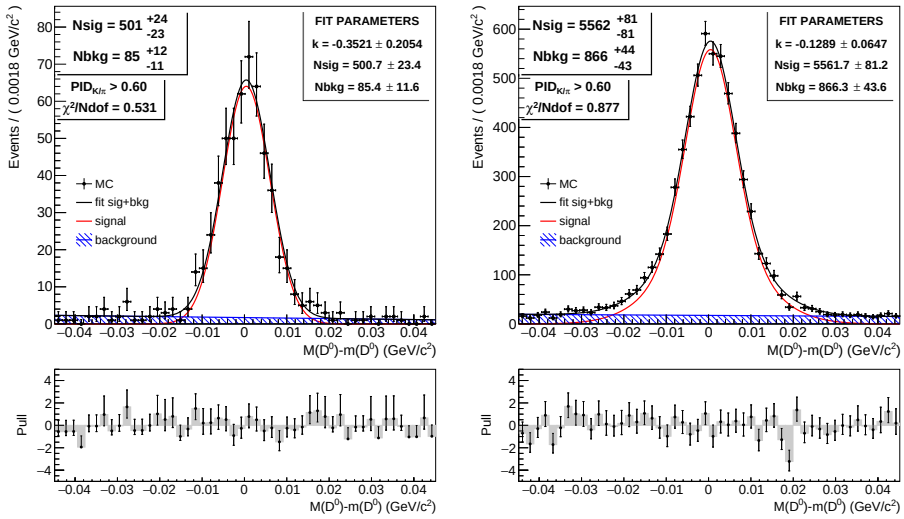

Slika 9.27: Porazdelitve mase mezonov D^0 za različni območji gibalnih količin in vpadnih kotov. Na sliki sta prikazana primera za mejo identifikacije nad 0,6. Parametre za opis oblike signalne funkcije smo fiksirali glede na vzorec s slike 9.26.

9.6.2 Rezultati simulacij

Uporabili smo simulacijo s 320 tisoč dogodki za fazo III in 18 tisoč dogodki za fazo II. Razdelili smo jih glede na vpadni kot in gibalno količino delca. Izbrali smo območje gibalnih količin med 0,5 GeV/c in 4,0 GeV/c, kjer pričakujemo optimalno delovanje detektorja ARICH. Vzorci kaonov in pionov so bili izbrani glede na to, ali je delec vstopil v geometrijsko pokritost ARICH-a.

9.6.2.1 Izkoristek identifikacije kaonov kot funkcija deleža napačno identificiranih pionov

Vzorce za obe fazi smo razdelili glede na gibalno količino p in kosinus vpadnega kota $\cos\theta$, kot prikazuje slika 7.13. Poleg tega smo odvisnosti pogledali tudi za celotne vzorce. Ker so delci izsevani zelo blizu interakcijske točke, njihovi vpadni koti ustrezajo tudi polarnemu kotu na ravnini detektorja ARICH.

Faza III

Simulacije kažejo, da ARICH dobro identificira kaone po celotnem območju vpadnih kotov in gibalnih količin, kot prikazuje slika 9.28. Ob zahtevi, da je napačno identi-

ficiranih pionov 5 %, pravilno identificiramo približno 90 % kaonov. Identifikacija ni enako učinkovita po celotnem območju, temveč je odvisna od vpadnega kota delcev in njihove gibalne količine. Primera učinkovitosti identifikacije kaonov za dva fiksna deleža napačno identificiranih pionov prikazuje slika 9.29.

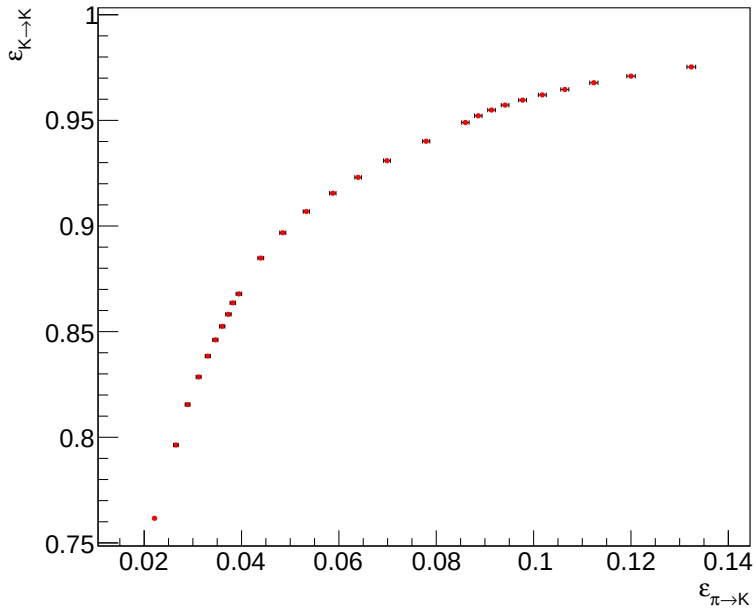

Slika 9.28: Delež pravilno identificiranih kaonov v odvisnosti od deleža napačno identificiranih pionov za celoten vzorec faze III.

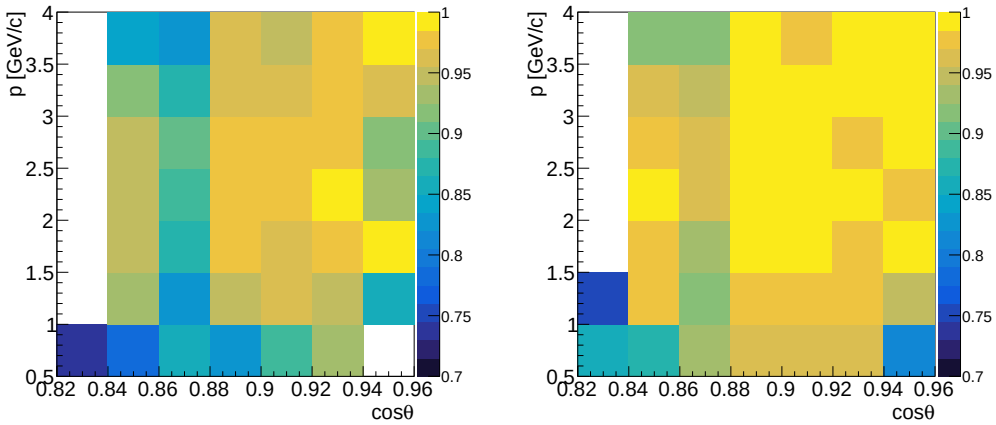

Slika 9.29: Deleži pravilno identificiranih kaonov v fazi III pri verjetnosti za napačno identificirane pione 5 % (levo) in 10 % (desno). Vrednosti pri deležih pravilno identificiranih kaonov pod 70 % niso prikazane zaradi slabše identifikacije na robu detektorja, kjer se večina fotonov odbije od zrcal.

Faza II

Notranji sledilni sistem (PXD+SVD) ni prisoten v fazi II, zato je rekonstrukcija počasnih delcev v slabša, relativni delež rekonstruiranih delcev z večjimi gibalnimi količinami pa višji. Ker so ti boljše identificirani, lahko z zahtevo po 5 % napačno identificiranih pionov pravilno identificiramo kar 92 % kaonov, kot prikazuje slika 9.30. Iz primerov izkoristkov identifikacije kaonov za dva fiksna deleža napačno identificiranih pionov na sliki 9.31 vidimo, da je identifikacija delcev pri vpadnih kotih nad 30° ($\cos\theta < 0.86$) manjša od 90 % pri 5 % napačno identificiranih pionov.

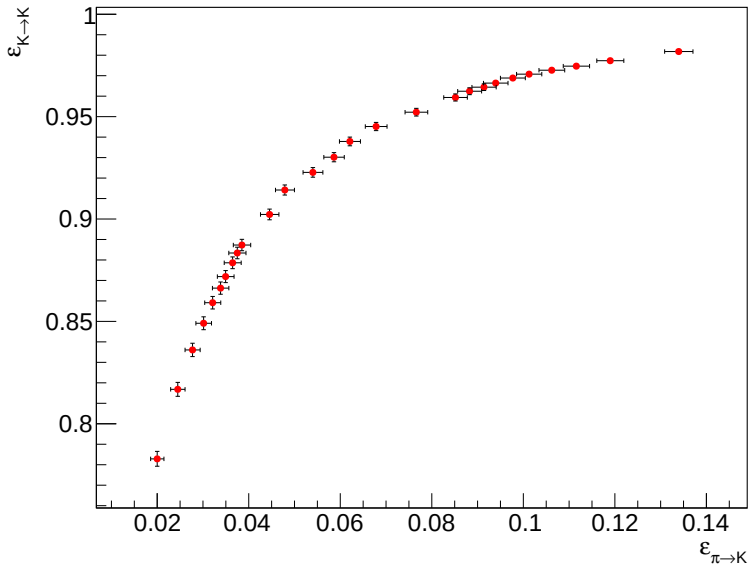

Slika 9.30: Delež pravilno identificiranih kaonov v odvisnosti od deleža napačno identificiranih pionov za celoten vzorec faze II.

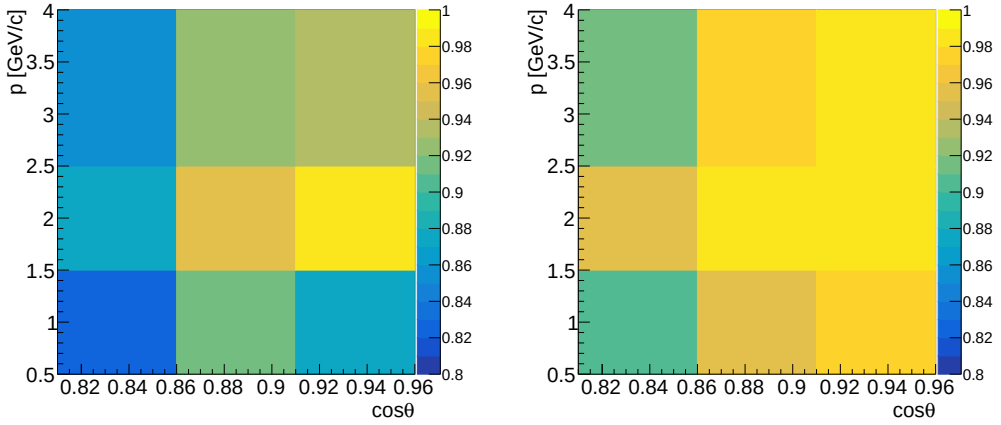

Slika 9.31: Deleži pravilno identificiranih kaonov v fazi II pri verjetnosti za napačno identificirane pione 5 % (levo) in 10 % (desno)

9.6.2.2 Učinkovitost identifikacije kaonov in deleži napačno identificiranih pionov v odvisnosti od gibalne količine nabitega delca

Odvisnost učinkovitosti identifikacije delcev smo pogledali tudi glede na razdrobljenost intervala gibalne količine v korakih 100 MeV/c za fazo II in 50 MeV/c za fazo III. Pri slednjih smo poleg celotnega območja vpadnega kota razlikovali še med tremi intervali z mejami $\cos\theta$ 0,81, 0,86, 0,91 in 0,96, ki ustrezajo kotom 35,9°, 30,7°, 24,5° in 16,3°. Rezultate smo klasificirali in med seboj primerjali na tri načine:

- $\varepsilon_{K/\pi\to K}$ za izbrano selekcijo $PID_{K/\pi} > 0{,}6$ in različne intervale vpadnih kotov (rezultati za fazo III so prikazani na sliki 9.32)
- $\varepsilon_{K/\pi\to K}$ za različne selekcije $PID_{K/\pi} > 0{,}6$ (rezultati za fazi III in II so prikazani na sliki 9.33)
- $\varepsilon_{K\to K}$ za različne fiksirane vrednosti $\varepsilon_{\pi\to K}$ (rezultati za fazi III in II so prikazani na sliki 9.34)

Najboljšo identifikacijo dobimo na intervalu med 2,0 GeV/c in 3,5 GeV/c.

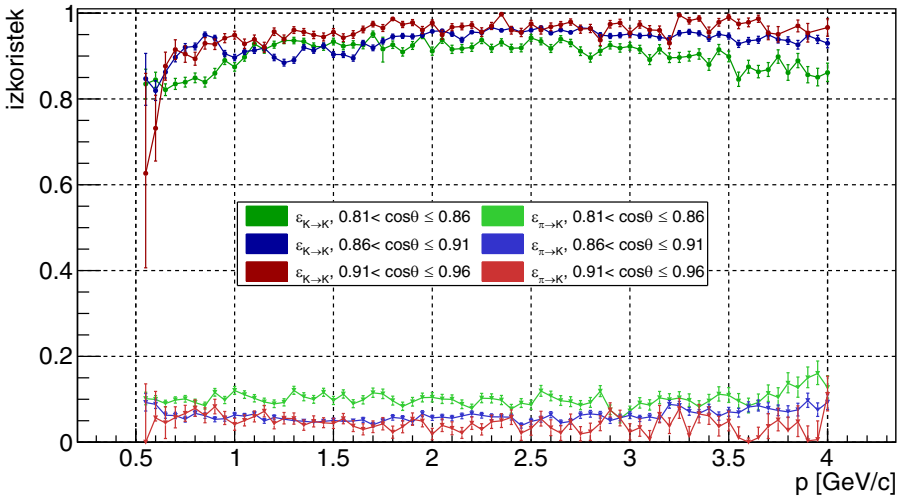

Slika 9.32: Deleži $\varepsilon_{K/\pi\to K}$ pri selekciji $PID_{K/\pi} > 0{,}6$ za fazo III. Prikazani so rezultati za tri intervale vpadnega kota delcev.

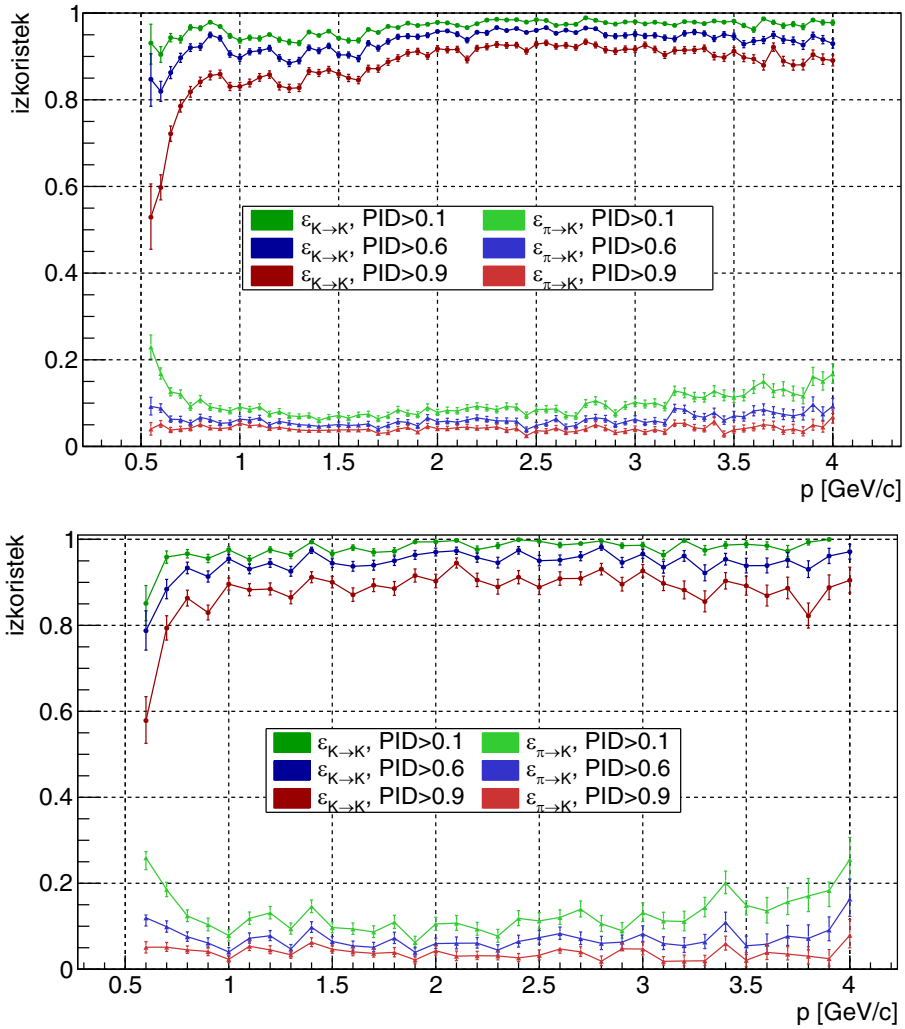

Slika 9.33: Deleži $\varepsilon_{K/\pi\to K}$ pri vstopnem kotu delca med 24,5° in 30,7° za fazo III (zgoraj) ter med 11,5° in 36,9° za fazo II (spodaj). Prikazani so rezultati za tri meje selekcije $PID_{K/\pi}$ (nad 0,1, 0,6 in 0,9).

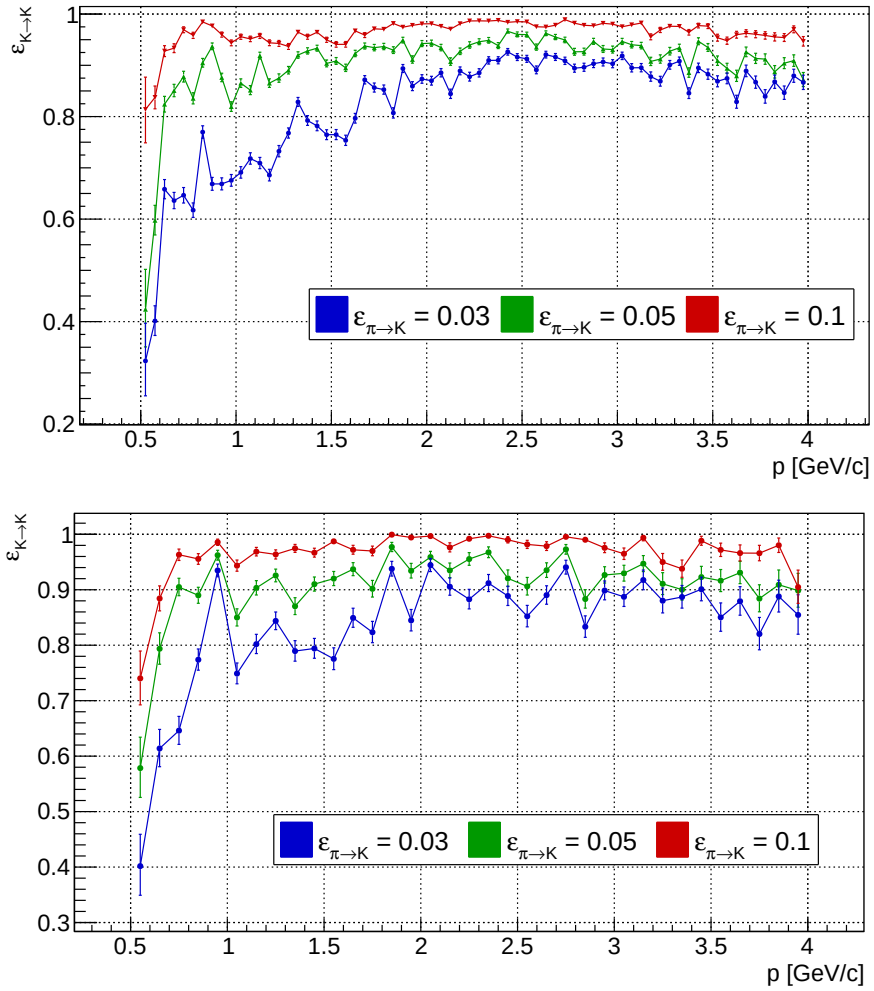

Slika 9.34: Deleži pravilno identificiranih kaonov pri vpadnem kotu delca med 24,5° in 30,7° za fazo III (zgoraj) ter med 11,5° in 36,9° za fazo II (spodaj). Prikazani so rezultati pri treh različnih deležih napačno identificiranih pionov.

9.6.2.3 Učinkovitost identifikacije kaonov in deleži napačno identificiranih pionov v odvisnosti od vpadnega kota nabitega delca

Odvisnost učinkovitosti identifikacije delcev smo pogledali tudi glede na razdrobljenost intervala kosinusa vpadnega kota v korakih 0,005 za fazo II in 0,0025 za fazo III. Pri slednjih smo poleg celotnega območja gibalne količine razlikovali še med tremi intervali z mejami 0,5 GeV/c, 1,5 GeV/c, 2,5 GeV/c in 4,0 GeV/c. Rezultate smo klasificirali in med seboj primerjali na tri načine:

- $\varepsilon_{K/\pi \to K}$ za izbrano selekcijo $PID_{K/\pi} > 0{,}6$ in različne intervale vpadnih kotov (rezultati za fazo III so prikazani na sliki 9.35)
- $\varepsilon_{K/\pi \to K}$ za različne selekcije $PID_{K/\pi} > 0{,}6$ (rezultati za fazi III in II so prikazani na slikah 9.36)
- $\varepsilon_{K \to K}$ za različne fiksirane vrednosti $\varepsilon_{\pi \to K}$ (rezultati za fazi III in II so prikazani na slikah 9.37)

Najboljšo identifikacijo dobimo za vpadne kote delcev med 25° in 30°.

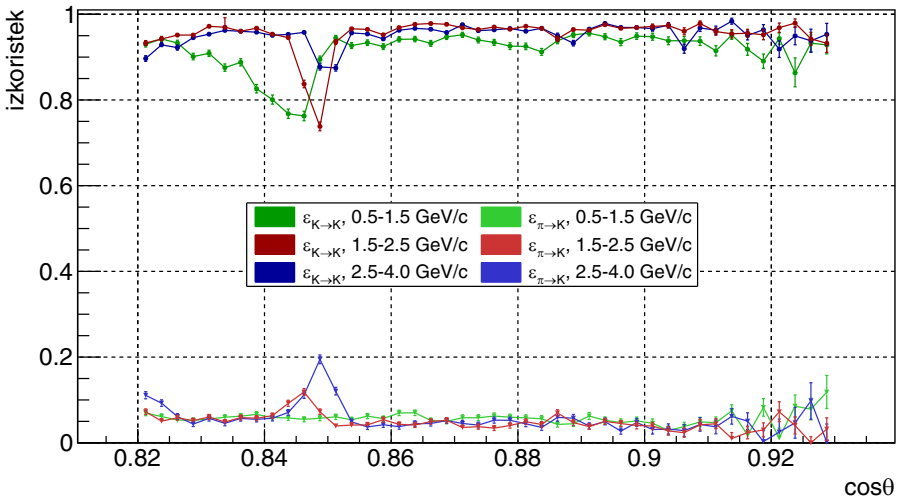

Slika 9.35: Deleži $\varepsilon_{K/\pi\to K}$ pri izbiri $PID_{K/\pi} > 0{,}6$ za fazo III. Prikazani so rezultati za tri intervale gibalne količine.

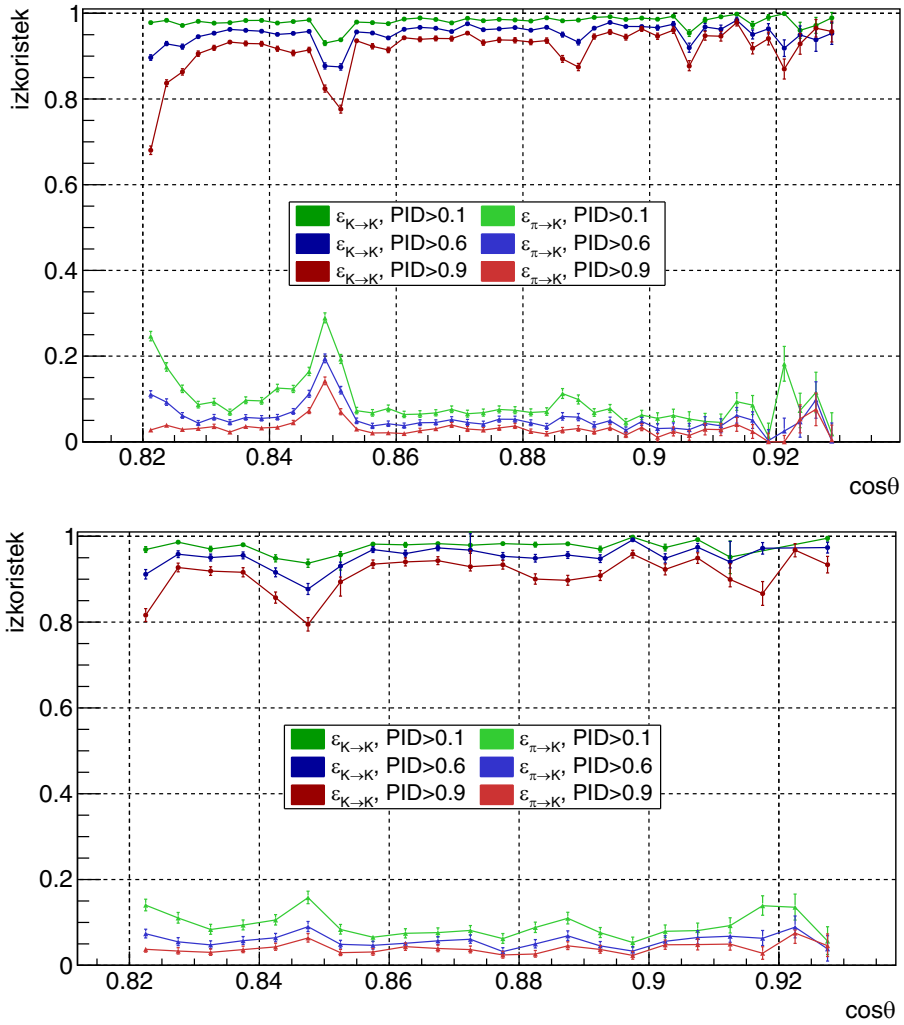

Slika 9.36: Deleži $\varepsilon_{K/\pi\to K}$ pri gibalni količini delca med 2,5 GeV/c in 4,0 GeV/c za fazo III (zgoraj) ter med 0,5 GeV/c in 4,0 GeV/c za fazo II (spodaj). Prikazani so rezultati za tri meje $PID_{K/\pi}$.

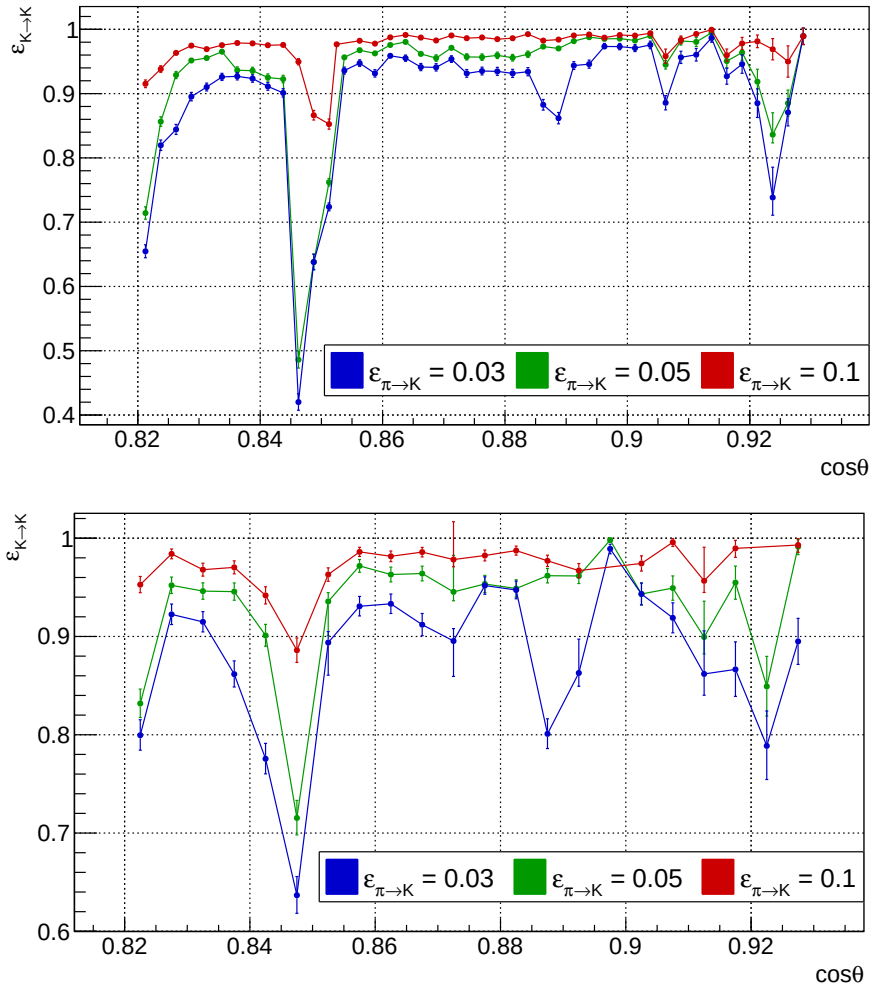

Slika 9.37: Deleži pravilno identificiranih kaonov pri gibalni količini delca med 2,5 GeV/c in 4,0 GeV/c za fazo III (zgoraj) ter med 0,5 GeV/c in 4,0 GeV/c za fazo II (spodaj). Prikazani so rezultati za tri deleže napačno identificiranih pionov.

9.6.3 Učinkovitost ločevanja kaonov od pionov v fazi II

Med fazo II smo zbrali vzorec podatkov z integrirano luminoznostjo 490 pb^{-1}. Zaradi visoke temperature znotraj ARICH-a smo večino časa podatke zajemali le s polovico detektorja, zaradi česar je statistika zbranih mezonov D nizka. Podatke smo analizirali preko dveh razpadnih kanalov, $D^{*+} \to D^0(\to K^-\pi^+)\pi_s^+$ in $D^0 \to K^-\pi^+$. Pri slednjem delcev nismo mogli identificirati neodvisno od informacije z ARICH-a, zato smo vsakemu nabitemu delcu enkrat pripisali maso kaona in drugič maso piona, ter v kombinaciji z drugim nabitim delcem določili invariantno maso mezona D^0. Zaradi omejene selekcije je kombinatorno ozadje pri razpadu $D^0 \to K^-\pi^+$ višje.

9.6.3.1 Razpadni kanal $D^{*+} \to D^0(\to K^-\pi^+)\pi_s^+$

Pri razpadnem kanalu $D^{*+} \to D^0(\to K^-\pi^+)\pi_s^+$ je statistika zelo nizka, zato ni bilo mogoče zanesljivo določiti izkoristkov identifikacije. Selekcijo delcev smo naredili na velikosti mas mezonov $1{,}91\,\mathrm{GeV/c^2} \leq M(K\pi\pi_s) \leq 2{,}11\,\mathrm{GeV/c^2}$ in $1{,}82\,\mathrm{GeV/c^2} \leq M(K\pi) \leq 1{,}91\,\mathrm{GeV/c^2}$ ter razliki mas $0{,}139\,\mathrm{GeV/c^2} \leq \Delta M \leq 0{,}160\,\mathrm{GeV/c^2}$. Po

uporabljeni selekciji smo dobili 72 negativno nabitih delcev iz razpada D^{*+}, ki so dosegli ARICH, kot prikazuje slika 9.38.

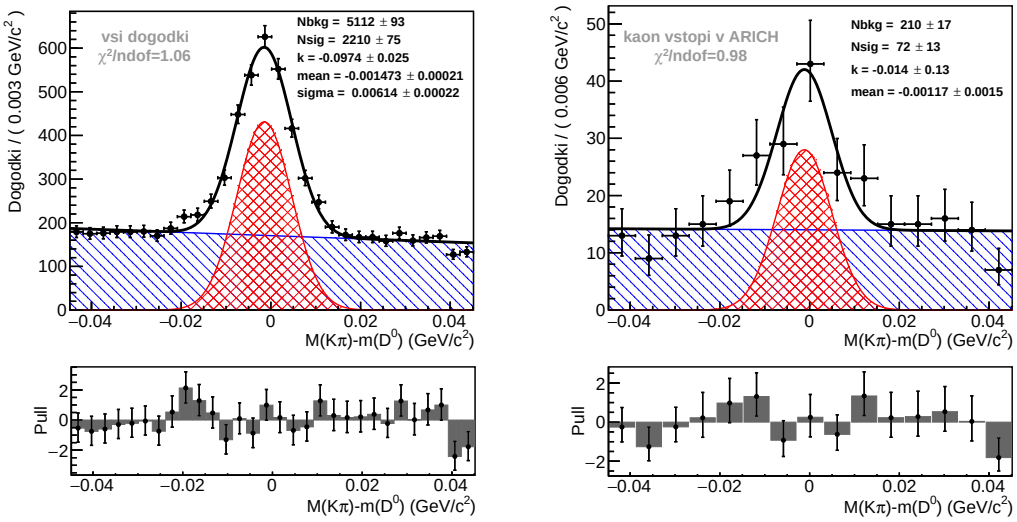

Slika 9.38: Porazdelitev deviacije invariantne mase D^0, kjer je gibalna količina kaona med 0,5 GeV/c in 4,0 GeV/c. Levo: Celotni vzorec, kjer nabiti delci priletijo v poljubni prostorski kot. Desno: Vzorec, kjer kaon vstopi v ARICH.

9.6.3.2 Razpadni kanal $D^0 \to K^-\pi^+$

Statistika nabitih delcev iz razpada mezona D^0, katerega izvor nas ne zanima, je desetkrat večja kot pri tistih, ki prihajajo iz mezona D^{*+}. Porazdelitev mas mezona D^0 za primera, kjer je kaon (pion) vstopil v ARICH, prikazuje slika 9.39 (9.40). Vidimo, da je vrh mase D^0 za razpade, kjer nabit delec vstopi v ARICH premaknjen glede na celotni vzorec, kar je najverjetneje posledica slabšega določanja sledi delcev v smeri naprej. Velikosti premikov signalnega vrha za razpade D^{*+} in D^0 ter pripadajoče število signalnih dogodkov so zbrani v tabeli 9.3.

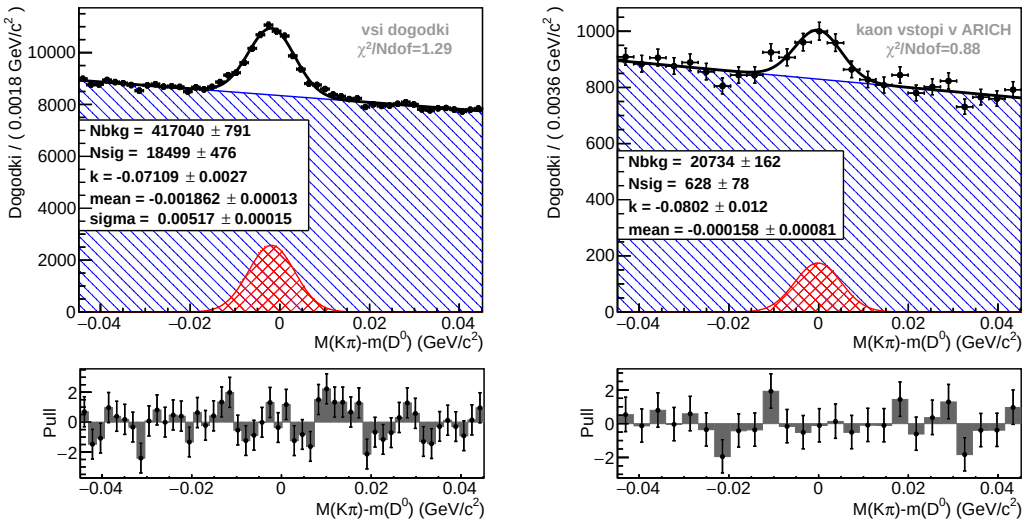

Slika 9.39: Porazdelitev invariantne mase D^0, kjer je gibalna količina kaona med 0,5 GeV/c in 4,0 GeV/c. Levo: Celotni vzorec, kjer nabiti delci priletijo v poljubni prostorski kot. Desno: Vzorec, kjer kaon vstopi v ARICH.

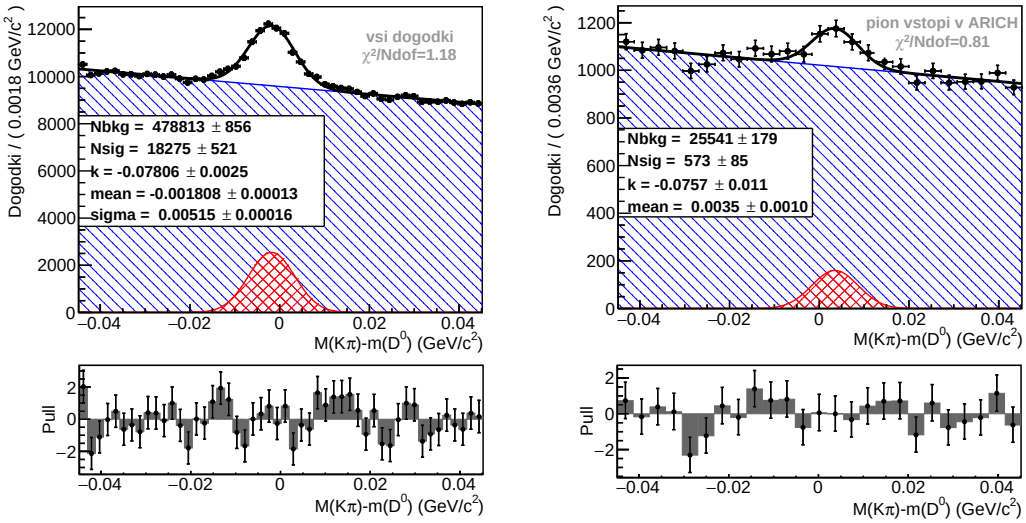

Slika 9.40: Porazdelitev invariantne mase D^0, kjer je gibalna količina piona med 0,5 GeV/c in 4,0 GeV/c. Levo: Celotni vzorec, kjer nabiti delci priletijo v poljubni prostorski kot. Desno: Vzorec, kjer pion vstopi v ARICH.

Tabela 9.3: Premiki signala, izračunani kot razlika srednjih vrednosti mase mezona D^0 za vzorec, kjer delec vstopi v ARICH, in celotni vzorec ter pripadajoče vrednosti signalnih dogodkov N_{sig}.

razpad	delec	premik [MeV/c^2]	N_{sig}	$N_{sig,premik}$	izguba N_{sig} [a]
D^{*+}	kaon	0,33	72 ± 13	72 ± 13	0 %
D^{*+}	pion	3,65	84 ± 14	92 ± 14	9 %
D^0	kaon	1,7	613 ± 78	628 ± 78	2 %
D^0	pion	5,3	434 ± 85	573 ± 85	24 %

[a] Delež izgube dogodkov, v primeru da fiksiramo srednjo vrednost Gaussove funkcije, ki ga izračunamo kot $\frac{N_{sig,premik}-N_{sig}}{N_{sig,premik}}$.

Na rekonstruiranih 600 dogodkih, kjer kaon (pion) vstopi v ARICH, smo preverili, kako učinkujejo rezi na mejah identifikacije $PID_{K/\pi}$ pri treh različnih vrednostih (0,1, 0,6 in 0,9), kot prikazujeta sliki 9.41 za kaone in 9.42 za pione. Leva histograma prikazujeta vzorec delcev, ki padejo nad mejo identifikacije $PID_{K/\pi}$, desna histograma pa vzorce delcev, ki padejo pod to mejo. Uporabljene so različne meje: 0,1 (zgoraj), 0,6 (sredina) in 0,9 (spodaj). Iz danih prilagajanj Gaussovih funkcij smo izračunali tudi izkoristke identifikacije, predstavljene v tabeli 9.4, ki pa so zaradi nizke statistike uporabljeni zgolj ilustrativno.

Tabela 9.4: Deleži pravilno identificiranih kaonov in napačno identificiranih pionov pri treh različnih mejah identifikacije $PID_{K/\pi}$.

$PID_{K/\pi}$	$\varepsilon_{K\to K}$[%]	$\varepsilon_{\pi\to K}$ [%]
0,1	95,7 ± 3,0	36,8 ± 8,8
0,6	89,3 ± 3,8	24,3 ± 9,1
0,9	76,4 ± 4,6	5,4 ± 8,1

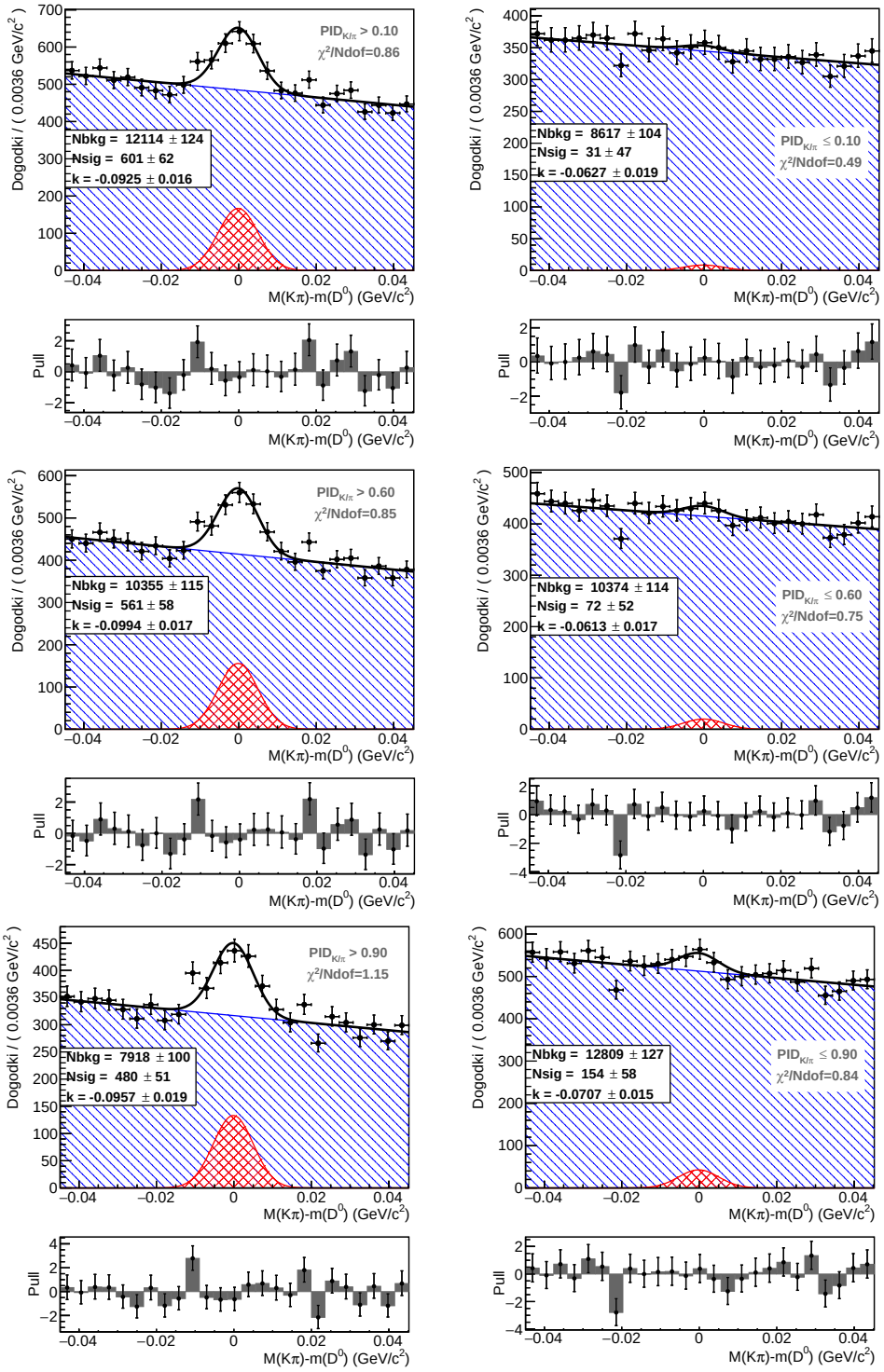

Slika 9.41: Deviacija invariantne mase mezona D^0 za vzorec, kjer je gibalna količina kaona med 0,5 GeV/c in 4,0 GeV/c, ta pa vstopi v geometrijsko območje ARICH-a. Leva stran prikazuje vzorec dogodkov, kjer kaon preživi rez selekcije $PID_{K/\pi}$, desna stran pa komplementarni del vzorca. Prikazani so rezultati različnih rezov $PID_{K/\pi}$: 0,1 (zgoraj), 0,6 (na sredini) in 0,9 (spodaj).

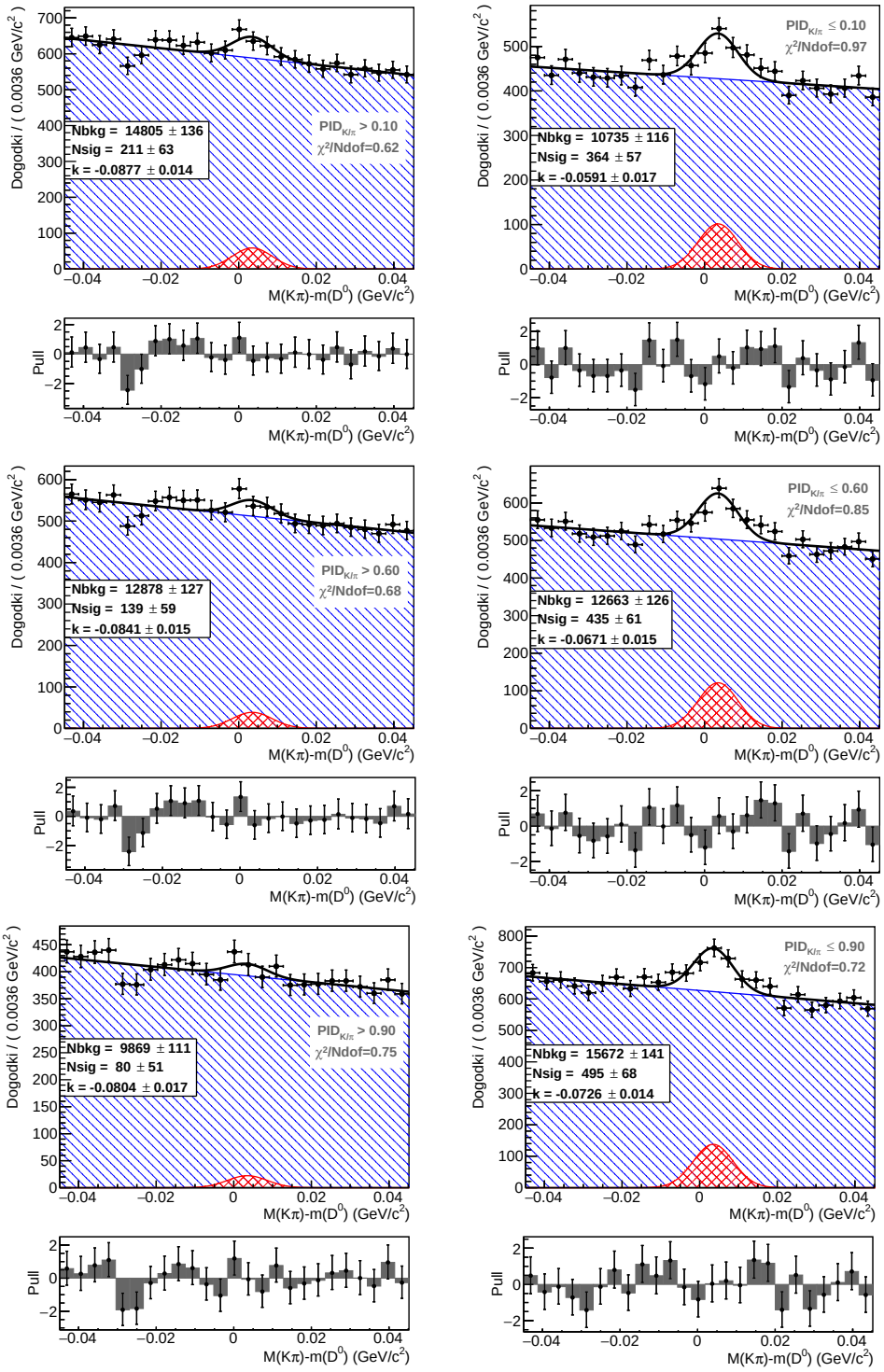

Slika 9.42: Deviacija invariantne mase mezona D^0 za vzorec, kjer je gibalna količina piona med 0,5 GeV/c in 4,0 GeV/c, ta pa vstopi v geometrijsko območje ARICH-a. Leva stran prikazuje vzorec dogodkov, kjer pion preživi rez selekcije $PID_{K/\pi}$, desna stran pa komplementarni del vzorca. Prikazani so rezultati različnih rezov $PID_{K/\pi}$: 0,1 (zgoraj), 0,6 (na sredini) in 0,9 (spodaj).

9.7 Zaključek

Detektor ARICH smo umerili pred sestavljanjem, ki je bilo končano leta 2017. V začetku leta 2018 smo pričeli s prvimi trki delcev pri nizki luminoznosti, s čimer smo preverili delovanje detektorskih komponent in sposobnost ločevanja med kaoni in pioni. Temperatura v detektorju je bila višja, kot smo načrtovali, saj hladilni sistem toplote ni učinkovito odvajal. Da bi preprečili prekomerno segrevanje, smo podatke zajemali s polovico detektorja ARICH naenkrat. Preverili smo tudi vpliv temperature na zaznavanje fotonov, pri čemer smo ugotovili, da ta močno vpliva na ojačanje signala. Pred zajemanjem podatkov pri višji luminoznosti smo nadgradili hladilni sistem, kar bo zmanjšalo končno temperaturo v detektorju, vendar bo potrebno detektor umeriti tudi med delovanjem, da preprečimo izgubo zaznanega signala zaradi premajhnega ojačanja.

Učinkovitost identifikacije kaonov in pionov smo ocenili z analizo razpadnega kanala $D^0 \to K^-\pi^+$ na podatkih iz faze II. Pri tem razpadnem kanalu smo z ARICH-em pravilno identificirali večji delež kaonov, vendar so zaenkrat tudi deleži napačno identificiranih pionov veliki. Pri upoštevanju selekcije $PID_{K/\pi} > 0{,}6$ smo dobili pravilno identificiranih $(89 \pm 4)\,\%$ kaonov, ob deležu napačno identificiranih pionov $(24 \pm 9)\,\%$. Večja napačna identifikacija je najverjetneje posledica nedokončne umeritve in neupoštevanja fizične poravnave ARICH-a znotraj detektorja Belle. Za bolj natančne študije potrebujemo večjo statistiko podatkov, ki jo pričakujemo po začetku zajemanja fizikalnih podatkov trkov, ki se bo predvidoma pričelo aprila 2019.